Transactions of the ASME®

Technical Editor, **T. H. OKIISHI (1998)**
Associate Technical Editors
Aeromechanical Interaction
R. E. KIELB (1999)
Gas Turbine (Review Chair)
A. KIDD (1997)
Heat Transfer
M. G. DUNN (1999)
Nuclear Engineering
H. H. CHUNG (1996)
Power
D. LOU (1998)
Turbomachinery
R. A. DELANEY (1998)

BOARD ON COMMUNICATIONS
Chairman and Vice-President
R. MATES

OFFICERS OF THE ASME
President, **R. J. GOLDSTEIN**
Executive Director, **D. L. BELDEN**
Treasurer, **J. A. MASON**

PUBLISHING STAFF
Managing Director, Engineering
CHARLES W. BEARDSLEY
Director, Technical Publishing
PHILIP DI VIETRO
Managing Editor, Technical Publishing
CYNTHIA B. CLARK
Managing Editor, Transactions
CORNELIA MONAHAN
Production Coordinator
VALERIE WINTERS
Production Assistant
MARISOL ANDINO

Transactions of the ASME, Journal of Turbomachinery (ISSN 0889-504X) is published quarterly (Jan., Apr., July, Oct.) for $185.00 per year by The American Society of Mechanical Engineers, 345 East 47th Street, New York, NY 10017. Periodicals postage paid at New York, NY and additional mailing offices. POSTMASTER: Send address changes to Transactions of the ASME, Journal of Turbomachinery, c/o THE AMERICAN SOCIETY OF MECHANICAL ENGINEERS, 22 Law Drive, Box 2300. Fairfield, NJ 07007-2300.
CHANGES OF ADDRESS must be received at Society headquarters seven weeks before they are to be effective. Please send old label and new address.
PRICES: To members, $40.00, annually; to nonmembers, $185.00.
Add $24.00 for postage to countries outside the United States and Canada.
STATEMENT from By-Laws. The Society shall not be responsible for statements or opinions advanced in papers or . . . printed in its publications (B7.1, Par. 3).

INDEXED by Applied Mechanics Reviews and Engineering Information, Inc.
Canadian Goods & Services Tax Registration #126148048

Journal of Turbomachinery

Published Quarterly by The American Society of Mechanical Engineers

VOLUME 119 • NUMBER 2 • APRIL 1997

TECHNICAL PAPERS

(Contents continued on p. 401)

(Contents continued)

TECHNICAL BRIEFS

ANNOUNCEMENTS

Bowed Stators: An Example of CFD Applied to Improve Multistage Compressor Efficiency

H. D. Weingold

R. J. Neubert

R. F. Behlke

G. E. Potter

Pratt & Whitney,
United Technologies Corporation,
East Hartford, CT 06108

Analysis of multistage compressor stator surface static pressure data reveals that the radial growth of suction surface corner separation prematurely separates core flow stator sections, limiting their pressure rise capability and generating endwall loss. Modeling of the stator flowfield, using a three-dimensional Euler analysis, has led to the development of "bowed" stator shapes, which generate radial forces that reduce diffusion rates in the suction surface corners, in order to delay the onset of corner separation. Experimental testing of the bowed stator concept in a three-stage research compressor has confirmed the elimination of suction surface corner separation, the resulting reduction of the endwall loss, and the increase in pressure rise capability of the stator core sections. This results in more robust pressure rise characteristics and substantially improved efficiency over the entire flow range of the compressor. The strong interaction effects of the bowed stator with the viscous endwall flowfield are shown to be predictable using a three-dimensional multistage Navier–Stokes analysis. This permits matching of the rotors to the altered stator exit profiles, in order to avoid potential stability limiting interactions. Application of bowed stators to a high bypass ratio engine eleven-stage high-pressure compressor has resulted in substantial improvement in efficiency, with no stability penalty.

Introduction

For aircraft engine applications, major drivers in compressor design are efficiency and weight, both of which translate into aircraft range or thrust-to-weight ratio. These drivers require the ability to optimize the design of rotor and stator rows within the multistage compressor, that is, to achieve the maximum design point efficiency with the minimum weight of rotors and stators, while maintaining sufficient off-design capability for adequate stall margin. To avoid weight penalties due to underloading of core flow stator sections, this optimization process may lead to stator designs that have some separation at the endwall corners. However, corner separations can grow rapidly as back-pressure is increased, limiting the incidence range of the stator row, and thus limiting the compressor stall range. Since operability must be provided, compressor stator rows typically have excess loading capability in the core region so that the endwalls can achieve the incidence range necessary to achieve required stall margin. The development of any technology that could eliminate or delay the onset of corner separation in stator rows could be translated immediately into improved efficiency and weight, by reducing the disparity in loading capability between core and endwall stator sections and permitting more favorable optimization of the stator rows. This paper describes the application of CFD methods to develop new "bowed" stator shapes that achieve this objective.

Previous investigators have examined several approaches to the stator endwall loss problem. The most successful of these approaches, endbends, now used in many aircraft engine applications, adds camber to the stator end sections at leading edge and trailing edge, to align the root and tip with the skewed onset flow at the stator row entrance and with the secondary flow overturning at the stator exit. Wisler (1985) reports a 10 percent reduction in stator endwall loss and delayed collapse of the endwall flow as the throttle is closed, due to application of endbends. Robinson et al. (1989) show that endbends can relieve the corner separation at the shrouded end of a stator. Behlke (1986) reported a further delay in corner separation by modifying the chordwise loading distribution of the stator endwall sections, describing this modification as a "second generation of controlled diffusion airfoils."

Tweedt et al. (1986) demonstrated that extending the leading edge forward at the root and tip, to create forward sweep, attracts high-momentum fluid to the endwall corner region, displacing low-momentum fluid. A 13 percent reduction in loss for a shrouded stator was reported. Tang and Chen (1988 and 1990) report that triangular leading edge extensions at the endwalls, forming vortex generators, were effective in reducing secondary flow vortex effects.

Peacock (1967) demonstrated in cascade testing that application of suction through a slot along the vane suction surface corners was effective in reducing the three-dimensional influences of the corner boundary layer, permitting high loadings to be achieved. More recently, Sturm et al. (1992) investigated the effects of blowing through slots at the airfoil corner and along the sidewall, reporting that sidewall blowing was effective in reducing corner losses.

Breugelmans et al. (1984) investigated the effects of vane dihedral and of spanwise curved vanes on secondary flow development in linear cascade tests. Shang et al. (1993), in linear cascade testing of more highly cambered sections, also investigated the effects of positively and negatively leaned vanes and curved vanes, describing many of the effects reported below, which were obtained analytically and in multistage compressor testing. Shang also reported separation at midspan of the curved vane configuration, an effect that was not observed in the current investigation. Wang et al. (1994) also report similar reductions in endwall loss but higher midspan loss for stationary cascade tests of curved diffusion cascades.

Contributed by the Turbomachinery Division for publication in the JOURNAL OF TURBOMACHINERY. Manuscript received by the Turbomachinery Division June 26, 1995. Associate Technical Editor: R. A. Delaney.

This paper, starting from a stator design technology level that employs controlled diffusion airfoil core sections, endbends, and second-generation controlled diffusion airfoil endwall sections, describes the use of advanced CFD capability to develop three-dimensional bowed stator shapes that generate aerodynamic forces in the endwall region to eliminate or further delay the onset of corner separation. Experimental data are presented, verifying the effectiveness of the bowed stator shape in reducing the effects of corner separation, and performance data are presented, quantifying the benefits in efficiency due to the application of this technology in a multistage compressor. A multistage three-dimensional Navier–Stokes analysis is shown to predict the large changes in the stator exit flowfield due to application of bowed stators, permitting rotor/stator matching in the multistage environment.

Discussion

Corner Separation Development in Compressor Stator Rows. Corner boundary layers are inherently more susceptible to separation than single surface boundary layers, under identical adverse pressure gradients, due to the added shear stresses imposed by the second surface. It is thus not surprising that the aft region of the suction surface corner, between a stator and the stationary end wall, is the most likely location for separation to be initiated in a compressor stator row. In this region, the boundary layer on both airfoil and corner surfaces has grown through the favorable pressure gradient region from the stator leading edge to the minimum pressure location, and is now subjected to an adverse pressure gradient as the trailing edge is approached. It is not unusual for such regions of corner separation to exist in well-designed compressor stators, even at the design point condition, since some separation may be present at the peak lift to drag point of many airfoils, which can correspond to a peak efficiency condition in a compressor. Data describing corner separation in stators are reported by Joslyn and Dring (1985), Cyrus (1986), Robinson et al. (1989), and Schulz et al. (1990). When the stator is subjected to increasing back pressure along a speed line, the region of corner separation tends to expand radially inward from the endwall toward midspan, the rate of growth of this region increasing as the compressor stall limit is approached. If both endwalls were originally separated, both corner separations will grow until a point is reached where one corner separation will dominate and grow rapidly in the radial direction, diverting flow to the opposite endwall, causing the corner separation region emanating from the opposite endwall to shrink. An example of this behavior is illustrated in Fig. 1, which was generated by analysis of surface static pressure data obtained in the third stator of a three-stage research compressor, **A,** as it was throttled from wide open to stall. Similar behavior is documented in the flow visualization data of Joslyn and Dring (1985), which were obtained on a large-scale, low-speed research compressor.

Weingold and Behlke (1987) described a procedure in which the measured surface static pressures and leading edge total pressure of a stator section could be analyzed, in an inverse manner, to deduce the inlet and exit conditions present at that section. This procedure has been extended to cascades with regions of separation on the suction surface, by modeling the effects of suction surface separation on the static pressure distribution of the pressure surface. Enforcement of momentum conservation from upstream to downstream, and requiring the blade forces to generate the changes in tangential momentum, permits closure of the model for separated stator sections. These conditions are automatically satisfied in the analysis for nonseparated sections.

A component of this analysis is the analysis of the boundary layer development on the suction surface of the stator section, from leading edge to the point of separation on the suction surface, consisting of a boundary analysis developed by

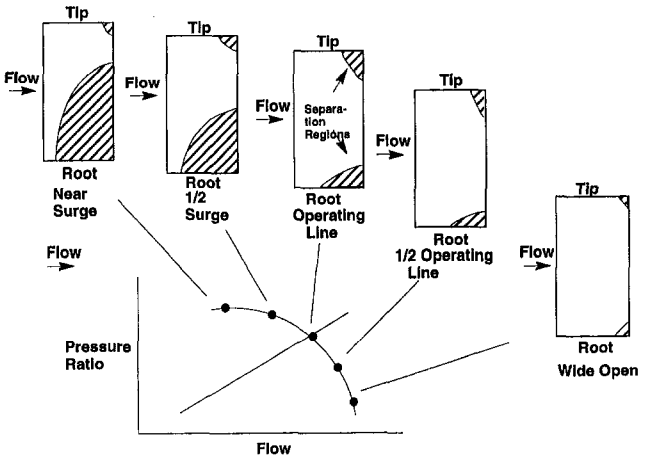

Fig. 1 Spanwise propagation of separation regions on the suction surface of the third stator of three-stage research compressor A, as it is back-pressured from wide-open throttle to stall at 100 percent design speed. Separation extent was deduced from analysis of surface static pressure data.

McNally (1970), combined with the transition model of Dunham (1972), the separation bubble model of Roberts (1979), and the mixing model of Stewart (1955). When applied to two-dimensional cascade data, Hobbs and Weingold (1984) and Weingold and Behlke (1987), where endwall corner separation has been eliminated through endwall and corner slot suction as per Peacock (1967), the predicted boundary layer separation point and the observed separation, based on analysis of the static pressure data, are in close agreement. When this analysis is applied to in-board stator sections that are affected by corner separation of the stator, the boundary layer calculation from leading edge to the observed separation point does not indicate a condition in which simple boundary layer separation should occur. This implies that if a two-dimensional cascade section were to be subjected to the inlet conditions deduced from the inverse analysis of the static pressure distribution, it would not separate at the observed separation point, but would continue to diffuse, generating additional turning and static pressure rise, relative to the identical section in the compressor stator. Thus, the radial expansion of the corner separation region, through three-dimensional flow within the boundary layer on the stator surface, causes premature inboard stator section separation at conditions that, in the absence of the corner separation, would not be separated, thus limiting the pressure rise capability of the inboard sections and generating increased losses. In conventional compressor design, based on S1–S2 surfaces, or axisymmetric throughflow and blade-to-blade surface analyses, this effect must be empirically introduced, since the blade-to-blade analysis will not predict this premature separation. Advances in computational fluid dynamics now permit calculation of these effects without resorting to empirical correlations.

Development of the Bowed Stator Concept. Based on the analysis of the three-stage compressor surface static pressure data, it was recognized that the loading limits imposed on the inboard sections by the separated corner boundary layer were imposing a substantial loss in potential stator performance, and that conversely, any strategy that would delay the onset of such corner separation could provide significant potential for improved performance. However, simply unloading the endwall sections to reduce the adverse pressure gradients was not desirable, since this would divert flow to the midspan region, creating undesirable flow distributions into downstream rows. A solution was sought in which the diffusion rate in the suction surface corner could be reduced, delaying corner separation, without significant change in flow distribution. To pursue this objective,

the effects of three-dimensional blade contouring, generating radial forces on the fluid in the endwall region, and the effects of such forces on the corner boundary layer were investigated, initially using a three-dimensional Euler analysis (Ni, 1981) and subsequently a three-dimensional Navier–Stokes analysis (Rhie, 1986), which became available at a later date.

Using the Euler analysis, the initial studies investigated the effects of dihedral on the static pressure gradients in the suction surface corner. The dihedral was imposed by tilting the stacking line of the stator in the circumferential direction, while sliding the unmodified airfoil sections on their conical flow surfaces. Imposing a dihedral, which was characterized by an acute angle between the stator pressure surface, and the ID (root) endwall, generated radial forces that diverted flow toward the ID. Its effect on the ID suction surface corner was to reduce the peak Mach number, and reduce the diffusion rate over the rear portion of the suction surface, thus lowering the local D factor, defined as $(V_{max} - V_2)/V_{max}$. This was considered to be a desirable effect since reduced local loading was anticipated to delay the onset of separation. The effect of this dihedral on the opposite wall, where an acute angle was generated between the endwall and the suction surface, was deleterious. The effect of the opposite dihedral, generating an acute angle between the suction surface and the ID endwall, had the opposite effect. Flow was diverted toward the tip (OD), the peak Mach number, diffusion rate, and local D factor in the suction surface corner at the OD were reduced, potentially delaying the onset of separation, while the effects at the ID were deleterious. Combining the two dihedrals into a bowed stacking line, which had acute angles between the pressure surface and the endwalls at both root and tip, while having a near radial stacking line over most of the span, was calculated to have the desirable effect of reduced diffusion rate in the suction surface corners at both ends of the stator, Fig. 2. Additionally, the flow distribution through the stator was not significantly affected. This effect is explained by a simple lifting line model of the bowed stator, Fig. 3, in which the airfoil is replaced by a vortex line located at its center of lift. If the bowed vortex line is replaced by a stepped vortex line, consisting of radial segments and tangential segments, it can be seen that the tangential vortex segments initially divert flow approaching the center of lift from the endwall toward midspan, and then redirect the flow back toward the endwall. This effect is strongest at the airfoil surface, since the tangential segments do not extend fully across the gap. In the suction surface corner, the meridional streamtube area increase, from upstream to the vortex line, diffuses the flow, reducing the peak Mach number. From the vortex

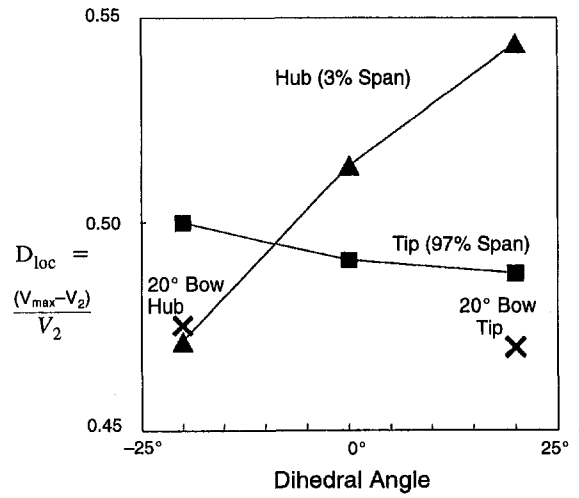

Fig. 2 Effect of tangential dihedral on the local loading parameter of stator hub and tip sections. Bow reduces the local loading parameter at both ends simultaneously.

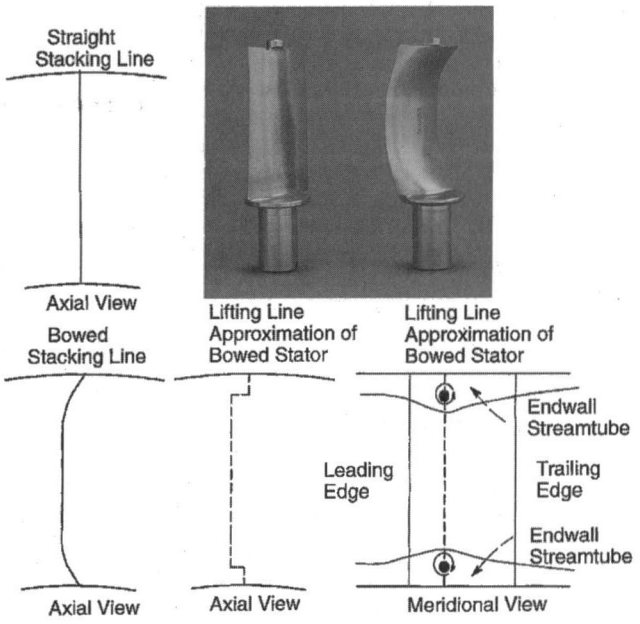

Fig. 3 Simplified lifting line model of bowed stator explains aerodynamic effects

line to the trailing edge, the meridional streamtube area decrease accelerates the flow, imposing a favorable pressure gradient, which reduces the adverse pressure gradient present in this region due to the stator turning, Fig. 4. Shang et al. (1993) reported flow visualization data, obtained in linear cascade testing for leaned and curved vanes, that confirm the separation trends deduced from the above-mentioned analytical study.

Experimental Verification—Baseline. Since the analyses used to calculate the effects of the bowed stacking line were, at this point, inviscid, an experimental program was undertaken to verify the accuracy of the predicted trends, and to evaluate the magnitude of their effect on the viscous flowfield. Three-stage research compressor **A** was selected as the baseline for this evaluation. This compressor was one of a series tested to optimize the aerodynamics of a typical group of middle stages of a transport engine high-pressure compressor (HPC). The initial compressor of this series modeled the middle stages of the PW2037 engine. Three-stage rig testing was conducted in a closed-loop facility at full scale and at Mach numbers and Reynolds numbers typical of the HPC middle stage environment (Behlke, 1986). The compressors in this series were fully instrumented with ID and OD endwall static pressures at inlet and exit of every rotor and stator row, leading edge PT and TT kielhead sensors at nine radial locations on each stator row,

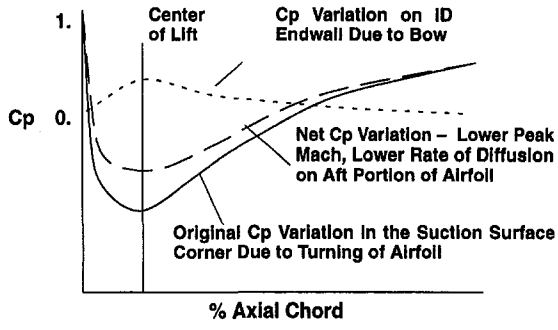

Fig. 4 Diffusion and reacceleration of the endwall streamtube due to bow is superimposed on the pressure distribution in the suction surface corner due to the airfoil camber. Result is reduced peak Mach number and reduced diffusion rate.

Table 1 Design parameters of the baseline three-stage compressor A

Number of Stages	3
Corrected Rotor Speed, rpm	7632
Corrected Mass Flow, lbs/sec(kg/sec)	41.3(18.43)
Overall Pressure Ratio	1.864
Peak Efficiency, Adiabatic	89.73%
Av. Reynolds No.	405,000
Avg. Tip Clearance/Span	.01
Inlet Hub Tip Ratio	.804
Avg. Aspect Ratio	2.03
Avg. Gap Chord Ratio	.95
Avg. Diffusion Factor	.47
Avg. $\Delta P/(P_0 - P)$	.41
Avg. Cx/U	.51
Avg. Reaction	.56

nine-element inlet PT and TT pole rakes, and nine-element exit PT and TT pole rakes circumferentially distributed downstream of several stator passages to average over a stator exit gap. Starting with the fourth compressor of this series, surface static pressure tap distributions were installed at seven radial locations on each stator row (3, 10, 20, 50, 80, 90, and 97 percent of span). Flow was measured using a calibrated venturi, and torque measurements were obtained for comparison to TT rise-based efficiency calculations. The baseline for this study, compressor **A,** employed controlled diffusion airfoils in the core regions, as in Hobbs and Weingold (1984), endbends, second-generation controlled diffusion airfoils in the endwall regions, as described in Behlke (1986), improved endwall loading distributions and rotor and stator counts that had been optimized during the middle stage rig test series to provide the optimum efficiency and stall margin of the series of compressors tested. Its design parameters are listed in Table 1. Compressor **A** achieved 89.73 percent adiabatic efficiency on the operating line and 17 percent surge margin.

Experimental Verification—Exit Stator Traverse Program. As an initial test, compressor **A** was reassembled and retested to obtain traverse data downstream of the trailing edge of the third stator. Traverse data were obtained $\frac{1}{2}$ chord downstream of the third stator exit plane, covering two stator gaps at nine radial locations. Performance and fixed instrumentation data were acquired at 90, 100, and 105 percent of design speed, from wide-open throttle to stall. Traverse data were acquired at 100 percent speed at four throttle settings; wide open, low operating line, operating line, and high operating line. Upon completion of the retest, the compressor was reassembled with a bowed stator replacing the conventional third stator row, and retested under the designation compressor **B.** The bowed stator design restacked the original stator sections as in Fig. 3, to achieve a 60 deg acute angle between the endwall and the stator pressure surface at each endwall, blending, through a parabolic distribution, into a radial stacking line at 40 and 60 percent span (Weingold et al., 1992). This distribution was derived through an analytical study, employing the Euler analysis, to develop bowed shapes that would provide the intended benefit in local D factor at the endwalls, without increasing it to dangerous levels in the compressor core. The leading edges at the endwalls were overcambered to align them with the predicted change in incidence due to the bowed stacking.

The surface static pressure data, converted to isentropic Mach number, for the third stator of the baseline compressor **A,** are illustrated in Fig. 5(*a*). On the operating line, it is evident that a significant region of separation extends from the OD wall inward beyond 80 percent span for this very efficient compressor. A region of separation is also evident at 3 percent span on the operating line, but appears to be absent at 10 percent span.

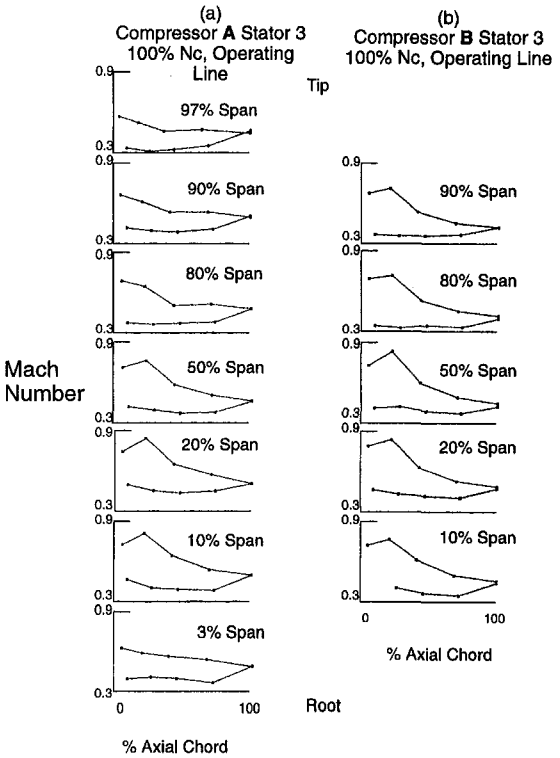

Fig. 5 Mach number distributions, derived from surface static pressure data: (A) indicates the presence of regions of separation at both root and tip of the third stator of three-stage research compressor A; (B) indicates that the bowed third stator of research compressor B has eliminated the OD separation

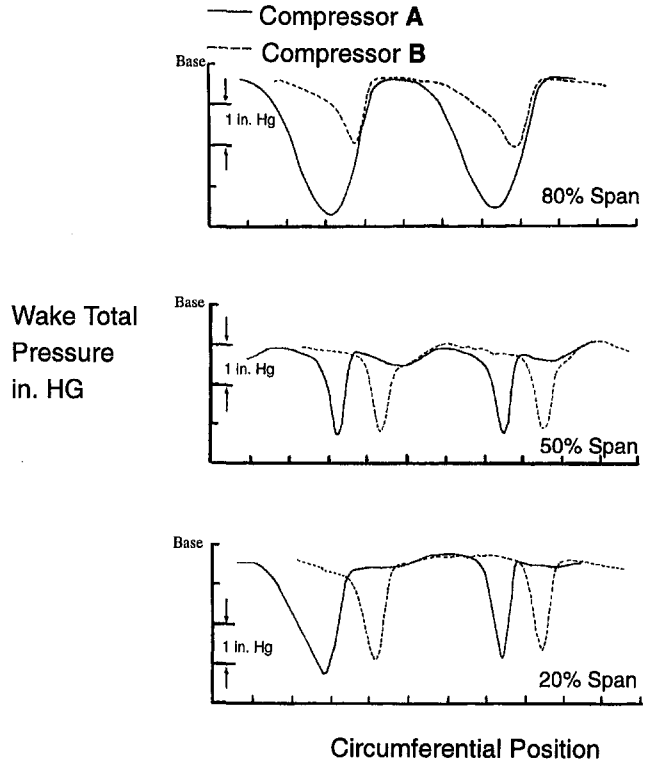

Fig. 6 Stator wake traverse data, acquired $\frac{1}{2}$ chord downstream of the trailing edges of the third stators of compressors A and B, indicate that the bowed stator of compressor B has significantly reduced the total pressure loss due to corner separations on the straight stator of compressor A

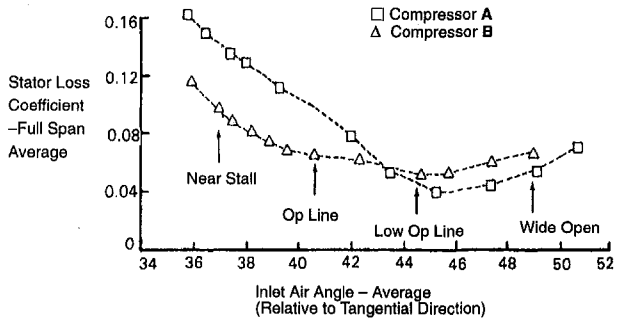

Fig. 7 Full span integrated losses are significantly lower for the bowed third stator of compressor B, relative to the straight stator of compressor A, from operating line to stall at 100 percent speed

Surface static pressure data for the bowed third stator of compressor **B,** Fig. 5(*b*), illustrate the absence of separation on the operating line at any span location. Comparison of the total pressure traverse data for the bowed stator compared to the baseline stator, Fig. 6, indicates that the bowed stator has dramatically reduced the total pressure defect resulting from the separated region of the baseline stator at 80 percent span. A smaller reduction in loss is observed at 20 percent span. Midspan is nearly unaffected. The full-span integrated loss of the two stators, derived from leading edge PT measurements and downstream PT rake data, is illustrated in Fig. 7, which covers the 100 percent speed characteristic from wide open to stall. Loss coefficient reduction of 0.04 is evident for the bowed stator from operating line to stall, corresponding to 36 to 28 percent reduction in overall stator loss. At flows above the operating line, the stall region of the baseline compressor exit stator gradually disappears, and the bowed stator loss advantage is gradually reduced. Toward wide-open throttle, the bowed stator has higher loss than the conventional stator due to higher wetted surface area. The conclusion drawn from the tests of the third stator was that the effects of the bowed stacking line on the viscous flowfield were substantial, and in the direction to be expected if the predicted reduced diffusion on the suction surface corner were sufficient to delay or eliminate corner separation. The continued effectiveness of the bowed stator, above the operating

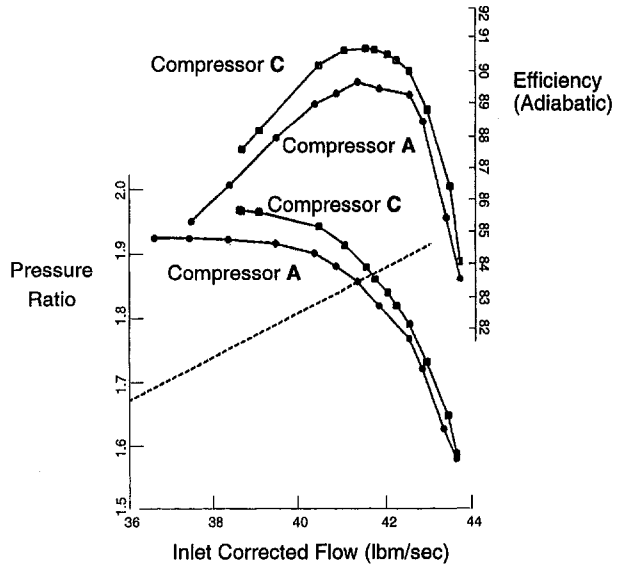

Fig. 8 Performance of compressor C, having bowed stators in all three stator rows, indicates significant improvement in efficiency and pressure rise capability over the entire 100 percent speed characteristic. A small reduction in stall margin is noted.

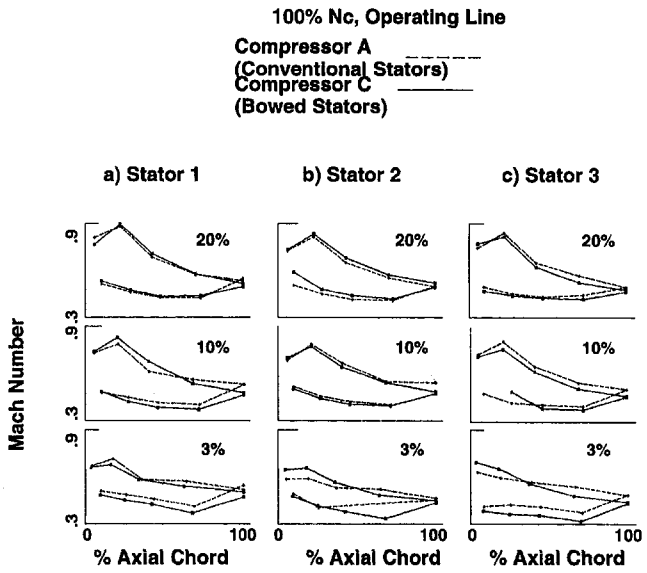

Fig. 9 Mach number distributions, derived from surface static pressure data, for the straight stators of compressor A and the bowed stators of compressor C indicate reduced root separation in all three rows

line toward compressor stall, is due to the radial pressure forces generated by bow being proportional to the lifting forces generated by the airfoil. As the compressor is back-pressured, the loading of the stator increases, and the radial pressure forces also increase, maintaining their effectiveness in delaying corner separation.

Experimental Verification—Performance Testing. To substantiate these effects further, and to quantify their effect on overall compressor performance, the compressor was reassembled using bowed stators, designed using the same principle described above, in all three stator rows. Since, at that time, there was no method to calculate the effects of bowed stators quantitatively on downstream profiles, no changes were made to the rotors or to the camber distributions of the stators of compressor **A** to compensate for these effects. This configuration, designated compressor **C,** demonstrated significant improvement in overall performance, as illustrated by the 100 percent speed pressure ratio and efficiency characteristics in Fig. 8. Operating line adiabatic efficiency increased by 1 percent,

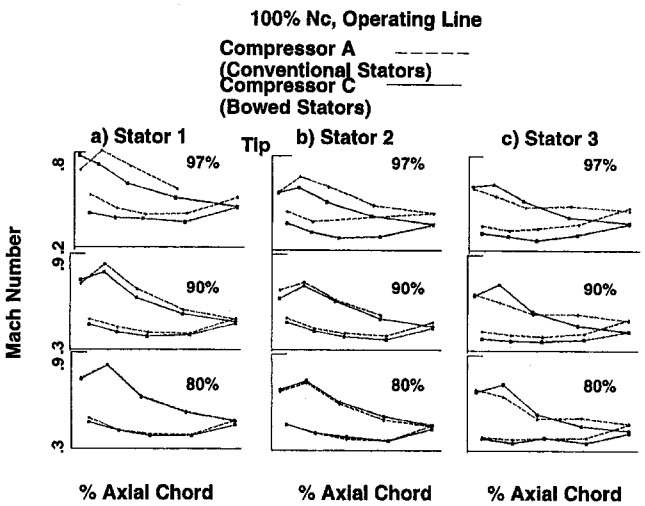

Fig. 10 Mach number distributions derived from surface static pressure data, for the straight stators of compressor A and the bowed stators of compressor C, indicate reduced tip separation in stator 3

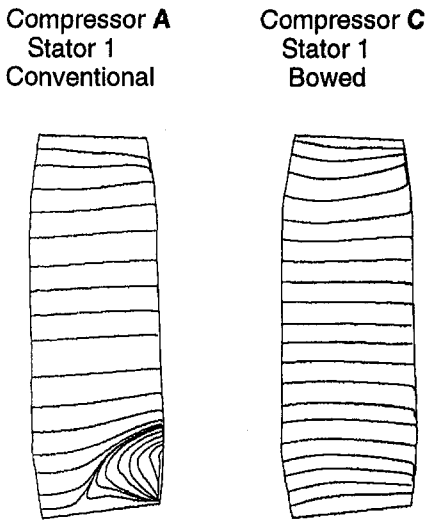

Fig. 11 Streakline patterns, calculated using the NASTAR Navier–Stokes analysis, indicate the presence of a separation region on the suction surface at the root of compressor A stator 1 at design conditions. The bowed stator 1 of compressor C is calculated to have no separation present at design conditions.

the efficiency improvement extending from the operating line through the stall point, and the pressure rise characteristic was stiffer. Flow capacity increased on the operating line by 0.85 percent. Similar effects were seen at 90 and 105 percent speed. A small reduction in stall margin, 3 percent, was present, due to mismatching of the rotors. Surface static pressure data show regions of reduced separation on all three stator rows, principally at the roots of stators 1, 2, and 3, Fig. 9(a–c) and at the tip of stator 3, Fig. 10(a–c).

Navier–Stokes Analysis. The results of the testing of bowed stators in a three-stage compressor indicate that there is a strong interaction between the radial forces generated by the bowed configuration and the viscous flow in the endwall region, and that these interaction effects extend well into the core flow region of the compressor. It is necessary to predict these interactions in order to match the rotor and stator incidence and loading distributions, and prevent adverse stability effects. The three-dimensional Navier–Stokes analysis, NASTAR (Rhie et al., 1995) has demonstrated the ability to predict these strong interactions. Figure 11 illustrates the NASTAR prediction of the flow streaklines in the suction surface corner region for the conventional and bowed stator designs of the first stators of compressors **A** and **C**, showing the elimination of separation over the inner 25 percent of span due to the bowed stator. A comparison of NASTAR predictions to surface static pressure data for the two cases is shown in Fig. 12(a, b), indicating both qualitative and quantitative prediction of the changes in blade forces due to the viscous interactions. In particular, at 10 and 20 percent of span, both data and analysis indicate, in Fig. 12, that the bowed stator suction surface sustains higher diffusion than the conventional stator. The consequent increase in area of the Mach number versus axial chord curves for these sections of the bowed stator indicates that they have higher loading and turning. NASTAR calculated total pressure contours, midway between stator 1 and rotor 2 for the conventional and bowed stators, Fig. 13, illustrate that bow has eliminated the high loss regions associated with corner separation, resulting in a nearly two-dimensional type flow over most of the span. The analysis predicts that, due to the elimination of the corner

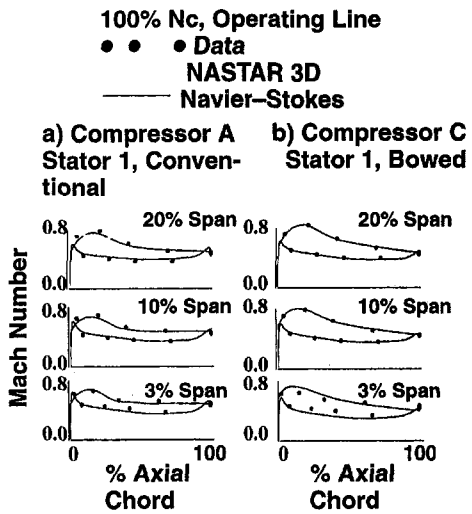

Fig. 12 The NASTAR Navier–Stokes analysis is capable of matching the surface static pressure data based Mach number distributions for the separated Stator 1 of compressor A (a), and the unseparated bowed stator 1 of compressor C (b)

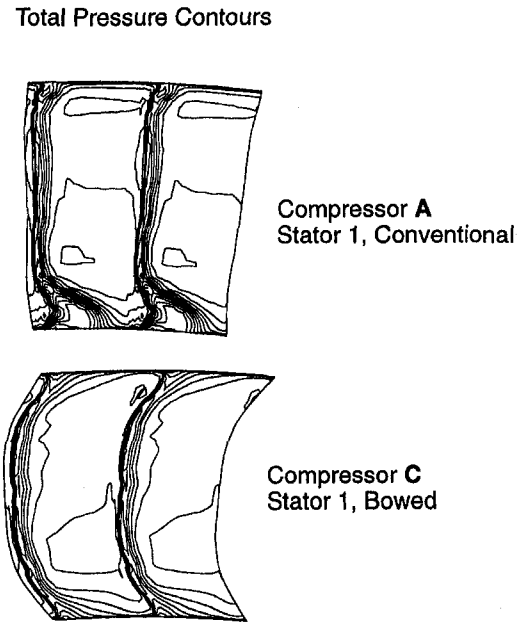

Fig. 13 Calculated total pressure contours illustrate that bow has eliminated the high loss regions due to corner separation, resulting in two-dimensional like flow over most of the span. Overall loss is reduced (total pressure contours are at equal spacing in both illustrations).

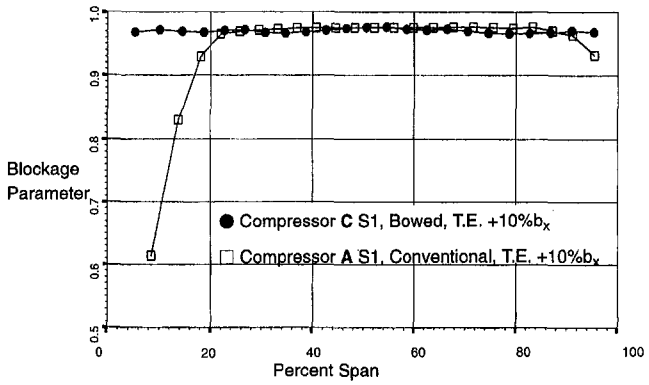

Fig. 14 Bowed first stator of compressor C is calculated to reduce blockage in the hub region significantly, relative to the straight stator of compressor A

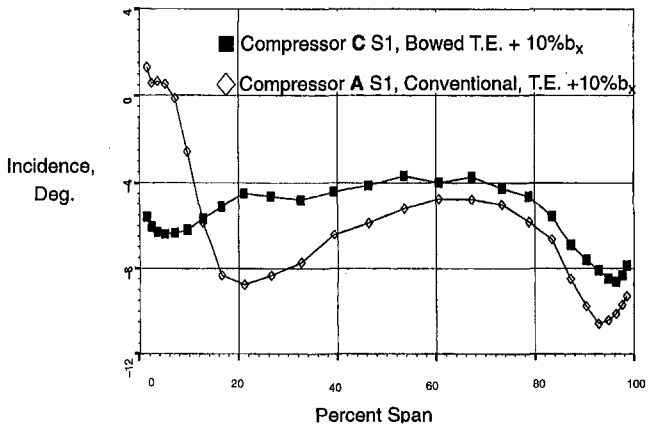

Fig. 15 Effect of reduced blockage in the hub region of stator 1 is an increase in incidence angle to rotor 2, from 20 to 100 percent span, for the bowed stator compressor C, relative to the straight stator compressor A

separation region at the root of stator 1, blockage is reduced in the root endwall region, Fig. 14. This causes the flow to shift radially inward to fill the formerly blocked region, increasing the turning and pressure rise of the stator root region. The flow shift also decreases the axial velocity component downstream of the bowed stator from 20 percent span to the tip. This increases incidence to the following rotor in the region from 20 percent span to the tip; incidence in the root region is decreased, Fig. 15. These incidence changes cause the rotor to work harder over the outer 80 percent of span, accounting for the increased flow capacity and speedline stiffness of compressor **C**, observed during the experimental program. Additionally, the rotor tip reaches its limit loading at a higher net flow, resulting in the observed reduction in stability. Using this information, a restagger or recamber could easily be accomplished to recover the lost stall margin of compressor **C**, while potentially further improving efficiency. The ability to predict these effects will permit avoidance of mismatching incidence in future bowed stator designs, without sacrifice of the beneficial reductions in stator loss.

Continuing Development. Bowed stators have now been tested in several additional compressor configurations, and the performance improvements described above have been found to be typical. The NASTAR analysis has been used to predict the aerodynamics of bowed stators and to optimize the matching of stator and rotor incidences for an 11-stage compressor, intended for use in the high spool of a high-bypass-ratio turbofan aircraft engine. This compressor, described by Lejambre et al. (1995), achieved substantial improvements in performance (+2 percent in efficiency) relative to its earlier design, employing conventional stators, without a stability penalty.

Conclusions

Stator suction surface corner separation spreads radially inward, as back pressure increases, prematurely separating airfoil sections that would otherwise not be separated under similar incident conditions.

Bowed stators generate radial forces on the flowfield that reduce diffusion rates in the suction surface corner and substantially delay or eliminate the formation of corner separation.

The elimination of corner separation permits the stator sections in the endwall region to operate without premature separation, generating reduced loss, reduced blockage, higher turning, and higher pressure rise.

Experimental testing has demonstrated that overall compressor efficiency may increase by 1 percent or more, typically, over substantial regions of the compressor operating envelope, due to the elimination of stator corner separation effects.

There is a strong interaction between the pressure distributions generated by the bowed stator configuration and the viscous flowfield in the endwall region. Without proper matching of rotors and stators, accounting for the effects of these interactions, reductions in stability can be experienced due to incidence increases to the rotor endwalls.

The NASTAR three-dimensional Navier–Stokes analysis has been shown capable of predicting these effects, which will permit the exploitation of bowed stator efficiency benefits without adverse stability effects.

Acknowledgments

The authors wish to extend their acknowledgments to John Andy, for performing many of the early CFD analyses, David Spear, for his extension of the inverse cascade analysis to separated flows, Kenneth Sawyer, R. Darton Marchant, John Horan, Ellis Canal, and Matthew Maciolek for their support of the experimental test program, and Aaron Gleixner and William Sprout for the NASTAR analyses of compressors **A** and **C**.

References

Behlke, R. F., 1986, "The Development of a Second-Generation of Controlled Diffusion Airfoils for Multistage Compressors," ASME JOURNAL OF TURBOMACHINERY, Vol. 108, pp. 32–40.

Breugelmans, F. A. H., Carels, Y., and Demuth, M., 1984, "Influence of Dihedral on the Secondary Flow in a Two-Dimensional Compressor Cascade," ASME *Journal of Engineering for Gas Turbines and Power,* Vol. 106, pp. 578–584.

Cyrus, V., 1986, "Experimental Study of Three-Dimensional Flow in an Axial Compressor Stage," ASME Paper No. 86-GT-118.

Dunham, J., 1972, "Prediction of Boundary Layer Transition on Turbomachinery Blades," AGARD-AG-164.

Hobbs, D. E., and Weingold, H. D., 1984, "Development of Controlled Diffusion Airfoils for Multistage Compressor Application," ASME *Journal of Engineering for Gas Turbines and Power,* Vol. 106, pp. 271–278.

Joslyn, H. D., and Dring, R. P., 1985, "Axial Compressor Stator Aerodynamics," ASME *Journal of Engineering for Gas Turbines and Power,* Vol. 107, pp. 485–493.

LeJambre, C. R., Zacharias, R. M., Biederman, B. P., Gleixner, A. J., and Yetka, C. J., 1995, "Development and Application of a Multistage Navier–Stokes Solver, Part II: Application to a High Pressure Compressor Design," ASME Paper No. 95-GT-343; accepted for publication in the JOURNAL OF TURBOMACHINERY.

McNally, W. D., 1970, "Fortran Program for Calculating Compressible Laminar and Turbulent Boundary Layers in Arbitrary pressure Gradients," NASA TN D-5681.

Ni, R.-H., 1981, "A Multiple Grid Scheme for Solving Euler Equations," AIAA Paper No. 81-1025.

Peacock, R. E., 1967, "Flow Control in the Corners of Cascades," Aeronautical Research Council Report ARC 27, 291 P.A. 1121.

Rhie, C. M., 1986, "A Pressure Based Navier–Stokes Solver Using the Multigrid Method," AIAA Paper No. 86-0207.

Rhie, C. M., Gleixner, A. J., Spear, D. A., Fischberg, C. J., and Zacharias, R. M., 1995, "Development and Application of a Multistage Navier–Stokes Solver, Part I: Multistage Modeling Using Body-forces and Deterministic Stresses," ASME Paper No. 95-GT-342; accepted for publication with ASME JOURNAL OF TURBOMACHINERY.

Roberts, W. B., 1979, "Calculation of Laminar Separation Bubbles and Their Effect on Airfoil Performance," AIAA Paper No. 79-0285.

Robinson, C. J., Northall, J. D., and McFarlane, C. W. R., 1989, "Measurement and Calculation of the Three-Dimensional Flow in Axial Compressor Stators, With and Without Endbends," ASME Paper No. 89-GT-6.

Schulz, H. D., Gallus, H. E., and Lakshminarayana, B., 1990, "Three Dimensional Separated Flow Field in the Endwall Region of an Annular Compressor Cascade in the Presence of Rotor–Stator Interaction: Part I—Quasi-Steady Flow Field and Comparison With Steady State Data," ASME JOURNAL OF TURBOMACHINERY, Vol. 112, pp. 669–678.

Shang, E., Wang, Z. Q., and Su, J. X., 1993, "The Experimental Investigations on the Compressor Cascades With Leaned and Curved Blades," ASME Paper No. 93-GT-50.

Stewart, W. L., 1955, "Analysis of Two-Dimensional Compressible Flow Loss Characteristics Downstream of Turbomachine Blade Rows in Terms of Basic Boundary Layer Characteristics," NACA TN 3515.

Sturm, W., Scheugenpflug, H., and Fottner, L., 1992, "Performance Improvements of Compressor Cascades by Controlling the Profile and Sidewall Boundary

Layers," ASME JOURNAL OF TURBOMACHINERY, Vol. 114, pp. 477–486.

Tang, Y.-P., and Chen, M.-Z., 1988, "An Experimental Investigation of a Vortex Flow Cascade," ASME Paper No. 88-GT-265.

Tweedt, D. L., Okiishi, T. N., and Hathaway, M. D., 1986, "Stator Endwall Sweep and Hub Shroud Influence on Compressor Performance," ASME JOURNAL OF TURBOMACHINERY, Vol. 108, pp. 224–232.

Wang, Z. Q., Su, J. X., and Zhong, J., 1994, "The Effect of the Pressure Distribution in a Three-Dimensional Flow Field of a Cascade on the Type of Curved Blades," ASME Paper No. 94-GT-409.

Weingold, H. D., and Behlke, R. F., 1987, "The Use of Surface Static Pressure Data as a Diagnostic Tool in Multistage Compressor Development," ASME JOURNAL OF TURBOMACHINERY, Vol. 109, pp. 123–129.

Weingold, H. D., Neubert, R. J., Andy, J. G., Behlke, R. F., and Potter, G. E., 1992, United States Patent 5,088,892, "Bowed Airfoil for the Compression Section of a Rotary Machine."

Wisler, D. C., 1985, "Loss Reduction in Axial-Flow Compressors Through Low-Speed Model Testing," ASME *Journal of Engineering for Gas Turbines and Power,* Vol. 107, pp. 354–363.

Y. Ohkita

H. Kodama

Aero-Engine & Space Operations,
Ishikawajima-Harima Heavy Industries,
Nishitama-gun, Tokyo, Japan

O. Nozaki

K. Kikuchi

A. Tamura

Thermofluid Dynamics Division,
National Aerospace Laboratory,
Chofu, Tokyo, Japan

Numerical and Experimental Investigation of Secondary Flow in a High-Speed Compressor Stator

A series of numerical and experimental studies have been conducted to understand the mechanism of loss generation in a high-speed compressor stator with inlet radial shear flow over the span. In this study, numerical simulation is extensively used to investigate the complex three-dimensional flow in the cascades and to interpret the phenomena that appeared in the high-speed compressor tests. It has been shown that the inlet radial shear flow generated by the upstream rotor had a significant influence on the stator secondary flow, and consequently on the total pressure loss. Redesign of the stator aiming at the reduction of loss by controlling secondary flow has been carried out and the resultant performance recovery was successfully demonstrated both numerically and experimentally.

Introduction

In the continuing quest for increased axial compressor performance, considerable attention has focused on three-dimensional flows in a cascade. The secondary flow due to inlet vortical flow is one type of three-dimensional flow and so far much theoretical and experimental work has been done on this subject (for example, Horlock and Lakshminarayana, 1973).

In order to understand this complicated phenomenon, detailed measurements are required in the passage of the cascade. For a high-speed compressor, however, it is difficult to carry out such measurements, so most of the experimental investigations on the three-dimensional flow in the compressor cascade have been limited to low-speed tests (for example, Joslyn and Dring, 1985; Dong et al., 1987; Cyrus, 1988; Schulz and Gallus, 1988).

In contrast, the development of computer power and numerical techniques in recent years has allowed the accurate calculation of flows within turbomachines for wide range of flow conditions. Copenhaver et al. (1993) and Mulac and Adamczyk (1992) successfully applied numerical simulation to examine the three-dimensional flow in the passage of high-speed compressors. Numerical simulation is expected to become one of the most useful tools to give detailed information in a high-speed compressor cascade.

In this paper, numerical analysis was used to understand the mechanism of secondary flow loss, which appeared in an aerodynamic tests of a high-speed compressor stator. The tests of the stator were carried out for two different inlet flows, which differ in the degree of spanwise shear. Those inlet flows were produced by two different rotors, which were designed to give the same inlet flow angle to the stator. It has been shown that the inlet flow with larger shear increased the stator loss considerably.

Numerical solutions indicated that the higher loss was attributed to intensified secondary flow by the inlet flow with larger shear. This implied some possibility to recover the stator performance by controlling the secondary flow. To demonstrate this possible improvement, redesign of the stator was carried out to suppress the secondary flow. Recovery of the stator performance was proved both numerically and experimentally.

Contributed by the International Gas Turbine Institute and presented at the 40th International Gas Turbine and Aeroengine Congress and Exhibition, Houston, Texas, June 5–8, 1995. Manuscript received by the International Gas Turbine Institute March 2, 1995. Paper No. 95-GT-229. Associate Technical Editor: C. J. Russo.

Effect of Inlet Shear on Secondary Flow

The measurements of stator performance were done with two different inlet flows produced by two different rotors. Numerical analyses have been carried out to understand the phenomena that appeared in the measurements.

Measurement of Stator Loss. The general arrangement of the test compressor is shown in Fig. 1. The rotor is located at 3 B_s upstream from the stator leading edge. Downstream of the stator, there are struts that are equally spaced circumferentially.

Stator inlet flow was measured by a five-hole yaw meter probe located at 0.9 B_s upstream from the stator leading edge. Total pressure, flow angle, and Mach number were obtained at 17 radial locations (from 2.5 percent to 95 percent span) by traversing the yaw meter.

Exit total pressures were measured at downstream of the struts (6 B_s downstream from the stator trailing edge). The measurement was done by circumferential traversing of the rake with eight radially spaced total pressure probes. The pitch of the traversing was 1.0 deg, which was equivalent to one sixth of the stator blade pitch.

To obtain the total pressure loss across the stator, streamline curvature throughflow analysis was carried out using the measured data at inlet and exit and then the loss was calculated on the same streamline.

The design parameters are summarized in Table 1. The stator is shrouded at both the hub and the tip.

The stator losses were measured for two different inlet flows (Types 1, 2) produced by two different rotors. These rotors were designed with different spanwise loadings so that they generate the different shear flows to the stator. However, they were designed to give the same flow angles to the stator. The two rotors have the same basic configuration, and were tested with the same tip clearance listed in Table 1.

The measured radial distribution of inlet total pressure, inlet Mach number and inlet flow angle are shown in Figs. 2, 3, and 4, respectively. The total pressure is normalized by the spanwise mass-averaged total pressure of Type 1 (P_{ref}). The values at the endwalls are given by extrapolating the measured data near the endwalls. It is seen in Fig. 3 that the shear of Type 1 is

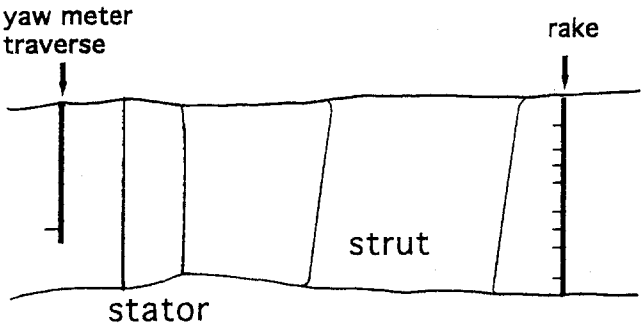

Fig. 1 Flow path and measuring planes

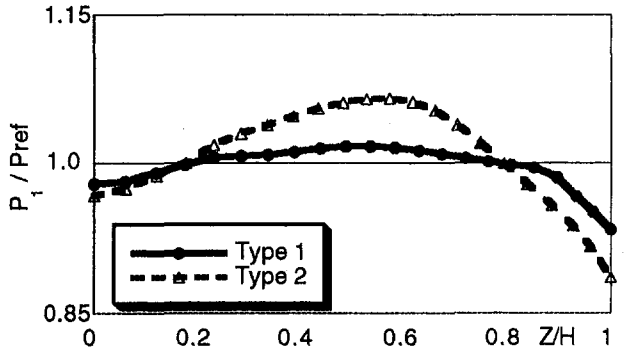

Fig. 2 Comparison of radial distribution of measured inlet total pressure between Type 1 and Type 2

Table 1 Design parameters

Stator	
Inlet flow angle	37 deg (at midspan)
Outlet flow angle	0 deg
Reynolds number	5.5×10^5
Number of blades	60
Pitch chord ratio	0.75 (at midspan)
Aspect ratio	3.0 (at midchord)
Rotor	
t/Cr	0.0037

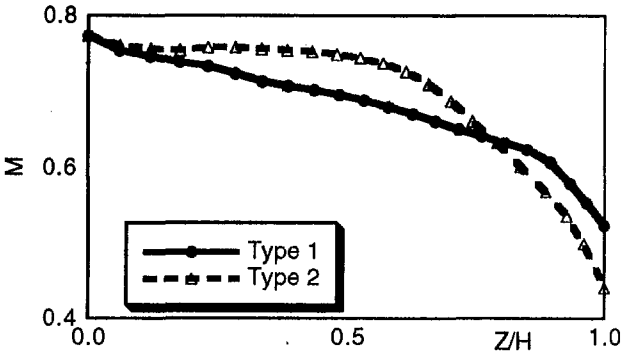

Fig. 3 Comparison of radial distribution of measured inlet Mach number between Type 1 and Type 2

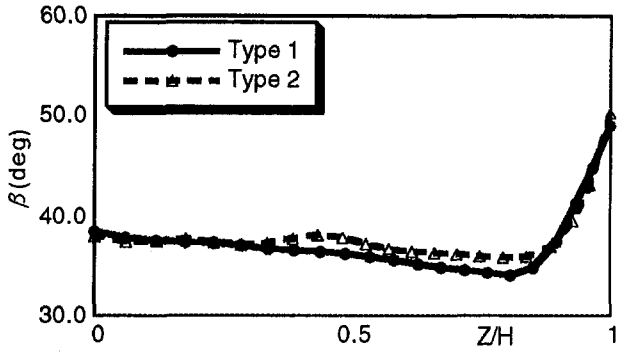

Fig. 4 Comparison of radial distribution of measured inlet flow angle between Type 1 and Type 2

relatively moderate, whereas in the case of Type 2 the large shear region extends from 60 percent span to the tip, and the Mach number of Type 2 is a little higher than Type 1 from the hub to 75 percent span.

Figure 4 shows that almost the same inlet flow angles were achieved. The difference of about 1.2 deg is seen in the outer half region but the difference is considered to give substantially no effect on the stator performance. It can be seen that almost the same degree of crossflow is formed near the tip in both cases. This crossflow is thought to be due to a rotor tip leakage flow.

A comparison of measured contours of constant total pressure loss between Type 1 and Type 2 is made in Fig. 5. The figure covers about a quarter of the full annulus. Two regions of high-pressure loss due to struts are seen in the figure at the same circumferential locations in both cases. While the wakes of the stator seem to be moderately smeared, loss cores that appear near the tip at the same interval of the stator blades have relatively high peak value. In the case of Type 1 the loss cores appear with small size near the tip, whereas the loss cores in the case of Type 2 spread out almost over the outer half span and the peak is located further inward from the tip end wall.

Nomenclature

B = axial chord length
C = chord length
H = height from hub to tip
M = Mach number
P = total pressure
t = tip clearance
u = velocity
X = normalized axial distance = (axial distance from stator leading edge)/(stator axial chord length)
Y_{55} = mass-averaged total pressure loss from 55 percent span to the tip $= \int_{55\%z}^{H} \int_0^{\tau} \rho u_x (\Delta P_{12}/P_1) dydz / \int_{55\%z}^{H} \int_0^{\tau} \rho u_x dydz \times 100$
Y_{75} = mass-averaged total pressure loss from 75 percent span to the tip $\int_{75\%z}^{H} \int_0^{\tau} \rho u_x (\Delta P_{12}/P_1) dydz / \int_{75\%z}^{H} \int_0^{\tau} \rho u_x dydz \times 100$
y = pitchwise coordinate
z = spanwise coordinate
β = flow angle, deg
ΔP_{12} = total pressure loss across the stator $= P_1 - P_2$
δ = normalized pressure loss; percent $(\int_0^{\tau} \rho u_x (\Delta P_{12}/P_1) dy / \int_0^{\tau} \rho u_x dy - \int_0^{H} \int_0^{\tau} \rho u_x (\Delta P_{12}/P_1) desdydz / \int_0^{H} \int_0^{\tau} \rho u_x dydz) \times 100$
ρ = density
τ = pitch

Subscripts

1 = upstream of the stator
2 = downstream of the stator
des = design value
ref = reference value
r = rotor
s = stator
x = axial component

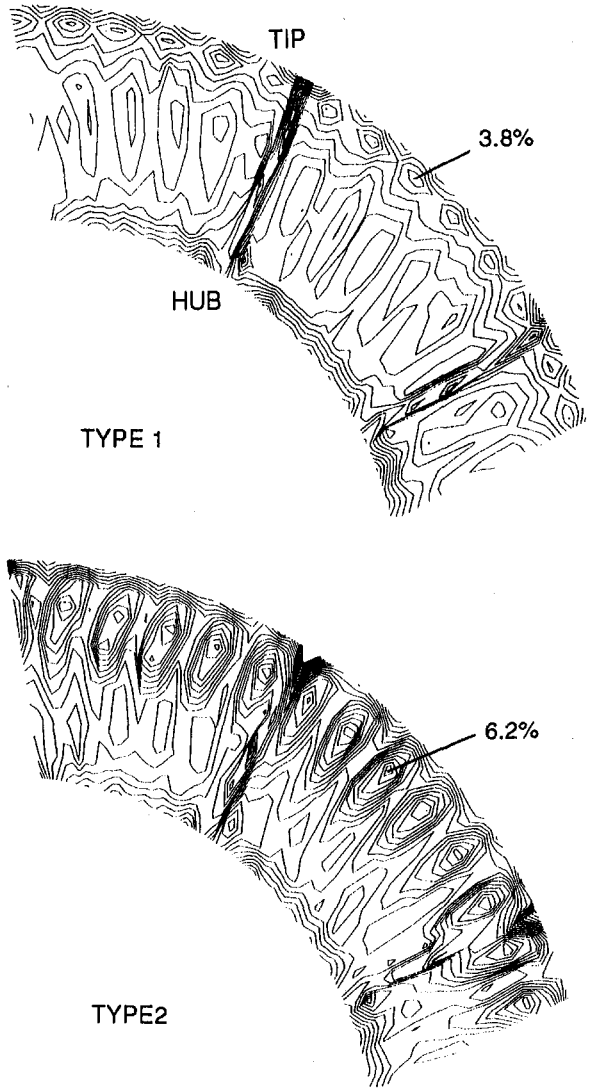

Fig. 5 Comparison of measured contours of constant pressure loss between Type 1 and Type 2

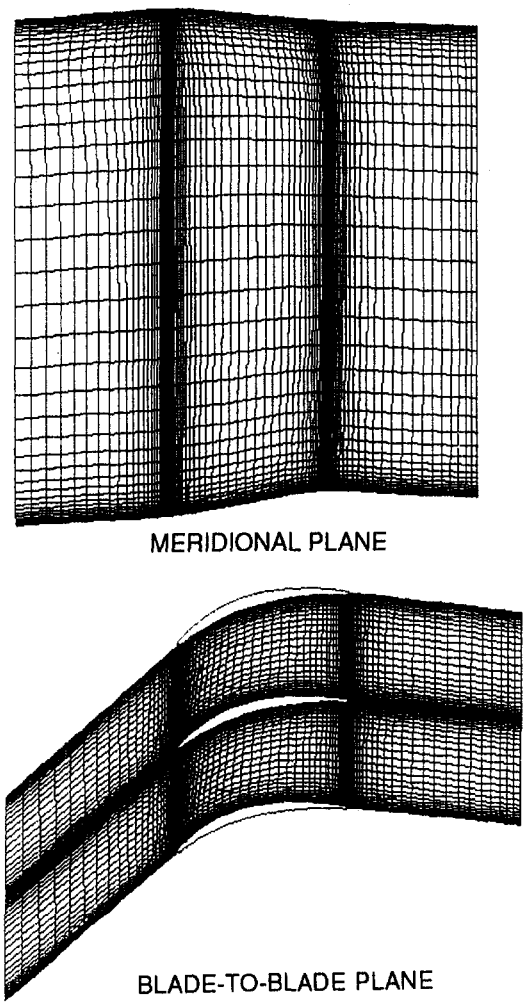

Fig. 7 Computational grid

The peak value of the loss core in the case of Type 2 is about 60 percent higher than in the case of Type 1.

The radial distribution of circumferentially mass-averaged pressure loss is presented in Fig. 6. Except near the endwalls, Type 2 shows higher pressure loss compared with Type 1. A slightly higher loss from 20 percent span to the midspan in Type 2 is probably due to higher inlet Mach number, whereas the large difference from the midspan to 80 percent span may be attributed to higher loss cores. The total difference over the span is equivalent to 50 percent of the design pressure loss of the stator. Note that the difference in Fig. 6 almost corresponds to the difference in the stator loss, although the pressure losses in the figure include not only the stator loss but also the strut loss and endwall friction loss from the stator trailing edge to the measured station.

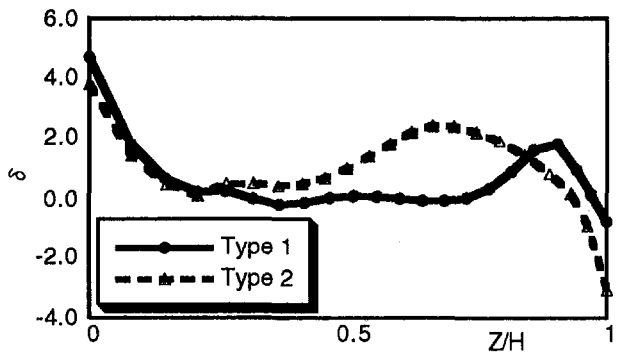

Fig. 6 Comparison of radial distribution of measured pressure loss between Type 1 and Type 2

Numerical Analyses of Secondary Flow. It was shown by the experiments that the loss cores were generated by the stator and that its magnitude was affected by the inlet flow conditions. But the mechanism of the loss core generation and the explanation of difference due to the inlet flows could not be ascertained from the present measurements. Therefore numerical simulations were carried out to investigate the flow phenomena that occurred in the stator.

The basic equations are the three-dimensional, compressible, Reynolds-averaged Navier–Stokes equations written for a generalized curvilinear coordinate system in which pressure, density, and velocity components are related to the energy for an ideal gas. The governing equations are solved using an implicit finite-difference scheme, by which the unsteady equations are solved for successive time steps until steady state is reached. The Baldwin–Lomax algebraic model with transition is used for calculating turbulent flow. A detailed description is given by Nozaki et al. (1993).

The computational grid used in this paper was an *H*-type grid as shown in Fig. 7 and it consists of 118 × 61 × 61 grid

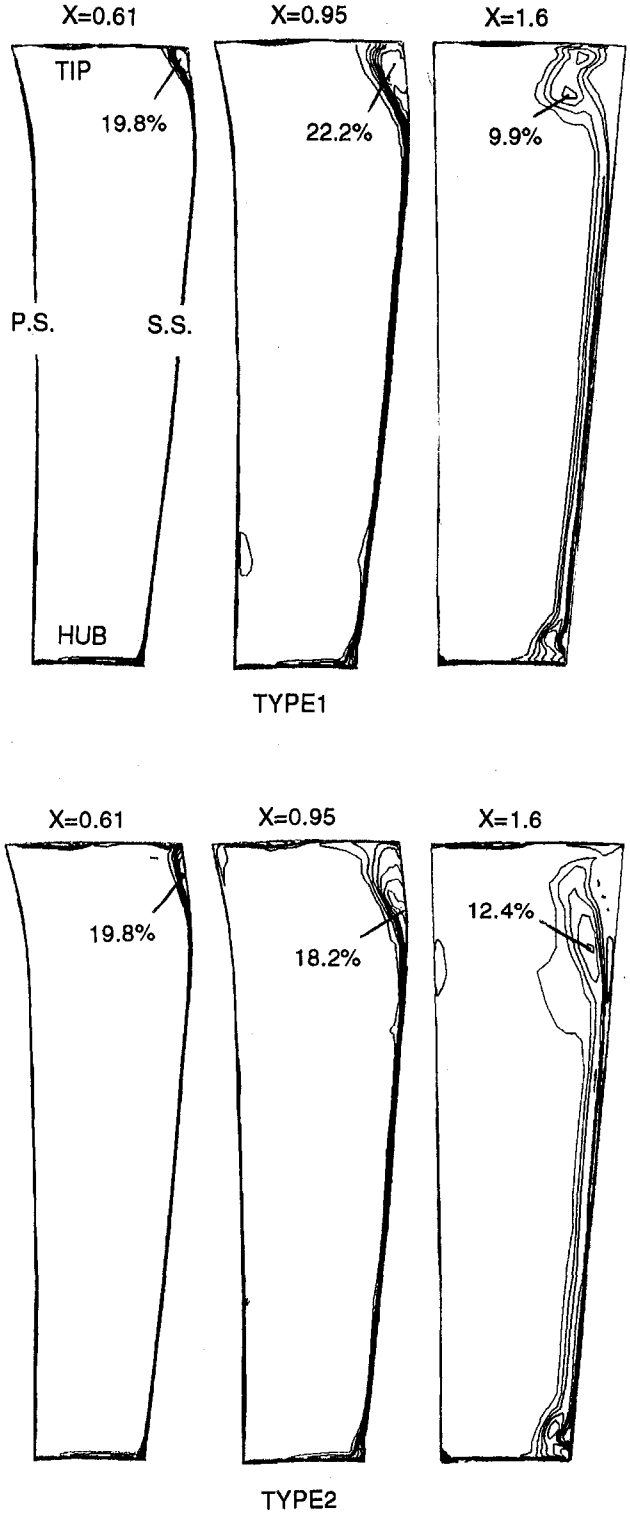

Fig. 8 Comparison of calculated contours of constant pressure loss between Type 1 and Type 2

points in axial, tangential, and radial directions respectively. The calculation region in the downstream was restricted to one axial chord distance.

Inlet boundary conditions are derived from the measurements. Measured total pressure and flow angle profile were imposed at the inlet boundary. Here thin boundary layers were assumed at both endwalls and were fitted to the measured total pressure profile. The total temperature profile obtained from throughflow analysis was also imposed at the inlet boundary.

Table 2 Comparison of mass-averaged total pressure loss from 75 percent span to the tip between type 1 and type 2

	Y_{75} (percent)	
X	Type 1	Type 2
0.61	0.31	0.43
0.95	0.49	0.52
1.6	0.70	0.92

At the exit boundary, static pressure was given such that the calculated inlet Mach number matched the measured profile.

The calculated contours of constant total pressure loss at several axial locations are compared in Fig. 8. The pressure loss across the stator was calculated on the same radial grid line. It can be seen in both cases that the loss core emerges at the corner of the endwall and suction surface, grows in the passage, and then the loss core peak reduces in magnitude downstream of the stator due to viscous dissipation. In the case of Type 1, the loss core proceeds downstream with little change in the radial location, whereas in the case of Type 2 the loss core is convected inward from the endwall. The features of loss cores at $X = 1.6$ are quite similar with those obtained in the experiment (Fig. 5).

The mass-averaged total pressure losses over the region dominated by the loss cores (from 75 percent span to the tip) are given in Table 2. The growth of loss in the case of Type 2 is already larger in the stator passage, and it makes a significant difference in the downstream of the stator. It should be noted that the profile loss of Type 2 in the region from 75 percent to the tip must be lower than that of Type 1 because of the lower inlet Mach number, so the net difference in the total pressure loss due to loss core is considered to be much larger than the difference appeared in Table 2. In the case of Type 1 a higher peak value of the loss core is seen at $X = 0.95$ in Fig. 8. It implies that, in the case of Type 1, higher local shear stress exists in the passage.

The radial distribution of circumferentially mass-averaged total pressure loss at $X = 1.8$ is shown in Fig. 9. Although the numerical calculations seem to have underestimated the magnitude of total pressure losses, the calculations successfully predicted the general trends of the measured profiles shown in Fig. 6. The significantly lower loss was predicted near the tip endwall as observed in the measured results. The numerical calculation showed that radially outward migration of relatively high total pressure fluid resulted in the lower loss prediction. In the region near the hub, there is little difference between the two cases. This feature agrees with the results of the measurement as seen in Fig. 6. This indicates that the secondary flow near the hub was not affected by the change in inlet flow to Type 2.

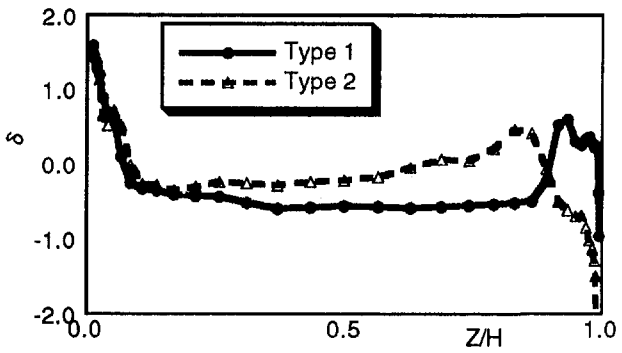

Fig. 9 Comparison of radial distribution of calculated pressure loss at $X = 1.8$ between Type 1 and Type 2

Figure 10 shows the calculated secondary velocity vectors in the planes at $X = 0.8$. Here the secondary velocities can be defined as the projections of total velocity vectors onto the plane perpendicular to the axial direction by assuming that the direction of primary flow is axial. The calculated secondary velocities show the passage vortex typically seen in the stator endwall region. There is a significant difference in the passage vortex between the two cases. In the case of Type 1, a small vortex is formed at the corner of endwall and suction surface, while in the case of Type 2, a fully developed vortex exists near the corner. This is because the inlet flow with larger shear in Type 2 intensified the secondary flow in the stator. It can also be seen in both cases that high secondary velocities exist near the corner with the flow directed toward suction surface on the endwall and radially inward on the suction surface.

The three-dimensional flow pattern for the case of Type 2 near the endwall and the suction surface is depicted in Fig. 11. The complex lines in the figure represent the paths of fluid particles that are transported from the tip endwall boundary layer into the stator. It is clearly visible that the endwall flow that was overturned to the suction surface side as a result of the transverse pressure gradient is then convected toward the midspan on the suction surface, and finally lifted off into the main stream. The formation of loss cores in Fig. 8 is explained in terms of the feeding of low-momentum endwall flow into the mainstream. The difference in the radial location between the loss core peak and the center of passage vortex also fits this explanation.

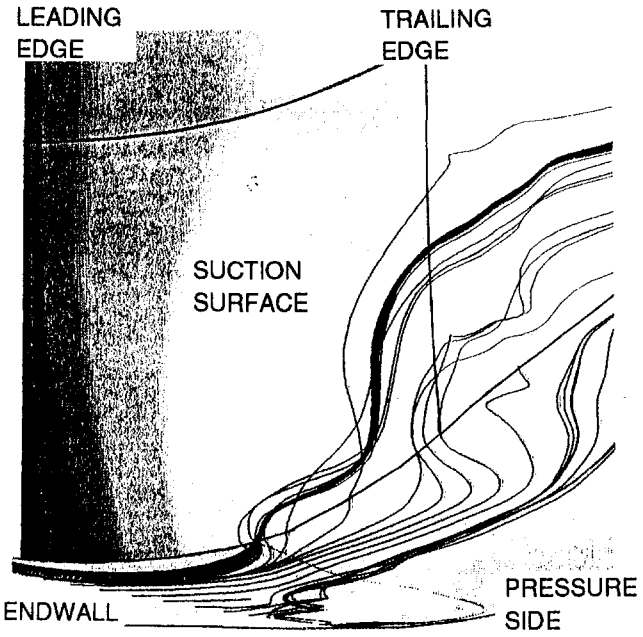

Fig. 11 Streakline of flow near the tip endwall for Type 2

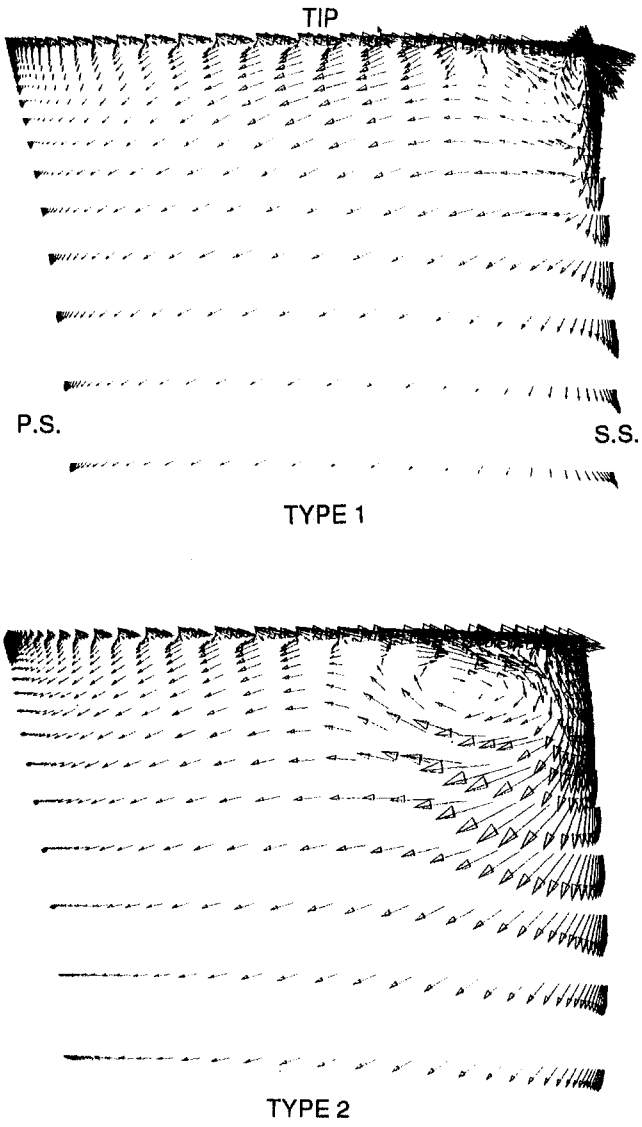

Fig. 10 Comparison of calculated secondary velocity vector at $X = 0.8$ between Type 1 and Type 2

Performance Recovery by Secondary Flow Control

It is expected that there is some possibility of performance recovery by reducing the secondary flow. In order to demonstrate the possibility, redesign of the stator was carried out. A secondary flow control design was applied to the spanwise region where secondary flow was dominant, that is, both end parts of 30 percent span. For the region other than both end regions, the existing stator geometry was maintained. Both the numerical and experimental investigations were conducted to confirm the performance recovery. The inlet conditions for the numerical and experimental investigations were obtained by a third rotor (Type 3), modified from the Type 2 rotor design to reduce the spanwise shear to the stator. Yet the spanwise shear was still much larger than the case of Type 1. In consequence of reduced shear, a slightly higher rotating speed of the Type 3 rotor was selected to produce the same level of shear as in Type 2. The resultant radial distributions of inlet total pressure, inlet Mach number, and inlet flow angle are shown in Figs. 12, 13, and 14, respectively. The inlet flow had the radial profile similar to Type 2, but a little higher flow. The flow angle is also slightly larger than that of Type 2.

Numerical Simulation for Redesigned Stator. Figure 15 shows calculated contours of constant total pressure loss. Note that the original stator shows higher losses compared to those shown in Fig. 8. This is attributed to a overall higher inlet Mach number as shown in Fig. 13. In the case of redesign, the peak value of the loss core is markedly reduced and the radial position of the peak remains closer to the endwall.

Table 3 shows the mass-averaged total pressure losses over the region dominated by the loss cores (from 55 percent span to the tip). It can be seen that most of the difference in the growth of loss occur in the stator passage. It indicates that the performance improvement by secondary flow control design particularly results from a reduction in high shear stresses due to secondary flow in the stator passage.

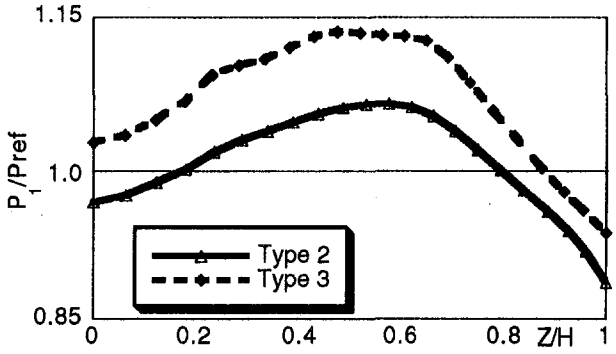

Fig. 12 Comparison of radial distribution of measured inlet total pressure between Type 2 and Type 3

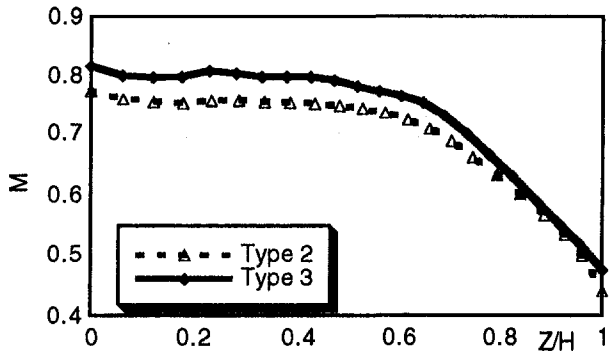

Fig. 13 Comparison of radial distribution of measured inlet Mach number between Type 2 and Type 3

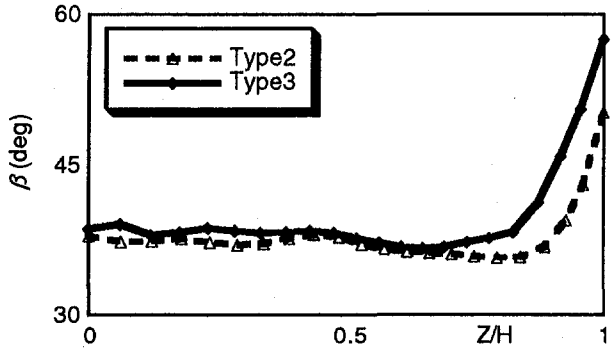

Fig. 14 Comparison of radial distribution of measured inlet flow angle between Type 2 and Type 3

The numerical calculations demonstrated that the redesigned stator would suppress the growth of secondary flow due to inlet large shear flow and lead to reduce the total pressure loss.

Experimental Evaluation of Redesigned Stator. In order to confirm the stator performance recovery experimentally, the measurements of the stators were carried out.

A comparison of measured contours of constant total pressure loss between the two stators is shown in Fig. 16. Although in the case of redesign, the loss cores are still large and the peak is located at nearly the same height of the span as for the original, the peak value of loss core is apparently reduced.

In the radial distribution of circumferentially mass-averaged total pressure loss shown in Fig. 17, improvement in the stator performance can be seen between 60 percent span and the tip. This is a consequence of the secondary flow controlled design applied to the stator tip region. On the other hand, there is little change between the two stators near the hub. We saw in Fig.

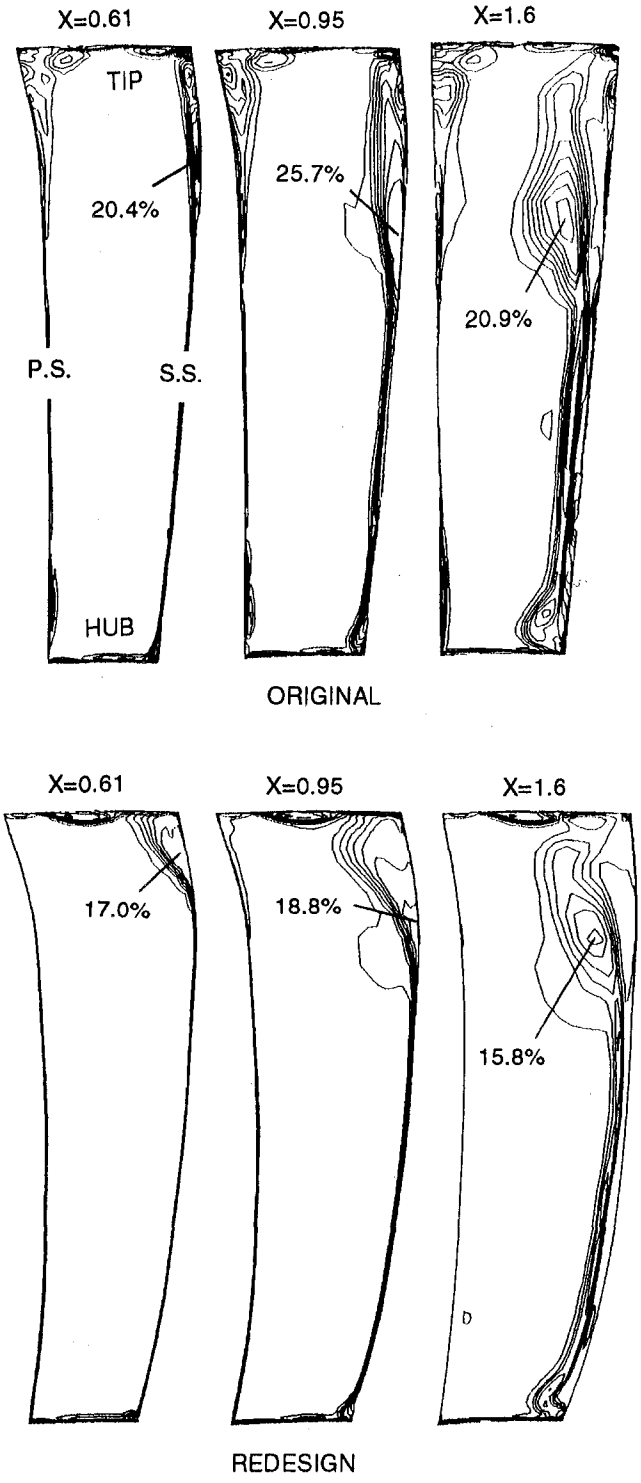

Fig. 15 Comparison of calculated contours of constant pressure loss between original and redesigned

Table 3 Comparison of mass-averaged total pressure loss from 55 percent span to the tip between original and redesigned stator

	Y_{55} (percent)	
X	Original	Redesign
0.61	0.63	0.41
0.95	1.1	0.53
1.6	1.3	0.92

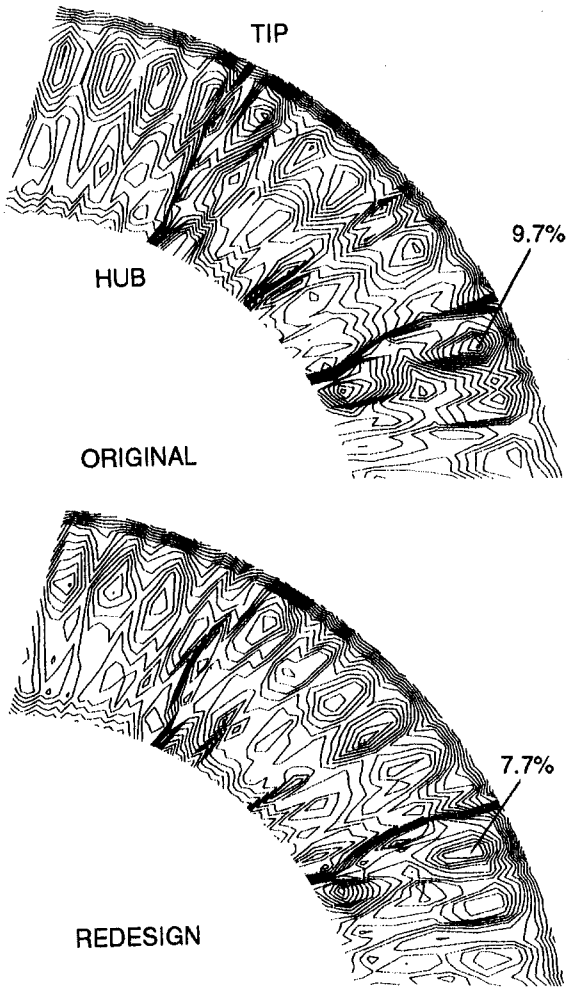

Fig. 16 Comparison of measured contours of constant pressure loss between original and redesigned

9 that the inlet flow has no influence on secondary flow near the hub. Figure 12 inlet flow case is the same. Therefore the stator performance in that region might not be worsened in the original stator. This is thought to be the reason why the secondary flow controlled design applied to the stator hub region was less effective.

In this case, the total difference was estimated to be about 23 percent of the overall total pressure loss of the original stator. The possibility of performance recovery using secondary flow controlled design was thus confirmed experimentally.

Conclusion

1 The effect of inlet radial shear flow on the performance of a high-speed compressor stator has been investigated experimentally and numerically. The numerical simulation supplied detailed results that could not be measured in a high-speed cascade flow.

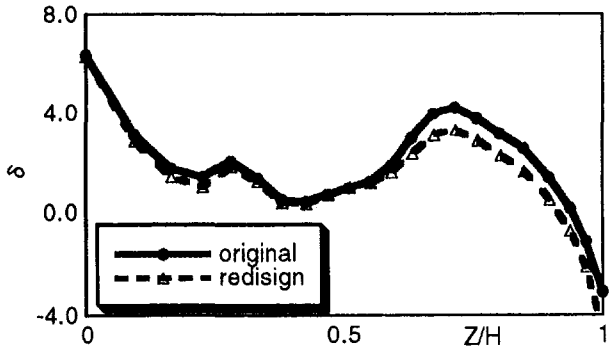

Fig. 17 Comparison of radial distribution of measured pressure loss between original and redesigned

2 The experiments have shown that an inlet radial velocity profile generated by the rotor has significant influence on the stator performance. A large radial shear flow increases the total pressure loss of the stator considerably.

3 Numerical simulation indicates that inlet large shear flow intensifies the passage secondary flow and forms a large loss core. It also implies that the loss increase is directly associated with the higher shear stresses due to intensified secondary flow.

4 Based on the understanding of loss mechanism, secondary flow control design was applied to the stator to recover the performance. Experiments and computations showed that performance recovery is possible to some extent.

5 Numerical simulation indicates that the performance improvement by secondary flow control design particularly results from a reduction in high shear stresses due to secondary flow in the stator passage.

References

Copenhaver, W. W., Hah, C., and Puterbaugh, S. L., 1993, "Three-Dimensional Flow Phenomena in a Transonic, High-Throughflow, Axial-Flow Compressor Stage," ASME JOURNAL OF TURBOMACHINERY, Vol. 115, pp. 240–248.

Cyrus, V., 1988, "The Effect of the Reynolds Number on the Three-Dimensional Flow in a Straight Compressor Cascade," ASME Paper No. 88-GT-269.

Dong, Y., Gallimore, S. J., and Hodson, H. P., 1987, "Three-Dimensional Flows and Loss Reduction in Axial Compressors," ASME JOURNAL OF TURBOMACHINERY, Vol. 109, pp. 354–361.

Horlock, J. H., and Lakshminarayana, B., 1973, "Secondary Flows: Theory, Experiment and Application in Turbomachinery Aerodynamics," *Annual Review of Fluid Mechanics*, Vol. 5, pp. 247–280.

Joslyn, H. D., and Dring, R. P., 1985, "Axial Compressor Stator Aerodynamics," ASME *Journal of Engineering for Gas Turbines and Power*, Vol. 107, pp. 485–493.

Mulac, R. A., and Adamczyk, J. J., 1992, "The Numerical Simulation of a High-Speed Axial Flow Compressor," ASME JOURNAL OF TURBOMACHINERY, Vol. 114, pp. 517–527.

Nozaki, O., Yamamoto, K., Kikuchi, K., Saito, Y., Sugahara, N., and Tamura, A., 1993, "Navier–Stokes Computation of the Three Dimensional Flow Fields Through a Transonic Fan Blade Row," ISABE-93-7030.

Schulz, H. D., and Gallus, H. E., 1988, "Experimental Investigation of the Three-Dimensional Flow in an Annular Compressor Cascade," ASME JOURNAL OF TURBOMACHINERY, Vol. 110, pp. 467–478.

Rotor Blade-to-Blade Measurements Using Particle Image Velocimetry

D. Tisserant

F. A. E. Breugelmans

Turbomachinery Department,
von Karman Institute for Fluid Dynamics,
Rhode-St.-Genèse, Belgium

The study of turbomachinery flow fields requires detailed experimental data. The rotating parts of turbomachines greatly limit the measurement techniques that can be used. Particle Image Velocimetry (PIV) appears to be a suitable tool to investigate the blade-to-blade flow in a rotor. The facility is a subsonic axial-flow compressor. The experimental apparatus enables the recording of a double-exposed photograph in a circumferential plane located at 85 percent of the blade height. The illumination plane has an axial direction and is provided by a pulsed ruby laser. The tracers used are submicron glycerine oil droplets. Data are processed by Young's fringes method. Measurements were performed at 3000, 4500, and 6000 rpm with velocities in the range of 30 to 70 m/s. Steady operating conditions are chosen in such a way that the effect of radial velocity on PIV measurements can be neglected. Experimental problems encountered included homogeneous seeding of the flow field and laser light scattering from blade surfaces. The uncertainty affecting the velocity determination corresponds to 2 percent of the measured value. For a given set of operating conditions, 10 PIV pictures are recorded. The periodic flow field is approximated by averaging the experimental data point by point. Upstream and downstream velocity triangles are confirmed by measurements obtained from pressure probes. PIV measurement results were found to be similar to those of a blade-to-blade potential-flow calculation.

Introduction

Several new optical techniques for nonintrusive flow investigation have been developed during the last two decades. Two classes of experimental technique are distinguished by Adrian (1986): The first results in flow information with low spatial resolution, whereas the second provides high spatial and temporal resolution in a flow region.

These topics characterize, respectively, the laser velocimetry system and the double-exposure techniques. Because of recent developments in computational and laser tools, the second class of optical diagnostic techniques has become increasingly attractive. In a Particle Image Velocimetry (PIV) application, a light sheet illuminates the flow field where tracers are introduced. Particle images are recorded at two different instants in time. The processing procedure consists of measuring the distance between two successive particle images. Knowing the time separation between two illuminations, it is possible to evaluate the velocity.

The first flow applications of the PIV technique were reported by Meynart (1983) and Adrian (1986). PIV is used in many turbulent-flow applications because it combines the advantages of flow visualization and quantitative measurement. The capabilities of this technique make it an ideal candidate for turbomachinery research, especially the instantaneous nature of the data recording in the case of unsteady or periodic phenomena. In 1987, Paone et al. (1988) performed measurements in the blade-to-blade plane of a centrifugal pump, whereas Bryanston-Cross et al. (1986) carried out experiments in a transonic turbine cascade.

With the development of three-dimensional unsteady computations, the requirement for experimental data in rotational flow increases. For that purpose, the feasibility of PIV measurements in a subsonic axial compressor rotor is demonstrated. The experiments were designed to measure velocities in the blade-to-blade plane. In rotating machines, the stream surfaces are considered to be axisymmetric. Consequently, the PIV technique can be applied as long as the illumination plane coincides with a stream surface.

Following a description of the experimental apparatus and the uncertainties affecting the measurements, a discussion of the experimental results and their validation by pressure tests will be reported. For each operating condition, a set of 10 PIV pictures of different blade passages with random blade position is recorded from which the periodic blade-to-blade flow is deduced and compared to results from a two-dimensional potential-flow prediction.

Experimental Conditions

Description of the Test Facility. The high-speed compressor facility is a semi-closed-loop system for the investigation of axial and radial compressors. The test section is large enough to house a multistage configuration.

PIV experiments are performed in a single stage. The rotor is formed by 24 blades of the NACA 65 family. Its tip radius is 200 mm and the hub-to-tip ratio is 0.5. An inlet provides a uniform axial flow at the entrance of the test section corresponding to the design operating conditions. The outlet flow goes into a collector, which is connected to an air cooler and it is finally discharged to the atmosphere of the facility room. The total-to-total compression ratio is 1.1.

There are four access ports to the test section, inclined at 45 deg with respect to the horizontal plane. Figure 1 is a sketch of the upper half of the rotor facility.

Experiments have been carried out at rotational speeds equal to 3000, 4500, and 6000 rpm. In this article, only the results at 3000 rpm are discussed. Similar conclusions can be formulated for the other speeds. The measurement plane is located at 85

Contributed by the International Gas Turbine Institute and presented at the 40th International Gas Turbine and Aeroengine Congress and Exhibition, Houston, Texas, June 5–8, 1995. Manuscript received by the International Gas Turbine Institute March 3, 1995. Paper No. 95-GT-99. Associate Technical Editor: C. J. Russo.

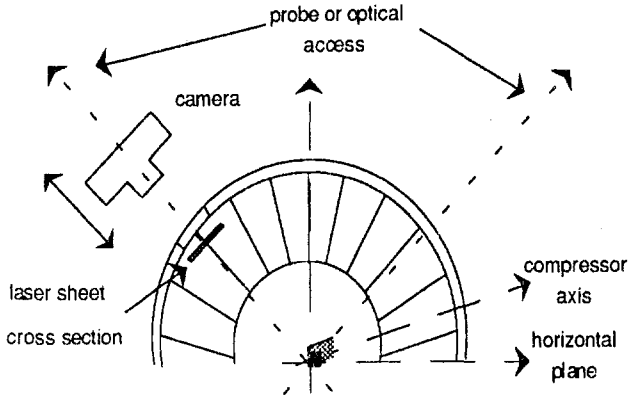

Fig. 1 Front view of the test section

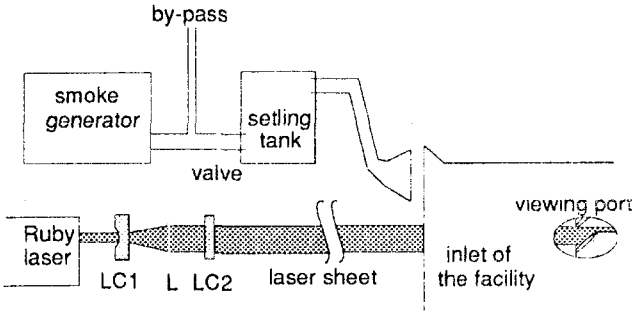

Fig. 3 PIV setup

percent of the blade height. Preliminary tests with yaw-flow-direction pressure probes were performed to determine the upstream and downstream flow conditions (Fig. 2). Uncertainties related to these tests and associated with the absolute velocity determination are equal to 0.25 percent of the measured value. The precision of the angle value is 0.2 deg and the rotational speed is kept constant within 10 rpm. The results of the pressure tests are:

Upstream	Downstream
$W_1 = 66.24$ m/s	$W_2 = 49.7$ m/s
$\beta_1 = 62.38$ deg	$\beta_2 = 50.52$ deg

The Reynolds number based on the chord and the inlet relative velocity is equal to 212,000. This indicates that the rotor is operating in a transitional regime.

PIV System. The light source is a high-energy pulsed ruby laser. It delivers 0.5 J per pulse of 30 ns duration. The light wavelength is 694.3 nm. An optical system formed by two cylindrical lenses (LC1, LC2) and a convergent one (L), sketched in Fig. 3, transforms the incident beam into a light sheet 40 mm wide and 1.5 mm thick. The laser sheet is introduced in front of the rotor. The laser is placed 1.5 m ahead of the facility.

A camera equipped with a focusing lens (Micro Nikkor) having a focal length equal to 55 mm is used to record the double exposed picture. It is fixed on the viewing port and centered on the window axis (Fig. 1). The camera translates along the radial direction to facilitate the focusing and to adjust the magnification factor to 0.5. Pictures are recorded on Kodak Technicalpan 2415. The F-number is adjusted to 2.8 and the camera is manually released. The time separation between two pulses is determined in such a way that the real displacement between two exposures is approximately 200 μm. Considering the inlet absolute velocity as a reference, the time delay is typically 5 μs for tests at 3000 rpm. This choice is imposed by the optimization of Young's fringes quality.

An accurate velocity measurement requires the use of submicron particles as flow tracers. The generation of glycerine oil vapor mixed with air provides a seeding which satisfies the previous requirement. The smoke circuit is sketched in Fig. 3. The amount of particles is adjusted through bypassing a part of the total mass flow. Before injection, smoke particles have to pass through a tank where the biggest ones condense and the rest lose their kinetic energy. They are naturally aspirated with the compressor flow. The contraction ratio of the facility defines the area of seeding. This means that the smoke outlet concentration is not the same as in the measurement plane and makes the setting of particle concentration difficult.

Data Processing. The basis of the data reduction system was laid down by Meynart (1983). The particle-image displacement is determined from the computation of the autocorrelation function of the photographic intensity distribution. It is done by the evaluation of two successive Fourier transforms. In case of high particle concentration, the relevant method is to perform the first Fourier transform optically. A small area of the PIV picture is reilluminated by a laser beam. Particle image pairs behave like doublets of a coherent light source, producing an interference pattern, the so-called Young's fringes. The distance between the fringes is inversely proportional to the particle-image displacement and the velocity angle can be deduced from the interference pattern angle.

The arrival of faster processor boards and the developments of Lourenco (1991) have led to the construction of a compact system (Fig. 4) articulated around a PC (processor 80386, 16 MHz) equipped with an array processor. A system of two convergent lenses (L1, L2) enables the adjustment of the interrogating laser-beam diameter as a function of the particle image size and concentration. Usually, this diameter is set to 0.5 mm. A spatial filter (F) eliminates the Gaussian noise around the laser

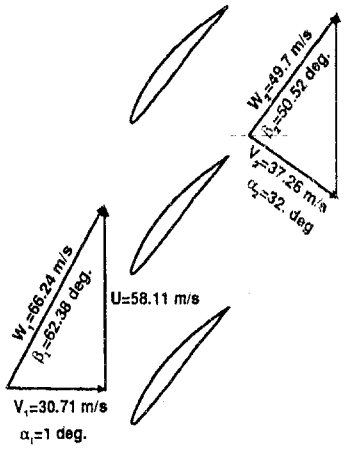

Fig. 2 Velocity triangles in the measurement plane

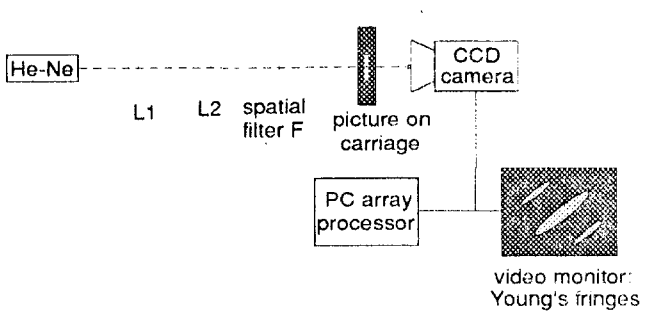

Fig. 4 Data processing system

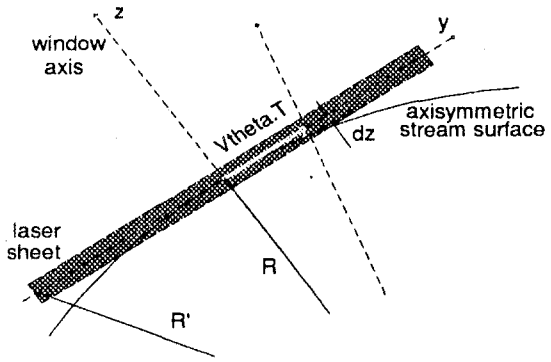

Fig. 5 Out-of-plane motion

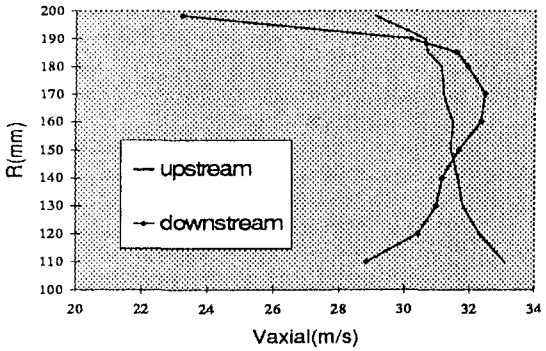

Fig. 6 Axial velocity distribution

spot. A video camera (512 × 512 pixels) records the fringe pattern and displays it on the video monitor. The computer digitizes the image with a frame grabber (DT2851). The second Fourier transform can therefore be computed and the velocity vector is determined. Three seconds of computation are necessary to get a vector.

Interrogating points are distributed on a structured grid of steps which can be fixed by the operator. The slide carriages are driven by a set of microcontrol motors controlled by two interfaces and the computer. The usual interrogation grid step is 0.4 mm.

Because of the random distribution of tracers in the flow or unexpected light reflection, erroneous vectors can be computed and results have to be filtered. This stage of the procedure is done point by point by checking the value of the signal-to-noise ratios. The velocity vector is also compared with its neighbors as an additional check. Usually, the processing of a whole picture lasts 3 hours, including the validation procedure, which typically causes the adjustment of 50 percent of the total number of vectors.

Measurement Uncertainties. Two types of errors are expected: Errors due to the three-dimensional flow motion and uncertainties involved with the technique itself. First, referring to the problem of out-of-plane motion described by Meynart and Lourenco (1984), errors due to PIV application in a cylindrical stream surface might be nonnegligible because the coincidence between the illumination plane and the stream surface is not effective on the whole laser sheet width. Figure 5 illustrates

Table 1 PIV uncertainties

absolute angle	0.6 deg.
absolute velocity	1.4 m/s
relative velocity	0.9 m/s
relative angle	1. deg.

Fig. 7 PIV photograph

this effect. The ratio (ϵ_x, ϵ_y) between erroneous displacement estimation and the real one is expressed in the following way:

$$\epsilon_x = 1 + \frac{dz}{dx} \tan \phi_x$$

$$\epsilon_y = 1 + \frac{dz}{dy} \tan \phi_y \qquad (1)$$

where dz is the out-of-plane displacement component, dx, the axial, and dy, the tangential in-plane one. ϕ_x, ϕ_y are the semi-angles of view.

When the flow is going through the blade row, it receives energy. The streamline deflection marks the transfer of momentum. It causes a change of the absolute tangential velocity component V_θ. Assuming that the flow is axisymmetric, the out-of-plane component dz due to the curvature difference between the laser plane and the stream surface is: $dz = R(1 - \cos(V_\theta T/R)) = 27 \times 10^{-9}$ m, with $R = 185$ mm, $V_\theta = 20$ m/s, and $T = 5$ μs. The semi-angle of view ϕ_x (or ϕ_y) is estimated by the ratio of the half laser sheet width with the camera objective focal length ($\phi_x = \phi_y = 20$ deg). Using Eq. (1), the out-of-plane errors are computed and they appear to be negligible ($\epsilon_x = 1.00005$, $\epsilon_y = 1.00008$, with $dx = 190$ μm and $dy = 120$ μm as typical values).

A second source of out-of-plane motion is the radial shift affecting streamlines through a blade row. Comparing the inlet to the outlet axial velocity distribution (Fig. 6), it becomes obvious that the flow does not remain purely axial because the profiles have different shapes. By joining radial positions

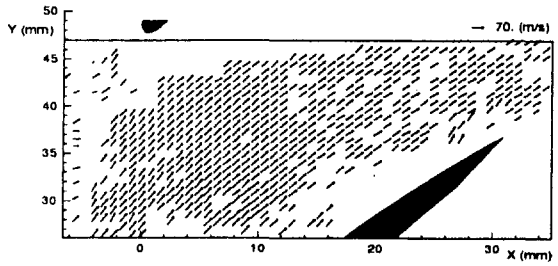

Fig. 8 Relative velocity vectors

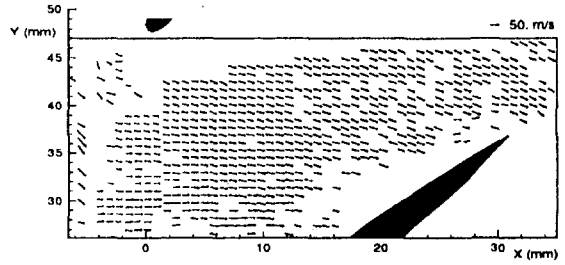

Fig. 9 Absolute velocity vectors

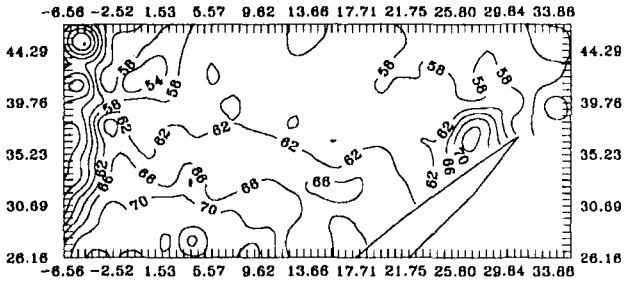

Fig. 10 Relative velocity contours (m/s)

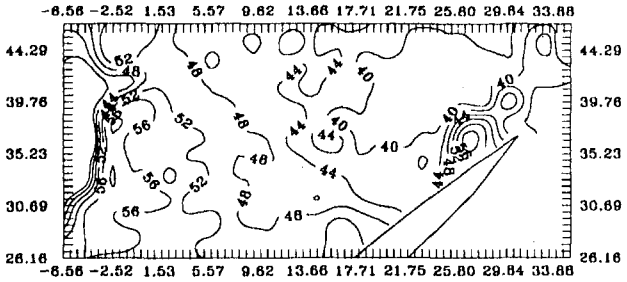

Fig. 11 Relative angle contours (deg)

corresponding to the same amount of mass flow ahead of and behind the blade, the slope of the stream surface is estimated to be equal to $dz/dx = 2.7 \times 10^{-3}$ (with $dx = 190$ μm). The associated error deduced from Eq. (1) is $\epsilon_x = 1.001$ and can be neglected.

In the same way, since the light plane coincides locally with the stream surface, fluid particles that are far from the laser-sheet center are in a cylindrical surface having a diameter equal to R' (Fig. 5). When the relative velocity is deduced from the absolute one, an error affects the determination of the circumferential velocity of these particles with respect to those close to the laser sheet middle. A geometric relationship enables the estimation of this error:

$$R'/R = \sqrt{1 + (l_o/2R)^2} = 1.0058$$

where l_o is the laser sheet width and $R = 185$ mm = the radial position of the measurement plane.

The second class of errors results from the different steps of the PIV technique. The main sources of uncertainty are the magnification factor determination and processing errors. An uncertainty equal to 1 percent of the magnification value results in the same amount of uncertainty affecting the velocity determination. The error due to the processing is estimated with the help of a computer-generated PIV picture with known particle displacement. The displacement component is determined within a range of 1 percent with respect to the measured value. Errors affecting the angle measurement are equal to 0.6 deg. Noting that the rotational speed is constant to within 10 rpm, the uncertainty corresponding to the different measured quantities is given in Table 1.

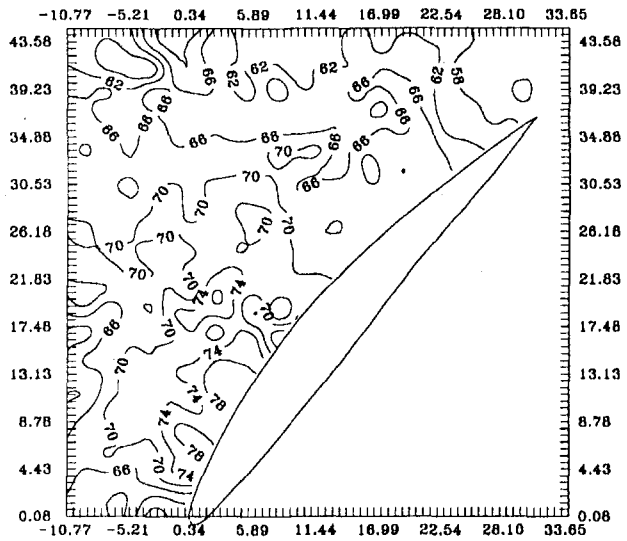

Fig. 12 Averaged relative velocity (m/s)

Discussion of Results

Instantaneous Flow Pictures. Figure 7 is a typical sample of the double-exposure image. The blade position in the view field is designated by the bright pattern caused by the laser reflection from the blade surface. The incoming laser sheet direction and blade stagger are not optimized. A large area at the pressure side is not illuminated. This drawback prevents us from making observations of the whole blade-to-blade flow.

In this picture, the particle image diameter is equal to 30 μm and the tracer concentration based on the planar image density multiplied by the laser sheet thickness is 28 particles per mm^3.

Figures 8 and 9 are examples, respectively, of instantaneous *relative* and *absolute* velocity-vector maps. The measurement grid step is 0.8 mm in the horizontal and vertical direction. The frame origin is fixed in the blade leading-edge position.

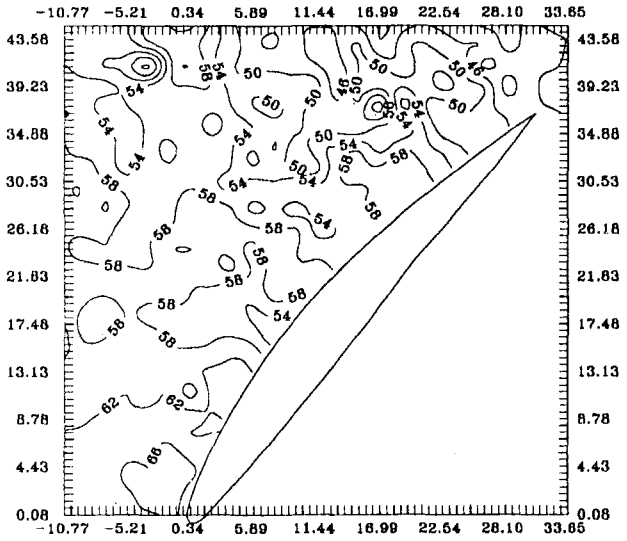

Fig. 13 Averaged relative angle (deg)

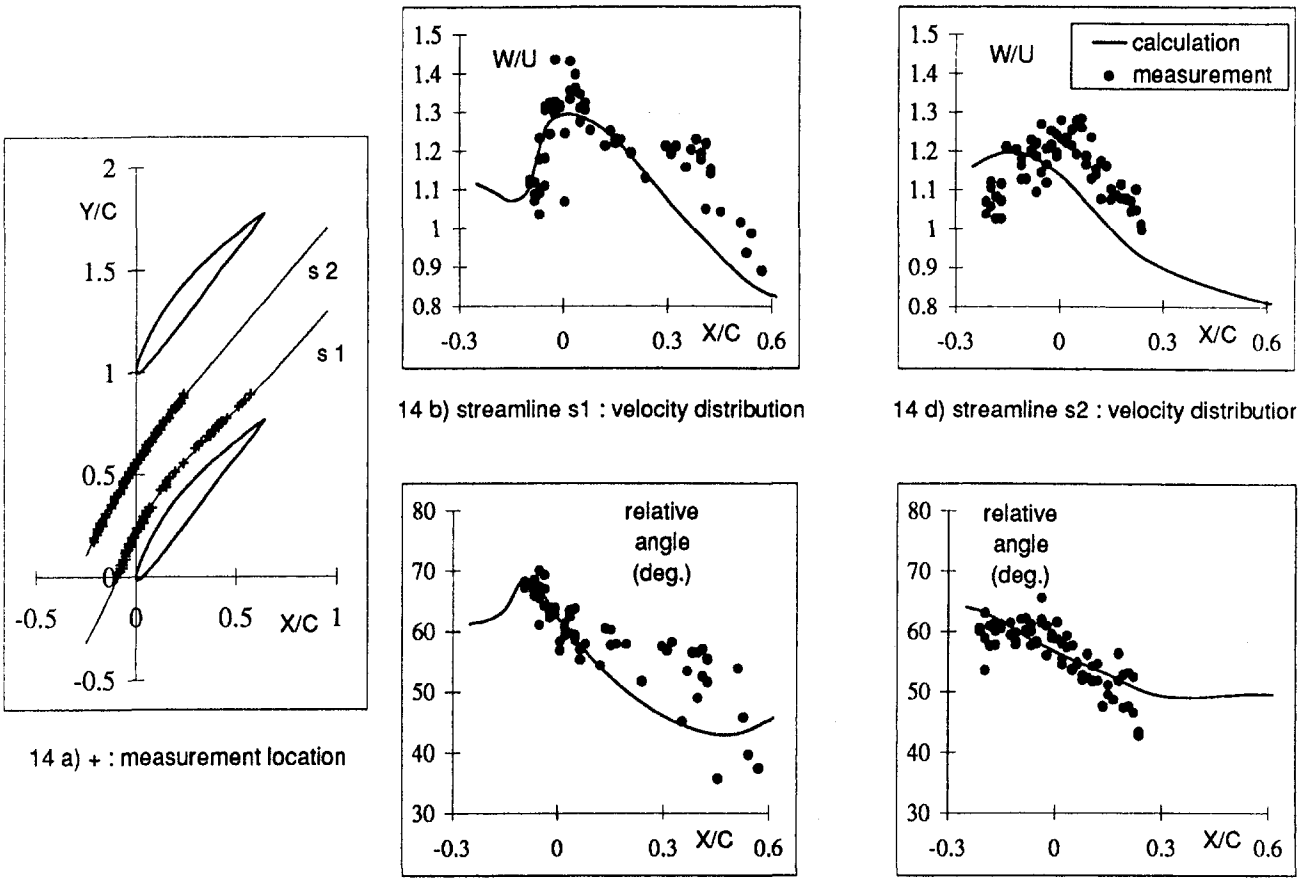

14 a) + : measurement location

14 b) streamline s1 : velocity distribution

14 d) streamline s2 : velocity distributior

Fig. 14 Comparison with a potential flow calculation

It is impossible to get measurements close to the blade surface because the light reflection saturates the photographic film locally. Most of the data losses are due to the absence or an overly low concentration of seeding. The presence of the laser apparatus in front of the facility implies that the tracers had to be introduced close to the flow entrance. Therefore, it creates some disturbances in the flow that affect the seeding uniformity.

The relative-velocity contours map presented in Fig. 10 resulted from the data interpolation of relative velocity vectors sketched on Fig. 8. The length scale is millimeters and the coordinates are expressed in the real frame attached to the blade leading edge. If the upstream and downstream PIV measurements values are compared to the velocity triangles (Fig. 2), the velocity magnitudes match. This observation is also verified for the relative angle (Fig. 11).

For the moment, any further conclusions about the amount of error will be affected by the fact that pressure measurements result from acquisition over a large number of periods, whereas optical data are instantaneous. The averaging of the optical measurements for comparison with mean observations will be discussed in the following section.

Approximation of the Steady Flow Conditions. For the same operating condition, a set of 10 PIV pictures with random blade position is recorded. The origin of the processing frame is defined in the blade leading edge position. It enables the superposition of all measured grids and computation of the average of data points located in the same position. The periodic flow field cannot be considered to be accurately determined. Because of the low number of pictures and the random blade position in the field of view, the experimental mean velocity results from the average of 3 to 10 instantaneous data. Nevertheless, the averaging procedure has a smoothing effect on the PIV data. Figures 12 and 13 are the resulting contour maps for the relative velocity and its angle. The flow-field width is equal to 1 pitch. The length scale is millimeters. By computing the average of inlet and outlet vertical data distribution, one gets quantities directly comparable with pressure-test results presented in Fig. 2. These quantities have the following values:

Upstream	Downstream
$W_1 = 67.82$ m/s	$W_2 = 59.19$ m/s
$\beta_1 = 61.25$ deg	$\beta_2 = 46.1$ deg

Compared to the pressure-test results, upstream conditions match very well, whereas higher downstream velocity (and therefore, lower relative angle) is estimated. Optical measurements are only obtained in an area close to the suction side, the region of highest velocity, which explains the differences observed downstream.

To demonstrate the ability of PIV to provide experimental data for code verification, a blade-to-blade potential-flow prediction has been compared with the average of the measurement grids. The computational code was implemented by Van den Braembussche (1984). It uses the singularity method. Flow comparisons are carried out along two streamlines, s1 and s2, respectively located 10 mm from the blade suction side and in the midpassage (Fig. 14(a)). The distance between the measurement position and the streamlines is at most 0.4 mm (equal to the half measurement grid step). Relative velocities and angle differences are examined (Figs. 14(b)), 14(c), 14(d), and 14(e)). Coordinates are nondimensionalized by the blade chord, $C = 47.9$ mm, and velocities are expressed with respect to the circumferential speed ($U = 58.11$ m/s).

The scattering of the experimental data confirms that the estimation of the periodic flow field is approximate and that the number of PIV samples should be increased to determine accurate mean velocities. The disturbances caused by the wake of the seeding injection system also contribute to these fluctuations.

In the first part of the streamline s1 ($X/C \leq 0.3$), measurement values are distributed around the calculated results with a maximum error equal to 10 percent of the velocity U, outside the region of velocity peak. Considering that the measurement uncertainty is 1.5 percent of the circumferential speed U, the maximum error is 8.5 percent of U or 4.9 m/s. Expressing this error with respect to the relative velocity range (W_1 = 66.24 m/s), the maximum difference between the prediction and the measurement is 7.5 percent of the measured value. Farther downstream on the streamline s1, measured velocities have higher values than those predicted. This difference is explained by the fact that the calculation does not take into account the contraction of the flow channel due to the three-dimensional effect. The contraction ratio is deduced from the ratio of the axial velocity measured from the pressure test. It is equal to 1.027. This contraction phenomenon may also explain the highest velocity peak value.

Concerning the relative-angle distribution along the streamline s1, two zones can be distinguished:

(*i*) a good agreement in the inlet part of the blade row
(*ii*) farther downstream, the measured angle fluctuates around higher values than those predicted.

This observation can be explained by the fact that the operating regime is transitional. So a boundary-layer stall is expected at the end of the blade suction side. It confirms also the measurement of a highest velocity peak.

Differences between prediction and measurement observed along the second streamline s2 have different characteristics than those noted along s1. The scattering of the PIV data is the same but, especially for the relative velocity measurement, there is a shift between the experimental and the numeric data. Higher velocities are also measured. Both effects might be a consequence of the blockage caused by the stall on the suction side. The relative angle determination is less sensitive to this phenomenon.

Conclusions and Future Developments

The application of PIV to the study of blade-to-blade flow in an axial-compressor rotor is motivated by two main features of the technique: instantaneous measurements and large spatial resolution. This permits a quick capture of the flow conditions. The data reduction performed afterward enables the determination of the stream parameters. PIV measurement resolution is linked to the uniform concentration of tracers in the flow. This requirement is the primary source of difficulties in applying the technique.

The comparison of optical measurements with conventional ones helps to demonstrate the ability of PIV in this experimental case. The estimation of the periodic flow field needs to be improved by increasing the number of instantaneous samples used in the mean velocity determination and keeping this number constant in all points of the flow map.

Progress can also be made by reducing the nonilluminated area. The idea is to introduce the laser sheet with its main direction angle close to the blade stagger. This can be achieved by using a laser-sheet probe, as did Bryanston-Cross et al. (1992). The application of a two-dimensional technique to study such a rotating flow is limited by the amount of out-of-plane motion. Three-dimensional effects are not always negligible and hence, the advent of three-dimensional PIV may eliminate these errors by the evaluation of the radial velocity component.

References

Adrian, R. J., and Yao, C. S., 1985, "Pulsed Laser Technique Application to Liquid and Gaseous Flow and the Scattering Power of Seed Materials," *Applied Optics*, Vol. 24, pp. 44–52.

Adrian, R. J., 1986, "Multi-point Optical Measurement of Simultaneous Vectors in Unsteady Flow—a Review," *International Journal Heat and Fluid Flow*, Vol. 7, pp. 127–145.

Bryanston-Cross, P. J., and Epstein, A. H., 1986, "The Application of Submicron Particle Visualization for (PIV) at Transonic Speeds," *Progress in Aerospace Science*, Vol. 27, pp. 237–265.

Bryanston-Cross, P. J., Towers, C. E., Judge, T. R., Towers, D. P., Harasgama, S. P., and Hopwood, S. T., 1992, "The Application of Particle Image Velocimetry (PIV) in a Short-Duration Transonic Annular Turbine Cascade," ASME JOURNAL OF TURBOMACHINERY, Vol. 114, pp. 504–509. No 91-GT-221.

Lourenco, L. M., 1991, private communication with M. L. Riethmuller.

Meynart, R., 1983, "Instantaneous Velocity Field Measurements in Unsteady Gas Flow by Speckle Velocimetry," *Applied Optics*, Vol. 22, pp. 535–540.

Meynart, R., and Lourenco, L. M., 1984, "Laser Speckle Velocimetry in Fluid Dynamics Applications," *Digital Image Processing in Fluid Mechanics*, von Karman Institute Lecture Series 1984.03.

Paone, N., Riethmuller, M. L., and Van den Braembussche, R. A., 1988, "Application of Particle Image Displacement Velocimetry to a Centrifugal Pump," *Proc. 4th Symposium on Application of Laser Techniques to Fluid Mechanics*, Lisbon, Paper No 6.

Van den Braembussche, R. A., 1984, "The Application of Singularity Method to Blade-to-Blade Calculations," *Thermodynamics and Fluid Mechanics of Turbomachinery*, NATO Advanced Sciences Institute Series, series E, *Applied Science*, A. S. Ucer, P. Stow, and C. Hirsch, eds., Vol. 97a, pp. 167–191.

The Influence of Large-Scale, High-Intensity Turbulence on Vane Aerodynamic Losses, Wake Growth, and the Exit Turbulence Parameters

F. E. Ames
Allison Engine Company,
Indianapolis, IN

M. W. Plesniak
School of Mechanical Engineering,
Purdue University,
West Lafayette, IN 47907

An experimental research program was undertaken to examine the influence of large-scale high-intensity turbulence on vane exit losses, wake growth, and exit turbulence characteristics. The experiment was conducted in a four-vane linear cascade at an exit Reynolds number of 800,000 based on chord length and an exit Mach number of 0.27. Exit measurements were made for four inlet turbulence conditions including a low-turbulence case ($Tu \approx 1$ percent), a grid-generated turbulence case ($Tu \approx 7.5$ percent) and two levels of large-scale turbulence generated with a mock combustor ($Tu \approx 12$ and 8 percent). Exit total pressure surveys were taken at two locations to quantify total pressure losses. The suction surface boundary layer was also traversed to determine losses due to boundary layer growth. Losses occurred in the core of the flow for the elevated turbulence cases. The elevated free-stream turbulence was found to have a significant effect on wake growth. Generally, the wakes subjected to elevated free-stream turbulence were broader and had smaller peak velocity deficits. Reynolds stress profiles exhibited asymmetry in peak amplitudes about the wake centerline, which are attributable to differences in the evolution of the boundary layers on the pressure and suction surfaces of the vanes. The overall level of turbulence and dissipation inside the wakes and in the free stream was determined to document the rotor inlet boundary conditions. This is useful information for assessing rotor heat transfer and aerodynamics. Eddy diffusivities and mixing lengths were estimated using X-wire measurements of turbulent shear stress. The free-stream turbulence was found to strongly affect eddy diffusivities, and thus wake mixing. At the last measuring position, the average eddy diffusivity in the wake of the high-turbulence close combustor configuration ($Tu \approx 12$) was three times that of the low turbulence wake.

Introduction

A designer's ability to predict turbine aerodynamic losses, wake characteristics, wake growth, and heat transfer to the blades is crucial to the development of the next generation of efficient and reliable turbines. Many complex flow features such as high levels of combustor and airfoil wake-generated turbulence, curvature, hot streaks, and secondary flows contribute to the difficulty in making such predictions. Current turbulence models are inadequate to capture the complex flow physics inherent to turbomachinery flows. Furthermore, inlet boundary conditions are often poorly defined, yet the inlet turbulence conditions significantly influence the turbine aerodynamics and heat transfer.

In the present study, a range of engine relevant turbulence scales and levels have been generated, and the resulting flow field and heat transfer (reported in Ames, 1994) to a vane in a linear cascade have been documented. Unlike most previous studies, a special turbulence generator was used to produce the large-scale, high-intensity turbulence typical of a gas turbine combustor. For comparison, a grid was used to generate smaller scale turbulence. The effect of turbulence scale was examined by comparing grid turbulence with combustor-simulator turbulence of the same intensity. Hot-wire anemometry was used extensively to document the inlet, intrapassage, and wake turbulence characteristics.

This paper focuses on the influence of inlet turbulence characteristics on wake losses, wake growth and development, and mixing within wakes. It also provides comprehensive documentation of turbulence characteristics of cascade exit flow, including the influence of a range of turbulence levels and scales on the wakes. The vane exit turbulence parameters such as the normal Reynolds stresses, dissipation rates, and length scales provide the inlet turbulence boundary conditions for the downstream rotor and impact the heat transfer, mixing, and aerodynamics of subsequent stages. Measurements of stagnation pressure losses through the cascade demonstrate the impact of high free-stream turbulence on vane profile losses.

Background. The primary cause of profile losses on turbomachinery airfoils is boundary layer growth and trailing edge blockage (Glassman, 1973). Hoheisel et al. (1987) found that free-stream turbulence and blade pressure gradient have a significant influence on boundary layer development, and thus impact losses across a turbine stage. Denton (1993) gives a comprehensive review of loss mechanisms in turbomachines, and suggests that mixing across gradients in the flow can result in increased losses even without the action of frictional forces. He relates total pressure losses to the creation of entropy. Boundary layer losses will depend on the cube of the ratio of the blade surface velocity to the upstream reference velocity integrated over the surface of the blade, implying that the suction surface

Contributed by the International Gas Turbine Institute and presented at the 40th International Gas Turbine and Aeroengine Congress and Exhibition, Houston, Texas, June 5–8, 1995. Manuscript received by the International Gas Turbine Institute. Paper No. 95-GT-290. Associate Technical Editor: C. J. Russo.

losses will be dominant. Separation bubbles will serve to thicken the boundary layers and result in additional entropy increases, or stagnation pressure losses.

Moore et al. (1987) found that more than one third of the losses in their cascade occurred downstream of the trailing edge, and attributed the loss in total pressure to deformation work primarily, $\rho\overline{w'^2}\partial W/\partial z$ near the midspan (dissipation of secondary kinetic energy). Mee et al. (1992) also reported significant wake mixing losses from their near-wake measurements in a transonic cascade. Gregory-Smith and Cleak (1992) measured the turbulence characteristics on a low-aspect-ratio rotor in a cascade with grid-generated free-stream turbulence of 5 percent. In the case with elevated free-stream turbulence they reported a 7 percent *increase* in the midspan loss coefficient, but a 12 percent *decrease* in the total loss coefficient (due to reduced core losses). Aside from Hoheisel et al. (1987) and Gregory-Smith and Cleak (1992), few investigators have examined the influence of inlet turbulence on losses across a turbine cascade.

High levels of turbulence are known to exist at the entrance to first stage nozzles. Bicen and Jones (1986) measured turbulence levels, based on the bulk exit velocity, ranging from 13 to 20 percent in a model can-type combustor. Ames and Moffat (1990) measured turbulence levels ranging from 15 to 17 percent at the exit of a mock combustor with energy scales (Lu) ranging from $\frac{1}{3}$ to $\frac{1}{2}$ of the exit height.

A number of investigators, starting with Hancock and Bradshaw (1983), have shown that both turbulence intensity and scale have an effect on the skin friction coefficient. Mayle (1992) believes that the onset of transition is controlled by the free-stream turbulence. Hoffmann and Kassir (1989) found that the free-stream turbulence intensity made the boundary layer more resistant to separation in adverse pressure gradients. In light of both the level of turbulence at the entrance to first-stage nozzles and the influence that the turbulence has been found to have on boundary layer development, the necessity to examine the influence of turbulence on losses and wake development is clear.

The development of the vane wake is important in that it provides the aerodynamic boundary condition for the rotor. Ladwig and Fottner (1993) found that incoming wakes had the greatest influence on losses when they entered the blade passage near the suction side of the blade. In addition, the wake generates turbulence characteristics that strongly influence the downstream airfoil heat transfer (Van Dresar and Mayle, 1988; Wittig et al., 1988; Dullenkopf et al., 1991; Dullenkopf and Mayle, 1994). Wake development and its turbulence characteristics are dependent on initial conditions. Weygandt and Mehta (1995) reported on the effect of laminar and turbulent initial boundary layers, and streamwise vortices that occur naturally as a secondary instability under some circumstances. Nakayama and Kreplin's (1994) study of wakes generated with asymmetries in the initial boundary layers on a splitter plate found that the magnitude of the Reynolds stress peaks downstream of the trailing edge is related to the surface friction in the boundary layers at the trailing edge and to the turbulence length scale. They also reported that locally, production does not equal dissipation, and that gradient diffusion models such as $k-\epsilon$ do not work well in cases where wake asymmetry is large.

In addition to wake turbulence, core turbulence can also have an important impact on turbine airfoil heat transfer. Arts et al. (1990) found significant increases in laminar heat transfer and early transition on a transonic turbine vane cascade due to 6 percent grid-generated turbulence. Ames and Moffat (1990), Van Fossen and Simoneau (1994), and Van Fossen and Ching (1994) found that both turbulence level and scale were important in correlating stagnation region heat transfer.

Objectives. The primary objective of this study was to investigate the influence of combustor-like inlet turbulence on turbine vane wake characteristics, development, and mixing.

Nomenclature

a = distance from trailing edge tip to origin of wake, see Eq. (3), cm
C = airfoil chord length, cm
Cd = drag coefficient = 2 Drag/($\rho U_\infty^2 d$), (per unit length)
C_f = skin friction coefficient
CL = cross-stream passage width, cm
d = trailing edge diameter, cm
D = leading edge diameter, cm
$\bar{e}_1$ = mass-averaged kinetic energy loss coefficient (Eq. (1))
$\bar{e}_2$ = mixed-out kinetic energy loss coefficient (Eq. (2))
l = mixing length = ν_m/v', cm
Lu = energy scale = $1.5|u'|^3/\epsilon$, cm
Lx = longitudinal integral scale, cm
M_{ex} = Mach number based on exit conditions
P = pressure, Pa
P_s = static pressure, Pa
$P_{s,ex}$ = mean static pressure measured at upper 8 exit static pressure ports and averaged, Pa
P_t = total pressure, Pa
Re = Reynolds number
Re_{ex} = exit Reynolds number = $(\rho_{ex} \cdot U_{ex} \cdot C)/\mu$
Tu = turbulence intensity = u'/U_∞
Tu_v = normal component turbulence intensity = v'/U_∞
Tu_o = turbulence level at reference position
T_t = stagnation temperature, K
U = local streamwise velocity, m/s
U_{defect} = defect velocity = $U_\infty - U$, m/s
$U_{max,def}$ = maximum defect velocity in the wake, m/s
u' = rms streamwise fluctuation velocity, m/s
$-\overline{u'v'}$ = primary Reynolds shear stress, m^2/s^2
v' = rms normal fluctuation velocity, m/s
w' = rms spanwise fluctuation velocity, m/s
W = width of the wake determined from the locations where the velocity defect equals one half of the peak velocity defect, cm
X_1 = distance between the probe tip and the vane tailing edge, cm
Y = normal distance from the surface, cm
Δ = change (mathematical symbol)
α_1 = cascade air exit angle, deg
δ_1 = displacement thickness, cm
δ_2 = momentum thickness, cm
δ_3 = energy thickness, cm
ϵ = turbulent dissipation, m^2/s^3
μ = dynamic viscosity, Pa s
ν = kinematic viscosity, m^2/s
ν_m = eddy viscosity, m^2/s
ρ = density, kg/m^3
σ = distance from the wake centerline to location where U_{defect} = $\exp(-1)U_{max,def}$
ω = total pressure loss coefficient = $(Pt_{in} - Pt_{ex})/(Pt_{in} - Ps_{ex})$
$\bar{\omega}$ = mass averaged total pressure loss coefficient

Subscripts

∞ = referenced to free-stream conditions
bgd = background
ex = referenced to exit static pressure tap plane location
in = referenced to inlet static pressure tap plane location
max = maximum
prb = probe correction
ss = suction surface boundary layer property
vane = referenced to vane static pressure

The turbulence characteristics of the wake and exit flow were carefully measured to provide useful information on the first-stage rotor inlet boundary condition, which is critical in assessing blade surface heat transfer. Additionally, this work provides a complete set of data for the calibration and validation of CFD models. For this study, two levels of simulated-combustor turbulence and one level of grid-generated turbulence were carefully characterized. Exit surveys were taken at two downstream locations to determine the distribution of total pressure, velocity, turbulent normal and shear stresses, and turbulent scales and dissipation rate. The data have been analyzed to help determine the influence of inlet turbulence on losses, wake growth, and wake mixing.

Experimental Facility and Techniques

The four-vane cascade used in this study is connected to an in-draft blower. The blower is rated at 1.13 m^3/s (2400 scfm) with a pressure rise of 10.3 kPa (1.5 psia). The Plexiglas walled cascade was originally built by Zimmerman (1990) to facilitate three component laser anemometry measurements. The cascade airfoils are 4.5 times scale C3X vanes. These vane profiles are two-dimensional slices from a first-stage nozzle for a helicopter engine. This vane geometry was previously used by Nealy et al. (1984) for determining heat transfer distributions in a warm cascade rig. The coordinates for the 4.5 times scale C3X vane geometry are given by Nealy et al. (1984). The vane true chord length is 14.493 cm and the axial chord is 7.816 cm. The vane spacing is 11.773 cm and the passage has a throat of 3.292 cm. The diameter of the leading edge is 2.337 cm and the diameter of the trailing edge is 0.340 cm. The stagger angle of the vane is 55.47 deg and the calculated air exit angle is 72.4 deg. The height of the vane is 7.62 cm. Note that the C3X was designed for operation at a transonic exit condition, where it has a slight adverse pressure gradient on the rear suction surface. At the low Mach number (M_{ex} = 0.27) at which these C3X cascade tests were run, this adverse pressure gradient is much more pronounced.

The arrangement of the four-vane cascade is shown schematically in Fig. 1. To monitor inlet static pressure uniformity, the cascade has a row of nine static pressure taps across two passages at the inlet, 3.68 cm upstream of the plane of the vane leading edges. The cascade is also instrumented with a row of nine static pressure taps spanning two passages at the exit (16.35 cm from the inlet plane or 9.37 cm axially downstream from the vane leading edges) to monitor exit static pressure uniformity. The inlet uniformity is set with bleed flow adjustments located below vane 1 and above vane 4. The exit flow uniformity is set by the tailboards, which pivot just downstream of the trailing edge of vanes 1 and 4. The exit probe access ports, which are labeled 1–8, accommodated 14.73-cm-long hot-wire and total pressure probes used to traverse the turbine passage and the exit. These probes were pivoted about the centerlines of the access ports using a slider linkage on a lead screw drive table. The inlet access ports, which are also labeled 1–8, accommodated inlet total pressure, temperature, and hot-wire probes used to reference and survey the inlet conditions. The location of the inlet probe access plane is 3.68 cm upstream from the vane leading edge plane.

Turbulence Generators. Four inlet turbulence boundary conditions were developed for this study. The conditions consisted of a low-turbulence (1.1 percent) base case, a grid-generated turbulence case to produce a moderate level (7.8 percent) of relatively small-scale (Lu = 1.36 cm) turbulence, and two cases with simulated combustor turbulence to produce moderate and high (8.3 and 12.0 percent) levels of relatively large-scale (Lu = 4.34 cm and 3.36 cm) turbulence. The inlet geometry for the low-turbulence condition consisted of an inlet filter to remove dust from the air, two nylon screens to reduce the inlet

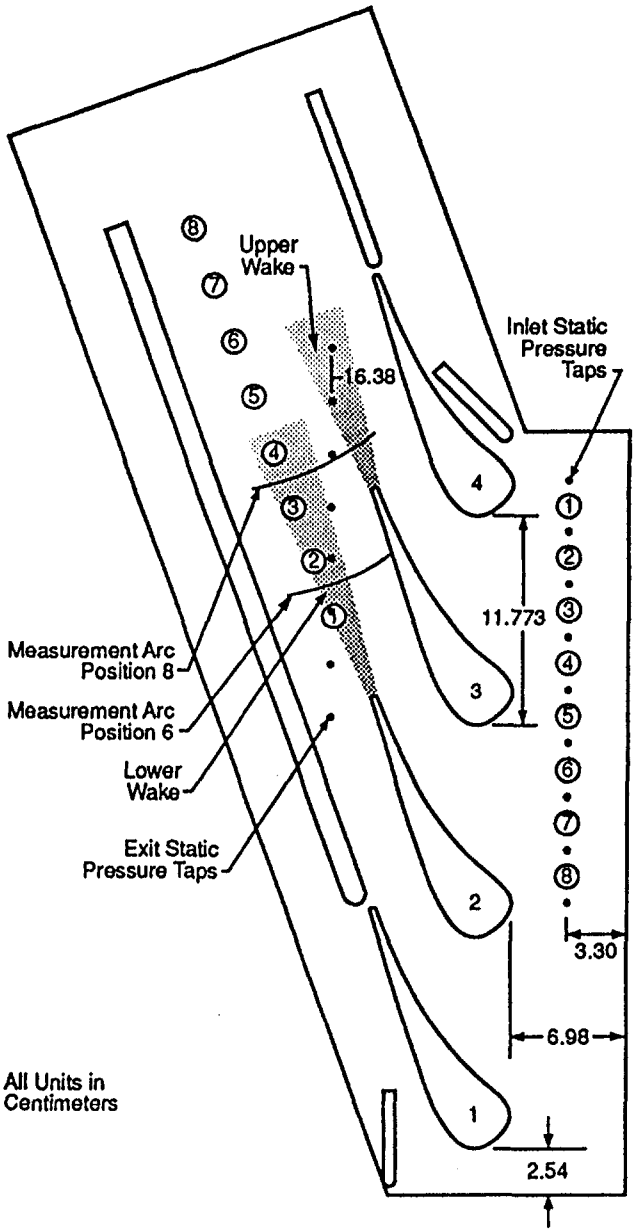

Fig. 1 Schematic of four vane cascade

velocity fluctuations, an eight-to-one two-dimensional contraction nozzle to reduce the level of the streamwise turbulence intensity, and a 25.4-cm-long, 7.62-cm-wide by 42.54-cm-high rectangular section, which was used to connect the two-dimensional nozzle to the cascade.

The inlet geometry for the grid-generated turbulence was the same as for the low-turbulence case, except that a grid was installed in the rectangular section. The grid was fabricated from 0.317 cm square steel bars, with a spanwise spacing of 1.524 cm and a pitchwise spacing of 1.588 cm, producing a 63 percent open area grid. It was positioned 19.7 cm from the vane leading edge plane to document the inlet characteristics at inlet access ports, 16 cm downstream of the grid. The grid was placed in a forward position (15.9 cm upstream of the vane leading edge plane) for all measurements except for documentation of the grid inlet conditions.

A schematic of the simulated combustor is shown in Fig. 2. Air enters into a 59.06 cm wide by 42.54 cm high plenum, where it is directed through the rear and side panels of the simulator liner. The flow through the back panel slots combines

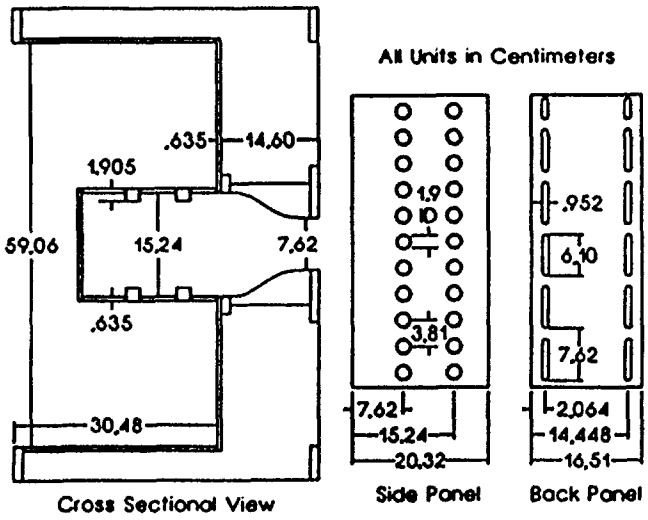

Fig. 2 Schematic of combustor turbulence simulator

with flow through the first row of holes in the side panels to create a recirculation zone inside the simulator liner. The second row of holes in the side panels simulates dilution jets. The simulator undergoes a two-to-one contraction from the liner into the inlet of the cascade through a 15.24-cm-long nozzle. The configuration with the combustor simulator closely attached to the cascade inlet is referred to as the "close combustor" [Comb(1)] configuration.

In the second combustor simulator configuration, a 25.4 cm rectangular spool is inserted between the combustor simulator and the cascade inlet. Thus, the turbulence generated in the combustor has sufficient time to decay to a level similar to that of the grid turbulence. The configuration with the rectangular spool inserted between the combustor simulator and the cascade is referred to as the "far combustor" [Comb(2)] configuration. A more complete description of the turbulence generators, the cascade, and the inlet conditions are given by Ames (1994). The inlet boundary layer is characterized by the momentum thickness Reynolds number, $Re_{\delta 2}$, which was 1288 for the low-turbulence case, 805 for the grid-turbulence case, 1253 for the Comb(2) configuration, and 1178 for the Comb(1) case.

Vane Pressure Distribution. The baseline pressure distribution for the low turbulence case is given in Fig. 3. The measured pressure distribution, shown with symbols, is compared to a numerical prediction based on a compressible stream function formulation. The analysis assumes the air exit angle is 72 deg. In general, the predicted and measured distributions compare well. The small differences between the predicted and measured pressure distributions are most likely due to the idealizations used in the stream function analysis. For example, the stream function analysis does not account for blockage due to development of the suction and pressure surface boundary layers, separation at the trailing edge, or the separation bubble on the suction surface (inferred from the momentum thickness for the high-turbulence cases compared to that for the low-turbulence cases).

Data Acquisition and Reduction. A PC-based data acquisition system was used in this study. Pressure measurements were made using a Scanivalve and two 6.89 kPa pressure transducers calibrated against a AMETEK dead-weight tester. Steady-state voltage signals were read using an HP 3456A digital multimeter with 100 nanovolt sensitivity and 2.5 microvolt accuracy. Signals were multiplexed using an HP 3497A scanner. Single element pitot probes with a 45 deg beveled end were used to measure the total pressure. The probes were not nulled due to their negligible directional sensitivity over the range of flow angles encountered. The pressure and hot-wire probes were traversed using two Unislide lead screw drive tables and an Anaheim Automation stepper motor controller. The hot-wire signals were acquired using an Analog Devices RTI-860 board with simultaneous sample and hold capability and a 200 kHz throughput (50 kHz per channel in simultaneous mode). The hot wires were powered with two DISA 55M system constant temperature anemometer bridges. The hot-wire signal was biased and amplified to take advantage of the full 12 bit resolution of the data acquisition card. The probes were calibrated in a low-turbulence jet and the calibration was fit with a fourth-order polynomial. Jorgensen's decomposition (see Frota, 1982) was used to determine the instantaneous velocity vector. For exit measurements with the X-wire, two 20 kHz active low pass filters were used to eliminate aliasing for spectra.

Pressure and thermocouple voltages were read 10 or more times for each data point using an integrating voltmeter. For mean measurements, single-wire voltages were read 16,384 times at each location, spaced at intervals of two or more time constants. Mean X-wire measurements were determined from 8192 independent points. Velocity time records for determining power spectra for both the single-wire and X-wire were determined from 40 records of 8192 realizations which were then averaged. The dissipation rate ϵ was estimated by fitting a line to the $-\frac{5}{3}$ slope inertial subrange region of the spectrum. Details of this procedure are given by Ames and Moffat (1990). The energy scale is defined as $Lu = 1.5|u'|^3/\epsilon$, similar to Hancock and Bradshaw (1983), except that ϵ is estimated from the inertial subrange portion of the spectrum rather than from the streamwise decay of turbulence.

Data Uncertainties. The data uncertainties were estimated based on the root mean square method (see Kline and McClintock, 1953). Determination of total pressure resulted in an absolute uncertainty of about 1 percent of the inlet dynamic head and about 0.25 percent of the exit dynamic head. The pitot probes were calibrated for the range of incidence angles encountered. Determination of the velocity from the pressure at the inlet and exit had an uncertainty of about 2 percent due to the uncertainty in the local static pressure. The mean velocity, as determined by single-wire anemometry, had an uncertainty of about 2 percent. A temperature compensation scheme was used to correct for the tunnel air temperature drift. The uncertainty in the turbulence level determined from the single wire was estimated to be about 3 percent. The X-wire velocity had an uncertainty of about 3 percent due to both random fluctuations and errors due to binormal fluctuations (w') combined with the probe angle of attack (see Wubben, 1991). The esti-

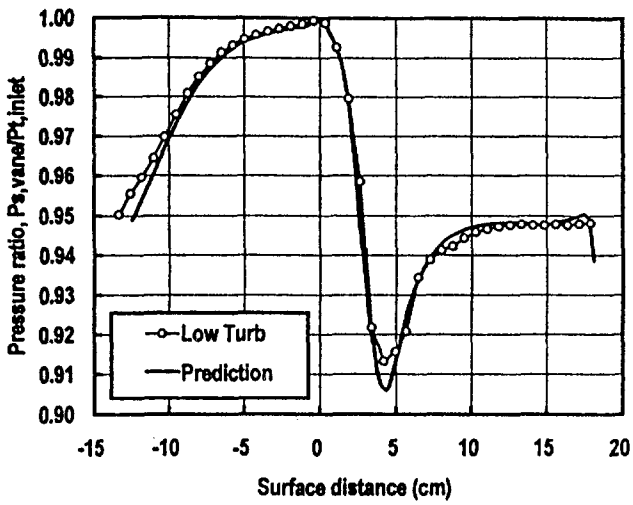

Fig. 3 Comparison of measured and predicted pressure profiles for low turbulence case, $M_{EX} = 0.27$

mated uncertainty in u' and v' was 4 percent for the X-wire at relatively low flow incidence angles (less than 7 deg), increasing for greater values. The estimated uncertainty in the shear stress, $-\overline{u'v'}$, ranged from $\pm 0.03|u'| \times |v'|$ for near zero angles of incidence to $\pm 0.05|u'| \times |v'|$ for incidence angles of 7 deg. The maximum flow angle encountered was 15 deg in the upper wake, where the uncertainty in $-\overline{u'v'}$ is $\pm 0.07|u'| \times |v'|$. Based on Wubben (1991), the error is expected to increase substantially for high levels of the spanwise turbulence, Tu_w, and larger angles of attack. In this study, Tu_w was not measured, but is expected to be comparable to Tu_v.

Experimental Results and Discussion

The exit conditions of the first-stage vane not only provide a means to assess vane profile loss but also constitute the inlet boundary conditions for the first-stage rotor. Identifying the influence of inlet turbulence on losses and the development of the wake is important for accurately predicting stage aerodynamic performance and assessing the effect of combustor and wake generated turbulence on rotor heat transfer. In this section, the main results of the total pressure, single-wire, and X-wire measurements will be presented and evaluated in terms of wake losses, growth, and turbulence characteristics. Only midspan results are presented because previous studies of the C3X vane cascade of the same geometry (Nealy et al., 1984) found that the exit profile was closely two-dimensional from 25 to 75 percent of the span and that secondary losses are predominantly confined to a region within one quarter of the span of the vane.

Wake Losses. Exit total pressure surveys were taken at midspan at positions 6 and 8 to determine profile losses for the different turbulence conditions. Figure 4 shows the total pressure loss profile from vane 2 taken at position 6 for the four turbulence conditions described previously. The inlet turbulence conditions are listed on the legend of this and subsequent figures. The survey starts from the suction surface of vane 3 and traverses the core region, pressure surface side and then the suction surface side of wake of vane 2 (see Fig. 1), crossing the wake centerline at 6.96 cm downstream of the trailing edge. Note that only a portion of the survey is plotted to emphasize details in the wake region. The peak total pressure loss is highest for the low-turbulence conditions and lowest for the close combustor [Comb(1)] condition. The close combustor pressure loss profile is the broadest in width, while that for the low-turbulence condition is the narrowest. Another feature that the profiles show is a loss, which occurs in the core of the flow well away from the edge of the wake or the suction surface boundary

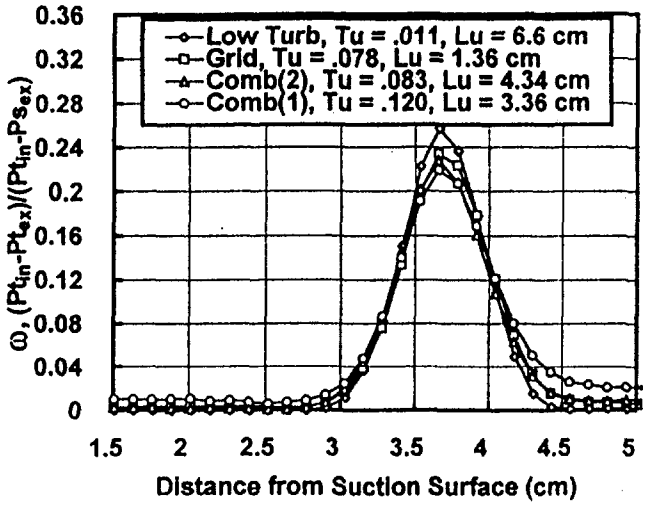

Fig. 4 C3X exit total pressure loss surveys, position 6, $M_{EX} = 0.27$

layer. This loss is clearly a strong function of the turbulence level, and is at least partly due to turbulent mixing across velocity gradients in the core of the flow. This "background loss" is negligible for the low-turbulence conditions but is very important for the close combustor (large-scale, high-intensity turbulence) condition.

The exit total pressure loss surveys for both the upper (vane 3) and lower (vane 2) wakes, taken from position 8, are shown in Fig. 5. Here the survey was taken from a reference position just outside the pressure surface side of the wake of vane 3, across the wake (crossing the centerline at $X_1 = 2.74$ cm), through the core region, and across the wake of vane 2 from the pressure surface side to the suction surface side (crossing its centerline at $X_1 = 13.39$ cm). Thus, the wake profiles were taken at $X_1/d = 20.5$ and 39.4 for the wake of vane 2 (lower wake), and $X_1/d = 8.06$ for the wake of vane 3 (upper wake). The cross-stream distance on the figures represents the distance from the reference position. The trends with respect to peaks, profile widths, and background losses are similar to, but even more pronounced than those described in Fig. 4. The suction surface side of the upper wake shows evidence of the effects of free-stream turbulence. The profile at the wake edge (between 1.2 and 1.5 cm) drops much more abruptly (on the suction surface side) for the low-turbulence wake, as compared to the higher turbulence wakes.

Some of the more important wake parameters for positions 6 and 8 downstream of vane 2 are tabulated in Table 1, including the mass-averaged total pressure loss, $\bar{\omega}$, and kinetic energy loss, $\bar{\epsilon}_1$ which agree closely due to a nearly incompressible exit Mach number of 0.27. These parameters provide information about the origin of the losses. The midspan or profile losses can be categorized into losses due to the development of boundary layers on the vane, losses due to separation at the trailing edge, and losses due to turbulence mixing outside of the vane boundary layers and wakes. The losses categorized as "background" losses seem high for the elevated turbulence level cases. However, both the level of turbulence kinetic energy and the dissipation rate increase significantly between the cascade inlet plane and the exit measurement stations, indicating that turbulent production in the core of the flow due to lateral and streamwise velocity gradients is extracting kinetic energy from the mean flow. Assuming that turbulence production roughly equals dissipation, it is estimated that at least a third and perhaps a half of the "background" losses can be attributed to turbulence production. Denton (1993) indicates that mixing process across velocity gradients in the flow can be a source of losses even when no frictional forces are present. The source of the remainder of these "background" losses is not currently understood.

Another significant source of loss is the suction surface boundary layer. The loss parameters and boundary layer parameters due to the suction surface boundary layer are listed with the subscript "ss" in Table 1. Note that C_f for the suction surface was determined by fitting the inner portion of the boundary layer velocity profile to Spaulding's expression (White, 1991). The suction surface boundary layer at position 6 is the source of 52 percent (low turbulence) to 61 percent (high turbulence) of the total losses. The pressure surface loss was estimated from an integral scheme and accounted for an additional 3 percent. Depending on the inlet turbulence condition, the background losses comprise between 0 and 19 percent of the total losses. The suction surface parameters at the trailing edge can be estimated by integrating C_f over the aft section of the vane to obtain the increase in momentum thickness. The other integral parameters can be estimated by assuming values for shape factors between position 6 and the trailing edge. The local wake kinetic energy loss, attributable to boundary layer skin friction, $\bar{\epsilon}_1$, can also be determined for the integral param-

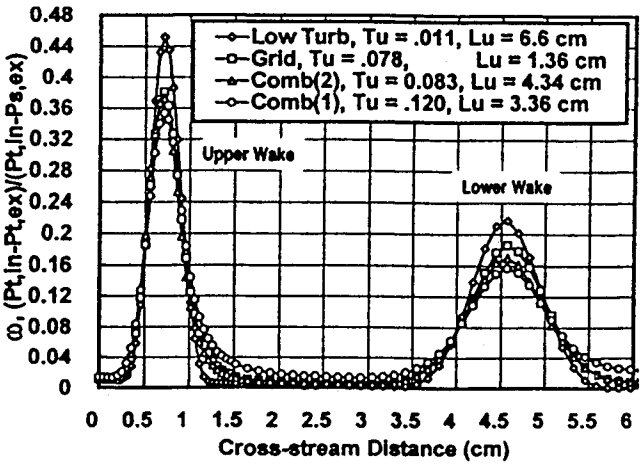

Fig. 5 Comparison of exit total pressure loss surveys, position 8, upper and lower wakes, $M_{EX} = 0.27$

eters as given by Eq. (7-67) of NASA SP-290 given below as Eq. (1).

The trailing edge blockage accounts for between 36 percent (low turbulence) to 27 percent [Comb(1)] of the total wake loss at position 6. Using the analysis from Chap. 7 of NASA SP-290 (Glassman, 1973), the trailing edge has a drag coefficient, which ranges from 0.127 to 0.158, and averages 0.145. The drag coefficient was estimated as twice the momentum thickness, δ_2, attributable to the trailing edge, divided by the trailing edge thickness, d. The trailing edge momentum thickness is the mixed-out wake momentum thickness minus the boundary layer momentum thickness adjusted for blockage.

The mixed-out loss, $\bar{e}_2$, can be determined from the integral parameters for incompressible flow, but it requires knowledge of the exit angle. The exit angle, α_1, was taken as the inverse cosine of the cross-stream distance, CL, divided by the vane spacing, 11.77 cm. At position 6, the cross-stream distance, CL, was determined from the distance between the suction surface of vane 3 and the centerline of the vane 2 wake. For position 8, CL was taken as the cross-stream distance between the peak velocity deficit location of the wakes of vane 2 and 3. Equation (7-82) of NASA SP-290 was used to determine $\bar{e}_2$, and is repeated below as Eq. (2):

$$\bar{e}_1 = \frac{\delta_3^*}{1 - \delta_1^*} \tag{1}$$

$$\bar{e}_2 = 1 - \frac{\sin^2\alpha_1\left(\dfrac{1-\delta_1^*-\delta_2^*}{1-\delta_1^*}\right)^2 + \cos^2\alpha_1(1-\delta_1^*)^2}{1 + 2\cos^2\alpha_1[(1-\delta_1^*)^2 - (1-\delta_1^*-\delta_2^*)]} \tag{2}$$

where δ_1^*, δ_2^*, and δ_3^*, are the dimensionless displacement, momentum and energy thicknesses, respectively.

The wake half-velocity widths, W, reported in Table 1 are uncorrected for shear displacement effects. In a velocity gradient, a total pressure probe tends to read a pressure that is off-center, since the probe averages the square of the velocity. According to Moffat (1980), the shift of the effective centerline toward the high velocity side is about 0.15 times the outer diameter. The outer diameter of the total pressure probe used was about 0.079 cm, so the correction for the displacement due to the probe (ΔY_{prb}) should be about 0.0118 cm. To apply this correction to the loss coefficients, $\bar{e}_{1,prb}$ and $\bar{e}_{2,prb}$, the coefficients were multiplied by $(1 + 2(\Delta Y_{prb})/W)$. At both positions 6 and 8, a comparison of the total losses shows that the low-turbulence case, the grid condition, and the far combustor case [Comb(2)] are all fairly consistent. The grid and far combustor have a reduced suction surface boundary layer loss but an increased "background" loss. The close combustor case [Comb(1)] has an elevated loss, primarily due to the "background" loss. Finally, to compare the mixed-out losses attributed only to the vane boundary layers and the trailing edge loss, the "background" loss was subtracted from the mixed-out kinetic energy loss coefficient $\bar{e}_{2,prb-bgd}$. At position 6, a comparison shows the net wake losses are fairly consistent, ranging from 0.442 to 0.458. A noticeable increase in losses occurs between position 6 and 8. Some of the increase in loss between the two stations could be due to slight differences in the upstream and downstream setup, the uncertainty in experimentally determining the loss coefficient, and the mixing out of spanwise nonuniformities in the flow. For the close combustor case, at least part of this increase in "background" losses appears to be due to mixing together of the two wakes.

Wake Growth Estimates. Single-wire profiles show the same trends as the total pressure profiles. Figure 6 shows the mean velocity deficit profiles for the wakes at position 6. Note that the velocity deficit is based on the average "free-stream" velocity at a distance of 3σ from the wake centerline. The single-wire measurements revealed a variation in the free-stream velocity outside the wake, so the 3σ point was chosen for consistency. Again, the low-turbulence wake has a deeper velocity deficit (by about 20 percent) and a narrower profile, while the high-turbulence wakes are shallower and broader. Figure 7 shows the velocity defect profiles taken from position 8 for the upper and lower wakes with trends similar to those discussed in Fig. 6. As in Fig. 6, there is an increased spreading of the upper wake on the suction surface side.

An analysis of the wake growth yields the parameters listed in Table 2. This analysis for cylinder wakes Hinze (1975) is considered valid for 50 or more diameters downstream from a cylinder. While the present wake data neither originate from a cylinder nor are they taken beyond 50 trailing edge diameters,

Table 1 Exit loss parameters, positions 6 and 8, $M_{EX} = 0.27$

Cond.	Low Turb.		Grid		Comb(2)		Comb(1)	
	Position		Position		Position		Position	
	6	8	6	8	6	8	6	8
Exit Conditions								
Ma_{ex}	.2689	.2703	.2698	.2691	.2701	.2706	.2704	.2696
P_t (kPa)	99.4	98.7	98.8	98.5	97.5	97.5	97.5	96.1
T_t (K)	292.2	296.8	293.1	296.6	293.1	296.1	293.1	298.5
α_1 (deg)	71.71	70.98	71.61	70.82	71.44	70.90	71.59	70.96
Wake parameters								
δ_1 (cm)	.0893	.1075	.0922	.1086	.0897	.1009	.1030	.1114
δ_2 (cm)	.0807	.0989	.0846	.1018	.0826	.0951	.0958	.1058
δ_3 (cm)	.1538	.1899	.1624	.1973	.1588	.1849	.1850	.2065
CL (cm)	3.694	3.837	3.714	3.867	3.688	3.851	3.719	3.842
W (cm)	.6217	.8956	.6714	.9554	.6972	.9703	.7637	.9965
Suction Surface Boundary Layer Parameters (Vane 3)								
$\delta_{1,ss}$ (cm)	.0683		.0559		.0555		.0565	
$\delta_{2,ss}$ (cm)	.0462		.0403		.0403		.0425	
$\delta_{3,ss}$ (cm)	.0796		.0713		.0718		.0767	
$Cf/2_{ss}$	.00143		.00175		.00174		.00181	
Loss Parameters								
$\bar{\omega}$	.0434	.0520	.0456	.0535	.0449	.0502	.0521	.0564
$\bar{\omega}_{max}$	.2569	.2170	.2339	.1857	.2282	.1696	.2191	.1564
$\bar{\omega}_{bgd}$	.0002	.0031	.0028	.0077	.0020	.0058	.0100	.0151
$\bar{e}_1$	.0428	.0511	.0449	.0526	.0443	.0493	.0513	.0555
$\bar{e}_{bgd}$	.0002	.0030	.0027	.0076	.0020	.0057	.0098	.0149
$\bar{e}_2$	.0443	.0523	.0462	.0534	.0454	.0501	.0523	.0559
$\bar{e}_{1,prb}$	.0443	.0523	.0465	.0538	.0457	.0505	.0528	.0567
$\bar{e}_{2,prb}$	.0460	.0538	.0479	.0548	.0470	.0513	.0540	.0573
$\bar{e}_{2,prb-bgd}$	.0458	.0508	.0452	.0472	.0450	.0456	.0442	.0424

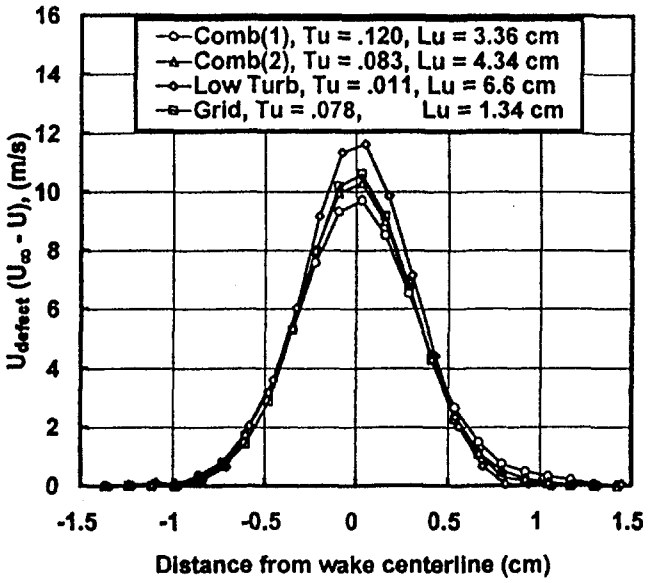

Fig. 6 Comparison of single-wire wake profiles, position 6, $M_{EX} = 0.27$

Table 2 Wake growth parameters (vane 2)

Distance from vane trailing edge to probe arc			
Position 6	X_1 = 6.965 cm		
Position 8	X_1 = 13.388 cm		
Position 6 wake			
Condition	W (cm)	$U_{max,def}/U_\infty$	Origin (a) (cm)
Low Turb	0.6828	0.1266	0.573
Grid	0.6852	0.1171	0.628
Comb(2)	0.7124	0.1120	1.242
Comb(1)	0.7425	0.1059	1.950
Position 8 wake			
Condition	W (cm)	$U_{max,def}/U_\infty$	Origin (a) (cm)
Low Turb	0.9884	0.1116	2.407
Grid	1.0032	0.0959	2.884
Comb(2)	1.0372	0.0883	4.008
Comb(1)	1.1172	0.0736	6.794

the analysis does provide a means to compare the relative growth of the wakes between stations 6 and 8 behind vane 2. Taking into account the single-wire probe holder length, the wire intersected the wake 6.96 cm and 13.39 cm downstream from the trailing edge of the vane at positions 6 and 8, respectively. In Table 2, the half-velocity width of the wake is based on the locations at which half the peak defect velocity occurs on each side of the wake centerline. Also, the ratio of the maximum defect velocity divided by the free-stream velocity is given. Based on the analysis of Hinze, the following equation can be used to estimate the origin, a, of the wake:

$$a = \frac{W^2}{0.1871d} - X_1 \tag{3}$$

where d is the trailing edge diameter (0.34 cm) and X_1 is the downstream distance from the trailing edge to the probe. The key feature of growth is shown by comparing the origin of the wakes between positions 6 and 8. All the wakes with elevated levels of free-stream turbulence show a substantial increase in the distance to the origin as compared to the low free-stream turbulence wake. For example, a increases from 0.573 to 2.407 cm in the low-turbulence case versus 1.950 to 6.794 cm in the highest turbulence case. This comparison supports the contention that the free-stream turbulence enhances spreading of the wakes, and therefore the mixing within the wakes.

Turbulence Parameters. Measuring the characteristics of the turbulence at the exit of the cascade helps to describe the wake in terms of pertinent mixing parameters and also to document the turbulence boundary condition for the rotor. Figure 8 shows the u' distribution taken at position 6. With increasing free-stream turbulence, the profiles exhibit elevated fluctuation levels in the suction surface boundary layer, through the passage, and across the wake. The wakes exhibit the characteristic double-peak behavior due to the occurrence of maximum velocity gradients on either side of the peak, with their resulting high production rates.

The v' distributions for position 6 are shown in Fig. 9. Near the suction surface of the upper vane, the v' distributions show a near-wall increase due to boundary layer production. Outside

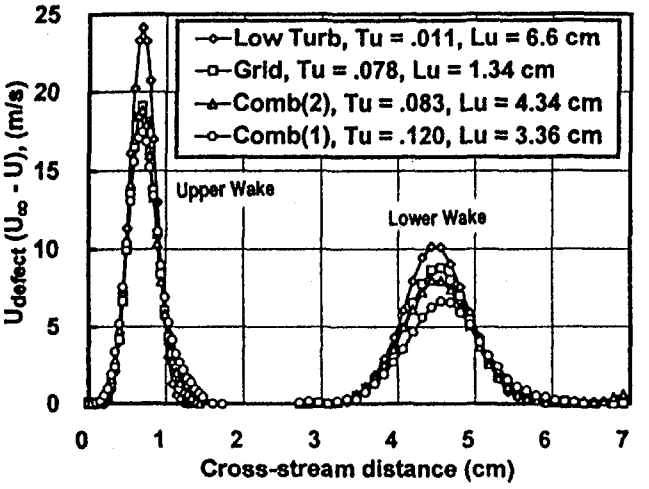

Fig. 7 Comparison of single-wire wake profiles, position 8, upper and lower wakes, $M_{EX} = 0.27$

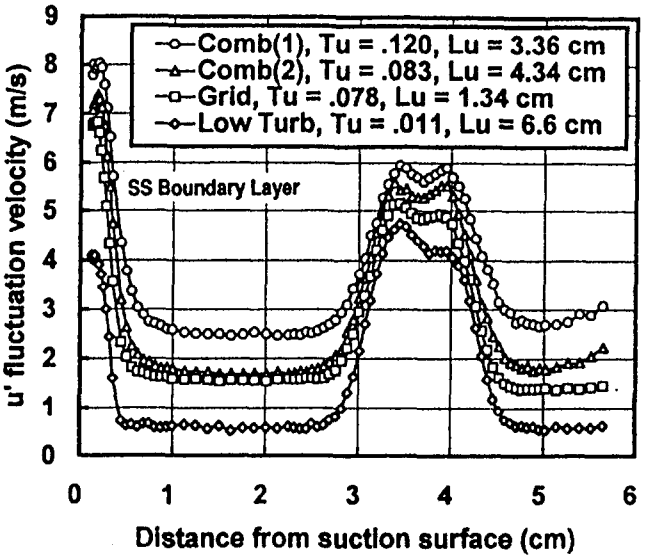

Fig. 8 Comparison of X-wire u' distributions, position 6, $M_{EX} = 0.27$

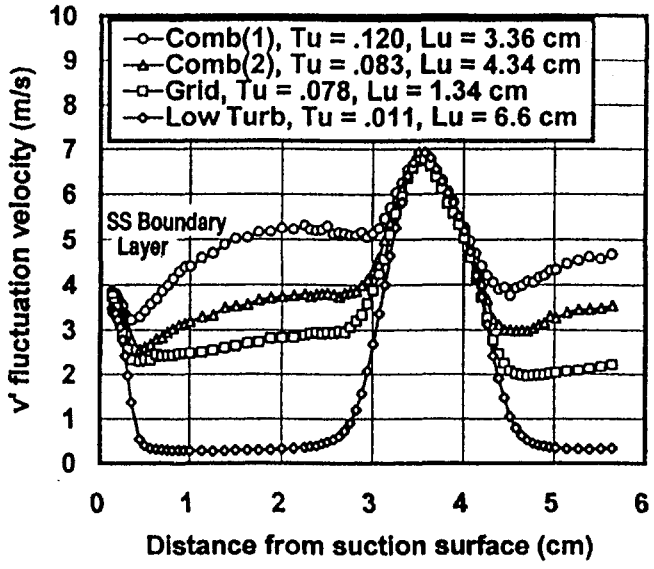

Fig. 9 Comparison of X-wire v' distributions, position 6, $M_{EX} = 0.27$

the boundary layer but close to the wall, the attenuation of v' due to the wall is evident in the profile. The energy in the v' component is redirected into the u' and w' components. On the side of the wake developing off the suction surface of vane 2, evidence of the history of v' attenuation is apparent. Note that the v' distributions are also skewed off-centerline toward the pressure surface. The pressure side of the wake has a higher initial velocity gradient than the suction surface due to its boundary layer profile, and this gradient results in high production rates.

The u' fluctuating velocity distributions taken at position 8 with an X-wire are shown in Fig. 10. These u' distributions agree very well with the single-wire u' distributions. Comparison of the level of u' in the region between the two wakes shown in Fig. 10 with that at position 6 (see Fig. 8) shows the level of u' is increasing in the streamwise direction. The straining that occurs through the turbine passage produces significant anisotropy. This increase in u' is due to the redistribution of the turbulence components, which slowly tends to return the turbulence to isotropy. The turbulence fluctuations themselves redistribute the high levels of energy in the v' and w' components into the u' component after the streamwise straining is stopped. The u' distributions though the wakes show the characteristic double peak behavior for both upper and lower wakes. The higher level of u' in the wake is skewed toward the suction surface side for the high free-stream turbulence cases. This skewed u' distribution is due to turbulence history effects remaining from the suction surface boundary layer. The dissipation levels around the peak on the wake suction surface side are about the same for all four cases.

The v' fluctuation distributions for position 8 are shown in Fig. 11. The notable feature is that the level of v' in the core flow is now the same as the level in the lower wake for the close combustor. Also, if we estimate the turbulent kinetic energy, TKE, at position 8 based on the approximation that $\overline{q'^2}/2 = (\overline{u'^2}/2 + 2 \times \overline{v'^2}/2)$, we find that the exit TKE is actually slightly greater than the inlet TKE.

In addition to u' and v' distributions shown in Figs. 9–11, Table 3 provides integral length scale, energy scale, and dissipation rate information at different locations in both the core flow and the wake. This information will provide boundary conditions for the downstream rotor. Ames (1997) found that vane pressure surface heat transfer augmentation correlates with $Tu_\infty Lu_\infty^{-1/3}\ \mathrm{Re}_{ex}^{1/3}$. While rotor heat transfer is complicated by the addition of intermittent wakes, the turbulence parameters and the mean velocity gradients are believed to be useful information for the assessment of rotor heat transfer and aerodynamics.

Wake Mixing. Vane wakes provide the hydrodynamic and thermodynamic boundary conditions for the downstream rotor. Accurate modeling of the mixing in wakes is important for accurate prediction of their development. This section examines the mixing, based on the experimental measurements, occurring in the wakes for the four turbulence conditions.

Table 2 documented the rapid growth of the wakes with elevated levels of free-stream turbulence. Enhanced mixing was inferred from this data. Figure 12 shows shear stress distributions taken at position 6 across the wake. Generally, the high-turbulence cases show deeper and broader shear stress profiles. Similar trends are shown in Fig. 13 for both the upper and lower wakes taken at position 8.

Figures 12 and 13 indicate that the pressure surface side of the wake is most affected by the different types of turbulence in terms of asymmetries in the magnitude of the Reynolds shear stress peaks on either side of the centerline. In addition, the level of v' is elevated on the pressure surface side of the wake with respect to the suction surface side (see Figs. 9 and 11), due to the enhanced production in the pressure surface side of the wake where the velocity gradient is greatest.

Not only are asymmetries in the profiles of shear stress and velocity fluctuations exhibited, but upon examination of Table 3, it becomes apparent that the dissipation rate on each side of

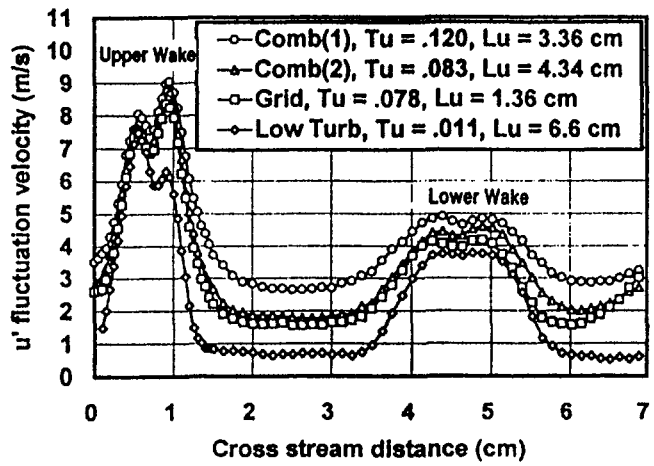

Fig. 10 Comparison of X-wire u' distributions, position 8, $M_{EX} = 0.27$

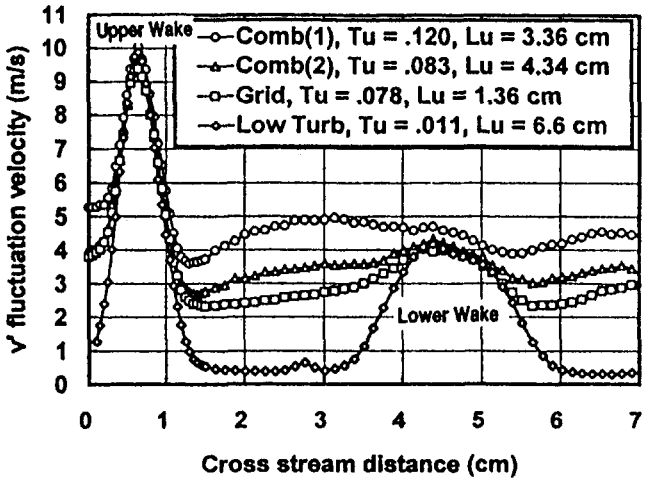

Fig. 11 Comparison of X-wire v' distributions, position 8, $M_{EX} = 0.27$

Table 3 Wake turbulence characteristics

	Tu	U (m/s)	Lx (cm)	Lu (cm)	ε (m^2/s^3)	Y (cm)	Pos
Comb(1)	0.0276	91.15	1.384	0.660	3622	2.032	core
Pos 6	0.0703	84.59	1.201	0.780	40416	3.452	-.71σ
	0.0751	80.25	0.980	0.691	47547	3.780	CL
	0.0698	83.66	1.819	1.313	22692	4.107	+.71σ
Comb(2)	0.0179	90.43	2.179	0.790	800	2.032	core
Pos 6	0.0671	83.59	1.130	0.709	37257	3.459	-.71σ
	0.0709	79.35	0.932	0.650	41053	3.780	CL
	0.0651	83.58	1.900	1.247	19415	4.102	+.71σ
Grid	0.0173	90.92	2.154	0.384	1508	2.032	core
Pos 6	0.0639	84.26	0.777	0.610	38485	3.475	-.71σ
	0.0679	75.35	0.691	0.572	41129	3.780	CL
	0.0622	83.38	1.207	0.963	21712	4.087	+.71σ
Low	0.0601	83.85	0.417	0.541	35554	3.452	-.71σ
Turb	0.0623	79.62	0.335	0.478	36953	3.759	CL
Pos 6	0.0548	83.54	0.574	0.777	18569	4.069	+.71σ
Comb(1)	0.0314	89.14	1.140	0.813	4060	2.159	core
Pos 8	0.0578	84.69	1.775	1.232	14275	4.229	-.71σ
	0.0589	82.28	1.702	1.110	15380	4.729	CL
	0.0536	85.46	2.306	1.588	9090	5.232	+.71σ
Comb(2)	0.0183	88.67	2.223	0.503	1266	2.159	core
Pos 8	0.0538	84.11	1.842	1.105	12601	4.181	-.71σ
	0.0553	80.81	1.400	0.848	15744	4.638	CL
	0.0528	84.24	2.289	1.420	9300	5.083	+.71σ
Grid	0.0200	88.99	1.882	0.531	1602	2.159	core
Pos 8	0.0499	83.98	1.539	0.907	12160	4.196	-.71σ
	0.0504	80.44	0.810	0.688	14455	4.651	CL
	0.0467	84.06	1.026	1.049	8656	5.103	+.71σ
Low	0.0464	83.33	0.579	0.716	12135	4.199	-.71σ
Turb	0.0485	79.42	0.579	0.648	13195	4.638	CL
Pos 8	0.0445	83.59	0.787	0.958	8072	5.075	+.71σ

the wake is quite different. In Table 3, the values of turbulence quantities on the wake centerline are compared to those at $\pm 0.71\sigma$. The maximum production is expected to occur at this location, based on analysis of the theoretical error function wake profile and assuming constant ν_m across the wake. At position 6, the magnitude of ϵ is typically 85 to 90 percent of the centerline value at -0.71σ (the pressure surface side) and only 50 percent of the centerline value at $+0.71\sigma$ (the suction surface side). At position 8, the corresponding values are 80 to 90 percent and 60 percent, respectively. Similar asymmetries were reported by Nakayama and Kreplin (1994). Their measurements indicated that the peak in production corresponds to the side of the wake which originates from the boundary layer with the larger C_f, and hence larger $\partial U/\partial y$. However, from a TKE balance, they found that locally production does not equal dissipation, especially in the strongly asymmetric wakes. The production peak is balanced by transverse diffusion, while the dissipation peak is offset toward the edge of the wake. Thus, the process of symmetrizing a wake originating from different initial boundary layers results in the production of TKE in the high shear region, and the diffusion to the edges of the wake, where dissipation occurs. This effect is most pronounced on the side of the wake with the larger production. The diffusion process is enhanced with the addition of free-stream turbulence.

A mean eddy diffusivity can be estimated from the shear stress measurements and the local velocity gradients. Table 4 lists estimates for the eddy diffusivity average across the wake in regions of high velocity gradient for the four conditions at

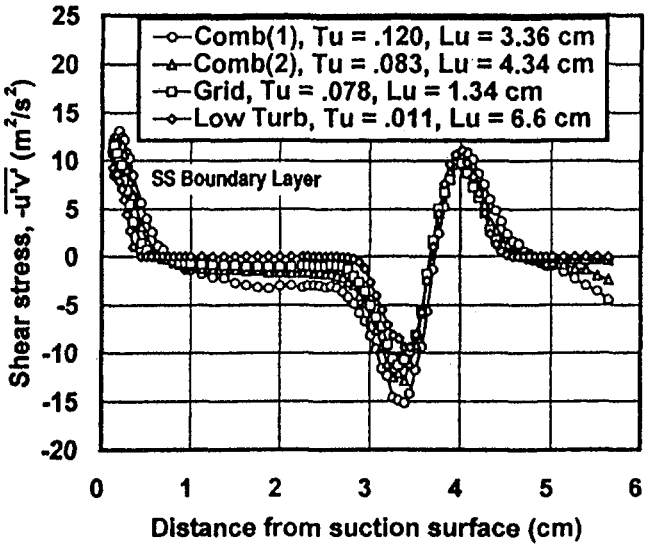

Fig. 12 Comparison of exit shear stress distributions, position 6, M_{EX} = 0.27

the two measurement positions. In addition, a mean local shear stress gradient, a mixing length (ℓ), the half-velocity width (W), the mean energy scale (Lu), and the maximum velocity deficit in the wake are given in the table. Note that the values of Lu in Table 4 represent the average of this parameter across the wake at a particular measurement plane, and thus are different than the local values listed in Table 3. The estimates show a substantial increase in eddy diffusivity for the flow with a turbulent core. In addition, the eddy diffusivity grows substantially in the streamwise direction for the turbulent flows. These results are generally consistent with the estimates obtained by applying the analysis of Hinze (1975) and Schlichting (1979) for cylinder wakes, which predicts that the mean value of eddy viscosity in the present low turbulence wakes should range from 0.0030 m^2/s to 0.0039 m^2/s.

For wakes developing in the presence of elevated levels of inlet turbulence, the mixing in the wake can be expected to be affected by the flow field turbulence as the turbulence is entrained into the wake. In the case of wake mixing, the combustor with spool [Comb(2)] has significantly enhanced mixing over the grid turbulence due to its larger scale. Based on Table 4, the

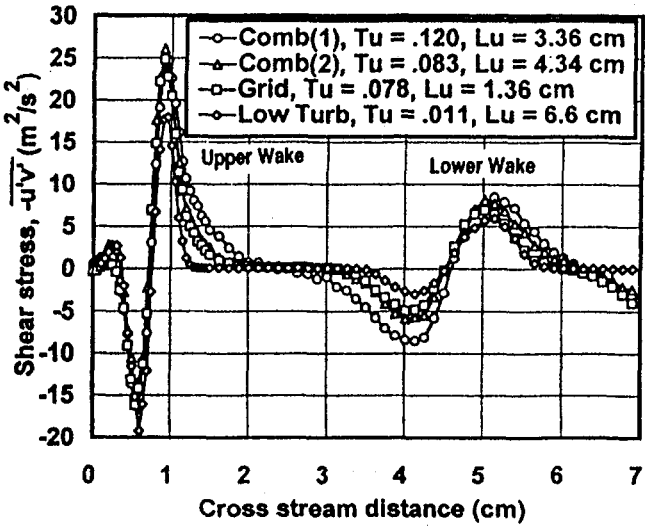

Fig. 13 Comparison of exit shear stress distributions, position 8, M_{EX} = 0.27

Table 4 Wake mixing and turbulence parameters

Position 6						
Cond.	|dU/dy| (1/s)	ν_m (m^2/s)	ℓ (cm)	Width (cm)	Lu (cm)	U_{max}, defect (m/s)
Comb(1)	1753	0.00694	0.124	0.7382	0.851	10.56
Comb(2)	1930	0.00556	0.104	0.7012	0.790	11.24
Grid	1981	0.00475	0.094	0.7006	0.635	11.52
LowTurb	2278	0.00410	0.079	0.6664	0.566	12.40
Position 8						
Cond	|dU/dy| (1/s)	ν_m (m^2/s)	ℓ (cm)	Width (cm)	Lu (cm)	U_{max}, defect (m/s)
Comb(1)	758	0.01060	0.257	1.0471	1.262	6.84
Comb(2)	978	0.00701	0.185	0.9866	1.074	8.23
Grid	1019	0.00572	0.162	0.9599	0.851	8.49
LowTurb	1189	0.00344	0.109	0.938	0.747	10.68

combustor with spool conditions shows a significant increase in eddy diffusivity over the grid turbulence. For example, at position 8 the values of ν_m for these two cases are 0.00701 and 0.00572 m^2/s, respectively. This enhanced diffusivity is also reflected by the wake width and peak velocity deficit.

The mixing length, l, defined as ν_m/v', is tabulated for comparison to the half-width and the energy scale in Table 4. For the low-turbulence case, the ratio l/W is expected to remain constant, especially in the far field where the characteristics of the wake have reached an equilibrium state. A comparison of l and W immediately shows that with elevated levels of free-stream turbulence, the mixing length in the wake no longer scales on the wake width. The ratio l/W also grows in the downstream direction. This growth demonstrates that as turbulence with the large-scale characteristics of the free-stream enters the wake, the mixing is enhanced. Another measure of a mixing length is the energy length scale, Lu. A comparison between l and Lu shows that at position 6 the ratios are consistent. Assuming isotropic turbulence and a value of the constant $C_\mu = 0.09$ in the standard $k-\epsilon$ model, the ratio l/Lu is calculated to be about 0.135. At position 6, the experimental data are reasonably consistent with this value. For the wake behind vane 2 (X_1 = 13.15 cm) at position 8, l/Lu averages 0.18 and is higher for the higher levels of turbulence.

Accurately predicting the development of wakes in the streamwise direction is dependent on our ability to model the mixing process. The comparison between the mixing length, l, and the wake width, W, indicated that a mixing length model would work adequately for a low-turbulence situation but not for the cases with elevated levels of free-stream turbulence. The comparison between the mixing length, l, and the energy scale, Lu, shows initially that Lu gives a reasonable estimate for the mixing length. However, as the larger-scale turbulence in the free stream begins to mix into the wake, the energy scale begins to underpredict the impact of these large-scale motions on the mixing process.

Conclusions

In this paper, the influence of free-stream turbulence on wake losses, wake growth, overall turbulence parameters, and on mixing were examined. Losses were broken down into losses that were found in the free stream and losses that were found in the wake. About 50 to 60 percent of the total losses could be attributed to the vane boundary layers, while 30 to 40 percent of the total losses were attributable to separation off the trailing edge of the vane. The remainder of the losses occurred in the core region of the flow. The cases with elevated levels of free-stream turbulence were found to correlate with significant losses in the "core" of the flow, or the part of the flow not expected to be influenced by the wake or the suction surface boundary layer. First-order estimates of turbulent production in this region indicated turbulent mixing in the core of the flow is responsible for at least one third to one half of these "background" losses. The origin of the remainder of these "background" losses is not presently understood.

The elevated free-stream turbulence was also found to have a significant effect on wake growth. Generally, the wakes with elevated turbulence were found to be broader and had smaller peak velocity deficits. Based on an estimate of the wake origins, the wakes with the free-stream turbulence spread faster than the low-turbulence case.

The overall level of turbulence and dissipation rate inside the wakes and in the free-stream was determined, and can be used as the inlet turbulence boundary condition in assessing the expected effects of free-stream and wake turbulence on rotor heat transfer. Additionally, an asymmetry in the dissipation rate was found, with the value on suction surface side typically half that at the centerline.

Eddy diffusivities and mixing lengths were estimated using X-wire measurements of Reynolds shear stress to quantify how turbulence affected mixing in the wake. The free-stream turbulence was found to affect eddy diffusivities strongly. The combustor at both levels of turbulence had a greater effect than the grid turbulence due to a larger turbulent scale. At the last measuring position, the average eddy diffusivity across the close combustor condition wake was three times the eddy diffusivity of the low-turbulence wake.

Acknowledgments

The authors would like to express our gratitude to NASA Lewis Research Center for funding this experimental study and also to Jim van Fossen, who served as the technical monitor. The authors would also like to acknowledge Allison Engine Company for providing the experimental facility where the work was performed.

References

Ames, F. E., and Moffat, R. J., 1990, "Heat Transfer With High Intensity, Large Scale Turbulence: The Flat Plate Turbulent Boundary Layer and the Cylindrical Stagnation Point," Report No. HMT-43, Thermosciences Division of Mechanical Engineering, Stanford University.

Ames, F. E., 1994, "Experimental Study of Vane Heat Transfer and Aerodynamics at Elevated Levels of Turbulence," NASA CR 4633.

Ames, F. E., 1997, "The Effects of Large-Scale, High Intensity Turbulence on Vane Heat Transfer," ASME JOURNAL OF TURBOMACHINERY, Vol. 119, p. 23.

Arts, T., Lambert de Rouvroit, M., and Rutherford, A. W., 1990, "Aero-thermal Investigation of a Highly Loaded Transonic Linear Turbine Guide Vane Cascade," Technical Note 174, von Karman Institute for Fluid Dynamics, Belgium.

Bicen, A. F., and Jones, W. P., 1986, "Velocity Characteristics of Isothermal and Combusting Flows in a Model Combustor," *Combust. Sci. and Technology*, Vol. 49, p. 1.

Denton, J. D., 1993, "Loss Mechanisms in Turbomachines," ASME JOURNAL OF TURBOMACHINERY, Vol. 115, pp. 621–656.

Dullenkopf, K., Schulz, A., and Wittig, S., 1991, "The Effect of Incident Wake Conditions on the Mean Heat Transfer of an Airfoil," ASME JOURNAL OF TURBOMACHINERY, Vol. 113, pp. 412–418.

Dullenkopf, K., and Mayle, R. E., 1994, "The Effects of Incident Turbulence and Moving Wakes on Laminar Heat Transfer in Gas Turbines," ASME JOURNAL OF TURBOMACHINERY, Vol. 116, p. 23.

Frota, M. F., 1982, "Analysis of the Uncertainties in Velocity Measurements and Technique for Turbulence Measurements in Complex Heated Flows With Multiple Hot-Wires," Ph.D. Dissertation, Dept. Mech. Engr., Stanford University.

Glassman, A. J., ed., 1973, *Turbine Design and Application*, Vols. 1–3, NASA SP-290.

Gregory-Smith, D. G., and Cleak, J. G. E., 1992, "Secondary Flow Measurements in a Turbine Cascade With High Inlet Turbulence," ASME JOURNAL OF TURBOMACHINERY, Vol. 114, p. 173.

Hancock, P. E., and Bradshaw, P. 1983, "The Effect of Free-Stream Turbulence on Turbulent Boundary Layers," ASME *Journal of Fluids Engineering,* Vol. 105, p. 284.

Hinze, J., 1975, *Turbulence,* 2nd ed., McGraw-Hill, New York.

Hoheisel, H., Kiock, R., Lichtfuss, H. J., and Fottner, L., 1987, "Influence of Free-Stream Turbulence and Blade Pressure Gradient on Boundary Layer and Loss Behavior of Turbine Cascades," ASME JOURNAL OF TURBOMACHINERY, Vol. 109, p. 210.

Hoffmann, J. A., and Kassir, S. M., 1989, "Effects of Free Stream Turbulence on Turbulent Boundary Layers With Mild Adverse Pressure Gradients," AIAA Paper No. 88-3757-CP.

Kline, S. J., and McClintock, F. A., Jan., 1953, "Describing Uncertainties in Single Sample Experiments," *Mech. Engr.,* Jan., p. 3.

Ladwig, M. and Fottner, L., 1993, "Experimental Investigations of the Influence of Incoming Wakes on the Losses of a Linear Turbine Cascade," ASME Paper No. 93-GT-394.

Mayle, R. E., 1991, "Role of Laminar-Turbulent Transition in Gas Turbine Engines," ASME JOURNAL OF TURBOMACHINERY, Vol. 113, pp. 509–537.

Mee, D. J., Baines, N. C., Oldfield, M. L. G., and Dickens, T. E., 1992, "An Examination of the Contributions to Loss on a Transonic Turbine Blade in Cascade," ASME JOURNAL OF TURBOMACHINERY, Vol. 114, pp. 155–162.

Moffat, R. J., 1980, "Experimental Methods in the Thermosciences," Dept. Mech. Engr., Stanford, University.

Moore, J., Shaffer, D. M., and Moore, J. G., 1987, "Reynolds Stress and Dissipation Downstream of a Turbine Cascade," ASME JOURNAL OF TURBOMACHINERY, Vol. 109, p. 258.

Nakayama, A., and Kreplin, H.-P., 1994, "Characteristics of Asymmetric Turbulent Near Wakes," *Phys. Fluids,* Vol. 6, No. 7, p. 2430.

Nealy, D. A., Mihelc, M. S., Hylton, L. D., and Gladden, H. J., 1984, "Measurements of Heat Transfer Distribution Over the Surfaces of Highly Loaded Turbine Nozzle Guide Vanes," ASME *Journal of Engineering for Gas Turbines and Power,* Vol. 106, pp. 149–158.

Schlichting, H., 1979, *Boundary Layer Theory,* 7th ed., McGraw-Hill, New York.

Van Fossen, G. J., and Ching, C. Y., 1994, "Measurements of the Influence of Integral Length Scale on Stagnation Region Heat Transfer," presented at the Fifth Int. Sym. on Transport Phenomena and Dynamics of Rotating Machinery (ISROMAC-5), Kaanapali, Maui, HI, Paper No. TP-16.

Van Fossen, G. J., and Simoneau, R. J., 1994, "Stagnation Region Heat Transfer: The Influence of Turbulence Parameters, Reynolds Number, and Body Shape," presented at the AIAA/ASME Thermophysics and Heat Transfer Conference, Colorado Springs, CO, June 20–23.

Van Dresar, N. T., and Mayle, R. E., 1988, "Stagnation Transfer Rates for Incident Flow With High Turbulence Intensities," ASME HTD-Vol. 101, p. 165.

Weygandt, J. H., and Mehta, R. D., 1995, "Three-Dimensional Structure of Straight and Curved Plane Wakes," *J. Fluid Mechanics,* Vol. 282, pp. 279–311.

White, F. M., 1991, *Viscous Fluid Flow,* 2nd ed., McGraw-Hill, New York.

Wittig, S., Schulz, A., Dullenkopf, K., and Fairbank, J., 1988, "Effects of Free-Stream Turbulence and Wake Characteristics on Heat Transfer Along a Cooled Gas Turbine Blade," ASME Paper No. 88-GT-179.

Wubben, F. J. W., 1991, "Single and Cross Hot-Wire Anemometry in Incompressible Flow," Report LR-663, Faculty of Aerospace Engineering, Delft University of Technology, The Netherlands.

Zimmerman, D. R., 1990, "Three-Dimensional Laser Anemometer Measurements in a Linear Turbine Vane Cascade," *Forum on Turbulent Flows—1990,* ASME FED-Vol. 94, p. 143.

Influence of Leading-Edge Geometry on Profile Losses in Turbines at Off-Design Incidence: Experimental Results and an Improved Correlation

M. W. Benner

S. A. Sjolander

Department of Mechanical and Aerospace Engineering, Carleton University, Ottawa, Ontario, Canada

S. H. Moustapha

Pratt & Whitney Canada, Inc., Longueuil, Quebec, Canada

The most recent correlations for turbine profile losses at off-design incidence include the leading-edge diameter as the only aspect of the leading-edge geometry that influences the losses. Cascade measurements are presented for two turbine blades that differ primarily in their leading-edge geometries. The incidence was varied over a range of ±20 deg and the results show significant discrepancies between the observed profile losses and those predicted by the available correlations. Using data from the present experiments, as well as cases from the literature for which sufficient geometric data are given, a revised correlation has been developed. The new correlation is a function of both the leading-edge diameter and the wedge angle, and it is significantly more successful than the existing correlations. It is argued that the off-design loss behavior of the blade is influenced by the magnitude of the discontinuity in curvature at the points where the leading-edge circle meets the rest of the blade profile. The wedge angle appears to be an approximate and convenient measure of the discontinuity in curvature at these blend points.

Introduction

Turbine design is an iterative process involving a trade-off between the aerodynamic performance at design and off-design conditions. Furthermore, the design will be influenced by non-aerodynamic factors. For example, durability considerations will impose certain cross-sectional area and maximum thickness requirements on the airfoils. These requirements might be met by using large leading-edge diameters. However, large leading-edge diameters will increase the losses and heat loads at the design condition, due to the increase in size of the associated horseshoe vortices. On the other hand, the large diameters will make the airfoils more tolerant to off-design incidence. Thus, a careful balance must be struck in the design process in an effort to satisfy a large number of sometimes conflicting requirements.

Empirical loss correlations and meanline analysis continue to play an important role in this process, particularly in the early stages of design. Therefore, there is an ongoing need to review and improve these correlations.

Probably the most widely used empirical loss system for axial turbines is that due to Ainley and Mathieson (1951). The Ainley and Mathieson system is a complete system in that it includes correlations for all the components of the loss and for both design and off-design conditions. It was subsequently modified by Dunham and Came (1970) to reflect the improved understanding of some aspects of the flow, notably the secondary flows. Further improvements to the design-point correlations were presented by Kacker and Okapuu (1982). Craig and Cox (1971) and a few other researchers have also proposed complete loss systems, but these are not as widely used as those based on Ainley and Mathieson's work.

Contributed by the International Gas Turbine Institute and presented at the 40th International Gas Turbine and Aeroengine Congress and Exhibition, Houston, Texas, June 5–8, 1995. Manuscript received by the International Gas Turbine Institute March 10, 1995. Paper No. 95-GT-289. Associate Technical Editor: C. J. Russo.

In 1990, Moustapha et al. (1990) reviewed the available correlations for profile and secondary losses at off-design conditions and compared them with a range of recent measurements. The authors concluded that the existing correlations do not adequately account for recent improvements in airfoil design and are no longer as reliable as they once were. Based on the substantial database of measurements they had collected, the authors devised new correlations for the profile and secondary losses. These were significantly more successful at correlating the data than the Ainley and Mathieson correlations. Drawing on the work of Mukhtarov and Krichakin (1969), and unlike Ainley and Mathieson, Moustapha et al. included the leading-edge diameter as a correlating parameter. The new off-design correlations were intended for use with the Kacker and Okapuu design-point correlations to form a complete loss system.

To verify the Moustapha et al. correlations and to investigate further the influence of the leading-edge geometry on the off-design behavior of turbine blades, an experimental study was initiated in a low-speed cascade wind tunnel. This paper presents the results obtained for the profile losses. Two blade designs, which differ mainly in their leading-edge geometries, have been investigated. Based on the results, an improved correlation for off-design profile losses is introduced.

Experimental Results

Cascade Test Section. All measurements presented here were obtained in the linear cascade test section shown schematically in Fig. 1. Two cascades, designated CC2 and CC3, were examined. The sets of five blades are mounted on a turntable which allows the incidence to be varied over a wide range. The side flaps and tailboards are used to adjust the inlet flow uniformity and the outlet flow periodicity.

The data for CC2 were obtained primarily during a study of the effects of axial velocity ratio (AVR) on turbine cascade measurements (Rodger et al., 1992). The endplates shown in the figure are adjustable and allow the divergence of the stream-

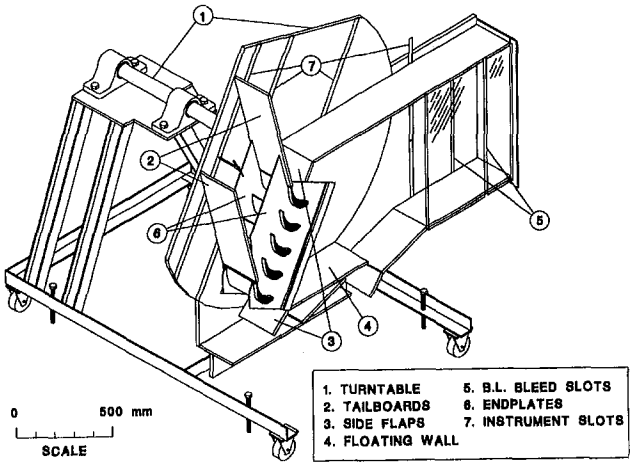

Fig. 1 Schematic of variable-incidence test section

tube through the cascade, and thus the axial velocity ratio, to be varied. For both cascades in the present study, the AVR was varied at each incidence to provide data over a range that included AVR = 1.0. The loss coefficients presented here are the interpolated values at AVR = 1.0. In addition to adjusting the AVR values, the spanwise distributions of the losses were examined at all values of incidence. In all cases there was a reasonable extent of constant loss about the midspan of the blade. Thus, the results are as two dimensional as can be reasonably achieved in a cascade of fairly low aspect ratio.

All measurements were made at a constant Reynolds number of $3.0 \pm 0.1 \times 10^5$, based on inlet velocity and true chord. The velocity at the cascade inlet was typically about 30 m/s so that conditions were essentially incompressible. The normal turbulence intensity at the cascade inlet is about 0.3 percent and most measurements were obtained under these conditions. The inlet turbulence intensity for CC3 was also increased to about 3 percent using a grid (Whitehouse et al., 1993), but this was found to have very little effect on the loss behavior of this blade: At both design and off-design incidence, differences in measured losses were close to the uncertainty in the measurements.

Blade and Cascade Geometries. The geometries of the two cascades are summarized in Fig. 2. Cascade CC2 represents the midspan section of a power turbine blade. This cascade has been used extensively in the past primarily for studies of off-design profile losses (e.g., Goobie et al., 1989; Tremblay et al., 1990; Rodger et al., 1992). After the development of the Moustapha et al. (1990) correlation, cascade CC3 was fabricated to examine further the influence of leading-edge geometry on the off-design losses. The two blades were designed for same inlet and outlet flow conditions using the same turbine-profile design system.

As shown in Fig. 2, CC3 has a leading-edge diameter roughly twice that of CC2. This would normally be expected to reduce the sensitivity to off-design incidence. To maintain similar blade pressure distributions for the two blades, which required that maximum thickness be essentially the same and at the same chordwise location, the leading-edge wedge angle for CC3 was reduced to 43 deg from the value of 52.4 deg used for CC2. Figure 3 shows that the pressure distributions measured for the two blades at the design incidence were in fact very similar.

Experimental Procedures. All flowfield measurements were obtained with a three-hole pressure probe. The probe tip had a width of 2 mm and a thickness of 0.7 mm. The probe pressures were measured with capacitive-type pressure transducers and recorded using a microcomputer-based data acquisition system. The corresponding flow quantities are estimated to have the following accuracies: total and dynamic pressures, ±1 percent of the local dynamic pressure; flow angles, ±0.5 deg; and mass-averaged total-pressure loss coefficients, ±5 percent. The values of incidence angle are estimated to be accurate to ±0.5 deg.

One blade from each cascade is also instrumented with 11 rows of static taps, each row having 43 taps. One of the taps is located on the trailing edge to give the base pressure. For the present measurements only the midspan rows of taps were used.

The locations of the upstream and downstream traverse planes are indicated in Fig. 2. The losses quoted later are fully mixed-out values calculated assuming mixing at constant area from the downstream plane.

Results for Off-Design Incidence. Figure 4 shows the measured profile loss coefficients for the two cascades as a function of incidence. The corresponding predictions using the classical Ainley and Mathieson (AM) and the Kacker and Oka-

Nomenclature

AVR = $\int_0^s Vx_2 d\dot{m} / \int_0^s Vx_1 d\dot{m}$ = axial velocity ratio
C = blade chord
$Cp = (P - P_1)/\frac{1}{2}\rho V_1^2$ = static pressure coefficient
$Cp_b = (P_b - P_2)/\frac{1}{2}\rho V_2^2$ = base pressure coefficient
Cx = blade axial chord
d = diameter of leading-edge circle
H = blade span
$i = \alpha_1 - \alpha_{1,\mathrm{des}}$ = incidence
$K = (\upsilon/V^2)(dV/dx)$ = acceleration parameter
M = Mach number
P = static pressure
P_b = base pressure
P_0 = total pressure
s = blade pitch or spacing
t = trailing-edge thickness
V = velocity
$w = s \cos \gamma$ = passage width
We = leading-edge wedge angle (in deg)
$Y = (P_{0_2} - P_{0_1})/\frac{1}{2}\rho V_2^2$ = total pressure loss coefficient
α = flow angle, measured from the axial direction
β = blade metal angle, measured from the axial direction
γ = blade stagger angle, specific heat ratio
δ = boundary layer thickness
$\delta^* = \int_0^\delta (1 - V/V_e)dy$ = boundary layer displacement thickness
$\theta = \int_0^\delta (V/V_e)(1 - V/V_e)dy$ = boundary layer momentum thickness
ρ = fluid density
υ = fluid viscosity
$\phi^2 = V_2^2/V_{2,is}^2$ = kinetic energy coefficient
= (actual outlet kinetic energy)/(kinetic energy for isentropic expansion)
$\chi = (d/s)^{-0.05} We^{-0.2} (\cos \beta_1/\cos \beta_2)^{-1.4} [\alpha_1 - \alpha_{1,\mathrm{des}}]$
= new incidence parameter (angles in deg)
$\chi' = (d/s)^{-1.6} (\cos \beta_1/\cos \beta_2)^{-2} [\alpha_1 - \alpha_{1,\mathrm{des}}]$ = Moustapha et al. incidence parameter (α_1 measured in deg)

Subscripts

des = value at the design point
e = boundary-layer edge value
P = profile value
x = axial direction
1, 2 = cascade inlet and outlet, respectively

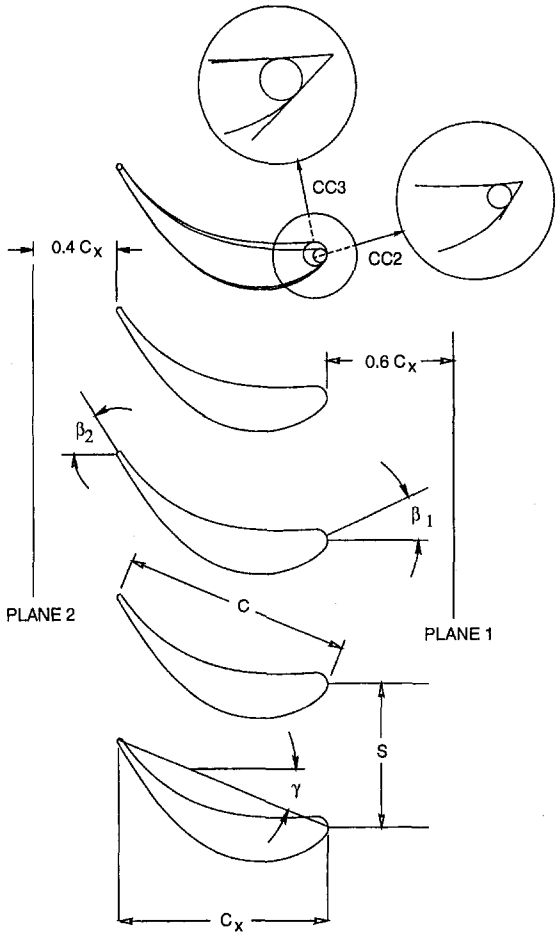

Cascade Parameters		
	CC3	CC2
Blade span, H (mm)	200	200
Blade spacing, S (mm)	110.7	110.7
True chord, C (mm)	162.3	162.8
Axial chord, Cx (mm)	149.4	150.0
Stagger angle, γ (deg.)	21.6	23.1
t_{MAX}/C	0.196	0.182
Inlet metal angle, β_1 (deg.)	25.5	29.3
Outlet metal angle, β_2 (deg.)	57.5	57.5
Leading-edge diameter (mm)	16.7	9.43
Leading-edge wedge angle (deg.)	43.0	52.4
Trailing-edge thickness (mm)	4.2	4.2

Fig. 2 Blade and cascade geometries

puu/Moustapha et al. (KOM) loss systems are also shown. The AM values are essentially the same for the two blades, since the only relevant parameter that varied was the maximum thickness-to-chord ratio, and it changed by only a small amount. While the KOM system matches the data somewhat better, the change in losses predicted by the Moustapha et al. correlation, due to the change in leading-edge diameter, was not reflected in the data for CC2 and CC3 at positive incidence. This suggests a need to re-examine the influence of leading-edge geometry on off-design profile losses.

It should be mentioned that data for CC2 had earlier been compared with the Moustapha et al. correlation with apparently better agreement than is shown here, notably at large positive

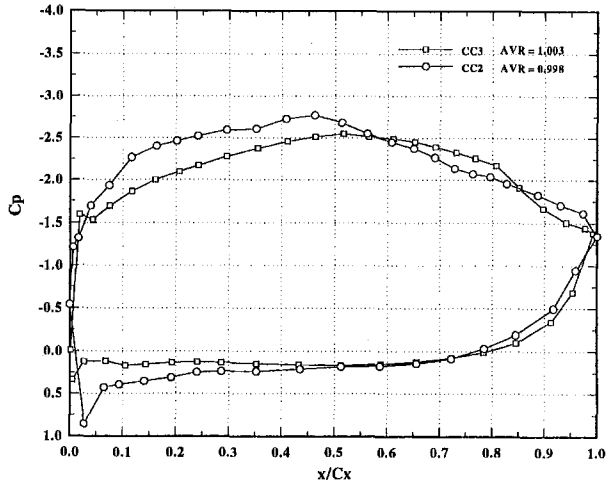

Fig. 3 Blade pressure distributions at design incidence

incidence (Tremblay et al., 1990). However, these earlier measurements were conducted at rather large values of axial velocity ratio (estimated at as high as 1.08 for +20 deg of incidence). Concern about the effect of this on the measurements led to the investigation of AVR by Rodger et al. (1992). This study showed that modest flow convergence (AVR > 1.0) has only a mild effect on the measured losses, provided there is no significant trailing-edge separation. However, when separation is present, the imposed favorable pressure gradient implied by AVR > 1.0 has the effect of shifting the separation point closer to the trailing edge. At a given incidence, this leads to lower profile losses than would be the case for more closely two-dimensional flow. As a result, the Tremblay et al. measurements gave lower losses at large positive incidence and therefore better agreement with the correlation.

For use in later discussion, some of the blade pressure measurements are also presented.

Figure 5 shows the variation in the blade pressure distributions at positive incidence for CC3. As incidence increases, a velocity overshoot appears on the suction side at the leading edge and, whereas at design incidence the flow is accelerated up to about midchord, at higher values of incidence the flow is decelerated along the full length of the suction surface. Figure 6 shows the pressure distributions for the two blades at +20 deg of incidence. The mismatch in static pressures at the trailing edge is probably the result of the difference in the axial velocity

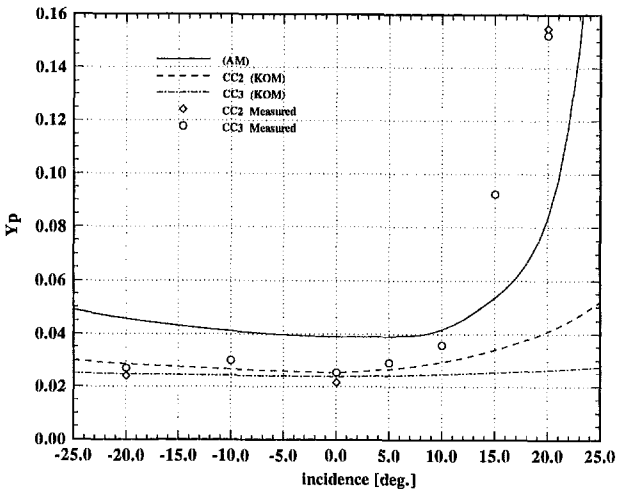

Fig. 4 Variation of midspan loss coefficients

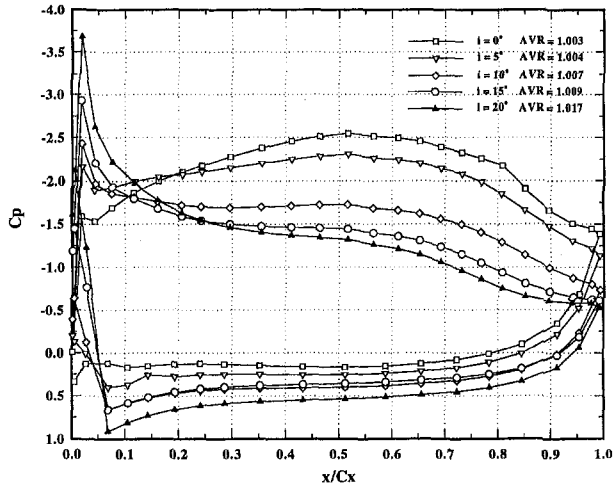

Fig. 5 Effect of positive incidence on blade pressure distributions (CC3)

ratios for the two sets of measurements. However, the difference in the suction peaks on the forward part of the blades seems to be too large to explain in this way. Nor does the uncertainty in the incidence angle seem adequate to explain the difference. In fact, the suction peak would have been expected to be milder for CC3 because of its larger leading-edge diameter. Instead, some other factor is evidently amplifying the suction peak.

As already noted, the agreement between the present measurements and the Moustapha et al. correlation was somewhat poor. This prompted a re-examination of the correlation and the results of this are presented next.

Improved Correlation

Discussion. As will be shown later, the Moustapha et al. correlation for off-design profile losses has been modified to include the effect of the leading-edge wedge angle. This resulted in a noticeable improvement in agreement with the present experimental data as well as with the data from the literature for which the wedge angle was available. This section examines the physical relationship between the leading-edge geometry and the profile losses, in an attempt to explain why the wedge angle should appear in the correlation.

The importance of the details of the leading-edge geometry has been recognized for some time. For example, Stow (1985) discusses the redesign of the leading edge of a turbine airfoil to remove a "spike," or local overshoot, in velocity very close to the leading edge. Stow does not explicitly identify the origin of the spike, but it appears to be associated with the blend point where the leading-edge circle meets the rest of the suction-side profile. It is plausible that a pressure disturbance would occur at this point since there would normally be a discontinuity in curvature there.

In his detailed examination of the boundary layer on a turbine rotor blade, Hodson (1985) likewise noted the occurrence of a sharp velocity overshoot at the blend point. As Hodson observed, this overshoot may often be missed in blade loading measurements since it is of short extent and can easily fall between static taps. This is almost certainly the case for the present measurements with CC2 and CC3. Hodson found that the bubbles quickly reattached since the velocity overshoot occurred in a region of overall favorable pressure gradient. In fact, he concluded that transition was not necessarily completed in the bubbles and that the subsequent favorable pressure gradient could in any case cause relaminarization of the boundary layer.

More recently, Walraevens and Cumpsty (1995) specifically examined the leading-edge flow using a plate mounted in a wind tunnel. The incidence and the free-stream turbulence were varied and both circular and elliptic leading edges were considered. Separation occurred at the same point, a short distance upstream of the blend point, under most conditions. The authors explicitly link the likelihood of separation to the magnitude of the discontinuity in curvature at the blend point. Thus, the appearance of separation was delayed to a higher angle of incidence for the elliptic leading edge because of its milder discontinuity in curvature. Raising the level of free-stream turbulence shortened the separation bubble somewhat but, for the circular leading edge in particular, did not prevent the appearance of the separation bubble or change the location of the separation. Boundary-layer measurements made downstream of the bubbles showed a substantial increase in momentum thickness as the extent of the bubble increased. This loss of momentum would be due to the mixing losses occurring in the free shear layer as well as the fact that the layer reattached turbulent. It should be noted that for all of the cases considered, the bubbles were reattaching in a region of adverse pressure gradient.

The profile losses are taken to include the loss production in the blade-surface boundary layers as well as at the trailing edge. With some simplifying assumptions, Denton (1993) relates the profile losses to the boundary layer parameters at the trailing edge and the trailing edge conditions as follows:

$$Y = \frac{2\theta}{w} + \left(\frac{\delta^* + t}{w}\right)^2 - \frac{C_{P_b} t}{w} \qquad (1)$$

where t is the trailing-edge thickness and w is the passage width. The first term accounts for the direct loss production in the boundary layers. The momentum thickness in this term is particularly influenced by the location of boundary-layer transition as well as by the mixing at the edge of any separation bubbles which may be present. The second term is the sudden-expansion loss at the trailing edge, where the blockage associated with the boundary-layer displacement thickness contributes to the effective change in area. The final term accounts for the retarding force that would be exerted by a low base pressure. The influence of the leading-edge geometry on the profiles losses should thus be explained mainly through its influence on the boundary-layer parameters at the trailing edge. This influence would be expected to make itself felt mainly up to the onset of trailing-edge separation, at which point the last two terms begin to dominate the losses. The boundary layers on the suction surface of turbomachinery blades are normally turbulent by the time they reach the trailing edge. Thus, although the onset of separation is influenced by the thickness of the incoming boundary layer, the angle of incidence at which separation begins should be determined mainly by the blade pressure distribution.

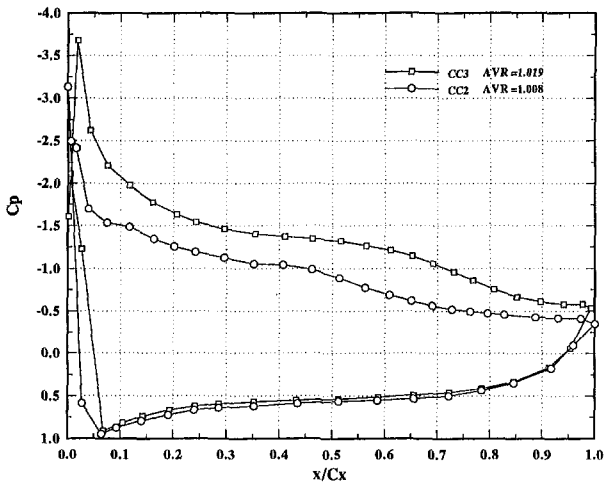

Fig. 6 Blade pressure distributions at +20 deg incidence

Therefore, any conclusions about the influence of the leading-edge geometry on losses are expected to hold mainly for negative incidence and for positive incidence up to the onset of significant trailing-edge separation.

In light of Eq. (1) and the earlier experimental studies, the following picture is proposed for CC2 and CC3.

Considering first the design incidence, both profiles experience a leading-edge velocity spike, although in the measured results (Fig. 3) this was evident only for CC3. Figure 7 shows the suction-surface velocity distributions for both profiles as predicted using a blade-to-blade potential flow code. It is clear that the spikes are directly related to the two blend points. The blend point for CC3 is farther from the leading edge, consistent with the smaller wedge angle. As noted earlier, the wedge angle was chosen to give roughly the same maximum thickness for the two profiles. However, on geometric grounds the smaller wedge angle will also tend to give a larger discontinuity in curvature at the blend point, and this is confirmed by the stronger velocity spike experienced by CC3. The strong adverse pressure gradient immediately after the spike may be sufficient to separate the boundary layer, which will be laminar at that point. Normally transition would occur quickly in a laminar separation bubble, which then allows it to reattach. However, since the overall pressure gradient quickly reverts to strongly favorable, a transitional or even laminar separation bubble should be able to reattach here. Furthermore, even if transition had commenced, it might well be followed by relaminarization due to the acceleration. The value of the acceleration parameter K is in fact higher than the suggested critical value (e.g., Mayle, 1991) of about 3×10^{-6} for a short length after the velocity spike. In any event, surface flow visualization conducted on the suction surface of both blades strongly suggested that transition occurred naturally over a distance from about 50 to 70 percent of the chord length. Thus, while separation bubbles might have been present, they were evidently very short and did not trigger transition. For both reasons, they would have had relatively little effect on the boundary-layer development and therefore on the losses generated on the blade surfaces.

The picture changes as the incidence becomes positive. As seen from Fig. 5, at positive incidence a normal overspeed develops at the leading edge. At the higher values of incidence a short separation bubble was also apparent from the surface flow visualization. Furthermore, once the incidence exceeds about 10 deg, the pressure gradient is adverse over essentially the whole of the suction surface. As a result of the adverse pressure gradient, the leading-edge separation will begin to have a greater influence on the losses: The bubble will tend to be longer, with greater loss production, and transition will probably

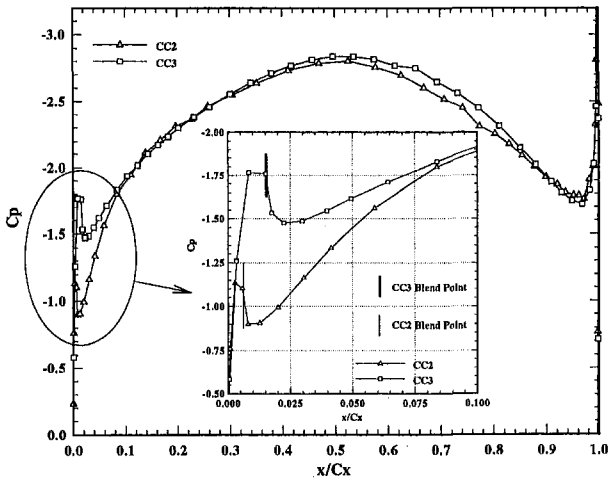

Fig. 7 Predicted flow around leading edge at design incidence (potential flow calculation)

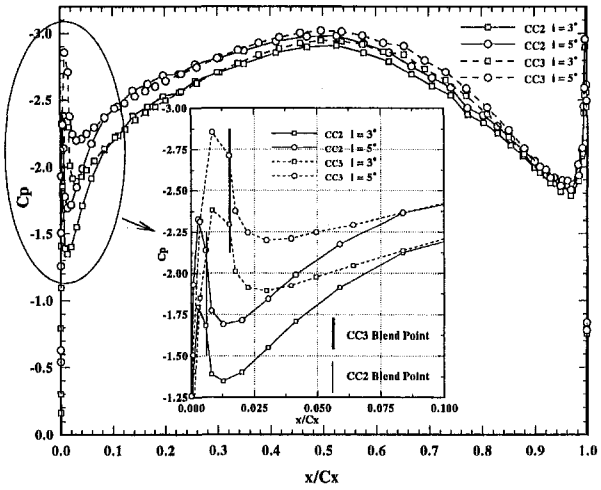

Fig. 8 Predicted flow around leading edge—effect of incidence (potential flow prediction)

be necessary for its reattachment. In turn, a geometric factor that tends to make the bubble larger will also tend to increase the losses. Potential-flow calculations for the flow in the leading-edge region of both blades are shown in Fig. 8 for a small range of positive incidence angles. It is seen that at a given incidence the velocity spike continues to be stronger for CC3 than for CC2, whereas one would have expected the larger diameter of CC3 to moderate the overshoot. The blade-surface measurements also showed consistently higher suction peaks for CC3, as indicated in Fig. 5. Thus, it appears that the curvature discontinuity continues to influence the flow by amplifying the normal suction peak at the leading edge. For these reasons, one would likewise expect the curvature discontinuity to continue to influence the profile losses, at least up to the appearance of significant separation at the trailing edge.

For negative incidence, the discontinuity in curvature at the pressure-side blend point comes into play to encourage the occurrence of a pressure-side separation bubble. This bubble is expected to reattach under most circumstances, but the mixing at the edge of this and the likely turbulent state of the subsequent boundary layer will increase the loss production on the pressure surface. Again, these losses will be influenced by the severity of the discontinuity in curvature through its influence on the appearance and chordwise extent of the separation bubble.

To summarize, it is believed, as has been suggested by a few other researchers, that the strength of the discontinuity in curvature at the leading-edge blend points will influence the trend in losses at off-design values of incidence. Obviously, it would be very inconvenient to have the curvature discontinuity appear explicitly in the profile-loss correlation. However, it is suggested that the value of the leading-edge wedge angle is a reasonable, approximate measure of the curvature discontinuity: larger values of wedge angle will tend to produce smaller discontinuities, and vice versa. Therefore, the use of the wedge angle in the revised correlation is interpreted as a convenient alternative to using the curvature discontinuity directly.

New Correlation. The new correlation is a revised version of the correlation of Moustapha et al. (1990). The latter correlation was based on data from 19 cascades. Unfortunately, the values of the leading-edge wedge angles were not quoted for all of these cascades. Therefore, the present correlation is based on a subset of 8 of the cascades from the earlier database together with data for CC2, CC3, and the three cascades of Perdichizzi and Dossena (1993), for a total of 13 cascades. Data for a very wide range of wedge angles and ratios of leading-edge diameter-to-spacing are included. Those sources of data

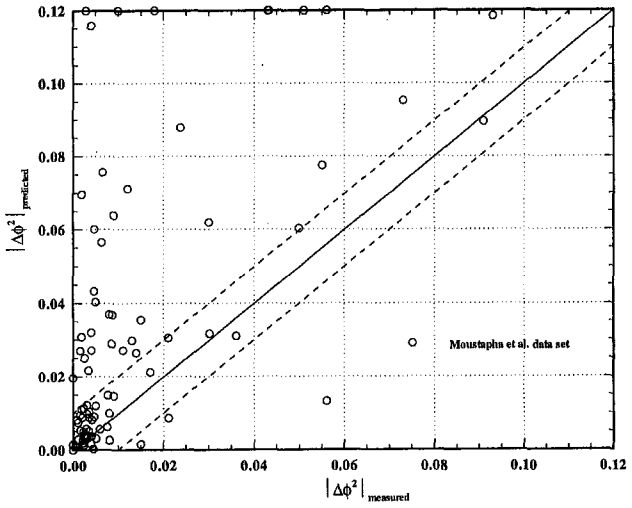

Fig. 9 Evaluation of Ainley and Mathieson profile loss correlation (predicted versus measured)

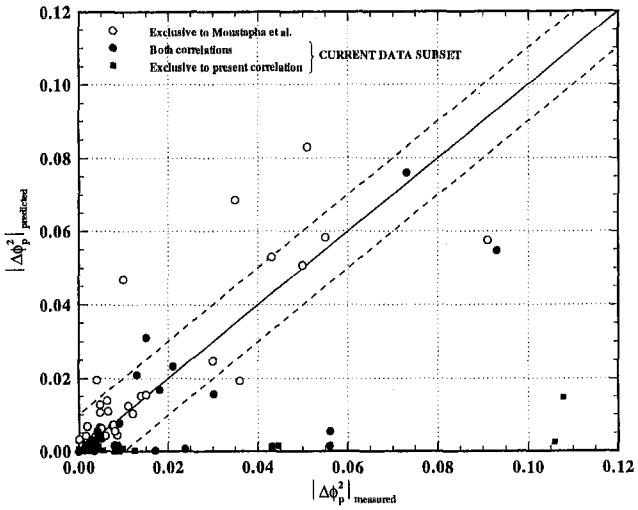

Fig. 11 Evaluation of Moustapha et al. correlation

that are in the open literature are identified in the list of references.

To demonstrate the improvements achieved with successive correlations, the data are compared with the Ainley and Mathieson, the Moustapha et al., and, finally, the new correlation.

Figure 9 compares the incremental losses predicted by the Ainley and Mathieson correlation with the measured values, expressed as changes to the kinetic-energy coefficient. Predicted values of $|\Delta\phi^2|$ that exceeded 0.12 have been plotted along the top edge of the figure. Ainley and Mathieson's correlation was based on cascade data obtained in the 1940s and 50s, whereas the measured values are mostly from cascades of recent design. As might be expected, the Ainley and Mathieson correlation does not reflect the improvements in turbine design and tends to overpredict the off-design losses.

Moustapha et al. correlated the incremental losses with the incidence, the channel acceleration, and the ratio of the leading-edge diameter to the spacing using the incidence parameter

$$\chi' = \left(\frac{d}{s}\right)^{-1.6}\left(\frac{\cos\beta_1}{\cos\beta_2}\right)^{-2}[\alpha_1 - \alpha_{1,\text{des}}].$$

The resulting correlation is shown in Fig. 10 and the evaluation of its accuracy is shown in Fig. 11. Comparison with Fig. 9 shows that it is significantly more successful than the Ainley and Mathieson correlation, although it still noticeably over or underpredicts the losses for some cascades.

The new correlation is shown in Fig. 12 and the corresponding evaluation in Fig. 13. The new incidence parameter takes the form

$$\chi = \left(\frac{d}{s}\right)^{-0.05} We^{-0.2}\left(\frac{\cos\beta_1}{\cos\beta_2}\right)^{-1.4}[\alpha_1 - \alpha_{1,\text{des}}].$$

As indicated, the influence of the leading-edge diameter is now much smaller and a significant dependence on wedge angle has been introduced. The revised correlation is seen to be considerably more successful in correlating the data. This applies equally to cascades CC2 and CC3, the data for which are included on the figures. Even the data at large positive incidence seem to be quite well correlated. However, the rapid rate of increase in the losses makes the collapse of the data appear slightly better than it actually is. This is evident from Fig. 13 where the largest differences between predictions and measurements are seen to occur at large values of incidence (that is, for large values of $|\Delta\phi^2|$). Nevertheless, the correlation must be regarded as

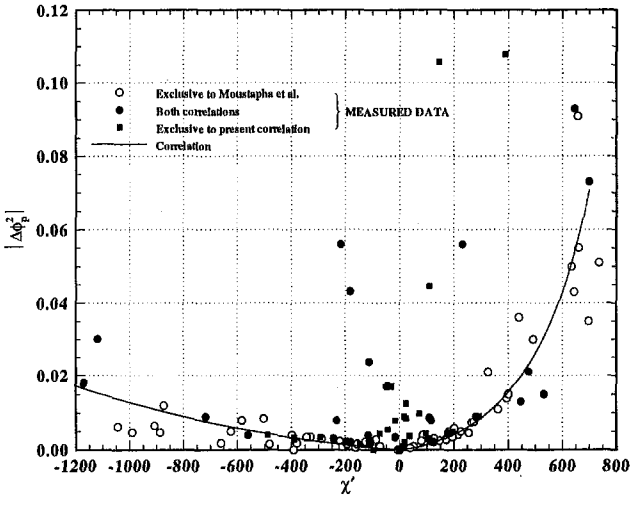

Fig. 10 Moustapha et al. (1990) correlation for profile losses at off-design incidence

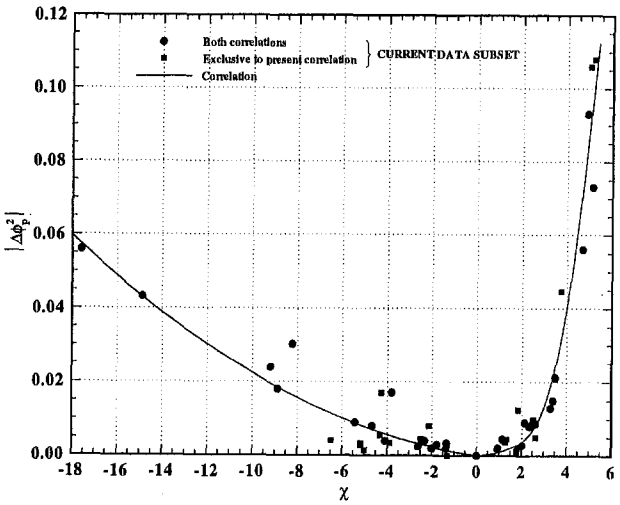

Fig. 12 Improved correlation for profile losses at off-design incidence

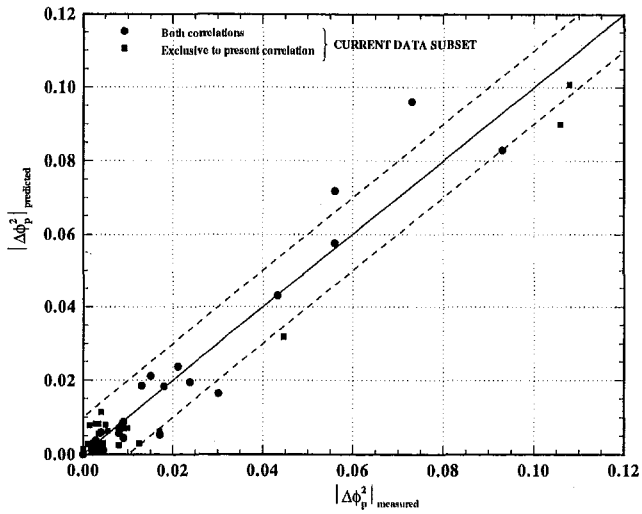

Fig. 13 Evaluation of improved correlation

excellent. For use in computations, the following polynomials have been fitted to the data:

$$\Delta\phi_P^2 = a_8\chi^8 + a_7\chi^7 + a_6\chi^6 + a_5\chi^5 + a_4\chi^4 + a_3\chi^3 + a_2\chi^2 + a_1\chi \quad (2a)$$

where

$$a_8 = +3.711 \times 10^{-7}, \quad a_7 = -5.318 \times 10^{-6},$$
$$a_6 = +1.106 \times 10^{-5}, \quad a_5 = +9.017 \times 10^{-5},$$
$$a_4 = -1.542 \times 10^{-4}, \quad a_3 = -2.506 \times 10^{-4},$$
$$a_2 = +1.327 \times 10^{-3}, \quad a_1 = -6.149 \times 10^{-5},$$

for $\chi \geq 0$, and

$$\Delta\phi_P^2 = 1.358 \times 10^{-4}\chi^2 - 8.720 \times 10^{-4}\chi \quad (2b)$$

for $\chi < 0$.

Like the Moustapha et al. correlation, the new one is expressed in terms of a change to the kinetic-energy coefficient, ϕ^2, because that parameter varies more weakly with Mach number than does, for example, the more usual total-pressure loss coefficient, Y. However, conversions between ϕ^2 and Y are easily made using

$$Y = \frac{\left[1 - \frac{\gamma - 1}{2} M_2^2 \left(\frac{1}{\phi^2} - 1\right)\right]^{-[\gamma/(\gamma-1)]} - 1}{1 - \left(1 + \frac{\gamma - 1}{2} M_2^2\right)^{-[\gamma/(\gamma-1)]}} \quad (3)$$

where M_2 is the Mach number at the outlet of the blade row.

Conclusions

Measurements have been made of the off-design profile losses for two turbine blades that differ primarily in their leading-edge geometries. The recent correlation of Moustapha et al. predicted that the blade with the larger leading-edge diameter would be considerably less sensitive to incidence. However, the losses were very similar for the two blades over a wide range of incidence angles. This prompted a re-examination of the influence of the leading-edge geometry on profile losses. It was found that a significantly better correlation could be obtained by including the leading-edge wedge angle as an additional and more influential correlating parameter. It is believed that the off-design behavior of the blade is influenced by the magnitude of the discontinuity in curvature at the blend points where the leading-edge circle joins the rest of the profile. The value of the wedge angle appears to give an approximate and convenient indication of the magnitude of this discontinuity in curvature.

The present results were obtained exclusively from blades employing leading-edge circles. It would appear that an elliptic leading edge allows a blade to be designed with milder curvature jumps at the blend points. This probably explains the reduced sensitivity to incidence usually attributed to elliptic leading edges.

Finally, although the present work has focused exclusively on the influence of the leading-edge geometry on the off-design profile losses, it is recognized that there are additional factors that should be investigated. These include the Reynolds number, the turbulence intensity, and the chordwise pressure distribution. The influence of the outlet Mach number is especially important and is still not well understood. It is planned to investigate some of these factors in future studies.

Acknowledgments

Financial support for this study provided by the Natural Sciences and Engineering Research Council of Canada and by Pratt & Whitney Canada Inc. is gratefully acknowledged.

References

Ainley, D. G., and Mathieson, G. C. R., 1951, "A Method of Performance Estimation for Axial Flow Turbines," ARC R&M 2974.

Aronov, B. M., Bogatyrev, A. G., Epifanov, V. M., Mamaev, B. I., and Shkurikhin, I. B., 1975, "Experimental Study of Blade Inlet Angle Influence on Profile Cascade Effectiveness," *Soviet Aeronautics*, Vol. 18, No. 3, pp. 82–86. [Data]

Craig, H. R. M., and Cox, H. J. A., 1971, "Performance Estimate of Axial Flow Turbines," *Proc. Institution of Mechanical Engineers*, Vol. 185, No. 32, pp. 407–424.

Denton, J. D., 1993, "Loss Mechanisms in Turbomachines," ASME JOURNAL OF TURBOMACHINERY, Vol. 115, pp. 621–656.

Dunham, J., and Came, P. M., 1970, "Improvements to the Ainley/Mathieson Method of Turbine Performance Prediction," ASME *Journal of Engineering for Power*, Vol. 92, pp. 252–256.

Goobie, S. M., Moustapha, S. H., and Sjolander, S. A., 1989, "An Experimental Investigation of the Effect of Incidence on the Two-Dimensional Performance of an Axial Turbine Cascade," *Proc. Ninth International Symposium on Air Breathing Engines*, Vol. 1, pp. 197–204.

Hodson, H. P., 1985, "Boundary-Layer Transition and Separation Near the Leading Edge of a High-Speed Turbine Blade," ASME *Journal of Engineering for Gas Turbines and Power*, Vol. 107, pp. 127–134.

Hodson, H. P., and Dominy, R. G., 1987a, "The Off-Design Performance of a Low-Pressure Turbine Cascade," ASME JOURNAL OF TURBOMACHINERY, Vol. 109, pp. 201–209. [Data]

Hodson, H. P., and Dominy, R. G., 1987b, "Three-Dimensional Flow in a Low-Pressure Turbine Cascade," ASME JOURNAL OF TURBOMACHINERY, Vol. 109, pp. 177–185. [Data]

Kacker, S. C., and Okapuu, U., 1982, "A Mean-Line Prediction Method for Axial Flow Turbine Efficiency," ASME *Journal of Engineering for Power*, Vol. 104, pp. 111–119.

Mayle, R. E., 1991, "The Role of Laminar–Turbulent Transition in Gas Turbine Engines," ASME JOURNAL OF TURBOMACHINERY, Vol. 113, pp. 509–537.

Moustapha, S. H., Kacker, S. C., and Tremblay, B., 1990, "An Improved Incidence Losses Prediction Method for Turbine Airfoils," ASME JOURNAL OF TURBOMACHINERY, Vol. 112, pp. 267–276.

Mukhtarov, M. K., and Krichakin, V. I., 1969, "Procedure of Estimating Flow Section Losses in Axial Flow Turbines when Calculating their Characteristics," *Teploenergetika*, Vol. 16(7), pp. 76–79.

Perdichizzi, A., and Dossena, V., 1993, "Incidence Angle and Pitch-Chord Effects on Secondary Flows Downstream of a Turbine Cascade," ASME JOURNAL OF TURBOMACHINERY, Vol. 115, pp. 383–391. [Data]

Rodger, P., Sjolander, S. A., and Moustapha, S. H., 1992, "Establishing Two-Dimensional Flow in a Large-Scale Planar Turbine Cascade," AIAA Paper No. 92-3066. [Data]

Stow, P., 1985, "Incorporation of Viscous-Inviscid Interactions in Turbomachinery Design," in *Thermodynamics and Fluid Mechanics of Turbomachinery*, A. S. Ucer, P. Stow, and Ch. Hirsch, eds., Nijhoff, Dordrecht, Vol. 2, pp. 887–921.

Tremblay, B., Sjolander, S. A., and Moustapha, S. H., 1990, "Off-Design Performance of a Linear Cascade of Turbine Blades," ASME Paper No. 90-GT-314. [Data]

Vijayaraghavan, S. B., and Kavanagh, P., 1988, "Effect of Free-Stream Turbulence, Reynolds Number, and Incidence on Axial Turbine Cascade Performance," ASME Paper No. 88-GT-152. [Data]

Walraevens, R. E., and Cumpsty, N. A., 1995, "Leading Edge Separation Bubbles on Turbomachinery Blades," ASME JOURNAL OF TURBOMACHINERY, Vol. 117, pp. 115–125.

Whitehouse, D. R., Moustapha, S. H., and Sjolander, S. A., 1993, "The Effect of Axial Velocity Ratio, Turbulence Intensity, Incidence, and Leading Edge Geometry on the Midspan Performance of a Turbine Cascade," *Canadian Aeronautics and Space Journal,* Vol. 39, No. 3, pp. 150–156. [Data]

Yamamoto, A., and Nouse, H., 1988, "Effects of Incidence on Three-Dimensional Flows in a Linear Turbine Cascade," ASME JOURNAL OF TURBOMACHINERY, Vol. 110, pp. 486–496. [Data]

Unsteady Flow Field Due to Nozzle Wake Interaction With the Rotor in an Axial Flow Turbine: Part I—Rotor Passage Flow Field

M. A. Zaccaria

B. Lakshminarayana

Center for Gas Turbines and Power,
The Pennsylvania State University,
University Park, PA 16802

The flow field in turbine rotor passages is complex with unsteadiness caused by the aerodynamic interaction of the nozzle and rotor flow fields. The two-dimensional steady and unsteady flow field at midspan in an axial flow turbine rotor has been investigated experimentally using an LDV with emphasis on the interaction of the nozzle wake with the rotor flow field. The flow field in the rotor passage is presented in Part I, while the flow field downstream of the rotor is presented in Part II. Measurements were acquired at 37 axial locations from just upstream of the rotor to one chord downstream of the rotor. The time-averaged flow field and the unsteadiness caused by the wake have been captured. As the nozzle wake travels through the rotor flow field, the nozzle wake becomes distorted with the region of the nozzle wake near the rotor suction surface moving faster than the region near the rotor pressure surface, resulting in a highly distorted wake. The wake is found to be spread out along the rotor pressure surface, as it convects downstream of midchord. The magnitude of the nozzle wake velocity defect grows until close to midchord, after which it decreases. High values of unresolved unsteadiness were observed at the rotor leading edge. This is due to the large flow gradients near the leading edge and the interaction of the nozzle wake with the rotor leading edge. High values of unresolved unsteadiness were also observed near the rotor pressure surface. This increase in unresolved unsteadiness is caused by the interaction of the nozzle wake with the flow near the rotor pressure surface.

Introduction

The flow around the blades of a turbine is highly unsteady. One of the major sources of unsteadiness is the aerodynamic interaction between the nozzle and rotor, which is called rotor–stator interaction. Rotor–stator interaction can affect the aerodynamic, structural, and thermal performance of a turbine. The rotor–stator interaction can be divided into two parts: potential flow and wake interactions. The potential flow gradients extend both upstream and downstream of the blade and they decay exponentially with a length scale of the order of the blade chord. If the axial gap between the blade rows is less than a chord (which it is in a typical axial flow turbine), then the potential influence can cause unsteadiness both upstream and downstream of the blades. However, the wake is convected downstream and has a far field rate of decay much lower than that of the potential flow. The wake will still be felt several chords downstream. But in most modern axial flow turbines, which have a rotor–stator spacing close to 20 percent of a blade chord, both the potential and wake effects occur together. As gas turbine designers try to reduce weight, and thus decrease the rotor–stator spacing, these effects will become more prominent.

Even though unsteady flow plays a major role in axial flow turbines, turbines are designed using three-dimensional steady flow calculation methods (Sharma et al., 1992). Empirical correlations are used to account for the effect of the unsteadiness. Because actual models of the loss-generating mechanisms in unsteady flow turbomachinery do not exist, these correlations are based on results from stationary cascade data and do not represent the actual fluid mechanics of the flow field (Sharma et al., 1985). Thus these correlations must be multiplied by some factor to obtain a good estimate of the actual losses that occur in turbines. Although these correlations have worked well in the design of existing turbines, they do not represent the true physics of the flow field and are only useful in the areas from which they were obtained, namely design point predictions and turbines, which are similar to existing designs (Hathaway, 1986). Thus, a more thorough knowledge of unsteady flow interactions is needed in order to increase both the design and off-design performance of existing turbines, and to design turbines that are considerably different than existing turbines. To obtain this knowledge, good time accurate data from inside the rotor are needed. This knowledge, in turn, can be used to model the unsteady flow mechanisms that are not currently in existing design codes.

Many researchers have investigated rotor–stator interaction. Greitzer (1985), Hathaway (1986), Gallus (1987), and Sharma et al. (1992) provide comprehensive surveys of unsteady flows in turbomachinery. Unfortunately, most of these investigations have been in isolated airfoils or axial flow compressors, and there are significant differences in the unsteady turbine flow field as compared to the unsteady compressor or isolated airfoil flow field (Sharma et al., 1985). This is because the flow field is accelerating in a turbine, whereas in a compressor the flow field is decelerating, and also because the flow turning is much larger in a turbine than in a compressor, thus causing stronger secondary flow in a turbine than in a compressor. Also there is

Contributed by the International Gas Turbine Institute and presented at the 40th International Gas Turbine and Aeroengine Congress and Exhibition, Houston, Texas, June 5–8, 1995. Manuscript received by the International Gas Turbine Institute March 15, 1995. Paper No. 95-GT-295. Associate Technical Editor: C. J. Russo.

the added effect of the horseshoe vortex in a turbine that does not occur in a compressor.

Only four groups have measured the unsteady flow field inside a turbine rotor; the groups at UTRC (Sharma et al., 1985; Dring et al., 1982), Cambridge (Hodson, 1985a), Allison/Calspan (Rao, et al., 1992) and at DFVLR (Binder et al., 1985, 1987; Binder, 1985). The Cambridge group measured the flow field at midspan (nozzle–rotor spacing is 50 percent of nozzle axial chord), the Allison/Calspan group measured the blade surface pressures at midspan (nozzle–rotor spacing is 22.5 percent of nozzle axial chord), the UTRC group measured the blade surface pressures and the rotor exit flow field (nozzle–rotor spacing is 65 percent of nozzle axial chord), and the researchers at DFVLR used a L2F velocimeter to measure two components of velocity and unresolved unsteadiness (axial and circumferential) at four axial planes inside of the rotor (nozzle–rotor spacing is 61 percent of nozzle axial chord). Three out of the four research groups had a nozzle–rotor spacing of 50 percent of nozzle axial chord or greater, which is not a realistic spacing for modern turbine designs. At this spacing the potential flow interactions will be very small and the nozzle wake will have decayed significantly by the time it enters the rotor passage. Typically, modern turbines have a nozzle–rotor spacing of around 25 percent or less nozzle axial chord. The only group to take measurements with a realistic nozzle–rotor spacing (Allison/Calspan), measured only the blade surface pressures at midspan (and did not measure the flow field between the blades). Thus there is a need for flow field measurements in a turbine rotor with a realistic nozzle–rotor spacing that will include both potential flow and wake interactions, which is the objective of this investigation.

Experimental Facility and Instrumentation

Experimental Facility. The Axial Flow Turbine Research Facility (AFTRF) of The Pennsylvania State University is an open circuit facility 0.9166 m (3 ft) in diameter and a hub to tip radius ratio of 0.73, with an advanced axial turbine blading configuration. The facility consists of a large bellmouth inlet, a turbulence-generating grid section, followed by a test section with a nozzle vane guide row and a rotor. There are 23 nozzle guide vanes and 29 rotor blades followed by outlet guide vanes. A window for LDV measurements covering the entire flow field from upstream of the nozzle to downstream of the rotor passage is also incorporated. Detailed design of the facility, performance, and geometric features are described by Lakshminarayana et al. (1996). Some important performance and geometrical parameters are as follows: hub/tip ratio = 0.7269, nozzle; chord (midspan) = 11.23 cm, turning angle = 70 deg, rotor; blade chord (midspan) = 9.294 cm, turning angle = 95.42 deg (tip), 125.69 deg (root), tip clearance = 1.27 mm; Reynolds number of nozzle flow (based on exit flow) = 10^6, mass flow rate = 11.05 kg/s, rotational speed = 1300 rpm. The vane-blade spacing is 22.6 percent of nozzle axial chord at midspan.

Laser-Doppler Velocimeter (LDV) System. The LDV is a two-color, four-beam, two-dimensional measuring system. It consists of a 5 W argon-ion laser tuned to the 488 nm (blue) and 514.5 (green) lines. The green and blue beam pairs are used to measure the axial and the tangential components of velocity, respectively. Rosco fog fluid, with a mean diameter of 1.1 μm and standard deviation of 1.9 μm, is used to seed the flow. Scattered light from the seed particles passing through the probe volume is collected on-axis. On-axis collection was used instead of off-axis to improve access into the rotor blade. The LDV system is mounted on an optical table attached to a mechanical traverse. The traverse can move horizontally and vertically, and can be tilted to achieve the measurement at the desired location in the turbine. The three linear degrees of freedom plus tilt enable positioning of the probe volume very accurately ($\pm$0.5 mm). The flow in the rotor is measured through a flat glass window. The glass is 3.175 mm ($\frac{1}{8}$ in.) thick. The

Nomenclature

C = nozzle axial chord at midspan
C_r = rotor axial chord at midspan
j = individual measurement window location in the rotor passage
k = turbulent kinetic energy
k = nozzle/rotor position
n = total number of measurements in each measurement window
NB = number of rotor blades
NRP = number of nozzle/rotor positions
NW = number of measurement windows
NWB = number of measurement windows per blade
PS = pressure surface
S = percentage pitchwise distance from the wake center at midspan (normalized by rotor pitch, positive on pressure side, negative on suction side)
S_r = percentage pitchwise distance in rotor passage (normalized by rotor pitch)
SS = suction surface
Tu_r = relative unresolved unsteadiness = $[\sqrt{(u')^2 + (v')^2}/W] \times 100$ percent (Eq. (9))
Tu_t = unresolved unsteadiness = $[\sqrt{(u')^2 + (v')^2}/U_m] \times 100$ percent (Eq. (12))
U_m = blade speed at midspan
u' = unresolved fluctuating velocity in axial direction
$\tilde{u}$ = periodic velocity in axial direction
V = absolute velocity
v' = unresolved fluctuating velocity in tangential direction
$\tilde{v}$ = periodic velocity in tangential direction
V_c = defect in absolute velocity at the nozzle wake center normalized by U_m
W = relative velocity
W_c = defect in relative velocity at the rotor wake center normalized by U_m
X_r = axial distance from rotor leading edge at midspan
Z = axial distance from nozzle or rotor trailing edge normalized by nozzle or rotor axial chord, respectively
δ^* = displacement thickness
ϵ = turbulent dissipation
θ = momentum thickness
ν_t = eddy viscosity
σ_k = constant in the turbulent kinetic energy equation

Subscripts

i = instantaneous
l = local
m = midspan
max = maximum
min = minimum
n = normal
r = rotor
r = relative
s = streamwise
r, θ, x = radial, tangential, axial directions
te = trailing edge

Superscripts

$\overline{}$ = ensemble-averaged properties
$=$ = time-averaged properties
$\cap$ = circumferentially mass-averaged properties
$\cdots$ = cycle-averaged properties
$'$ = fluctuating quantity
$\sim$ = periodic quantity
$\cup$ = phase-lock averaged

rotor and endwalls were painted with a high-temperature flat black paint to reduce surface reflections. Regular flat black paint was first used, but the laser beams burned off the paint.

The LDV system is free to acquire velocity measurements whenever a seed particle crosses the LDV probe volume. In the rotor flow field, this results in the random acquisition of many velocity measurements during every rotor revolution. Thus to relate a measurement event to the rotor position, an optical shaft encoder has been attached to the turbine shaft. This encoder divides one revolution of the rotor into 6000 counts and since there are 29 rotor blades, this comes to 207 counts per rotor passage. One rotor passage is then divided into 50 measurement windows, each which has 4.1 counts and is 1.72 mm in length at midspan. Each velocity measurement is tagged with the angular position of the rotor by means of the optical encoder. At each survey point, approximately 120,000 velocity measurements were acquired. Since all the velocity components were spatially phase-locked averaged (see next section), and this results in a representative rotor passage with 50 measurement windows, there were 2400 velocity measurements on average in each measurement window.

Since a two-dimensional LDV is used for measurements in the AFTRF, only the properties in the axial and tangential directions are measured. In order to reduce the reflections of the laser beams from the glass window on the receiving optics, the LDV system is offset in the tangential directions by 7.6 deg. This causes the tangential velocity to be in error by a small amount (<1 percent), which was considered acceptable. To process the data, two counter-type signal processors (one for each channel) are interfaced with an IBM PC compatible computer. The coincidence window for the two components of velocity is 10 μs.

LDV measurements are subject to numerous errors, most of which can be quantified. A complete error analysis for these measurements is given by Zaccaria (1994). Based on this error analysis, the uncertainty for a 95 percent confidence level is as follows; outside the rotor wake, 0.4 and 2.8 percent, respectively, for the ensemble-averaged velocity and the unresolved component of velocity, inside the rotor wake, 4.0 and 14.8 percent for ensemble averaged and unresolved velocity, respectively.

Measurement Procedure and Data Processing. Figure 1 shows the LDV measurement locations in the rotor. Measurements have been acquired at 37 axial measurement locations from just upstream of the rotor ($X_r/C_r = -0.088$) to one chord downstream of the rotor. Each measurement location is at midspan. Since a two-dimensional LDV was used for measurements in the rotor, only the velocities in the axial and tangential directions are measured. To account for the nonuniformity of the rotor absolute inlet flow field, measurements were made at six tangential locations in the absolute frame equally spaced over one nozzle pitch. These six tangential locations represent six different relative positions between the nozzle and the rotor (labeled nozzle/rotor locations 1–6) or if viewed from the nozzle frame of reference, six different time-resolved positions of the rotor in relation to the nozzle.

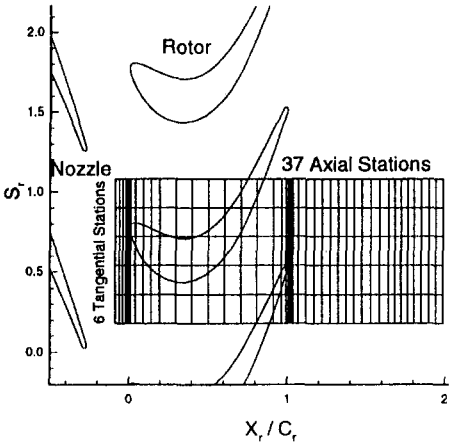

Fig. 1 Rotor LDV measurement locations

Each rotor passage is divided into 50 measurement windows, which means that there are measurements at 50 circumferential locations across the rotor pitch. Every instantaneous velocity measurement was recorded. After all instantaneous velocity measurements were acquired for the particular survey point, the velocity is then ensemble averaged at each measurement window according to

$$\bar{V} = \frac{1}{n}\sum_{i=1}^{n} V_i \tag{1}$$

where $\bar{V}$ is the ensemble-averaged velocity, V_i is the instantaneous velocity measured at a particular rotor measurement window, and n is the total number of measurements in that measurement window. The unresolved velocity for each measurement window can also be calculated as

$$V' = V_i - \bar{V} \tag{2}$$

and the corresponding variance as

$$\overline{(V')^2} = \frac{[\sum_{i=1}^{n} (V_i - \bar{V})^2]}{(n-1)} \tag{3}$$

The level of unresolved unsteadiness in each measurement window is determined by the variance.

Since the flow field between the rotor passages was demonstrated to be periodic (see Zaccaria, 1994), all the ensemble average velocity components were spatially phase-lock averaged as follows:

$$\breve{G}_j = \frac{\sum_{m=1}^{N_{RB}} G_{j,m}}{N_{RB}} \tag{4}$$

where G represents either the ensemble-averaged velocity or variance, the subscript m determines the particular rotor passage, and j is the measurement window location relative to the mth rotor passage and N_{RB} is the number of rotor blades. The successive application of Eq. (4) results in a description of the flow field at 50 equally spaced shaft positions across a representative rotor passage (Fig. 2). Since all results presented from now on are spatially phase-lock averaged, the superscript $\cup$ will be dropped hereafter.

For the LDV measurements in the rotor, the instantaneous velocity, V_i, is decomposed as follows:

$$V_i = \bar{\bar{V}} + \tilde{V} + V' \tag{5}$$

where $\bar{\bar{V}}$ is the time-averaged velocity, $\tilde{V}$ is the periodic velocity, and V' is the unresolved velocity component as calculated in Eq. (2). The decomposition for the phase-locked averaged rotor blade passage is shown in Fig. 2. The periodic unsteady velocity results from the relative motion of the rotor with respect to the nozzle, while the unresolved unsteady velocity is any flow field fluctuation that is not correlated with the rotor speed, such as turbulence and vortex shedding. The time-averaged velocity $\bar{\bar{V}}$ is obtained by averaging all the ensemble-averaged velocities in each measurement window as follows:

$$\bar{\bar{V}} = \frac{1}{\mathrm{NWB}}\sum_{j=1}^{\mathrm{NWB}}\left[\frac{1}{N_{RB}}\sum_{m=1}^{N_{RB}} \bar{V}_{j,m}\right] \tag{6}$$

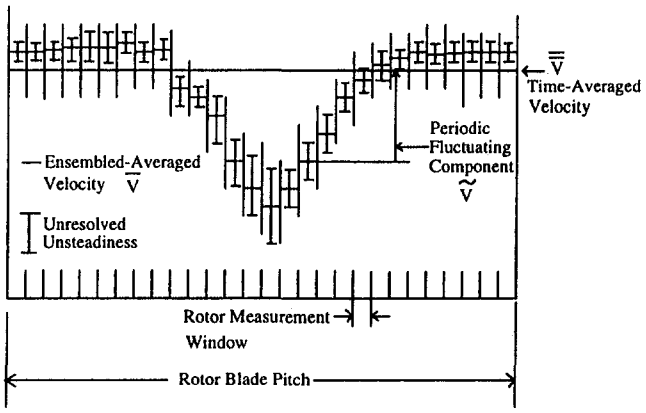

Fig. 2 Velocity decomposition for phase-lock averaged rotor blade (only 25 windows shown for clarity)

where NWB is the number of measurement windows per blade. The time-averaged velocity is a time average of all measurements acquired at a fixed point in space. The periodic velocity is then obtained from

$$\hat{V} = \bar{V} - \bar{\bar{V}} \tag{7}$$

From this velocity decomposition, the axial, tangential, and cross-velocity correlations (both periodic and unresolved) can be computed, also.

One typical velocity triangle in the free stream and one typical velocity triangle in the wake are shown in Fig. 3. The velocity defect in the nozzle wake produces a slip velocity in the relative frame toward the rotor suction surface. A more detailed discussion of this phenomenon is provided later in this paper.

Experimental Results

It should be emphasized here that the experimental procedure and data processing are designed to obtain spatial and "temporal" measurements (i.e., rotor shaft positions, not real time) of the wake–rotor interaction generated unsteadiness in the rotor. The laser is located at a fixed position relative to the nozzle wake for each nozzle/rotor location, hence, the averaging is based on identical rotor–nozzle blade positions. These measurements are similar to those reported by earlier investigators (e.g., Hathaway, 1986). Only representative data in the present turbine are presented in this paper. A more comprehensive data set and its interpretation can be found in Zaccaria (1994).

Cycle-Averaged Properties. The cycle-averaged values are obtained by averaging the ensemble-averaged (and phase-lock averaged) properties in each rotor measurement window for one nozzle/rotor location over the six nozzle/rotor locations (see Fig. 1) as follows:

$$\dddot{G}_j = \frac{1}{N_{\mathrm{NRP}}} \sum_{k=1}^{N_{\mathrm{NRP}}} \bar{G}_{j,k} \tag{8}$$

where G represents any flow parameter (such as velocity or unresolved unsteadiness), the superscript ... stands for cycle averaged property, N_{NRP} is the number of nozzle/rotor positions (6), the subscript j represents the individual measurement window location in the rotor passage, and the subscript k = 1 to 6 denotes a particular nozzle/rotor position. All the rotor flow field contour plots presented in this paper are for one ensemble-averaged (and phase-lock averaged) rotor blade pitch, which is doubled so that two rotor pitches are shown in the contour plots. Since the LDV was oriented at 7.6 deg to the circumferential direction (in order to reduce reflections from the laser beam on the casing window from saturating the photomultipliers), there is a shadow region on the blade suction side where no measurements could be obtained. This is shown in Fig. 4(*a*).

The cycle-averaged LDV data at the farthest measurement location upstream of the rotor ($X_r/C_r = -0.088$) were mass averaged over one rotor pitch and compared with mass-averaged five hole probe data closest to this location ($X_r/C_r = -0.080$ or 16 percent of nozzle axial chord downstream of the nozzle). Measurements were made with a five-hole probe data at 50 circumferential locations over one nozzle pitch. The agreement is excellent with the absolute velocity being 0.98 percent of each other ($\hat{V}/U_m = 1.6119$ for the five-hole probe and $\hat{\bar{V}}/U_m = 1.6278$ for the LDV) and the absolute flow angles being within 0.30 percent of each other ($\hat{\alpha} = 70.42$ deg for the five-hole probe and $\hat{\bar{\alpha}} = 70.63$ deg for the LDV). The five-hole probe measurements were acquired in the stationary frame of reference, which is equivalent to the cycle-averaged LDV data, and thus they were only circumferentially mass averaged.

Relative Velocity and Relative Flow Angle. The cycle-averaged relative velocity normalized by mean rotor speed (U_m) is presented in Fig. 4(*a*). (The bar over the velocity and angle notation in this paper's figures represents ensemble averaging.) This figure shows the flow acceleration through the blade passage. The velocity accelerates gradually on the suction side from the leading edge to $X_r/C_r = 0.80$, after which it levels off and becomes fairly uniform until the trailing edge. On the pressure side the velocity change is fairly gradual from the leading edge to the trailing edge. The effect of the leading edge on the flow field is clearly shown with the flow decelerating as the leading edge is approached. The relative total velocity, just upstream of the leading edge, decelerates to a value of $\dddot{W}/U_m = 0.2$. This can be seen more clearly in Fig. 4(*b*), which presents an enlargement of the flow field near the rotor leading edge. Downstream of the blade, the rotor wake decays to negligible values within half a chord length downstream of the blade. The rotor wake thickness is small. The rotor wake is discussed in more detail in Part II of this paper.

Figures 5(*a*, *b*) present the cycle-averaged relative flow angle. The relative flow angle shows the characteristic large change in flow angle for a turbine rotor, with the flow being turned around 110 deg in the rotor passage. The effect of the leading edge on the flow field is also evident by the large change of flow angle at the leading edge. The blade-to-blade profiles of the cycle-averaged relative flow angle, presented in Fig. 5(*a*), show that the rotor leading edge has a significant effect on the flow field even 9 percent of the rotor axial chord upstream of the leading edge, with the change in flow angle being 18 deg across the passage at this location. This effect increases as the rotor leading edge is approached with the change in angle increasing to 35 deg just upstream of the rotor leading edge.

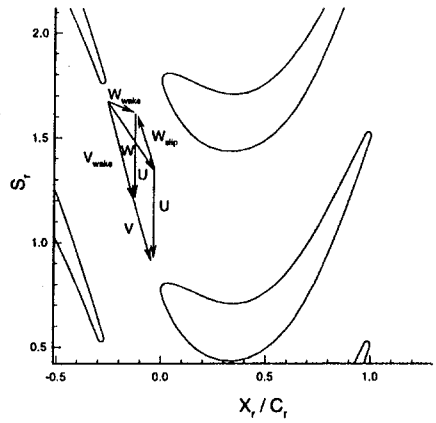

Fig. 3 Rotor inlet velocity triangles

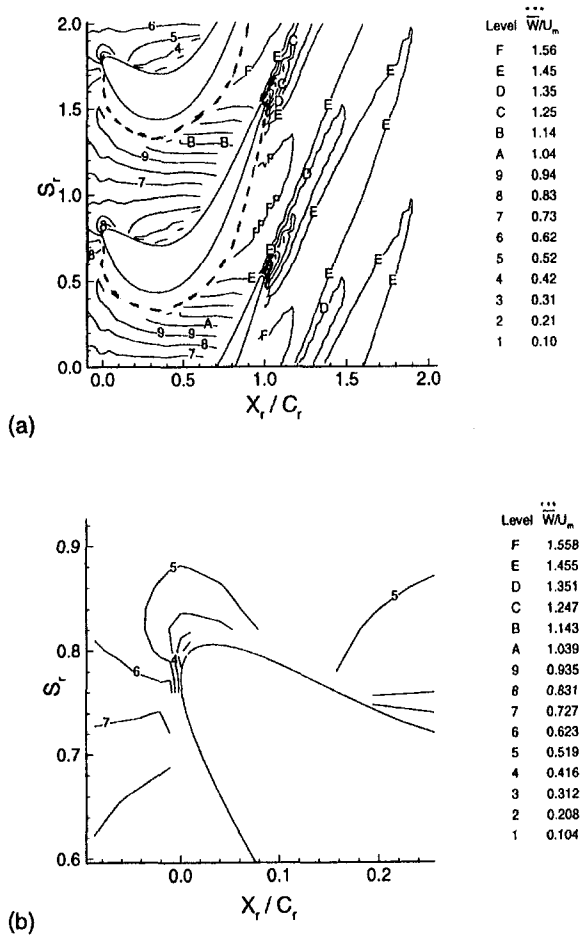

Fig. 4 Cycle averaged relative total velocity ($\bar{\bar{W}}/U_m$) (measurements were not obtained in the region between the dotted line and the rotor suction surface, shown in Figure 4(*a*), due to optical blockage)

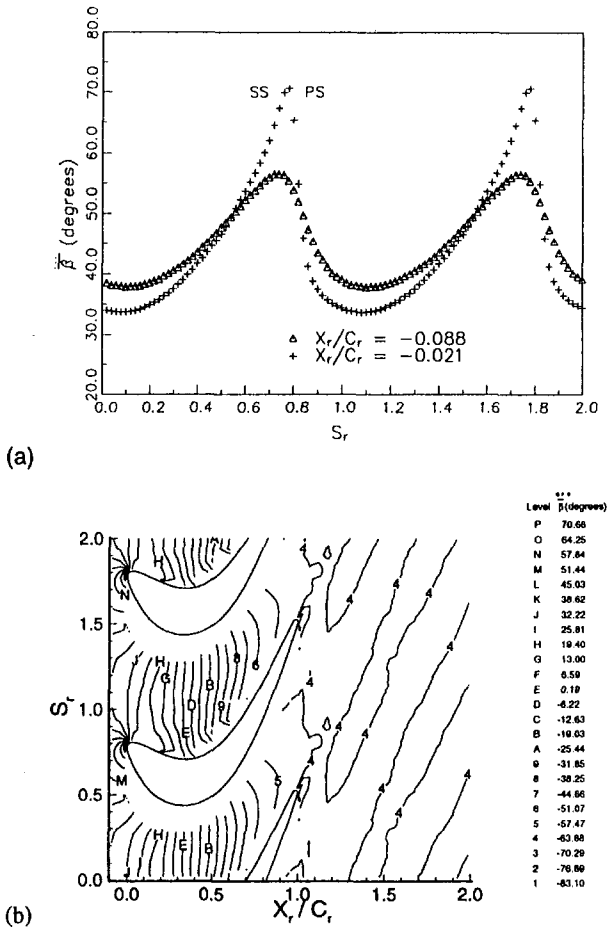

Fig. 5 Cycle-averaged relative flow angles ($\bar{\bar{\beta}}$)

Unresolved Unsteadiness. The cycle-averaged relative unresolved unsteadiness, shown in Fig. 6, is defined as follows:

$$Tu_r = \frac{\sqrt{\overline{(u')^2} + \overline{(v')^2}}}{W} \times 100 \text{ percent} \tag{9}$$

where

$$\overline{u'^2} = \frac{[\sum_{i=1}^{n} (V_{x_i} - \bar{V}_x)^2]}{(n-1)} \tag{10}$$

and

$$\overline{v'^2} = \frac{[\sum_{i=1}^{n} (V_{\theta_i} - \bar{V}_\theta)^2]}{(n-1)} \tag{11}$$

where $\bar{V}$ is the ensemble-averaged (and phase-lock averaged) velocity, V_i is the instantaneous velocity measured at a particular rotor measurement window, and n is the total number of measurements at that measurement window. The relative unresolved unsteadiness is then cycle averaged using Eq. (8). The unresolved unsteadiness defined by Eqs. (9), (10), and (11) includes all the turbulence fluctuations in the nozzle wake, and those produced by the rotor (e.g., wakes) and other unsteadiness not associated with the shaft or blade frequency. The relative unresolved unsteadiness is low inside the rotor passage and high in the rotor wake. The highest level is observed near the leading edge. This is demonstrated more clearly in Fig. 7, which is a blade-to-blade profile of cycle-averaged relative unresolved unsteadiness just upstream of the rotor leading edge. Figure 8 shows the cycle-averaged unresolved unsteadiness at the leading edge with the unresolved unsteadiness (Tu_r) normalized by the mean rotor speed instead of the local relative velocity. The unresolved unsteadiness is defined by:

$$Tu_t = \frac{\sqrt{\overline{(u')^2} + \overline{(v')^2}}}{U_m} \times 100 \text{ percent} \tag{12}$$

The unresolved unsteadiness is then cycle averaged using Eq. (8). High levels of unresolved unsteadiness are still visible at

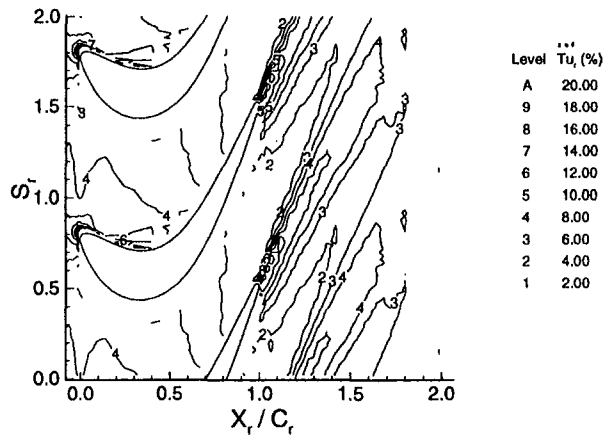

Fig. 6 Cycle-averaged relative unresolved unsteadiness ($\bar{\bar{Tu}}_r$)

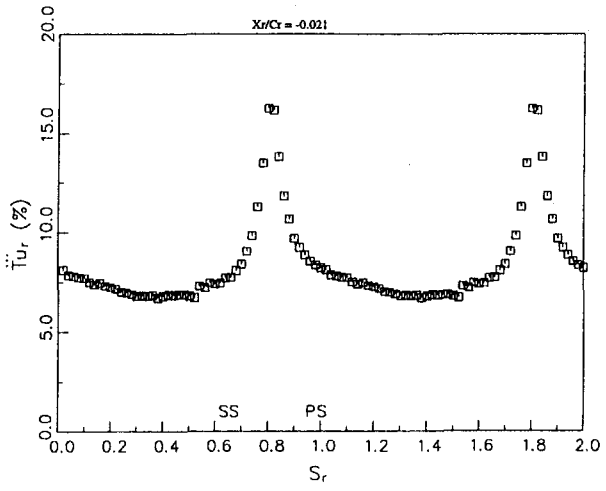

Fig. 7 Cycle-averaged relative unresolved unsteadiness ($\overline{Tu_r}$)

the leading edge. This demonstrates that the increase in relative unresolved unsteadiness at the rotor leading edge shown in Figs. 7 and 8 is not only due to low relative velocities, but also to an increase in the absolute magnitude of the velocity fluctuations. This agrees with the results of Hobson and Shreeve (1993), who measured an increase in the absolute magnitude of the velocity fluctuations at the leading edge of a compressor cascade, and this can be explained by examining the turbulent kinetic energy equation, which is

$$\frac{\partial k}{\partial t} + V_i \frac{\partial k}{\partial x_i} = \frac{\partial}{\partial x_i}\left(\frac{\nu_t}{\sigma_k}\frac{\partial k}{\partial x_j}\right) - \overline{v_i' v_j'}\frac{\partial V_i}{\partial x_j} - \epsilon \qquad (13)$$

I II III IV V

where term I is the rate of change of kinetic energy (k), term II is the convection term, III is the diffusion term, IV is the production term, and ϵ is the dissipation. In Eq. (13), $\overline{v_i' v_j'}$ is the turbulent fluctuating velocity correlation. The kinetic energy is a measure of the intensity of the velocity fluctuations. As the leading edge is approached, the large increase in mean flow velocity gradients near the leading edge causes an increase in the production term, which overshadows the dissipation, diffusion, and convection terms. Thus, the unresolved unsteadiness should increase as the leading edge of the blade is approached. In addition, the unresolved unsteadiness is observed to be higher near the pressure side. This is due to the interaction of the nozzle wake with the flow near the rotor pressure surface, which is discussed in the next section.

Rotor Time-Resolved Flow Field Including Nozzle Wake Propagation Through the Rotor. To understand the propagation of the nozzle wake through the rotor, one needs to look at the flow field in the rotor at different relative positions of the rotor with respect to the nozzle. This will show the chopping of the nozzle wake and its transport through the rotor, and is accomplished by looking at the rotor flow field at the six different nozzle/rotor blade locations measured (as shown in Fig. 1).

There are several criteria that can be used to identify the nozzle wake in the rotor passage. Compared to the free-stream flow field outside of the wake, the wake has a velocity defect, higher unresolved unsteadiness, a variation in flow angle across the nozzle wake, and higher shear stress. These criteria will be used in this section to determine the presence and propagation of the nozzle wake through the rotor passage.

An indication of the level of the interaction between the nozzle and rotor flow field can be assessed by examining the ratio of the time it takes the rotor to traverse one nozzle pitch versus the time it takes for fluid particles to travel through the rotor blade passage. This is called the reduced frequency and it is given by

$$\Omega = \frac{C_r/V_x}{S/U_m} \qquad (14)$$

where Ω is the reduced frequency, C_r is the rotor axial chord, V_X is the axial velocity at the inlet to the rotor, and S is the nozzle pitch. This ratio determines the number of nozzle wakes in each rotor passage at any instant in time. For the turbine in this investigation, the reduced frequency is 1.5, which means that there should be one and a half nozzle wakes in each rotor passage for each nozzle/rotor blade location, which is demonstrated in the following paragraphs.

Relative Unresolved Unsteadiness. Figures 9 shows the relative unresolved unsteadiness at six different nozzle/rotor locations. They represent six different "snapshots" of the rotor flow field, and since these six different locations are equally spaced over one nozzle pitch, they can be viewed sequentially from nozzle/rotor location one to location six and then back to one again. Examining position 2 first, a region of increased unresolved unsteadiness upstream of the rotor leading edge can be seen as compared to the cycle averaged relative unsteadiness upstream of the rotor presented in Fig. 4. This is the nozzle wake. Moving to position 3, the nozzle wake enters the rotor passage, and is subsequently chopped into individual segments by the rotor blades. The nozzle wake is bowed because the convection velocity at midpitch is higher than at the rotor leading edge. These individual segments of the nozzle wake can now move independently of each other, resulting in a mismatch between segments that were originally part of the same nozzle wake by the time they reach the rotor exit. There is also increased unresolved unsteadiness near the pressure surface of the rotor blade, just downstream of the point where the nozzle wake interacts with the rotor pressure surface. This increase in unresolved unsteadiness is a result of the interaction of the nozzle wake with the flow near the rotor pressure surface.

At position 4, the nozzle wake is becoming distorted as it travels through the rotor passage, with the region of the nozzle wake near the rotor suction surface moving faster than the region near the pressure side. This distortion of the nozzle wake is due to the large differential in the convection velocity between the pressure and suction surface, especially at the leading edge. Moving to positions 5 and 6, the distortion of the nozzle wake is continuing with the nozzle wake turning clockwise in the rotor passage. Continuing onto positions 1 and 2, the nozzle wake has turned more than 30 deg from its orientation at the rotor leading edge and it is now parallel to the rotor pressure

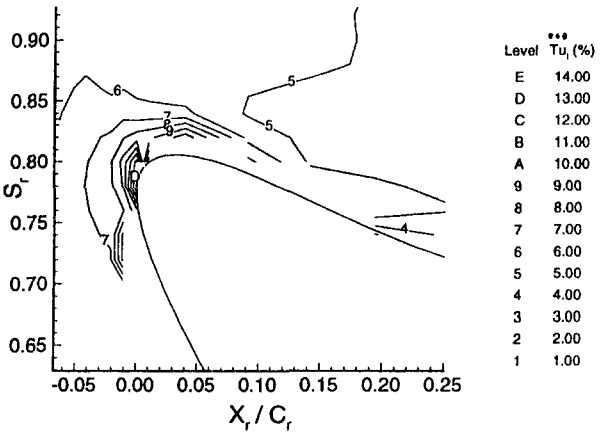

Fig. 8 Cycle-averaged unresolved unsteadiness ($\overline{Tu_t}$)

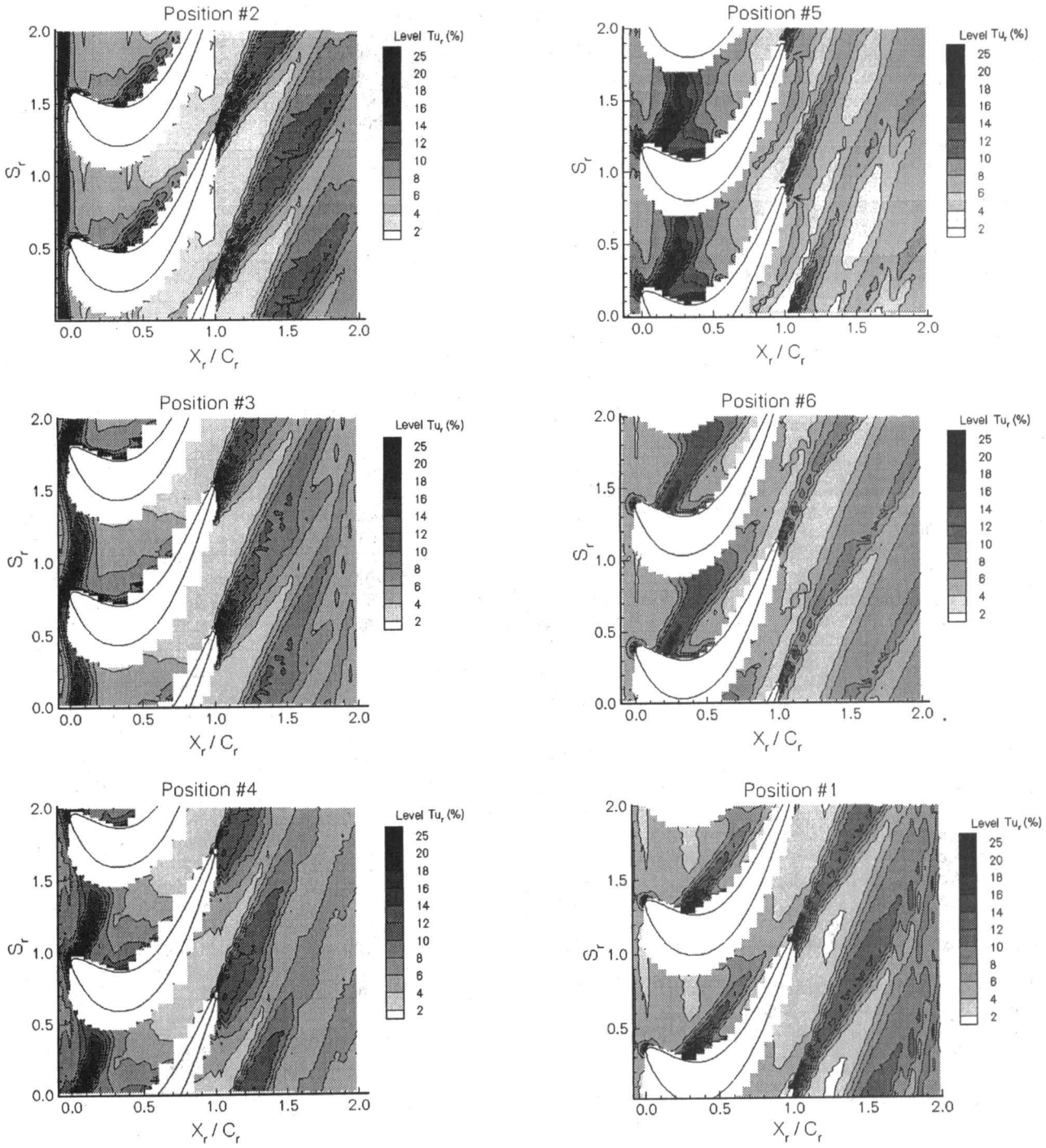

Fig. 9 Relative unresolved unsteadiness (Tu_r) at the six nozzle/rotor positions

surface. At position 3, the nozzle wake is stretched along the rotor pressure surface. Thus, it cannot be easily identified in the rotor passage since it is close to the rotor pressure surface, which cannot be measured by the LDV. This is in contrast to other measurements of the nozzle wake in the rotor passage (Hodson, 1985a; Binder et al., 1985) and computations (Hodson, 1985b; Korakianitis, 1992) who show that at the rotor trailing edge, the nozzle wake still spans the rotor passage from the pressure to suction surfaces. The reason for this can be found by looking at the blade surface velocity distributions. In both Hodson's and Binder's turbine rotors, the difference between the pressure and suction surface velocities is much less than the difference between the pressure and suction surface velocities for the AFTRF rotor. (Korakianitis (1992) calculates the flow in Binder's turbine rotor, while Hodson (1985b) calculates the flow in his own turbine rotor.) At midchord, the suction surface to pressure surface velocity ratio of the AFTRF turbine rotor is twice that of Hodson's and Binder's turbine rotors suction to pressure surface velocity ratios. This large difference between the pressure and suction surface velocities in the AFTRF turbine rotor causes the region of the nozzle wake near the rotor suction surface to travel much more rapidly than the region of the nozzle wake near the pressure surface. Thus by the time the nozzle wake near the rotor suction surface has reached the rotor trailing edge, it has rotated so that it hugs the pressure surface. In Hodson's and Binder's turbine rotors, the

difference between the pressure surface and suction surface velocities is not as great, thus the nozzle wake does not turn as much and by the time it reaches the rotor trailing edge it still spans the rotor passage from the pressure to suction surface.

Using an average convection velocity along the AFTRF rotor pressure surface between $X_r/C_r = 0.50$ and $X_r/C_r = 1.0$ (where the nozzle wake is located at position 2) to calculate the distance the nozzle wake moves between each position, the nozzle wake should be completely inside the rotor wake after six nozzle/rotor locations. Thus six nozzle/rotor locations from position 2 is position 2.

This is confirmed by examining the flow field downstream of the rotor. It can be seen that the flow field is not the same at every nozzle/rotor position, but changes from one position to another. Sharma et al. (1985) also noticed this phenomenon downstream of their rotor. Measuring the flow field at 10 percent axial chord downstream of a rotor with a three-sensor hot wire, they showed that there are two distinct flow fields downstream of the rotor, which they called the minimum and maximum interaction between the nozzle and rotor wakes. The maximum interaction occurs when the nozzle wake is directly inside the rotor wake while the region outside the wake shows low total unsteadiness. The minimum interaction occurs when the upstream nozzle wakes are between the rotor wakes, which is shown by the high unsteadiness in this region. A similar feature can be seen in the AFTRF rotor flow field just downstream of the rotor (from the trailing edge to one half chord downstream). The maximum interaction occurs at position 2 with high relative unsteadiness in the rotor wake (maximum relative unsteadiness of 16 percent at $X_r/C_r = 1.12$) and low unsteadiness in the region between the wakes (relative total unsteadiness of 4 percent at $X_r/C_r = 1.12$). This low relative unsteadiness region occupies more than 60 percent of the rotor pitch at 10 percent axial chord downstream of the rotor trailing edge.

The minimum interaction occurs at position 5 with the low relative unsteadiness region between the wakes ($Tu_r = 4$ percent) occupying only 15 percent of the rotor pitch at $X_r/C_r = 1.10$. At this location the maximum relative unsteadiness in the rotor wake is 12 percent as compared to 16 percent at the maximum interaction. This is because the nozzle wake is located between the rotor wakes at position 5, causing higher relative unsteadiness in between the rotor wakes, while at position 2 the nozzle wake is located in the rotor wake, thus causing higher relative unsteadiness in the rotor wake.

Unresolved Velocity Cross Correlations. The cross correlation of fluctuating axial and tangential velocity components of the unresolved velocity for each nozzle/rotor position, shown in Fig. 10, is defined as follows:

$$\overline{u'v'} = \frac{\sum_{i=1}^{n} [(V_{x_i} - \bar{V}_x)(V_{\theta_i} - \bar{V}_\theta)]/n}{U_m^2} \times 100 \text{ percent} \quad (15)$$

The unresolved velocity cross correlation in the nozzle wake is higher than in the surrounding fluid. These higher velocity cross correlation regions are located in the same regions where the nozzle wake was identified by examining the relative total unsteadiness, relative total velocity (not shown, see Zaccaria, 1994), and relative flow angle contours (not shown, see Zaccaria, 1994), thus providing added confidence for the existence of the nozzle wake. The unresolved velocity cross correlation starts out being negative in the nozzle wake at position 2. (The nozzle wake is located upstream of the rotor blade at this position.) At position 3, the velocity cross correlation changes sign in the region of the nozzle wake near the pressure surface, with this region being positive while the region of the nozzle wake near the suction surface is negative. Continuing on to the next locations, the turning and the distortion of the nozzle wake can be seen. These figures show that as the nozzle wake travels downstream through the rotor passage it thins out near the rotor pressure surface and thickens near the rotor suction surface. This is due to the nozzle wake acting like a negative jet. Examining positions 1 and then 2, the nozzle wake is seen to have elongated and thinned out considerably. This is a result of two reasons. The first is an inviscid phenomenon, which was discussed by Smith (1966), and is due to the fact that vorticity must be conserved in the nozzle wake, thus as the wake length grows, the wake width must become smaller. The second is a result of the large variation in convective velocity across the rotor pitch. Since the velocity is faster along the rotor suction surface than near the pressure surface, the region of the wake near the suction surface moves faster than the region near the pressure surface. Thus the wake stretches, becoming narrower and longer.

The maximum unresolved cross correlation (in the rotor passage) occurs near the nozzle wake center at most of the positions. The correlation is negligible at other locations in the rotor blade passage. One would expect the correlation to be higher inside the blade boundary layer, but no data are available in this region to confirm this.

Downstream of the rotor trailing edge, one can see the flow field is not the same at every nozzle/rotor position, but changes from one position to another, similar to the unsteadiness plots. For the region just downstream of the trailing edge at the maximum interaction (position 2), the unresolved velocity cross correlation is high in the near-rotor wake (at $X_r/C_r = 1.04$ it is a maximum of -3.0) and is low (zero) in the free-stream region outside of the rotor wake. This low unresolved velocity cross correlation region occupies over 60 percent of the rotor pitch at $X_r/C_r = 1.12$. The minimum interaction position (position 5) has a lower peak value of unresolved velocity cross correlation in the rotor wake (maximum unresolved velocity cross correlation of -2.0 at $X_r/C_r = 1.04$) than the value at the maximum interaction region (position 2) and a higher unresolved velocity cross correlation in the region between the rotor wake (maximum unresolved velocity cross correlation of 0.40 at $X_r/C_r = 1.12$) as compared to the value at the maximum interaction position. The low unresolved velocity cross correlation ($\overline{u'v'} = 0$) occupies only 25 percent of the blade pitch at $X_r/C_r = 1.1$. This is because at the maximum interaction position, the nozzle wake is inside the rotor wake, thus causing higher unresolved velocity cross correlations in the wake and outside the rotor wake the unresolved velocity cross correlations are low, while at the minimum interaction position the nozzle wake is located between the rotor wake, thus causing higher unresolved velocity cross correlations in the region between the rotor wake.

Nozzle Wake Characteristics Inside the Rotor Passage. An understanding of the steady and unsteady characteristics of turbine nozzle and rotor wakes is important for the efficient design of axial flow turbomachinery. A major cause of noise and vibration characteristics of turbomachinery is wakes. Turbine wakes represent a source of loss in efficiency, since the mixing of the wakes with the free stream inside the rotor passage dissipates energy. The characteristics of the wake, including the decay characteristics and the path that it follows, are important in the design of the following blade rows. This information is essential for both the prediction of the aerodynamic and mechanical performance of a turbine and for building quieter turbomachines.

Absolute Velocity. The absolute velocity profiles of the nozzle wake upstream of the rotor blade, in the rotor blade passage, and downstream of the rotor blade are presented in Figs. 11 and 12, respectively. The measurements upstream of the rotor were acquired with the five-hole probe and are taken from Zaccaria and Lakshminarayana (1995). For the measurements in and downstream of the rotor, each axial location, plotted in Fig. 12, represents the axial location for each nozzle wake segment where the maximum velocity defect occurs. The nozzle/rotor

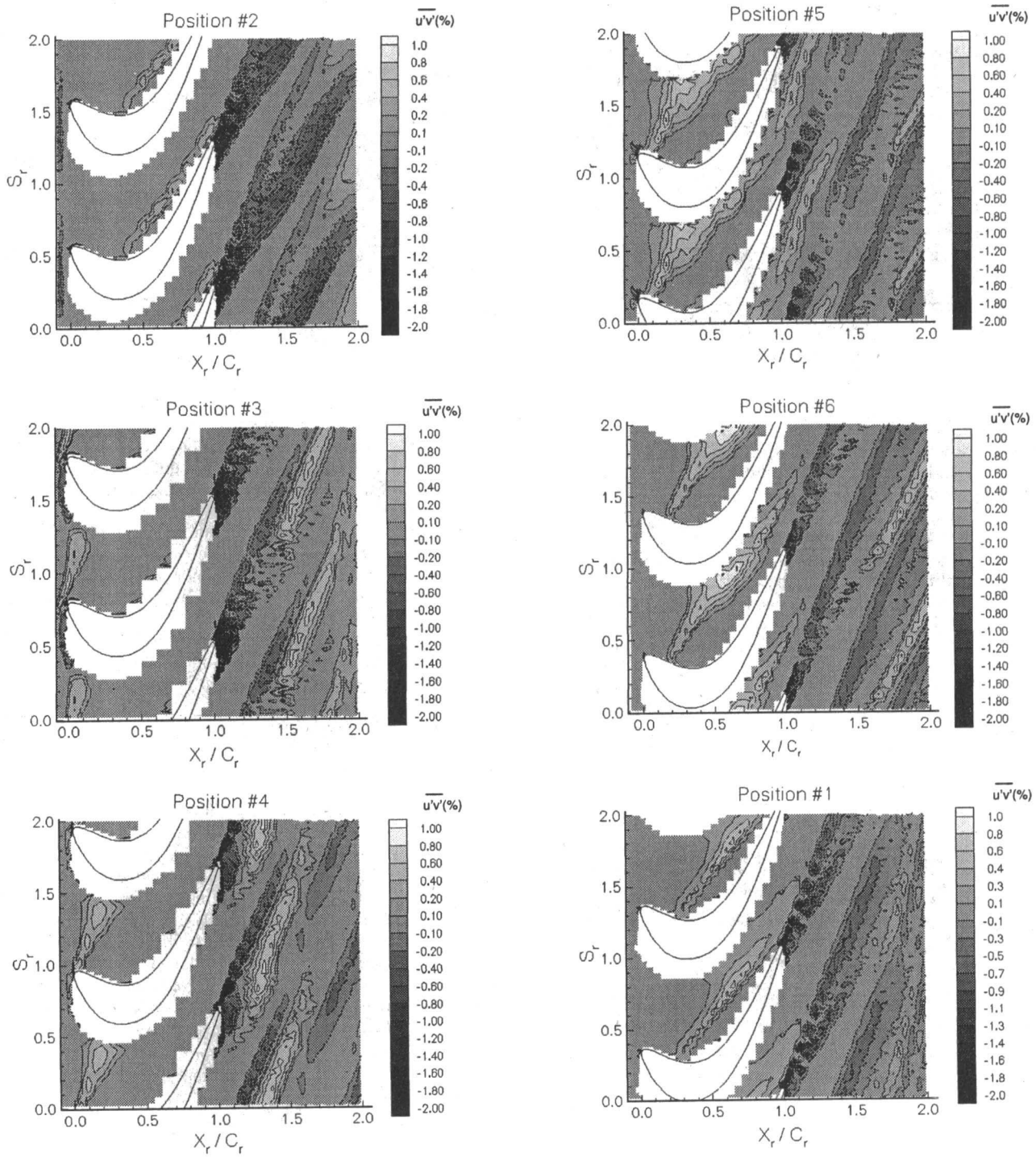

Fig. 10 Unresolved velocity correlation ($\overline{u'v'}$) at the six nozzle/rotor positions

position in which the nozzle wake segment is located is also given in Fig. 12 in parentheses next to the axial location. A nozzle wake segment is defined as follows: As the nozzle wake enters the rotor passage, it is divided into individual segments as it is chopped by the rotor leading edge and these segments subsequently propagate through the rotor passage independent of each other. The data are displayed over two rotor blade pitches (the data from one rotor pitch is doubled) to aid interpretation.

Upstream of the rotor, the nozzle wake decays very rapidly as the rotor leading edge is approached. As the nozzle wake moves through the rotor passage, the absolute magnitude of its defect grows and then decreases. Downstream of the rotor trailing edge, the nozzle wake defect remains constant until $X_r/C_r = 1.64$. (The nozzle wake is the smaller of the two velocity defects in the flow field downstream of the rotor while the rotor wake is the larger defect.) The variation in nozzle wake defect is demonstrated more clearly in Fig. 13, which shows the nozzle wake defect normalized by the local maximum velocity. The wake defect is the difference between the local minimum and maximum velocity in the wake. (The local maximum velocity is defined as the velocity that would exist at the same location as the wake center line in the absence of nozzle wake. This is interpolated from the wake profiles shown in Fig. 12.) This is

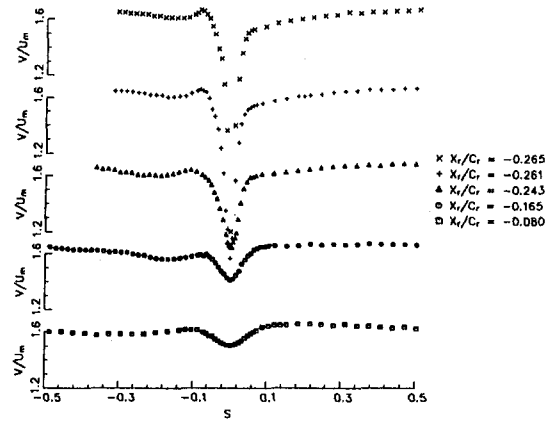

Fig. 11 Nozzle wake velocity (V/U_m) profiles upstream of rotor (five-hole probe measurements)

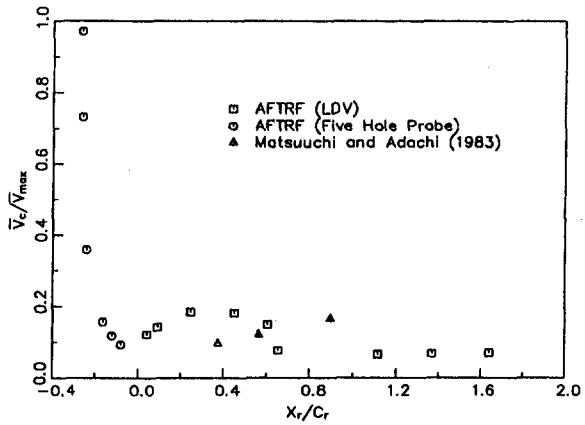

Fig. 13 Variation of peak nozzle wake velocity defect in rotor passage

consistent with the normalization of the nozzle wake velocity defect upstream of the rotor measured by a five-hole probe (see Zaccaria and Lakshminarayana, 1995), which is also presented in this figure. Examining this figure, one can see that the velocity defect decreases sharply from the nozzle trailing edge (located at $X_r/C_r = -0.27$) to the rotor leading edge. This rapid decay is due to pressure gradients, high turbulence intensities, and wake centerline curvature and the influence of the downstream rotor. The relative motion between the rotor and the nozzle causes periodic variations in the potential flow field around the blades which causes the wake to decay faster. A more detailed discussion of the nozzle wake decay between the nozzle and rotor is given in Zaccaria and Lakshminarayana (1995).

The nozzle wake then enters the rotor passage where the velocity defect increases from the rotor leading edge up to $X_r/C_r = 0.30$ and decreases after that until the trailing edge. Downstream of the trailing edge the velocity defect is constant. Matsuuchi and Adachi (1983) have observed a similar feature in their axial flow fan. The maximum velocity defect for each upstream stator wake segment in their axial flow fan rotor is presented also in Fig. 13. As the stator wake travels through the rotor its velocity defect increases. This is because, according to Hill et al. (1963), a positive (adverse) pressure gradient slows the wake decay and if the pressure gradient is large enough the wake decay will be stopped completely and the wake will grow in size. This is what is happening here, since there is an adverse pressure gradient in a compressor rotor.

The reasons for the velocity defect increase and decrease in the turbine rotor are more complex. A possible explanation can be given by examining the mass-averaged cycle-averaged relative velocity, presented in Fig. 14. Also shown in this plot is a comparison of the LDV data to the mass-averaged relative velocity derived from the five-hole probe downstream of the nozzle. The comparison between the data derived from the two measuring techniques is excellent, being within 1.0 percent of each other at $X_r/C_r = -0.08$. The relative velocity decreases slightly from the leading edge until $X_r/C_r = 0.30$, increases sharply from $X_r/C_r = 0.40$ until the trailing edge, and then is constant downstream of the trailing edge. The change in wake defect seems to correspond to the relative velocity change, with the defect increasing until $X_r/C_r = 0.30$ and then decreasing downstream of $X_r/C_r = 0.40$. Downstream of the rotor trailing

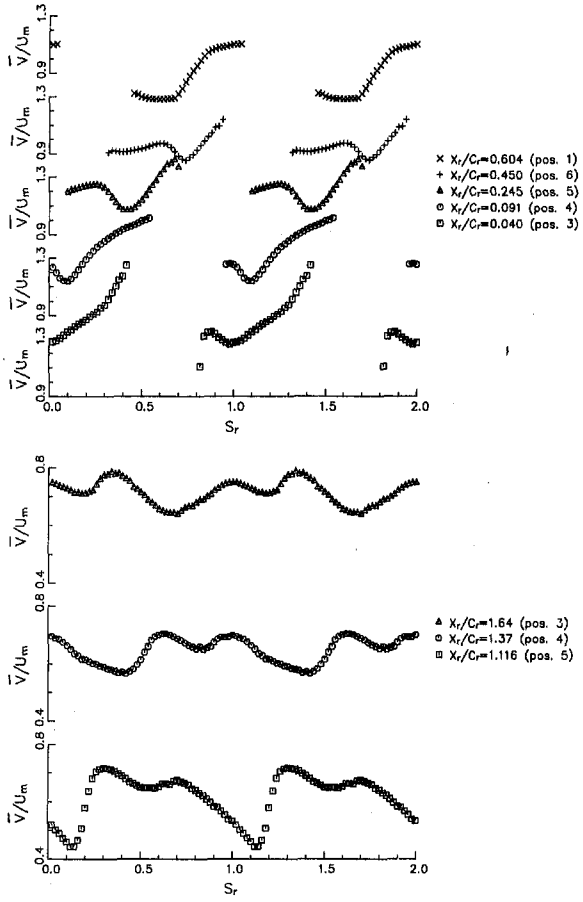

Fig. 12 Nozzle wake velocity ($\bar{V}/U_m$) profiles in rotor passage

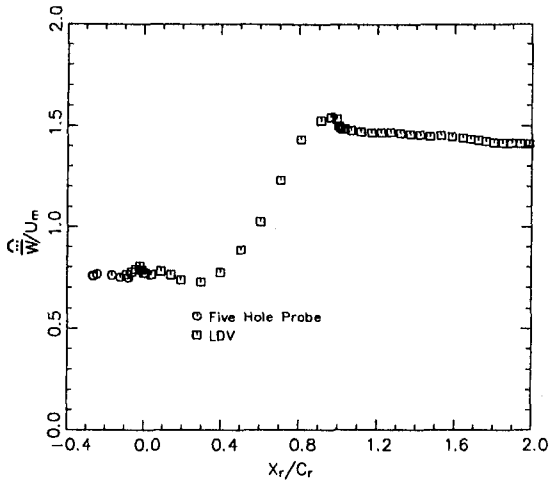

Fig. 14 Mass-averaged, cycle-averaged relative velocity ($\ddot{\bar{W}}/U_m$)

edge, the wake defect is constant. As discussed earlier, Raj and Lakshminarayana (1973) found that the wake decay rate corresponds to the variation in wake edge velocity. In the region where the relative velocity decreases, the nozzle wake velocity defect increases. Between $X_r/C_r = 0.40$ and the trailing edge, the relative velocity increases, resulting in a favorable pressure gradient, which causes the nozzle wake to decay.

Unresolved Unsteadiness and Velocity Cross Correlations. Blade-to-blade profiles of unresolved unsteadiness (defined by Eq. (12)) at the axial location where the maximum unresolved unsteadiness occurs in each nozzle wake segment are shown in Fig. 15. The unresolved unsteadiness is normalized by U_m here in order to compare the fluctuating velocity at different axial locations, since the velocity outside of the nozzle wake changes significantly in the rotor. One interesting feature is that the peak magnitude of unresolved unsteadiness in the nozzle wake does not decay continuously as it travels through and downstream of the rotor passage. This is also established in Fig. 16, which presents the peak unresolved unsteadiness for each nozzle wake segment. The peak unsteadiness increases slightly from the rotor leading edge to $X_r/C_r = 0.30$ after which it decreases dramatically.

This increase and decrease in unresolved unsteadiness are related to the nozzle wake velocity defect increase and decrease in the rotor passage shown in Fig. 16. Where the nozzle wake velocity defect increases in the rotor passage (from the rotor leading edge to $X_r/C_r = 0.30$), the unresolved unsteadiness increases and where the nozzle wake decays (from $X_r/C_r = 0.40$ to the rotor trailing edge) the nozzle wake unresolved unsteadiness decays. An additional effect that could cause the decrease in unresolved unsteadiness from $X_r/C_r = 0.40$ to the rotor trailing edge can be seen by examining Fig. 14, which is the mass-averaged cycle-averaged relative velocity in the rotor. The relative velocity increases sharply downstream of $X_r/C_r = 0.30$ and since the unsteadiness decays in an accelerating flow field, the maximum unsteadiness in each nozzle wake segment decreases also. Downstream of the rotor trailing edge, the nozzle wake unsteadiness increases in magnitude until at one half chord downstream of the rotor it is at the same value as it is at the rotor inlet. Sharma et al. (1985) also notice in their axial flow turbine that the nozzle wake unsteadiness downstream of the rotor is the same order of magnitude as it is upstream of the rotor. Another interesting feature of this flow field can be seen downstream of the rotor in Fig. 15. Close to the trailing edge, the unsteadiness of the rotor wake is much higher than the nozzle wake. As the wakes travel downstream, the unsteadiness in the rotor wake decreases while the nozzle wake unsteadiness increases until about one half chord downstream of the rotor the unsteadinesses for both the nozzle and rotor wakes are equal in magnitude.

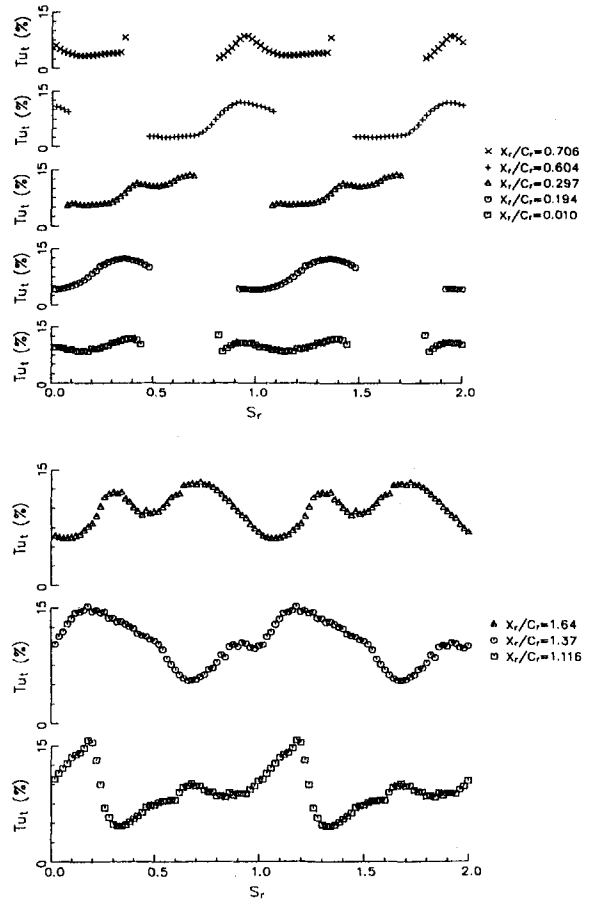

Fig. 15 Nozzle wake unresolved unsteadiness (Tu_t) in rotor passage

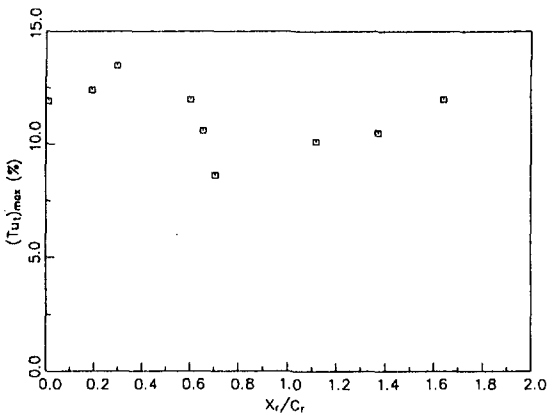

Fig. 16 Variation of peak nozzle wake unresolved unsteadiness $(Tu_t)_{max}$ in rotor passage

Blade-to-blade profiles of unresolved velocity cross correlation (defined by Eq. (15)) at the axial location where the maximum unresolved velocity cross correlation occurs in each nozzle wake segment are presented in Fig. 17. As the nozzle wake travels through the rotor passage, the velocity cross correlation grows until midchord, after which is decreases sharply. This is clear from Fig. 18, which is the variation of peak unresolved velocity cross correlation in each nozzle wake segment. The unresolved velocity cross correlation increases as the nozzle wake travels through the rotor passage until midchord, after which it decreases. This decrease occurs at the same location as the decrease in unresolved unsteadiness and they are probably related.

Concluding Remarks

The rotor flow field was measured at midspan with a two component LDV to gain a better understanding of the steady and unsteady flow field in a turbine rotor. Detailed measurements were also made near the leading edge. These measurements show that the rotor leading edge has a major influence on the flow field, with large velocity gradients and flow angle changes in the vicinity of the leading edge. The rotor leading edge has an influence on the flow field even 9 percent of the rotor axial chord upstream of the leading edge, with the change in flow angle between the free stream and stagnation region being 18 deg at this location. This effect increases as the rotor leading edge is approached with the change in flow angle increasing to 35 deg just upstream of the rotor leading edge.

High levels of relative unresolved unsteadiness also exist near the leading edge. As the leading edge is approached, a large

increase in the mean flow velocity gradients cause an increase in the production of unresolved unsteadiness that overshadows its dissipation. Higher levels of relative unresolved unsteadiness are also observed near the rotor pressure surface. This increase in unresolved unsteadiness is due to the interaction of the nozzle wake with the flow near the pressure surface.

The nozzle wake can be easily identified in the rotor passage. As the nozzle wake travels through the rotor flow field, the nozzle wake becomes distorted, since the region of the nozzle wake near the rotor suction surface moves faster than the region near the rotor pressure surface. The wake is found to be spread out along the rotor pressure surface, as it convects downstream of midchord. As the nozzle wake moves through the rotor passage, the magnitude of the velocity defect increases from the leading edge until $X_r/C_r = 0.30$, after which it decreases. This can be explained by examining the mass-averaged cycle-averaged relative velocity. The relative velocity decreases from the rotor leading edge until $X_r/C_r = 0.30$; this causes the nozzle wake velocity defect to increase. Downstream of $X_r/C_r = 0.30$, the relative velocity increases, resulting in a favorable pressure gradient, which causes the nozzle wake to decay. Downstream of the rotor trailing edge the nozzle wake velocity defect is nearly constant.

The unresolved unsteadiness in the nozzle wake does not decrease steadily as the nozzle wake travels through the rotor passage. Instead, the peak magnitude of the unresolved unsteadiness in the nozzle wake increases initially and then decreases as the nozzle wake travels through the rotor passage, until at one half chord downstream of the rotor trailing edge it is at the same value as it was upstream of the rotor.

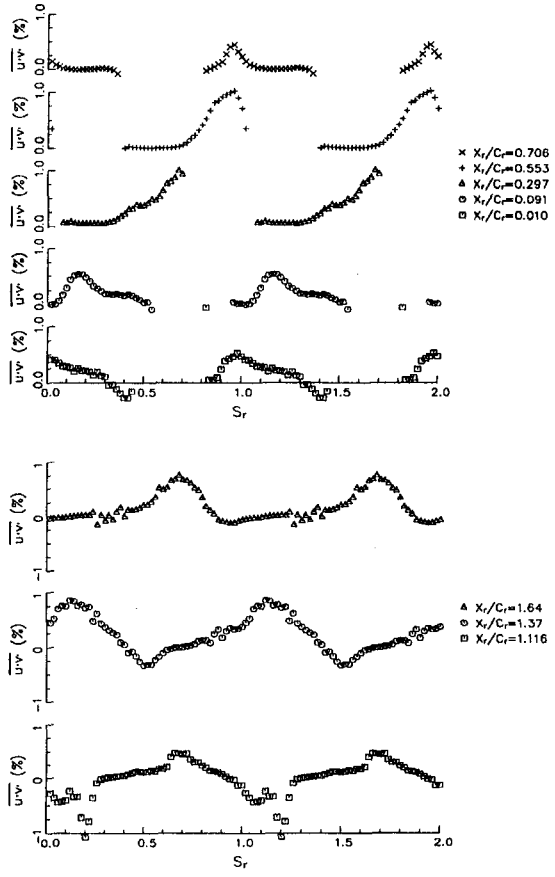

Fig. 17 Nozzle wake unresolved velocity correlation ($\overline{u'v'}$) in rotor passage

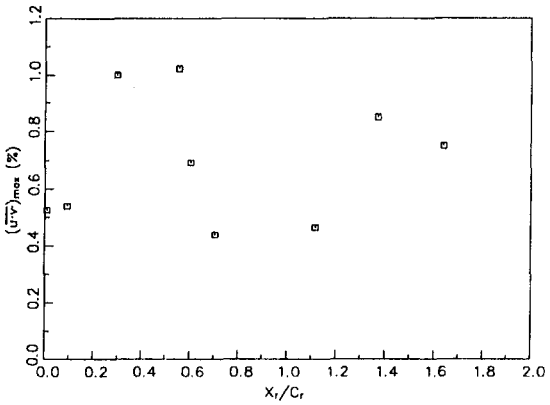

Fig. 18 Variation of peak nozzle wake unresolved velocity correlation $(\overline{u'v'})_{max}$ in rotor passage

Acknowledgments

This work was supported by NASA through Grant NSG3-555, with R. Boyle, K. Civinskas, and J. Schwab as technical monitors. Their helpful suggestions are also acknowledged. The LDV system used in this investigation was acquired with funds provided by NSF through equipment grant MSME-85-06626. The assistance of D. Ristic and S. Khalatov in acquiring the LDV data is gratefully acknowledged.

References

Binder, A., 1985, "Turbulence Production Due to Secondary Vortex Cutting in a Turbine Rotor," ASME *Journal of Engineering for Gas Turbines and Power,* Vol. 107, pp. 1039–1046.

Binder, A., Forster, W., Kruse, H., and Rogge, H., 1985, "An Experimental Investigation Into the Effect of Wakes on the Unsteady Turbine Rotor Flow," ASME *Journal of Engineering for Gas Turbines and Power,* Vol. 107, pp. 458–466.

Binder, A., Forster, W., Mach, K., and Rogge, H., 1987, "Unsteady Flow Interaction Caused by Stator Secondary Vortices in a Turbine Rotor," ASME JOURNAL OF TURBOMACHINERY, Vol. 109, pp. 251–257.

Dring, R. P., Joslyn, H. D., Hardin, L. W., and Wagner, J. H., 1982, "Turbine Rotor–Stator Interaction," ASME *Journal of Engineering for Power,* Vol. 104, pp. 729–742.

Dring, R. P., Joslyn, H. D., and Blair, M. F., 1987, "The Effects of Inlet Turbulence and Rotor/Stator Interactions on the Aerodynamics and Heat Transfer of a Large-Scale Rotating Turbine Model," NASA-CR-179469, Vol. 4.

Gallus, H. E., 1987, "Unsteady Aerodynamic Measurements on Rotors," in: *AGARD Manual on Aeroelasticity in Axial-Flow Turbomachines, Vol. 1, Unsteady Turbomachinery Aerodynamics,* pp. 11-1 to 11-18.

Greitzer, E. M., 1985, "An Introduction to Unsteady Flow in Turbomachines," in: *Thermodynamics and Fluid Mechanics of Turbomachinery,* Vol. II, pp. 967–1025.

Hathaway, M., 1986, "Unsteady Flows in a Single-Stage Transonic Axial-Flow Fan Stator Row," NASA TM-88929.

Hill, P. G., Schaub, U. W., and Senoo, Y., 1963, "Turbulent Wakes in Pressure Gradients," ASME *Journal of Applied Mechanics,* Vol. 30, pp. 518–524.

Hobson, G. V., and Shreeve, R. P. S., 1993, "Inlet Turbulence Distortion and Viscous Flow Development in a Controlled Diffusion Compressor Cascade at Very High Incidence," AIAA *Journal of Propulsion and Power,* Vol. 9, No. 3, pp. 397–407.

Hodson, H. P., 1985a, "Measurements of Wake-Generated Unsteadiness in the Rotor Passages of Axial Flow Turbines," ASME *Journal of Engineering for Gas Turbines and Power,* Vol. 107, pp. 467–476.

Hodson, H. P., 1985b, "An Inviscid Blade-to-Blade Prediction of a Wake-Generated Unsteady Flow," ASME *Journal of Engineering for Gas Turbines and Power,* Vol. 107, pp. 337–344.

Korakianitis, T., 1992, "On the Prediction of Unsteady Forces on Gas Turbine Blades: Part 1—Description of the Approach," ASME JOURNAL OF TURBOMACHINERY, Vol. 114, pp. 114–122.

Lakshminarayana, B., Camci, C., Halliwell, I., and Zaccaria, M., 1996, "Design and Development of a Turbine Research Facility to Study Rotor–Stator Interaction Effects," *Int. J. Turbo and Jet Engines,* Vol. 13, pp. 155–172.

Matsuuchi, K., and Adachi, T., 1983, "Measurement of the Three-Dimensional Unsteady Flow Inside a Rotor Blade Passage of an Axial Flow Fan," JSME Paper No. 83-TOKYO-IGTC-67.

Raj, R., and Lakshminarayana, B., 1973, "Characteristics of the Wake Behind a Cascade of Airfoils," *J. Fluid Mech.,* Vol. 61, part 4, pp. 707–730.

Rao, K. V., Delaney, R. A., and Dunn, M. G., 1992, "Vane-Blade Interaction in a Transonic Turbine, Part I—Aerodynamics," AIAA Paper No. 92-3323.

Sharma, O. P., Butler, T. L., Joslyn, H. D., and Dring, R. P., 1985, "Three-Dimensional Unsteady Flow in an Axial Flow Turbine," AIAA *Journal of Propulsion,* Jan.-Feb., pp. 29–38.

Sharma, O. P., Pickett, G. F., and Ni, R. H., 1992, "Assessment of Unsteady Flows in Turbines," ASME JOURNAL OF TURBOMACHINERY, Vol. 114, pp. 79–90.

Smith, L. H., 1966, "Wake Dispersion in Turbomachines," ASME *Journal of Basic Engineering,* Vol. 88, p. 66.

Zaccaria, M., 1994, "An Experimental Investigation into the Steady and Unsteady Flow Field in an Axial Flow Turbine," Ph.D. Thesis, Pennsylvania State University.

Zaccaria, M., and Lakshminarayana, B., 1995, "Investigation of Three Dimensional Flow Field at the Exit of Turbine Nozzle," AIAA *Journal of Propulsion and Power,* Vol. 11, p. 55.

Unsteady Flow Field Due to Nozzle Wake Interaction With the Rotor in an Axial Flow Turbine: Part II—Rotor Exit Flow Field

M. A. Zaccaria

B. Lakshminarayana

Center for Gas Turbines and Power,
The Pennsylvania State University,
University Park, PA 16802

The two-dimensional steady and unsteady flow field at midspan in a turbine rotor has been investigated experimentally using an LDV with an emphasis on the interaction of the nozzle wake with the rotor flow field. The velocity measurements are decomposed into a time-averaged velocity, a periodic velocity component, and an unresolved velocity component. The results in the rotor passage were presented in Part I. The flow field downstream of the rotor is presented in this paper. The rotor wake profiles and their decay characteristics were analyzed. Correlations are presented that match the decay of the various wake properties. The rotor wake velocity defect decays rapidly in the trailing edge region, becoming less rapid in the near and far wake regions. The rotor wake semi-wake width increases rapidly in the trailing edge region and then grows more gradually in the near and far wake regions. The decay of the maximum unresolved unsteadiness and maximum unresolved velocity cross correlations is very rapid in the trailing edge region and this trend slows in the far wake region. In the trailing edge region, the maximum periodic velocity correlations are much larger than the maximum unresolved velocity correlations. But the periodic velocity correlations decay much faster than the unresolved velocity correlations. The interactions of the nozzle and rotor wakes are also studied. While the interaction of the nozzle wake with the rotor wake does not influence the decay rate of the various wake properties, it does change the magnitude of the properties. These and other results are presented in this paper.

Introduction

An understanding of the steady and unsteady characteristics of turbine nozzle and rotor wakes is important for efficient design of axial flow turbomachinery used in land, space, naval, and aircraft applications. The rotor–stator interaction due to upstream wakes is a major source of noise, vibration, unsteady heat transfer, flutter, and unsteady flow in turbomachinery. Turbine wakes represent a source of loss in efficiency, since the mixing of the wakes with the free stream dissipates energy. The characteristics of the wake, including the decay and the path that it follows, are important in the design of the following blade rows. This information is essential for both the prediction of the aerodynamic and mechanical performance of a turbine and for building quieter turbomachines. An understanding of the wake development and its decay is also essential because of the role it plays in the rotor–stator interaction (see Part I). The objective of the research reported in this paper it to understand the steady and unsteady characteristics of the rotor wake caused by the upstream nozzle wake.

Although there has been extensive research done on compressor rotor wakes (see Reynolds and Lakshminarayana, 1979, and Ravindranath and Lakshminarayana, 1980), not much work has been done on turbine rotor wakes. Sitaram and Govardhan (1986) reported the wake of a turbine rotor cascade blade at midspan at seven axial locations. The only reported measurement of a wake from a turbine rotor is from Dring et al. (1987), and the rotor wake was measured at only one axial location. Thus, there is a need for a comprehensive survey of turbine wakes from a turbine rotor.

Contributed by the International Gas Turbine Institute and presented at the 40th International Gas Turbine and Aeroengine Congress and Exhibition, Houston, Texas, June 5–8, 1995. Manuscript received by the International Gas Turbine Institute March 15, 1995. Paper No. 95-GT-296. Associate Technical Editor: C. J. Russo.

Rotor Wake Characteristics

A complete discussion of the experimental facility, instrumentation, data analysis procedure, and definition of the averaging is given in part I. The rotor wake can be classified into three different categories: the trailing edge region, the near wake and the far wake. The trailing edge region is confined to the area just downstream of the trailing edge. The velocity defect is very large in this region. In the near wake region, the physical characteristics of the blade and the aerodynamic loading on the blade have a major impact on the development of the wake, causing the wake to be asymmetric. The wake defect is of the same order of magnitude as the mean velocity in this region. In the far wake the wake structure is almost symmetric and the physical characteristics and the aerodynamic loading have minor effects on the development of the wake. The velocity defect is also small in the far wake region. Typically, the trailing edge region extends to a few percent of chord, near wake up to about 20 to 30 percent chord, and the far wake beyond that.

Cycle-Averaged Properties. Figures 1(*a*) and 1(*b*) show the cycle-averaged relative velocity profiles at several axial locations in the rotor wake. (All velocities presented in this paper are ensemble averaged and phase-lock averaged. The averaging procedures are described in detail in part I.) The velocity gradients in the tangential direction are very large just downstream of the rotor trailing edge. This feature results from the develop-

ment of the flow as it transitions from the blade boundary layer to the wake. Farther downstream the gradient becomes much smaller due to wake spreading and mixing with the free stream as well as interchange of momentum and energy on either side of the wake. Also, the wake profiles are asymmetric about the wake center due to the differential growth of the boundary layer on the two surfaces of the blade. The suction side of the wake has a larger width than the pressure side wake, since the suction surface boundary layer at the blade trailing edge is larger than the pressure surface boundary layer. As the wake moves downstream, the differences between the pressure side and the suction side of the wake diminish until $X_r/C_r = 1.22$, where the wake profile becomes nearly symmetric about the wake center. The wake decay is fairly rapid, with very little left of it at two chords downstream.

The cycle-averaged unresolved unsteadiness (normalized by U_m to show the absolute level of the fluctuations and defined by Eq. (12) in part I) is presented in Figs. 2(*a*) and 2(*b*). The unresolved unsteadiness is highest near the trailing edge and decreases farther downstream. The high values near the trailing edge result from the vortex street shed from the trailing edge and the high production of turbulence in this region. The unsteadiness profiles have a dip in unsteadiness at the wake center with higher values of unsteadiness on either side of the dip. This is to be expected since the unsteadiness is zero on the blade surface with the maximum value occurring slightly away from the surface. This dip in unsteadiness disappears due to wake spreading and mixing, as the wake travels downstream. The highest unsteadiness is observed on the pressure side of the wake, which demonstrates that the pressure surface boundary layer has a higher unsteadiness than the suction surface boundary layer. This is due to the interaction of the nozzle wake with the flow near the pressure surface, which was discussed in part I. This increases the unresolved unsteadiness, which persists even in the wake. The maximum unsteadiness occurs close to the wake center in the near wake. Farther downstream, the maximum unsteadiness occurs away from the wake center due to the spread of the wake.

The cycle-averaged unresolved velocity cross correlation in the streamwise-normal coordinate system is shown in Figs. 3(*a*) and 3(*b*) and is defined as follows:

$$\overline{u_s' v_n'} = \frac{\overline{u'v'}(\cos^2 \bar{\beta} - \sin^2 \bar{\beta}) + (\overline{u'^2} - \overline{v'^2}) \cos \bar{\beta} \sin \bar{\beta}}{U_m^2} \times 100 \text{ percent} \quad (1)$$

where, unlike in part I (Eq. (15)), $(\overline{u'v'})$ is not normalized by U_m^2 and is defined as follows:

$$\overline{u'v'} = \frac{\sum_{i=1}^{n} [(V_{x_i} - \bar{V}_x)(V_{\theta_i} - \bar{V}_\theta)]}{n}$$

and the subscript i represents instantaneous velocity, the superscript represents the ensemble-averaged and phase-lock-averaged velocity in each rotor measurement window, and β is the relative flow angle. The unresolved unsteady velocity cross correlations for streamwise-normal coordinate system $(\overline{u_s' v_n'})$ is then cycle averaged using Eq. (8) in part I. The streamwise-normal coordinate system is used to aid physical interpretation. The unresolved velocity cross correlation is very small in the free stream and reaches a maximum value in the wake center. This is to be expected since the unresolved velocity cross correlation results from velocity and turbulence intensity gradients. The velocity cross correlation changes sign near the wake center due to the opposite velocity gradients on either side of the wake center, but close to the trailing edge the zero unresolved velocity cross correlation does not occur at the point of minimum velocity. Other researchers, such as Lakshminarayana and Reynolds (1979) also see this feature in their rotor wakes. In the near

Nomenclature

C_r = rotor axial chord
H = shape factor
j = individual measurement window location in the rotor passage
k = nozzle/rotor position
L = semi-wake width
n = total number of measurements in each measurement window
NB = number of rotor blades
NRP = number of nozzle/rotor positions
NW = number of measurement windows
NWB = number of measurement windows per blade
PS = pressure surface
s = streamwise distance
S_r = percentage pitchwise distance in rotor passage (normalized by rotor pitch)
SS = suction surface
Tu_r = relative unresolved unsteadiness $= \sqrt{(\overline{u'^2} + \overline{v'^2})}/W \times 100$ percent
Tu_t = unresolved unsteadiness $= \sqrt{(\overline{u'^2} + \overline{v'^2})}/U_m \times 100$ percent
U_m = blade speed at midspan
u' = fluctuating (unresolved) velocity in axial direction
$\tilde{u}$ = periodic velocity in axial direction
$\overline{u_s' v_n'}$ = unresolved unsteady velocity cross correlation in streamwise-normal coordinate system
V = absolute velocity
v' = fluctuating (unresolved) velocity in tangential direction
$\tilde{v}$ = periodic velocity in tangential direction
V_c = defect in absolute velocity at the wake center normalized by U_m
W = relative velocity
W_c = defect in relative velocity at the wake center normalized by U_m
W_o = rotor wake free-stream velocity
X_r = axial distance from rotor leading edge at midspan
Y = percentage pitchwise distance in the rotor wake with wake center equal to zero (normalized by rotor pitch)
Z = axial distance from rotor trailing edge normalized by rotor axial chord
α = absolute tangential flow angle or yaw angle (measured from axial direction)
α_p = primary flow angle
β = relative tangential flow angle or yaw angle (measured from axial direction)
β_o = rotor blade outlet angle
δ^* = displacement thickness (Eq. (14))
Θ = momentum thickness (Eq. (13))

Subscripts

h = hub
i = instantaneous
l = local
m = midspan
max = maximum
min = minimum
n = principle normal direction
r = rotor
s = streamwise direction
s = stator
r, θ, x = radial, tangential, axial directions
te = trailing edge

Superscripts

$\overline{\quad}$ = ensemble-averaged and phase-lock-averaged properties
$=$ = time-averaged properties
$\cdots$ = cycle-averaged properties
$'$ = fluctuating quantity
$\sim$ = periodic quantity

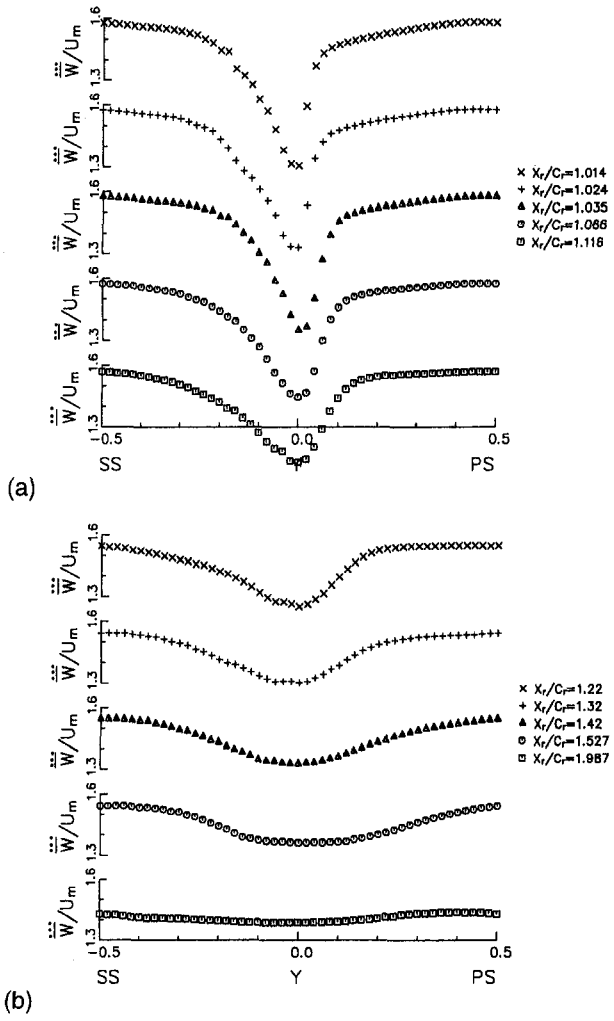

Fig. 1 Rotor wake cycle-averaged relative velocity ($\dddot{W}/U_m$) profiles

wake, the unresolved velocity cross correlation profiles are asymmetric about the wake center, with the magnitude of the cross correlation on the pressure side being larger than the magnitude on the suction side. The difference in the unresolved velocity cross correlation between the pressure and suction side of the wake decreases as the wake travels downstream until $X_r/C_r = 1.22$.

The relative flow angle in the cycle-averaged rotor wake, shown in Fig. 4, demonstrates that just downstream of the rotor trailing edge, the flow is overturned on the suction side of the wake and underturned on the pressure side of the wake. This is due to the difference in flow direction on the pressure and suction surfaces of the rotor. This over and underturning of the flow angle decreases rapidly from a maximum of 17 deg difference at the trailing edge to a 3 degree difference in flow angle at 10 percent chord downstream.

Cycle-Averaged Wake Decay Properties. A knowledge of the rate of decay for the rotor wake defect is necessary for an understanding of the rotor–stator interaction discussed earlier. The decay of the velocity defect is influenced by the pressure gradient, turbulence intensity, curvature, and viscous effects. The velocity defect decay for the cycle-averaged rotor wake is shown in Fig. 5. The wake velocity defect is the difference between the local minimum and maximum velocity in the wake. The very rapid decay in the trailing edge region results from the high unresolved unsteadiness and possibly the three-dimensional effects in this region. In the near and far wake regions, the velocity defect decay is less rapid. The rotor wake velocity defect is also compared to the decay of the AFTRF nozzle wake, and the decay of two linear rotor cascades, those of Sitaram and Govardhan (1986) and Ho and Lakshminarayana (1996), who computed the flow field in Gregory-Smith's rotor cascade (Gregory-Smith et al., 1988), which has similar flow turning as the present turbine rotor. The AFTRF rotor velocity defect decays much slower than the velocity defects of the other blades. This is in contrast to a compressor rotor wake, which decays faster than the wake of a compressor cascade. This reason for this is not understood as of yet. It is possible that the low-momentum fluid from other spanwise locations is being convected into the midspan wake and thus causing the midspan wake to be deeper and to decay slower. Future measurements at midspan and other spanwise locations that include the radial velocity are needed to verify this.

Schlichting's (1979) analysis indicates that a plane wake defect decays far downstream according to

$$V_c/V_{\max} \propto S^{-1/2} \tag{2}$$

where V_c is the velocity defect, $V_{\max}$ is the maximum velocity in the free stream outside of the wake, and S is streamwise distance. Using this relationship to correlate the rotor wake velocity defect results in the following equation:

$$\frac{\dddot{W}_c}{\dddot{W}_{\max}} = 0.14\left(\frac{Z}{\cos\beta_o}\right)^{-0.5} \tag{3}$$

where $\dddot{W}_c$ is the cycle-averaged velocity defect, $\dddot{W}_{\max}$ is the

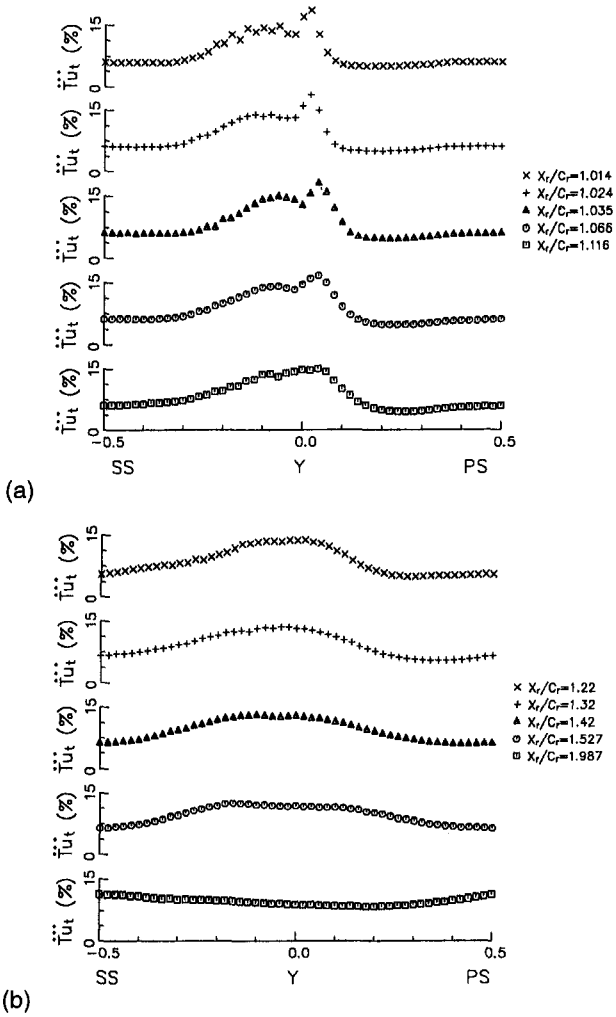

Fig. 2 Rotor wake cycle-averaged unsteadiness ($\dddot{T}u_t$) profiles

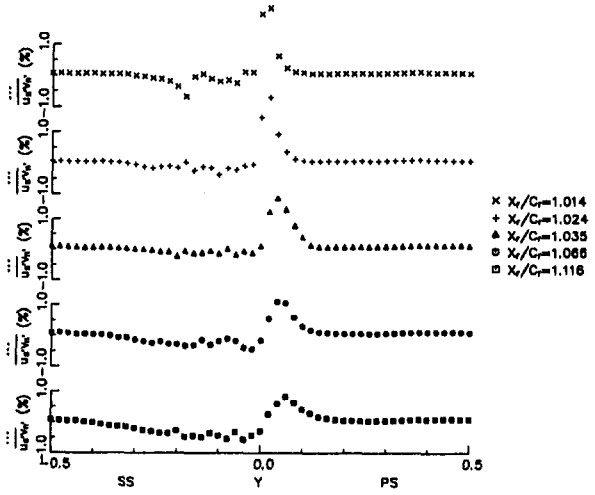

(a)

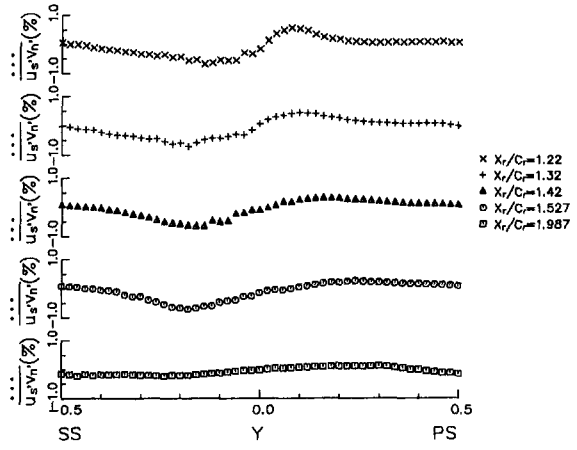

(b)

Fig. 3 Cycle-averaged unresolved streamwise-normal velocity correlation ($\overline{u_s'v_n'}$) profiles downstream of rotor

cycle-averaged maximum relative velocity in the free stream outside of the wake, $Z/\cos\beta_o$ is the streamwise distance downstream of the rotor (Z is the axial distance downstream of the rotor with $Z = 0.0$ at the trailing edge and β_o is the rotor blade outlet angle). This correlation can be seen to match the data quite well over most the region downstream of the rotor in Fig. 5. It is not good in the immediate vicinity of the rotor trailing edge ($Z/\cos\beta_o < 0.2$). In this region, the flow is very complex and is dominated by flow separation and trailing edge vortices along with the high levels of total unsteadiness; thus, the wake decays much faster than farther downstream. The constant in Eq. (3), 0.14, depends on the aerodynamic properties of the blade such as blade loading and turbulence intensity. These properties need to be included for a more general wake decay correlation.

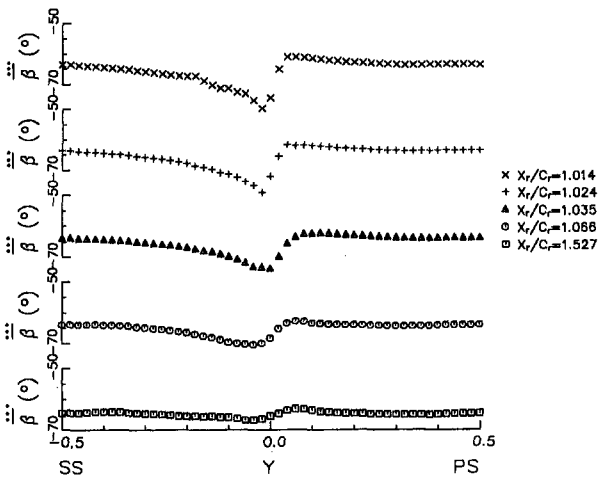

Fig. 4 Rotor wake cycle-averaged relative flow angle ($\overline{\beta}$) profiles

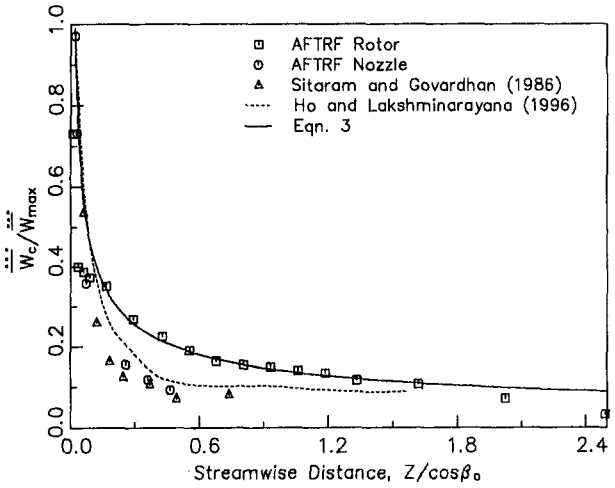

Fig. 5 Decay of cycle-averaged rotor wake velocity defect

The variation of the cycle-averaged rotor semi-wake width with streamwise distance is shown in Fig. 6. Semi-wake width is defined as the width of the wake where the total relative velocity defect is half. The data from the Sitaram and Govardhan's (1986) rotor cascade is also presented there for comparison. Both wake widths increase rapidly just downstream of the trailing edge (in the trailing edge region) and then grow more gradually in the near and far wake regions. Very far downstream (beyond $Z/\cos\beta_o = 1.5$), the AFTRF rotor wake width grows at a much slower rate.

Schlichting's (1979) analysis indicates that the increase of rotor semi-wake width is proportional to streamwise distance as follows:

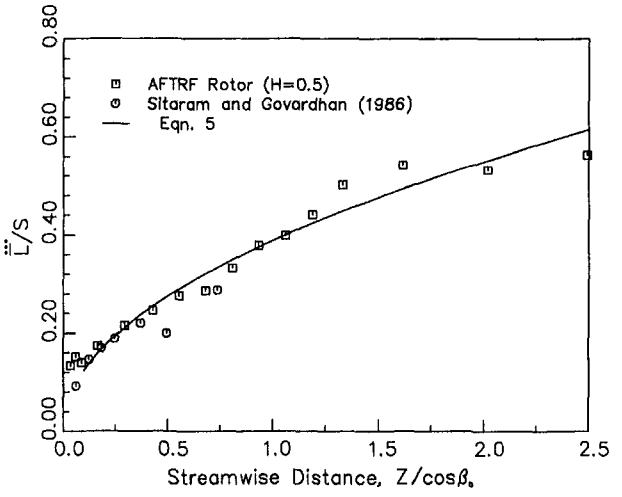

Fig. 6 Variation of cycle-averaged semi-wake width with streamwise distance

$$L \propto S^{1/2} \quad (4)$$

where S is streamwise distance and L is semi-wake width (the wake width at half the maximum velocity defect). Using Eq. (4), the measured variation of semi-wake width over most of the streamwise distance can be represented by the equation

$$L/S = 0.389(Z/\cos\beta_o)^{1/2}$$

$$\text{for} \quad 0.088 < (Z/\cos\beta_o) < 2.5 \quad (5)$$

The semi-wake width variation of Sitaram and Govardhan (1986) turbine rotor also matches this equation. Their turbine rotor has loading similar to the AFTRF turbine rotor (AFTRF rotor flow turning is 110 deg and Sitaram and Govardhan's rotor flow turning is 120 deg). Since wake width depends on the aerodynamic properties of the blade and this should be a function of the blade loading, the constants in Eq. (5) should include blade and flow properties.

An interesting feature in the variation of semi-wake width is observed between the trailing edge and near wake regions. The semi-wake width is nearly constant from the trailing edge to about $Z/\cos\beta_o = 0.1$. It then increases steadily beyond $Z/\cos\beta_o = 0.1$. Reynolds et al. (1979) also see this feature in their compressor rotor wake width. It is possible that this phenomenon is a characteristic of rotor wakes, since the turbine cascade wake width does not have this constant wake width near the trailing edge, and that it is caused by the effect of three-dimensional flow (radial flows) inside the wake, which are not present in cascade wakes. The radial transport of mass, momentum, and energy could be responsible for the constant wake width between the trailing edge and near wake regions, although the wake defect is decaying steadily there.

The decay of the maximum relative cycle-averaged unresolved unsteadiness, and the maximum axial and tangential components of cycle-averaged unresolved unsteadiness, are presented in Fig. 7. The relative unresolved unsteadiness is defined by Eq. (9) in part I while the relative unresolved axial and tangential unsteadinesses are defined as follows:

$$Tu_x = \frac{\sqrt{\overline{u'^2}}}{W} \times 100 \text{ percent}$$

$$Tu_\theta = \frac{\sqrt{\overline{v'^2}}}{W} \times 100 \text{ percent}$$

where $\sqrt{\overline{u'^2}}$ and $\sqrt{\overline{v'^2}}$ are defined in Eqs. (10) and (11) in part I, respectively. These values are then cycle averaged using Eq. (8) in part I. While the unsteadiness is very high in the trailing edge region, it decays rapidly as the wake travels downstream. In the far wake region, beyond $Z/\cos\beta_o = 1.50$, the relative unsteadiness has decayed to its magnitude upstream of the rotor blade. The relative unsteadinesses do not all decay at the same rate; each can be shown to decay at a rate given by

$$(Tu)_{\max} = K\left(\frac{Z}{\cos\beta_o}\right)^n \quad (6)$$

according to Raj and Lakshminarayana (1976), where K and n assume different values for each component. For the AFTRF turbine rotor, the rate of decay of the maximum cycle-averaged relative unresolved unsteadiness and the axial and tangential unsteadinesses are given by this equation with the constants as indicated in Fig. 7.

Equation (6) matches the data quite well, as seen in Fig. 7. The good match of Eq. (6) with both Raj and Lakshminarayana's (1976) compressor rotor maximum unsteadiness and the AFTRF turbine rotor data shown here gives confidence that a generalized correlation is feasible for the decay of the correlation of unresolved unsteady velocity downstream of turbine and compressor rotors. Since the exponent n varies from -0.18 to -0.27 for the turbine rotor and -0.19 to -0.24 for the streamwise and normal components of relative unsteadiness in the compressor rotor (see Raj and Lakshminarayana, 1976), assuming the exponent is equal to -0.22 will give a fairly good fit for the expression. The constant K depends on factors such as the blade drag coefficient, the free-stream unsteadiness, the mean velocity, and the blade curvature. Including the effect of these factors in the equation could collapse the data into a universal curve and lead to a good correlation.

The decay of the maximum cycle-averaged unresolved velocity cross correlation in the streamwise-normal coordinate system is presented in Fig. 8. The unresolved velocity cross correlation is very high in the trailing edge region and decays very rapidly as the wake travels downstream. The rate of decay seems to follow the same trend as the decay of the relative unsteadinesses. Using an equation of the form of Eq. (6), the decay rate of the maximum cycle-averaged unresolved velocity cross correlation can be correlated to distance as follows:

$$(\overline{u_s' v_n'})_{\max} = 0.335\left(\frac{Z}{\cos\beta_o}\right)^{-0.644} \quad (7)$$

This correlation agrees with the data quite well, as can be seen in Fig. 8.

The decay of the maximum auto and cross correlations of fluctuating velocity, both cycle-averaged periodic and unresolved, is shown in Figs. 9, 10, and 11. The periodic unsteady velocity, defined by Eq. (7) in part I, is caused by the relative motion between the blade rows, while the unresolved unsteady velocity is flow field fluctuation that is not correlated with the rotor speed, such as turbulence and vortex shedding. The components of the unresolved velocity cross correlations are defined as follows:

$$\overline{v_p' v_q'} = \frac{\sum_{i=1}^{n} [(V_{p_i} - \bar{V}_p)(V_{q_i} - \bar{V}_q)]/n}{U_m^2} \times 100 \text{ percent} \quad (8)$$

while the components of the periodic velocity cross correlation are defined as:

$$\overline{\tilde{v}_p \tilde{v}_q} = \frac{\sum_{i=1}^{n} [(\bar{V}_p - \bar{\bar{V}}_p)(\bar{V}_q - \bar{\bar{V}}_q)]/n}{U_m^2} \times 100 \text{ percent} \quad (9)$$

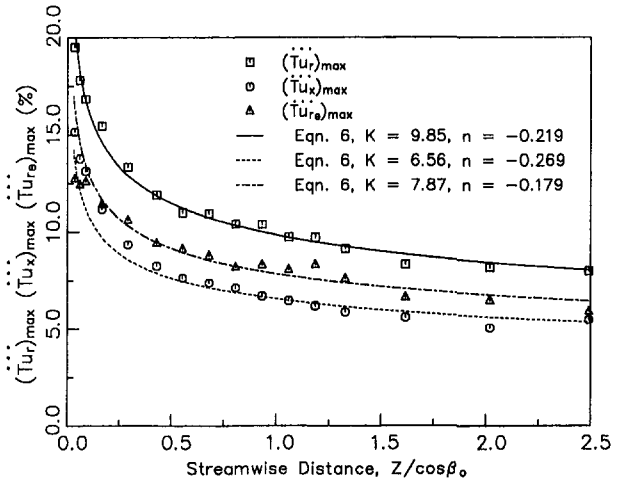

Fig. 7 Decay of rotor wake cycle-averaged maximum relative unresolved unsteadiness

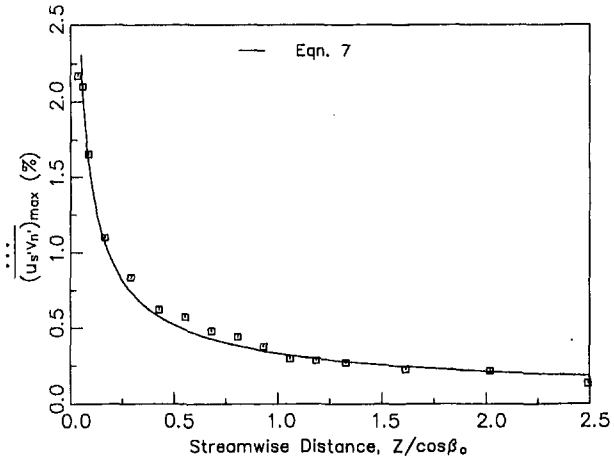

Fig. 8 Decay of rotor wake cycle-averaged maximum unresolved velocity correlation

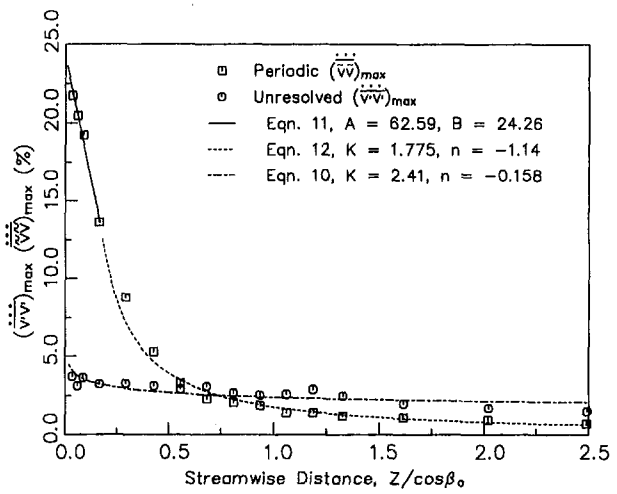

Fig. 10 Decay of rotor wake cycle-averaged maximum unresolved $(\overline{v'v'})_{max}$ and periodic velocity correlations $(\tilde{v}\tilde{v})_{max}$

where the subscripts p and q correspond to the axial and/or tangential velocity components, the overbar over the velocity components corresponds to both ensemble and phase-lock averaging, V_i is the instantaneous velocity, and $\bar{V}$ is the time-averaged velocity (see Fig. 2 in part I). The components of velocity cross correlations are then cycle averaged using Eq. (8) in part I.

For all three correlations, the maximum periodic unsteady velocity correlations are much larger than the maximum unresolved correlations in the trailing edge region. This is because the periodic velocity correlations are due to the periodic variation in velocity over the rotor blade pitch, which is large in the rotor wake. However, the periodic correlations decay much faster than the unresolved correlations so that the maximum periodic axial velocity correlation ($\overline{\tilde{u}\tilde{u}}$) is less than the maximum unresolved axial velocity correlation ($\overline{u'u'}$) downstream of $Z/\cos\beta_o = 0.25$, while the magnitude of the maximum periodic tangential velocity correlation ($\overline{\tilde{v}\tilde{v}}$) becomes lower than the maximum unresolved tangential velocity correlation ($\overline{v'v'}$) downstream of $Z/\cos\beta_o = 0.75$. While the maximum periodic unsteady velocity cross correlation ($\overline{\tilde{u}\tilde{v}}$) decays more rapidly than the maximum unresolved velocity cross correlation ($\overline{u'v'}$), the magnitude of the maximum periodic cross correlation is never lower than the magnitude of the maximum unresolved cross correlation. Both decay to negligible values in the far wake. These findings are useful in the analysis of multistage compressors and turbines, through the use of the averaging technique developed by Adamczyk (1985). These indicate that the periodic stresses are important and overshadow the flow in the near wake region ($Z/\cos\beta_o < 0.25$), and beyond this the correlations due to both the periodic and unresolved fluctuations are important. The decay of the maximum cycle-averaged unresolved velocity correlation reflects the same trend as the relative unsteadiness and can be modeled using Eq. (6) as follows:

$$(\overline{v_p'v_q'})_{max} = K\left(\frac{Z}{\cos\beta_o}\right)^n \tag{10}$$

where the subscripts p and q correspond to the axial and/or tangential velocity components and the constants K and n take different values for each component, which are given in Figs. 9, 10, and 11. The decay of the maximum periodic velocity correlations, on the other hand, only follow this trend in the near and far wake regions; in the trailing edge region the decay is linear. Thus, in the trailing edge region, the maximum cycle-

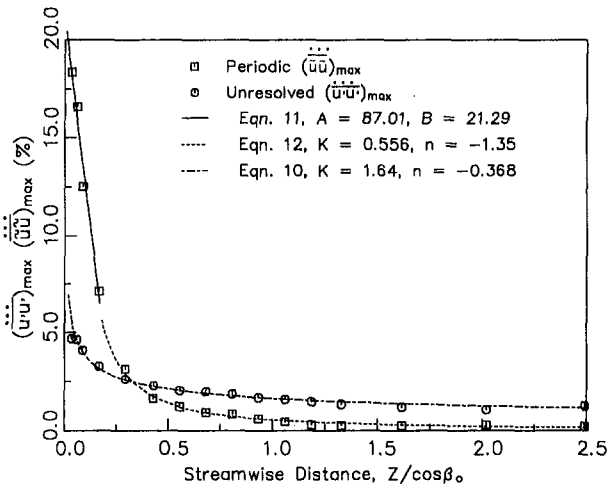

Fig. 9 Decay of rotor wake cycle-averaged maximum unresolved $(\overline{u'u'})_{max}$ and periodic $(\overline{\tilde{u}\tilde{u}})_{max}$ velocity correlations

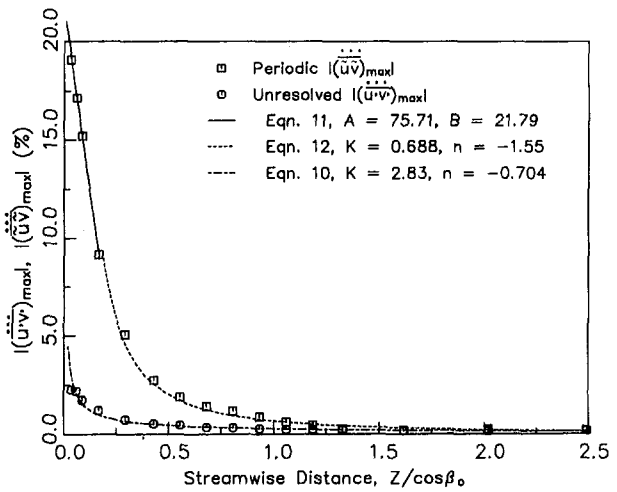

Fig. 11 Decay of rotor wake cycle-averaged maximum unresolved $|\overline{u'v'}|_{max}$ and periodic velocity correlations $|\overline{\tilde{u}\tilde{v}}|_{max}$

averaged periodic velocity correlation decay rates conform to the following relationship:

$$\overline{(\tilde{v}_p\tilde{v}_q)}_{\max} = -A\left(\frac{Z}{\cos\beta_o}\right) + B \tag{11}$$

while in the near and far wake regions the maximum periodic velocity decay rate correspond to the equation:

$$\overline{(\tilde{v}_p\tilde{v}_q)}_{\max} = K\left(\frac{Z}{\cos\beta_o}\right)^n \tag{12}$$

where $0.17 < Z/\cos\beta_o < 2.5$ and the constants A, B, K, and n assume different values for each component of unsteadiness given in Figs. 9, 10, and 11. These correlations correspond the experimental data quite closely. They also give added confidence that Eq. (6) can be used to model correctly both the decay of each component of the Reynolds stress tensor and the periodic velocity correlations. Since the periodic velocity correlations also correspond to the velocity defect, these correlations could be used to model the total velocity defect decay.

The cycle-averaged wake momentum thickness and shape factor variations downstream of the rotor are shown in Figs. 12 and 13. The momentum thickness for the rotor wake was determined using the equation

$$\Theta = \frac{1}{S_r}\int_0^{S_r}\frac{\overline{W}}{\overline{W}_o}\left(1 - \frac{\overline{W}}{\overline{W}_o}\right)rd\theta \tag{13}$$

where the integration was performed in the tangential direction over one blade spacing. The displacement thickness is defined by the expression,

$$\delta^* = \frac{1}{S_r}\int_0^{S_r}\left(1 - \frac{\overline{W}}{\overline{W}_o}\right)rd\theta \tag{14}$$

where the integration was also performed over one blade spacing in the tangential direction. Knowing δ^* and Θ, the wake shape factor in the wake can be found using the following equation:

$$H = \frac{\delta^*}{\Theta} \tag{15}$$

which is shown in Fig. 13.

Figure 12 shows that the momentum thickness increases from the trailing edge to $Z/\cos\beta_o = 0.4$, then decreases as the wake travels downstream until $Z/\cos\beta_o = 1.0$. It then becomes nearly constant between $Z/\cos\beta_o = 1.0$ to 1.6, and beyond $Z/\cos\beta_o = 1.6$, it decreases. Both Raj and Lakshminarayana (1973) and Ravindranath (1979) explained the variation in momentum thickness in their compressor cascade and rotor wakes, respectively, on the basis of the von Karman momentum integral equation with zero wall shear stress as follows:

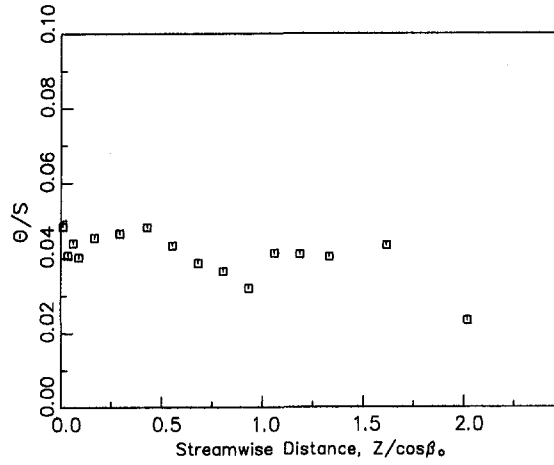

Fig. 12 Variation of rotor wake cycle-averaged momentum thickness with streamwise distance

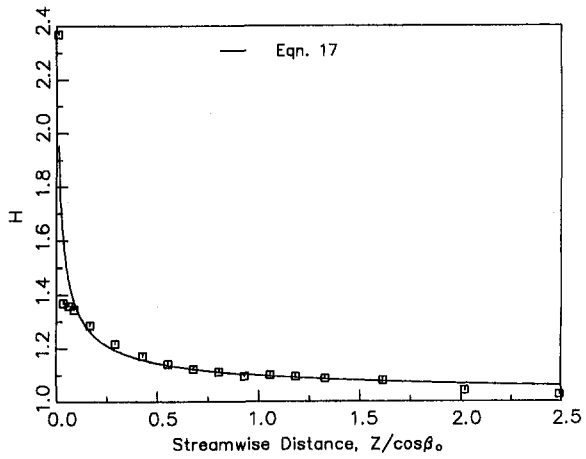

Fig. 13 Variation of rotor wake cycle-averaged shape factor with streamwise distance

$$\frac{d\Theta}{ds} + (2 + H)\frac{\Theta}{W_o}\frac{dW_o}{ds} = 0 \tag{16}$$

where s is the streamwise distance in the wake and W_o is the free-stream velocity. Equation (16) shows that the increase or decrease of Θ depends on the variation of W_o. If W_o increases, then Θ decreases, and if W_o decreases, then Θ increases. The downstream variation of Θ cannot be explained on the basis of this equation. The variation of the wake edge velocity downstream of the rotor does not correspond to the variation of the momentum thickness. A possible reason for this is the three-dimensional effects (radial outward flow) inside the wake.

The variation of shape factor with streamwise distance is presented in Fig. 13. The shape factor decreases sharply in the trailing edge region and then decreases at a slower rate as the wake travels downstream. The high value of shape factor just downstream of the trailing edge ($H = 2.37$) shows that the flow has a tendency to separate there. Since a turbine blade has a thick trailing edge, the flow does have a tendency to separate there. Other researchers, such as Hobson and Lakshminarayana (1990), have also predicted flow separation at the trailing edge of a turbine blade.

The variation of the shape factor with streamwise distance downstream of the trailing edge of an isolated airfoil was given by Spence (1953),

$$\left(1 - \frac{1}{H}\right) = \left(1 - \frac{1}{H_{te}}\right)\left[40\left(\frac{Z}{\cos\beta_o}\right) + 1\right]^{-1/2} \tag{17}$$

where H_{te} is the shape factor at the trailing edge. Raj and Lakshminarayana (1973) demonstrated that Eq. (17) can be used to predict the variation of shape factor accurately downstream of a compressor cascade. Figure 13 shows the comparison of this equation with the experimentally measured shape factor. In the trailing edge region the comparison is not good, but farther downstream, Eq. (17) accurately predicts the magnitude of shape factor. The poor agreement in the trailing edge region is due to the largely three-dimensional nature of the flow in the trailing edge region, flow separation, and the presence of the trailing edge vortex system.

Rotor Wake Profiles at Various Nozzle/Rotor Passage Relative Positions. Figures 14(*a*, *b*) show the relative velocity profiles in the rotor wake at different axial locations close to the rotor trailing edge. The data are presented at two selected nozzle/rotor locations that have large difference in flow properties between them (locations 3 and 5). The wake width at position 3 is wider than that at position 5, while the defect is larger at position 3 than at position 5. This is because the nozzle wake is located inside the rotor wake at position 3 and is located in the free-stream region outside of the rotor wake at position 5. While the magnitude of the minimum velocity in the wake center is similar close to the trailing edge at both positions, the free-stream velocity is different. The nozzle wake causes the free-stream relative velocity to be lower at position 5 than the free-stream velocity at position 3. Furthermore, the nozzle wake in position 3 causes an uneven velocity distribution inside the rotor wake, especially near the trailing edge (X_r/C_r = 1.0 to 1.035).

The unresolved unsteadinesses (Eq. 12 in part I) in the rotor wake at nozzle/rotor positions 3 and 5 are shown in Figs. 15(*a*, *b*). At both positions the unsteadiness is asymmetric about the wake centerline, which results from the different unresolved unsteadiness profiles in the blade surface boundary layers upstream of the trailing edge. The unsteadiness is much higher in the rotor wake. The region of increased unsteadiness occurs over a larger area at position 3 than at position 5 due to the presence of the nozzle wake inside of the rotor wake at position 3. On the other hand, the free-stream region of position 5 contains twice the magnitude of unresolved unsteadiness as the free-stream region of position 3 (10 percent as compared to 5 percent at position 3). This also results from the nozzle wake, which is located in the free-stream region of position 5.

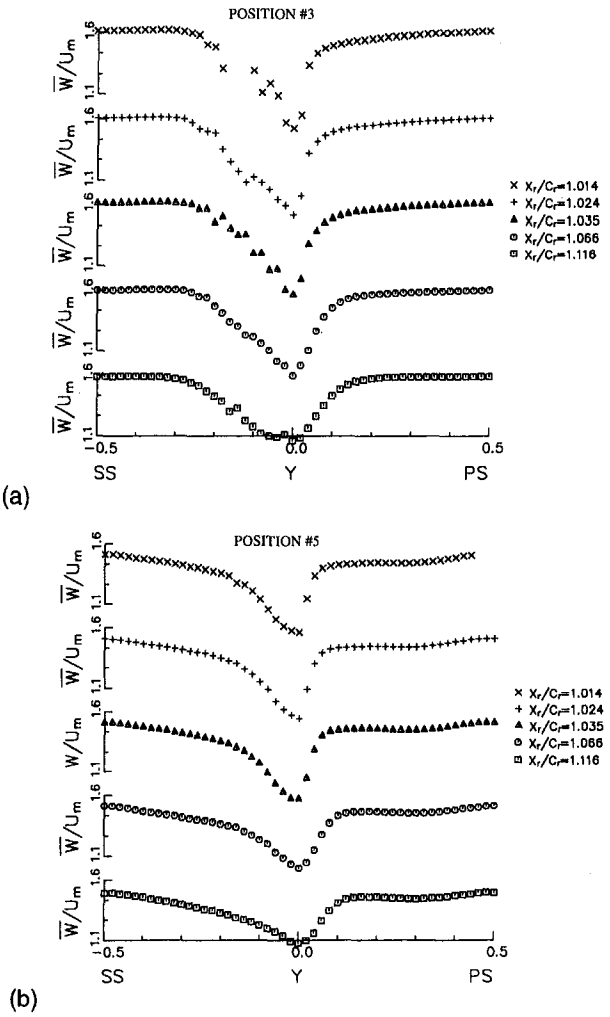

Fig. 14 Rotor wake relative velocity ($\overline{W}/U_m$) profiles

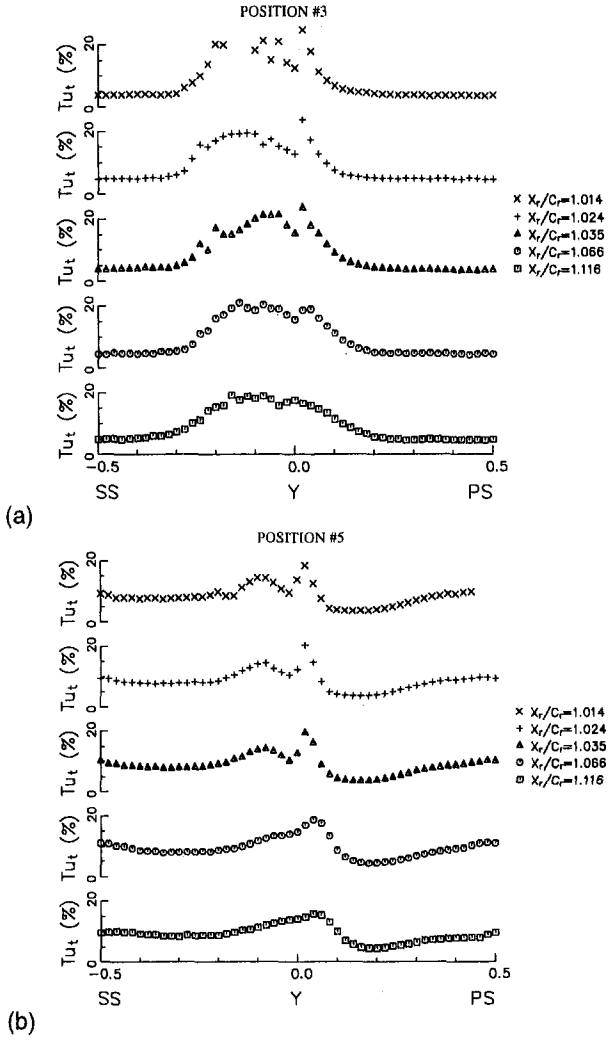

Fig. 15 Rotor wake unresolved unsteadiness (Tu_t)

The unresolved velocity cross correlation in the streamwise-normal coordinate system at nozzle/rotor positions 3 and 5 are presented in Figs. 16(*a*, *b*). The magnitude of unresolved velocity cross correlation on the pressure side of the rotor wake at position 3 is twice that on the pressure side of the rotor wake at position 5. This is caused by the transport of the nozzle wake toward the pressure side as explained in part I of this paper. On the suction side of the rotor wake at position 5, the unresolved velocity cross correlation is negligible, while the suction side of the wake at position 3 contains a large area of negative unresolved velocity cross correlation. The higher unresolved velocity cross correlation in the rotor wake at position 3 results from the presence of the nozzle wake inside the rotor wake at this position.

A noticeable difference between the relative flow angle in the rotor wake at these two nozzle/rotor positions is seen in Figs. 17(*a*, *b*). At position 3, the overturning on the suction side rotor wake is larger than the overturning on the suction side rotor wake of position 5, while the overturning in the free-stream region outside of the rotor wake at position 5 is higher than that in the free-stream region of position 3. The higher overturning regions result from the presence of the nozzle wake in these areas. Considerable variation in relative flow angle

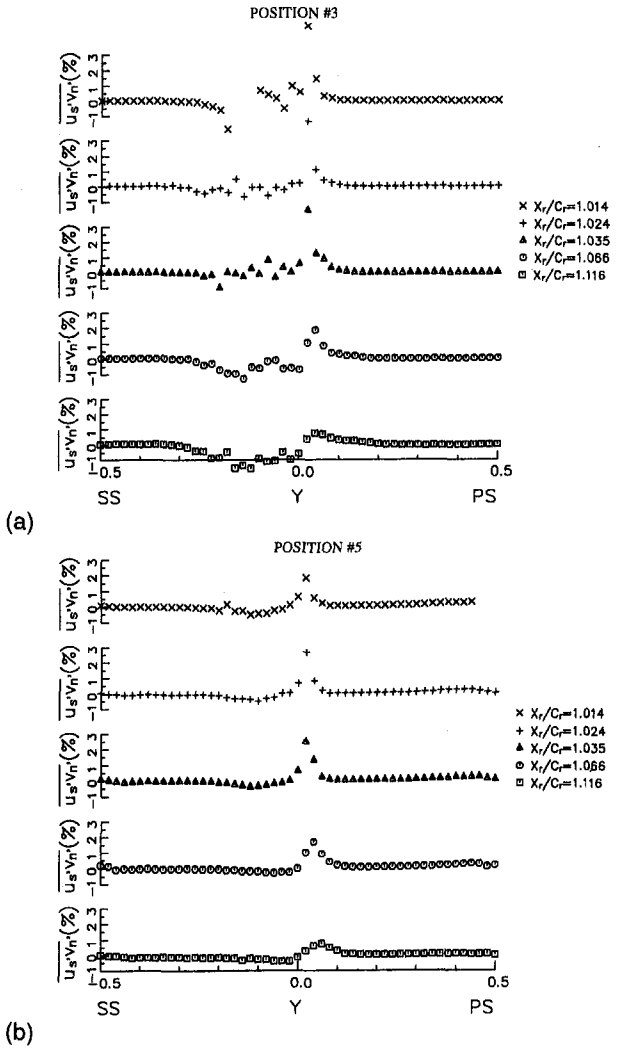

Fig. 16 Rotor wake unresolved velocity correlation ($\overline{u_s' v_n'}$)

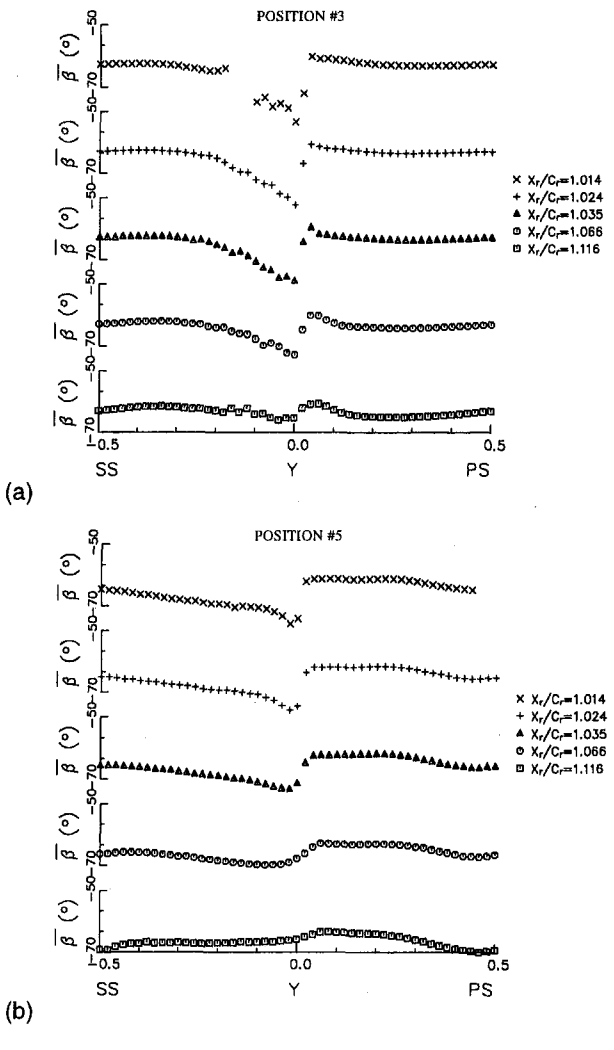

Fig. 17 Rotor wake relative flow angle ($\bar{\beta}$)

across the wake is observed at all positions. This is especially pronounced at position 3 in the near wake region. The underturning region, even though small, is observed on the pressure side of the wake at position 3. The flow angle variations are much larger at position 3 due to the presence of the nozzle wake inside the rotor wake.

Figures 14–17 show that the rotor wake properties vary between individual nozzle/rotor relative positions. Thus one can conclude that the rotor wake is not steady in the rotor time frame. This can be seen more clearly by looking at Figs. 18 and 19, which show the relative velocity profiles and unresolved unsteadiness in the rotor wake just downstream ($X_r/C_r = 1.066$) of the rotor trailing edge at all six nozzle/rotor positions. There is a variation in both the velocity profile inside the wake and in the free stream for all six positions (there is an 8 percent difference between the highest and lowest free-stream velocity and an 18 percent difference in velocity inside the wake). The lowest velocity at the wake center occurs at position 3 due to the presence of the nozzle wake inside the rotor wake at this position. At position 4, the nozzle wake has moved toward the rotor wake free-stream region (see part I of this paper). This causes the suction side wake width to increase and the free-stream velocity to decrease, since the nozzle wake is located partly in the suction side of the rotor wake and partly in the free-stream region. The wake center velocity increases at position 5, while the free-stream velocity decreases due to movement of the nozzle wake out of the rotor wake and into the free-stream region at this position.

The unresolved unsteadiness, presented in Fig. 19, shows the increased levels of unsteadiness on the suction side of the rotor

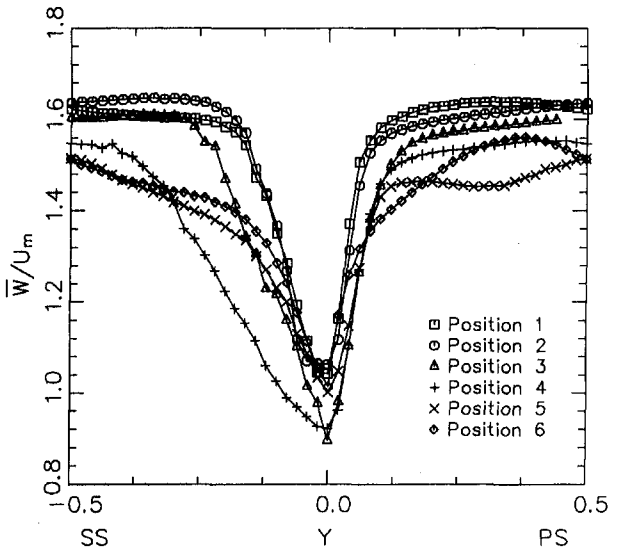

Fig. 18 Rotor wake relative velocity ($\bar{W}/U_m$) profiles at $X_r/C_r = 1.066$

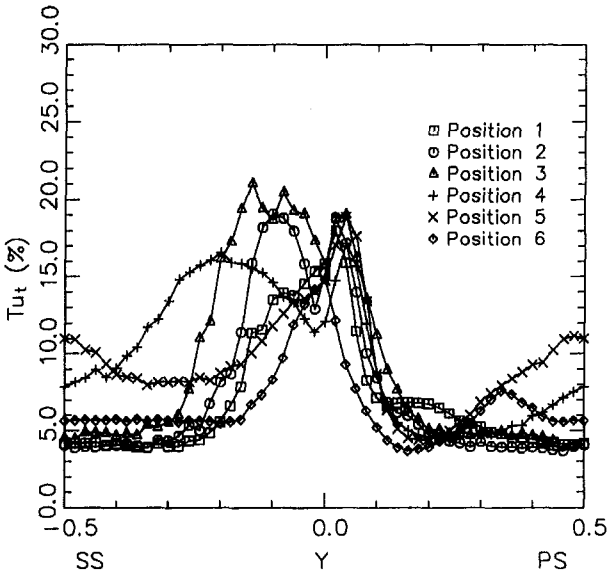

Fig. 19 Rotor wake unresolved unsteadiness (Tu_t) at X_r/C_r = 1.066

wake at position 3 due to the presence of the nozzle wake. At position 4, the level of the unsteadiness has decreased in the wake but has increased in the free-stream region since the nozzle wake is now partially in the rotor wake and partially in the free-stream region. At position 5, the nozzle wake has moved entirely into the free-stream region, as shown by the higher level of unsteadiness in the free-stream region and lower level in the rotor wake.

The decay of the velocity defect in the rotor wake with streamwise distance is shown in Fig. 20 for each of the different nozzle/rotor positions. The decay rate for each of the positions is similar, but the magnitudes of the velocity defects are different at each streamwise location. In the trailing edge and near wake region the defects for positions 3 and 4 are larger than the defects at 5 and 6 due to the presence of the nozzle wake inside the rotor wake at positions 3 and 4. Thus, while the nozzle wake does not seem to have an impact on the velocity defect decay rate, it does influence the magnitude of the velocity defect. Furthermore, positions 3 and 4 have the lowest defect from the trailing edge to $z/\cos\beta_o = 0.5$. Thus the nozzle wake tends to augment mixing of the wake resulting in a lower defect. Far downstream, position 1 has the higher wake velocity defect.

The nozzle wake interaction with the rotor wake also affects the rotor wake semi-wake width, as shown in Fig. 21. The semi-

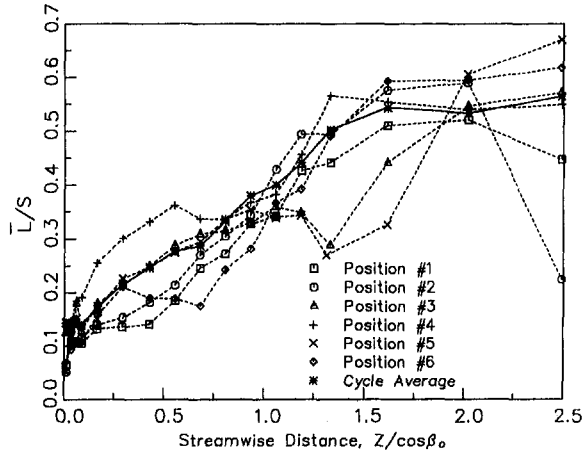

Fig. 21 Variation of rotor wake semi-wake width with streamwise distance for each nozzle/rotor location

wake width is defined as the width of the wake at half the defect of total velocity. The rate of increase in wake width for each of the nozzle/rotor positions is similar, but the magnitude of the semi-wake width at each streamwise location is not the same for each nozzle/rotor location. In the trailing edge and near wake regions, the rotor semi-wake widths for positions 3 and 4 are larger in magnitude than the semi-wake widths for positions 5 and 6 due to the presence of the nozzle wake inside the rotor wake at positions 3 and 4. Thus, just as for the velocity defect, the nozzle wake influences the magnitude of the semi-wake width. It is interesting to note that position 4 has the highest rate of increase in wake width from $z/\cos\beta_o$: 0.0 to 0.5. This is caused by the fact that the nozzle wake is in the outer edge between the wake and free stream, which influences the mixing and wake spreading. Far downstream the wake width for this position is the lowest. A similar trend is observed for position 3. Position 1, consistent with the wake defect (Fig. 19), has the lowest wake width of all the positions from $z/\cos\beta_o = 0.0$ to 0.5.

Figures 22 and 23 present the decay of the maximum unresolved unsteadiness and maximum unresolved velocity cross correlation in the streamwise-normal coordinate system, respectively. Just as with the velocity defect and the semi-wake width, the rate of decay is similar for all six nozzle/rotor positions; just the magnitude of the unsteadiness and shear stress is different for each streamwise location. Therefore, the nozzle wake interaction with the rotor wake does not change the rate of decay or increase of the various properties, but it does change

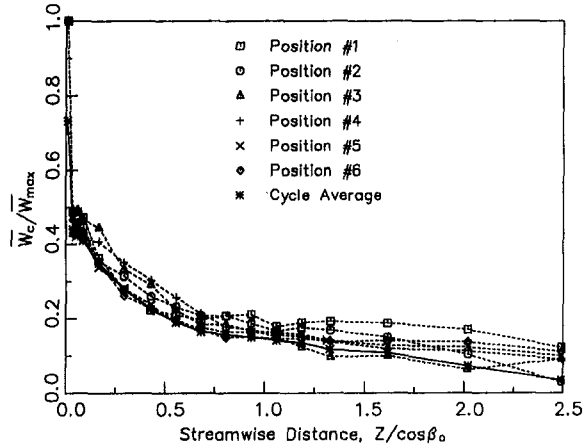

Fig. 20 Decay of rotor wake velocity defect with streamwise distance for each nozzle/rotor location

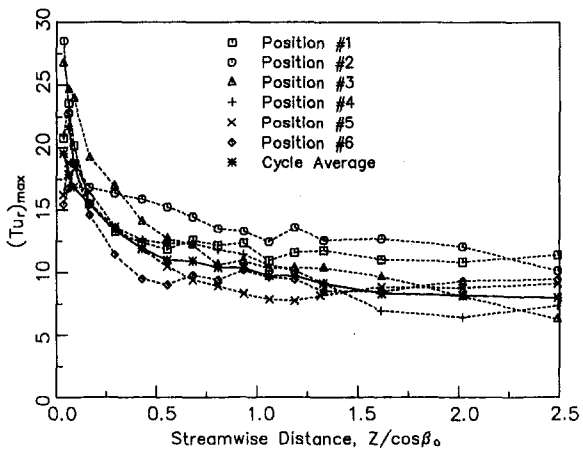

Fig. 22 Decay of maximum relative unresolved unsteadiness $(Tu_r)_{max}$ with streamwise distance for each nozzle/rotor location

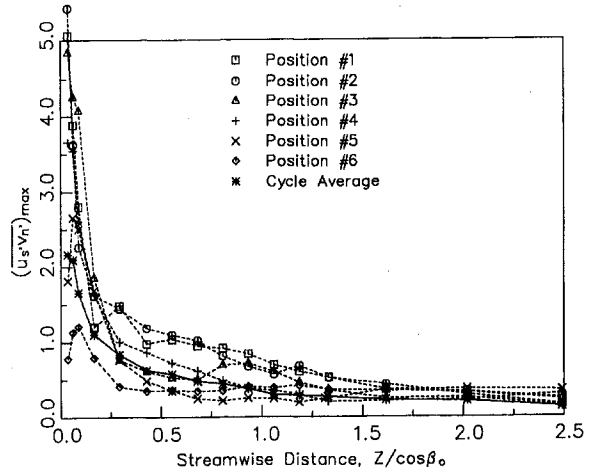

Fig. 23 Decay of maximum unresolved velocity correlation ($\overline{u_s' v_n'}$) with streamwise distance for each nozzle/rotor location

the magnitude of the properties for each nozzle/rotor position at each streamwise location. In the near wake, position 3 has the highest unresolved unsteadiness and velocity cross correlation, and the values at position 5 are the lowest of all the position at most axial locations. This is consistent with the conclusions derived earlier.

Conclusions

The rotor wake flow field was measured at midspan with a two-component LDV to gain a better understanding of the rotor wake properties and its decay characteristics. The rotor wake unresolved unsteadiness is highest in the trailing edge region and decreases farther downstream. This is caused by the vortex street shed from the trailing edge and the production of unresolved unsteadiness in this region. Also in the trailing edge region, the unresolved unsteadiness profiles are asymmetric with a dip in unsteadiness at the wake center. The asymmetry and dip in unresolved unsteadiness disappear as the rotor wake travels downstream. The streamwise-normal unresolved velocity cross correlation in the rotor wake is also asymmetric close to the rotor trailing edge, becoming symmetric farther downstream.

The rotor wake velocity defect decays much slower than the velocity defect of turbine cascades. The semi-wake width is nearly constant from the trailing edge to about $Z/\cos\beta_o = 0.1$, beyond which it increases steadily. Decay of the maximum unresolved unsteadiness and maximum unresolved velocity cross correlation is very rapid in the trailing edge region and this trend slows in the far wake region. In the trailing edge region, the maximum periodic velocity correlations are much larger than the maximum unresolved velocity correlations. But the periodic velocity correlations decay much faster than the unresolved correlations.

The rotor wake shape factor decreases sharply in the trailing edge region and then decreases at a slower rate farther downstream. The variation of the rotor wake shape factor with streamwise distance downstream of the rotor was found to match the correlation developed by Spence (1953) quite well in the near and far wake regions and not as well in the trailing edge region.

The rotor wake is not steady in the rotor time frame, since the rotor wake properties vary between individual nozzle/rotor locations. At the positions where the nozzle wake is inside the rotor wake, the wake center velocity is lower, the unresolved unsteadiness, unresolved velocity cross correlation in the streamwise-normal coordinate system, and the overturning are higher compared to the positions where the nozzle wake is not inside the rotor wake. At the positions where the nozzle wake is located in the free-stream region outside of the rotor wake, the free-stream velocity is lower, the unresolved unsteadiness is higher, and the flow overturning is higher in the free-stream region as compared to the positions where the nozzle wake is not located in the rotor wake free-stream region. While the interaction of the nozzle wake with the rotor wake does not influence the rate of decay or increase of the various wake properties, it does change the magnitude of the properties.

Acknowledgments

This work was supported by NASA through Grant No. NSG3-555, with R. Boyle, K. Civinskas, and J. Schwab as technical monitors. Their helpful suggestions are also acknowledged. The LDV system used in this investigation was acquired with funds provided by NSF through equipment grant No. MSME-85-06626. The help of D. Ristic and S. Khalatov in the acquiring of the LDV data is gratefully acknowledged.

References

Adamczyk, J. J., 1985, "Model Equations for Simulating Flows in Multistage Turbomachines," ASME Paper No. 85-GT-226.

Dring, R. P., Joslyn, H. D., and Blair, M. F., 1987, "The Effects of Inlet Turbulence and Rotor/Stator Interactions on the Aerodynamics and Heat Transfer of a Large-Scale Rotating Turbine Model," NASA-CR-179469, Vol. 4.

Gregory-Smith, D. G., Graves, C. P., Walsh, J. A., 1988, "Growth of Secondary Losses and Vorticity in an Axial Turbine Cascade," ASME JOURNAL OF TURBOMACHINERY, Vol. 110, pp. 1–8.

Ho, Y. H., and Lakshminarayana, B., 1996, "Computational Modeling of Three-Dimensional Flow Through a Turbine Rotor Cascade With Strong Secondary Flows," ASME JOURNAL OF TURBOMACHINERY, Vol. 118, pp. 250–261.

Hobson, G., and Lakshminarayana, B., 1990, "Computation of Turbine Flow Fields With Navier–Stokes Equations," AIAA Paper No. 90-2122.

Lakshminarayana, B., and Reynolds, B., 1979, "Turbulence Characteristics in the Near Wake of a Compressor Rotor Blade," AIAA *Journal,* Vol. 18, No. 11, pp. 1354–1362.

Raj, R., and Lakshminarayana, B., 1973, "Characteristics of the Wake Behind a Cascade of Airfoils," *J. Fluid Mech.,* Vol. 61, part 4, pp. 707–730.

Raj, R., and Lakshminarayana, B., 1976, "Three-Dimensional Characteristics of Turbulent Wakes Behind Rotors of Axial Flow Turbomachinery," ASME *Journal of Engineering for Power,* Vol. 98, pp. 218–228.

Ravindranath, A., 1979, "Three-Dimensional Mean and Turbulence Characteristics of the Near Wake of a Compressor Rotor Blade," M. S. Thesis, Department of Aerospace Engineering, The Pennsylvania State University.

Ravindranath, A., and Lakshminarayana, B., 1980, "Mean Velocity and Decay Characteristics of the Near and Far-Wake of a Compressor Rotor Blade of Moderate Loading," ASME *Journal of Engineering for Power,* Vol. 102, pp. 535–548.

Reynolds, B. D., and Lakshminarayana, B., 1979, "Characteristics of Lightly Loaded Fan Rotor Blade Wakes," NASA CR-3188.

Reynolds, B., Lakshminarayana, B., and Ravindranath, A., 1979, "Characteristics of the Near Wake of a Compressor or a Fan Rotor Blade," AIAA *Journal,* Vol. 17, No. 9, pp. 959–967.

Schlichting, H., 1979, *Boundary Layer Theory,* McGraw-Hill, New York.

Sitaram, N., and Govardhan, M., 1986, "Effect of Incidence Angle on Wake Characteristics of High Deflection Turbine Rotor Linear Cascade," presented at 9th Australasian Fluid Mechanics Conference, Auckland, Dec.

Spence, D. A., 1953, British Aero. Research Council C. P., No. 125.

D. E. Halstead

D. C. Wisler

GE Aircraft Engines,
Cincinnati, OH 45215

T. H. Okiishi
Iowa State University,
Ames, IA 50011

G. J. Walker
University of Tasmania,
Hobart, Tasmania

H. P. Hodson
University of Cambridge,
Cambridge, United Kingdom

H.-W. Shin
GE Aircraft Engines,
Cincinnati, OH 45215

Boundary Layer Development in Axial Compressors and Turbines: Part 3 of 4— LP Turbines[1]

This is Part Three of a four-part paper. It begins with Section 11.0 and continues to describe the comprehensive experiments and computational analyses that have led to a detailed picture of boundary layer development on airfoil surfaces in multistage turbomachinery. In this part, we present the experimental evidence that we used to construct the composite picture for LP turbines that was given in the discussion in Section 5.0 of Part 1. We present and interpret the data from the surface hot-film gages and the boundary layer surveys for the baseline operating condition. We then show how this picture changes with variations in Reynolds number, airfoil loading, and nozzle–nozzle clocking.

11.0 Format for Data Presentation and Interpretation

This section describes the format we use to present our results and the techniques we use to identify transition.

11.1 Space–Time (s–t) Diagrams and Line Plots. The time history of the developing boundary layer is described by s–t diagrams, which show contour plots of ensemble-averaged random unsteadiness and skew measured with surface hot-film gages. Airfoil surface length is plotted along the abscissa and time, in units of wake passing period, is plotted along the ordinate. Examples are shown in Figs. 28(a, b). The color red on the contour plots represents the highest values of the variable measured, and the color blue represents the lowest. There is a linear variation of ten equal increments (changes in color) between red and blue. Reference color legends are shown only in Fig. 28. For all other color contour plots, the highest value of the quantity (plotted in red) is given in the figure caption as Q_{10} and the lowest value (plotted in blue) as Q_0. The reader can refer to the reference color legends to decode the values the colors represent.

Important regions of the s–t diagram are identified by letters A, B, etc., and points of specific interest are identified by numbers 1, 2, etc. Trajectories W, X, Y, and Z are drawn at selected percentages of the wake passing period. Trajectory W always extends along the wake-induced path.

Distributions of quasi wall shear stress, random unsteadiness, and skew are also shown as line plots. Black lines through the black symbols on the plots denote the time-average of the data, as seen in Figs. 28(c, d, e). Colored lines denote values along trajectories W, X, Y, and Z. The dashed lines, shown for quasi-wall shear stress only, denote the minimum and maximum values of the unsteady data. These dashed lines do not represent error bars.

11.2 Identifying Transition. In a manner identical to that for the compressor, we identify transition regions and infer values of intermittency from the variations in skew and random unsteadiness along the airfoil surface. Since skew provides a measure of the asymmetry in fluctuations of wall shear stress about the mean, its value is positive when the transitional flow is more laminar than turbulent. Its value is negative when the transitional flow is more turbulent than laminar. Therefore as shown in Fig. 12(d) of Part 2, skew is zero prior to transition onset (intermittency $\gamma = 0$), skew reaches a maximum positive value at $\gamma \approx 0.25$, skew is zero at the midpoint of transition $\gamma \approx 0.50$, skew is a negative maximum at $\gamma \approx 0.75$, and skew is zero when transition is complete, $\gamma = 1.0$. At the same time skew is varying in this manner, the random unsteadiness increases from a laminar level at $\gamma = 0$ to a peak value at $\gamma \approx 0.50$. It then decreases in value as transition is completed. Thus peak random unsteadiness occurs near zero skew and 50 percent intermittency.

Since it is easy to identify where intermittency is 0.75 from skew data, we have selected $\gamma = 0.75$ as a figure of merit for identifying the location where the wake-induced strips are capable of generating effective calmed regions. This provides consistency for comparison purposes.

12.0 Boundary Layer Development for LP Turbines

This section describes the development of the boundary layer along the embedded, second-stage nozzle airfoils of the LP turbine operating at baseline Test Point 5A. It provides the evidence for the composite picture for the turbine baseline given as Fig. 10(b) in the discussion in Section 5.0.

The relative clocking of nozzles N1 and N2 was selected to reduce the influence of the N1 wakes on the N2 boundary layers. For completeness, we have tabulated the locations of

[1] Editor's note: Parts 1 and 4 of this paper were published in the January 1997 issue of the JOURNAL OF TURBOMACHINERY. Part 2 will be published in the July 1997 issue.

Contributed by the International Gas Turbine Institute and presented at the 40th International Gas Turbine and Aeroengine Congress and Exhibition, Houston, Texas, June 5–8, 1995. Manuscript received by the International Gas Turbine Institute April 7, 1995. Paper No. 95-GT-463. Associate Technical Editor: C. J. Russo.

the laminar, transitional, and turbulent regions for our turbine test cases in Table 6 at the end of Part 3.

The $s-t$ diagrams, which show ensemble-averaged contour plots of random unsteadiness and skew, are presented in Figs. 28(*a, b*) for the suction surface of the nozzle. They are the turbine equivalent of the compressor results shown in Figs. 13(*a, b*). Four trajectories, labeled W, X, Y, and Z, are drawn at a speed of 0.7 V_∞, which is an average of the leading and trailing boundary speeds of a turbulent spot. These trajectories are not straight lines because the free-stream velocity, V_∞, varies through the airfoil passage. Trajectory W is drawn through the wake-induced transitional/turbulent strips.

The distribution of turbulence intensity entering the nozzle row, shown as curve TI in Fig. 28(*a*), has several distinct levels. Along the wake-induced path W, the turbulence intensity was about 4.6 percent. In the path between wakes, there were three levels of 2.7, 3.4, and 1.7 percent. These three levels result from the dispersion of the upstream nozzle wakes as will be shown in Section 15.0. Trajectories X, Y, and Z, which are located in time at 20, 42 and 76 percent of the wake passing period following trajectory W, originate upstream along paths having the three respective levels of turbulence intensity.

The composite picture in Fig. 10(*b*) described the boundary layer as developing along two separate but coupled paths: the wake-induced path, which consists of regions A, B, and C; and the path between wakes, which consists of regions A, D, E, F, and G. These paths are examined below.

12.1 The Wake-Induced Path. As wakes from the upstream airfoil row convect along the downstream airfoil, a boundary layer on the downstream airfoil develops along a wake-induced path, which lies approximately under the convecting wake. The wake-induced path begins in Figs. 28(*a, b*) at the leading edge, goes through points 2–3 in laminar region A and continues through both the wake-induced transitional strip B and the wake-induced turbulent strip C to the trailing edge of the airfoil.

The Laminar Region (A). For the baseline test condition, a laminar boundary layer begins at the leading edge of the suction surface and continues downstream. This region is classified as laminar because it has low random unsteadiness and zero skew, seen respectively as the blue region A in Fig. 28(*a*) and the blue/green region A in Fig. 28(*b*).

The portion of region A that interests us here occupies about 20–25 percent of the wake passing period. It lies approximately under the convecting wakes and extends from the leading edge along points 2–3 to about 32 percent SSL. Wake-induced trajectory W passes through this portion. Along 2–3, the laminar boundary layer is subjected to periodic and random unsteadiness from the passage of the rotor wakes. This appears as a slightly higher (but still low) level of random unsteadiness seen as the lighter blue area along points 2–3 in Fig. 28(*a*). The skew along 2–3 is still near zero in Fig. 28(*b*) and wall shear stress is decreasing for trajectory W in Fig. 28(*c*). This portion of region A constitutes the beginning of the wake-induced path.

Region A for the turbine has an even greater streamwise extent than that for the compressor in Fig. 13 of Part 2. This is due to the larger extent of the favorable pressure gradient existing along the turbine suction surface.

Wake-Induced Transitional Strip (B). There is a significant increase in random unsteadiness and skew along the path of the rotor wakes near 32 percent SSL at point 3 in Figs. 28(*a, b*) and along the red wake-induced trajectories W in Figs. 28(*d, e*). These changes, which are in phase with the peak values of inlet turbulence intensity shown as curve TI in the figure, mark the start of wake-induced transition. The changes occur when disturbances in the convecting rotor wake penetrate into the laminar boundary layer of region A and initiate turbulent spots. The streamwise location of transition onset coincides with the small region of local diffusion near 35 percent SSL in Fig. 7(*b*).

This transitional flow appears convecting in time as wake-induced transitional strip B in the $s-t$ diagrams in Figs. 28(*a, b*). For this nozzle, the strip extends from 32 to 80 percent SSL. There is clear definition of both the leading boundary of region B, which lies between points 9 and 4 in Figs. 28(*a, b*), and the trailing boundary between 4 and 10. The leading and trailing boundary velocities of the strip are inferred from the figure to be about 0.9 V_∞ and 0.5 V_∞, respectively. The trajectories for these two convection velocities form the boundaries of region B. These velocities are consistent with the propagation rates of the leading and trailing boundaries of turbulent spots observed by other researchers. Outside the boundary layer the wake convects at the free-stream velocity 1.0 V_∞, which in Fig. 28(*a*) is greater than (i.e., leads) the leading boundary of strip B.

The evidence that region B is a transitional strip is virtually identical to that for the compressor discussed in Section 7.1 of Part 2.

- The variation of skew along trajectory W in Figs. 28(*b, e*) is typical of transition. The skew increases from zero at point 3 (32 percent SSL) marking transition onset. It reaches a positive maximum at 4 (45 percent SSL) and decreases to zero around 5 (55 percent SSL) where inter-

Nomenclature

A = laminar region on $s-t$ diagram
B = wake-induced transitional strip on $s-t$ diagram
C = wake-induced turbulent strip on $s-t$ diagram
D = calmed region on $s-t$ diagram
E = region of transition between wakes on $s-t$ diagram
F = region of turbulent boundary layer between wakes on $s-t$ diagram
G = calmed region on $s-t$ diagram
h = height through boundary layer normal to surface
LE = leading edge
PSL = pressure surface length from LE to TE of airfoil
Q_0 = lowest value (blue) of quantity in reference color legend for color figures
Q_{10} = highest value (red) of quantity in reference color legend for color figures
Re = Reynolds number for turbine = V_{ex} (SSL)/n
$\overline{\text{Re}}$ = stage-averaged Reynolds number = $0.5(\text{Re}_{\text{rotor}} + \text{Re}_{\text{stator}})$
s = distance, the abscissa in the distance–time ($s-t$) diagram
SSL = suction surface length from LE to TE of airfoil
t = time, the ordinate in the distance–time ($s-t$) diagram
TE = trailing edge
TI = turbulence intensity
u = streamwise velocity within boundary layer
V = velocity
V_∞ = velocity at edge of boundary layer (free-stream velocity)
W, X, Y, Z = trajectories on $s-t$ diagrams at constant fraction of free-stream velocity
γ = intermittency
δ = boundary layer thickness
${}_q\tau_w$ = quasi wall shear stress

Subscripts

avg = average

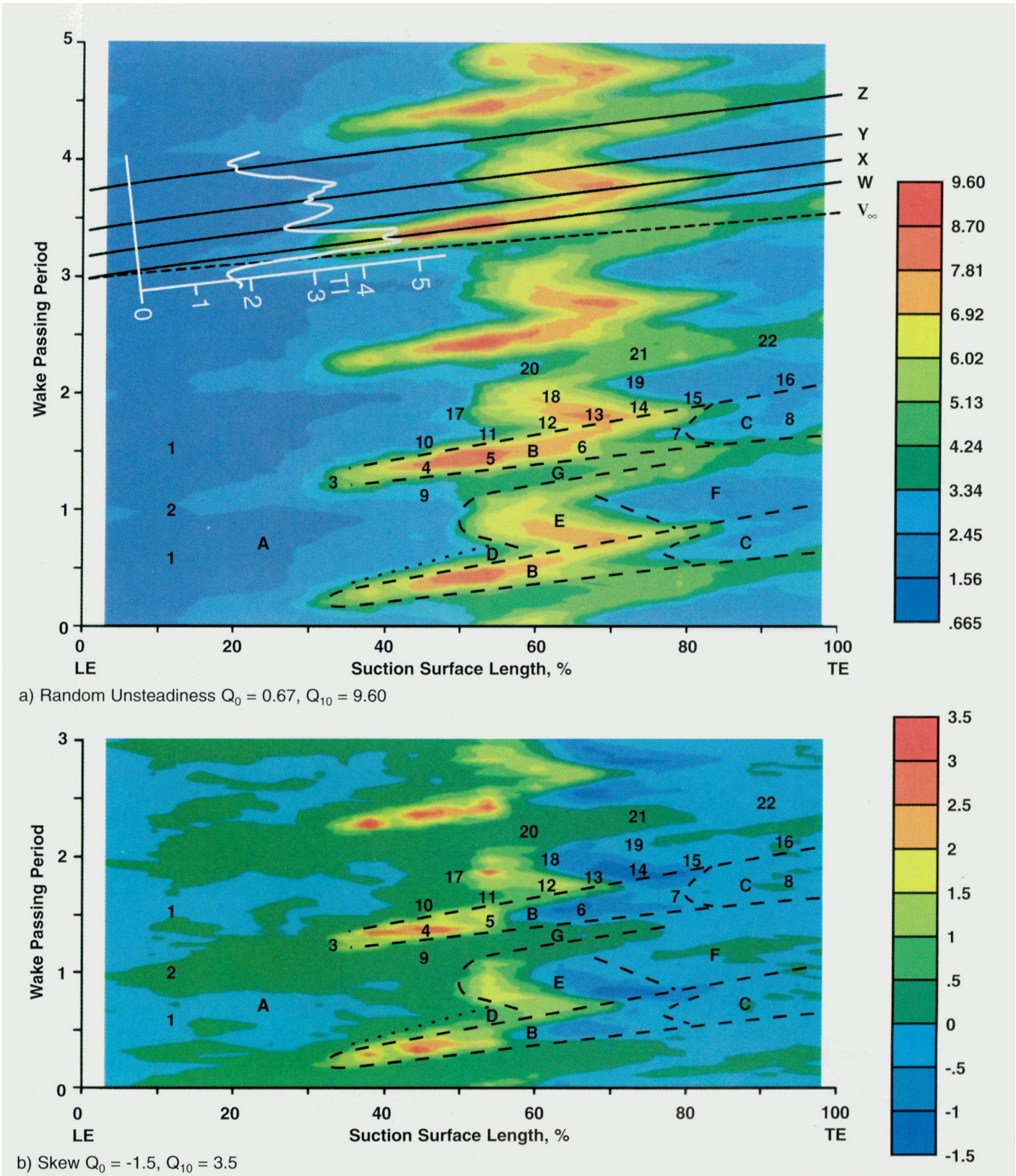

Fig. 28 Shear stress characteristics on suction surface of second stage nozzle N2, $\overline{Re}$ = 5.27 × 10^5, turbine baseline, Test Point 5A. (*a–b*) *s–t* diagram, (*c–e*) Trajectories *W*, *X*, *Y*, *Z*.

mittency is 0.5. A negative minimum occurs near 6 (65 percent SSL) where intermittency is inferred to be about 0.75. Skew increases to zero by 7 (80 percent SSL) upon completion of transition where intermittency is about one.

- The pattern of random unsteadiness in Figs. 28(*a, d*) is also characteristic of transition. The unsteadiness increases along 3–4, indicating transition onset, reaches a maximum (red) at 5, and subsequently decreases in amplitude along 5–6–7 as transition is completed. By 7 the levels are at those seen in the turbulent (green–blue) regions of the boundary layer on this airfoil. Peak random unsteadiness occurs at point 5 in Fig. 28(*a*) where skew

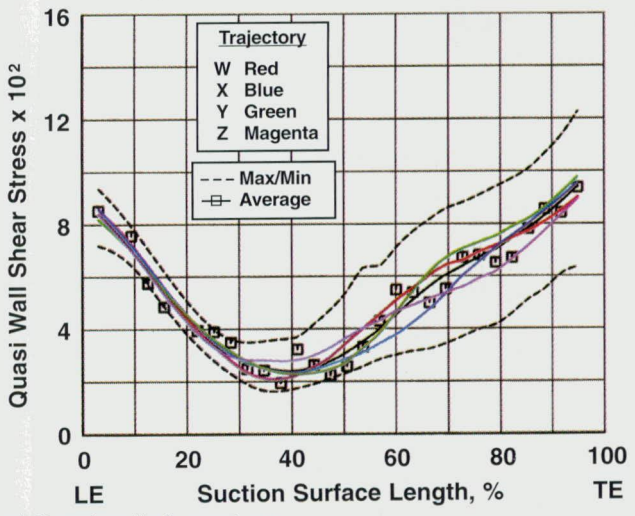

c) Quasi wall shear stress

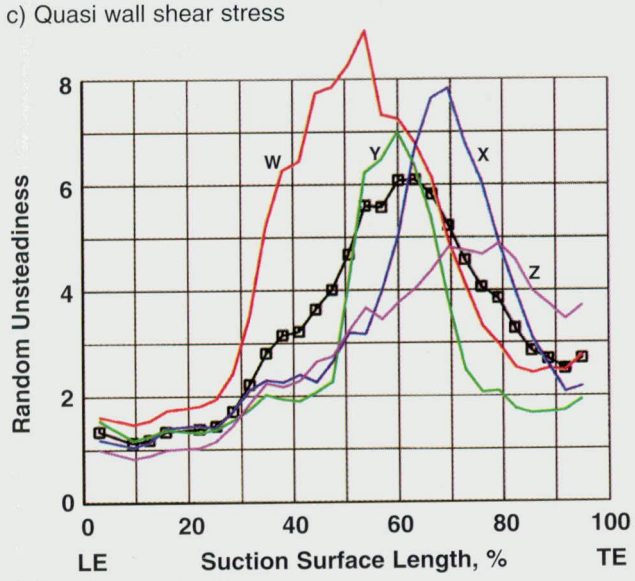

d) Random unsteadiness

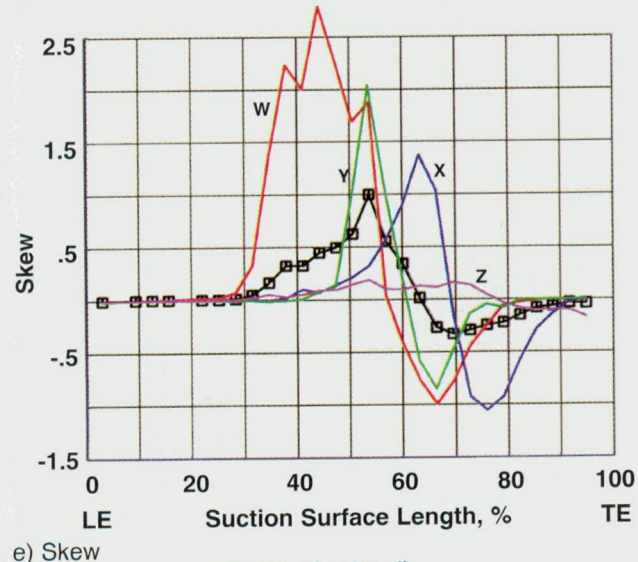

e) Skew

Fig. 28 (Continued)

is zero in Fig. 28(*b*), indicating intermittency $\gamma \approx 0.50$. This is the midpoint of transition. Comparing red trajectories in Figs. 28(*d, e*) shows these details in line plots.

- The boundary layer surveys and raw traces are indicative of transition as discussed in Sections 12.3 and 12.4.

The discovery that these strips are transitional in nature and not turbulent means that the process of wake-induced transition does not immediately produce a fully turbulent strip with an intermittency of one, as assumed by some researchers.

Wake-Induced Turbulent Strip (C). When transition is complete, the wake-induced transitional strip *B* becomes a wake-induced turbulent strip identified as region *C* in Figs. 28(*a, b*). Region *C* extends along points 7–8 from 80 percent SSL to the trailing edge of the airfoil. Random unsteadiness has decreased to the lower relative levels seen as the blue color in Fig. 28(*a*), and the skew has returned to zero in Fig. 28(*b*). This indicates the transition process had been completed and the boundary layer is turbulent. Convective velocities associated with the leading and trailing boundaries of turbulent strip *C* were found to be 0.9 V_∞ and 0.5 V_∞, respectively.

12.2 The Path Between Wakes. The development of the boundary layer is now described along the path between wakes. This path begins at the leading edge, goes through point 1 in laminar region *A*, continues through the laminar region to include also the calmed region, and then goes through the transition and turbulent regions between wakes, *E* and *F*, respectively, as it continues to the trailing edge.

The Laminar Region (A). The portion of laminar region *A* that is of interest here occupies most of the wake passing period. It lies between the rotor wakes where the laminar boundary layer is subjected only to disturbances from other than the upstream rotor wakes. This portion extends from the leading edge near points 1 to about 50 percent SSL. It is identified by low levels of random unsteadiness (blue area in Fig. 28(*a*)), zero skew (blue/green area in Fig. 28(*b*)) and decreasing wall shear stress for trajectories *X*, *Y*, and *Z* in Fig. 28(*c*).

The Calmed Region (D). As described in Section 4.2 and associated Fig. 9 of Part 1, the turbulent spots produced within wake-induced transitional strip *B* generate a calmed region that follows the transitional strip in time. This calmed region appears in the path between wakes as region *D* in Figs. 28(*a, b*). Region *D* is characterized by low random unsteadiness, near zero skew, and elevated levels of shear stress.

Although there is no visual evidence that allows us to identify the calmed region from the ensemble-averaged results presented in Figs. 28(*a, b*), its existence will clearly be seen in the raw data. The boundary of region *D* is obtained from raw data traces as the limit where the high shear relaxes asymptotically to low-shear values. This boundary for our data lies along a trajectory of about 0.35 V_∞, which is marked as the dotted line in Figs. 28(*a, b*). Since the relaxation is asymptotic and the appearance of turbulent spots is random, the boundary has some uncertainty.

By comparing the size of the compressor's calmed region *D* in Fig. 13(*a*) with that of the turbine's in Fig. 28(*a*), one can see the calmed region for the turbine is considerably less extensive. As discussed in Section 5.1 of Part 1, this results from differences in time scales based on boundary layer thickness and differences in reduced frequency, which for the turbine is about one-half that for the compressor. As a result, turbulent spots and associated calmed regions have, in a relative sense, less time to grow as they convect along the turbine nozzle in comparison to the compressor stator. Consequently, the transitional behavior between wakes for most of the turbine passage is affected primarily by the level of free-stream turbulence entering the nozzle.

How effective is this particular calmed region in Fig. 28(*a*)? We reason that the effectiveness of the calmed region in suppressing flow separation and transition onset between wakes is a function of the level of intermittency within the transitional strip and the extent of the calmed region between wakes. As

described in Section 11.2, intermittency levels can be inferred from the skew distributions. For this case, the location of 0.75 intermittency does not occur until about 65 percent SSL, which is well past the region of transition onset between wakes. Consequently we judge the calming effect in region D to be weak.

Transition Between Rotor Wakes (E, G). Between wakes, the flow undergoes bypass transition induced by disturbances other than those associated with wakes from the rotor immediately upstream. These regions of transitional flow are labeled E and G in Figs. 28(a, b). Transition between wakes begins on average at 52 percent SSL, which is 20 percent SSL farther downstream than that for region B. This difference is consistent with the lower levels of turbulence intensity between rotor wakes.

The transition processes in regions E and G are described for the three trajectories X, Y, and Z, which originate upstream along paths that respectively have turbulence intensities of 2.7, 3.4, and 1.7 percent. Along the path between wakes, there is a clear correlation between the streamwise location of transition onset and the variation of turbulence intensity across a wake passing period.

Trajectory X cuts through the calmed region D and region E just behind transitional strip B. Transition along trajectory X, which is delayed relative to that along trajectory Y, is indicated in Figs. 28(b, e) by positive/zero/negative/zero skew at points 12, 13, 14, and 15, respectively. The delay in transition onset (appearance of increased random unsteadiness) for trajectory X relative to Y in Figs. 28(a, d) is caused by the lower level of entering turbulence intensity of 2.7 percent and by the small calmed effect. It is not possible to separate these two causes using the data.

Trajectory Y cuts through the portion of region E along points 17–19 that is most influenced by the higher turbulence levels. The calmed region has no influence along this trajectory. The variation in random unsteadiness and the cycle of skew in Figs. 28(a, b, d, e) is typical of the transition picture described previously.

Trajectory Z, cutting through region G along points 20–22, has the lowest inlet turbulence intensity of 1.7 percent. Region G results from the low level of inlet turbulence intensity and the calming effects following turbulent spots formed in region E. Transition onset along Z occurs at point 20 near 60 percent SSL. The variation in random unsteadiness and skew in Figs. 28(d, e) clearly show transition is not completed before the trailing edge. On an instantaneous basis, the raw data will show nonturbulent calmed flow extending to the trailing edge of the nozzle for up to 40 percent of the wake-passing events.

Turbulent Region Between Wakes (F). The region of turbulent boundary layer downstream of the flow that undergoes transition between wakes is labeled F in Figs. 28(a, b). The fluctuations in shear stress at point 16 are similar to that at point 8. The random unsteadiness in region F is lower than that for the transitional flow in region E but higher than that for the laminar flow in region A. The skew is near zero.

The boundaries between regions C and F from about 80 percent SSL to the trailing edge cannot be readily distinguished from the random unsteadiness and skew. However, they can be distinguished in the boundary layer surveys. Higher random unsteadiness in region G can be distinguished around point 22, where calmed regions intermittently reach the trailing edge.

12.3 Boundary Layer Surveys. The results presented so far show only what is happening on the airfoil surface. Additional understanding of the state of the boundary layer was achieved by also studying the boundary layer profiles.

Surveys of the boundary layer were obtained at midspan along the nozzle suction surface at streamwise locations of 50, 68, 82, and 94 percent SSL. Boundary layer profiles for trajectories W, X, Y, and Z of Fig. 28(a) are presented in Figs. 29(a–d). The time-averaged profile is shown as a dashed line. Height above the nozzle surface is normalized by the time-averaged boundary layer thickness measured at the given streamwise location instead of the local time-varying value. This allows the thickness of the various boundary layers to be distinguished. Velocity is normalized by the local free-stream value of each individual profile. Curve fits of the data were done systematically using a spline fit with weighted averaging and zero velocity imposed at the wall. No custom-tailoring was employed. However, since the turbine boundary layers were very thin (less than 0.8 mm or 0.030 in. at 50 percent SSL), measurements on a normalized basis could not be made as close to the wall as those for the compressor. As a result, there is greater uncertainty in the values of the integral parameters computed using the curve fits of the profiles. This uncertainty decreases with Reynolds number as the boundary layer thickens. Due to the high camber of the turbine nozzle, surveys upstream of 50 percent SSL could not be made.

Ensemble-averaged distributions of the boundary layer integral parameters, obtained by integration of the profile curve fits, are given in Figs. 30(a–d) for one wake passing period. Displacement and momentum thicknesses are normalized by nozzle suction surface length. Time-averaged values are provided along the right-hand side of each figure.

Profile Shapes. For the predominantly favorable pressure gradient of the turbine, there is only a small distinction between the velocity profiles for wake-induced trajectory W and those for trajectories X and Y in Figs. 29(a–d). This is in contrast to the findings for the compressor in Fig. 15, where in the presence of an adverse pressure gradient, the profile for trajectory W was clearly thicker than the others and of a different character.

However, the turbine profile for trajectory Z in Figs. 29(a–d) is clearly distinguished from the others. This trajectory cuts through region G, which is perturbed by the low inlet turbulence and exhibits calmed effects. The boundary layer along trajectory Z is still transitional at the trailing edge and is noticeably thinner than the others.

Integral Parameters. There are two major messages obtained from the integral parameters in Fig. 30. First, the maximum values occur along the wake-induced path W and the minimum values occur along trajectory Z. This is consistent with transition starting farther upstream along W. Second, all values of shape factor are consistent with attached flow.

The nonsymmetric distributions of displacement and momentum thickness around trajectory W in Figs. 30(a, b) are noteworthy. The values of each parameter are significantly lower along trajectory Z ahead of the wake-induced strip than they are along trajectories X and Y behind it. This is likely due to the long streamwise extent of transitional flow in region G along trajectory Z.

12.4 Analysis of Raw Data. The raw data are examined because they show evidence for important flow features, such as the calmed effect and velocities of individual turbulent spots, that cannot be seen in ensemble-averaged data.

Instantaneous time traces of quasi wall shear stress, presented in A-C coupled format, are shown in Fig. 31 for the suction surface of the second-stage nozzle. The traces were obtained simultaneously. Trajectories W through successive wake passing periods are given numerical subscripts. Areas of importance are encircled and identified with a number.

The Laminar Region A. Time traces for the perturbed laminar region A of Fig. 28(a) extend along the first 25 percent of the airfoil in Fig. 31. Traces near the leading edge contain only low-amplitude fluctuations indicative of a laminar boundary layer. At 25 percent SSL, stronger periodic variations associated with the jet-wake effect, which in turbines transports rotor wake

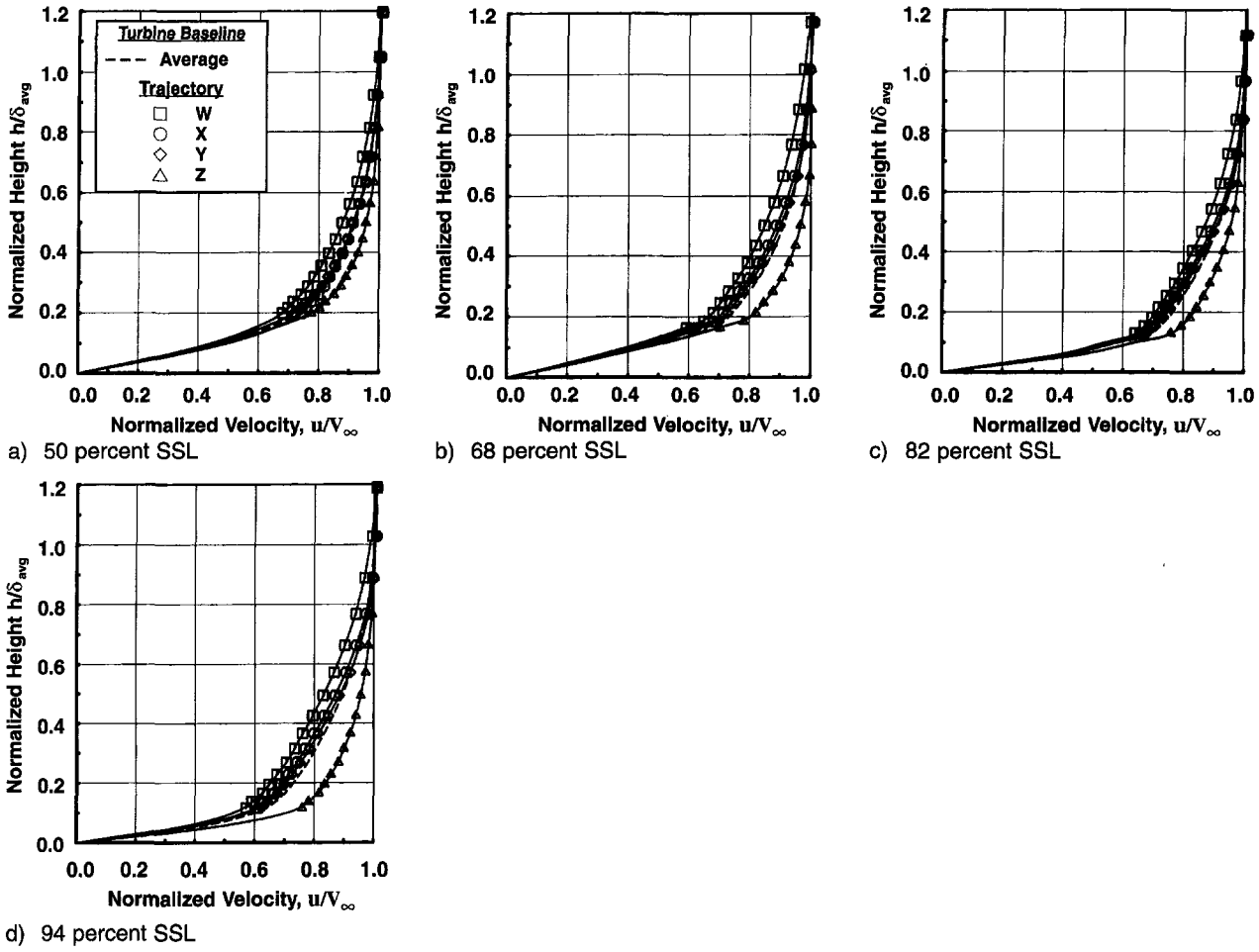

Fig. 29 Boundary layer profiles for turbine baseline along Trajectories *W*, *X*, *Y*, and *Z* in Fig. 28(*a*). Suction surface of second-stage nozzle, profiles normalized by time-average boundary layer thickness, Re = 5.27 × 10^5, Test Point 5A.

fluid toward the nozzle suction surface, are evident as illustrated by encircled area 1. The ensemble-mean distributions, superimposed on the figure as dashed lines at 25 and 32 percent SSL, further illustrate the periodic nature of this jet-wake effect. Characteristics of jet-wake interaction that would produce these features were documented by Hodson (1985).

Wake-Induced Transitional Strip B. Wake-induced transition is clearly underway by 32 percent SSL. Turbulent spots originate in the vicinity of the *W* trajectories such as those shown along W_4 in area 2. The time period between successive spots does not correlate as closely with wake passing as that seen for the compressor. Instead, spots both lead and lag the equally spaced *W* trajectories. Convection velocities appear to vary as well. The average convection velocities of the spots along W_1 and W_2 are somewhat less than 0.7 V_∞ while those along W_4 and W_5 are somewhat greater. At 44 percent SSL, turbulent events of varying amplitude occur for each passing wake as seen by the various magnitudes of marker "3" in the figure.

Calmed Region D. The calmed regions are identified in Fig. 31 as areas of elevated but decaying shear stress following turbulent spots. An example is seen as area 4. The downstream boundary of the region is determined by locating where flow breakdown occurs and constructing a trajectory from the origin of the strip to the breakdown point. The green trajectory of 0.35 V_∞ is an example. The average temporal extent of the turbulent spots and the associated calmed regions are significantly less than those for the compressor as described previously in Section 12.2.

Transition Between Wakes E. The onset of transition between the wake-induced strips takes place near 50 percent SSL prior to maximum velocity. Single-spot events in area 5 and multiple-spot events in area 6 mark transition onset in Fig. 31. The relative locations of the spots between wake events coincide with the regions of elevated free-stream turbulence described previously in the introduction of Section 12.0. The presence of numerous spots at 63 percent SSL makes it impossible, in general, to distinguish the wake from the non-wake-induced areas at this location. Downstream of maximum velocity, the turbulent events continue to engulf the remaining laminar flow. By 85 percent SSL, transition is nearly complete.

Along trajectories Z_2 and Z_3, which begin at 70 percent SSL in Fig. 31, areas of calmed flow persist all the way back to the trailing edge, as illustrated by areas 7 and 8. Due to their elevated levels of shear stress, these areas of nonturbulent boundary layer do not separate even in the presence of the mild adverse pressure gradient in this region. As expected, these events coincide with region *G* in Fig. 28(*a*).

No evidence of T–S waves was found. Rather, the flow in the region between wakes undergoes bypass transition.

12.5 The Pressure Surface. The boundary layer development along the pressure surface is shown for Test Point 5D in Fig. 32. These measurements are presented at the cruise Re = 1.80 × 10^5 for consistency with a later comparison. However, results along the pressure surface were found not to vary appreciably with Reynolds number.

A short region of laminar boundary layer exists from the leading edge to about 10 percent PSL. This appears as the blue

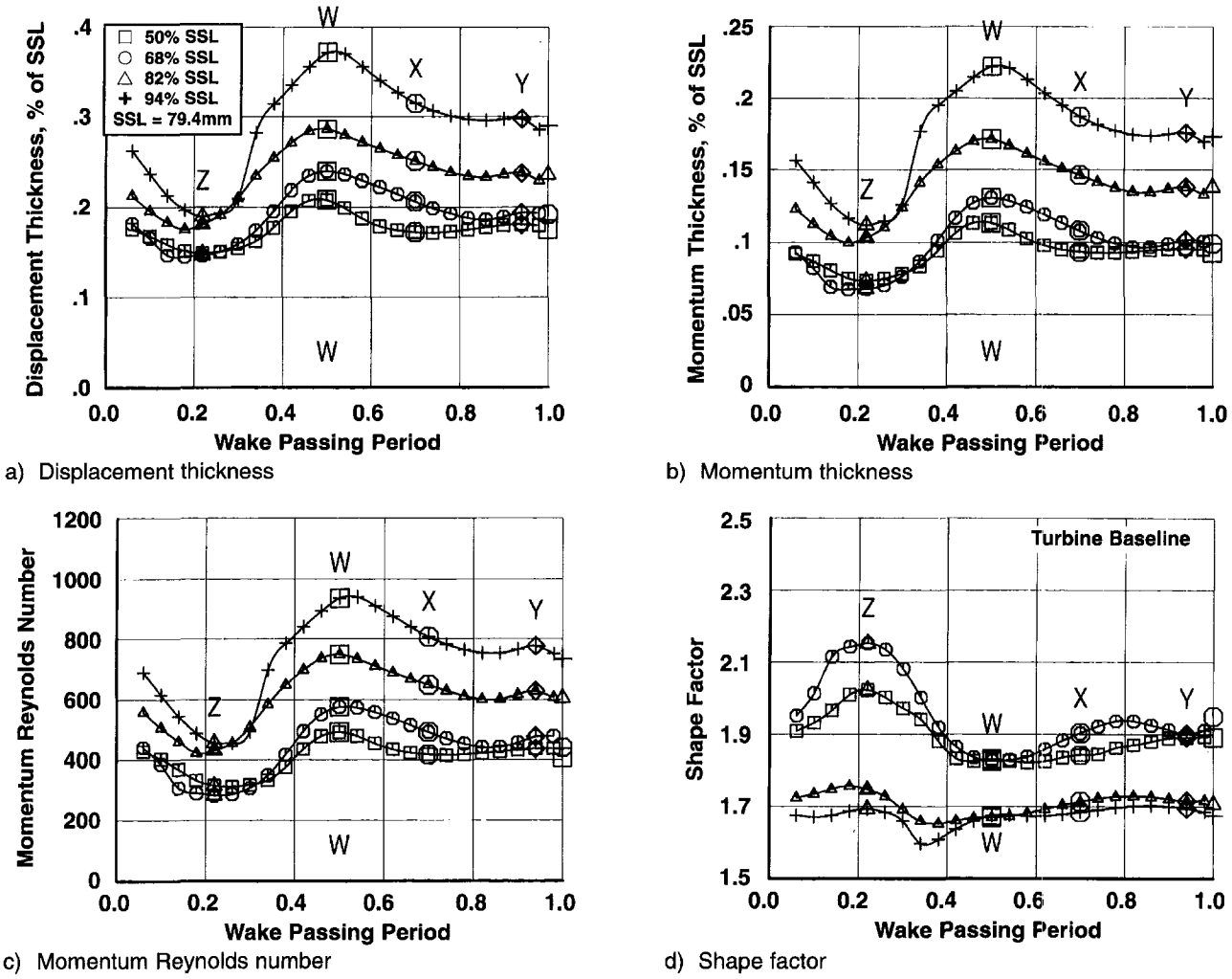

Fig. 30 Variation of integral boundary layer parameters across wake-passing period for turbine baseline, suction surface second-stage nozzle. Trajectories *W*, *X*, *Y*, and *Z* from Fig. 28(*a*) are identified. $\overline{Re} = 5.27 \times 10^5$, Test Point 5A.

color and is marked region *A*. Transition, which begins near the leading edge in the region of adverse pressure gradient, is completed relatively quickly compared to that on the suction surface.

For the wake path, transition occurs in a wake-induced transitional strip shown by the red-orange-yellow region *B*. Transition begins at about 10 percent PSL and is completed by about 40 percent PSL. The skew (not shown) has a general appearance of transition but it is less pronounced than that for the suction surface. Following region *B*, there is a turbulent boundary layer marked *C*, which remains attached until the trailing edge.

Between wakes, transition occurs in the strong adverse pressure gradient from about 12 to 30 percent PSL in region *E*. The turbulent boundary layer *F*, which follows from region *E*, remains attached to the trailing edge.

13.0 Reynolds Number Effects on Turbine Boundary Layers

This section examines the influence of Reynolds number on LP turbine boundary layers. It provides the evidence for Fig. 10(*d*) in the discussion in Section 5.0. It shows that as Reynolds number is reduced from the high values at take-off to low values at cruise, the wake-induced transitional strips weaken and move toward the trailing edge. The location of transition onset between wakes also moves toward the trailing edge. This conclusion was similar to that for compressors. The turbine findings are evaluated relative to those for the baseline in Section 12.0. The results are listed in Table 6.

The Reynolds number tests for the embedded second stage of the LP turbine were conducted at stage-averaged Reynolds numbers of 5.27×10^5, 3.96×10^5, and 2.71×10^5 for take-off conditions and 1.80×10^5 and 1.19×10^5 for cruise conditions. These are test points 5A, 5B, 5C, 5D, and 5E, respectively.

13.1 Picture Constructed From Surface Film Data

Cruise (Low) Reynolds Numbers. The *s–t* diagram of random unsteadiness for the cruise (low) Reynolds number of 1.19×10^5 is shown in Fig. 33(*a*). This flow picture is markedly different from that at the high (baseline) Reynolds number shown in Fig. 28, and in abbreviated form in Fig. 33(*b*).

The striking feature of Fig. 33(*a*) is the very great extent of laminar region *A* and the near absence of wake-induced transitional strips penetrating this laminar region. The favorable pressure gradient for this airfoil extends to about 62 percent SSL, as seen in Fig. 7(*b*). Transition onset does not occur until 73 percent SSL along the wake-influenced trajectory *W*. This is well into the region of mild diffusion. The subsequent wake-induced region is labeled *B* in the figure. Between wakes, a significant calmed region *D* develops which inhibits flow separation. However, some evidence of transition between wakes, denoted by region *E*, is present as well. Transition in both regions *B* and *E* extends to the trailing edge. Even at this low

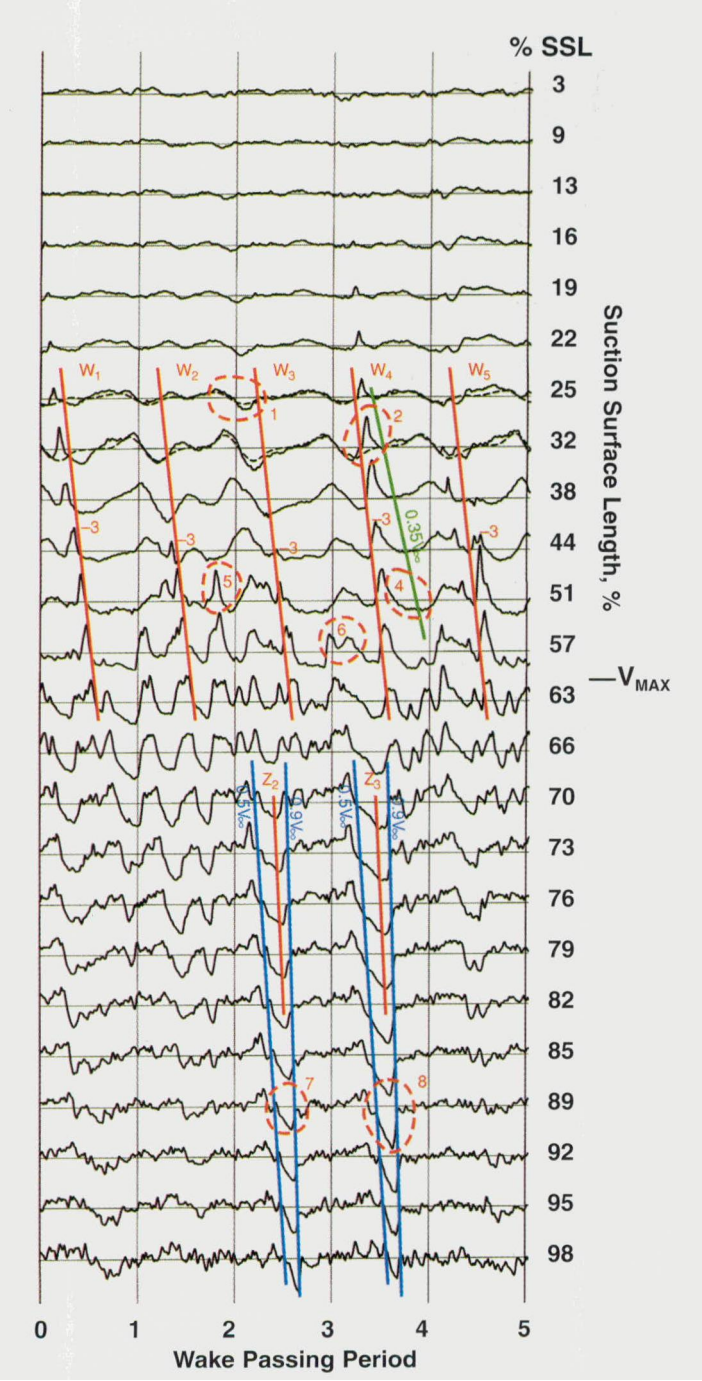

Fig. 31 Raw time traces from surface hot-film gages operated simultaneously on the suction surface of second-stage nozzle N2, Turbine Test Point 5A

Reynolds number, no flow separation was observed. The results for the cruise $\overline{\text{Re}} = 1.80 \times 10^5$ were similar.

Take-off (Higher) Reynolds Numbers. The s–t diagrams of random unsteadiness for take-off $\overline{\text{Re}} = 2.70 \times 10^5$ and 5.27×10^5 are shown in Fig. 33(b). As Reynolds number is increased from cruise values through the take-off range, Figs. 33(a, b) show quite a compelling picture of transition as regions B, C, D, E, and F move progressively upstream and become more defined. Transition onset for the wake-induced strips moves from 73 to 71 to 48 to 34 to 32 percent SSL as Reynolds number is progressively increased. (Not all of these data are shown.) At take-off Reynolds numbers, transition onset is influenced by the short region of slight adverse pressure gradient near 35 percent SSL in Fig. 7(b). The beginning of transition between wakes moves from 80 to 76 to 60 to 52 to 52 percent SSL. For $\overline{\text{Re}} = 2.70 \times 10^5$ in the upper region of Fig. 33(b), the high levels of random unsteadiness at the trailing edge indicate that transition along both the wake and non-wake paths has not yet been completed.

At take-off Reynolds numbers, the calmed effect has much less impact on the transition process for turbines than it has for compressors and transition and is tied more closely to the level and variation of free-stream turbulence entering the blading. For cruise Reynolds numbers, however, calmed effects played an important role in suppressing laminar separation.

Quasi Wall Shear Stress. Distributions of quasi wall shear stress for the various Reynolds numbers are shown in Fig. 34. For the two cruise Reynolds numbers (Test Points 5D and 5E), the shear stress continues to decrease in a manner characteristic of laminar boundary layers until the onset of transition at about 80–90 percent SSL. For $\overline{\text{Re}} = 1.80 \times 10^5$, shear stress along all of the trajectories W through Z exhibit the same features.

For the higher Reynolds numbers, average shear stress in Fig. 34 begins to increase between 40 and 50 percent SSL, indicating transition onset occurring much earlier than at cruise values.

13.2 Boundary Layer Surveys. Surveys of the boundary layer were obtained for the cruise (low) $\overline{\text{Re}} = 1.80 \times 10^5$ at the same locations as those for the take-off Reynolds number shown in Fig. 29. Compared to the profiles for the take-off Reynolds numbers, the profiles for the cruise Reynolds numbers (not shown) are less full. Profiles W and X at 50 percent SSL are clearly laminar. Trajectories W through Z take on a transitional character as one moves toward the trailing edge.

The integral parameters, shown in Fig. 35, have a somewhat different character than those in Fig. 30. The distributions about W are now more symmetric at cruise than they are at take-off. The lower values associated with region G along trajectory Z at take-off are not present at cruise since transition everywhere has moved well aft on the airfoil. At cruise Reynolds number the boundary layers are thicker, as expected, with maximum values lying under the wake-disturbed region W. The maximum-to-minimum ratios of both displacement thickness and momentum Reynolds number in Fig. 35 are about 1.4 compared to a value of about 2.0 for the take-off Reynolds number in Fig. 30.

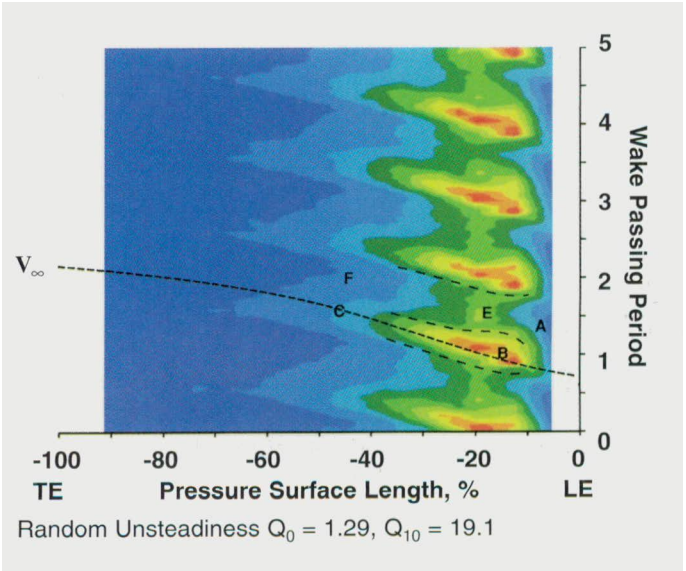

Fig. 32 Shear stress characteristics on pressure surface of second-stage nozzle, $\overline{\text{Re}} = 1.80 \times 10^5$, turbine baseline, Test Point 5D

Table 6 Effect of Reynolds number and loading on boundary layer development for turbines. Tabulated numbers give locations of regions along suction surface of airfoil in percent SSL.

REGION		$\overline{Re} \times 10^{-5}$ OR LOADING LEVEL	TEST POINT	A LAMINAR REGION		B WAKE-INDUCED TRANSITIONAL STRIP			C WAKE-INDUCED TURBULENT STRIP		D CALMED REGION	E TRANSITION BETWEEN WAKES			F TURBULENT BETWEEN WAKES	
				L	T_B/T_E	L	$0.5\gamma/0.75\gamma$	T	L	T	Effective	L	0.5γ	T	L	T
TURBINE	NOZZLE	5.27	5A	LE	32/52	32	56/66	80	80	TE	Low	52	62	73	73	TE
		3.96	5B	LE	34/52	34	65/73	83	83	TE	Low	52	66	84	84	TE
		2.71	5C	LE	48/60	48	76/85	93	93	TE	Low	60	82	TE	—	—
		1.80	5D	LE	71/76	71	90/–	TE	—	—	High	76	93	TE	—	—
		1.19	5E	LE	73/80	73	90/–	TE	—	—	High	80	—	TE	—	—
TURBINE	ROTOR	Intermediate	6A	LE	50/57	50	66/72	84	84	TE	Low	57	84	TE	—	—
		Increased (High)	5B	LE	25/53	25	42/64	80	80	TE	Low	53	78	TE	—	—
TURBINE	NOZZLE	Low	7A	LE	52/62	52	70/76	91	91	TE	Low	62	95	TE	—	—
		Increased (High)	5B	LE	34/52	34	65/73	83	83	TE	Low	52	66	84	84	TE

* Separation
L ≡ Leading boundary of region
T ≡ Trailing boundary of region
γ ≡ Intermittency
T_B ≡ Trailing boundary of laminar region along wake-induced transitional strip B (Trajectory W)
T_E ≡ Trailing boundary of laminar region for transition between wakes E (Trajectory Y)

Values of shape factor vary between 2 and 2.6 at cruise Reynolds numbers, indicating that no flow separation occurred. These values are somewhat higher than those for take-off conditions.

13.3 Analysis of Raw Data for Cruise Reynolds Number. An abbreviated set of instantaneous time traces (raw data) of quasi wall shear stress for the cruise Reynolds number of 1.19×10^5, Test Point 5E, are shown in Fig. 36. The most striking feature of these traces is the absence of any transitional flow along the first three quarters of the nozzle suction surface. In contrast, wake-induced transition occurred as early as 30 percent SSL for the baseline test case as shown in Fig. 31.

For cruise Reynolds numbers, wake-induced transition is not evident until 79 percent SSL, as noted from the turbulent events labeled "1" in Fig. 36. Distinct calmed regions, examples of which are labeled "2" for various streamwise locations, develop behind the wake-induced events as they convect downstream. This calming effect produces elevated levels of nonturbulent shear stress between the turbulent events. The asymptotically decreasing wall shear through the above-mentioned calmed regions indicates that the boundary layer between wake-induced strips remains attached. This is especially evident when the calmed effect is strong.

Instantaneous time traces obtained at the higher cruise Reynolds number of 1.80×10^5 (Test Point 5D) contained identical features to those described above. Values of shape factor from this latter test condition in Fig. 35(*c*) provide further evidence that no flow separation of the nonturbulent flow occurs prior to the trailing edge in spite of the mild adverse pressure gradient. This is in contrast to conventional boundary layer calculations which predict laminar separation to occur prior to 80 percent SSL for this blading. This feature is discussed in Part 4.

At 98 percent SSL, significant regions of nonturbulent flow persist. An intermittency level of only about 0.6–0.7 was inferred visually from numerous traces at this trailing-edge location.

14.0 Loading Effects on Boundary Layers

This section examines the influence of airfoil loading on boundary layer development for embedded stages of LP turbines. It provides the evidence for Fig. 10(*f*) of the discussion in Section 5.0. It shows that decreasing the loading weakens the wake-induced transitional strips as they move downstream. The findings are evaluated relative to those for the baseline. The results are listed in Table 6.

14.1 Loading Effects for the Suction Surface. Loading effects were evaluated systematically for the embedded second stage of the LP turbine. Since the results for the rotor and nozzle were similar, we chose to show the rotor results because they illustrate the additional feature of "beating" as described below. *S–t* diagrams of random unsteadiness are presented for intermediate and increased loading, Test Points 6A and 5B, respectively. For intermediate loading, it is important to note from Fig. 7(*a*) that a continuous flow acceleration was maintained from the leading edge to maximum velocity. In contrast, at increased loading, a region of local diffusion occurs near 25 percent SSL. Data for Test Point 6A were obtained at design rpm. The Reynolds number is about 15 percent greater than that for Test Point 5B. However, based on the results just presented in Section 13.1, this difference is not significant.

The shear stress characteristics for the turbine rotor R2 at intermediate loading Test Point 6A are presented in Fig. 37. The random unsteadiness in Fig. 37(*a*) shows a large extent of laminar region *A*. Wake-induced transition in region *B* does not begin until about 50 percent SSL. A small region of turbulent boundary layer, *C*1, follows region *B* near the trailing edge. Between wakes, transition begins in region *E* and the flow between wakes remains transitional at the trailing edge.

The difference in the transitional character of regions *B* and *E* is seen by comparing the skew for trajectories *W* and *Y* in Fig. 37(*b*). Wake-induced trajectory *W* has completed the zero-positive-zero-negative-zero transition cycle of skew while trajectory *Y* has only completed about half of the cycle, even though the two trajectories begin their initial rise at about the same percent SSL.

At increased rotor loading in Fig. 38(*a*), the wake-induced strips *B* now begin at about 25 percent SSL near the location of local diffusion. Transition between wakes in region *E* moves upstream to about 53 percent SSL. The skew for trajectory *W* in Fig. 38(*b*) begins its cycle at about 25 percent SSL, well ahead of that for trajectory *Y* between wakes. Tran-

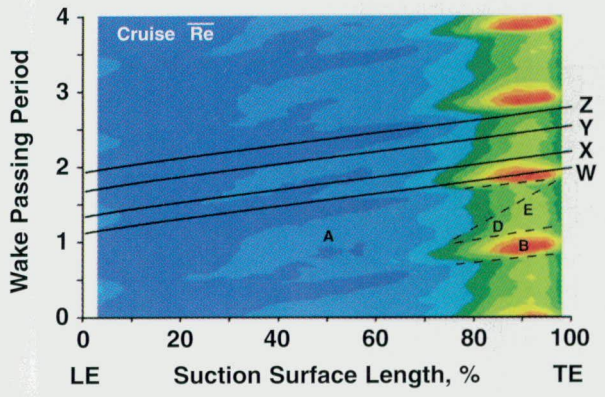

a) Cruise $\overline{Re}$ = 1.19x10^5, Test Point 5E, Q_0 = 1.13, Q_{10} = 23.73

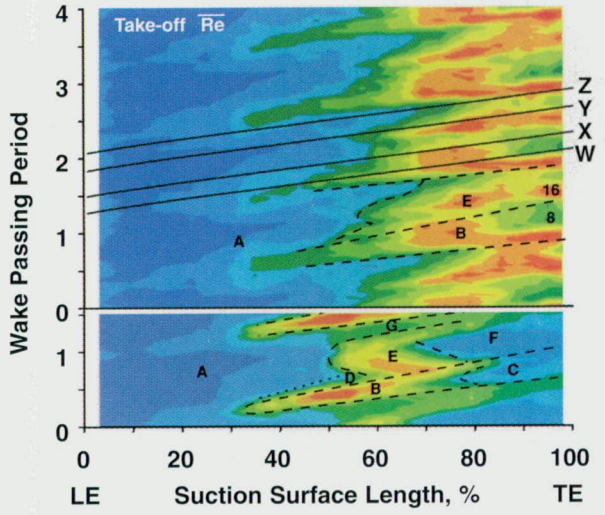

b) Take-off, (upper portion) $\overline{Re}$ = 2.7 x 10^5, Test Point 5C, Q_0 = 1.20, Q_{10} = 11.20 (lower portion) Re = 5.27 x 10^5, Test Point 5A, from Fig. 28

Fig. 33 Reynolds number effect on boundary layer development. Suction surface, turbine nozzle N2. Data shown as *s–t* diagrams of random unsteadiness.

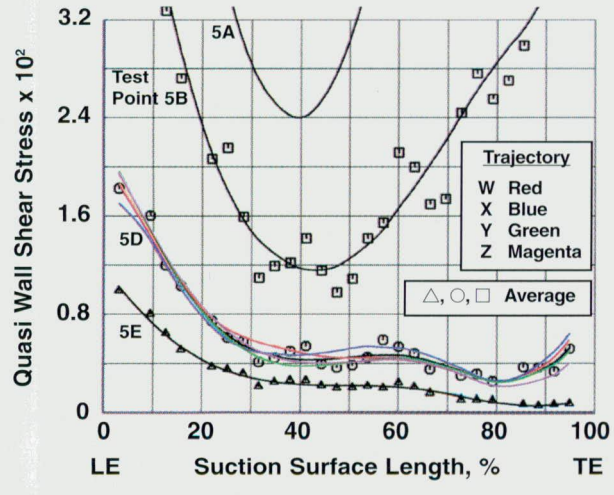

Fig. 34 Reynolds number effect on quasi-wall shear stress. Suction surface, turbine nozzle N2. Time averaged values shown for Test Points 5A from Fig. 28(*c*), 5B, 5D, and 5E. Trajectories *W*, *X*, *Y*, and *Z* also shown for Test Point 5D.

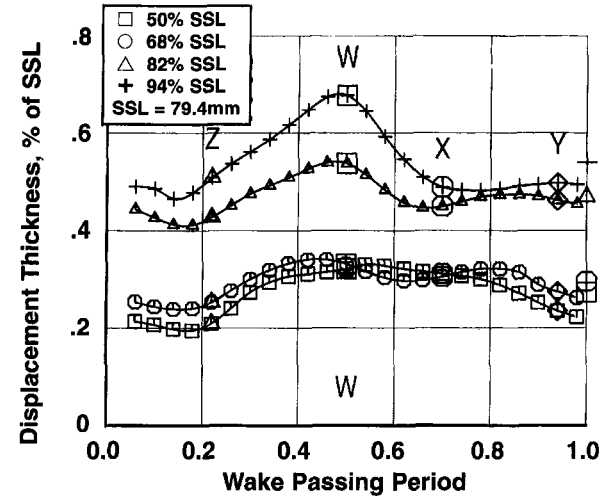

a) Displacement thickness

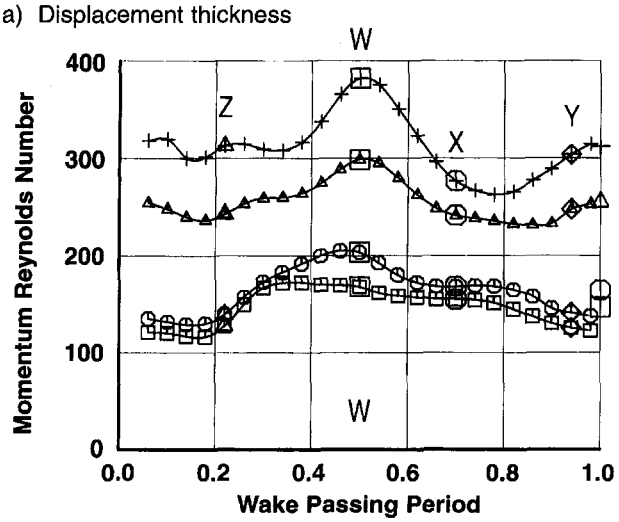

b) Momentum Reynolds number

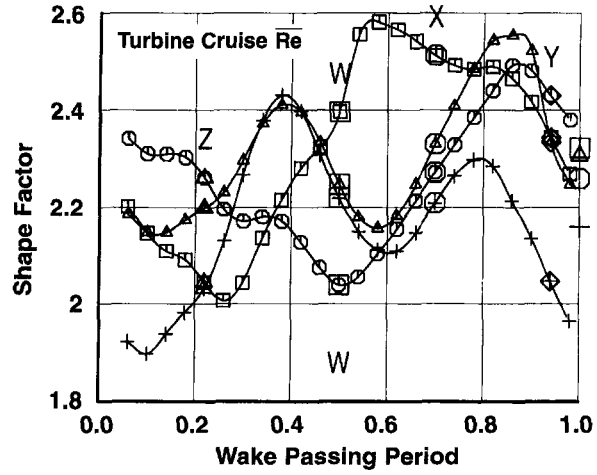

c) Shape factor

Fig. 35 Variation of integral boundary layer parameters across wake-passing period for turbine cruise Reynolds number, suction surface of the second-stage nozzle. $\overline{Re}$ = 1.80 × 10^5, Test Point 5D.

sition for trajectory *W* is complete by 75–80 percent SSL while it is only just over half complete for trajectory *Y* between wakes.

An additional feature of the wake-passing events in the rotor *s–t* diagrams of Figs. 37(*a*) and 38(*a*) is the ''beating'' pattern,

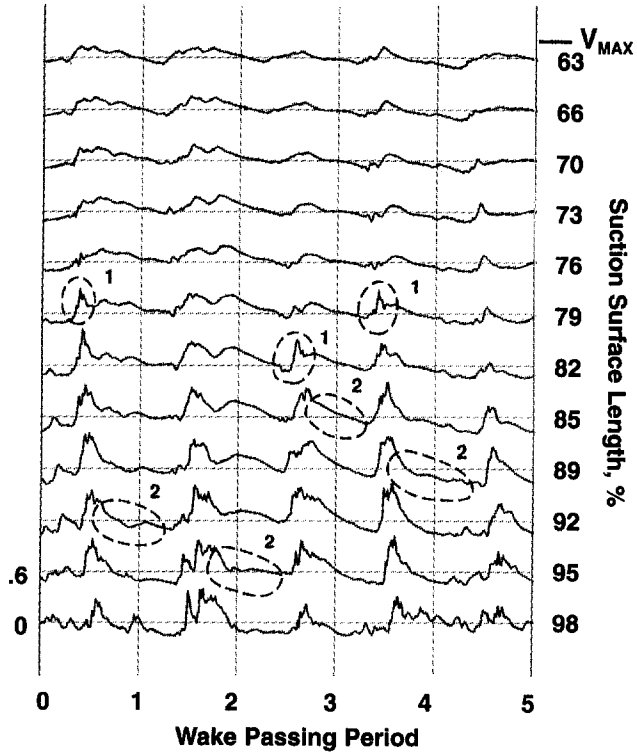

Fig. 36 Instantaneous time traces (raw data) from surface hot-film gages for turbine cruise Reynolds number. Gauges operated simultaneously. Suction surface of second-stage nozzle, $\overline{Re} = 1.19 \times 10^5$, Test Point 5E.

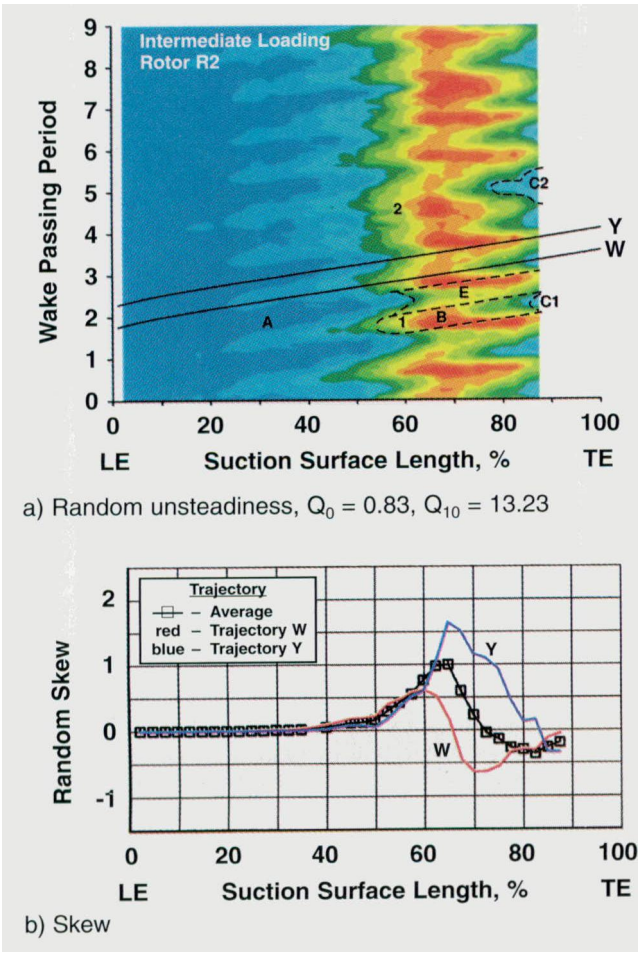

Fig. 37 Loading effect on rotor boundary layer development. Suction surface, turbine rotor R2. Intermediate loading, Test Point 6A.

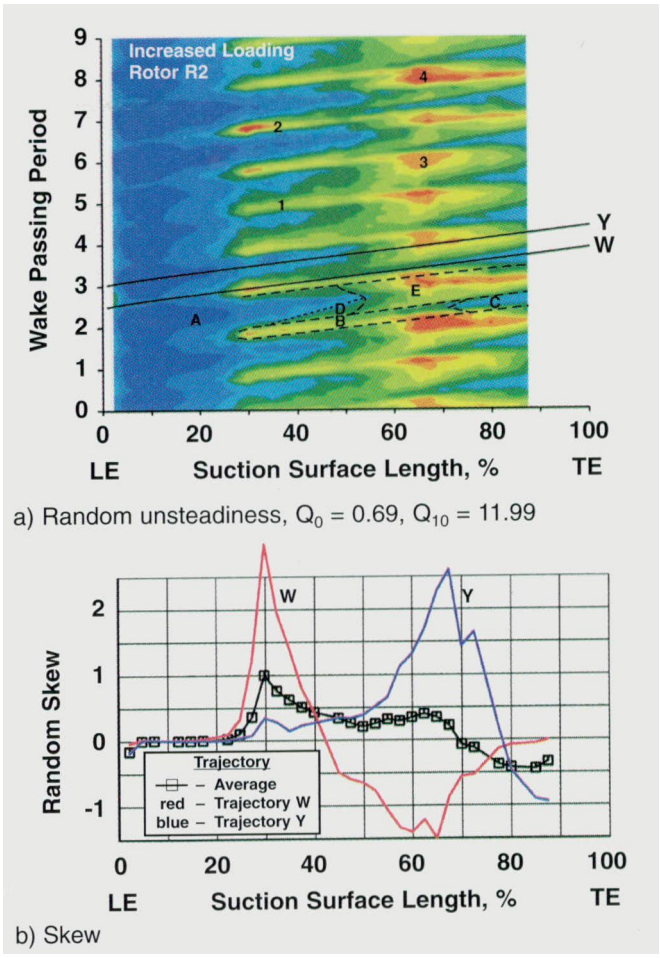

Fig. 38 Loading effect on rotor boundary layer development. Suction surface, turbine rotor R2. Increased loading, Test Point 5B.

which occurs at the frequency difference associated with the differing vane count. Nozzle N1 has 82 airfoils while Nozzle N2 has 108 airfoils. Consequently, the N1/N2 orientation varies with circumferential position. This causes a beating effect on boundary layer development as can be seen by comparing the wake-induced strips at points 1 and 2 in each of the figures. Behind point 2 in Fig. 37(*a*), where the interaction is stronger, transition is completed sooner and the region of turbulent boundary layer at *C*2 is larger than that at *C*1 where the interaction is weaker. In Fig. 38(*a*) this effect can also be seen by comparing points 3 and 4 between wakes.

14.2 Loading Effects for Pressure Surface. We return to the nozzle results to evaluate the effect of loading on boundary layer development along the pressure surface. At decreased loading in Fig. 39(*a*) (Test Point 7B), the high negative incidence and strong adverse pressure gradient near the leading edge (see Fig. 7) cause flow separation at the leading edge with reattachment at about 5 to 8 percent PSL. At increased loading in Fig. 39(b), the high incidence allows the flow to remain attached as described previously in Section 12.5.

15.0 Nozzle–Nozzle Interaction (Clocking Effects)

This section examines the effect that clocking nozzle N1 relative to nozzle N2 has on boundary layer development on embedded nozzle N2. It provides the evidence for Fig. 10(*h*) of the discussion in Section 5.0. It shows clocking effects can produce quite different boundary layers on the suction surfaces of the LP blading.

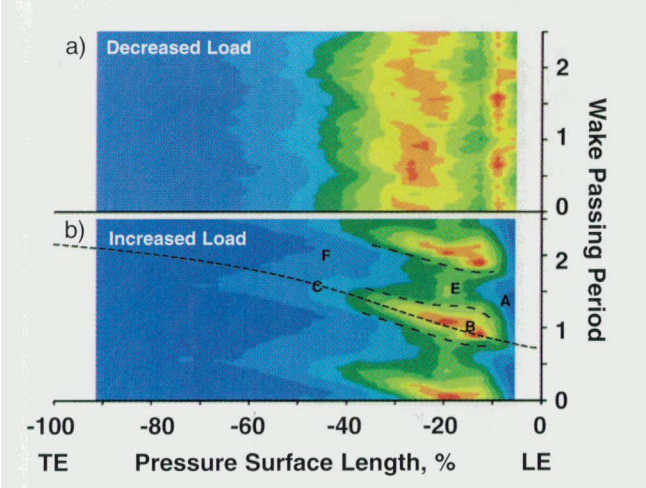

Fig. 39 Loading effect on boundary layer development. Pressure surface, turbine nozzle N2, s–t diagram of random unsteadiness. (a) Decreased loading Test Point 7B, Q_0 = 2.37, Q_{10} = 17.57. (b) Increased loading Test Point 5D, Q_0 = 1.29, Q_{10} = 19.09.

15.1 Wake Interaction. Significant wake interaction (dispersion) occurs in a LP turbine as upstream nozzle wakes convect through the downstream rotor (Arndt, 1993). This situation is illustrated in Fig. 40(a), which shows the upstream nozzle wakes (lightly shaded regions in the figure) being stretched and turned as they convect through the following rotor. Instrumentation placed at the measurement plane shown downstream of the rotor in the figure will detect both the rotor wakes and the dispersed wake segments of the nozzle. This combined wake signature will vary depending upon the circumferential position of the instrumentation relative to the upstream nozzle.

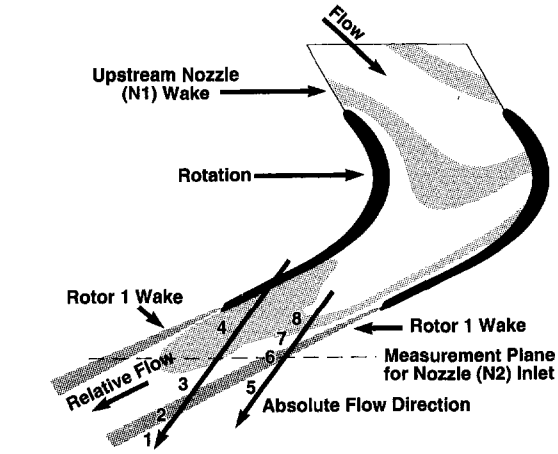

a) Sketch of wake convection (after Denton, 1993).

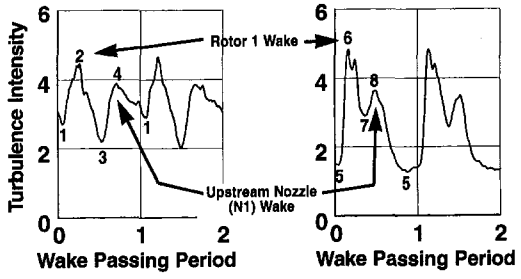

b) 60% relative pitch c) 20% relative pitch

Fig. 40 Wake convection in a multistage LP turbine

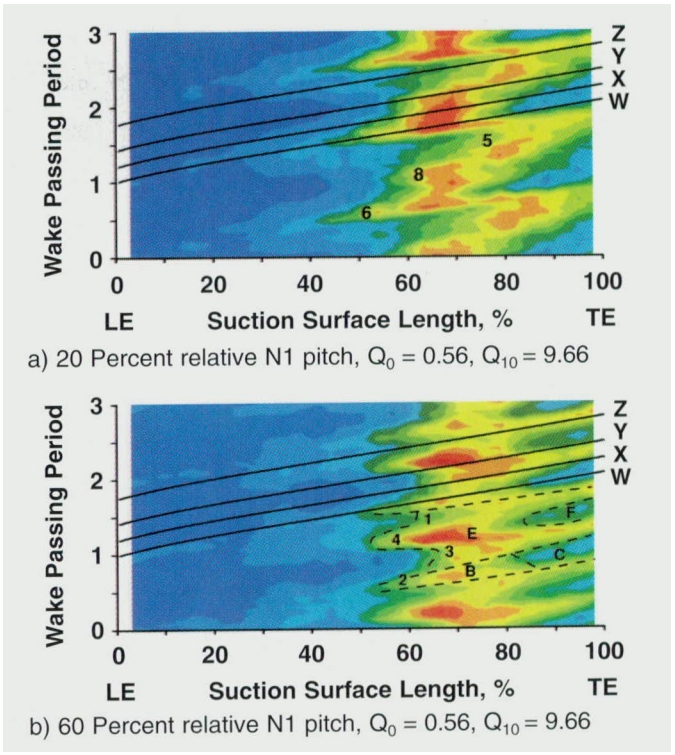

Fig. 41 Effect of nozzle one (N1) clocking on boundary layer development along nozzle two (N2). Turbine suction surface, Test Point 6A.

Figure 40(a) relates to our test configuration in that the upstream nozzle is nozzle N1 and the rotor is rotor R1 as seen in Fig. 4. Two clocking examples are illustrated by the two parallel arrows shown in Fig. 40(a); one arrow is located at 60 percent relative N1 pitch, and the other at 20 percent relative pitch. The arrows show the absolute flow direction the wakes take past a stationary probe placed at each of the two clocking positions. The rotor in Fig. 40(a) is shown frozen at an instant in time. If one allows the "film to roll" (i.e., the rotor to rotate), specific wake features, identified by the numbers adjacent to each arrow, will convect past the stationary instrumentation in the absolute frame (i.e., along the arrow). This unsteadiness pattern will be felt by our downstream nozzle N2.

As the wakes convect past the 60 percent relative N1 pitch location in Fig. 40(a), the instrumentation (and nozzle N2 when aligned with the arrow) will see a turbulence intensity pattern as measured along absolute flow trajectory 1-2-3-4 marked in the figure. The number "2" identifies the peak TI within the R1 wake and "4" denotes the peak TI within the N1 wake segment. This measured pattern of turbulence intensity is shown in Fig. 40(b). Similarly at 20 percent relative N1 position in Fig. 40(a), the TI pattern follows along 5-6-7-8, with the measured values shown in Fig. 40(c). For reference, all nozzle results presented up to this point were obtained with nozzle N1 at 40 percent relative pitch to nozzle N2. The turbulence pattern for this orientation is superimposed onto Fig. 28(a).

15.2 Effect of Nozzle Clocking on the Boundary Layer. The boundary layer development for the two clocking positions described above is shown in Fig. 41. The numbers superimposed on the figures correspond to those in Fig. 40, which identify various levels of turbulence intensity. As observed previously, transition onset at each numbered location in Fig. 41 follows closely the variation in inlet turbulence intensity shown by the time-traces in Figs. 40(b, c).

The flow picture from Fig. 41(a) is very similar to that observed for the baseline in Fig. 28. Its periodic variation is primarily at the blade passing frequency. On the other hand,

the picture in Fig. 41(b), which corresponds to Fig. 10(h), shows the development of two distinct transitional/turbulent strips. One is due to the wake of Rotor R1 and the other is due to the wake segment of Nozzle N1. Periodic variations in the boundary layer occur at twice the blade passing frequency at the trailing edge.

These measurements clearly show that at least two upstream bladerows are required in test vehicles in order to produce the actual disturbance environment, including the nozzle–nozzle clocking effect, that is present in embedded stages.

Conclusions

Conclusions about boundary layer development in LP turbines drawn from our experiments are included at the end of Part 1.

References

Arndt, N. 1993, "Blade Row Interaction in a Multistage Low-Pressure Turbine," ASME JOURNAL OF TURBOMACHINERY, Vol. 115, pp. 137–146.

Denton, J. D., 1993, "Loss Mechanisms in Turbomachines," ASME JOURNAL OF TURBOMACHINERY, Vol. 115, pp. 621–656.

Hodson, H. P., 1985, "Measurements of Wake-Generated Unsteadiness in the Rotor Passages of Axial Flow Turbines," ASME *Journal of Engineering for Gas Turbines and Power*, Vol. 107, pp. 467–476.

Measurement of Gust Response on a Turbine Cascade

A. P. Kurkov

B. L. Lucci

National Aeronautics and Space Administration,
Lewis Research Center,
Cleveland, OH 44135

The paper presents benchmark experimental data on a gust response of an annular turbine cascade. The experiment was particularly designed to provide data for comparison with the results of a typical linearized gust-response analysis. Reduced frequency, Mach number, and incidence were varied independently. Except for the lowest reduced frequency, the gust velocity distribution was nearly sinusoidal. For the high-inlet-velocity series of tests, the cascade was near choking. The mean flow was documented by measuring blade surface pressures and the cascade exit flow. High-response pressure transducers were used to measure the unsteady pressure distribution. Inlet-velocity components and turbulence parameters were measured using hot wire. In addition to the synchronous time-averaged pressure spectra, typical power spectra are included for several representative conditions.

Introduction

In recent years there has been a renewed interest in theoretical and experimental treatments of the gust response mainly to provide better tools and foundations for predicting unsteady forces on turbomachinery blades. For the current state of the art in the field, the reader is referred to the paper by Manwaring and Wisler (1993). They conducted a series of experiments in a large, low-speed facility. The experiments provided aerodynamic forced-response measurements on a compressor stator and a turbine nozzle, and included the measurement of gust inlet-velocity profiles. The excitation was provided by the rotor wakes and a rotating distortion. However, experimental data are still needed in a transonic-flow regime where most of the current turbomachinery operates. It is known that transonic effects are important in flutter phenomena (see, for example, Kurkov and Mehmed, 1993), and hence, it is expected that they will also be significant for the forced excitation.

The object of the current experiment is to fill this gap and to provide systematic variation of several key parameters, which should help the evaluation of the gust analyses. In order to conform to the usual assumptions made in the frequency-domain analyses, the wake-generating rotor and the turbine cascade were widely separated and the gust was nearly sinusoidal (for the majority of the tests) and of small amplitude. Note that the nature of the disturbance in this experiment is vorticial, and the data, therefore, represent a response to this type of gust.

This paper is only concerned with detailed presentation of experimental data. A follow-up paper will include detailed comparisons with analytical results obtained using a linearized two-dimensional code that is based on a potential steady-flow solution and includes inviscid-viscous interaction. The article series will be completed by presenting structural-response data and analysis.

Test Facility

The air entered the bellmouth and passed through the annulus to the rotor consisting of radial pins, either 0.317 or 0.476 cm ($\frac{1}{8}$ or $\frac{3}{16}$ in.) in diameter. The wakes from the pins were convected by the main flow into a turbine cascade. The rotor pins and the turbine cascade are depicted in Fig. 1. The rotor induced a swirl of 3 to 5 deg into the mean flow. The direction of rotation determined the sign of the swirl component, which provided a convenient way of changing the flow incidence. Nominally, the flow into the cascade was axial. For the current experiment, cascade turning angle was 61 deg, the blade chord angle relative to the axial was 38 deg, and the distance between the rotor and the cascade leading edge was 3.9 axial chords. The chord length was 6.35 cm, the axial chord was 4.75 cm, and annulus outside and inside diameters were 40.64 and 27.13 cm, respectively. The cascade consisted of 23 blades that extended in the radial direction spanning the annulus.

The power was delivered to the rotor through a long shaft that extended vertically through the inner pipe of the annulus. The shaft exits the outer pipe at the 90 deg bend close to the floor level and is terminated by a belt-driven pulley, which transmits the power from the electric motor.

Test Matrix

The number of pins on the rotor was either 24, 12, or 6. The pin diameter for the 24-pin configuration was 0.317 cm and for 12- and 6-pin configurations it was 0.476 cm. The pin diameter was increased for the last two configurations in order to reduce the number of harmonics in the wake. The reduced frequency,

$$\omega = \frac{N_w \omega_r c_h}{U_1},$$

was varied by changing the number of pins on the rotor, N_w. In this equation, the shaft angular velocity is denoted by ω_r, the blade chord by c_h, and the axial inlet velocity by U_1. Subscript 1

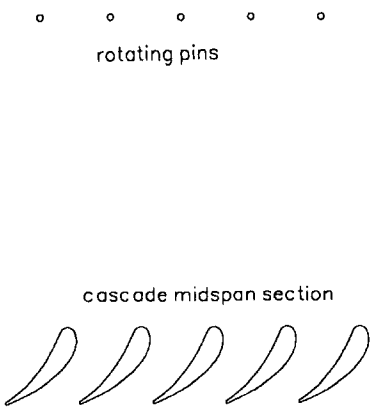

Fig. 1 Rotor–stator configuration

Contributed by the International Gas Turbine Institute and presented at the 40th International Gas Turbine and Aeroengine Congress and Exhibition, Houston, Texas, June 5–8, 1995. Manuscript received by the International Gas Turbine Institute February 13, 1995. Paper No. 95-GT-96. Associate Technical Editor: C. J. Russo.

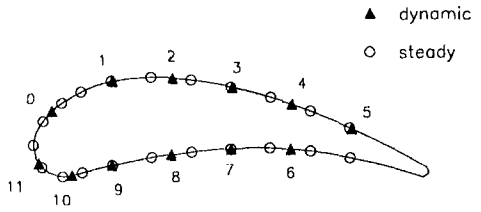

Fig. 2 Instrumentation ports

denotes the station downstream of the bellmouth and upstream of the rotor. In subsequent sections, subscripts 2 and 3 denote the station downstream of the rotor and upstream of the cascade, and the station downstream of the cascade, respectively. Substituting the value for the blade cord, this equation can be expressed as

$$\omega = 0.375 \frac{N_w}{\phi}$$

where ϕ is the flow coefficient, defined as the ratio of axial inlet velocity to the rotational velocity at midspan rotor radius. Throughout the test, the flow coefficient was kept constant at 0.9. Thus, for the available N_w's, the reduced frequency values were 10, 5, and 2.5. The inlet Mach number was either 0.2 or 0.27. At the higher inlet Mach number the flow in the blade passage throat was near choking at the midspan radius. To maintain the desired flow coefficient, the shaft speeds for these two Mach numbers were on the average 4290 and 5790 rpm. The Reynolds numbers corresponding to low and high inlet velocities were 2.7×10^5 and 3.6×10^5, based on blade chord.

Positive and negative values of incidence corresponded to two directions of rotation. Because of the inlet-flow symmetry relative to axial direction, it was sufficient to survey the wake for only one direction of rotation. The incidence values were

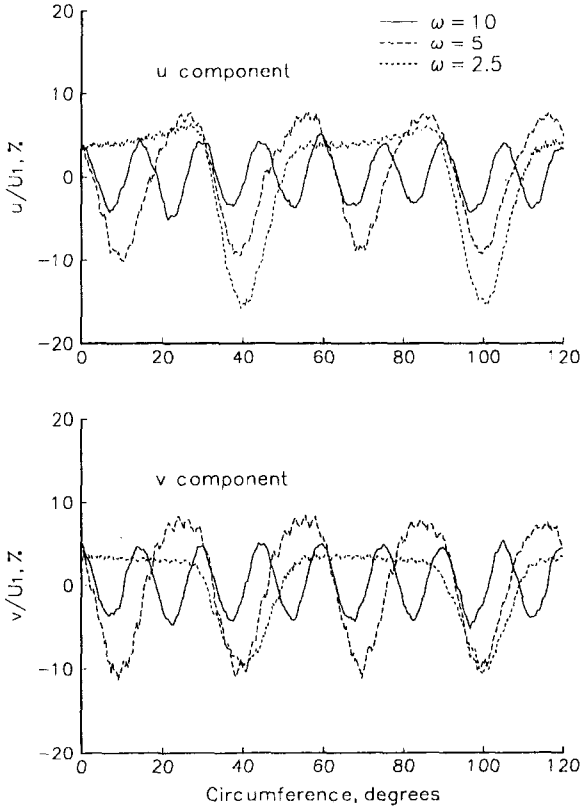

Fig. 3 Inlet velocity profiles, $M_1 = 0.27$

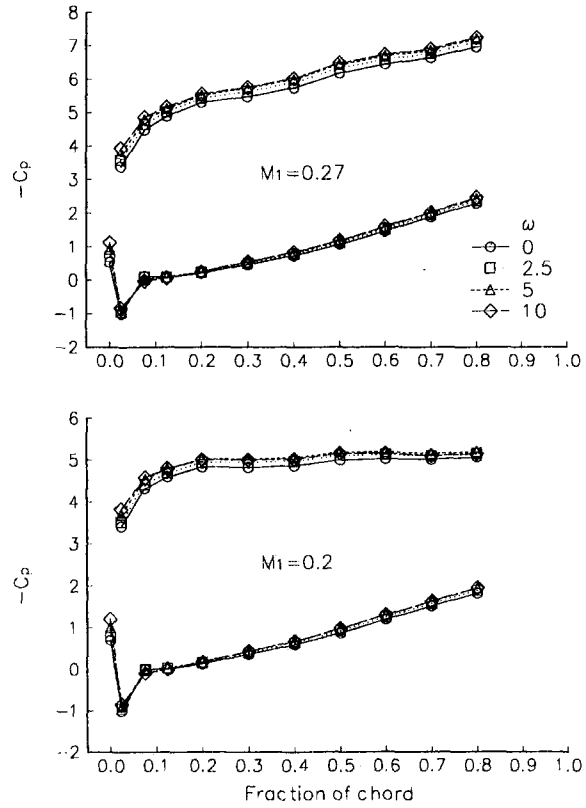

Fig. 4 Mean pressure coefficients, $\beta_2 > 0$

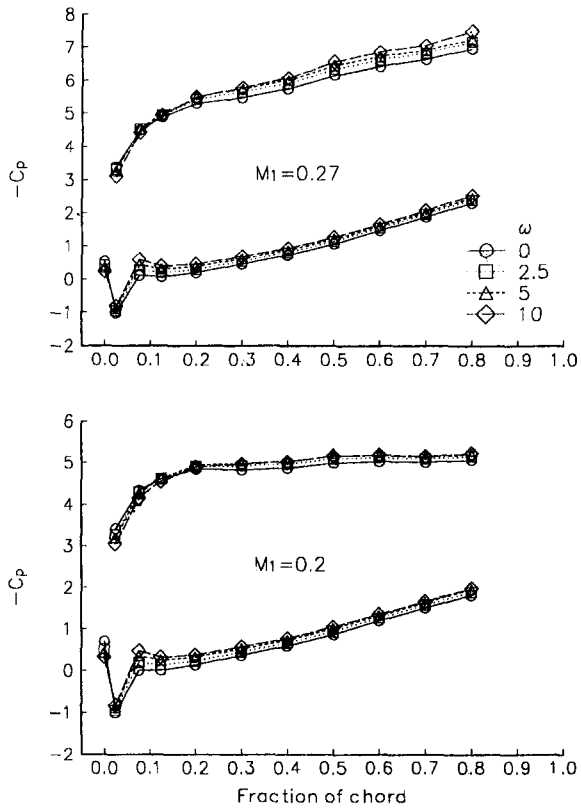

Fig. 5 Mean pressure coefficients, $\beta_2 < 0$

Table 1 Time-averaged inlet-velocity spectra

ω	M_1	β_2	Harmonic amplitude (percent) and phase (deg), u/U_1						Harmonic amplitude (percent) and phase (deg), v/U_1					
			1		2		3		1		2		3	
2.5	0.2	4.59	7.36	-78.9	4.34	29.2	1.59	141.2	6.60	-76.8	3.78	26.34	1.38	138
	0.27	5.17	7.76	-69.2	5.36	55.5	2.35	-178.3	5.48	-58.6	3.23	57.4	1.29	178
5	0.2	3.85	7.70	74.4	1.03	-8.9	--------	--------	6.95	71.8	0.50	-20.8	--------	--------
	0.27	3.52	8.01	63.0	1.06	-20.1	--------	--------	8.67	65.5	1.16	-31.4	--------	--------
10	0.2	3.24	4.40	-11.6	--------	--------	--------	--------	4.87	-10.8	--------	--------	--------	--------
	0.27	2.98	4.07	8.02	--------	--------	--------	--------	4.54	8.46	--------	--------	--------	--------

between 3 and 5 deg and depended mainly on the rotor pin diameter. Numerical incidences in this paper are reported as deviations from the nominal design axial inlet-flow direction.

Note that when changing the direction of rotation, the interblade phase angle also changes the sign. Taking into account the number of rotor pins and the number of blades, the interblade phase angles for positive and negative rotations are close to ± 360, ± 180, or ± 90 for reduced frequencies of 10, 5, and 2.5, respectively. The last change is the most significant, and, therefore, for reduced frequency of 2.5 the change in incidence is coupled with a substantial change in interblade phase angle.

Experimental Measurements

The inlet condition was defined by the barometric pressure, inlet temperature at the bellmouth inlet, and several static pressure measurements on the inside and outside wall of the annulus downstream of the bellmouth. The cascade exit flow was surveyed at the blade midspan radius over a circumference in excess of one blade pitch with a five-hole probe. This station was one axial chord length downstream of the cascade trailing edge.

The cascade inlet-velocity components at the midspan radius were measured with a hot wire. To simulate the far-field frozen gust condition, the cascade was removed for these measurements, and the inner and outer spacer rings were installed in its place to maintain the same annulus geometry. The hot-wire measurements were made at the axial location corresponding to the cascade leading-edge position.

The single-wire method was implemented essentially as given by Bruun (1990) for the mean velocity and by Fujita and Kovasznay (1968) for the mean-square turbulence velocities. For each wake point, four data runs were obtained corresponding to four different angles of the wire relative to the axial flow direction. (The run reproducibility was well within the measurement accuracy.) Only two wire angles were needed for the mean flow velocity components. For the turbulence velocities, the four wire angles allowed the equations to be solved by the least-square method. Wire calibration was performed in the test facility at the station just downstream of the bellmouth. After the wire was calibrated, it was transferred together with the actuator to the wake measurement station downstream of the rotor. IFA-100 anemometer (TSI Inc.) was used to process hot-wire signals. The analog signals were digitized at 150 or 200 kHz for the low- and high-shaft-speed runs. Prior to calculating mean-square turbulence parameters, the hot-wire data were digitally filtered using a 256-point finite impulse response filter (Rabiner and McGonegal, 1979).

The steady-state blade-pressure distribution was measured with a specially instrumented hollow blade provided with 21 surface pressure taps. For the steady-state conditions the flow was axial and the rotor was replaced with spacer rings to preserve the axial geometry. Because the rotor induces a small swirl into the mean flow, this blade was also used for unsteady tests to evaluate the effect of the swirl. Long tubes leading to the transducers eliminated all unsteadiness from the data. Separate transducers were used for each port. They were automatically calibrated in approximately 20-min intervals, identical to the other steady-state transducers.

The dynamic pressures on the blade surfaces were measured by 3.45 N/cm^2 (5 psi) differential transducers manufactured by Kulite Semiconductor Products, Inc. (LQ-125 series). The transducers were mounted in a hollow blade at the midspan radius and were recessed slightly from the blade surface. The diameter of the sensitive area was 1.8 mm, and the natural frequency was 70 kHz. Because of the high curvature at the leading-edge stagnation point, a smaller transducer (XCS 062) with the sensitive area diameter of 0.71 mm and the natural frequency of 150 kHz was used at this location. The back sides of the transducers were connected to a reference pressure source, which was selected so that the measured differential pressure was within the transducer limits. A separate reference was used for the transducers on the pressure and the suction sides of the blade. With the instrumented blade installed in the tunnel, the transducer calibration was performed prior to each research run by reducing the pressure to the back sides of the diaphragms below the atmospheric, while maintaining quiescent conditions in the wind tunnel.

The five-hole probe, manufactured by United Sensor & Control Corp. (prism type, model DA-125), was nulled in the yaw direction. For the pitch angle, and the total and static pressures, the free-jet calibration curves were used.

The steady-state data were acquired using the Central Data Processing Facility, while all dynamic data were recorded locally. A Concurrent 6350 series computer was used to digitize and analyze the data. For pressure signals, 13 channels were acquired simultaneously using a 12-bit digitizer and a sample and hold module. The sampling rate was either 75 or 103 kHz, depending on the shaft speed. The unsteady pressure data were filtered at 20 kHz using an 8-pole-6-zero, constant-delay, low-pass filter.

The once-per-revolution signal was generated by a high-response fiber-optic sensor. The probe, positioned on the outside wall opposite the rotor pins, transmitted the light to and collected the reflected light from a rotating pin that had a polished tip. (The tips of the remaining pins were painted black.) The probe diameter was 3.175 mm and its frequency response was 150 kHz. The probe output, usually between 2 and 4 V, depended on the gap between the probe tip and the pins.

The locations of the steady-state and dynamic ports on the instrumented blades are given in Fig. 2. (Note that separate blades were used for the two measurements.) The dynamic ports are numbered for later reference. Blade and pressure-port coordinates are given in tabular form in the appendix. The blade coordinates are listed in Table 1A in terms of lower (subscript L) and upper (subscript U) contours. The units in this table are inches, as specified in the drawing. The X axis is horizontal and tangent to the two points on the lower surface in Fig. 2, and the Y axis is vertical and tangent to the point $X_L = 0$, $Y_L = 0.192$ in. If shown, the axis of rotation in Fig. 2 would be tilted 38 deg relative to the X axis (see also Fig. 1). The leading-

edge radius that completes the contour of the lower surface between the X and Y tangency points is 0.192 in., and the trailing-edge radius is 0.034 in. Tables 2A and 3A in the appendix list the measured X coordinates in inches of the steady-state and dynamic pressure ports (which are also identified by the port number shown in Fig. 2).

The 12-bit digitizer provided sufficiently high dynamic range so that both ac and dc components for the hot wire and the unsteady pressure signals could be captured. An exception was the port 3 pressure transducer (Fig. 2), which had a large dc zero shift and, therefore, had to be ac coupled.

The unsteady signals were digitized to the memory in a contiguous stream that comprised at least 200 revolutions. The data analysis was performed subsequent to the test. This minimized the test time and provided the best accuracy, since test conditions did not have to be maintained over an extended period. The once-per-revolution signal was used to sort the data into the consecutive revolution periods. Because the digitizing rate for all tests was in excess of 1024 points per revolution, 1024 approximately equidistant points could be selected for each revolution. For the spatial time-domain distributions (1024 points), the data were averaged over the total of 200 revolutions; however, for the spectral analyses, the length of the averaged segment was 8 revolutions (8192 points) resulting in approximately 25 averages. Thus the resolution for the phase-synchronous spectra was $\frac{1}{8}$ engine order (E). For the power spectra, the averaging was performed in the frequency domain resulting in 25 averages for each of the 4096 frequency points.

Because the discrete Fourier transforms included an integral number of revolutions and, therefore, in the case of forced response an integral number of cycles, the spectral amplitudes were essentially confined to single-frequency lines. This also made windowing unnecessary.

Results

Inlet-Velocity Profiles. Figure 3 presents the unsteady axial (u), and circumferential (v) time-averaged velocity components expressed as percents of inlet velocity U_1 for the inlet Mach number $M_1 = 0.27$, and the three reduced frequencies of 10, 5, and 2.5. The results for the inlet Mach number of 0.2 are quite similar. The corresponding synchronously averaged

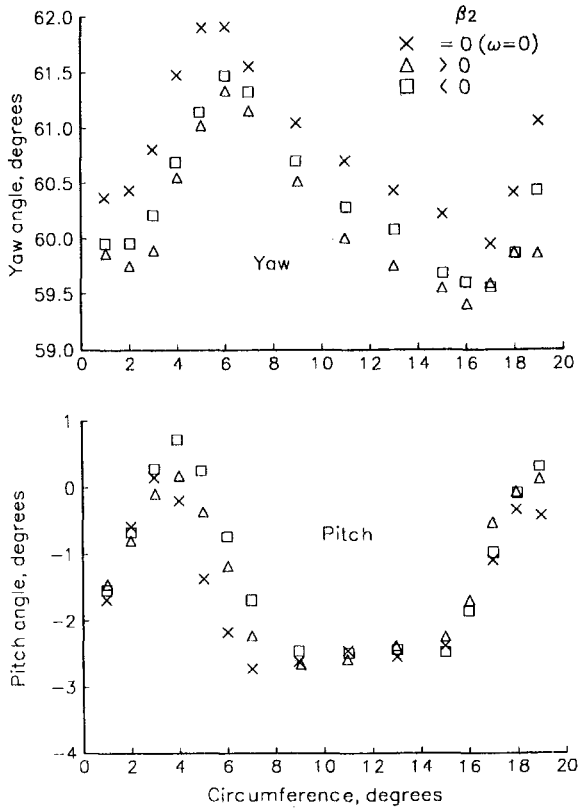

Fig. 6 Exit angles, $\omega = 10$, $M_1 = 0.27$

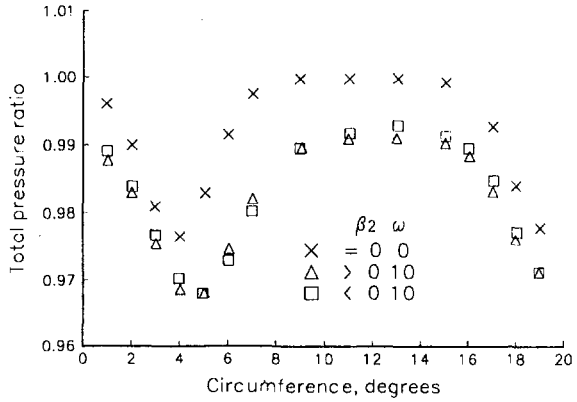

Fig. 7 Exit total pressure ratio, $M_1 = 0.27$

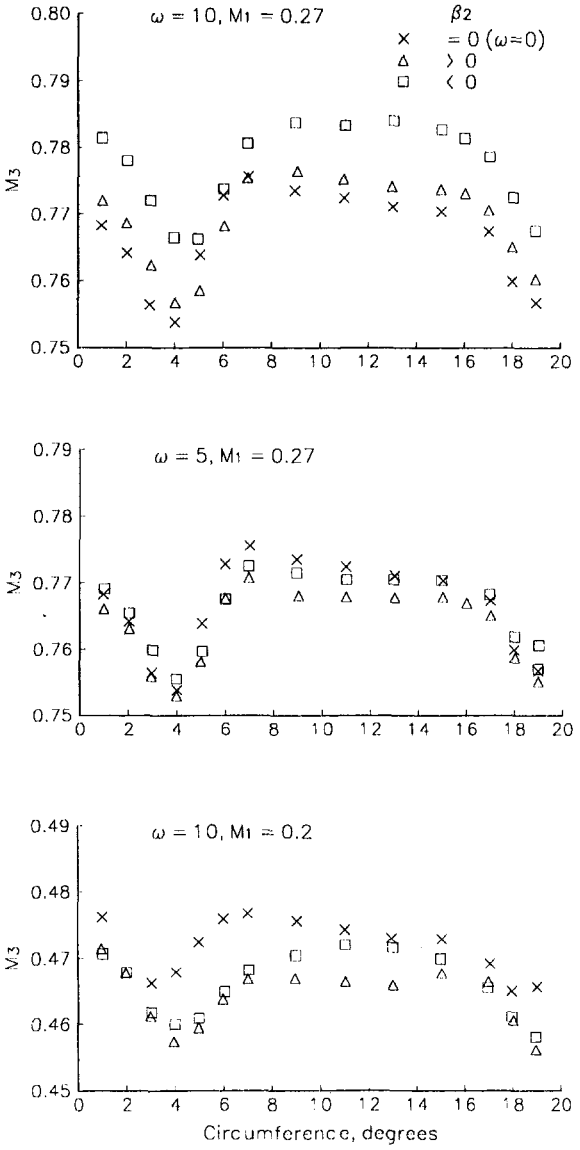

Fig. 8 Exit Mach number

Table 2 Time-averaged first harmonics of the unsteady blade pressures

M_1	ω	β_2	Amplitudes [percent $\rho_1 U_1^2/2$] and phase angles [radians]											
			0	1	2	3	4	5	6	7	8	9	10	11
0.27	10.00	-2.98	13.45	10.31	4.79	4.61	4.30	1.75	5.74	6.66	4.69	1.83	4.29	8.37
			-0.13	-0.28	-0.42	0.36	0.30	-0.17	-0.48	-0.38	-0.29	-0.08	-0.04	0.27
		2.98	6.57	4.94	1.21	1.12	1.49	0.90	1.02	1.23	1.86	3.14	7.25	8.89
			-0.49	0.17	0.06	-0.25	-0.26	0.48	0.16	0.30	0.40	0.41	0.35	-0.02
	5.00	-3.52	33.57	24.66	12.88	4.19	3.51	9.69	19.56	20.87	19.67	18.24	24.06	14.50
			-0.20	-0.28	-0.30	-0.28	0.02	0.10	0.06	0.09	0.12	0.15	0.12	0.36
		3.52	25.77	10.25	2.46	5.46	9.38	14.45	4.89	5.04	5.25	6.88	14.97	16.73
			-0.20	-0.35	-0.06	0.04	0.05	0.09	-0.44	-0.42	-0.43	-0.46	-0.48	0.18
	2.50	-5.17	29.95	13.61	5.11	2.51	2.62	3.24	11.75	13.55	14.62	16.28	23.60	12.64
			0.27	0.22	0.16	0.02	0.07	0.14	-0.18	-0.18	-0.18	-0.19	-0.23	-0.03
		5.17	20.17	1.76	8.98	11.70	15.78	20.12	9.28	8.82	9.08	10.27	17.15	16.32
			-0.39	0.06	0.02	0.04	0.02	0.05	0.06	0.06	0.07	0.09	0.12	-0.16
0.20	10.00	-3.24	12.34	10.54	6.84	4.19	1.95	1.50	5.23	4.74	3.69	2.42	4.65	8.29
			-0.10	-0.29	-0.42	0.44	0.27	-0.08	0.49	-0.37	-0.22	-0.03	-0.02	0.31
		3.24	5.43	4.01	1.61	1.13	0.79	1.06	0.89	1.17	1.77	2.73	5.82	7.26
			0.49	0.16	-0.02	-0.17	-0.33	0.38	0.17	0.30	0.39	0.41	0.34	-0.05
	5.00	-3.85	35.50	22.73	10.37	3.23	2.00	5.03	12.23	15.41	16.42	16.97	23.67	14.84
			-0.15	-0.23	-0.27	-0.35	0.27	0.17	0.12	0.15	0.19	0.22	0.19	0.40
		3.85	20.39	6.63	7.19	7.12	5.85	4.03	6.11	5.91	5.84	7.55	16.20	18.86
			-0.15	-0.48	0.30	0.27	0.24	0.16	-0.36	-0.36	-0.39	-0.44	-0.46	0.19
	2.50	-4.59	32.76	14.95	5.56	1.23	1.37	2.48	9.71	11.72	13.11	15.40	23.44	10.76
			0.31	0.27	0.24	0.15	-0.09	-0.20	-0.19	-0.18	-0.18	-0.18	-0.22	-0.03
		4.59	13.26	8.52	11.58	11.88	11.48	10.80	4.67	5.18	6.27	8.36	15.56	17.21
			-0.37	0.18	0.13	0.14	0.11	0.09	0.13	0.12	0.12	0.13	0.17	-0.15

spectral results are presented in Table I, where β_2 denotes the incidence in the cascade leading-edge plane. From these results it follows that the gust was nearly sinusoidal for the reduced frequencies of 10 and 5. Amplitudes were larger for the reduced frequencies of 5 and 2.5, because larger diameter rotor-pins were used for these runs. The incidences for these reduced frequencies were also somewhat higher in magnitude. For the reduced frequency of 2.5 the first two harmonics were significant.

Steady and Mean Pressures. The steady-state blade pressure distribution was obtained for the axial inlet flow without the rotor and corresponds to $\omega = 0$ label in the figures. For the nonzero reduced frequencies, there was a mean incidence present relative to the axial flow direction, which somewhat affected the distribution of the pressure coefficient,

$$C_p = \frac{p - p_1}{\rho_1 U_1^2/2}$$

where p denotes the static pressure and ρ the density (see Figs. 4 and 5). At the 0.075 chord fraction in Fig. 5 on the pressure surface, the pressure coefficient is reduced for $\omega = 10$ relative to other reduced frequencies. (Note that pressure coefficient is negative for positive ordinates.) At the inlet Mach number of 0.27, in this figure there is also a reduction of pressure coefficient on the suction side of the rear portion of the blade for $\omega = 10$. On the other hand, the gust amplitude (Table I) does not appear to be a strong factor for the mean pressure coefficient distributions.

Exit Flow. The exit-flow station was one axial chord downstream of the cascade trailing edge. The distributions of the yaw and pitch angles for one blade passage are presented in Fig. 6 for the inlet Mach number of 0.27 and the reduced frequency of 10. Distributions for other reduced frequencies and inlet Mach numbers were quite similar. Figure 7 presents the total pressure plot for the conditions for which the loss was the maximum. The total pressure ratio depended mainly on the Mach number and the reduced frequency.

The exit Mach number distribution exhibited dependence on the inlet Mach number, the incidence, and the reduced frequency, as illustrated in Fig. 8. The differential increase in the exit Mach number for $\omega = 10$, $M_1 = 0.27$, and $\beta_2 < 0$ supports the observed drop in the mean pressure coefficient in the aft portion of the blade on the suction side in Fig. 5.

Unsteady Pressure Spectra. The first harmonics of synchronously averaged, complex, pressure spectra are presented in Table 2. The amplitudes are given in percent of the inlet dynamic pressure (first row for each β_2) and phase angles are given in radians (second row). The second and third harmonics for the unsteady pressures were significant for the reduced frequency of 2.5, just as for the inlet velocity spectra. Thus, for this value of reduced frequency, the time-domain experimental results will be affected, to some extent, by the higher harmonics. In the frequency domain, the amplitudes of the second harmonic for the reduced frequency of 2.5 result in qualitatively similar distribution to that corresponding to the first harmonic for reduced frequency of 5.

The amplitudes for the reduced frequencies of 5 and 2.5 are larger than the amplitude for the reduced frequency of 10 because of the larger rotor pins used for these frequencies. Thus, the results for the reduced frequency of 10 more nearly represent the small amplitude sinusoidal disturbance usually assumed for gust analyses in the frequency domain.

The amplitude distribution in Table 2 is strongly dependent on the reduced frequency and incidence. Mach number dependence is weak for negative incidences; however, for positive

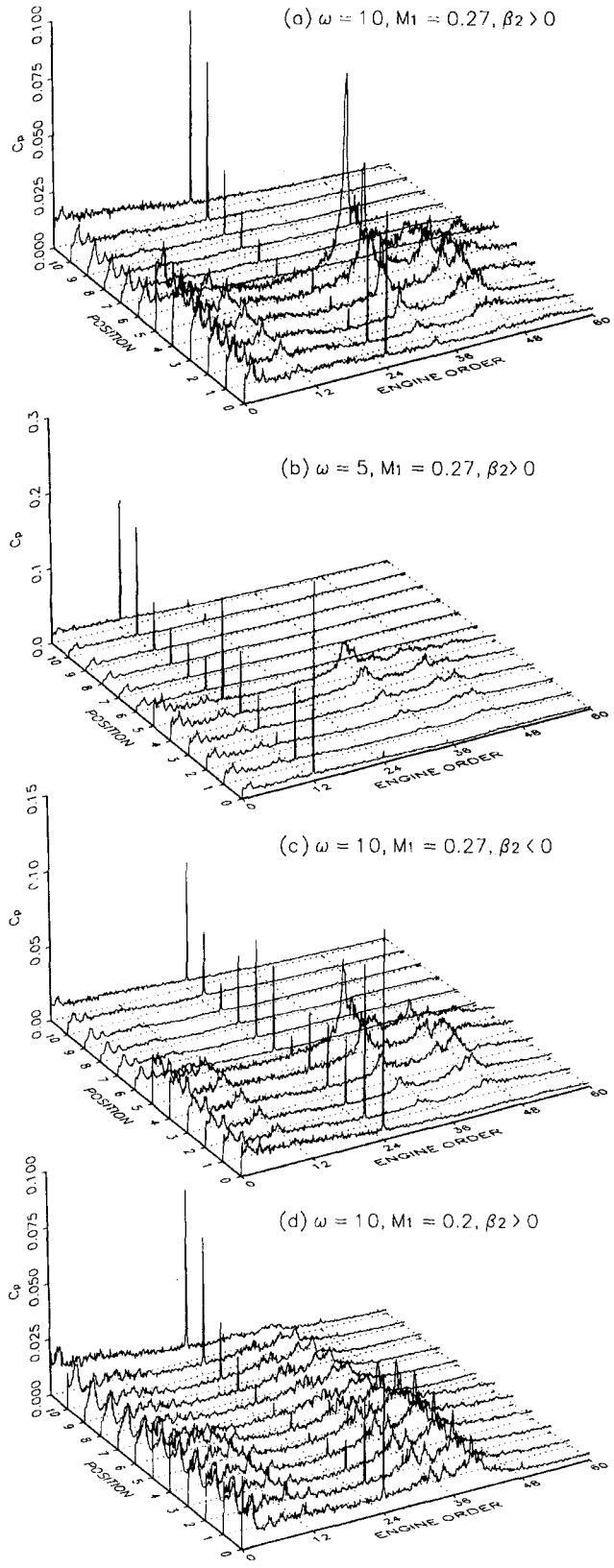

Fig. 9 The rms pressure spectra

incidences and lower reduced frequencies it is significant. For example, a steep amplitude variation on the suction side of the blade near the leading edge (positions 0, 1, and 3) is present for $M_1 = 0.27$, $\omega = 2.5$, and $\beta_2 > 0$. Since the wavelength of the disturbance is the largest for this reduced frequency, one would not expect such a steep variation in the unsteady-pressure amplitude at this condition. For $M_1 = 0.2$, the amplitude variation is much less at these locations.

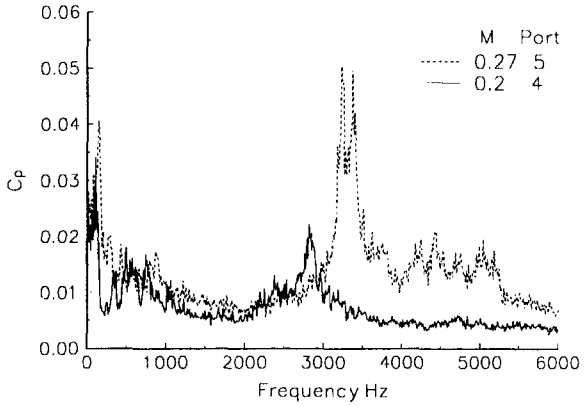

Fig. 10 Clean inlet rms pressure spectra

The representative root-mean-square (rms) spectra are illustrated in Fig. 9. The synchronous peaks in these spectra are virtually identical with the corresponding peaks in the time-average spectra in Table 2; however, they also include the non-synchronous origin and the random pressure fluctuations. The frequency units are engine orders; thus, the synchronous peaks appear at the frequency equal to the number of rotor pins. The position-axis units correspond to blade port numbers in Fig. 2; thus, position 0 corresponds to the port nearest to the leading edge on the suction surface side, and 11 corresponds to the port nearest to the leading edge on the pressure side.

In addition to the synchronous peaks, the dominant feature in the spectra is the pressure excitation in Fig. 9(*a*) at position 5 on the suction side. It reaches its maximum of 0.093 at the frequency of 33 E, or 3182 Hz. Apparently, this disturbance is related to the broad-band turbulence excitation on the suction side of the blade. It is evident that amplification of this disturbance is a function of inlet Mach number, reduced frequency, and incidence. For reduced frequency of 10 and negative incidence, Fig. 9(*c*), the corresponding peak amplitude is 0.065 at 33 E or 3177 Hz. Note that only at reduced frequency of 10 did the high-frequency pressure fluctuations peak at an integral engine order.

Figure 9 also indicates that while the broad-band turbulent excitation in the higher-frequency range is confined to the suction side at the inlet Mach number of 0.27, it is also significant on the pressure side at Mach 0.2. The peak excitation at the inlet Mach number of 0.2 in Fig. 9(*d*) has amplitude of 0.034 and frequency of 39.125 E or 2815 Hz. (Note that the rotational speed was lower for this Mach number.)

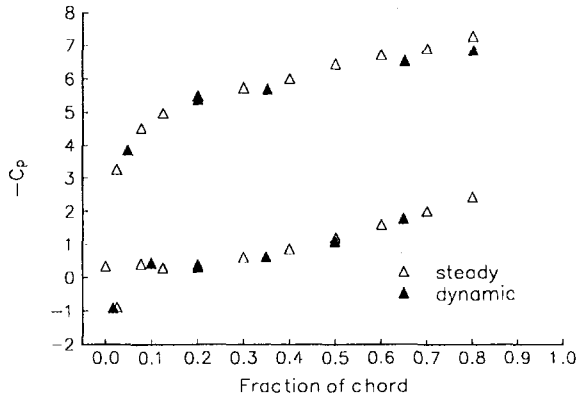

Fig. 11 Mean pressures, $M_1 = 0.27$, $\omega = 5$, $\beta_2 < 0$

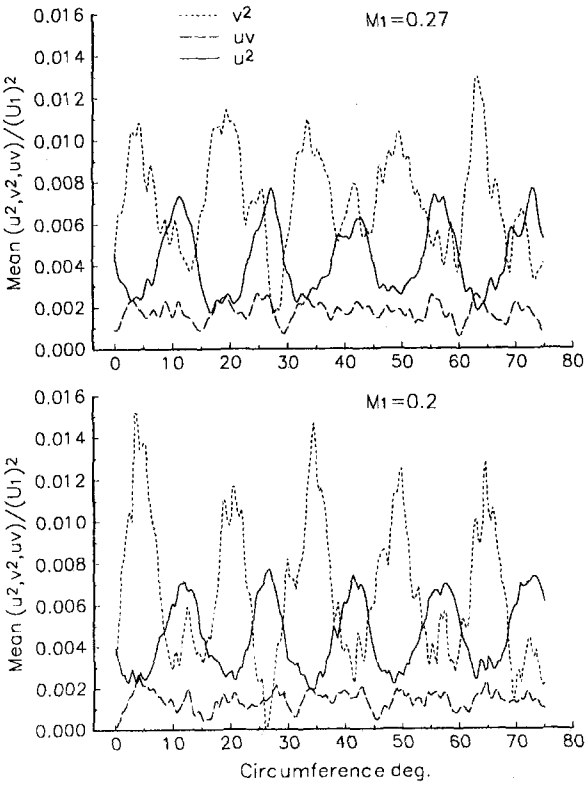

Fig. 12 Mean-square fluctuating velocities, ω = 10

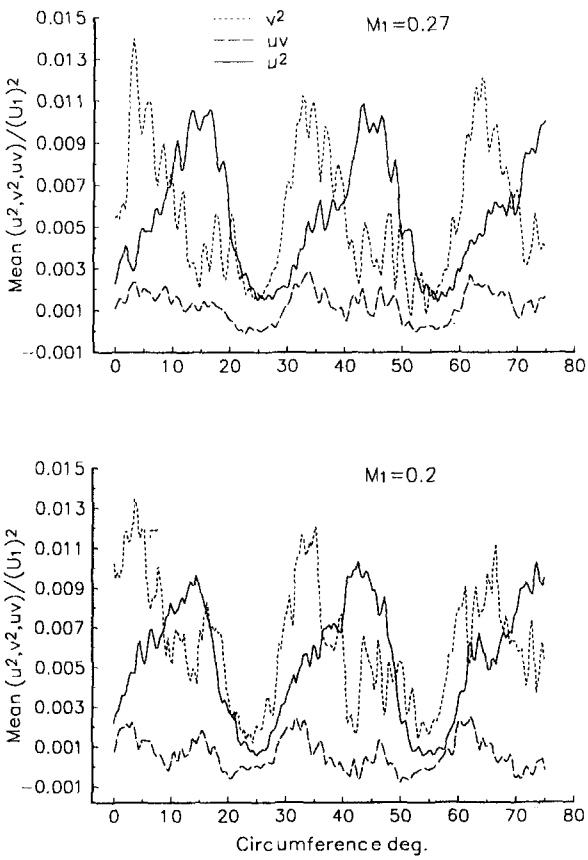

Fig. 13 Mean-square fluctuating velocities, ω = 5

The rms pressure spectra for the clean-inlet case (i.e., no rotor) and the inlet Mach numbers of 0.27 and 0.2 are shown in Fig. 10. For the Mach number of 0.27, the spectrum corresponds to port 5. The low-frequency peak amplitude is 0.0406 at the frequency of 138.9 Hz. The two high-frequency peaks have amplitudes of 0.0510 and 0.0496 at the corresponding frequencies of 3220 and 3359 Hz. For the clean-inlet Mach number of 0.2 the spectrum corresponds to port 4 (for which it was maximum). The low- and high-frequency peak amplitudes and frequencies are 0.03408 and 138.9 Hz, and 0.0223 and 2807.6 Hz.

The clean-inlet results together with forced excitation results for the entire test matrix show that under forced excitation there is a small frequency shift for the peak high-frequency turbulence excitation relative to the clean inlet. The peak-response frequency is mainly a function of Mach number. The highest magnification factor of pressure fluctuations under forced excitations is about 2. It occurs at a reduced frequency of 10 and positive incidence at an integral engine order frequency. Within the range of gust amplitudes encountered in the test, the gust amplitude does not strongly influence the peak response, since it occurred at a reduced frequency for which the gust amplitude was the smallest. In no case was the amplitude of the pressure fluctuations under forced excitation lower than the corresponding clean-inlet amplitude.

Note that, although there is no indication of separation (i.e., no flattening of C_p distribution) on the suction side of the blade for the conditions of Fig. 9(a) (see Fig. 4), if the flow separates past the last measuring station on the suction surface, the observed magnification of random pressures in Fig. 9(a) may result because of proximity of separation point, as observed by Schulz et al. (1990).

Since both the dc and ac components of the dynamic pressure were recorded, one can derive the average pressure distribution from the dynamic pressure measurements and compare it to the mean pressure distribution obtained with the steady-state-type instrumentation. This is illustrated in Fig. 11 for the reduced

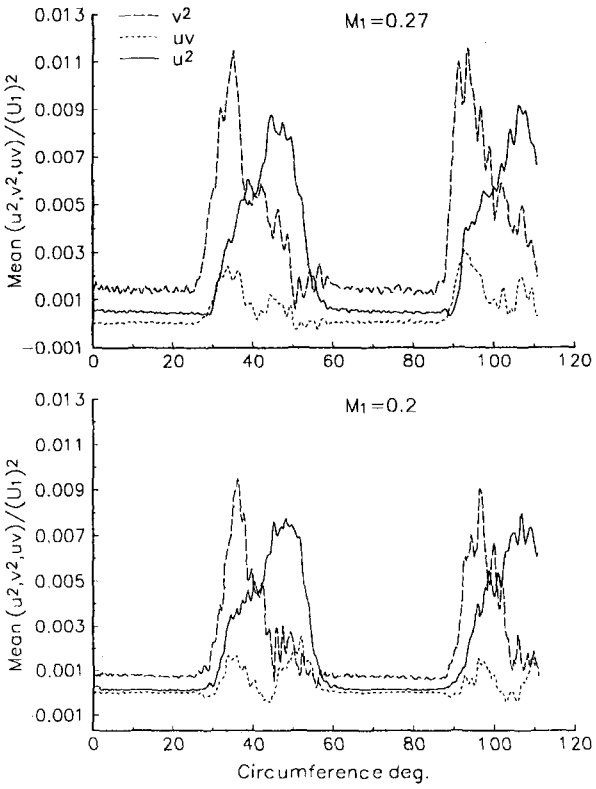

Fig. 14 Mean-square fluctuating velocities, ω = 2.5

frequency of 5, the inlet Mach number of 0.27, and the negative incidence. The slightly higher values of pressures (and hence the lower values of the negative pressure coefficient in Fig. 11) in the aft portion of the blade on the suction side are probably caused by the small differences in the blade contours between the steady-state and the dynamically instrumented blades, and the contribution due to the turbulence (Mattingly, 1983). These results are typical for majority of the test conditions.

Wake Turbulence. Wake turbulent velocity fluctuations are included in the paper because it is possible that some of the observed behavior in the experimental results depends on the turbulence level in the wake. Figures 12–14 present the mean-square distribution of turbulent velocities. The Reynolds stress component uv is small for all conditions and v^2 appears to be significantly higher than u^2 at reduced frequency of 10. (Without explicit notation, it is implied in the paper that all second-order velocity parameters are mean-square values averaged over about 200 revolutions.) Moreover, at this reduced frequency u^2 and v^2 are out of phase. At reduced frequencies of 5 and 2.5, these two components are more nearly equal and more nearly in phase.

At reduced frequency of 2.5 (Fig. 14) there are periods of low turbulence intensity because the wakes did not merge. The turbulence intensity between the wakes corresponds to free-stream turbulence. Perhaps the previously noticed steep unsteady pressure variation in the forward part of the blade suction surface (port 1) for $\omega = 2.5$, $\beta_2 > 0$, and $M_1 = 0.27$ arises because the prolonged periods of high- and low-turbulence-intensity fluctuations may influence the unsteady flow structure in this region. Some support for this argument follows from the work of Liu and Rodi (1991), who noticed that the transition point is frequency dependent for wakes that have not merged. It appears that for nonsinusoidal gust, it would be valuable to include detailed boundary layer measurements in addition to the unsteady pressure. If there is a separation bubble in the region of this pressure port at the stated conditions, one would expect a low value of the unsteady-pressure amplitude according to Schulz et al. (1990).

Concluding Remarks

For the two-out-of-three reduced frequencies in the experiment, a nearly sinusoidal gust has been generated, allowing a parametric study of the reduced frequency effects in the time and frequency domains. The incidence variation at each reduced frequency was accomplished without a change in the inlet Mach number or the flow coefficient. The gust amplitude varied somewhat with the reduced frequency; however, it did not appear to have a dominant effect.

Unsteady, synchronous-response blade pressures are strongly dependent on reduced frequency and incidence. Mach number dependence is weak for negative incidence and significant for positive incidence at lower reduced frequencies.

The mean blade-pressure distribution is to some extent dependent on the reduced frequency, particularly for the negative incidence and the higher inlet Mach number.

At the reduced frequency of 10, the inlet Mach number of 0.27, and the positive incidence, a magnification of the turbulent pressure fluctuations on the suction side of the aft portion of the blade resulted in a significant excitation concentrated at an integral engine order much higher than the synchronous excitation frequency.

References

Bruun, H. H., 1990, "Signal Analysis Method of *X* Hot-Wire Anemometry," in: *The Heuristics of Thermal Anemometry, Proc. ASME Fluids Engineering Division,* D. E. Stock et al., eds., ASME FED-97, Toronto, Canada, pp. 53–58.

Fujita, H., and Kovasznay, S. G., 1968, "Measurement of Reynolds Stress by a Single Rotated Hot Wire Anemometer," *The Review of Scientific Instruments,* Vol. 39, pp. 1352–1355.

Kurkov, A. P., and Mehmed, O., 1993, "Optical Measurement of Unducted Fan Flutter," ASME JOURNAL OF TURBOMACHINERY, Vol. 115, pp. 189–196.

Liu, X., and Rodi, W., 1991, "Experiments on Transitional Boundary Layers With Wake-Induced Unsteadiness," *Journal of Fluid Mechanics,* Vol. 231, pp. 229–256.

Manwaring, S. R., and Wisler, D. C., 1993, "Unsteady Aerodynamics and Gust Response in Compressors and Turbines," ASME JOURNAL OF TURBOMACHINERY, Vol. 115, pp. 724–740.

Mattingly, G. E., 1983, "Volume Flow Measurements," in: *Fluid Mechanics Measurements,* R. J. Goldstein, ed., Hemisphere, New York.

Rabiner, L. R., and McGonegal, C. A., 1979, "FIR Windowed Filter Design Program-WINDOW," in: *Programs for Digital Signal Processing,* IEEE Press, New York.

Schulz, H. D., Gallus, H. E., and Lakshminarayana, B., 1990, "Three-Dimensional Separated Flow Field in the Endwall Region of an Annular Compressor Cascade in the Presence of Rotor–Stator Interaction: Part 2—Unsteady Flow and Pressure Field," ASME JOURNAL OF TURBOMACHINERY, Vol. 112, pp. 679–688.

APPENDIX

Blade and Pressure-Port Coordinates

Table 1A Blade coordinates

X_L	0.000	0.050	0.100	0.150	0.200	0.250	0.300	0.350	0.400	0.450	0.500	0.550	0.600	0.650
Y_L	0.192	0.063	0.023	0.005	0.000	0.009	0.021	0.034	0.046	0.057	0.068	0.079	0.090	0.099
X_L	0.700	0.750	0.800	0.850	0.900	0.950	1.000	1.050	1.100	1.150	1.200	1.250	1.300	1.350
Y_L	0.109	0.118	0.126	0.134	0.141	0.148	0.154	0.160	0.164	0.168	0.172	0.174	0.176	0.178
X_L	1.400	1.450	1.500	1.550	1.600	1.650	1.700	1.750	1.800	1.850	1.900	1.950	2.000	2.050
Y_L	0.178	0.178	0.176	0.174	0.172	0.168	0.164	0.159	0.153	0.146	0.138	0.130	0.121	0.111
X_L	2.100	2.150	2.200	2.250	2.300	2.350	2.400	2.442	2.450	2.489	--------	--------	--------	--------
Y_L	0.100	0.088	0.076	0.062	0.048	0.033	0.017	0.003	0.000	0.034	--------	--------	--------	--------
X_U	0.000	0.042	0.050	0.100	0.150	0.200	0.250	0.300	0.350	0.400	0.450	0.500	0.550	0.600
Y_U	0.192	0.312	0.321	0.384	0.431	0.469	0.499	0.525	0.546	0.563	0.577	0.589	0.597	0.604
X_U	0.650	0.700	0.750	0.800	0.850	0.900	0.950	1.000	1.050	1.100	1.150	1.200	1.250	1.300
Y_U	0.609	0.612	0.613	0.613	0.611	0.608	0.604	0.599	0.592	0.585	0.576	0.567	0.556	0.545
X_U	1.350	1.400	1.450	1.500	1.550	1.600	1.650	1.700	1.750	1.800	1.850	1.900	1.950	2.000
Y_U	0.532	0.519	0.505	0.490	0.475	0.459	0.442	0.424	0.405	0.386	0.366	0.346	0.324	0.302
X_U	2.050	2.100	2.150	2.200	2.250	2.300	2.350	2.400	2.450	2.472	2.489	--------	--------	-------
Y_U	0.279	0.256	0.232	0.207	0.182	0.156	0.130	0.103	0.075	0.063	0.034	--------	--------	------

Table 2A Steady-state pressure port locations (Fig. 2)

X_L	0.000	0.058	0.188	0.312	0.502	0.748	0.999	1.247	1.491	1.745	1.995
X_U	0.000	0.063	0.188	0.300	0.490	0.743	0.995	1.246	1.496	1.747	1.991

Table 3A Dynamic pressure port locations (Fig. 2)

PORT	11	10	9	8	7	6
X_L	0.039	0.247	0.500	0.873	1.248	1.621
PORT	0	1	2	3	4	5
X_U	0.119	0.499	0.879	1.256	1.629	2.005

Free Vortex Theory for Efficiency Calculations From Annular Cascade Data

A. J. Main

M. L. G. Oldfield

G. D. Lock[1]

T. V. Jones

Department of Engineering Science,
Oxford University,
Oxford, United Kingdom

This paper describes a new three-dimensional theory to calculate the efficiency or loss of nozzle guide vane annular cascades from experimental area traverse measurements of the compressible downstream flow. To calculate such an efficiency, it is necessary to mix out the measured flow computationally to either a uniform state or one that is a function of radius only. When this is done by conserving momentum, mass, and energy flow, there is a remaining degree of freedom in that the radial distribution of circumferential velocity can be chosen. This extra freedom does not arise in two-dimensional cascades. The new method mixes the flow out to a free (i.e., irrotational) vortex. This is preferred to existing methods in that it gives a physically realistic flow and also provides a unique, lossless, isentropic reference flow. The annular cascade efficiency is then uniquely defined as the ratio of the mixed-out experimental kinetic energy flux to the ideal isentropic kinetic energy flux at the same mean radius static pressure. The mathematical derivation of this method is presented. This new theory has been used to process data obtained from a large, transonic, annular cascade in a blowdown tunnel. A four-hole pyramid probe, mounted on a computer-controlled traverse, has been used to map the passage flowfield downstream of the nozzle guide vanes. Losses calculated by the new method are compared with those calculated from the same data using earlier analysis methods.

1 Introduction

The experimental measurement of blade row efficiency is crucial to the prediction and understanding of loss in modern gas turbines. Denton (1993) provides a thorough survey of loss mechanisms in turbomachines. This reference contains a comprehensive bibliography and reviews the main issues in this field. The present paper presents a fully three-dimensional free vortex theory for the calculation of a unique efficiency from experimental area traverses of the three-dimensional flow field downstream of an annular cascade, and illustrates the use of the new method.

Calculations of the loss or efficiency of turbomachinery components from experimental measurements always assume, either explicitly or implicitly, some ideal, lossless process with which the performance of the real component is compared. Usually this ideal process is defined as taking place between the input and output states of the real process. In a turbine stage, for example, the real work-out can be compared to the ideal work from an isentropic process with the same upstream conditions, mass flow, and downstream pressure. It is usually assumed that there is a unique, uniform, mixed-out, downstream flow state which can be used. In the case of the annular cascade with swirling exit flow, there is no such state.

For cascade tests, there is no work done, and so efficiency is defined in terms of the measured and ideal kinetic energy fluxes leaving the blade row. For two-dimensional turbine cascades, the procedure is well established. In Fig. 1 the uniform upstream flow at plane 1 passes through the cascade blade row, and is measured at the traverse plane $2A$. It is then computationally *mixed out* to a uniform flow at plane 2. On an enthalpy–entropy diagram (Fig. 2) the real process is from 1 to 2 and the ideal isentropic from 1 to $2s$.

The blade row isentropic efficiency can then be defined as

$$\eta = \frac{h_{02} - h_2}{h_{01} - h_{2s}}, \tag{1}$$

and the loss as

$$\zeta = \frac{(h_{01} - h_{02}) + (h_2 - h_{2s})}{h_{02} - h_2}. \tag{2}$$

Usually, there is no net heat transfer from the blade row, and the first term in the numerator of Eq. (2) disappears. Denton (1993) notes that the second term

$$h_2 - h_{2s} \approx T_2(s_2 - s_1) = T_2\Delta s \tag{3}$$

and that, consequently, losses can be analyzed in terms of entropy production.

Various *mixing-out* methods such as mass averaging and continuity averaging have been defined, and these are discussed by Oates (1984); the disadvantage of these is that, for flow in a constant-area duct with no side-wall friction (and uniform total temperature), the mass-averaged total pressure decreases while the continuity-averaged total pressure increases.

Amecke (1970) proposed a way of considering the flow exiting a cascade of linear blades. Using the four independent conservation equations of mass, momentum parallel to the blade row, momentum perpendicular to the blade row, and energy, he considered flow at constant total temperature. Using Taylor series expansions, for a flow of average Mach number in the range of 0.8 to 1.2, he solved these four conservation equations to give averaged, so-called *mixed-out,* values of the Mach number, the flow angle, and the total pressure. From these, the mixed-out values of the density, the two velocity components, and the static pressure may be calculated, such that the mixed-out flow is fully known. This method gives a mixed-out total pressure that remains the same in the case of a constant area duct with no side-wall friction where the flow is at a constant

[1] Present address: School of Mechanical Engineering, University of Bath, Bath, United Kingdom.

Contributed by the International Gas Turbine Institute and presented at the 40th International Gas Turbine and Aeroengine Congress and Exhibition, Houston, Texas, June 5–8, 1995. Manuscript received by the International Gas Turbine Institute February 22, 1995. Paper No. 95-GT-186. Associate Technical Editor: C. J. Russo.

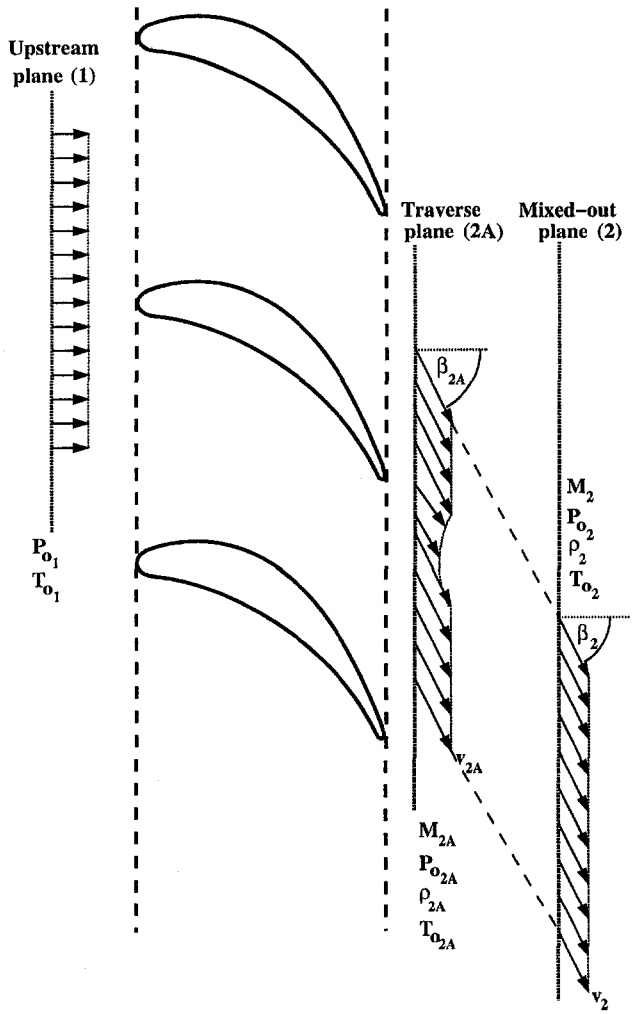

Fig. 1 The theoretical mixing process

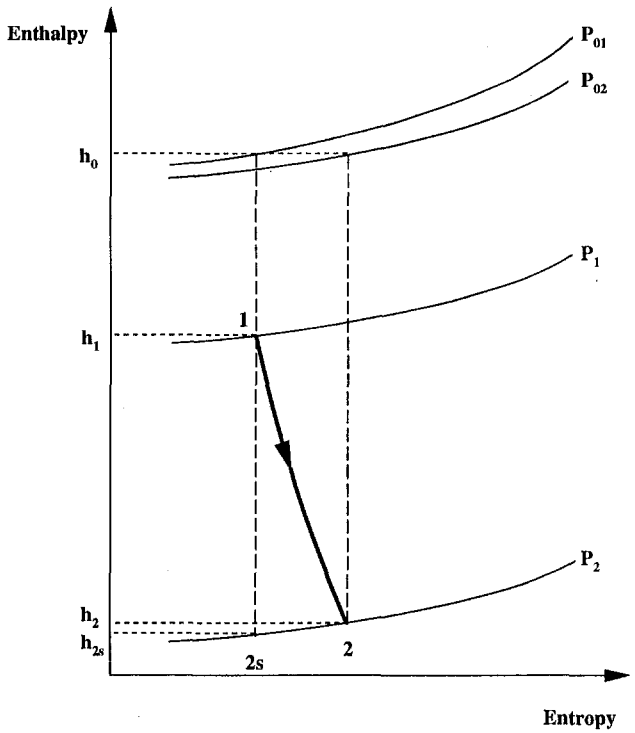

Fig. 2 Enthalpy/entropy diagram for the flow through a blade row

total temperature. Nicholson (1981) and Oldfield et al. (1981) extended Amecke's analysis to the situation in which the total temperature is not constant, to allow for the case of cooled blades.

For the annular nozzle guide vane cascade shown in Fig. 3, the highly swirling exit flow exit flow must have a radial pressure gradient. For realistic flows, there cannot be single static pressure in the exit flow and the radial static pressure distribution must be determined. States 2 and 2*s* in Fig. 2 then must be defined in terms of averaged enthalpies and entropies to enable the use of Eqs. (1), (2), and (3). Equation (3) does not offer a way out of this dilemma, as Δs will depend on the mixed-out state chosen and an average T_2 must be determined. It will be shown that there is a choice of mixed-out states, but that only one has a realistic corresponding isentropic flow state.

Various averaging techniques have been devised for annular cascades. These include mass-averaging and numerical averaging methods. In 1983, an AGARD Advisory Group produced a report on averaging methods in use at that time (Pianko and Wazelt, 1983). Their conclusion was that, in the case of compressor stages, the choice of averaging technique made a significant difference to the efficiency while, in the case of turbine stages, the differences were far less marked. Few of the methods described in this report were applicable to the case of swirling flow. However, in each of those methods that are applicable, constant values of the physical variables are calculated at a single, arbitrary value of the radius. The primary method of the report is from Dzung (1971), in which the average values of the physical variables are calculated at one *swirl-averaged* radius using the four conservation equations and the equation of state. The efficiency may only be calculated from this by assum-

Nomenclature

a = local speed of sound
c_{ax} = axial chord
c_p = specific heat capacity, constant pressure
c_v = specific heat capacity, constant volume
h = specific enthalpy
M = Mach number
$\dot{m}$ = mass flow rate
P = pressure
r = radius
r_{avg} = average radius
r_i = inner radius
r_o = outer radius
s = entropy
T = absolute temperature
$\mathbf{V}$ = velocity vector
v_a = axial velocity
v_r = radial velocity
v_θ = circumferential velocity
w = relative velocity
α = pitch angle
β = yaw angle
γ = ratio of specific heats
ζ = loss
η = efficiency
θ = angle around the annulus
ρ = density
ω = angular velocity

Subscripts

1 = cascade inlet
2 = mixed-out plane
2A = measurement plane
2u = traverse line for linear cascade
0 = stagnation conditions
2s = insentropic flow in mixed-out plane
c = coolant
e = cascade exit
s = constant entropy

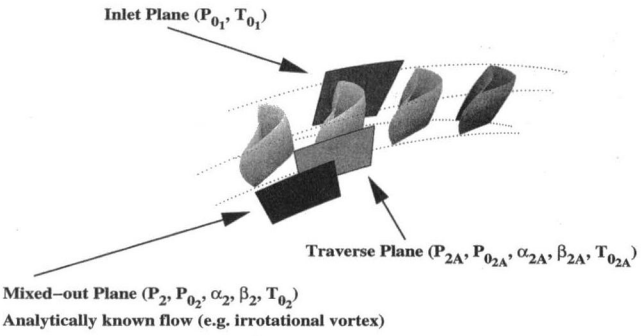

Fig. 3 A three-dimensional representation of the theoretical mixing process behind an annular cascade

ing that the values of the flow variables obtained at this swirl-averaged radius are the same throughout the flowfield. However, Appendix A describes this method in detail and demonstrates that, although this analysis is mathematically realizable, there is no physical basis for it.

Another method for *mixing out* the swirling exit flow is to consider it to be made up of radially spaced layers of two-dimensional flow (Dominy and Harding, 1989). Using the analysis of Amecke (1970), the flow at each radial position is mixed out as a two-dimensional flow. This results in a distribution of values of the flow variables, dependent on the radius. The efficiency may be calculated by dividing the integral of the real enthalpy variation by the integral of the ideal enthalpy variation. Appendix B examines this method in detail and explains that this analysis has no radial mixing, giving a mixed-out flow that is not required to satisfy radial pressure equilibrium, i.e., a flow that is not physically realizable.

It can be argued that in a real turbine stage the nozzle guide vane exit flow does not mix out fully before entering the following turbine blade row. It may even be possible that the turbine can recover some of the kinetic energy that would be lost in the mixing process. Certainly, efficiencies and losses can be calculated at the traversing plane, but they would be specific to that plane. Additionally, h_{2s} in Eqs. (1) and (2) or T_2 in Eq. (3) would have to be defined.

Efficiencies could be defined by using the principle of available work (e.g., Horlock, 1992). This requires reference pressure and temperature, and is more suitable for complete engines than for evaluating component tests, carried out at the correct nondimensional flow parameters, but at different pressure and temperature from the engine.

2 Free Vortex Method for Mixing Out Annular Cascade Flow

This section presents the first analysis to computationally mix out the measured flow exiting an annular blade row to a fully three-dimensional compressible flow. Derived from Crocco's Theorem, this method utilizes all four conservation equations, and the equation of state, to mix the flow out to an irrotational vortex flow, and uses no arbitrary factors.

In mixing out the measured annular cascade flow at the traverse plane $2A$ in Fig. 3 to the mixed out plane 2, the radial swirl velocity distribution at plane 2 must then be chosen. Using the nomenclature in Figs. 1–3, two of the many possible choices are:

- A forced vortex (v_a = constant and $v_\theta \sim r$).
- A free (or irrotational) vortex (v_a = constant and $v_\theta \sim 1/r$).

The requirements of the mixed-out flow are as follows:

(a) The flow must be a physically realizable and three dimensional.
(b) The flow satisfies the four conservation equations and the equation of state.
(c) There is a realistic isentropic flow with which the mixed-out flow may be compared.
(d) The flow has constant total temperature.
(e) The flow is self-sustaining, i.e., there is no shear stress.

The Dzung (1971) method (Appendix A) does not satisfy (a) and (c). The two-dimensional method (Appendix B) does not satisfy (a), (c), or (e) and has no radial mixing. The only self-sustaining, swirling flow in an annulus is the forced vortex. However, Crocco's Theorem states that, for a steady flow,

$$T\nabla s = \nabla h_0 - \mathbf{V} \wedge (\nabla \wedge \mathbf{V}). \tag{4}$$

This means that, if the flow is defined to have constant γ and T_0 (i.e., constant h_0), then the only isentropic flow is one with zero vorticity. A forced vortex has nonzero vorticity, whereas a free vortex in an annulus does have zero vorticity.

Hence, there is no flow that satisfies all the conditions listed above. Consequently, in order that there is an isentropic reference flow, the requirement that the flow be self-sustaining is disregarded.

Free Vortex Equations. Consider the flow through the annular cascade between the traverse measurement plane (subscript $2A$ in Fig. 3) and the mixed-out plane (subscript 2 in Fig. 3). In the mixed-out plane there is a free vortex, i.e.,

$$v_{a_2} = L, \quad v_{\theta_2} = \frac{K}{r} \quad \text{and} \quad v_{r_2} = 0, \tag{5}$$

where K and L are constants. The gas is assumed to be ideal. The mixed-out flow is defined to have constant total temperature T_{0_2} and hence constant total enthalpy h_{0_2}. Furthermore, the flow has zero vorticity and, invoking Crocco's Theorem, is thus homentropic. Consequently there exists a constant E such that

$$E = \frac{\rho_2}{P_2^{1/\gamma}} \tag{6}$$

everywhere in the mixed-out flow.

For an annular flow in radial equilibrium, and with constant axial velocity and no radial velocity,

$$\frac{1}{\rho}\frac{dP}{dr} = \frac{v_\theta^2}{r}. \tag{7}$$

Hence for the mixed-out flow this equation can be integrated to give

$$P_2 = \left[A - \left(\frac{\gamma - 1}{2\gamma}\right)\frac{EK^2}{r^2}\right]^{\gamma/(\gamma-1)}, \tag{8}$$

where A is a constant.

Conservation Equations. The conservation of mass for the flow described in Fig. 3 yields

$$I_A = \int_{r_i}^{r_o}\int_0^{2\pi} \rho_{2A} v_{a_{2A}} r d\theta dr = 2\pi \int_{r_i}^{r_o} \rho_2 v_{a_2} r dr\,; \tag{9}$$

the conservation of linear momentum (axially) yields

$$I_B = \int_{r_i}^{r_o}\int_0^{2\pi} [\rho_{2A} v_{a_{2A}}^2 + P_{2A}] r d\theta dr$$

$$= 2\pi \int_{r_i}^{r_o} [\rho_2 v_{a_2}^2 + P_2] r dr; \tag{10}$$

the conservation of angular momentum yields

$$I_C = \int_{r_i}^{r_o} \int_0^{2\pi} \rho_{2A} v_{a_{2A}} v_{\theta_{2A}} r^2 d\theta dr$$

$$= 2\pi \int_{r_i}^{r_o} \rho_2 v_{a_2} v_{\theta_2} r^2 dr; \quad (11)$$

and the conservation of energy yields

$$\int_{r_i}^{r_o} \int_0^{2\pi} c_{p_{2A}} T_{0_{2A}} \rho_{2A} v_{a_{2A}} r d\theta dr = 2\pi \int_{r_i}^{r_o} c_{p_2} T_{0_2} \rho_2 v_{a_2} r dr. \quad (12)$$

The radial velocity component only appears in the energy equation through the total enthalpy, $c_p T_0 = c_p T + 0.5(v_a^2 + v_\theta^2 + v_r^2)$. The free vortex method is fully three dimensional.

Case 1: Adiabatic and No Film Cooling. In the adiabatic case where there is no film cooling, the conservation of energy gives $h_{01} = h_{02}$. Both c_p and γ are constant everywhere so $T_{0_2} = T_{0_1}$.

Case 2: Nonadiabatic and/or Film Cooling. In the nonadiabatic case $T_{0_{2A}}$ will vary. When film cooling is present the coolant gas may be different to that of the mainstream. For example, foreign gas can be used to simulate a colder, higher density, coolant flow (Teekaram et al., 1989). Then γ_{2A} and $c_{p_{2A}}$ may vary. In either (or both) of these situations, Eqs. (9) and (12) may be normalized by the isentropic sonic conditions $\rho_{2A}^* a_{2A}^*$ (see Amecke, 1970; Nicholson, 1981; and Oldfield et al., 1981) to yield

$$I_Y = \int_{r_i}^{r_o} \int_0^{2\pi} \frac{P_{0_{2A}}}{P_{0_1}} \sqrt{\frac{T_{0_1}}{T_{0_{2A}}}} \Theta_{2A} \cos \beta_{2A} \cos \alpha_{2A} r d\theta dr$$

$$= 2\pi \int_{r_i}^{r_o} \frac{P_{0_2}}{P_{0_1}} \sqrt{\frac{T_{0_1}}{T_{0_2}}} \Theta_2 \cos \beta_2 r dr \quad (13)$$

and I_Z equal to

$$\int_{r_i}^{r_o} \int_0^{2\pi} c_{p_{2A}} \frac{P_{0_{2A}}}{P_{0_1}} \sqrt{\frac{T_{0_{2A}}}{T_{0_1}}} \Theta_{2A} \cos \beta_{2A} \cos \alpha_{2A} r d\theta dr$$

$$= 2\pi \int_{r_i}^{r_o} c_{p_2} \frac{P_{0_2}}{P_{0_1}} \sqrt{\frac{T_{0_2}}{T_{0_1}}} \Theta_2 \cos \beta_2 r dr. \quad (14)$$

In these equations

$$\tan \beta = \frac{v_\theta}{v_a}, \quad \sin \alpha = \frac{v_r}{v} \quad (15)$$

and

$$\Theta = \frac{\rho v}{\rho^* a^*}$$

$$= \sqrt{\frac{2}{\gamma - 1}} \sqrt{\left(\frac{\gamma + 1}{2}\right)^{(\gamma+1)/(\gamma-1)}}$$

$$\times \left(\frac{P}{P_0}\right)^{1/\gamma} \sqrt{1 - \left(\frac{P}{P_0}\right)^{(\gamma-1)/\gamma}} \quad (16)$$

where

$$v = \sqrt{v_\theta^2 + v_a^2 + v_r^2} \quad (17)$$

and

$$v_a = v \cos \beta \cos \alpha, \quad v_r = v \sin \alpha \quad \text{and}$$

$$v_\theta = v \sin \beta \cos \alpha. \quad (18)$$

The double integrals I_Y and I_Z on the left-hand sides of Eqs. (13) and (14) may be evaluated from the experimental data. Note that $c_{p_{2A}}$ can be calculated from the concentration of the foreign gas. The mixed-out total temperature may then be calculated from

$$T_{0_2} = \frac{1}{c_{p_2}} \frac{I_Z}{I_Y} T_{0_1}. \quad (19)$$

Alternatively, T_{0_2} may be calculated directly from the steady flow energy equation

$$-\dot{q} + \dot{m}_1 c_{p_1} T_{0_1} + \dot{m}_c c_{p_c} T_{0_c} = \dot{m}_2 c_{p_2} T_{0_2}, \quad (20)$$

if a value for the net heat transfer rate to the blade $\dot{q}$ is assumed or calculated independently.

Calculating the Mixed-Out Flow. The mixed-out flow conditions are obtained by solving Eqs. (9), (10), and (11). The general analysis presented here is applicable even in the cases of varying temperatures and coolant concentrations. The left-hand side of Eq. (9), I_A, is the mass flow rate through the cascade, which may be determined independently, using an orifice plate. Alternatively, if $T_{0_{2A}}$ is known, I_A may be calculated directly from measurements of P_{02A}, M, α_{2A}, and β_{2A} in the traverse plane, i.e.,

$$I_A = \int_{r_i}^{r_o} \int_0^{2\pi} \frac{\frac{1}{2}\rho_{2A} v_{2A}^2}{P_{0_{2A}}} \frac{2P_{0_{2A}}}{v_{2A}} \cos \beta_{2A} \cos \alpha_{2A} r d\theta dr, \quad (21)$$

using the using isentropic relations:

$$\frac{\frac{1}{2}\rho v^2}{P_0} = \frac{\gamma}{\gamma - 1} \left(\frac{P}{P_0}\right)^{1/\gamma} \left[1 - \left(\frac{P}{P_0}\right)^{(\gamma-1)/\gamma}\right], \quad (22)$$

$$v_{2A} = \mathrm{M} \sqrt{\frac{\gamma R T_0}{1 + \left(\frac{\gamma - 1}{2}\right)\mathrm{M}^2}}, \quad (23)$$

and

$$\mathrm{M} = \sqrt{\frac{2}{\gamma - 1} \left[\left(\frac{P_0}{P}\right)^{(\gamma-1)/\gamma} - 1\right]}. \quad (24)$$

In a similar manner, Eq. (22) can be used together with Eqs. (15) and (17) to evaluate the left-hand sides of Eqs. (10) and (11) (I_B and I_C) from the data obtained in the traverse measurement plane.

Define the integrals J_A and J_B as follows:

$$J_A(X) = 2\pi \int_{r_i}^{r_o} \left[1 - \frac{X^2}{r^2}\right]^{1/(\gamma_2 - 1)} r dr \quad (25)$$

and

$$J_B(X) = 2\pi \int_{r_i}^{r_o} \left[1 - \frac{X^2}{r^2}\right]^{(\gamma_2)/(\gamma_2 - 1)} r dr, \quad (26)$$

where

$$X^2 = \left(\frac{\gamma_2 - 1}{2\gamma_2}\right) \frac{EK^2}{A} \quad (27)$$

and

$$\gamma_2 = \frac{\dot{m}_1 c_{p_1} + \dot{m}_c c_{p_c}}{\dot{m}_1 c_{v_1} + \dot{m}_c c_{v_c}}. \tag{28}$$

This form for X, $J_A(X)$, and $J_B(X)$ is derived from Eqs. (6) and (8), which give P_2 and ρ_2 in terms of A, E, and K. Using Eq. (22), Eqs. (9) to (11) become

$$I_A = ELA^{1/(\gamma_2-1)} J_A(X), \tag{29}$$

$$I_B = LI_A + A^{\gamma_2/(\gamma_2-1)} J_B(X) \tag{30}$$

and

$$I_C = EKLA^{1/(\gamma_2-1)} J_A(X), \tag{31}$$

where I_A, I_B, and I_C are known, having been calculated from the downstream measurements.

Hence, we have three equations (Eqs. (29), (30), and (31)) in four unknowns (A, E, K, and L), together with the parameter X (given by Eq. (27)). A fourth equation is required in order to produce a unique solution. This equation is obtained from knowing the value of T_{0_2} by one of the methods described above. Using Eq. (22) for the mixed-out flow together with Eqs. (5), (6), and (8) yields

$$P_{0_2} = \left[A + \left(\frac{\gamma_2 - 1}{2\gamma_2} \right) EL^2 \right]^{\gamma_2/(\gamma_2-1)}. \tag{32}$$

Hence P_{0_2} is a constant, as would be expected in potential (i.e., irrotational) flow. Evoking the equation of state and Eq. (6) yields

$$E = \frac{P_{0_2}^{(\gamma_2-1)/\gamma_2}}{R_2 T_{0_2}}, \tag{33}$$

where

$$R_2 = \frac{\dot{m}_1 c_{p_1} + \dot{m}_c c_{p_c}}{\dot{m}_1 + \dot{m}_c} - \frac{\dot{m}_1 c_{v_1} + \dot{m}_c c_{v_c}}{\dot{m}_1 + \dot{m}_c}$$

$$= \frac{\dot{m}_1 R_1 + \dot{m}_c R_c}{\dot{m}_1 + \dot{m}_c}. \tag{34}$$

Combining Eqs. (32) and (33) expresses the total temperature in terms of the four unknown constants, i.e.,

$$T_{0_2} = \frac{A + \left(\frac{\gamma_2 - 1}{2\gamma_2} \right) EL^2}{ER_2}. \tag{35}$$

The mixed-out flow is obtained by reducing Eqs. (27), (29), (30), (31), and (35) to the following two equations:

$$X[LX]\frac{I_B}{I_A} J_A(X) = [LX]^2 J_A(X) + \frac{I_C^2}{I_A^2}\left(\frac{\gamma_2 - 1}{2\gamma_2} \right) J_B(X) \tag{36}$$

and

$$[LX]^2 = \left(\frac{2\gamma_2}{\gamma_2 - 1} \right) R_2 T_{0_2} X^2 - \frac{I_C^2}{I_A^2}. \tag{37}$$

These equations may be solved numerically to yield values for L and X. Then the other constants may be evaluated sequentially by

$$K = \frac{I_C}{I_A}, \tag{38}$$

$$E = \frac{I_C}{KLJ_A(X)} \left[\frac{I_B - LI_A}{J_B(X)} \right]^{-(1/\gamma_2)} \tag{39}$$

and

$$A = ER_2 T_{0_2} - \left(\frac{\gamma_2 - 1}{2\gamma_2} \right) EL^2. \tag{40}$$

With this solution, all the constants in the expressions for the velocities, the pressure, the total pressure, and the density are known. Hence, the mixed-out free vortex flow is completely defined.

Discussion. It should be noted that the solution given above includes any effect of coolant (either cold gas or foreign gas) and temperature variation. In order to evaluate I_A, I_B, and I_C, measurements of M, $P_{0_{2A}}$, α_{2A}, and β_{2A} are required. In the case of foreign gas coolant, it is also necessary to measure the concentration of foreign gas at each position in the traverse plane in order to calculate a mass average value of $c_{p_{2A}}$. If T_{0_2} is to be evaluated using Eqs. (9) to (12), then it is necessary to measure $T_{0_{2A}}$ (and the concentration of foreign gas, if used) in addition to M, $P_{0_{2A}}$, α_{2A}, and β_{2A}.

3 Calculation of Ideal Flow and Efficiency

The free vortex mixing method is now used to calculate blade row efficiencies in the simplest case: adiabatic flow with no film cooling. The more complex calculation of efficiency for the nonadiabatic case and the case with foreign-gas film cooling will be discussed in a future paper.

Using the same approach demonstrated in section 2, it is possible to calculate the ideal (isentropic) flowfield (subscript $2s$). For the adiabatic situation with no coolant flow, the following conditions are taken:

1 $P_{0_{2s}} = P_{0_1}$.
2 $T_{0_{2s}} = T_{0_2} = T_{0_1}$.
3 Mass is conserved.
4 Ideal static pressure at average radius = mixed-out real static pressure at average radius. (An alternative would be to make the average static pressures at the inner and outer annulus walls the same.)

The isentropic relations

$$E = \frac{P_{0_2}^{(\gamma-1)/\gamma}}{RT_{0_2}} \quad \text{and} \quad E_s = \frac{P_{0_1}^{(\gamma-1)/\gamma}}{RT_{0_1}}. \tag{41}$$

can be combined, together with condition 2, to yield

$$\frac{E_s}{E} = \left(\frac{P_{0_1}}{P_{0_2}} \right)^{(\gamma-1)/\gamma}. \tag{42}$$

Since the isentropic flow is also an irrotational vortex, Eq. (35), together with condition 2 gives

$$T_{0_{2s}} = \frac{A_s}{E_s R} + \left(\frac{\gamma - 1}{2\gamma} \right) \frac{L_s^2}{R}$$

$$= \frac{A}{ER} + \left(\frac{\gamma - 1}{2\gamma} \right) \frac{L^2}{R} = T_{0_2}. \tag{43}$$

Condition 4 gives

$$A - \left(\frac{\gamma - 1}{2\gamma} \right) \frac{EK^2}{r_{av}^2} = A_s - \left(\frac{\gamma - 1}{2\gamma} \right) \frac{E_s K_s^2}{r_{av}^2}. \tag{44}$$

Table 1 Tunnel conditions for aerodynamic traverse measurements

Case	M_e	Re_e	P_{01} bar	P_e bar
M^-	0.82	1.53×10^6	1.68	1.09
Design	0.96	1.97×10^6	2.00	1.11
M^+	1.11	1.97×10^6	1.95	0.91

The conservation of mass yields

$$I_A = 2\pi \int_{r_i}^{r_o} EL\left[A - \left(\frac{\gamma - 1}{2\gamma}\right)\frac{EK^2}{r^2}\right]^{1/(\gamma-1)} rdr$$

$$= 2\pi \int_{r_i}^{r_o} E_s L_s\left[A_s - \left(\frac{\gamma - 1}{2\gamma}\right)\frac{E_s K_s^2}{r^2}\right]^{1/(\gamma-1)} rdr. \quad (45)$$

Equations (43) to (45) are three equations in three unknowns (A_s, K_s, and L_s), since E_s is determined by Eq. (42). Hence, the ideal flow may be determined by solving these equations numerically. The isentropic efficiency and loss may then be calculated from Eqs. (1) and (2).

4 Efficiency Measurements

Experimental Measurements. Full-area traverses have been performed downstream of an annular cascade of nozzle guide vanes (NGVs) in the Oxford University Blowdown Tunnel (Martinez-Botas et al., 1993, 1995), which can achieve independent variation of Mach number and Reynolds number over a wide range of engine-representative conditions. The tunnel is a transient facility (run times of ~5 s) and a traverse mechanism and four-hole pyramid probe were used to map the NGV exit plane. Details of the probe and traverse mechanism can be found from Main (1994) and Main et al. (1994, 1995).

Measurements were made in two axial positions (relative to the leading edge of the NGV) at each of three tunnel conditions. The three tunnel conditions are given in Table 1. Contours of experimental measurements of normalized total pressure, isentropic Mach number, and swirl and pitch angles at the design condition over an arc equivalent to one and a half vane passages are shown in Fig. 4 (Main et al., 1995).

Efficiency Calculations. The fully three-dimensional free vortex method for calculating the efficiency of a blade row from downstream aerodynamic measurements has been applied to the data presented above. In addition, efficiency calculations have been performed using the two-dimensional and Dzung methods (Appendices A and B). The results from all three methods are shown in Table 2. The absolute accuracy of these measurements is $< \pm 0.6$ percent. When comparing efficiencies at different conditions and with different mixing methods using the same data, the relative accuracy is better ($< \pm 0.2$ percent).

These results demonstrate a slight reduction of the blade row efficiency as the Mach number through the cascade is increased through the transonic region, due to the losses resulting from shock waves.

The other important feature is that the efficiencies obtained from the downstream traverses at 117 percent c_{ax} are greater than those from the measurements at 134 percent c_{ax}. One possible reason for this is the increase in the loss due to the mixing out of the total pressure loss in the boundary layers on the annulus walls. While the mixing operation should ensure that the efficiency remains constant regardless of traverse position, this assumes that the flowfield everywhere is known. However, due to the size of the probe and the influence of the endwall on the probe measurements, measurement of the flow variables near the endwalls was not possible. Consequently, the values of the flow variables were obtained by extrapolation from the measured values near this region, so that the integrals required for the efficiency calculations could be calculated.

In the experiment there is additional loss due to the boundary layer shear on the annulus walls in the 134 percent c_{ax} case that is not accounted for in the 117 percent c_{ax} calculations. Shock activity in the annulus between 117 and 134 percent axial chord

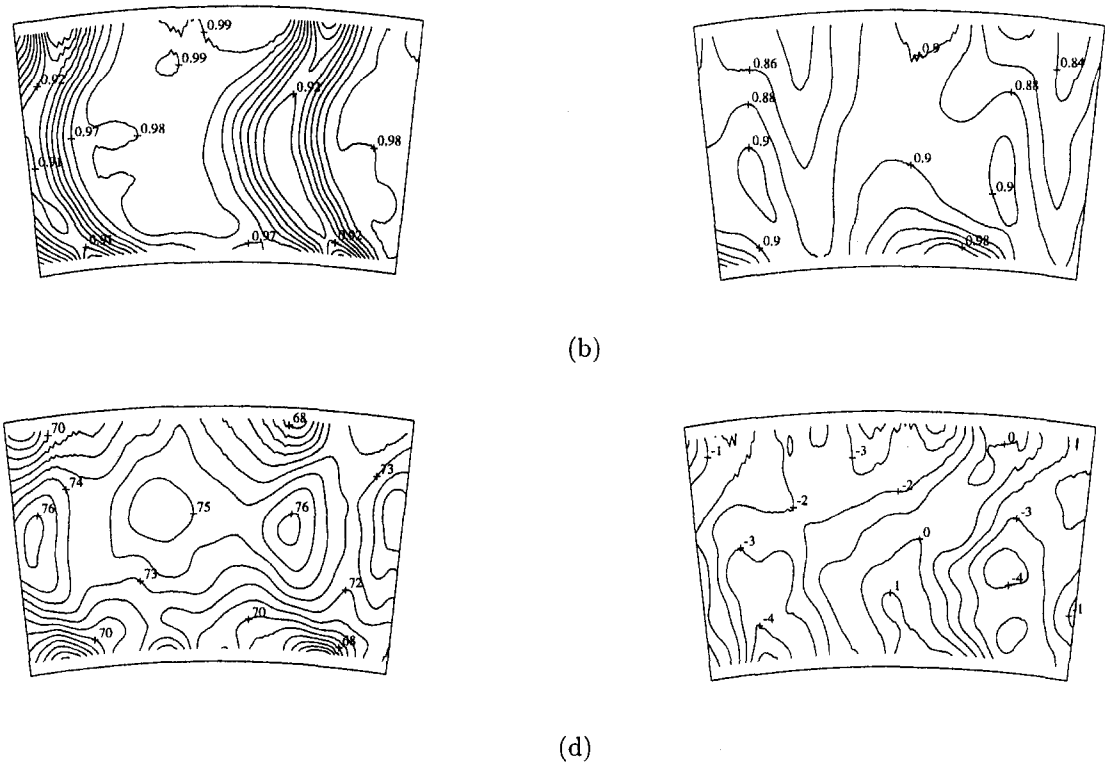

Fig. 4 Contour plots of the main flow variables: (*a*) normalized total pressure, (*b*) isentropic Mach number, (*c*) swirl angle, (*d*) pitch angle

Table 2 Values of the primary efficiency obtained by three methods

Case	c_{ax}	Isentropic efficiencies		
		Free Vortex	2-D	Dzung
M^-	117%	96.11%	96.07%	96.05%
M^-	134%	95.60%	95.53%	95.53%
Design	117%	95.86%	95.74%	95.80%
Design	134%	95.43%	95.44%	95.37%
M^+	117%	95.40%	94.93%	95.35%
M^+	134%	94.65%	94.54%	94.60%

cannot affect the conservation of mass, momentum, and energy equations in the mixing-out process, and so do not affect the final mixed-out loss except by changing the annulus wall boundary layers.

The results from all three methods demonstrate good agreement. With one exception, the maximum difference of the value of efficiency at any condition and position is 0.12 percent.

5 Discussion

The close agreement of the efficiencies calculated by the three methods is, on first glance, surprising, and could suggest that there is no advantage in employing the free vortex method. The agreement is probably due to the particular radial distribution of the circumferentially averaged swirl velocity of the flow studied. This is related to the axial component of the vorticity. Each method mixes down to a particular vorticity distribution: The free vortex method mixes to zero axial vorticity; the Dzung method mixes to a constant circumferential velocity with nonzero vorticity; the two-dimensional method has no radial mixing, and so conserves the circumferentially averaged axial vorticity. The calculated loss depends on how much mixing (and hence entropy generation) is required to get from the measurement plane state to the mixed out vorticity distribution for each method.

The free vortex theory is fully three dimensional and takes into account all three components of the measured exit flow. It has a sound physical basis, and provides a computationally mixed-out state for experimental results, which also has a unique lossless isentropic reference flow. For these fundamental reasons, it is the preferred method, even though the results are not significantly different for the data analyzed so far.

Measurements of efficiency in other flows, with higher levels of axial vorticity, may not yield such agreement between the three methods. Numerical experiments that add different vorticity distributions to the measured flow would clarify this issue.

6 Conclusions

The new free vortex method derived here has been used to mix out downstream area traverse measurements numerically in an annular nozzle guide vane cascade to a unique steady flow state. The blade-row efficiencies calculated by applying this method to area traverse measurements in a blowdown annular cascade have been shown to differ only slightly from those obtained from earlier methods. These earlier methods, the two-dimensional method and the Dzung, swirl-averaged radius method, do yield efficiencies but are inherently flawed in that they mix the flow to states that cannot be physically obtained in annular flow as they do not satisfy radial pressure equilibrium. Additionally, the two-dimensional method uses a series expansion limited to the transonic range of exit flows.

The free vortex method is preferable, as it mixes the measured downstream flowfield into a unique, physically realizable, irrotational, annular flow. The method also computes a fully defined, lossless isentropic flowfield, which must also be in the form of an irrotational vortex. This ideal flow has the same mean-radius static pressure as the mixed-out measured flow. As both flows are completely known, the isentropic efficiency and loss can easily be calculated from the ratio of the mixed-out experimental kinetic energy flux to the ideal isentropic kinetic energy flux using Eqs. (1) and (2). Although the new method is more sophisticated, it does not involve significantly more computational effort, and is not limited to transonic flows.

This new method is not only applicable to annular cascade flow. It can be used to mix the measured flow downstream of compressor or turbine stages when the downstream flow is not purely axial. It is, indeed, applicable to the mixing out of any annular flowfield containing significant amounts of swirl.

Acknowledgments

This work was funded by Rolls Royce plc and the Defence Research Agency. The authors wish to thank both organizations for their support, advice, and assistance in this project and for permission to publish the paper. Thanks also to Mr. C. R. B. Day for his help in processing some of the data.

References

Amecke, J., 1970, "Anwendung der transsonischen Ähnlichkeitsregel auf die Strömung durch ebene Schaufelgitter," *VDI Forschungsheft,* Vol. 540, pp. 16–28.

Denton, J. D., 1993, "Loss Mechanisms in Turbomachines," ASME JOURNAL OF TURBOMACHINERY, Vol. 115, pp. 621–656.

Dominy, R. G., and Harding, S. C., 1989, "An Investigation of Secondary Flows in Nozzle Guide Vanes," AGARD-CP-469, Paper No. 7.

Dzung, L. S., 1971, "Konsistente Mittlewerte in der Theorie der Turbomaschinen für Kompressible Medien," *BBC-Mitt.,* Vol. 58, Pages 485–492.

Horlock, J. H., 1992, *Combined Power Plants: Including Combined Cycle Gas Turbine,* Pergamon, Oxford.

Main, A. J., 1994, "Annular Turbine Cascade Aerodynamics," DPhil thesis, Oxford University.

Main, A. J., Day, C. R. B., Lock, G. D., Oldfield, M. L. G., and Rose, M. G., 1994, "Calibration of a Four-Hole Pyramid Probe for Loss Measurement in a Transonic Cascade Tunnel," presented at the 12th Symposium on Measuring Techniques for Transonic and Supersonic Flow in Cascades and Turbomachines, Prague.

Main, A. J., Day, C. R. B., Lock, G. D., Oldfield, M. L. G., and Rose, M. G., 1995, "Area Traversing Downstream of an Annular Cascade of Nozzle Guide Vanes in a Short-Duration Blowdown Tunnel Using a Four-Hole Pyramid Probe," presented at the 1st European Conference on Turbomachinery: Fluid Dynamic and Thermodynamic Aspects, University Erlangen, Germany, Mar. 1–3.

Martinez-Botas, R. F., Main, A. J., Lock, G. D., and Jones, T. V., 1993, "A Cold Heat Transfer Tunnel for Gas Turbine Research on an Annular Cascade," ASME Paper No. 93-GT-248.

Martinez-Botas, R. F., Lock, G. D., and Jones, T. V., 1995, "Heat Transfer Measurements in an Annular Cascade of Transonic Gas Turbine Blades Using the Transient Liquid Crystal Technique," ASME JOURNAL OF TURBOMACHINERY, Vol. 117, pp. 425–431.

Nicholson, J. H., 1981, "Experimental and Theoretical Studies of the Aerodynamic and Thermal Performance of Modern Gas Turbine Blades," D.Phil. Thesis, Oxford University.

Oates, G. C., 1984, *Aerodynamics of Gas Turbine and Rocket Propulsion,* AIAA Education Series, pp. 185–191.

Oldfield, M. L. G., Schultz, D. L., and Nicholson, J. H., 1981, "Loss Measurements Using a Fast Traverse in an ILPT Transient Cascade," presented at the *Symposium on Measuring Techniques for Transonic and Supersonic Flow in* Cascades and Turbomachines, Lyon, France.

Pianko, M., and Wazelt, F., eds., 1983, "Suitable-Averaging Techniques in Non-uniform Internal Flows," AGARD Advisory Report AGARD-AR-182.

Teekaram, A. J. H., Forth, C. J. P., and Jones, T. V., 1989, "The Use of Foreign Gas to Simulate the Effects of Density Ratios in Film Cooling," ASME JOURNAL OF TURBOMACHINERY, Vol. 111, pp. 57–62.

APPENDIX A

Dzung or Swirl-Averaged Radius Efficiency

The swirl-averaged radius method was devised by Dzung (1971) and is applicable to flows exiting both stator and rotor blade rows. This method uses the four conservation equations for the rotating relative system. The analysis was done for the general case of varying annulus dimensions. In order to facilitate a more direct comparison with the free vortex mixing method, a constant annulus is used to demonstrate the conservation equations.

Conservation of mass:

$$I_A = \int_{r_i}^{r_o}\int_0^{2\pi} \rho_{2A} w_{a_{2A}} r d\theta dr = 2\pi \bar{\rho}_2 \bar{w}_{a_2}. \quad (46)$$

Conservation of linear momentum:

$$I_B = \int_{r_i}^{r_o}\int_0^{2\pi} (\rho_{2A} w_{a_{2A}}^2 + P_{2A}) r d\theta dr$$

$$= 2\pi(\bar{\rho}_2 \bar{w}_{a_2}^2 + \bar{P}_2). \quad (47)$$

Conservation of angular momentum:

$$I_C = \int_{r_i}^{r_o}\int_0^{2\pi} (\omega r + w_{\theta_{2A}}) \rho_{2A} w_{a_{2A}} r^2 d\theta dr$$

$$= 2\pi \bar{r}(\omega \bar{r} + \bar{w}_{\theta_2}) \bar{\rho}_2 \bar{w}_{a_2}. \quad (48)$$

Conservation of energy:

$$I_D = \int_{r_i}^{r_o}\int_0^{2\pi} \left(h_{2A} + \frac{w_{2A}^2}{2} - \frac{(\omega r)^2}{2} \right) \rho_{2A} w_{a_{2A}} r d\theta dr$$

$$= 2\pi \left(\bar{h}_2 + \frac{\bar{w}_2^2}{2} - \frac{(\omega \bar{r})^2}{2} \right) \bar{\rho}_2 \bar{w}_{a_2}. \quad (49)$$

If ω is set to zero and w is replaced by v, then these four equations are also valid for a stationary blade row. These four conservation equations are used together with the calorific equation of state $\bar{h} = \bar{h}(\bar{\rho}, \bar{P})$ to give five equations in six unknowns ($\bar{P}$, $\bar{\rho}$, $\bar{h}$, $\bar{w}_a$, $\bar{w}_\theta$, and $\bar{r}$).

To obtain a solution, Dzung postulates that all terms in Eq. 48 be averaged on a swirl basis. This means that the corresponding terms on both sides of this equation be equated to give:

$$\int_{r_i}^{r_o}\int_0^{2\pi} w_{\theta_{2A}} \rho_{2A} w_{a_{2A}} r^2 d\theta dr = 2\pi \bar{r}\, \bar{w}_{\theta_2} \bar{\rho}_2 \bar{w}_{a_2} \quad (50)$$

and

$$\int_{r_i}^{r_o}\int_0^{2\pi} \omega \rho_{2A} w_{a_{2A}} r^3 d\theta dr = 2\pi \omega \bar{r}^2 \bar{\rho}_2 \bar{w}_{a_2}. \quad (51)$$

This arbitrary method creates the requisite sixth equation to provide a unique solution for the flow exiting a rotor blade row, and calculates the values of the flow variables at this value of the radius.

For the situation of the flow exiting a stator blade row, it is necessary to define a completely nominal value of the radius to mix the flow out at. The obvious value of the radius to chose for this is the average of the inner and outer radii at the measurement position. For this situation, $\bar{c}_{p_2}$, $\bar{\gamma}_2$ and $\bar{R}_2$ may be calculated from the concentration of gases as before and $\bar{T}_{0_2}$ is given by

$$\bar{T}_{0_2} = \frac{I_D}{\bar{c}_{p_2} I_A}. \quad (52)$$

Then these equations reduce to solving

$$I_A \bar{R}_2 \bar{T}_{0_2}$$

$$= I_B \bar{v}_{a_2} - I_A \bar{v}_{a_2}^2 \left[\frac{\bar{\gamma}_2 \bar{R}_2 \bar{T}_{0_2}}{\bar{\gamma}_2 \bar{R}_2 \bar{T}_{0_2} - \frac{\bar{\gamma}_2 - 1}{2}\left(\bar{v}_{a_2}^2 + \frac{I_C^2}{I_A^2 \bar{r}} \right)} \right] \quad (53)$$

for $\bar{v}_{a_2}$. The other variables may be calculated subsequently by

$$\bar{v}_{\theta_2} = \frac{I_C^2}{I_A^2 \bar{r}}, \quad (54)$$

$$\bar{T}_{0_2} = \frac{I_D}{\bar{c}_{p_2} I_A}, \quad (55)$$

$$\bar{P}_2 = \frac{I_B - (I_A \bar{v}_{a_2})}{\pi(r_o^2 - r_i^2)} \quad (56)$$

and

$$\bar{P}_{0_2} = \bar{P}_2 \left(1 + \left(\frac{\bar{\gamma}_2 - 1}{2} \right) \left[\frac{\bar{v}_2^2}{\bar{\gamma}_2 \bar{R}_2 \bar{T}_{0_2} - \left(\frac{\bar{\gamma}_2 - 1}{2} \right) \bar{v}_2^2} \right] \right)^{\bar{\gamma}_2/(\bar{\gamma}_2 - 1)}. \quad (57)$$

To obtain a value of the efficiency using this method, it is necessary to make the unrealistic assumption that the values of the flow variables calculated at the average radius is the value of those variables everywhere in the mixed-out flow. The ideal enthalpy variation is that which corresponds to an isentropic expansion from the state at the inlet to the blade row (P_{0_1}, T_{0_1}) down to the state ($\bar{P}_{0_2}$, $\bar{T}_{0_2}$, $\bar{P}_2$) at the exit to the blade row. Since the flow is the same everywhere, Eq. (1) can be used. For an ideal gas, $h = c_p T$ and for an isentropic process,

$$\frac{T}{T_0} = \left(\frac{P}{P_0} \right)^{(\gamma - 1)/\gamma}. \quad (58)$$

Hence, the primary efficiency for the situation without coolant flow is given by:

$$\eta = \frac{\bar{T}_{0_2} \left[1 - \left(\frac{\bar{P}_2}{\bar{P}_{0_2}} \right)^{(\gamma_2 - 1)/\gamma_2} \right]}{T_{0_1} \left[1 - \left(\frac{\bar{P}_2}{\bar{P}_{0_1}} \right)^{(\gamma_2 - 1)/\gamma_2} \right]}. \quad (59)$$

The Dzung method uses the four conservation equations and the equation of state, as does the free vortex method. However, there are three major differences. Firstly, the irrotational vortex method contains sufficient equations to determine a unique solution, whereas the Dzung method requires an arbitrary assumption to determine a unique solution. Secondly, the Dzung analysis only produces average values of the flow variables at an average radius, whereas the irrotational vortex method is a complete three-dimensional flow. Finally, the Dzung method is not physically attainable, as it is not a constant area mixing calculation.

APPENDIX B

Two-Dimensional Mixing

The mixing method most commonly used for linear cascades is that devised by Amecke (1970). In this, Amecke uses the four conservation equations, but does not allow for temperature variation. Nicholson (1981) and Oldfield et al. (1981) extended this analysis to include temperature variation. The conservation equations and subsequent analysis are detailed below for this latter, more general situation.

Conservation of mass:

$$\frac{1}{t}\int_0^t \rho_{2u} v_{2u} \cos \beta_{2u} du = \rho_2 v_2 \cos \beta_2 = \rho_2^* a_2^* I_A. \quad (60)$$

Conservation of momentum perpendicular to the cascade front:

$$\frac{1}{t}\int_0^t (\rho_{2u} v_{2u}^2 \cos^2 \beta_{2u} + P_{2u})du$$

$$= \rho_2 v_2^2 \cos^2 \beta_2 + P_2 = P_{0_1} I_B. \quad (61)$$

Conservation of momentum parallel to the cascade:

$$\frac{1}{t}\int_0^t \rho_{2u} v_{2u}^2 \cos \beta_{2u} \sin \beta_{2u} du$$

$$= \rho_2 v_2^2 \cos \beta_2 \sin \beta_2 = P_{0_1} I_C. \quad (62)$$

Conservation of energy:

$$\frac{1}{t}\int_0^t T_{0_{2u}} \rho_{2u} v_{2u} \cos \beta_{2u} du = T_{0_2} \rho_2 v_2 \cos \beta_2 = \rho_2^* a_2^* I_D. \quad (63)$$

These equations are solved using a Taylor series expansion in M*, valid for the range of Mach numbers 0.8 to 1.2, to yield

$$M_2^{*^2} = \left(\frac{\gamma + 1}{2}\right)^{2/(\gamma-1)} \left(\frac{I_B}{I_O}\right)^2$$

$$\times \left[\frac{1}{2} - \left(\frac{2}{\gamma + 1}\right)^{2/(\gamma-1)} \left(\frac{I_O}{I_B}\right)^2 + \frac{\gamma + 1}{2\gamma}\left(\frac{I_C}{I_B}\right)^2\right]$$

$$- \sqrt{\frac{1}{4} - \left(\frac{2}{\gamma + 1}\right)^{2/(\gamma-1)} \left(\frac{I_O}{I_B}\right)^2 + \frac{\gamma^2 - 1}{4\gamma^2}\left(\frac{I_C}{I_B}\right)^2}, \quad (64)$$

$$\frac{P_2}{P_{0_2}} = \left[1 - \frac{\gamma - 1}{\gamma + 1} M_2^{*^2}\right]^{\gamma/(\gamma-1)}, \quad (65)$$

$$\sin \beta_2 = \frac{I_C}{I_O} \frac{\Theta_2}{2\left(\frac{\frac{1}{2}\rho_2 v_2^2}{P_{0_2}}\right)} \quad (66)$$

and

$$\frac{P_{0_2}}{P_{0_1}} = \frac{I_O}{\Theta_2 \cos \beta_2}, \quad (67)$$

where Θ_2 and $\frac{1}{2}\rho_2 v_2^2/P_{0_2}$ are given by Eqs. (16) and (22) and I_O is given by

$$I_O = I_A \sqrt{\frac{I_D}{I_A}}. \quad (68)$$

Dominy and Harding (1989), at Cambridge University, applied this method, without any temperature variation, to the situation of flow exiting an annular cascade. The Amecke analysis is applied to each radial position to give average values of the flow variables at each radial position. Then the efficiency may be calculated from

$$\eta_{\text{primary}} = \frac{H_{0_2} - H_2}{H_{0_2} - H_{0_{2s}}} \quad (69)$$

where

$$H = \int h d\dot{m}. \quad (70)$$

It must be noted that this does not generate a true mixed-out flow, as there is no mixing in the radial direction. This analysis also generates an isentropic flow to be compared with the mixed-out flow, which has a radial variation in total pressure with no physical mechanism to account for the variation. The other major difference from the free vortex method is that Amecke's method relies on a Taylor series expansion, resulting in a limited range of validity.

Throughflow Method for Turbomachines Applicable for All Flow Regimes

S. V. Damle

T. Q. Dang

Department of Mechanical and Aerospace Engineering, Syracuse University, Syracuse, NY 13244

D. R. Reddy

Internal Fluid Mechanics Division, NASA Lewis Research Center, Cleveland, OH 44135

A new axisymmetric throughflow method for analyzing and designing turbomachines is proposed. This method utilizes body-force terms to represent blade forces and viscous losses. The resulting equations of motion, which include these body-force terms, are cast in terms of conservative variables and are solved using a finite-volume time-stepping scheme. In the inverse mode, the swirl schedule in the bladed regions (i.e., the radius times the tangential velocity rV_θ) is the primary specified flow quantity, and the corresponding blade shape is sought after. In the analysis mode, the blade geometry is specified and the flow solution is computed. The advantages of this throughflow method compared to the current family of streamline curvature and matrix methods are that the same code can be used for subsonic/transonic/supersonic throughflow velocities, and the proposed method has a shock capturing capability. This method is demonstrated for designing a supersonic throughflow fan stage and a transonic throughflow turbine stage.

Introduction

Throughflow calculation methods are the most useful tools in the design of turbomachines (Cumpsty, 1989). These methods are most commonly used in the design mode. In this mode, the annulus and blade geometries are designed having prescribed the stagnation temperature rise/drop across the blade rows and some estimates of the blade row performance. Another application of these throughflow methods is the prediction of the flow-field given the annulus and blade profiles when used in the analysis mode.

There are two popular approaches for the throughflow calculation: the streamline curvature throughflow method (Smith, 1966) and the matrix throughflow method (Marsh, 1966). The streamline curvature throughflow method solves the so-called radial equilibrium equation, which is cast in terms of primitive variables. The matrix throughflow method solves the so-called principal equation, which is cast in terms of the streamfunction. Neither of these methods can deal with transonic or supersonic throughflow velocities accurately.

In view of recent developments and capabilities of simulating fully three-dimensional flows in multistage turbomachines with robust time-marching algorithms for the Euler/Navier–Stokes equations, the usefulness of integrating them in a design system with a time-marching throughflow method has been stressed. The idea of developing a throughflow method using the body-force field concept to represent blade rows in conjunction with existing time-marching algorithms for the Euler/Navier–Stokes equations was suggested by Miller and Reddy (1991). They proposed an axisymmetric viscous/inviscid "passaged-averaged" throughflow package to be integrated with their three-dimensional design/analysis system for turbomachine blades, called the NASA LERC Turbomachinery Design/Analysis System.

In this paper, a formal theoretical development of a throughflow method based on the conservative-variable formulation is given. This method can be used to design and analyze multistage turbomachines in the axisymmetric limit and is applicable in the subsonic/transonic/supersonic flow regimes. In this paper, expressions are developed for the body-force terms used to model (1) the presence of blade rows, and (2) viscous effects via loss models. Other body-force terms such as those associated with the "passage-averaged" equations can in principle be included in this formulation (Adamczyk, 1985). Finally, the equations derived include a blockage term, which can be used to model blade thickness and viscous effects.

The proposed throughflow method can be used in both the analysis and inverse modes. In the analysis mode, the blade profiles (actually the flow angle or the S2 streamsurface) are prescribed, and the axisymmetric flowfield is computed. In the design mode, the swirl schedule $rV_\theta(r, z)$ is prescribed in the bladed regions, and the blade profiles (actually the flow angle or the S2 streamsurface) are computed. The formulation of the proposed throughflow method is conceptually similar to the one proposed by Spurr (1980).

This paper is arranged as follows. The description of the theory is first presented. Next, the numerical techniques employed to solve the governing equations and the method of implementing boundary conditions are summarized. Results of two design studies, a supersonic throughflow fan stage and a transonic throughflow turbine stage, are then presented. Finally, concluding remarks are given.

Theoretical Background

The use of a distributed body-force field to model turbomachine flowfield was first proposed by Marble (1964). This concept has been used extensively in throughflow methods (Dang and Wang, 1992; Denton, 1978; Hirsch and Warzee, 1976; Marsh, 1966). In a throughflow approximation, the body force can be seen to be composed of two components, one due to the pressure force exerted on the blades, and the other due to viscous and multistage effects. In this section, we develop expressions for the blade and viscous body forces.

Blade and Viscous Body Force Fields. The expression for the blade body-force field is first developed. We begin by noting two important characteristics of the blade body-force field. First, the blade body force must be zero everywhere except in the bladed region. Second, the blade body force must point in the direction normal to the blade surface since it represents entirely the reaction on the fluid of ideal pressure forces on the blades.

Contributed by the International Gas Turbine Institute and presented at the 40th International Gas Turbine and Aeroengine Congress and Exhibition, Houston, Texas, June 5–8, 1995. Manuscript received by the International Gas Turbine Institute March 21, 1995. Paper No. 95-GT-395. Associate Technical Editor: C. J. Russo.

On using these two properties, the blade body-force field denoted by $\mathbf{F}_B$ can be expressed as

$$\mathbf{F}_B \approx B(r, z)\nabla\alpha \tag{1}$$

where the constant α surface defined as $\alpha = \theta - f(r, z)$ denotes the blade surface, and thus $\nabla\alpha$ is a vector normal to the blade surface (Dang and Wang, 1992). Conceptually, the constant α surface corresponds to the S2-surface concept proposed by Wu (1952), and it is approximately the blade surface. In Eq. (1), the function $B(r, z)$ is related to the change in the fluid's angular momentum imparted by the blade rows and/or viscous effects.

Next, an expression for the viscous body force is developed. In general, viscous losses occurring in the blade passage can be included in the body-force term $\mathbf{F}_L$, which can be expressed as

$$\mathbf{F}_L = -L(r, z)\frac{\mathbf{W}}{|\mathbf{W}|} \tag{2}$$

This form models viscous effects as a retarding force, which is opposite in direction to the local velocity direction, assuming that $L(r, z)$ is positive. The function $L(r, z)$ represents the magnitude of the viscous loss and can be varied depending on the degree of sophistication required.

The simplest loss model involves the specification of an entropy field distribution $s(r, z)$ in the flow passage (Bosman and Marsh, 1974). In this case, the function $L(r, z)$ can be related to the entropy field through Crocco's equation (see appendix)

$$L(r, z) = \frac{T}{|\mathbf{W}|}\mathbf{W}\cdot\nabla s \tag{3}$$

where T is the local static temperature. As an example, the entropy field can be constructed as follows. Given the adiabatic stage efficiency, the net mass-averaged entropy rise across the stage can be computed. In addition, if the shapes (i.e., not magnitude) of the radial variation in entropy increase at the outlet of the stage and the axial variation in entropy increase within the blade rows are given, then the entropy field can be constructed.

On using the expression for the viscous body force in Eq. (3), the magnitude of the blade body force $B(r, z)$ can be derived. In the appendix, it is shown that the tangential component of the momentum equation yields an expression for the function B in Eq. (1)

$$B = \mathbf{V}\cdot\nabla(rV_\theta) + rL\frac{W_\theta}{|\mathbf{W}|} \tag{4}$$

In the case of a loss-free turbomachine ($L = 0$), Eq. (4) states that the blade body force is related to the change in the fluid's angular momentum per unit mass along the meridional streamline. In the presence of viscous effects, Eq. (4) indicates that the strength of the blade body force is modified for a given increase in rV_θ. Finally, we note that the blade body force must vanish at the blade trailing edge (i.e., the Kutta condition) and outside the bladed region.

Equations of Motion. The equations to be solved here are the axisymmetric unsteady equations of motion expressed in terms of the conservative variables, e.g.

$$\frac{\partial\mathbf{U}}{\partial t} + \frac{1}{r}\frac{\partial(r\mathbf{E})}{\partial r} + \frac{\partial\mathbf{G}}{\partial z} = \rho b(\mathbf{S} + \mathbf{S}_B + \mathbf{S}_L) \tag{5}$$

In Eq. (5), the conservative-variable vector $\mathbf{U}$, the flux vectors $\mathbf{E}$ and $\mathbf{G}$, and the source vector $\mathbf{S}$ are defined as

$$\mathbf{U} \equiv \begin{bmatrix} b\rho \\ b\rho V_r \\ b\rho V_\theta \\ b\rho V_z \\ b\rho e_t \end{bmatrix} \quad \mathbf{E} \equiv \begin{bmatrix} b\rho V_r \\ b(\rho V_r^2 + p) \\ b\rho V_r V_\theta \\ b\rho V_r V_z \\ b\rho V_r H_o \end{bmatrix}$$

$$\mathbf{G} \equiv \begin{bmatrix} b\rho V_z \\ b\rho V_z V_r \\ b\rho V_z V_\theta \\ b(\rho V_z^2 + p) \\ b\rho V_z H_o \end{bmatrix}$$

$$\mathbf{S} \equiv \begin{bmatrix} 0 \\ \left((p + \rho V_\theta^2)/r + \dfrac{p}{b}\dfrac{\partial b}{\partial r}\right)/\rho \\ -V_r V_\theta/r \\ (p/\rho b)\dfrac{\partial b}{\partial z} \\ 0 \end{bmatrix} \tag{6}$$

In these relations, $b = b(r, z)$ is the blockage factor, which can be used to model blade thickness and takes on the form

$$b(r, z) = 1 - \frac{\theta_p - \theta_s}{2\pi/N_b} \tag{7}$$

where $(\theta_p - \theta_s)$ represents the blade thickness in radian, and N_b is the number of blades. The source vector $\mathbf{S}_B$ models the blade rows as a distributed body-force field. On using Eqs. (1) and (4), the source vector $\mathbf{S}_B$ takes on the form

Nomenclature

b = blockage function (Eq. (7))
B = magnitude of the blade body-force (Eq. (4))
e_t = stagnation internal energy = $\mathbf{V}^2/2 + C_vT$
f = blade wrap angle, rad
$\mathbf{F}_B$ = blade body force (Eq. (1))
$\mathbf{F}_L$ = viscous body force (Eq. (2))
H_o = stagnation enthalpy normalized to RT_{01}
I = rothalpy normalized to RT_{01}
L = loss distribution function (Eq. (3))
p = static pressure normalized to P_{01}
P_0 = stagnation pressure normalized to P_{01}
R = ideal gas constant
(r, θ, z) = cylindrical coordinate system
s = entropy normalized to R
T = temperature normalized to T_{01}
T_0 = stagnation temperature normalized to T_{01}
$\mathbf{V}$ = absolute velocity normalized to $\sqrt{RT_{01}}$
$\mathbf{W}$ = relative velocity normalized to $\sqrt{RT_{01}}$
α = blade surface = $\theta - f(r, z)$, rad
ρ = density normalized to P_{01}/RT_{01}
η_{st} = adiabatic stage efficiency
ω = rotational speed normalized to $\sqrt{RT_{01}}/r_{tip}$

Subscripts

(r, θ, z) = r, θ, and z components
tip = at tip radius of rotor blade
1, 2 = conditions at inlet and outlet
s, p = suction and pressure surfaces

$$\mathbf{S}_B = \begin{bmatrix} 0 \\ \mathbf{F}_B \cdot \hat{e}_r \\ \mathbf{F}_B \cdot \hat{e}_\theta \\ \mathbf{F}_B \cdot \hat{e}_z \\ \mathbf{V} \cdot \nabla H_o \end{bmatrix}$$

$$= \begin{bmatrix} 0 \\ -\left[\mathbf{V} \cdot \nabla(rV_\theta^*) + rL\dfrac{W_\theta}{\mathbf{W}}\right]\dfrac{\partial f}{\partial r} \\ \left[\mathbf{V} \cdot \nabla(rV_\theta^*) + rL\dfrac{W_\theta}{\mathbf{W}}\right]/r \\ -\left[\mathbf{V} \cdot \nabla(rV_\theta^*) + rL\dfrac{W_\theta}{\mathbf{W}}\right]\dfrac{\partial f}{\partial z} \\ \omega[\mathbf{V} \cdot \nabla(rV_\theta^*)] \end{bmatrix} \quad (8)$$

In Eqs. (6) and (8), both V_θ and V_θ^* denotes the tangential velocity component. However, these quantities are to be interpreted as follows. The quantity V_θ is computed using the θ component of the momentum equation (i.e., third component of Eq. (5)). On the other hand, the quantity V_θ^* is prescribed in the inverse mode and is evaluated using the flow-tangency condition in the analysis mode. Clearly, in the inverse mode, when the solution converges, the computed value of rV_θ is identically equal to the prescribed rV_θ^* distribution.

The source vector $\mathbf{S}_L$ models viscous losses as a distributed body-force field. On using Eq. (2), the source vector $\mathbf{S}_L$ takes on the form

$$\mathbf{S}_L = \begin{bmatrix} 0 \\ \mathbf{F}_L \cdot \hat{e}_r \\ \mathbf{F}_L \cdot \hat{e}_\theta \\ \mathbf{F}_L \cdot \hat{e}_z \\ 0 \end{bmatrix} = \begin{bmatrix} 0 \\ -L\dfrac{W_r}{|\mathbf{W}|} \\ -L\dfrac{W_\theta}{|\mathbf{W}|} \\ -L\dfrac{W_z}{|\mathbf{W}|} \\ 0 \end{bmatrix} \quad (9)$$

Finally, we note that in Eq. (5), we have neglected all the perturbation terms that would result from circumferentially averaging the equations of motion (Jennions and Stow, 1985). However, these correlation terms can easily be incorporated into the equations as source terms. Other effects such as correlations associated with the average-passage equation system of Adamczyk (1985) can also be included in the equations as source terms.

Inverse Mode. In the inverse mode, the swirl distribution $rV_\theta^*(r, z)$ is prescribed in the bladed regions. The computed quantities are the blade profiles as described by $f(r, z)$. This quantity is obtained by enforcing the flow-tangency condition along the blade surface,

$$\mathbf{W} \cdot \nabla\alpha = 0 \rightarrow V_r\frac{\partial f}{\partial r} + V_z\frac{\partial f}{\partial z} = \frac{V_\theta^*}{r} - \omega \quad (10)$$

In the inverse mode, f is updated periodically during the time-marching process of the unsteady equations of motion (i.e., Eq. (5)) to steady state. The new value for f is then used to update the source vector $\mathbf{S}_B$ given in Eq. (8). In order to solve this initial-value problem, a boundary condition for f needs to be prescribed. This boundary condition is taken from the prescribed blade stacking position (Dang and Wang, 1992).

We note that the swirl distribution rV_θ^* is a useful quantity to prescribe in the inverse mode because it is directly related to the work input/output of the rotor blades (i.e., from the Euler Turbine Equation). For the stator vanes, the swirl distribution is the most appropriate quantity to prescribe because the function of these vanes is to remove swirl (in a compressor) or add swirl (in a turbine) to the flow.

Analysis Mode. In the analysis mode, the blade geometry function $f(r, z)$ is prescribed and the flow solution is computed. In this mode, the magnitude of the blade body force is adjusted so that the flow-tangency condition is satisfied. This is accomplished by adjusting the blade body force through $rV_\theta^*(r, z)$ in Eq. (8) using the flow-tangency condition along the blade surface. This condition yields the following algebriac relation:

$$\mathbf{W} \cdot \nabla\alpha = 0 \rightarrow rV_\theta^* = r^2\left(\omega + V_r\frac{\partial f}{\partial r} + V_z\frac{\partial f}{\partial z}\right) \quad (11)$$

In the analysis mode, the quantity rV_θ^* is computed periodically during the time-marching process of the unsteady equations of motion (i.e., Eq. (5)) to steady state. The new value for rV_θ^* updated using Eq. (11) is used to update the source vector $\mathbf{S}_B$ given in Eq. (8).

Numerical Technique

The unsteady equation of motion given in Eq. (5) is marched to steady-state using the cell-centered finite-volume Runge–Kutta time-stepping scheme proposed by Jameson et al. (1981). This scheme consists of discretizing the integral form of Eq. (5) using a finite-volume technique, which reduces to a centered-difference approximation on a uniform square grid. Blended nonlinear second- and fourth-difference artificial dissipations are needed to prevent oscillations in the numerical solutions. The resulting system of ODEs is then integrated using the explicit four-stage Runge–Kutta time-stepping scheme. The details of this algorithm are not given here and can be found in Jameson et al. (1981). We note that no acceleration technique was implemented in our computer code.

Boundary Conditions at Inflow Boundary. The usual method of imposing boundary conditions based on the theory of incoming and outgoing characteristic waves is adopted here. If the incoming flow is supersonic, then all five characteristic variables are specified at the inflow boundary. In the present study, we specify the following conditions at the inflow boundary: the stagnation pressure P_{01}, the stagnation temperature T_{01}, the Mach number M_1, the radial velocity V_{r1}, and the tangential velocity $V_{\theta 1}$. If the incoming flow is subsonic, then four flow conditions can be specified at the inflow boundary, and one flow condition is extrapolated from the solutions inside the computational domain. In the present study, we specify P_{01}, T_{01}, V_{r1}, $V_{\theta 1}$, and we extrapolate the static pressure p_1 using a first-order space-extrapolation technique.

Boundary Conditions at Outflow Boundary. The same procedure based on the theory of incoming and outgoing characteristic waves is used at the outflow boundary. If the exit flow is supersonic, then all five characteristic variables must be extrapolated from the solutions inside the computational domain. In the present study, we extrapolate the five conservative variables using a first-order space-extrapolation technique. If the exit flow is subsonic, then one characteristic variable must be specified, and the remaining four characteristic variables must be extrapolated from the solutions inside the computational domain. In the present study, we specify the exit static pressure p_2, and we extrapolate for the remaining four primitive variables.

Boundary Conditions Along Hub and Shroud. The slip condition is imposed along the hub and shroud boundaries. In the cell-centered formulation, the mass, momentum, and energy

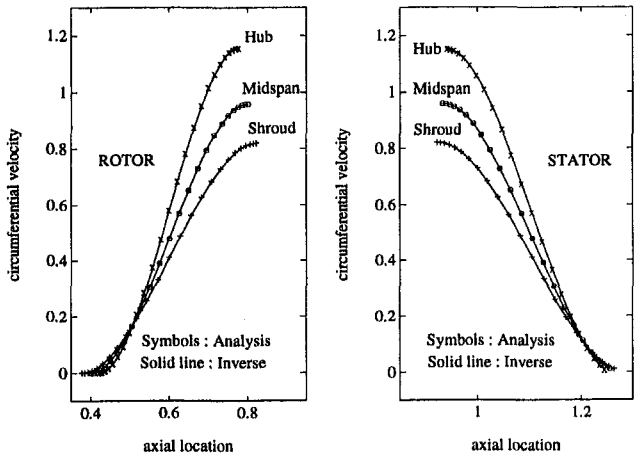

Fig. 1 Comparison of V_θ axial distribution for STF fan stage (normalized to $\sqrt{RT_{01}}$)

fluxes across the cell boundaries coinciding with the hub and shroud are set to zero, and the pressure force acting on these boundaries are extrapolated from the cell-centered values.

Results

The first example presented is the design and analysis of a single-stage Supersonic ThroughFlow (STF) fan. This fan has performance specifications similar to the one designed at NASA Lewis (Schmidt et al., 1987). In this design, the annulus has constant hub and shroud radii, with the hub-to-tip radius ratio of 0.7. In order to keep the blade solidity relatively constant at all radial locations, the blade axial chord is increased in the radial direction. The fan stage has 44 rotor blades and 52 stator blades. The rotor rotational speed ω (normalized to $\sqrt{RT_{01}}/r_{tip}$) is set at 1.575, the overall change in rV_θ across the rotor (normalized to $r_{tip}\sqrt{RT_{01}}$) is set at 0.815, and the adiabatic stage efficiency η_{st} is assumed to be 90 percent (a relatively high number for a STF fan stage). These inputs yield a designed fan pressure ratio of 2.7. The mesh employed in the following calculations has 96 cells in the axial direction and 24 cells in the radial direction.

The solid lines in Fig. 1 show the prescribed axial distributions of the circumferential velocity V_θ in the rotor and stator regions along the hub, midspan, and shroud stations. Both rotor and stator blades are designed using free-vortex distributions. The rotor is designed to increase the fluid angular momentum per unit mass rV_θ from 0 to 0.815, and the stator is designed to deswirl the flow completely (Fig. 2).

In the bladed regions, the prescribed blockage function $b(r, z)$ varies between 85 percent at the hub and 95 percent at the tip. This blockage function is used to model the blockage effect due to blade thickness. No flow blockage was imposed in nonbladed regions. Figure 3 illustrates the prescribed entropy field employed in this calculation. This loss distribution was generated by assuming an adiabatic stage efficiency of 90 percent.

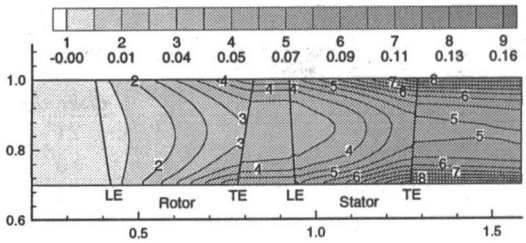

Fig. 3 Prescribed entropy field for STF fan stage (normalized to gas constant R)

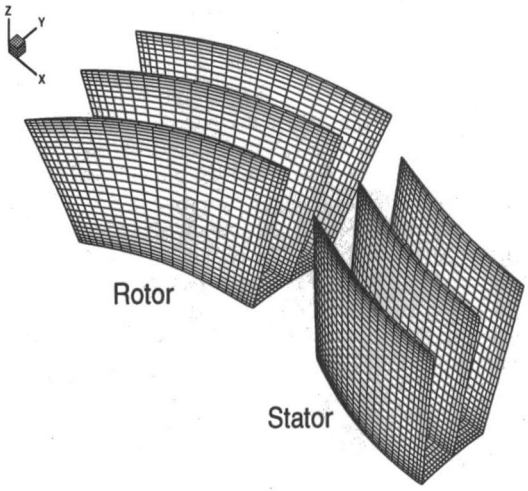

Fig. 4 Designed STF blade geometries

The loss is equally divided in the stator and rotor regions, and is proportioned more at the hub/shroud regions than at the midspan region.

Figure 4 illustrates the blade geometries calculated by the inverse mode. Figure 5 shows the contour plot of the absolute Mach number. This figure shows the presence of a high-Mach-number region in the stator at the hub (maximum Mach number is on the order of 3.3), indicating the potential existence of high shock losses for this design.

For completeness, numerical results of the Mach number, static pressure and blade angle at the leading and trailing edges are tabulated in Table 1 at the hub/midspan/shroud locations.

Next, the analysis mode of the code is used to verify the solutions given by the inverse mode. To carry out this consistency check, the flowfield through the STF fan blade shown in Fig. 4 is analyzed using the analysis mode of the code. This consistency check is carried out to confirm that the designed blade profiles do produce the prescribed swirl distributions. Figure 1 illustrates excellent comparisons of the axial distributions of the circumferential velocity V_θ at the hub/midspan/shroud locations between the prescribed values in the inverse mode (solid lines) and the values predicted by the analysis mode

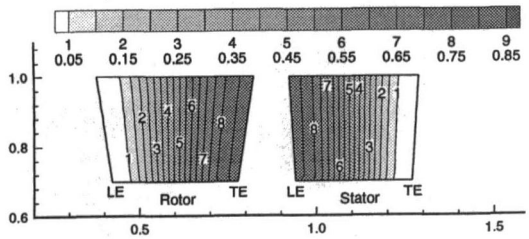

Fig. 2 Prescribed rV_θ for STF fan stage (normalized to $r_{tip}\sqrt{RT_{01}}$)

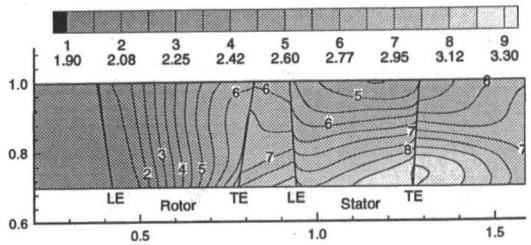

Fig. 5 Absolute Mach number for STF fan stage

Table 1 STF fan stage design results

STF fan		Rotor		Stator	
		LE	TE	LE	TE
Relative/	hub	2.32	2.69	3.21	3.29
Absolute	midspan	2.48	2.67	2.88	2.97
Mach No.	shroud	2.66	2.72	2.72	2.58
Static	hub	0.136	0.070	0.054	0.044
Pressure	midspan	0.133	0.094	0.093	0.078
p/P_{01}	shroud	0.131	0.109	0.115	0.131
Blade	hub	-32	1	27	0
Angle	midspan	-37	-9	23	0
(degree)	shroud	-42	-18	20	0

(symbols). Other results such as the Mach number and the static pressure also show excellent agreements between the results given by the inverse and analysis calculations.

Finally, we present an attempt to improve this STF fan design. This task is carried out to demonstrate the shock-capturing capability of the proposed throughflow method. The present design can be improved in two areas. First, the Mach number contour shown in Fig. 5 suggests the need to reduce the Mach number in the stator along the hub in order to minimize shock losses that are inherent in the blade-to-blade plane. Second, the numerical results show that the average exit static pressure is well below the inlet static pressure. The inlet static pressure (normalized to P_{01}) is 0.13, and the average outlet static pressure is on the order of 0.08. In an actual engine design, the flow is slowed down in the diffuser through a weak oblique shock wave before entering the fan. Then, the bypass flow leaving the fan is expanded through a nozzle to ambient pressure. Hence, the exit static pressure should only be slightly lower than the fan inlet static pressure. To correct for these deficiencies, we propose to modify the hub geometry. Since the flow is supersonic in the stator region, we can improve this design by simply reducing the flow area in the stator region. The reduction in flow area will result in the deceleration of the flow and the accompanied increase in static pressure. We note that since the flow is supersonic, the contouring of the hub geometry must be done carefully to minimize shock losses.

Figures 6 and 7 illustrate comparisons of the absolute Mach number and static pressure about three different designs. Design A is the original design with constant hub and shroud radii. Designs B and C both have constant tip radius. However, the hub radius (normalized to r_{tip}) in Design C is chosen to vary smoothly from 0.7 at the inlet to 0.78 at the outlet, while the hub radius in Design B varies from 0.7 at the inlet to 0.8 at the outlet at a faster rate than Design C. These design calculations were carried out with the same swirl and blockage distributions

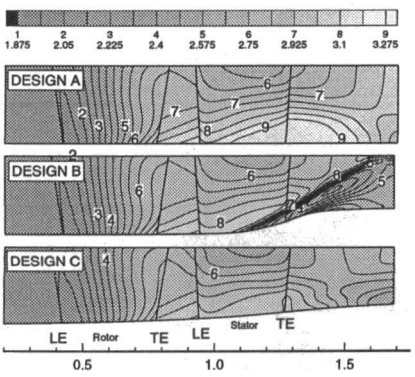

Fig. 6 Comparison of absolute Mach number for STF fan stage

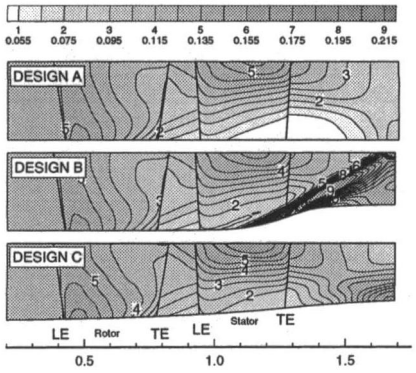

Fig. 7 Comparison of static pressure for STF fan stage (normalized to P_{01})

as in the previous STF fan design study. However, the viscous loss model was removed from these calculations to isolate the effects of entropy rise across shocks that may be present in the new design (i.e., Design B and Design C).

The contour plots shown in Figs. 6 and 7 indicate that the hub geometry in Design C is an improvement over the original design (Design A) in terms of (1) reducing the maximum Mach number in the stator region (maximum Mach number is reduced from 3.3 to 3.0), and (2) increasing the exit static pressure (the average exit static pressure is increased from 0.08 to 0.12). In Design B, although the region of high Mach number is also reduced, a strong oblique shock appears at the stator midchord location along the hub. Figure 8 illustrates a comparison of the entropy field for these three designs. This figure clearly shows the presence of a strong oblique shock in Design B, while Design C has no shock. We note that the magnitude of the entropy rise across this oblique shock is higher than the input viscous loss employed in the previous STF fan design (Fig. 3), indicating that shock losses in Design B reduce the stage efficiency significantly. In fact, the calculated stage stagnation pressure ratio in Design A and Design C is 2.93, while the calculated stage stagnation pressure ratio in Design B is 2.6.

The use of the proposed throughflow method to improve the STF fan-stage design illustrates the unique capability of the method to handle flows with strong shocks. Existing throughflow methods (streamline curvature and matrix methods) would not have been able to predict the oblique shock in Design B. In the design stage of the turbomachine annulus in supersonic-flow applications, the shock-capturing capability is very important since the throughflow method must be able to differentiate between shocked and shock-free design. We note that even though shocks present in axisymetric throughflow solutions may not be accurate since the actual flow is fully three dimensional,

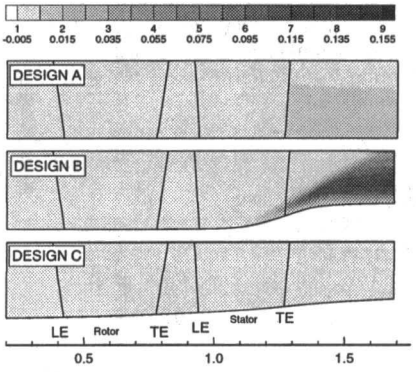

Fig. 8 Comparison of entropy for STF fan stage (normalized to gas constant R)

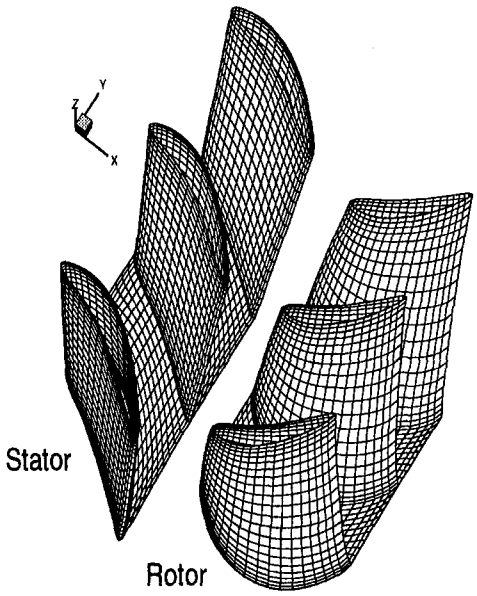

Fig. 9 Designed turbine blade geometries

preventing the appearance of shock waves in throughflow solutions will likely reduce shock losses in the "real" three-dimensional problem.

The second example to be presented is the design of a generic transonic throughflow turbine stage. In this study, the rotor rotational speed ω is set at 0.92, the overall change in rV_θ across the rotor is set at -0.73, and the stage efficiency η_{st} is assumed to be 87 percent. These inputs correspond to a designed stage stagnation pressure ratio of 0.40. The mesh distribution employed in this calculation has 90 cells in the axial direction and 20 cells in the radial direction.

The prescribed swirl distribution for this turbine stage is similar in shape to the one used in the STF fan, although the magnitude is different. In this example, the stator is designed to increase the fluid angular momentum per unit mass rV_θ from 0 to 0.73, and the rotor is designed to convert all the tangential momentum to shaft power. Both stator and rotor blades are designed using free-vortex distributions. The prescribed blockage function $b(r, z)$ varies between 55 percent at the hub and 85 percent at the tip. The loss distribution was generated by assuming an adiabatic stage efficiency of 87 percent. The loss is equally divided in the stator and rotor regions, and is proportioned more at the hub/shrould regions than at the midspan region.

Figure 9 illustrates the blade geometries calculated by the inverse mode. The designed turbine stage has 36 stator blades and 46 rotor blades. Figure 10 shows the contour plot of the

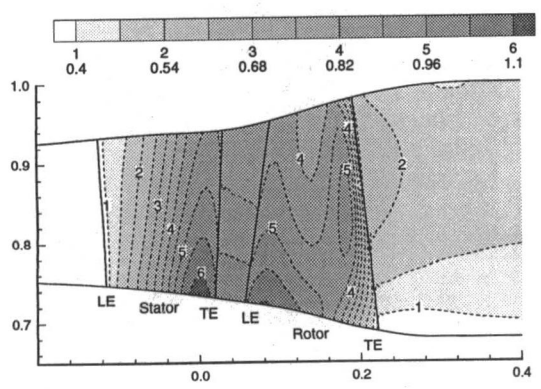

Fig. 10 Absolute Mach number for transonic turbine stage

Table 2 Transonic turbine fan stage design results

Turbine		Stator		Rotor	
		LE	TE	LE	TE
Relative/ Absolute Mach No.	hub	0.31	1.05	1.01	0.74
	midspan	0.33	0.98	0.91	0.98
	shroud	0.36	0.92	0.88	1.11
Static Pressure p/P_{01}	hub	0.917	0.435	0.460	0.344
	midspan	0.912	0.494	0.531	0.299
	shroud	0.913	0.520	0.545	0.295
Blade Angle (degree)	hub	0	62	36.4	-56.8
	midspan	0	56.3	12.5	-49.3
	shroud	0	50.7	-10.6	-52.9

absolute Mach number in the meridional plane. This figure shows the presence of a supersonic-flow region in the intrabladed region along the hub. For completeness, numerical results of the Mach number, static pressure, and blade angle at the blade leading and trailing edges are tabulated in Table 2 at the hub/midspan/shroud locations.

Concluding Remarks

A newly developed throughflow method for turbomachine flowfield design/analysis using modern shock-capturing techniques is proposed. This method utilizes body-force terms to represent the presence of blade rows and viscous losses. Expression for the blade body force is derived from the basic flow equations. To demonstrate the capability of the method to handle viscous effects, a simple viscous loss model is used to represent losses via a body-force term. The method solves the time-dependent equations of motion, cast in terms of the conservative variables and including the body-force terms, using a four-stage Runge–Kutta time-stepping scheme and a finite-volume formulation. The primary advantages of this throughflow method over the conventional streamline curvature and matrix throughflow methods are that (1) transonic and supersonic throughflow velocities can readily be computed, and (2) a shock-capturing technique is available.

The proposed throughflow method can be used in both the inverse and analysis modes. In the analysis mode, the annulus and blade geometries are prescribed, and the method calculates the axisymmetric flowfield. In the inverse mode, both the annulus and the swirl schedules in the bladed regions are prescribed, and the method calculates the corresponding blade geometries and the remaining flow solution. In this paper, design studies of a Supersonic ThroughFlow (STF) fan stage and a transonic throughflow turbine stage are presented. The STF fan-stage design studies include design calculations with strong shocks.

As the purpose of this work is to introduce a newly developed throughflow method for the design/analysis of turbomachine flowfields, several assumptions are used in this initial study. For example, the blade deviation angles are taken to be zero so that the flow angles are assumed to be the same as the blade angles. Also, the loss model employed in this study is relatively rudimentary. With the use of these assumptions, it is clear that the method in its present form is still incomplete to be considered a design tool, and hence *no comparisons* with test data are presented in this paper.

Acknowledgments

This research was supported by the NASA Lewis Research Center under grant NAG3-1585 (Dr. David Miller, Technical Monitor) and the CASE Center at Syracuse University. The

authors would like to thank David Allen and Richard Ziomkowski for their assistance in carrying out the STF-fan calculations.

References

Adamczyk, J. J., 1985, "Model Equation for Simulating Flows in Multistage Turbomachinery," ASME Paper No. 85-GT-226.

Bosman, C., and Marsh, H., 1974, "An Improved Method for Calculating the Flow in Turbo-Machines, Including a Consistent Loss Model," *Journal of Mechanical Engineering Science,* Vol. 16, No. 1, pp. 25–31.

Cumpsty, N. A., 1989, *Compressor Aerodynamics,* Longman Scientific & Technical.

Dang, T. Q., and Wang, T., 1992, "Design of Multi-stage Turbomachinery Blading by the Circulation Method: Actuator Duct Limit," ASME Paper No. 92-GT-286.

Denton, J. D., 1978, "Throughflow Calculations for Transonic Axial Flow Turbines," ASME *Journal of Engineering for Power,* Vol. 100, pp. 212–218.

Hirsch, C., and Warzee, G., 1976, "A Finite-Element Method for Through-Flow Calculations in Turbomachines," ASME *Journal of Fluids Engineering,* Vol. 98, pp. 403–421.

Jameson, A., Schmidt, W., and Turkel, E., 1981, "Numerical Solution of the Euler Equations by Finite Volume Methods Using Runge-Kutta Time-Stepping Schemes," AIAA Paper No. 81-1259.

Jennions, I. K., and Stow, P., 1985, "The Quasi-Three-Dimensional Turbomachinery Blade Design System: Part I—Throughflow Analysis; Part II—Computerized System," ASME *Journal of Engineering for Gas Turbines and Power,* Vol. 107, pp. 301–314.

Lyman, F. A., 1993, "On Conservation of Rothalpy in Turbomachines," ASME JOURNAL OF TURBOMACHINERY, Vol. 115, pp. 520–526.

Marble, F. E., 1964, "Three-Dimensional Flow in Turbomachine," *High Speed Aerodynamics and Jet Propulsion,* Vol. 10, Sec. C, Princeton University Press, pp. 83–166.

Marsh, H., 1966, "A Digital Computer Program for the Through-flow Fluid Mechanics in an Arbitrary Turbomachine Using a Matrix Method," Aeronautical Research Council, R&M 3509.

Miller, D., and Reddy, D. R., 1991, "The Design/Analysis of Flows Through Turbomachinery—A Viscous/Inviscid Approach," AIAA Paper No. 91-2010.

Schmidt, J. F., Royce, M. D., Wood, J. R., and Steinke, R. J., 1987, "Supersonic Through-flow Fan Design," AIAA Paper No. 87–1746.

Smith, L. H., 1966, "The Radial-Equilibrium Equation of Turbomachinery," ASME *Journal of Engineering for Power,* Vol. 88, pp. 1–12.

Spurr, A., 1980, "The Prediction of 3D Transonic Flow in Turbomachinery Using a Combined Throughflow and Blade-to-Blade Time Marching Method," *International Journal of Heat and Fluid Flow,* Vol. 2, No. 4, pp. 189–199.

Wu, C. H., 1952, "A General Theory of Three-Dimensional Flow in Subsonic and Supersonic Turbomachines of Axial, Radial and Mixed-Flow Types," NACA TN 2604.

APPENDIX

Viscous Body Force

The general form of Crocco's equation is

$$-\mathbf{W} \times (\nabla \times \mathbf{V}) = -\nabla I + T\nabla s + \mathbf{F}_B + \mathbf{F}_L$$

Substituting the expressions for the blade and viscous body forces given in Eqs. (1) and (2) into this equation, we have

$$-\mathbf{W} \times (\nabla \times \mathbf{V}) = -\nabla I + T\nabla s + B\nabla\alpha - L\frac{\mathbf{W}}{|\mathbf{W}|}$$

On taking the dot product of $\mathbf{W}$ with this equation, and noting that $\mathbf{W} \cdot \nabla I$ is zero from the conservation law of rothalpy along streamlines (Lyman, 1993), and that $\mathbf{W} \cdot \nabla\alpha$ is zero from the flow tangency condition along the blade surfaces, we obtain

$$L(r, z) = \frac{T}{|\mathbf{W}|}\mathbf{W} \cdot \nabla s$$

We note that since the entropy always increases along the direction of flow, L is always positive as required by the loss model.

Blade Body Force

The momentum equation for steady flow is

$$\rho(\mathbf{V} \cdot \nabla)\mathbf{V} = -\nabla p + \rho\mathbf{F}_B + \rho\mathbf{F}_L$$

On using the expressions for the body force terms given in Eqs. (1) and (2), the θ component of this equation reads, for axisymmetric flows

$$V_\theta V_r + rV_r\frac{\partial V_\theta}{\partial r} + rV_z\frac{\partial V_z}{\partial z} = B - rL\frac{W_\theta}{|\mathbf{W}|}$$

Solving for B yields

$$B(r, z) = \mathbf{V} \cdot \nabla rV_\theta + rL\frac{W_\theta}{|\mathbf{W}|}$$

Outside the bladed region, B vanishes and the equation reduces to

$$\mathbf{V} \cdot \nabla rV_\theta = -rL\frac{V_\theta}{|\mathbf{V}|}$$

In the absence of viscous losses, this equation is a statement of conservation of angular momentum along a streamline. When losses are present, the entropy increases along the direction of flow and the equation shows that the angular momentum decreases in the direction of flow (Bosman and Marsh, 1974).

Finite Volume Scheme With Quadratic Reconstruction on Unstructured Adaptive Meshes Applied to Turbomachinery Flows

M. Delanaye

J. A. Essers

Aerodynamics Group,
Institute of Mechanics and Aeronautics,
The University of Liège,
Liège, Belgium

This paper presents a new finite volume cell-centered scheme for solving the two-dimensional Euler equations. The technique for computing the advective derivatives is based on a high-order Gauss quadrature and an original quadratic reconstruction of the conservative variables for each control volume. A very sensitive detector identifying discontinuity regions switches the scheme to a TVD scheme, and ensures the monotonicity of the solution. The code uses unstructured meshes whose cells are polygons with any number of edges. A mesh adaptation based on cell division is performed in order to increase the resolution of shocks. The accuracy, insensitivity to grid distortions, and shock capturing properties of the scheme are demonstrated for different cascade flow computations.

Introduction

The main advantage of unstructured grids is to provide an efficient tool to mesh geometrically complex domains. Indeed, even for a simple blade row, the use of a one-block structured mesh can be very problematic and can lead to large grid distortions. However, this problem can be partly solved by using the multiblock structured technique, which splits the complex geometry into simpler subdomains that can be meshed individually. The difficulties of this approach lie in the necessity to design sophisticated algorithms to transfer data correctly from one block to another without loosing accuracy.

Another important advantage of unstructured grids is relatively easy adaptation, which is difficult to achieve with the multiblock structured technique. Indeed, we want to obtain a solution offering a high resolution of the complex flow features. Directly creating a mesh to reach this objective without knowing the solution is quite difficult in practice. Fortunately, unstructured grids can be adapted by adding or removing nodes according to some flow characteristics, such as gradients or higher order derivatives.

A drawback of unstructured grids lies in the need for indirect addressing due to the unstructured character of the connectivity between nodes. This does not allow the best use of the architecture of vector computers, and increases the CPU time with respect to structured solvers. Nevertheless, the ability of clustering nodes in regions of interest can dramatically decrease the total number of grid points that would be used by a structured technique to obtain the same resolution.

Unstructured meshes usually tend to be very irregular. For them, accurate schemes are much more difficult to design. Most classical schemes are generally very dependent on the grid quality.

The main aim of this paper is to present a scheme whose accuracy is weakly dependent on grid distortions. It is based on a finite volume cell-centered approach and used to solve the two-dimensional Euler equations. The advective derivatives are discretized with an upwind technique based on Van Leer's flux vector splitting. The advective flux balance is accurately computed using a third-order Gauss quadrature. A Riemann problem is solved at each quadrature point of the cell edges by using the right and left extrapolations of the conservative variables obtained from an original quadratic reconstruction in the control volumes. The resulting scheme is demonstrated to exhibit a spatial second-order accuracy even for very irregular meshes. For such a high-order scheme, the monotonicity of the computed solution is not guaranteed. A special procedure has been developed to ensure a monotone solution by switching to a classical TVD scheme in the vicinity of discontinuities. As we are presently only interested in steady flows, a solution is obtained from a pseudo-unsteady approach with variable time stepping.

An adaptation technique based on mesh enrichment by cell division is applied in order to increase the resolution of discontinuities. For this purpose, the code is implemented to deal with any kind of polygonal cell.

The Finite Volume Scheme

The two-dimensional Euler equations governing time-dependent inviscid and compressible plane flows are written in their differential form as follows:

$$\partial_t \mathbf{s} + \partial_x \mathbf{f} + \partial_y \mathbf{g} = 0 \tag{1}$$

$\mathbf{s}$ is the vector of conservative variables; $\mathbf{f}$ and $\mathbf{g}$ denote the advective fluxes in cartesian coordinates.

The scheme is based on the finite volume cell-centered approach. A set of conservative variables is computed at each node located at the center of gravity of the corresponding cell. The Euler equations are integrated in their conservative form on the control volume S. By using the Gauss theorem, the system (1) becomes:

$$\int_S \partial_t \mathbf{s} dS + \oint_{\partial S} [\mathbf{f} n_x + \mathbf{g} n_y] d(\partial S) = 0 \tag{2}$$

Contributed by the International Gas Turbine Institute and presented at the 40th International Gas Turbine and Aeroengine Congress and Exhibition, Houston, Texas, June 5–8, 1995. Manuscript received by the International Gas Turbine Institute March 2, 1995. Paper No. 95-GT-234. Associate Technical Editor: C. J. Russo.

$\mathbf{n}$ is the outward normal of ∂S. Assuming $\partial_t \mathbf{s}$ spatially constant inside the control volume, we obtain:

$$\frac{d\mathbf{s}_i}{dt} + \frac{1}{S_i} \oint_{\partial S_i} [\mathbf{f} n_x + \mathbf{g} n_y] d(\partial S) = 0 \tag{3}$$

$\mathbf{s}_i$ is the set of conservative variables associated with the control volume S_i, and refers to the variables at the node i.

We do not make any assumption about the shape of the control volume S_i, which can be any polygon with an arbitrary number N_i of edges (Fig. 1). The contour integral in Eq. (3) is computed with the summation of the fluxes through each edge of the control volume:

$$\frac{d\mathbf{s}_i}{dt} + \frac{1}{S_i} \sum_{k=1}^{N_i} \mathbf{f}_n^k = 0 \tag{4}$$

where: $\mathbf{f}_n^k = (\mathbf{f}_k n_x^k + \mathbf{g}_k n_y^k)\delta_k$; δ_k is the length of edge k.

The global accuracy of the scheme depends on the way the flux $\mathbf{f}_n^k$ is computed. This calculation is performed by a numerical integration of the flux functions using the n-point Gauss quadrature:

$$\mathbf{f}_n^k = \delta_k \sum_{j=1}^{n} \omega_j [\mathbf{f}(x_j^k, y_j^k) n_x^k + \mathbf{g}(x_j^k, y_j^k) n_y^k] \tag{5}$$

where (x_j^k, y_j^k) are the coordinates of the Gauss quadrature point j used to evaluate the advective fluxes, ω_j denoting the weight associated with this point. By using n quadrature points, the formula (5) allows the exact integration of polynomials with degree $2n - 1$. We want to reach the second-order spatial accuracy for the advective term of Eq. (2). In other words, if $\mathbf{f}$ and $\mathbf{g}$ were quadratic polynomials of the Cartesian coordinates, we should be able to compute $(1/S_i) \oint_{\partial S_i} [\mathbf{f} n_x + \mathbf{g} n_y] d(\partial S)$ exactly. This is possible only with at least two quadrature points. Hence, on each edge of the mesh, two advective flux evaluations are required to obtain the second-order accuracy. In comparison, the first-order classical finite volume scheme and the TVD schemes based on linear extrapolations use only one quadrature point located at the middle of the edge. It can easily be demonstrated that these schemes are respectively only zeroth-order or first-order accurate on irregular meshes (Essers et al., 1993).

However, as shown by Essers et al. (1993), a scheme using one quadrature point can exhibit the second-order accuracy even on very irregular grids. Nevertheless, this has to be achieved by applying a nonconservative correction to the scheme. In the work presented here, the use of two quadrature points allows us to meet the required accuracy while preserving the full conservativity.

Right and left extrapolations $\mathbf{s}_R$ and $\mathbf{s}_L$ of the conservative variables are computed at the quadrature points on each edge. Advective fluxes are then obtained from flux vector splitting (Van Leer, 1982).

The technique used to compute these extrapolations is sometimes called "reconstruction." In our approach, it is based on a truncated Taylor series expansion around the right and left neighbors of the edge to obtain the right and left extrapolated values at the quadrature points (Fig. 1). For example, $\mathbf{s}_R$ is given by:

$$\mathbf{s}_{R_j}^k = \mathbf{s}_R^k + (\mathbf{r}_j^k - \mathbf{r}_R^k)^T \nabla \mathbf{s}_R^k + \tfrac{1}{2} (\mathbf{r}_j^k - \mathbf{r}_R^k)^T \mathcal{H}_R (\mathbf{r}_j^k - \mathbf{r}_R^k) \tag{6}$$

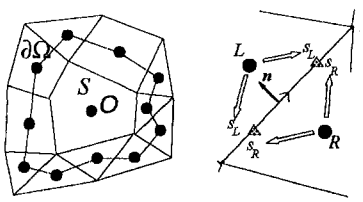

Fig. 1 Control volume, extrapolation

where $\mathbf{r}$ is the position vector, and $\mathcal{H}$ the Hessian matrix of each conservative variable:

$$\mathcal{H} = \begin{bmatrix} \partial_{xx}^2 \mathbf{s} & \partial_{xy}^2 \mathbf{s} \\ \partial_{xy}^2 \mathbf{s} & \partial_{yy}^2 \mathbf{s} \end{bmatrix} \tag{7}$$

It can be proved (see, e.g., Essers et al., 1993) that in order to obtain second-order accuracy for the advective derivatives, the relative error on the flux integral should be third-order at least. That requirement is met by formula (6) if the gradients and the second-order derivatives in the Hessian matrix are respectively computed with a second and a first-order accuracy.

There are different possibilities to choose the stencil for computing the gradients and the Hessian matrix. In the ENO schemes, the stencil is adaptive (Vankeirsbilck, 1993). The nodes supporting the reconstruction are chosen at each iteration in regions with smooth variations in order to maintain the monotonic behavior of the numerical solution. The main disadvantage of this method is the high CPU requirements. For that reason, our reconstruction is based on a fixed stencil. The numerical gradient and Hessian matrix are obtained by linear combinations of nodal values. The constant coefficients of these discretizations are computed in a preprocessing step. They are stored in memory and used during the whole calculation. However, that storage requires a large amount of memory. Indeed, five double-precision real numbers times the number of neighbors have to be stored for each control volume. However, thanks to the present trend to produce computers with increasing capacity, that requirement should not be considered as a major problem.

Computation of the Hessian Matrix

For unstructured meshes, the computation of second-order derivatives with the required accuracy is not an easy task. Our procedure is based on the least-squares technique. Let us consider a function f known at the nodes of the mesh. We want to reconstruct a quadratic piecewise approximation in each control volume from:

$$f_{\text{rec}} = f_O + (\mathbf{r} - \mathbf{r}_O)^T \nabla f_O + \tfrac{1}{2} (\mathbf{r} - \mathbf{r}_O)^T \mathcal{H}_O (\mathbf{r} - \mathbf{r}_O) \tag{8}$$

We expect this approximation to be the best possible in the least-squares sense, i.e., we wish to minimize the distance between f_{rec} and f at the neighbors of node O. The stencil of the reconstruction then includes all the neighbors of O, i.e., all nodes whose control volume has at least one edge or one vertex in common with the one of O (Fig. 1).

These conditions can be expressed by a system of N_Ω equations, where N_Ω is the number of neighbors of O. This technique is formally similar with that presented by Barth (1993). However, Barth minimizes the distance between f_{rec} and a continuous quadratic interpolation of f on each control volume. This condition is applied at each quadrature point of the control volume. The resulting number of equations obtained with that method is two times larger when compared with our method.

The unknowns of the system are the first and second derivatives appearing in Eq. (8). Therefore, a $N_\Omega \times 5$ linear system has to be solved for each control volume:

$$\begin{bmatrix} \Delta x_1 & \Delta y_1 \tfrac{1}{2} \Delta x_1^2 \tfrac{1}{2} \Delta y_1^2 & \Delta x_1 \Delta y_1 \\ \vdots & & \\ \Delta x_{N_\Omega} & \cdots & \Delta x_{N_\Omega} \Delta y_{N_\Omega} \end{bmatrix} \begin{bmatrix} \partial_x f_O \\ \partial_y f_O \\ \partial_{xx}^2 f_O \\ \partial_{yy}^2 f_O \\ \partial_{xy}^2 f_O \end{bmatrix} = \begin{bmatrix} \Delta f_1 \\ \vdots \\ \Delta f_{N_\Omega} \end{bmatrix} \tag{9}$$

with $\Delta_i \odot = \odot_i - \odot_O$.

This overdetermined system is approximately solved by using the least-squares approach. The numerical approximations of first and second-order derivatives obtained by that technique can be proved to meet the accuracy requirements, i.e., $\mathcal{O}(h^2)$ and $\mathcal{O}(h)$, respectively. We could use this procedure to reconstruct the conservative variables in Eq. (6). However, from our experience, the resulting scheme was not found to be very robust for strongly distorted meshes. Up to now, that difficulty remains unexplained. Notice that most classical linear stability analyses, which are only applicable to regular grids, cannot be used for that purpose. For that reason, we actually used another procedure described below to compute the first derivatives. Nevertheless, Eq. (9) provides an accurate estimate of the second-order derivatives to be used in Eq. (6), which is schematically denoted as follows:

$$\begin{bmatrix} \partial^2_{xx} f_O \\ \partial^2_{yy} f_O \\ \partial^2_{xy} f_O \end{bmatrix} \simeq \mathbf{D}_2[f_O \quad f_1 \quad \ldots \quad f_{N_\Omega}]^T \tag{10}$$

Computation of the Gradients

A well-known method to compute the gradients, which is widely used by many researchers, is to apply the Gauss theorem on a contour $\partial\Omega$ defined by the neighbors of the control volume (Fig. 1):

$$\nabla f = \frac{1}{\Omega} \oint_{\partial\Omega} f \mathbf{n} d\partial\Omega \tag{11}$$

However, a careful accuracy investigation proves that such a numerical gradient is only first-order. By using a Taylor series expansion of f around node O in Eq. (11), it can be demonstrated that the second-order accuracy is obtained if and only if O is the center of gravity of Ω, which only occurs for regular meshes. The integral in Eq. (11) is discretized by a summation of the contributions of the linear segments of $\partial\Omega$ obtained from the trapezoidal rule. It can be expressed by the following linear combination:

$$\nabla f = \mathbf{D}_1[f_O \quad f_1 \quad \ldots \quad f_{N_\Omega}]^T \tag{12}$$

Expanding f around node O in Eq. (12) leads to the truncation error $\mathbf{E}$:

$$\mathbf{E} = \mathbf{Er}[\partial^2_{xx} f_O \quad \partial^2_{yy} f_O \quad \partial^2_{xy} f_O]^T \tag{13}$$

where $\mathbf{Er}$ is a 2×3 matrix containing constant coefficients of order h. By using Eq. (10) to estimate the second order derivatives, second-order accuracy in the evaluation of the gradients can be recovered by subtracting $\mathbf{E}$ from the right-hand side of formula (12), leading to:

$$\nabla f = (\mathbf{D}_1 - \mathbf{ErD}_2)[f_O \quad f_1 \quad \ldots \quad f_{N_\Omega}]^T \tag{14}$$

Monotonicity

The scheme as presented above cannot be used directly to solve problems with shocks or contact discontinuities. Because of its high accuracy, oscillations occur in the vicinity of these regions. To overcome this type of problem, much work has been done to get monotone higher order schemes. Two main important classes of schemes were developed. The first one corresponds to the so-called "TVD schemes (Harten, 1983)" based on the use of limiters. The second includes the "ENO schemes (Shu and Osher, 1988)." The advantage of the latter is the possibility to get high-order accuracy very close to shocks. ENO schemes are based on an adaptive stencil, which is quite time consuming. The basic characteristic of TVD schemes is to go progressively from a "linear reconstruction scheme" to a classical "constant reconstruction scheme" by using a limiter. Their advantage lies in a low cost thanks to a fixed stencil. They do, however, lead to a local reduction of the accuracy. Furthermore, the limiters were mostly designed from one-dimensional concepts.

Like ENO schemes, we keep the quadratic reconstruction scheme unmodified as close as possible to discontinuities, where we move to a classical TVD scheme with linear reconstruction. To do so, we need a tool to detect shocks, and contact discontinuities, and regions where numerical oscillations occur for any reason. That tool is a straightforward generalization to unstructured meshes of a detector proposed by Essers et al. (1995). It is based on first and second-order derivatives of the static pressure and Mach number. Indeed, the static pressure seems to be the most sensitive variable to detect shocks, while the Mach number is well suited for contact discontinuities. The two following quantities are computed at each node:

$$d_1 = \frac{k_1}{\Delta p} \max \|\mathbf{d}_k \nabla f_k\| \tag{15}$$

$$d_2 = \frac{k_2 L}{\Delta p} \max \frac{1}{\|\mathbf{d}_k\|} \|\mathbf{d}_k^T \mathcal{H}_k(f) \mathbf{d}_k\| \tag{16}$$

$\forall k = 1, \ldots, N_\Omega$, where $\mathbf{d}_k = \mathbf{r}_k - \mathbf{r}_O$. f denotes the Mach number or the static pressure.

The coefficients k_1, k_2 are generally chosen close to 0.5, d_1 and d_2 are normalized by a characteristic variation of pressure Δp and variation length L. The final detector σ dependent on d_1 and d_2 is given by:

$$\sigma = 1 - \min [\max^2 (d_1, d_2), 1] \tag{17}$$

If d_1, d_2 are larger than 1, σ becomes close to 0, and the region with sharp gradients or oscillations is detected. On the other hand, when d_1, d_2 are very small, the region is considered to be "smooth," and σ is close to 1. Finally, σ is made discrete by using the formula below:

$$\begin{aligned} &\text{if } \sigma < \alpha \Rightarrow \sigma = 0 \\ &\text{if } \sigma \geq \alpha \Rightarrow \sigma = 1 \end{aligned} \tag{18}$$

where α is a user-given constant (typically, $\alpha \simeq 0.5$) The discrete value of σ and the TVD limiter ϕ are used as follows in the reconstruction of the conservative variables:

$$\mathbf{s}^k_{R_j} = \mathbf{s}^k_R + \phi'(\mathbf{r}^k_j - \mathbf{r}^k_R)^T \nabla^{1st} \mathbf{s}^k_R + \sigma_R[-(\mathbf{r}^k_j - \mathbf{r}^k_R)^T \mathbf{Er}_R \nabla^2 \mathbf{s}^k_R + \tfrac{1}{2}(\mathbf{r}^k_j - \mathbf{r}^k_R)^T \mathcal{H}_R(\mathbf{r}^k_j - \mathbf{r}^k_R)]$$

∇^{1st} is a symbolic notation for the numerical gradient given by Eq. (11), ∇^2 is the vector of second derivatives (Eq. (10)). The same formula holds for $\mathbf{s}_L$. The modified limiter ϕ' is given by:

$$\phi' = \phi(1 - \sigma) + \sigma \tag{19}$$

In the regions of shocks, $\sigma = 0$ and ϕ' can be any classical TVD limiter, while in smooth regions $\sigma = 1$ and the fully quadratic scheme is used ($\phi' = 1$). In most of our calculations, we use the limiter developed by Van Albada et al. (1982) except if stated otherwise.

Adaptive Refinement

One of the main advantage of unstructured meshes is the easy adaptation to local flow features. The scheme presented in this paper is very accurate in smooth regions, but near shocks, higher resolution could be obtained using an adaptation of the mesh. There are different ways to adapt a mesh. The first one is to relocalize the nodes without increasing their number. This method is essentially used in structured meshes (see, e.g., Ingram et al., 1993). The second one increases the number of nodes by dividing existing cells (Kallinderis and Baron, 1989) (mesh enrichment). This procedure is fast and quite easy to

implement, but can lead to very unsmooth meshes. The last one, which is the most complicated, consists in a complete remeshing of the domain as suggested by Peraire et al. (1987). Among these methods, we chose the mesh enrichment approach for the following reasons: Our scheme is designed for completely arbitrary shape of control volume, and our high-order reconstruction does not loose accuracy on strongly distorted meshes. To adapt the mesh, we need a tool to select the cells to be refined. Therefore, the detector σ defined above is also used to flag the cells. Because our meshes are mostly made of triangles or/and quadrangles, we only treat the refinement procedure for these elements. Triangles and quadrangles are divided into four triangles and four quadrangles, respectively, as shown in Fig. 2. Difficulties occur when we have to refine a mesh that has already been refined. In that case, triangles or quadrangles containing more than three or four edges, respectively, are usually obtained. The technique to refine a quadrangle with more than four edges is the following:

- Select all edges to be divided. An edge is marked when at least one of its neighbors has to be divided.
- Create the new vertices located at the center of each marked edge.
- For each cell to be refined, create a list of all the vertices belonging to it (old and new ones).
- In the list of vertices, select the ones corresponding to the corners of the element, and use them to define a bilinear (linear) transformation from a unit square (triangle) (Fig. 3).
- By using this transformation, it is easy to select the closest vertices (new or old) to the center of each edge of the unit square. These are used to refine the element.
- Remove all the new vertices that are not used to divide a cell.

A similar technique is applied to the triangles. Generally three or four adaptations are sufficient to get a nice solution. This method is quite crude. A better job can be done by refining directionally according to the values of some gradients, which reduces the number of cells. Research is presently being carried out to modify the adaptation procedure in that way.

Time Integration

A pseudo-time-dependent approach with variable time stepping is used to compute updated values of the conservative variables at time level $(n + 1)$ from their known level (n). Time integration of Eq. (3) is performed with a multistep Runge–Kutta scheme. We essentially use three or four-step schemes that are only first-order accurate in time and introduce purely transient additional dissipative effects that do not influence the steady solution. The coefficients and number of steps are chosen from a trade-off between the maximum allowable CFL number and the strength of transient dissipative effects.

Boundary Conditions

The boundary conditions are imposed via a weak formulation based on the modification of the fluxes through boundary edges.

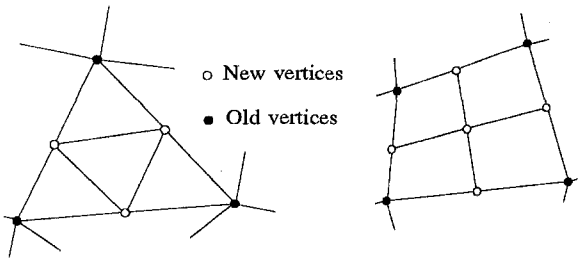

Fig. 2 Cell division

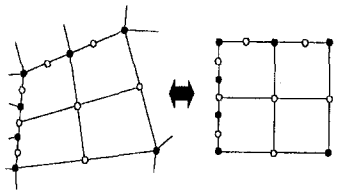

Fig. 3 Cell transformation

For solid walls, the normal velocity is set to zero and the momentum fluxes only depend on the pressure, which is extrapolated from the interior nodes. At subsonic inflow boundaries, the total pressure, the total temperature, and the flow angle are prescribed, while the pressure is imposed for subsonic outflow boundaries. The periodicity between boundaries is achieved by using dummy nodes outside the computational domain to reconstruct the solution in boundary control volumes.

Results

The first result presented is the computation of the Ringleb's flow. This test case was proposed by Chiocchia (1985) to validate Euler codes. The solution is analytically obtained by a hodograph transformation. It depends on two parameters: the inverse of the streamline function (k) and the velocity (q). By choosing two streamlines, and regarding them as rigid walls, we can simulate the flow in a curved duct. The constant velocity lines are circles. The exact solution is symmetric with respect to the geometric axis (Fig. 4(a)). This test case is very interesting to show the effect of the numerical dissipation of a scheme on the solution. Indeed, the dissipation will create an asymmetric solution. We choose a geometry defined from the following values:

$$k = 0.8 \quad \text{inner wall}$$
$$k = 0.4 \quad \text{outer wall}$$
$$q = 0.3 \quad \text{inflow and outflow boundaries}$$

The inflow Mach number is equal to 0.30273. The Mach number reaches its maximum value 0.8567 at the intersection of the inner wall with the axis of symmetry. The mesh (Fig. 4(b)) used for this computation is rather coarse (616 nodes) in order to emphasize the numerical dissipative effects. Figures 4(c) and 4(e), respectively, show the computed Mach isolines obtained with the linear reconstruction and the quadratic reconstruction schemes. The former scheme leads to an asymmetric solution near the inner wall. On the other hand, the quadratic reconstruction performs very well. Indeed, its numerical solution is almost symmetric and identical with the exact one. The effect of the numerical dissipation of the schemes clearly appears on the total pressure isolines (Fig. 4(d) and 4(f)). For both schemes, the numerical dissipation obviously occurs in the region with the largest solution variations (inner wall). For the linear reconstruction scheme, the dissipation is larger (1.5 percent of total pressure loss) and also takes place farther downstream. By using the quadratic reconstruction scheme, the maximum total pressure loss is reduced by a factor of 3 (0.5 percent). Notice that the accuracy of the inner wall Mach number distribution computed with the quadratic scheme is very good despite the relatively coarse mesh used (Fig. 4(g)).

The second test case is the computation of the flow in the supercritical compressor cascade of Sanz (1984). This shockless profile has been designed by this author with a hodograph-related method coupled with a boundary layer correction. The main characteristics of the flow are the following:

$$\text{inlet Mach number:} \quad M_1 = 0.711$$
$$\text{inlet flow angle:} \quad \alpha_1 = 30.81 \text{ deg}$$
$$\text{exit Mach number:} \quad M_2 = 0.544$$

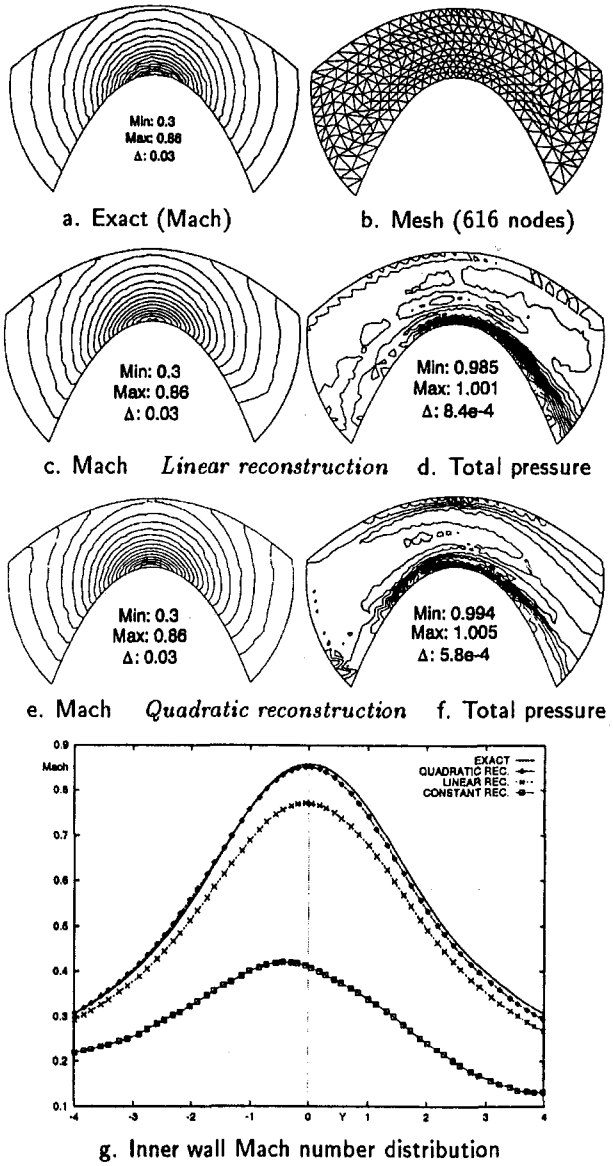

Fig. 4 Ringleb's flow

The main difficulty of this test case is to compute the deceleration on the suction side without numerically generating a shock. Many authors (see, e.g., Denton, 1983) have found an irregular Mach number distribution based on the geometry proposed by Sanz. A smooth Mach number distribution is, however, obtained with a slightly modified geometry generated by the inverse method of Léonard and Van den Braembussche (1992a) in the region of the suction side plateau. Figure 5(b) shows the very good agreement between the computed isentropic Mach number and the exact solution. No shock appears on the suction side during the deceleration. However, a small deviation with the exact solution takes place at the trailing edge. Indeed, the geometry (Denton et al., 1990) is open, and no particular attention has been paid to the trailing edge discretization.

The supersonic staggered wedge cascade is an analytical test case that was proposed by Denton et al. (1990) to test Euler codes. The inlet and outlet conditions are:

$$\text{inlet Mach number:} \quad M_1 = 1.6$$

$$\text{inlet flow angle:} \quad \alpha_1 = 60 \text{ deg}$$

$$\text{outlet static to inlet total pressure:} \quad p_2/p_{o1} = 0.3536$$

An advancing front method was used to create the initial mesh containing 1774 cells. The final mesh (Fig. 6(a)) (9874 cells) has been obtained after three adaptations based on the pressure detector. The new cells created are clustered near the shocks (Fig. 6(a)). To limit the computational cost, the adaptation has been turned off at the end of the domain, as suggested by Holmes (1989). The minmod limiter has been applied in Eq. (19). Notice in Fig. 6(a) that the control volumes where the detector σ did automatically switch to zero, are actually located near shocks. The evolution of the isentropic Mach number is presented in Fig. 6(b)). A close agreement is found with the reference solution of Holmes (1989). The shock on the suction side is monotone, while a small wiggle appears in the pressure side shock. As in Holmes' results, the trailing shock impinging on the corner is fully absorbed by the expansion arising from this corner. A small deviation with the exact solution occurs after the expansion.

The last test case is a very high turning blade ($\theta = 80$ deg) proposed by Sieverding (1990). The computation of the flow around this transonic turbine blade is well known to be difficult, and shows the limitation of inviscid calculations to predict realistic phenomena. Indeed, the main difficulty lies in the description of the flow near the rounded trailing edge (Fig. 7(c)), where an inviscid computation leads to severe unphysical accelerations and decelerations. In practice, the viscous effects cause the flow to detach from the wall and to create a wake. In order to overcome that difficulty, the wall impermeability boundary condition is not imposed to some edges of the trailing edge, which allows the flow to detach from the blade, thus creating an artificial wake (Léonard and Van den Braembussche, 1992b). The computed flow corresponds to the following inlet and outlet conditions:

$$\text{inlet flow angle:} \quad \alpha_1 = 1.9 \text{ deg}$$

$$\text{outlet isentropic Mach number:} \quad M_2 = 1.0$$

The grid for computing this test case demonstrates the high flexibility of unstructured meshes (Fig. 7(c)). It consists of a

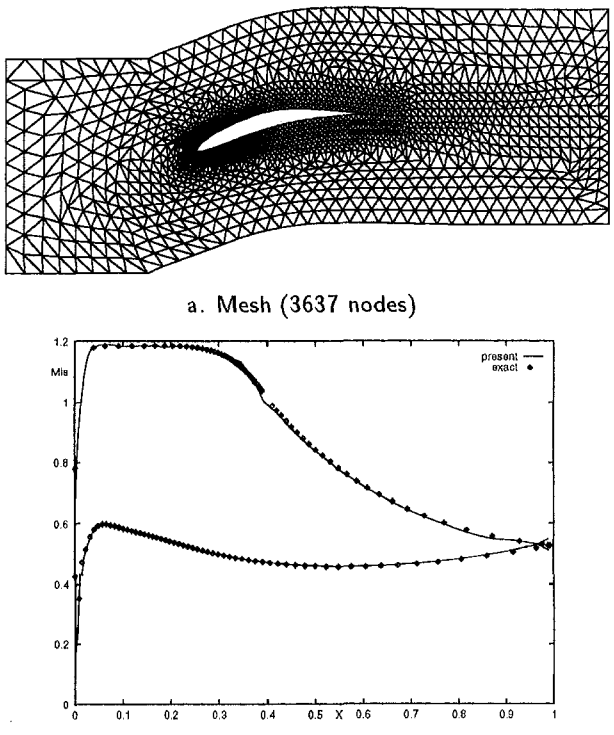

Fig. 5 Sanz supercritical compressor cascade

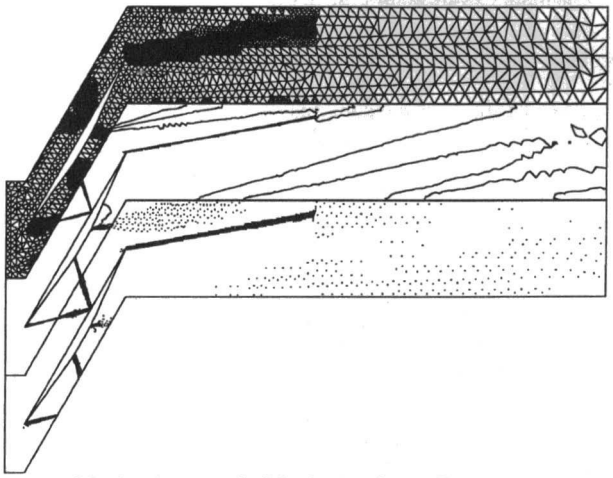

a. Mesh - Isentropic Mach number - Detector

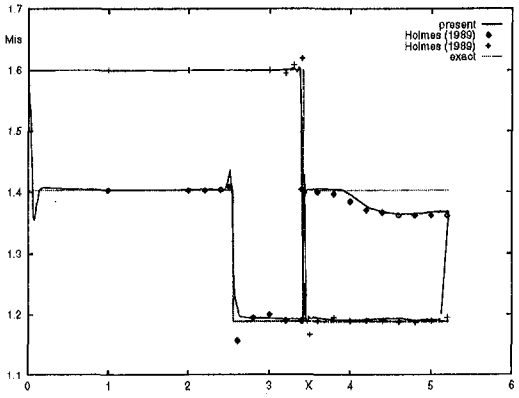

b. Wall isentropic Mach number

Fig. 6 Staggered wedge cascade

grid with rectangular cells in the wake and around the blade, as well as a triangulated mesh outside. An O-type mesh surrounds the blade, while the grid in the wake is of H-type. The total number of nodes is equal to 3858. Note that this mesh has not been adapted.

A stable solution is reached after a residual decay by three orders of magnitude. No further convergence could be obtained because of a stagnation of the maximum residual values in the critical trailing edge region. This is, however, not believed to be due to our scheme but essentially to the very artificial numerical treatment of the trailing edge. Figures $7(a)$ and $7(b)$ show the isodensity pattern and the Schlieren photograph of the flow. We can remark that the shocks detected by the experiments are well predicted by the numerical simulation. Figure 8 provides a comparison with experimental data for the wall isentropic Mach number. The numerical solution agrees well with experiments on the pressure side and on the first part of the suction side after the stagnation point. Nevertheless, the shock created at the trailing edge and impinging on the suction side is located upstream of the experimental location, which modifies the further evolution of the flow. This effect is most probably due to the artificial wake created at the trailing edge. The computed reattachment shock appears to be created upstream of its experimental location. Therefore a full Navier–Stokes calculation in the trailing edge region seems to be required to obtain a more accurate solution.

Conclusion

A new cell-centered finite volume technique for solving steady-state solutions of the two-dimensional Euler equations has been presented. The discretization of the advective derivatives is based on a high-order Gauss integration of the fluxes on the control volume sides coupled with an original quadratic reconstruction of the conservative variables. The use of the Van Leer's flux vector splitting allows us to obtain accurate shock captures. In order to achieve monotonicity in the vicinity of the discontinuities, a special procedure switches the quadratic reconstruction to a limited linear reconstruction (TVD scheme). The code has been implemented to deal with any kind of cells, which provides a very high flexibility. An adaptation technique based on cell division is applied in order to increase the resolution of shocks. The refinement criterion is based on normalized first and second-order derivatives of the pressure and the Mach number. The high accuracy of the method has been demonstrated with the computation of two analytical test cases: the Ringleb flow, and the Sanz supercritical compressor cascade. The adaptation procedure and the monotonicity technique have been tested on the supersonic staggered wedge cascade. A mixed triangular–rectangular mesh has been used to obtain the

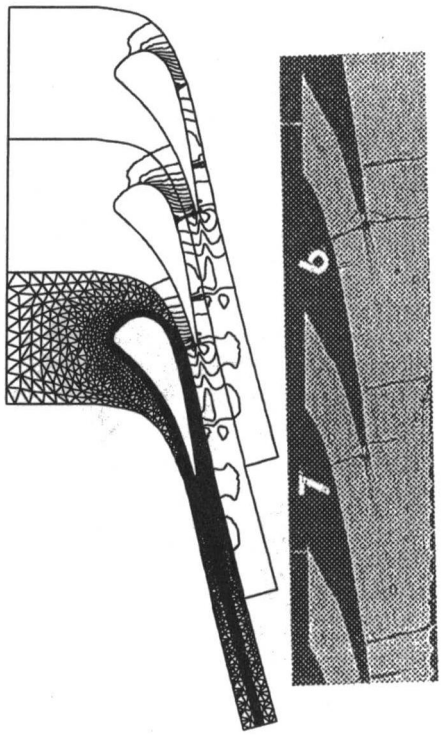

a. Iso-density - Mesh b. Schlieren (Sieverding, 1990)

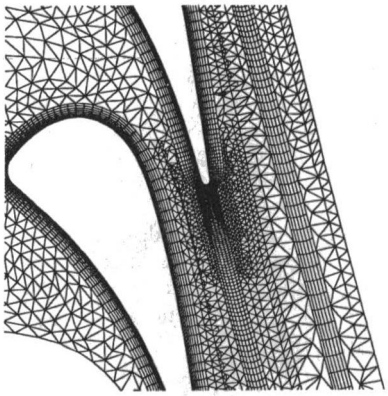

c. Close-up of trailing edge

Fig. 7 Transonic turbine cascade

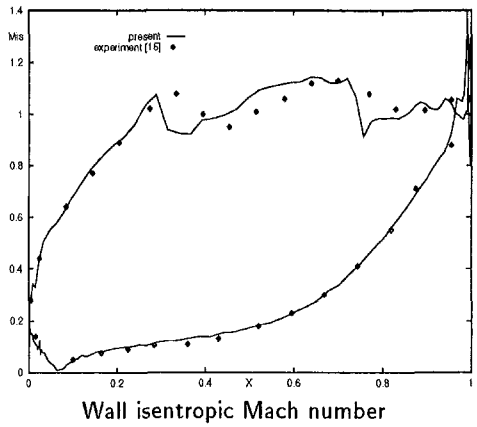

Fig. 8 Transonic turbine cascade

flow around a very high turning transonic blade cascade, which demonstrates the high flexibility of unstructured meshes.

Future work will be focused on the discretization of the Navier–Stokes equations, and the use of an implicit time-integration scheme based on Krylov related methods (Brown and Saad, 1990) in order to increase the robustness and to accelerate the convergence of the code. Directional refinement and coarsening techniques will also be implemented.

Acknowledgments

We wish to acknowledge P. Rogiest and Dr. O. Léonard for their helpful suggestions and support during this work.

References

Barth, T. J., 1993, "Recent Developments in High Order K-Exact Reconstruction on Unstructured Meshes," *Proc. 31st AIAA Aerospace Sciences Meeting and Exhibit,* Reno, AIAA Paper No. 93-0668.

Brown, P. N., and Saad, Y., 1990, "Hybrid Krylov Methods for Nonlinear Systems of Equations," *SIAM Journal on Scientific and Statistical Computing,* Vol. 11, pp. 450–481.

Chiocchia, G., 1985, "Exact Solutions to Transonic and Supersonic Flows," AGARD Technical Report AR-211, pp. 4.1–4.14.

Denton, J. D., 1983, "An Improved Time-Marching Method for Turbomachinery Flow Calculation," ASME *Journal of Engineering for Power,* Vol. 105, pp. 514–524.

Denton, J. D., Hirsch, Ch., and Meauzé, G., 1990, "Analytical Test Cases for Cascades," AGARD Technical Report AR-275, pp. 19–31.

Essers, J. A., Delanaye, M., and Rogiest, P., 1993, "An Upwind-Biased Finite-Volume Technique Solving Compressible Navier–Stokes Equations on Irregular Meshes. Applications to Supersonic Blunt-Body Flows and Shock-Boundary Layer Interactions," *Proc. 11th AIAA CFD Conference,* Orlando, AIAA Paper No. 93-3377, Vol. 2, pp. 861–869.

Essers, J. A., Delanaye, M., and Rogiest, P., 1995, "An Upwind-Biased Finite-Volume Technique Solving Compressible Navier–Stokes Equations on Irregular Meshes," *AIAA Journal,* to be published.

Harten, A., 1983, "High Resolution Schemes for Hyperbolic Conservation Laws," *Journal of Computational Physics,* Vol. 49, pp. 357–393.

Holmes, D. G., 1989, "2D Inviscid Test Cases Results," VKI Lecture Series 1989–06.

Ingram, C. L., McRae, D. S., and Benson, R. A., 1993, "Time Accurate Simulation of a Self Excited Oscillatory Supersonic External Flow With a Multiblock Solution Adaptive Mesh Algorithm," *Proc. 11th AIAA CFD Conference,* Orlando, AIAA Paper No. 93-3387, Vol. 2, pp. 970–977.

Kallinderis, Y. G., and Baron, J. R., 1989, "Adaption Methods for a New Navier–Stokes Algorithm," *AIAA Journal,* Vol. 27, pp. 37–43.

Léonard, O., and Van den Braembussche, R., 1992a, "Design Method for Subsonic and Transonic Cascade With Prescribed Mach Number Distribution," ASME JOURNAL OF TURBOMACHINERY, Vol. 114, pp. 553–560.

Léonard, O., and Van den Braembussche, R., 1992b, "Permeable Wall Boundary Conditions for Transonic Airfoil Design," *Proc. 1st European CFD Conference,* Brussels, Vol. 2, pp. 689–695.

Peraire, J., Vahdati, M., Morgan, K., and Zienkiewicz, O. C., 1987, "Adaptive Remeshing for Compressible Flow Computations," *Journal of Computational Physics,* Vol. 72, pp. 449–466.

Sanz, J. M., 1984, "Improved Design of Subcritical and Supercritical Cascades Using Complex Characteristics and Boundary Layer Correction," *AIAA Journal,* Vol. 22, pp. 950–956.

Shu, C. W., and Osher, S., 1988, "Efficient Implementation of Essentially Non-oscillatory Shock-Capturing Schemes," *Journal of Computational Physics,* Vol. 77, pp. 439–471.

Sieverding, C. H., 1990, "Experimental Test Cases for Cascades," AGARD Technical Report AR-275, pp. 139–151.

Van Albada, G. D., Van Leer, B., and Roberts, W. W., 1982, "A Comparative Study of Computational Methods in Cosmic Gas Dynamics," *Astronomy and Astrophysics,* Vol. 108, pp. 76–84.

Vankeirsbilck, P., 1993, "Algorithmic Developments for the Solution of Hyperbolic Conservation Laws on Adaptive Unstructured Grids (Applications to the Euler Equations)," Ph.D. Thesis, Katholiek Universiteit van Leuven and Von Karman Institute, Belgium.

Van Leer, B., 1982, "Flux-Vector Splitting for the Euler Equations," *Lecture Notes in Physics,* Vol. 170, pp. 507–512.

Heat Transfer Predictions for Two Turbine Nozzle Geometries at High Reynolds and Mach Numbers

R. J. Boyle
NASA Lewis Research Center,
Cleveland, OH 44135

R. Jackson
DRA Pyestock,
Farnborough, Hants, United Kingdom

Predictions of turbine vane and endwall heat transfer and pressure distributions are compared with experimental measurements for two vane geometries. The differences in geometries were due to differences in the hub profile, and both geometries were derived from the design of a high rim speed turbine (HRST). The experiments were conducted in the Isentropic Light Piston Facility (ILPF) at Pyestock at a Reynolds number of 5.3 × 10^6, a Mach number of 1.2, and a wall-to-gas temperature ratio of 0.66. Predictions are given for two different steady-state three-dimensional Navier–Stokes computational analyses. C-type meshes were used, and algebraic models were employed to calculate the turbulent eddy viscosity. The effects of different turbulence modeling assumptions on the predicted results are examined. Comparisons are also given between predicted and measured total pressure distributions behind the vane. The combination of realistic engine geometries and flow conditions proved to be quite demanding in terms of the convergence of the CFD solutions. An appropriate method of grid generation, which resulted in consistently converged CFD solutions, was identified.

Introduction

Confidence in the validity of three-dimensional Navier–Stokes predictions for turbine aerodynamic performance and surface heat transfer characteristics increases when computations are shown to predict measured values for cases that approach actual engine geometry and flow conditions. For example, the engine Reynolds and Mach numbers, as well as the turbulence intensity, should be matched as closely as possible. Confidence levels increase when the test geometry incorporates features that are part of a three-dimensional design philosophy. A turbine vane design philosophy could include convergence in the meridional plane, as well as underturning of the vane in the endwall region to reduce secondary losses. When design considerations such as these are present, blade and endwall heat transfer may be substantially different from values measured in either a linear or annular cascade with constant section vane geometry. Comparisons with experimental turbine blade heat transfer data, which include both endwall and blade results, provide a significant test of three-dimensional Navier–Stokes analyses, since the endwall heat transfer is significantly affected by secondary flow patterns. The blade heat transfer is more two dimensional in nature. Blair (1974), and Boyle and Russell (1990) presented endwall heat transfer distributions obtained in linear cascades for large-scale vanes, at relatively low Mach numbers. York et al. (1984) obtained similar data, but at transonic Mach numbers. Arts and Heider (1994) presented vane and endwall heat transfer measurements obtained at transonic Mach numbers in an annular cascade with constant radii endwalls.

Test cases with hubs and shrouds of constant radii, and with blades of little or no twist, provide useful information for predicting aerodynamic and heat transfer behavior. However, turbine blading employed in actual engines typically has vanes with significant endwall convergence and twisted blades. Comparing predictions for test cases with these geometric features increases confidence in the ability of the analysis to predict aerodynamic and heat transfer performance at actual engine conditions.

The previously cited experimental data are for geometries with constant radii hub and shroud surfaces, and with little or no blade twist. A series of experiments measuring turbine aerodynamics and surface heat transfer utilizing a vane geometry representative of an actual engine have been conducted in the DRA Isentropic Light Piston Facility (ILPF). Kingcombe et al. (1989) presented the overall performance and detailed vane heat transfer and aerodynamic measurements for a transonic turbine. Vane measurements were given for a range of Reynolds numbers at an exit Mach number of 1.14. Harasgama and Wedlake (1991) presented experimental surface pressure and heat transfer distributions on the vane and on the hub and casing endwalls for a range of Reynolds and Mach numbers. Both of these references were for a vane with reduced turning at the hub and tip casing, but with constant radius endwalls. Chana (1992) measured vane, hub, and tip heat transfer and pressure distributions using the same vane geometry for two different hub contour geometries.

In recent years a number of three-dimensional Navier–Stokes predictions for vane and/or rotor heat transfer have been presented. Choi and Knight (1988), Hah (1989), and Ameri and Arnone (1994) showed comparisons with large scale–low speed heat transfer data of Graziani et al. (1980) using both algebraic and two-equation turbulence models. Chima et al. (1993) developed an algebraic turbulence model, which was used to compare vane endwall heat transfer predictions over a range of Reynolds numbers with the experimental data of Boyle and Russell (1990). In addition to predictions for isolated blade rows, three-dimensional Navier–Stokes heat transfer analyses have been performed for entire turbine stages. Boyle and Giel (1992), and Ameri and Arnone (1992) showed comparisons with the experimental heat transfer data of Dunn et al. (1994)

Contributed by the International Gas Turbine Institute and presented at the 40th International Gas Turbine and Aeroengine Congress and Exhibition, Houston, Texas, June 5–8, 1995. Manuscript received by the International Gas Turbine Institute February 16, 1995. Paper No. 95-GT-104. Associate Technical Editor: C. J. Russo.

and Blair (1994). Heider and Arts (1994) showed comparisons of predicted heat transfer with the data of Arts and Heider (1994) using the Baldwin–Lomax turbulence model. Except for the comparisons of Heider and Arts (1994), these comparisons have been for subsonic conditions. It remains to be seen whether algebraic models can predict turbine heat transfer as accurately as two-equation models for high Mach and Reynolds number cases.

The ideal turbulence model would give accurate heat transfer predictions with little computational overhead. Algebraic turbulence models require less computational effort compared to multiple equation models. They also have the advantage in that empirical correlations can be easily incorporated into the modeling to account for effects such as transition and augmentation of the leading edge heat transfer due to free-stream turbulence. However, if the algebraic models are not accurate, their use is not warranted. Ameri and Arnone (1994) showed heat transfer predictions using algebraic and two-equation models. Their results indicated that the degree of agreement with the experimental data was not significantly improved using a two-equation turbulence model. Results using either turbulence model were in good agreement with the experimental data. Other factors, such as the thermal boundary condition and spanwise grid density, resulted in heat transfer variations as large as between the two turbulence models. Algebraic models also require less CPU time per time step, and less core memory than higher order models. Ameri and Arnone (1994), showed that heat transfer predictions using two-equation models required nearly twice the CPU time to converge, compared with an algebraic model solution. The high-Reynolds-number cases investigated herein require large-size grids, which favors algebraic models. Also, use of higher-order models would have required additional computer simulations to determine the effects of the assumed value of the inlet length scale on the predicted heat transfer. The length scale at the inlet was not known, and Ameri and Arnone (1992) showed that blade surface heat transfer is significantly affected by the assumed value for the length scale at the inlet boundary.

As the result of a cooperative agreement between NASA Lewis Research Center and the Defence Research Agency (DRA, Pyestock), a study was undertaken to predict the turbine vane heat transfer of two geometric configurations. The predictions are compared with the experimental measurements of Chana (1992). These measurements included pressure and heat transfer distributions on the vane surfaces as well as the hub and tip casings. Pressure and heat transfer distributions were measured on the vane, hub, and shroud surfaces for two different hub endwall geometries. In addition, the total pressure distribution behind the vane was measured for one configuration. These data are for a high Reynolds number of $Re_2 = 5.3 \times 10^6$, and at a pressure ratio corresponding to an exit Mach number of 1.2. The high Reynolds number requires small grid spacing in the near-wall region. This, in turn, results in large computational grids. Because of the large computational grids, and indications that algebraic turbulence models would give accurate heat transfer predictions, algebraic turbulence models were used. Heat transfer comparisons are shown using three different models for turbulent eddy viscosity. Predictions were made for the vane surface, hub, and casing heat transfer. Also, the ability of the analyses to predict surface static pressures and the total pressure distribution behind the vane is examined. The reason for comparing predicted wake profiles with measurements is that these comparisons may shed light on the differences in the heat transfer results. Good agreement in the downstream pressure distributions indicates that the analysis predicted secondary flows correctly.

Description of Computational Analysis

Two different steady state three-dimensional Navier–Stokes computer code analyses were used. One computer code, referred to as TRAF3D, is the finite volume analysis described by Arnone et al. (1992). The other code, referred to as RVC3D, is the finite difference analysis described by Chima (1991) and by Chima and Yokota (1988). The reason for using two Navier–Stokes analyses is to help insure that the conclusions drawn from this work are applicable to a range of CFD analyses, and that they are not specific to any one formulation. While the two Navier–Stokes analyses had different approaches to the discretization, they were similar in other respects. Both analyses used a Runge–Kutta scheme to march the solution in time, and both employed implicit residual smoothing.

The code TRAF3D uses the turbulence model developed by Baldwin and Lomax (1978). The RVC3D code uses either of two turbulence models. One is a variation of the Baldwin–Lomax model, and results obtained using this model are labeled as Chima's model. The other is a variation of the Cebeci–Smith (1974) model, and results obtained using this model are labeled as Cebeci–Smith results. Chima et al. (1993) discuss the implementation of these two models. Unless stated otherwise, references to the TRAF3D code imply the Baldwin–Lomax turbulence model, and references to the RVC3D code imply Chima's turbulence model. Both of these models use the Baldwin–Lomax transition criterion. The transition criterion in the Baldwin–Lomax model does not account for the effects of free-stream turbulence. Since these tests, and actual engine operation, are at relatively high levels of turbulence, the transition criterion of Mayle (1991) was incorporated into the turbulence model. Also, high free-stream turbulence results in leading edge Frössling numbers significantly greater than unity. The model of Smith and Kuethe (1966) was used to account for the effects of free-stream turbulence. Pr and Pr_t were held constant at 0.70 and 0.90, respectively.

The inlet total pressure was 5.0 bars. The inlet total temperature was 440 K, and the surface temperature was 290 K. The hub static-to-total pressure ratio was 0.42. The Reynolds number based on exit conditions, and true chord was 5.3×10^6. A uniform temperature boundary condition was imposed on all solid boundaries. Spanwise radial equilibrium was assumed at the exit boundary of the calculation domain. At each spanwise

Nomenclature

c = true chord
c_x = axial chord
d = distance from surface
k = thermal conductivity
M_{IS} = isentropic Mach number
Nu = Nusselt number based on true chord and $k(T_1')$
P' = total pressure
Pr = Prandtl number
Pr_t = turbulent Prandtl number
Re_2 = exit true chord Reynolds number
s = surface distance
T' = total temperature
Tu = turbulence intensity
U = velocity
y_1^+ = normalized distance of first grid line
θ = momentum thickness
μ_t = turbulent eddy viscosity
ρ = density

Subscripts

EXIT = exit of computational domain
INLET = inlet of computational domain
M = measurement plane
S = surface of blade
1 = inlet, or surface
2 = outlet, or surface

location the exit static pressure was allowed to vary in the circumferential direction. The average static pressure was specified at the hub exit, but the pitchwise variation was determined from the internal flow field. The hub and tip inlet full boundary layer thicknesses were determined from measurements to be 9 percent of axial chord. Uniform total conditions were specified for the inlet core flow, and uniform static pressures were specified through the inlet boundary layers. The inlet temperature and velocity profiles through the boundary layers were determined using flat plate correlations. The friction factor and Stanton number are first determined from the specified inlet boundary layer thickness. Once these quantities are found, the profiles are determined from correlations given by Kays and Crawford (1980). Using a simple power law for the inlet temperature profile produces an erroneous result, since the power law gives an infinite gradient at the wall.

The primary convergence criterion was to examine the solution to see that the variables of interest were not changing with increased iterations. The primary variable of interest was surface heat transfer, because it converged at a slower rate than surface pressures. Because of the large CPU requirements, most cases were not started from a simple initial flow field, but, when a parameter was changed, the previous solution was used as an initial guess. If the new parameter value produced a small change in the flow field, the residuals did not necessarily increase significantly initially. With this approach, relying on "orders of magnitude" decreases in residuals was impractical. Low residuals relative to initial values without restart were verified, but were not the primary convergence measure. The inlet and exit mass flows differed by less than 1 percent at convergence.

Discussion of Results

Figure 1(*a*) shows a meridional view of the two configurations. They differ in the shape of the hub. For presentation purposes, these configurations are labeled B for bellmouth, and S for the S-contoured hub. Configuration B has lower acceleration near the front portion of the vane than configuration S for the same pressure ratio. The meridional view only indicates a part of the acceleration, since the flow is turned from axial to an average of about 70 deg.

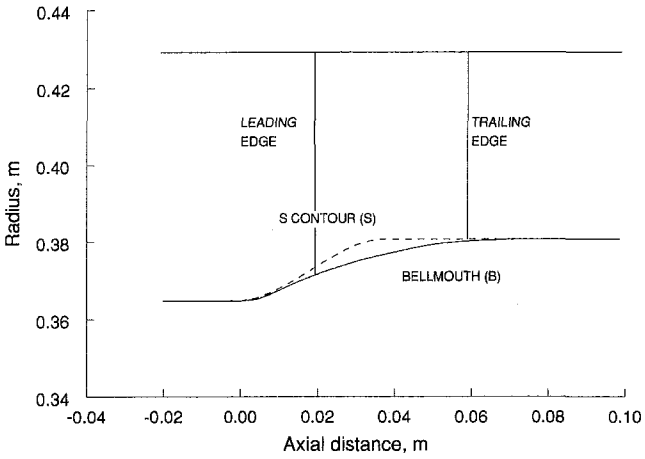

Fig. 1(*a*) Meridional view of vane configuration

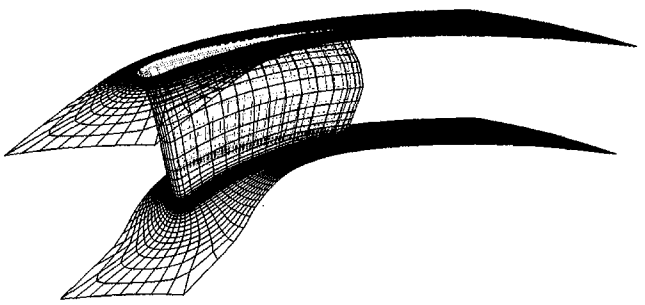

Fig. 1(*b*) Typical grid used for analysis

Figure 1(*b*) shows the vane profile with the hub configuration B. The vane trailing edge angle varies from hub to tip. The highest amount of turning occurs near midspan, and the lowest amount of turning at the hub endwall. This figure also shows the C-type grids used for the analysis. C-type grids were chosen in order to obtain good resolution of the flow field, and hence heat transfer, in the leading edge region.

Grid Generation. For the test Reynolds numbers, the desired near-wall spacing was 1×10^{-5} of c_x to obtain maximum values of y_1^+ of approximately one, which are needed to insure accurate results. Two approaches were taken for grid generation. A common grid was used for both flow analysis codes. Best results were obtained using an embedded grid with a nonmatching condition along the cut line. A program, TCGRID, developed by Chima (1990), was initially used to obtain the grids used in the finite difference analysis. This program generates a series of two-dimensional fully elliptical grids in the blade-to-blade plane based on Sorenson's (1980) grid generation procedure. These grids, typically seven in number, are then stacked and interpolated to give a grid for each value of the spanwise index. For a $177 \times 49 \times 65$ grid, the seven blade-to-blade grids are interpolated to give 65 blade-to-blade plane grids. For a three-dimensional grid, the grid control parameters should be the same for each blade-to-blade section. Satisfactory three-dimensional grids with the desired near-wall spacing were not obtained using recommended orthogonality constraint parameter values. Relaxing the parameters gave unrealistic flow solutions, probably due to excessive grid stretching.

The approach finally taken for the finite difference analysis was to use the grid generation code developed for the finite volume flow analysis code, as described by Arnone et al. (1992). In this approach the blade-to-blade grids are calculated in two steps. First a coarse grid, suitable for an Euler analysis, is generated using Sorenson's (1980) technique. A grid with the desired near-wall spacing is then embedded within the coarse blade-to-blade grid. The resulting blade-to-blade grids are then stacked to yield the three-dimensional grid. Typically, the degree of orthogonality at the wall is less for an embedded grid than for a fully elliptical grid. For turbine blade grids, the degree of orthogonality is significantly improved if the constraint of matching grid lines along the cut line emanating from the trailing edge stagnation point to the downstream boundary is removed. In contrast to the two-dimensional results presented by Boyle and Ameri (1997), it was found that the convergence of the three-dimensional finite difference code, RVC3D, was significantly improved by not imposing a matching condition along the cut line. The finite volume analysis, TRAF3D, of Arnone et al. (1992) was developed to use grids that did not require a matching condition along the cut line.

For each configuration the grid size was $177 \times 49 \times 65$. There were 56 increments on the pressure side of the cut line in the wake region. There were 32 increments along the pressure side of the blade, and 64 increments along the suction side. There were 24 increments on the suction side of the wake region cut line.

Surface Pressures. Figure 2 shows a comparison of the predicted and experimental isentropic Mach numbers, as determined from the static to total pressure ratio, for both configurations. Even though the passage geometry is complex, there is little spanwise variation in either the predicted or measured surface pressures. The computations are consistent with the experimental data in predicting the spanwise variation in pressures. These results were obtained using the TRAF3D code, and predictions using the RVC3D code were nearly identical.

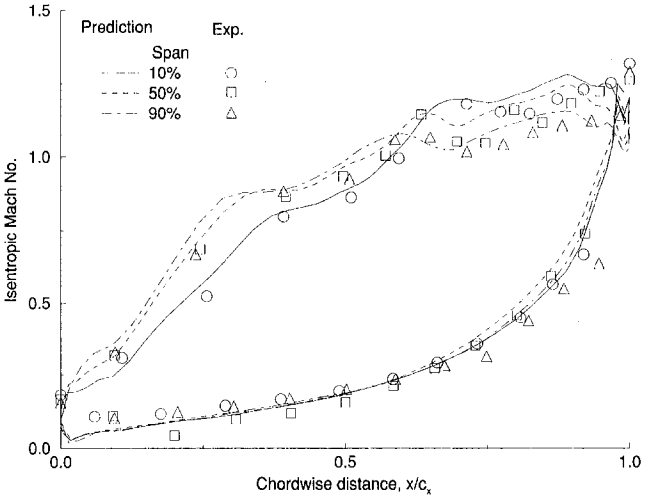

Fig. 2 Vane surface pressure distribution

Both CFD codes require the specification of either a uniform or average hub exit boundary pressure. Arts et al. (1990) have shown, for a similar vane, that when the exit Mach number exceeds unity, there was a considerable pitchwise variation in the midspan static pressure. At 0.42 chords behind the vane the maximum-to-minimum variation in static pressure was 11 percent of the dynamic pressure at a Mach number of 0.85, and increased to 23 percent at a Mach number of 1.1. The results shown in Fig. 2 are for a hub exit Mach number of 1.2. The blade surface pressure distribution was sensitive to the specified exit pressure. The tip exit pressure corresponded to an isentropic Mach number near unity, and had significantly less pitchwise variation than the hub exit pressure. Since only a few pressures were available to determine the appropriate exit boundary condition, the tip exit pressure was used. In the analysis, the hub exit pressure was adjusted so that the tip exit pressure matched the experimental value.

Figures 3 and 4 compare predicted and experimental hub and tip endwall isentropic Mach numbers for both configurations. Predictions were the same using either analysis, and the agreement with the data is good. Measurements, using approximately 53 taps per surface, extended from $0.06c_x$ upstream of the leading edge to $0.13c_x$ downstream of the trailing edge. The predictions, which extend beyond the blade region, show the pitchwise variation in isentropic Mach number to be greater for the hub than for the tip.

Heat Transfer Comparisons. In this section predicted and measured vane and endwall heat transfer are compared. Predictions of surface pressure distributions were nearly identical using either flow analysis. However, predictions of surface heat transfer were different between the two analyses. Since the analyses incorporated different turbulence models, these differences could be due to either the analyses themselves, or in the turbulence models. It will be shown that the primary difference in the heat transfer results between the two analyses is due to the choice of turbulence model.

Comparisons of the predicted and measured vane surface Nusselt numbers are given in Fig. 5 using the Baldwin--Lomax turbulence model, and in Fig. 6 using Chima's turbulence model. Except for the suction surface transition region, there is little spanwise variation in the experimental Nusselt number. Even though the variation is not large, the results show that the midspan region of the suction and pressure surfaces have higher heat transfer than near either endwall. The peak suction surface heat transfer occurs at transition, and is highest for the data at 50 and 98 percent of span. The leading edge region heat transfer is relatively low compared to the average suction surface value. This results from the endwall convergence, which gives lower inlet velocities compared with constant radius endwalls.

The TRAF3D analysis agrees well with the data at the leading edge, $s/c_x = 0$, for both configurations. However, this analysis overpredicts the pressure surface heat transfer prior to transition, which occurs at the location of minimum heat transfer. The RVC3D analysis underpredicts the midspan heat transfer at the leading edge, but is in good agreement with the pressure surface data prior to transition. The difference is a consequence of the TRAF3D prediction incorporating the Smith and Kuethe (1966) model to account for the effects of free-stream turbulence on laminar heat transfer, while the RVC3D prediction did not include a model for this effect. Without this model both analyses gave the same leading edge heat transfer rates.

The predicted suction surface transition occurs downstream of the experimental location. This is a consequence of the way Mayle's (1991) transition model was implemented. In this model the start of transition occurs when $\mathrm{Re}_\theta = 400Tu^{-5/8}$. The measured upstream Tu was 6.5 percent. It was assumed that the fluctuations remained constant to determine the local Tu for the transition criterion. The upstream Mach number was 0.14, so that the local calculated Tu at transition was approximately 1 percent. If the turbulence intensity is held constant, the predicted suction surface transition location occurs closer to the leading edge than is shown by the data. The results of Young et al. (1992), lead to the expectation that the primary effect of high free-stream Tu was to cause early transition. They showed that the effects of high free-stream Tu are at a minimum when either Re_θ, or the length scale to boundary layer thickness ratio is large. Re_θ is large on the endwalls, and the boundary layer thickness is small on the vane.

Both predictions show the correct spanwise variation in suction surface heat transfer after transition, where the highest values are at midspan and the lowest values are at 2 percent of the span. However, both analyses overpredict the amount of spanwise variation. This may not be due to defects in the turbulence model, since, as is shown in a subsequent figure, the vane suction surface heat transfer changes very rapidly near the endwall. The measurements may have averaged the heat transfer rates for a region close to the endwall.

The two predictions differ in the calculated heat transfer in the near-wall region at 2 and 98 percent of span. This is especially evident near the leading edge for configuration S. The RVC3D prediction shows much higher heat transfer levels near the endwalls compared to midspan. The TRAF3D prediction shows smaller spanwise variation in this region. This is due to different assumptions made in the respective analyses. In the RVC3D code the eddy viscosity at a point is calculated from:

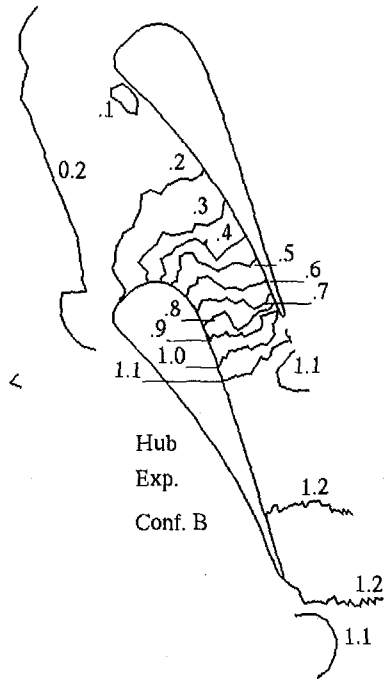

Fig. 3(*a*) Experimental M_{IS} for configuration B hub

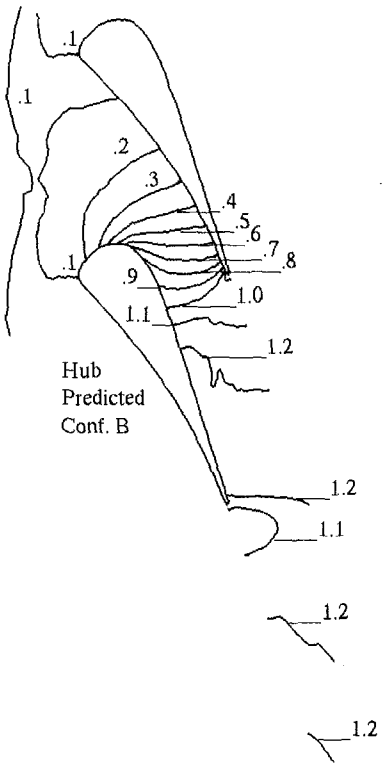

Fig. 3(*b*) Predicted M_{IS} for configuration B hub

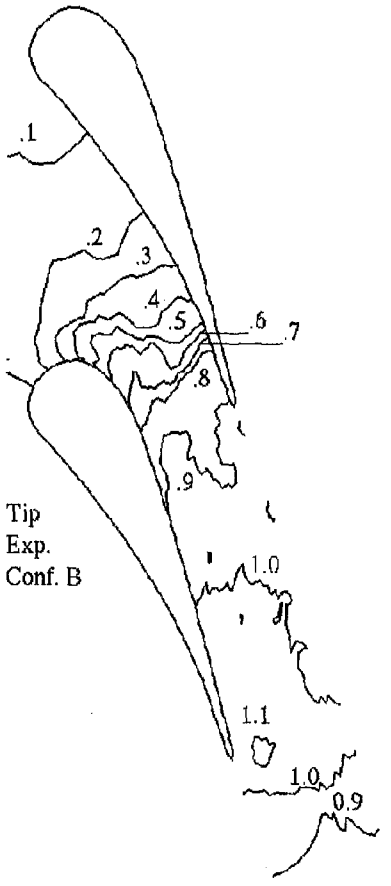

Fig. 3(*c*) Experimental M_{IS} for configuration B tip

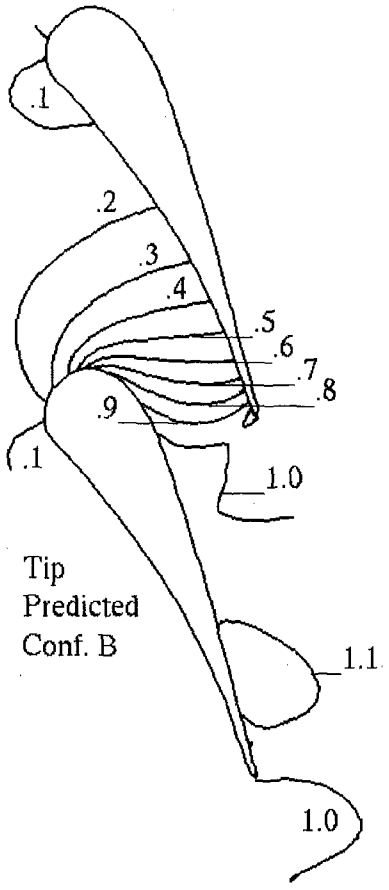

Fig. 3(*d*) Predicted M_{IS} for configuration B tip

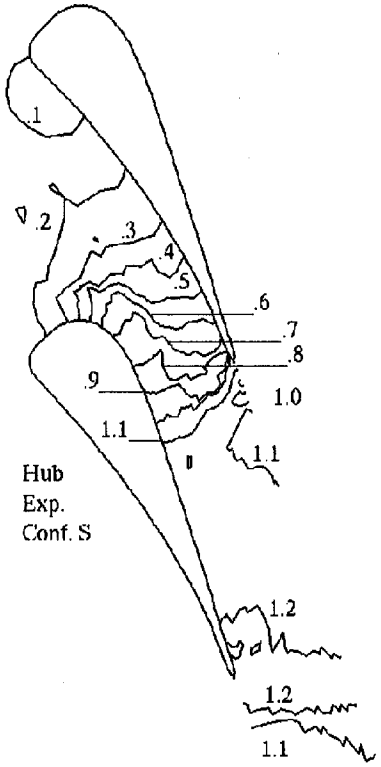

Fig. 4(*a*) Experimental M_{IS} for configuration S hub

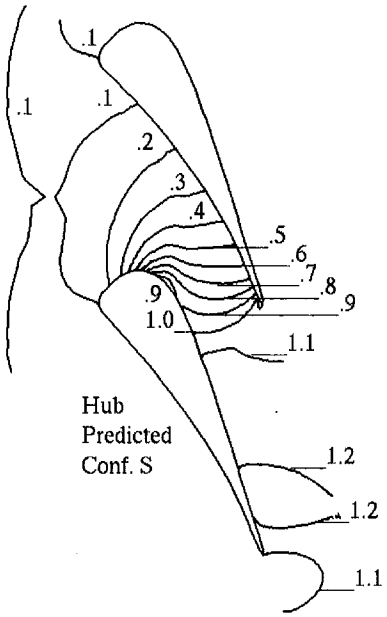

Fig. 4(*b*) Predicted M_{IS} for configuration S hub

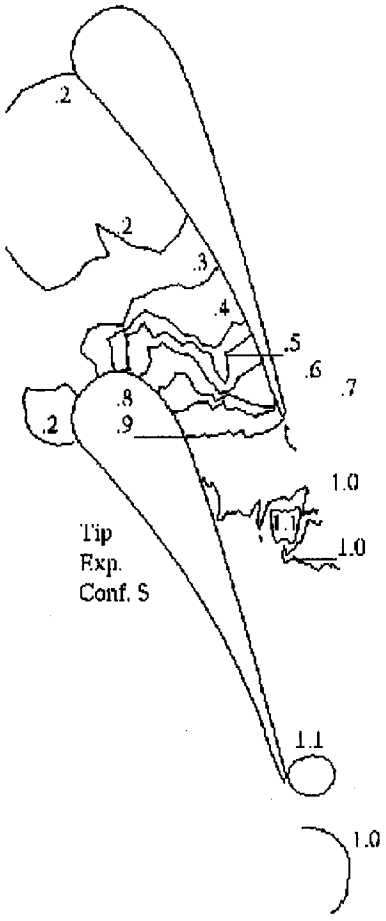

Fig. 4(*c*) Experimental M_{IS} for configuration S tip

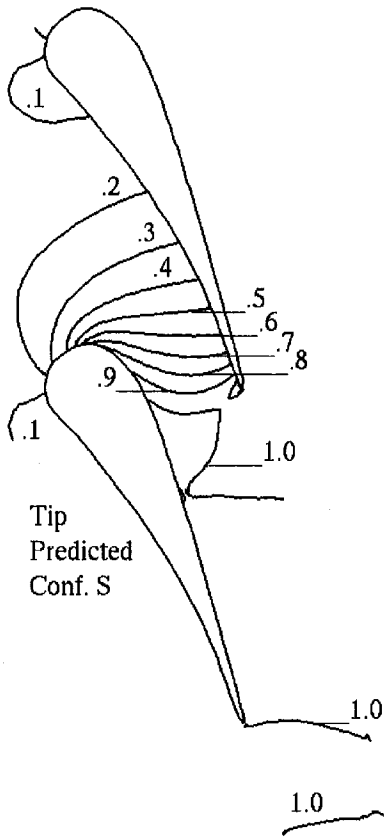

Fig. 4(*d*) Predicted M_{IS} for configuration S tip

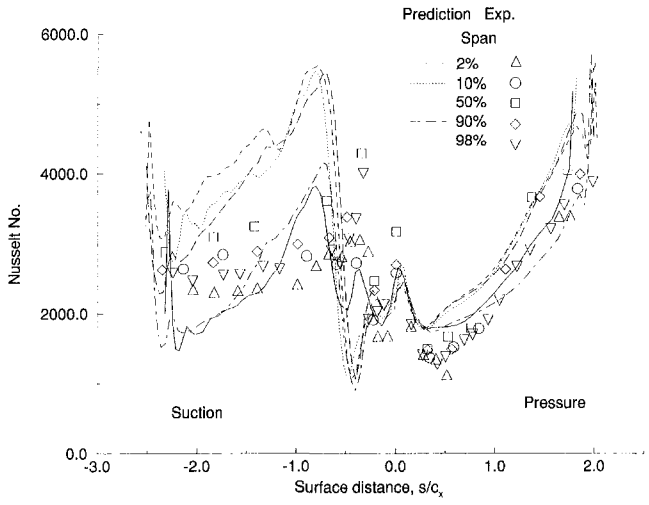

a- Configuration B

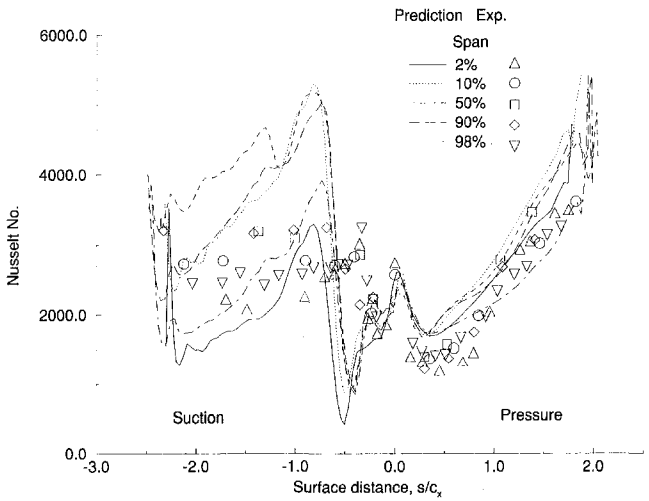

b- Configuration S

Fig. 5 Heat transfer, Baldwin–Lomax (TRAF3D) model

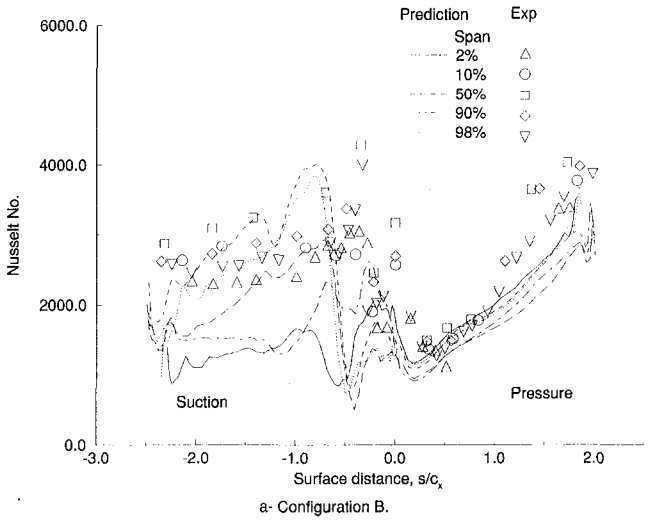

a- Configuration B.

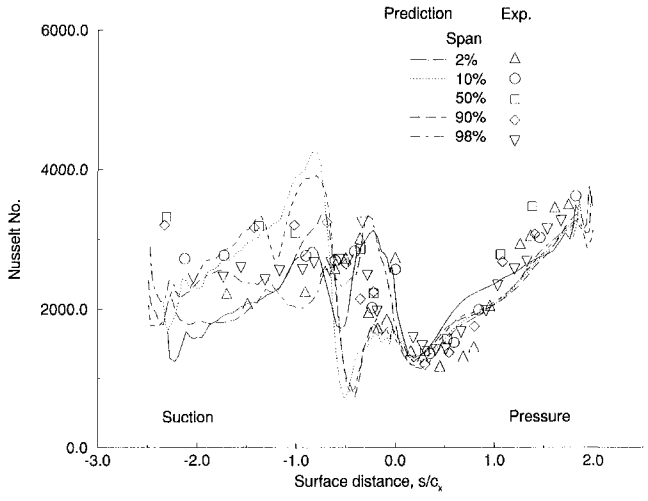

b- Configuration S

Fig. 6 Heat transfer, Chima's (RVC3D) model

$$\mu_t = \sqrt{(\mu_t)_1^2 + (\mu_t)_2^2}.$$

$(\mu_t)_1$ is found by considering only the effect of the blade surface, and $(\mu_t)_2$ is found by considering only the effect of the endwall surface. Also, the length scale used for both values of μ_t is the Buleev length scale, which can be approximated as the minimum distance to either surface. The TRAF3D code, however, weighs the individual contributions to the eddy viscosity:

$$\mu_t = R(\mu_t)_1 + (\mu_t)_2(1 - R)$$

and

$$R = d_2^2/(d_2^2 + d_1^2).$$

For each value of μ_t the length scale is the normal distance to the appropriate wall. In the corner region the eddy viscosity in the RVC3D code can be nearly 40 percent greater than the maximum value from one surface. In this same region the TRAF3D assumption limits the value to the greater of the two values. Consequently, the RVC3D assumption gives greater eddy viscosity in the corner region, even for the same turbulence model assumptions. The results in Figs. 5 and 6 show that the RVC3D code assumption regarding the eddy viscosity is in better agreement with the experimental data.

Predictions were also made using the RVC3D code with the Cebeci–Smith turbulence model. Except for the differences noted due to the implementation of the models, the Cebeci–Smith results were similar to the Baldwin–Lomax results shown in Fig. 5.

Other differences in predicted heat transfer between the two turbulence models can be highlighted if transition effects are absent. Figure 7 shows a contour plot of Nu as a function of span and surface distance for configuration B, and assuming fully turbulent flow. Similar results were obtained for configuration S. This figure shows comparisons of predictions for five different cases, and illustrates the effect of varying the turbulence model using the two flow solvers. The horizontal axis is the surface distance along the suction and pressure surfaces of the vane. Because of the endwall contour, the leading edge is at the location of maximum span. Figure 7(a) shows Nu for the TRAF3D code with the Baldwin–Lomax turbulence model. Figures 7(b, c, d) show RVC3D code results with Chima's turbulence model, the Cebeci–Smith turbulence model, and the Baldwin–Lomax turbulence model, respectively. These three figures show the surface heat transfer for different turbulence models using the same flow solver and grid. The Cebeci–Smith model gives the highest vane heat transfer. The other two models give similar surface heat transfer. Comparing the heat transfer in Figs. 7(a) and 7(d) shows differences in heat transfer between the two flow solvers for the same turbulence model.

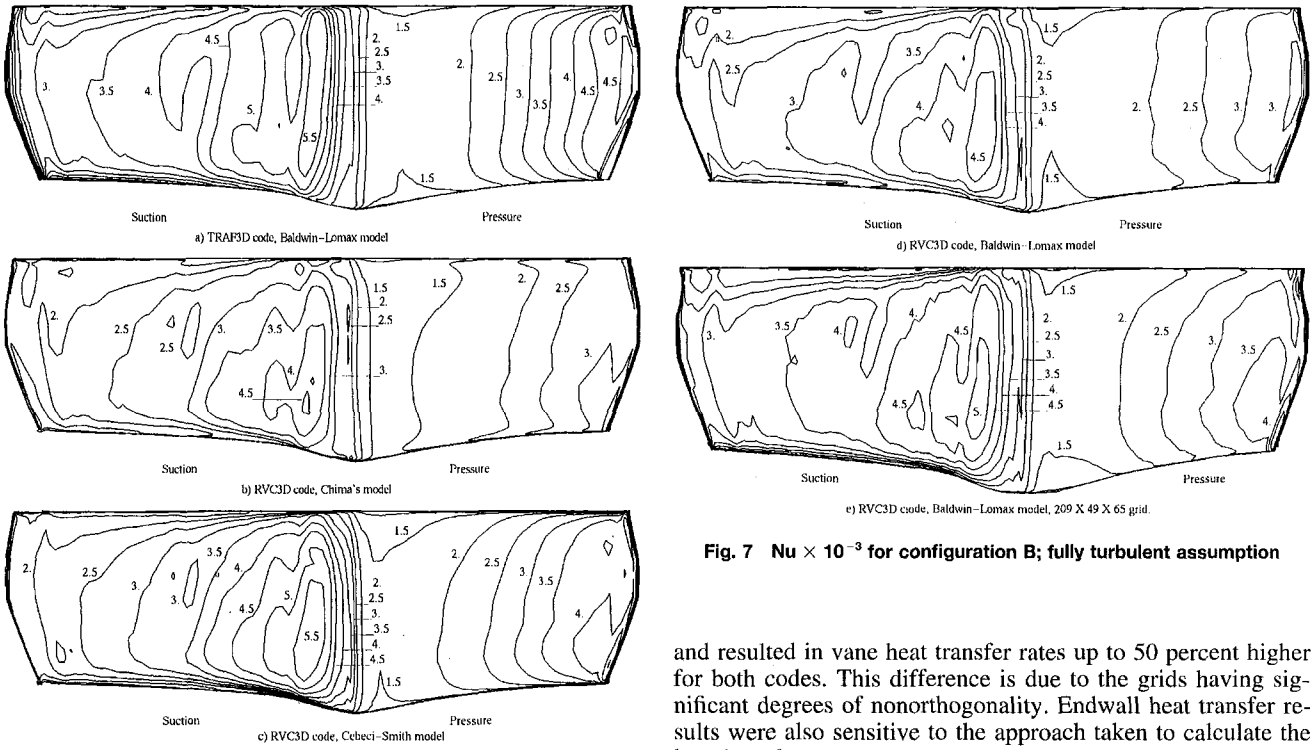

Fig. 7 Nu $\times 10^{-3}$ for configuration B; fully turbulent assumption

The differences are on the same order as the differences among the three turbulence models. The differences are not due to either differences in the implementation of the turbulence model, or to inherent differences between the codes. If the μ_t from the converged TRAF3D case was used in the RVC3D code, and the μ_t calculation bypassed, the heat transfer was the same as in Fig. 7(*d*). The differences are due to the RVC3D code exhibiting a greater grid sensitivity than the TRAF3D code. Figure 7(*e*) shows the vane heat transfer using a finer grid in the streamwise direction. Overall, this grid was about 20 percent larger, but had a 50 percent increase in the number of grid lines (from 32 to 48 increments), along the pressure surface. Sixteen increments were also added to the suction surface. The results in Fig. 7(*e*) are in closer agreement with the Fig. 7(*a*) results. When the TRAF3D analysis was run with the finer grid, the vane heat transfer was nearly identical to that shown in Fig. 7(*a*).

In an effort to understand the differences among the results, the manner in which the models were implemented was investigated. The TRAF3D code uses Sutherland's Law to determine the variation of viscosity, and hence conductivity, with temperature. The RVC3D code uses a power law for this variation. Using the power law variation in the TRAF3D code did not change the predicted heat transfer.

The Baldwin–Lomax model was applied everywhere in the flow field. In the RVC3D code a distinction was made, based on an input variable, between a "near wall" region and the entire flow field. For a j index greater than j_{EDGE}, the turbulent eddy viscosity was set to the outer region value, independent of where the crossover between the inner and outer regions occurred. Extending j_{EDGE} to the grid size index resulted in no significant change in the predicted heat transfer. Only when the turbulent eddy viscosity was suppressed completely for j values greater than j_{EDGE} was the heat transfer reduced by 10 to 15 percent.

Both codes calculate the length scale in the same manner. For the vane or endwall the length scale is calculated as the normal distance from the grid line (RVC3D) or cell center (TRAF3D) to the appropriate surface. Taking the distance along the grid line for the length scale overestimates the length scale, and resulted in vane heat transfer rates up to 50 percent higher for both codes. This difference is due to the grids having significant degrees of nonorthogonality. Endwall heat transfer results were also sensitive to the approach taken to calculate the length scale.

Figures 8 and 9 compare predictions of endwall heat transfer with experimental data for both analyses for configurations B and S, respectively. The experimental data extended from $0.11\,c_x$ upstream of the leading edge to $0.11\,c_x$ beyond the vane trailing edge. There were between 28 and 39 heat transfer measurements on each endwall. Upstream of the blade leading edge there was little variation in endwall heat transfer. The inlet Nu was calculated to be 1245. While the choice of the transition location noticeably affected the vane surface heat transfer, the location of transition on the vane had no noticeable effect on endwall heat transfer. Based on the measured inlet boundary layer thickness, the inlet endwall boundary layers was taken as fully turbulent.

The predictions shown in these figures are for a 177 × 49 × 65 grid. There was no significant difference in the predictions when a 209 × 49 × 65 grid, or a 177 × 49 × 89 grid was used.

Comparing Figs. 8(*a*) and 9(*a*) shows that configuration B had a somewhat lower hub heat transfer in the leading edge region, and a slightly higher heat transfer in the throat region. The predictions with any of the turbulence models do not show any significant differences between the two configurations in the leading edge region. This is somewhat surprising, since, as is shown in Fig. 1, this is the region where there is a difference in the hub contour. In the throat region the Baldwin–Lomax model predicts the same hub heat transfer for either configuration, with a peak value that closely agrees with the measurements. Chima's turbulence model underpredicts the peak heat transfer in the throat region, and is generally lower than the experimental data for most of the passage. The Cebeci–Smith model overpredicts the peak heat transfer in the throat region, but generally agrees well with the experimental data.

In the tip region the experimental data are, as expected, relatively the same for both configurations. Again, there is a slightly higher throat region heat transfer for configuration B. The tip data show a region of high heat transfer at the top of the suction surface for configuration B, but not for configuration S.

The predictions show the high heat transfer to be confined to only a small region of the tip endwall. Both the hub and tip predictions show the same relative agreement with the data for either hub configuration.

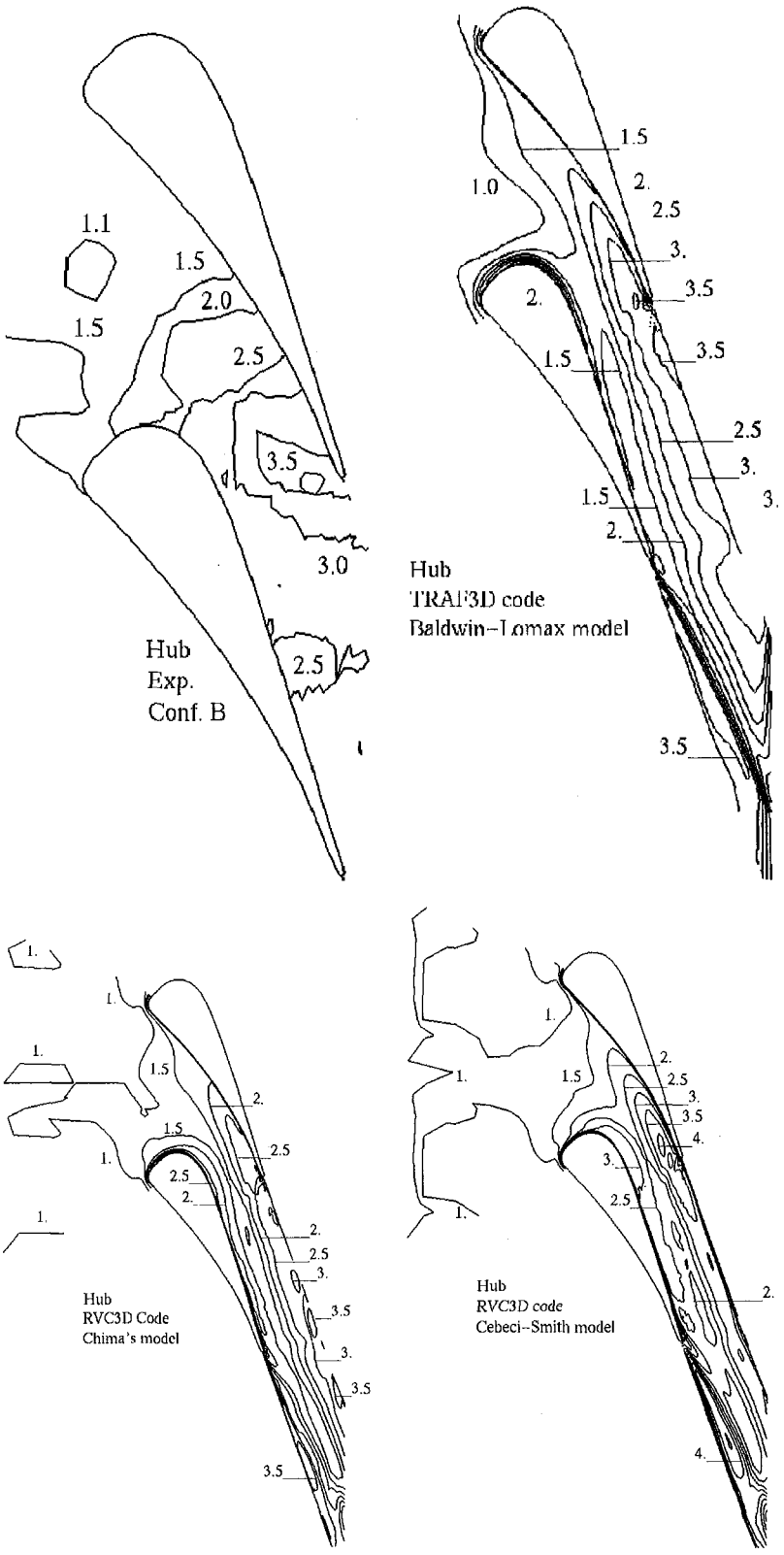

Fig. 8 Nu × 10^{-3} for configuration B

The experimental data show a slightly higher tip endwall heat transfer level compared to the hub endwall for both configurations. The predictions also show higher heat transfer on the tip endwall for a small region near the suction surface, close to the peak of the blade. This behavior is consistent with the experimental vane data shown in Fig. 5. At this vane surface region, the data, especially for configuration B, show higher heat transfer at 98 percent of span than at 2 percent of span. Along the suction surface region for either configuration the Baldwin–Lomax results show lower heat transfer than the other predictions. The other two predictions agree better with the data in this region. The

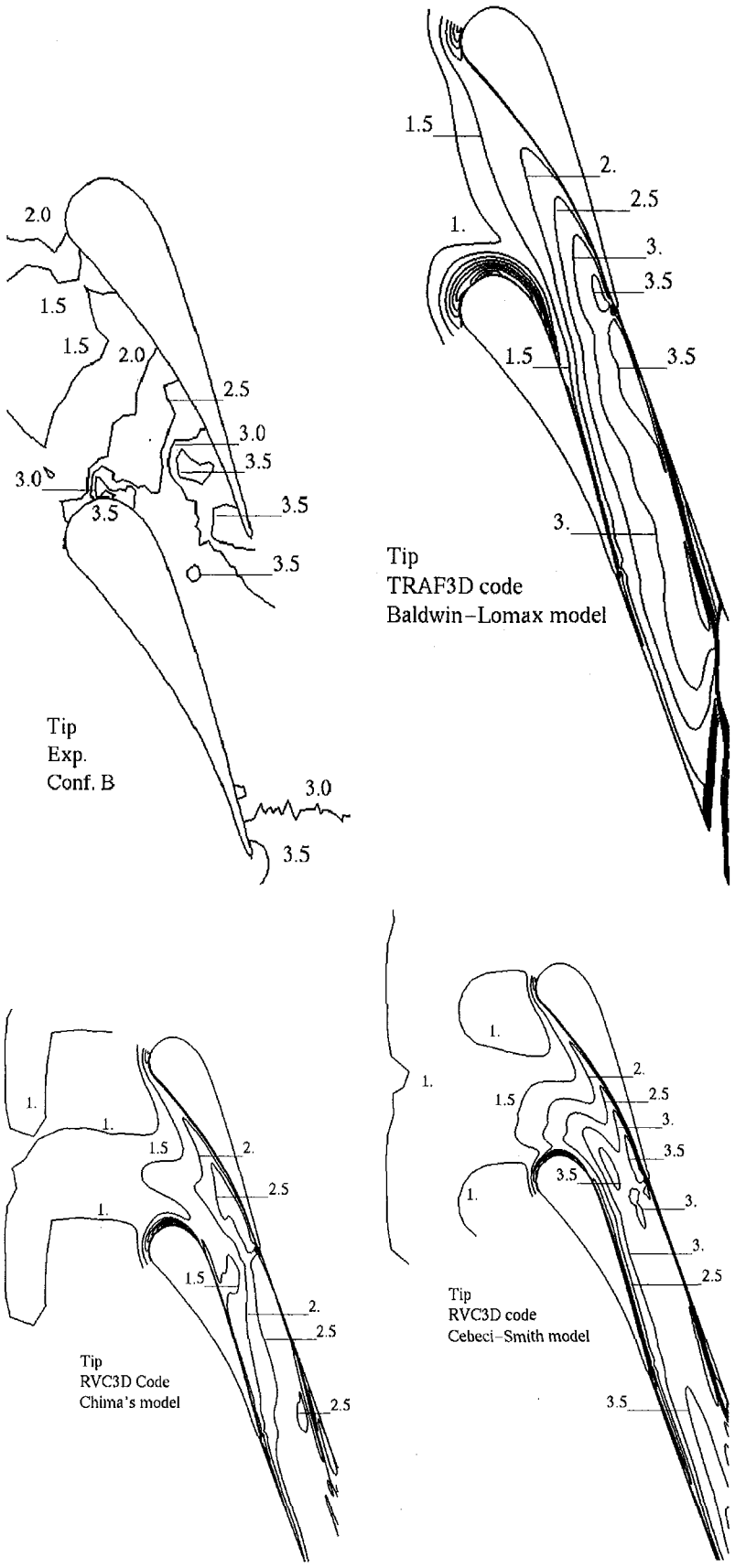

Fig. 8 Continued

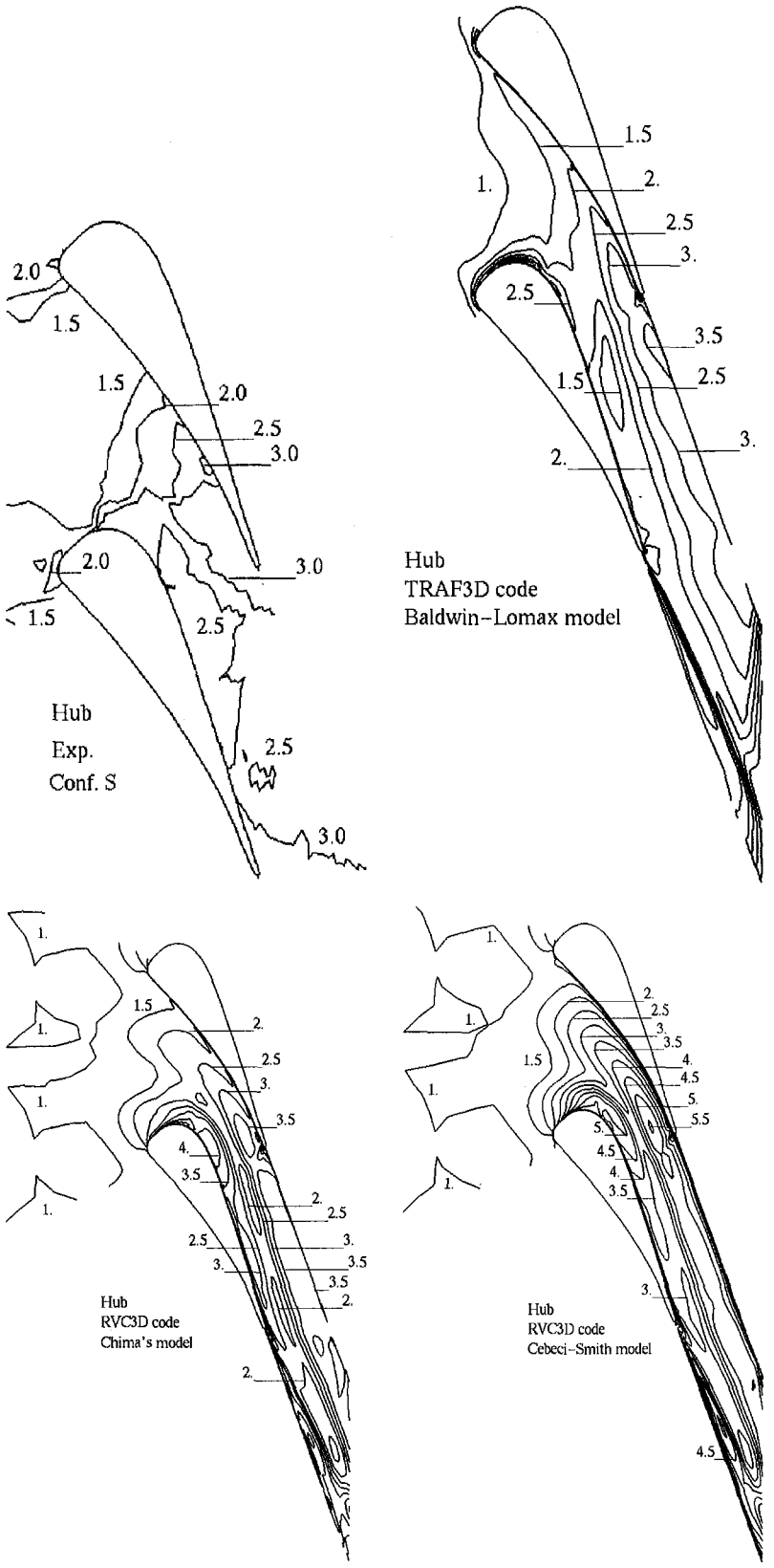

Fig. 9 Nu $\times$ 10^{-3} for configuration S

better agreement is partly is due to differences in the turbulence models, and partly due to the way in which μ_t is calculated. The summation used in the RVC3D code results in greater eddy viscosity in the corner region compared with approach taken in the TRAF3D code. Using the TRAF3D approach in the RVC3D code resulted in lower endwall heat transfer close to the suction surface.

In an overall sense, the Cebeci–Smith turbulence model tends to overpredict the endwall heat transfer, but to be in reasonably good agreement with the data. The Baldwin–Lomax results

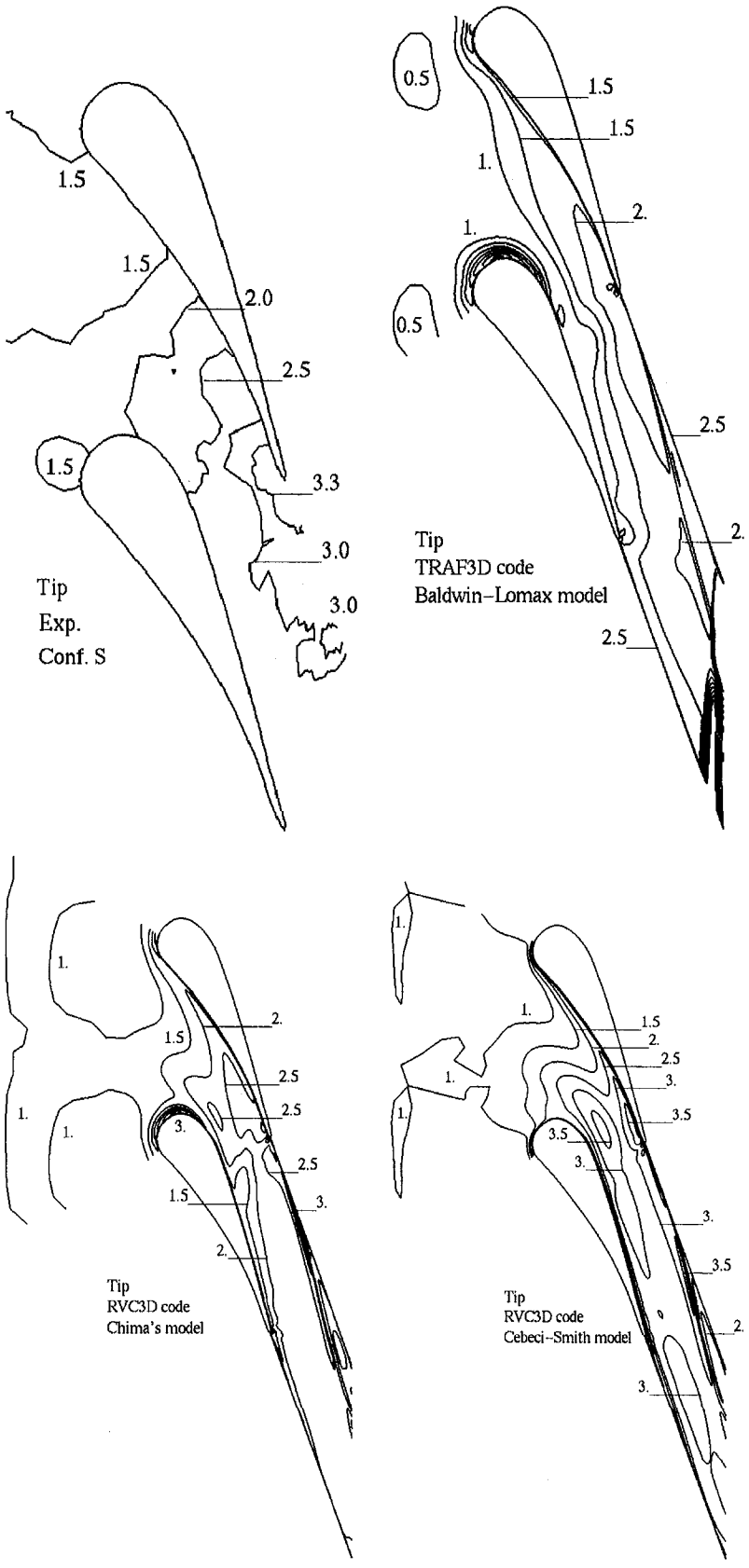

Fig. 9 Continued

underpredict the heat transfer in the region near the suction surface, but agree reasonably well with the data elsewhere. Chima's model underpredicts the heat transfer. This is especially true for the maximum heat transfer in the throat region.

Total Pressure Distribution. Figure 10 compares the total pressure distributions at 0.20 axial chords downstream of the trailing edge. Both computed results overpredict the depth of the wake, but correctly predict the spanwise variation in the

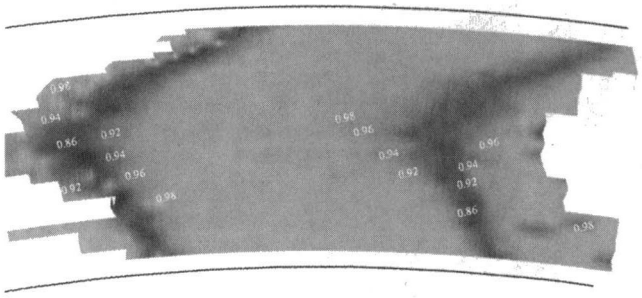

Fig. 10(*a*) Experimental data of Chana

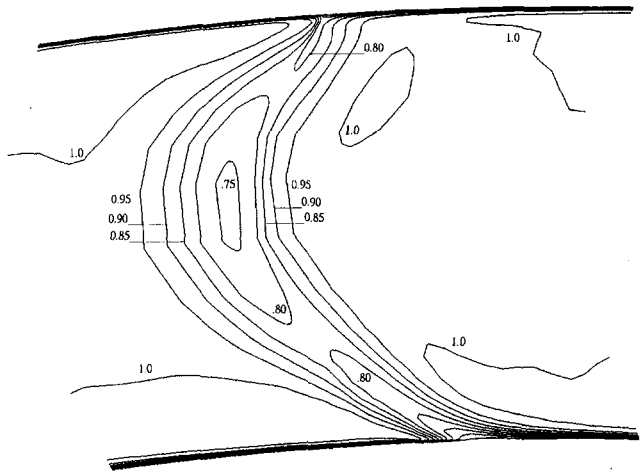

Fig. 10 (*b*) TRAF3D code, Baldwin-Lomax model

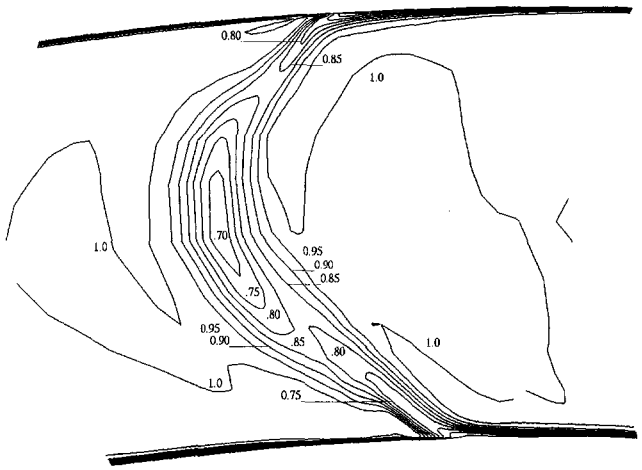

Fig. 10 (*c*) RVC3D code, Chima's model

Fig. 10 Total pressures $0.2c_x$ behind vane

wake characteristics. The wake is thickest, and has moved further in the tangential direction, near midspan. Near midspan the minimum experimental total pressure ratio was 0.84. The RVC3D results were very similar for either turbulence model, and had a minimum total pressure ratio of 0.67. The TRAF3D results had a minimum total pressure ratio of 0.74. The spanwise variation in the location of the minimum pressure shows that the parabolic variation in flow turning with span is well predicted. Also, both predictions are in agreement with the experimental data in that the wake is widest near midspan. The overprediction of the depth of the wake is consistent with the results shown by Boyle and Ameri (1997) in a two-dimensional analysis of the effects of grid topology on the aerodynamic and heat transfer characteristics of a high turning transonic vane. The tendency to overpredict the wake depth is not confined to the CFD methodologies used for this work. Results of the ASME compressor rotor test case for Rotor 37 (Strazisar, 1994) showed that many analyses overpredicted the wake depth for the transonic compressor rotor.

The analyses predict a wake that is both too narrow and too deep. These effects compensate to some degree, and the pitchwise-averaged total pressure downstream of the rotor is reasonably well predicted. This is illustrated in Fig. 11 where the spanwise variation in pitchwise-averaged total pressure is shown. Both the experimental data and predictions were area averaged in the blade-to-blade direction to obtain these results. The experimental data extend from 6 to 94 percent of span, and show very low loss regions near the endwalls. The maximum experimental loss occurs near midspan. Both predictions give too large a loss between the hub and midspan. The hub region is one of minimum static pressure, so that in the region between hub and midspan, overall loss is sensitive to shock losses.

Concluding Remarks

Heat transfer predictions were made using a finite difference (RVC3D) and a finite volume (TRAF3D) computer code for two vane geometries typical of actual engine applications. The test conditions of $M_2 = 1.2$, and $Re_2 = 5.6 \times 10^6$ provided a severe test of the code's computational capability. Convergence was heavily influenced by the choice of grid topology. The grid generation procedure described by Arnone et al. (1992) resulted in grids that gave satisfactory results for both codes. These grids were generated by embedding a near-wall grid. Primarily because of the required near-wall spacing of $1 \times 10^{-5}\ c_x$, it was found that using a nonmatching condition along the cut line was highly desirable in terms of obtaining converged solutions.

Solutions obtained with both codes converged in approximately the same number of CPU hours. Typically, the grids used were 560,000 points, and the solution was obtained in two hours on a Cray C90 computer.

As expected, the surface pressure distribution converged more rapidly than the surface heat transfer. Since the solution was stopped only after the heat transfer distributions were seen not to change over a large number of iterations, the actual convergence for either code may have taken somewhat less than two hours.

Both computational analyses correctly predicted the spanwise variation in vane surface pressures, and the endwall static pressures for both experimental configurations. Best agreement with the data was achieved when the predicted exit static pressure was matched to the measured tip value. There was a larger

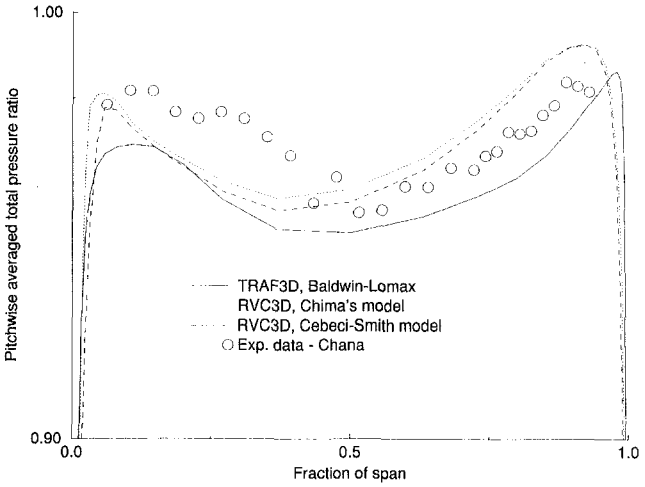

Fig. 11 Spanwise total pressure variation

pitchwise static pressure variation at the hub than at the tip. To minimize uncertainty, measured tip, rather than hub, values should be used for exit boundary pressures.

Blade heat transfer predictions agreed reasonably well with the data for the pressure side of either vane for all turbulence model assumptions. On the suction surface of the blade Chima's turbulence model produced results that agreed best with the data. This was independent of the choice of the transition model. The location of transition on the suction surface using Mayle's model was bounded by the choice of local *Tu* used in the model. Assuming constant *Tu* resulted in early transition, and assuming the fluctuation constant resulted in transition too far aft on the vane suction surface.

Differences in predicted endwall heat transfer among the different turbulence models were greater than the differences in experimental heat transfer between the two configurations. The results with the Cebeci–Smith turbulence model were in reasonably good agreement with the data, but tended to overpredict the peak heat transfer. The approach taken in the RVC3D code to determine μ_t in the corner region gave better agreement with the data compared to the approach taken in the TRAF3D code. There were significant heat transfer variations using the different turbulence models. Therefore, cases with significant variations in Reynolds number should be examined to determine if the degree of agreement with the data remains the same. This would increase the level of confidence in whichever turbulence model is used for predictions.

Both computer analyses correctly predicted the spanwise variation in the wake behind the vane. Both analyses predicted too low a value for the minimum total pressure in the wake region. This appeared to be due to underprediction of pitchwise mixing. The spanwise distribution of the pitchwise averaged total pressure was well predicted. The analyses and the data showed minimum total pressure loss close to both endwalls.

Acknowledgments

Contributions to the resourcing of this work were made by the National Aeronautics and Space Administration and by the United Kingdom's Ministry of Defence and the Department of Trade and Industry.

References

Ameri, A. A., and Arnone, A., 1992, "Navier–Stokes Heat Transfer Predictions Using Two-Equation Turbulent Closures," Paper No. AIAA-92-3067.

Ameri, A. A., and Arnone, A., 1994, "Prediction of Turbine Blade Passage Heat Transfer Using a Zero and a Two-Equation Turbulent Model," ASME Paper No. 94-GT-122.

Arnone, A., Liou, M.-S., and Povinelli, L. A., 1992, "Navier–Stokes Solution of Transonic Cascade Flows Using Non-periodic C-Type Grids," AIAA *Journal of Propulsion and Power*, Vol. 8, No.2, pp. 410–417.

Arts, T., Lambert de Rouvroit, M., and Rutherford, A. W., 1990, "Aero-Thermal Investigation of a Highly Loaded Transonic Linear Turbine Guide Vane Cascade," von Karman Institute for Fluid Dynamics, Technical Note 174.

Arts, T., and Heider, R., 1994, "Aerodynamic and Thermal Performance of a Three Dimensional Annular Transonic Nozzle Guide Vane. Part I: Experimental Investigation," Paper No. AIAA-94-2929.

Baldwin, B. S., and Lomax, H., 1978, "Thin-Layer Approximation and Algebraic Model for Separated Turbulent Flows," Paper No. AIAA-78-257.

Blair, M. F., 1974, "An Experimental Study of Heat Transfer and Film Cooling in Large-Scale Turbine Endwalls," ASME *Journal of Heat Transfer*, Vol. 96, pp. 525–529.

Blair, M. F., 1994, "An Experimental Study of Heat Transfer in a Large-Scale Turbine Rotor Passage," ASME JOURNAL OF TURBOMACHINERY, Vol. 116, pp. 1–13.

Boyle, R. J., and Russell, L. M., 1990, "An Experimental Determination of Stator Endwall Heat Transfer," ASME JOURNAL OF TURBOMACHINERY, Vol. 112, pp. 547–558.

Boyle, R. J., and Giel, P.W., 1992, "Three-Dimensional Navier–Stokes Heat Transfer Predictions for Turbine Blade Rows," Paper No. AIAA-92-3068.

Boyle, R. J., and Ameri, A., 1997, "Grid Orthogonality Effects on Predicted Turbine Midspan Heat Transfer and Performance," ASME JOURNAL OF TURBOMACHINERY, Vol. 119, pp. 31–38.

Chana, K. S., 1992, "Heat Transfer and Aerodynamics of a High Rim Speed Turbine Nozzle Guide Vane With Profiles End Walls," ASME Paper No. 92-GT-243.

Cebeci, T., and Smith, A. M. O., 1974, *Analysis of Turbulent Boundary Layers*, Academic Press, New York.

Chima, R. V., 1987, "Explicit Multigrid Algorithm for Quasi-Three-Dimensional Flows in Turbomachinery," AIAA *Journal of Propulsion and Power*, Vol. 3, No. 5, pp. 397–405.

Chima, R. V., and Yokota, J. W., 1988, "Numerical Analysis of Three-Dimensional Viscous Internal Flows," AIAA Paper No. 88-3522; NASA TM-100878.

Chima, R. V., 1990, Private Communication.

Chima, R. V., 1991, "Viscous Three-Dimensional Calculations of Transonic Fan Performance," AGARD Propulsion and Energetics Symposium on Computational Fluid Mechanics for Propulsion, San Antonio, TX, May 27–31.

Chima, R. V., Giel, P. W., and Boyle, R. J., 1993, "An Algebraic Turbulence Model for Three-Dimensional Viscous Flows," AIAA Paper No. 93-0083; NASA TM-105931.

Choi, D., and Knight, C. J., 1988, "Computations of 3D Viscous Linear Cascade Flows," *AIAA Journal*, Vol. 26, No. 12, pp. 1477–1482.

Dunn, M. G., Kim, J., Civinskas, K. C., and Boyle, R. J., 1994, "Time-Averaged Heat Transfer and Pressure Measurements and Comparison With Prediction for a Two-Stage Turbine," ASME JOURNAL OF TURBOMACHINERY, Vol. 116, pp. 14–22.

Graziani, R. A., Blair, M. F., Taylor, R. J., and Mayle, R. E., 1980, "An Experimental Study of Endwall and Airfoil Surface Heat Transfer in a Large Scale Turbine Blade Cascade," ASME *Journal of Engineering for Power*, Vol. 102, No. 2, pp. 1–11.

Hah, C., 1989, "Numerical Study of Three-Dimensional Flow and Heat Transfer Near the Endwall of a Turbine Blade Row," AIAA Paper No. 89-1689.

Harasgama, S. P., and Wedlake, E. T., 1991, "Heat Transfer and Aerodynamics of a High Rim Speed Turbine Nozzle Guide Vane Tested in the RAE Isentropic Light Piston Cascade (ILPC)," ASME JOURNAL OF TURBOMACHINERY, Vol. 113, No. 4, pp. 384–391.

Heider, R. and Arts, T., 1994, "Aerodynamic and Thermal Performance of a Three Dimensional Annular Transonic Nozzle Guide Vane. Part II: Assessment of a 3D Navier–Stokes Solver," Paper No. AIAA-94-2930.

Kays, W. M., and Crawford, M. E., 1980, *Convective Heat and Mass Transfer*, McGraw-Hill, New York.

Kingcombe, R. C., Harasgama, S. P., Leversuch, N. P., and Wedlake, E. T., 1989, "Aerodynamic and Heat Transfer Measurements on Blading for a High Rim-Speed Transonic Turbine," ASME Paper No. 89-GT-228.

Mayle, R. E., 1991, "The Role of Laminar–Turbulent Transition in Gas Turbine Engines," ASME JOURNAL OF TURBOMACHINERY, Vol. 113, pp. 509–537.

Smith, M. C., and Kuethe, A. M., 1966, "Effects of Turbulence on Laminar Skin Friction and Heat Transfer," *Physics of Fluids*, Vol. 9, pp. 2337–2344.

Sorenson, R. L., 1980, "A Computer Program to Generate Two-Dimensional Grids About Airfoils and Other Shapes by the Use of Poisson's Equation," NASA TM 81198.

Strazisar, A. J., 1994, Private Communication.

York, R. E., Hylton, L.D., and Mihelc, M. S., 1984, "Experimental Endwall Heat Transfer and Aerodynamics in a Linear Vane Cascade," ASME *Journal of Engineering for Gas Turbines and Power*, Vol. 106, pp. 159–167.

Young, C. D, Han, J. C., Huang, Y., and River, R. B., 1992, "Influence of Jet-Grid Turbulence on Flat Plate Turbulent Boundary Layer Flow and Heat Transfer," ASME *Journal of Heat Transfer*, Vol. 96, pp. 525–529.

Simulation of Heat Transfer From Flow With High Free-Stream Turbulence to Turbine Blades

E. Fridman
College of Engineering,
The University of Toledo,
Toledo, OH 43612

The present investigation is devoted to one of the most difficult problems in the gas turbine industry: predicting the heat transfer to turbine blades. It is known that one of the important factors that affects heat transfer coefficients is a significant level of turbulence in the flow that surrounds a turbine blade. The influence of free-stream turbulence on heat transfer coefficients for a flat plate boundary layer with zero pressure gradient or in the vicinity of the stagnation point of a circular cylinder is investigated numerically. An algebraic relaxation-length model of turbulence is applied in order to simulate real situations in flows with a high level of free-stream turbulence. The results, temperature and velocity profiles, and heat transfer and drag coefficients, are compared with available experimental data. The proposed method is recommended for practical calculations of heat transfer coefficients on turbine blades.

Introduction

It is known that one of the important factors that affect heat transfer to turbine blades is a significant level of gas stream turbulence. Even though a number of studies, both experimental and theoretical, have been devoted to the investigation and prediction of the influence of free-stream turbulence on heat transfer and friction coefficients, still there is no general prediction correlation or solution for this problem.

A large body of experimental data has been accumulated for flow patterns that typically take place near a turbine blade. These patterns are the flow near the forward stagnation point of a blunt body and the flow along a flat plate. The data obtained by Kestin (1966), Sikmanovic et al. (1974), Dyban et al. (1975), O'Brien and VanFossen (1985), Mehendale et al. (1991), and many others show a significant increase of the heat transfer coefficients in the vicinity of the forward stagnation point of a circular cylinder. Even though the quantitative results differ, the qualitative conclusions about the increase in heat transfer over the low free-stream turbulence case are consistent.

With regard to flow patterns along a flat plate with and without pressure gradient, the researchers' opinions have been divided as to whether free-stream turbulence has any effect on the laminar and turbulent boundary layers. Thus Kestin (1966), Junkhan and Serovy (1967), and Consigny and Richards (1982) report no effect of free-stream turbulence on local heat transfer. They suggest that the free-stream turbulence only alters the location of the transition region, moving it to a lower Reynolds number. Another opinion is that there is a significant influence of free-stream turbulence on local heat transfer in the laminar boundary layer, which is supported by Smith and Kuethe (1966), Dyban and Epik (1985), as well as in the turbulent boundary layer, which is supported by Smith and Kuethe (1966), Dyban and Epik (1985), Charnay et al. (1976), Simonich and Bradshaw (1978), Pedisius et al. (1979), Blair (1983), and Maciejewski and Moffat (1992).

An early attempt to predict the influence of free-stream turbulence on the laminar boundary layer near the forward stagnation point of a circular cylinder was made by Smith and Kuethe (1966). Their approach was based on the Reynolds equations for averaged motion and the assumption that eddy viscosity is proportional to the longitudinal component of fluctuating velocity $\overline{u_\infty'^2}$ and the distance from the surface $\nu_T = C\sqrt{\overline{u_\infty'^2}}y$, where C is the constant defined from their experimental data.

This approach was further developed by authors who were using different closure models for the Reynolds-averaged equations. Miyazaki and Sparrow (1977) applied a relationship for the mixing length, modified for the case of the nonzero turbulent free stream. Traci and Wilcox (1975) employed the Saffman turbulence model and defined turbulent viscosity as $\nu_T = E/\sqrt{\omega}$, where E is the turbulent kinetic energy and ω is pseudo-vorticity. For functions E and ω, two more differential equations were solved. The two-equation $k-\epsilon$ model was applied by Wang et al. (1985) to account for the free-stream turbulence effect on heat transfer to turbine airfoils at low Reynolds numbers. McDonald and Kreskovsky (1974) considered the turbulent boundary layer on a flat plate. They were using the Bradshaw et al. (1967) turbulence model, which related $\overline{u'v'}$ to the energy of turbulent fluctuations, k. The influence of the free-stream turbulence was taken into account by modifying the equation $-\overline{u'v'} = ak$ into the equation $-\overline{u'v'} = a[k + f(y/\delta)k_\infty]$, where a is the structural coefficient and $f(y/\delta) = (1 - \cos \pi y/\delta)/2$. This modification allowed for a direct effect of free-stream turbulence upon the Reynolds stresses to be taken into account. The latter investigators, unlike the others, did a comparison of the predicted results with experimental data not only for heat transfer coefficients but also for velocity profiles. The modified relation for $\overline{u'v'}$ that was used in these calculations allowed them to obtain velocity profiles that are typical for a turbulent boundary layer with nonzero free-stream turbulence. This became possible because the relation for $\overline{u'v'}$ accounted for nonzero Reynolds stresses in the region close to the outer edge of the boundary layer with nonzero free-stream turbulence. The Boussinesq hypothesis that was employed in the rest of the investigations mentioned above did not allow for such results.

In the present study, the relaxation model of turbulence (Dyban and Fridman, 1987) is applied in order to simulate laminar, transitional, and turbulent flows with nonzero free stream turbulence. Flows in the vicinity of the stagnation point of a circular

Contributed by the International Gas Turbine Institute and presented at the ASME Cogen-Turbo, Vienna, Austria, August 23–25, 1995. Manuscript received by the International Gas Turbine Institute May 19, 1995. Paper No. 95-CTP-4. Associate Technical Editor: C. J. Russo.

cylinder and flows along a flat plate were considered. A comparison of the results of calculations with corresponding experimental data was performed for heat transfer and friction coefficients, as well as for temperature and velocity profiles.

Relaxation Model

The calculation method described in the present study is based on the Reynolds-averaged equations of motion and energy:

$$\frac{\partial u}{\partial x} + \frac{\partial v}{\partial y} = 0$$

$$u\frac{du}{dx} + v\frac{du}{dy} = -\frac{1}{\rho}\frac{\partial \tau_{ef}}{\partial y} - \frac{1}{\rho}\frac{dP}{dx}$$

$$u\frac{\partial T}{\partial x} + v\frac{\partial T}{\partial y} = -\frac{1}{\rho c_p}\frac{\partial q_{ef}}{\partial y} \qquad (1)$$

with the boundary conditions

$$u = v = 0,\ T = T_w \quad \text{when} \quad y = 0$$

$$u \to U(x),\ T \to T_\infty \quad \text{when} \quad y \to \infty. \qquad (2)$$

The system of equations (1) with the boundary conditions (2) gives the solution for both laminar (or as we call it "pseudolaminar") and turbulent boundary layers when the free stream contains turbulent fluctuations. A "pseudolaminar" boundary layer is a flow that contains characteristics of both laminar flow (the Reynolds number is below the transition Reynolds number) and turbulent flow (the momentum and heat transfer processes occur more intensively than in classical Blausius laminar flow).

The system (1)–(2) contains unknown effective shear stresses τ_{ef} and effective heat flux q_{ef} that are defined by the formulas

$$\tau_{ef} = \tau + \tau_T = \tau - \rho\overline{u'v'} \qquad (3)$$

$$q_{ef} = q + q_T = q - \rho c_p \overline{v'T'}. \qquad (4)$$

In order to define unknown turbulent shear stresses $\tau_T = -\rho\overline{u'v'}$, the Boussinesq hypothesis is usually employed

$$-\overline{u'v'} = \nu_T \frac{\partial u}{\partial y} = (\nu_{ef} - \nu)\frac{\partial u}{\partial y}. \qquad (5)$$

It is known that Eq. (5) does not work for flow patterns where the time-averaged product of velocity fluctuations $\overline{u'v'}$ and gradient velocity $\partial u/\partial y$ do not simultaneously approach zero. As Fig. 1 shows, this situation takes place at the outer edge of the boundary layer when the level of turbulence in the free stream is significant. Indeed, when $y = \delta$, the value of $|\overline{u'v'}|$ differs noticeably from zero, and this difference increases with the increasing of the level of free-stream turbulence. At the same time, the velocity gradient is practically equal to zero in the region close to the outer edge of the boundary layer. As numerical experiments have shown (Fridman, 1989), this was the reason the predicted velocity and temperature profiles obtained with the Boussinesq hypothesis did not follow the experimental data in the wake region.

The velocity profile in a turbulent boundary layer can be presented as (Kader and Yaglom, 1980):

$$u^+ = \frac{1}{K}\ln y^+ + C + \frac{\Pi_0}{K}\omega_0, \qquad (6)$$

where the following values for constants $K = 0.4$, $C = 5.1$, and $\Pi_0 \sim 0.5$, and for wake function $\omega_0 = 2[3(y/\delta)^2 - 2(y/\delta)^3]$ in the fully developed turbulent boundary layer are recommended.

Experiments have shown (Blair, 1983; Maciejewski and Moffat, 1992) that under the influence of the free-stream turbulence, parameter Π_0 decreases and in some cases becomes negative. As was mentioned above, this fact is impossible to simulate using the Boussinesq hypothesis for turbulent stresses. Figure 2 presents the comparison of the predicted velocity profiles obtained with the Boussinesq hypothesis and with the relaxation model of turbulence used as closures for the Reynolds-averaged equations (1). As one can see, the profiles obtained with Boussinesq hypothesis fail to simulate effect of the free-stream turbulence on the wake component of the boundary layer. A similar situation exists for the temperature profiles. This is one of the reasons the present investigation employs the relaxation model

Nomenclature

$a = k/\rho c_p$ = thermal diffusivity
c_f = skin friction coefficient
c_p = fluid specific heat
$E = (u'^2 + v'^2 + w'^2)/2\ k = 2*E$ = turbulent kinetic energy
l = mixing length
L_x, L_y = relaxation scales in longitudinal and transverse directions
$L_{x\theta}$, $L_{y\theta}$ = thermal relaxation scales in longitudinal and transverse directions
Nu_D = Nusselt number based on cylinder diameter
Pr = Prandtl number
Pr_T = turbulent Prandtl number
q = heat flux
Re_D = Reynolds number based on cylinder diameter
Re** = Reynolds number based on momentum thickness
$R_T = \nu_T/\nu$ = turbulent Reynolds number
Re_θ^{**} = Reynolds number based on enthalpy thickness
Re_x = Reynolds number based on plate location
St = Stanton number
T = mean temperature
T' = temperature fluctuation
Tu = ratio of rms velocity fluctuation to mean value
$u^+ = u/u_*$ = mean velocity scaled on inner variables
u_* = friction velocity
U = mean convective velocity
u, v = longitudinal and transverse components of mean velocity
u', v' = longitudinal and transverse components of turbulent velocity
x, y = Cartesian coordinates
$y^+ = yu_*/\nu$ = dimensionless distance from the wall
δ = momentum boundary layer thickness
δ^* = displacement thickness
δ_θ = thermal boundary layer thickness
ϵ = kinetic energy dissipation rate
ν = viscosity
ρ = fluid density
τ = shear stresses
ω_0, ω_θ = wake functions for velocity and temperature profiles
K = empirical constant, $l = Ky$
$\Theta = (T_w - T)/(T_w - T_\infty)$-dimensionless temperature
$\Theta+ = \Theta/\Theta_* = q_w/\rho c_p u_*(T_w - T_\infty)$-dimensionless temperature scaled on inner variables

Subscripts

ef = effective
T = turbulent
tr = transition point
w = wall
δ = outer edge of boundary layer
θ = thermal boundary layer
0 = zero free-stream turbulence
∞ = free stream

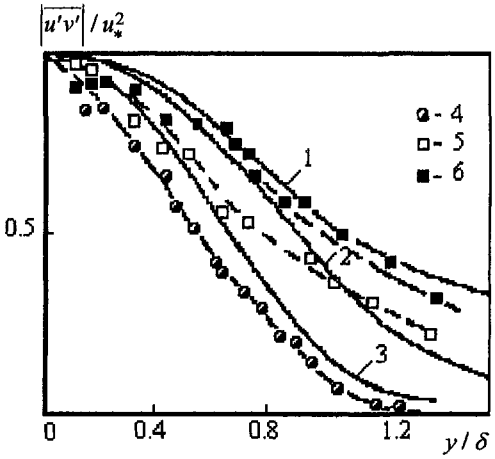

Fig. 1 Turbulent shear stresses in the presence of free-stream turbulence; present calculations: 1— $\nu_{T_\delta}/\nu_{T_0} = 10$; 2–5; 3–1 ($Tu_\infty = 0$); experiment (Dyban and Epik, 1985): 4— $\nu_{T_\delta}/\nu_{T_0} = 1$; 5–3.6; 6–13.6

of turbulence and does not employ the Boussinesq equation for turbulent stresses.

Another reason is that it has been shown (Hinze, 1976) that in turbulent flow, memory effects can be significant. To account for memory effects, Hinze (1976) represents turbulent stresses with two parts: The first one is defined by the local gradients of averaged motion (Boussinesq hypothesis), and the second one is characterized by memory effects and described in terms of local gradients:

$$-\overline{u'v'} = (\nu_{ef} - \nu)\frac{\partial u}{\partial y} + L_x\frac{\partial \overline{u'v'}}{\partial x} + L_y\frac{\partial \overline{u'v'}}{\partial y} \qquad (7)$$

The larger the scale of turbulent motion and the more uniform the velocity field ($\partial u/\partial y \to 0$), the more pronounced will be the memory effects.

The main idea of the proposed method is that, instead of the Boussinesq hypothesis, it uses relaxation equation (7) for turbulent stresses in order to simulate real situations that take place in the boundary layer, which has nonzero free-stream turbulence.

Similarly, for turbulent heat flux:

$$-\overline{v'T'} = \rho(a_{ef} - a)\frac{\partial T}{\partial y} + L_{x_\theta}\frac{\partial \overline{v'T'}}{\partial x} + L_{y_\theta}\frac{\partial \overline{v'T'}}{\partial y}. \qquad (8)$$

The present model is a continuation of the approach that is proposed by Dyban and Epik (1985). In accordance with this approach, the effective coefficient of momentum transfer in the free stream is defined by an existing relations, for example:

$$\nu_T = 0.1125\frac{E^2}{\epsilon}.$$

Then for the boundary layer, the coefficients of heat and momentum transfer are defined as

$$\nu_{ef} = \nu + \nu_T f(R_T) \qquad (9)$$

$$a_{ef} = \frac{\nu}{\mathrm{Pr}} + \frac{\nu_T}{\mathrm{Pr}_T} f(R_T), \qquad (10)$$

where $f(R_T) = (1 + 10.7/R_T)^{-1}$ is the modified Rotta damping function (Dyban and Epik, 1978) that depends on the local turbulent Reynolds number and accounts for the molecular transport in the near-wall region.

The main difficulty in using Eq. (7) is defining the longitudinal L_x and the transverse L_y relaxation scales. Loytsyanskiy (1982) applied the relaxation equation to a flow with a strong longitudinal pressure gradient. In this study, he interpreted the relaxation scales, L_x and L_y, as the Prandtl mixing lengths in the longitudinal and transverse directions, respectively. For longitudinal mixing length, the expression $L_x = ax$ was proposed while the transverse mixing length was assumed to be small in comparison with the longitudinal mixing length (strong longitudinal gradient); thus $L_y \approx 0$.

Following Loytsyanskiy (1982), the present study treats the relaxation scales as the mixing lengths and accounts for one preferable direction of the heat and momentum transfer. For a flat-plate boundary layer with zero pressure gradient and nonzero free-stream turbulence, the main direction of transfer is the transverse, y, direction. Therefore, unlike Loytsyanskiy (1982), the longitudinal relaxation scale is assumed to be negligible, $L_x \approx 0$, in comparison with the transverse one. For the transverse relaxation scale, L_y, the following expression is adopted (Dyban and Fridman, 1987):

$$L_y = l_\delta\left[1 - \exp\left(-5\left(\frac{y}{\delta}\right)^3\right)\right]. \qquad (11)$$

The function (11) coincides with the mixing length in the outer part of the boundary layer, which decreases with decreasing distance from the wall, due to the reduction of the relaxation effect in the near-wall region.

The mixing length is defined by the formula (Dyban and Epik, 1985)

$$l_\delta = \delta\left(0.08 + 0.042\left(\frac{\nu_{T_\delta}}{\nu_{T_0}}\right)^{0.8}\right), \qquad (12)$$

that is obtained by summarizing the corresponding experimental data.

Then Eqs. (7) and (8) combine to become:

$$-\overline{u'v'} = (\nu_{ef} - \nu)\frac{\partial u}{\partial y} + L_y\frac{\partial \overline{u'v'}}{\partial y} \qquad (13)$$

and

$$-\overline{v'T'} = (a_{ef} - a)\frac{\partial T}{\partial y} + L_{y_\theta}\frac{\partial \overline{v'T'}}{\partial y}, \qquad (14)$$

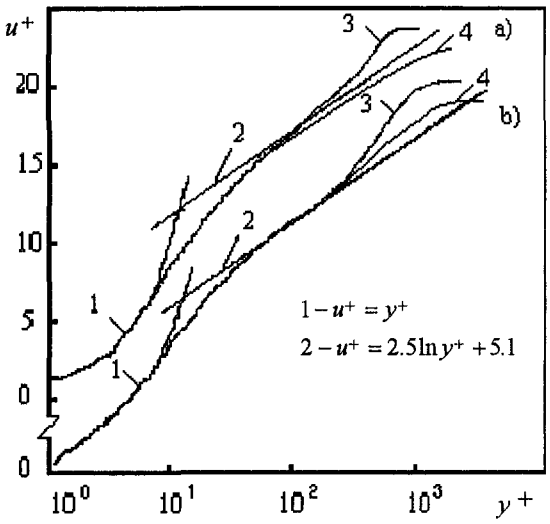

Fig. 2 The velocity profiles predictions; 3—the Boussinesq hypothesis; 4—the relaxation model; $\nu_{T_\delta}/\nu_{T_0} = 10$; (*a*) Re = 1500; (*b*) Re** = 3000**

where the thermal relaxation scale in the transverse direction, L_{y_θ}, is defined by relations similar to the Eqs. (11) and (12):

$$L_{y_\theta} = \delta_\theta \left[0.08 + 0.042 \left(\frac{\nu_{T_\delta}}{\nu_{T_0}} \right)^{0.8} \right] \times \left[1 - \exp\left(-5 \left(\frac{y}{\delta_\theta} \right)^3 \right) \right]. \quad (15)$$

The eddy viscosity that is defined by Eq. (9) can be represented as:

$$\frac{\nu_{ef}}{\nu} = 1 + \frac{\nu_{ef_\delta} - \nu}{\nu} F\left(\frac{y}{\delta} \right), \quad (16)$$

where $F(y/\delta) = (\nu_{ef} - \nu)/(\nu_{ef_\delta} - \nu)$, the function that describes the eddy viscosity inside the boundary layer, is given by:

$$F\left(\frac{y}{\delta} \right) = \frac{y}{\delta} \left(2 - \frac{y}{\delta} \right) \left[1 + 2 \left(1 - \frac{y}{\delta} \right)^2 \right] \times \left[1 - \exp\left(- \frac{y^+}{a} \right) \right]^3 \quad (17)$$

Thus, the effective eddy viscosity for a "pseudolaminar" boundary layer can be presented as:

$$\left(\frac{\nu_{ef}}{\nu} \right)_{LBL} = 1 + \frac{\nu_{T_\delta}}{\nu} f(R_{T_\delta}) F\left(\frac{y}{\delta} \right). \quad (18)$$

In a turbulent boundary layer, the free-stream turbulence does not always cause the turbulent viscosity to increase. As experiments show (Dyban and Epik, 1985), intensification of the heat and momentum transfer takes place in cases where the value of turbulent viscosity in the free stream, ν_{T_δ}, is larger than ν_{T_0} (the value of turbulent viscosity in a turbulent boundary layer for which free-stream turbulence is zero). The turbulent viscosity, ν_{T_0}, is defined by one of the well-known formulas:

$$\nu_{T_0} = 0.0165 U \delta^* \quad \text{or} \quad \nu_{T_0} = 0.065 u_* \delta. \quad (19)$$

Figure 3 presents the experimental functions for turbulent viscosity at different values of parameter ν_{T_δ}/ν_{T_0}. As one can see, the turbulent viscosity in the near-wall region scales on $u_* \delta$. The main change in this turbulent viscosity behavior occurs in the outer part of the boundary layer. Therefore, turbulent viscosity inside the boundary layer is described as the sum of two functions, one for the near-wall region and the other for the rest of the boundary layer:

$$\left(\frac{\nu_{ef}}{\nu} \right)_{TBL} = 1 + \frac{\nu_{T_0}}{\nu} F\left(\frac{y}{\delta} \right) \times \left\{ f(\mathrm{Re}_{T_0}) + c \left(\frac{\nu_{T_\delta}}{\nu_{T_0}} - 1 \right) f(\mathrm{Re}_{T_\delta}) \frac{\left[1 - \exp\left(-b \frac{y}{\delta} \right) \right]^3}{\left[1 - \exp\left(- \frac{y^+}{a} \right) \right]^3} \right\} \quad (20)$$

In order to describe the flow pattern in the transition region, the function of the longitudinal intermittency (Loytsyanskiy, 1970) is used:

$$\gamma = 1 - \exp\left[-0.1 \left(\frac{\mathrm{Re}^{**}}{\mathrm{Re}^{**}_{tr}} \right)^6 \right], \quad (21)$$

where the Reynolds number that corresponds to the point of the transition Re^{**}_{tr} is defined by the empirical relation (Suprun, 1988):

$$\mathrm{Re}^{**}_{tr} = 163[1 + \exp(1.816 - Tu\%)] \exp\left[\frac{(\mathrm{Re}_{ef_\delta} - 1)^{0.3}}{7} \right] \times [1 + 0.175(\mathrm{Re}_{ef_\delta} - 1)^{0.3}] \quad (22)$$

When the flow approaches the transition region, the Reynolds number Re** approaches the transition Reynolds number Re^{**}_{tr} and the function γ abruptly increases, modeling the laminar-to-turbulent transition process.

Finally, the turbulent viscosity for all flow conditions is defined as

$$\frac{\nu_{ef}}{\nu} = \left(\frac{\nu_{ef}}{\nu} \right)_{LBL} (1 - \gamma) + \left(\frac{\nu_{ef}}{\nu} \right)_{TBL} \gamma, \quad (23)$$

where $(\nu_{ef}/\nu)_{LBL}$ is given by Eq. (18) and $(\nu_{ef}/\nu)_{TBL}$ is given by Eq. (20). For flow patterns with undisturbed free stream ($Tu_\infty = 0$), Eq. (23) becomes

$$\nu_{ef} = \nu(1 - \gamma) + \left[\nu + \nu_{T_0} f(\mathrm{Re}_{T_0}) F\left(\frac{y}{\delta} \right) \right] \gamma, \quad (24)$$

which reflects the contribution of the molecular and eddy transfer processes in the transition region.

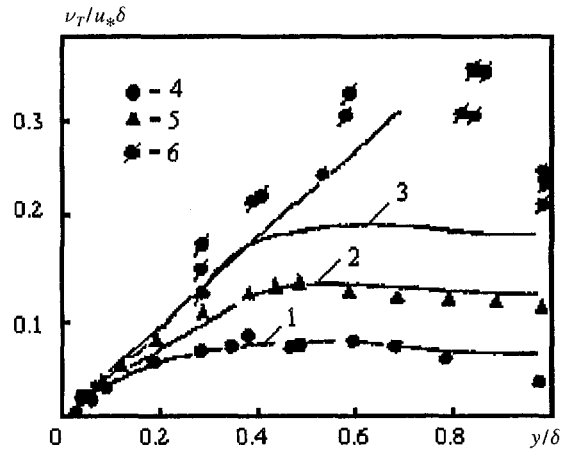

Fig. 3 Effective coefficient of turbulent viscosity in the turbulent boundary layer with nonzero stream turbulence; present calculations: 1—ν_{T_δ}/ν_{T_0} = 1; 2—5; 3—10; experiment (Dyban and Epik, 1985): 4—1; 5—3; 6—8.8

Numerical Procedure

The numerical solution of the system (1) has been carried out by the finite difference method with variables x, $\ln(1 + y/a_1\sqrt{x})$. Logarithmic transformation of the transverse coordinate provided a larger number of grid points in the near-wall region. Thus, there were a few grid points in the laminar sublayer. The Crank–Nicolson implicit scheme that was employed for finite-difference approximation of Eqs. (1) is usually considered unconditionally stable and has second-order accuracy $O(\Delta x)^2 + O(\Delta y)^2$. The solution of the discretization equations was obtained by TriDiagonal-Matrix Algorithm.

The system (1) was solved by iterations. The first iteration was the numerical solution of the equations (1) with the boundary conditions (2) and the Boussinesq hypothesis for turbulent stresses (5). Then the velocity and temperature profiles ob-

tained in the first iteration were used to define $\overline{u'v'}$ and $\overline{v'T'}$ from relaxation relations, Eqs. (13) and (14).

The boundary layer thickness obtained in the first iteration can be used to define new boundary conditions for $U(x)$ and $T(x)$ at the outer edge of the boundary layer. From the second (momentum) equation of the system (1) considered at the outer edge of the boundary layer ($\partial u/\partial y \to 0$) and Eq. (13), one can get:

$$U\frac{dU}{dx} = -\frac{1}{\rho}\frac{dP}{dx} + \frac{\partial}{\partial y}\left(L_y\frac{\partial\overline{u'v'}}{\partial y}\right)_{y=\delta}. \quad (25)$$

Then, for flow along a flat plate, $dP/dx = 0$, after integrating Eq. (25), the velocity distribution became

$$U(x) = \left[2\int_0^x \frac{\partial}{\partial y}\left(L_y\frac{\partial\overline{u'v'}}{\partial y}\right)_{y=\delta} dx + U_\infty^2\right]^{0.5}. \quad (26)$$

Similarly, the temperature distribution can be obtained from the third (energy) equation of the system (1) and Eq. (14):

$$T(x) = \int_{x_0}^x \frac{1}{U(x)}\frac{\partial}{\partial y}\left(L_{y_\theta}\frac{\partial\overline{v'T'}}{\partial y}\right)_{y=\delta} dx + T(x_0) \quad (27)$$

Equations (26) and (27) show that the boundary conditions for free stream $u = U_\infty$ and $T = T_\infty$ will not be satisfied at the outer edge of the boundary layer, $y = \delta$, where δ obtained in the first iteration by using the Boussinesq hypothesis. It also follows from Eqs. (26) and (27) that for flow patterns with high levels of free-stream turbulence it is impossible to define the correct value for boundary layer thickness by using the Boussinesq hypothesis. In the present investigation the value for boundary layer thickness was obtained in the second and improved in the following iterations.

Iterations were repeated until the magnitude of errors for $|\overline{u'v'}|/u_*^2$ approached ± 1 percent from its max value, which corresponds to the absolute value of approximately ± 0.1 cm^2/s^2.

In order to test the described method, the simulations of the momentum and the thermal laminar, transitional, and turbulent boundary layers with zero free-stream turbulence were performed in a wide range of the Reynolds numbers $Re_x = 9 \times 10^4 \div 2 \times 10^7$. The results of calculations for the temperature and velocity profiles, heat transfer and friction coefficients, and the thicknesses of the boundary layers are in agreement with available experimental data and corresponding theoretical relations (Dyban and Fridman, 1987).

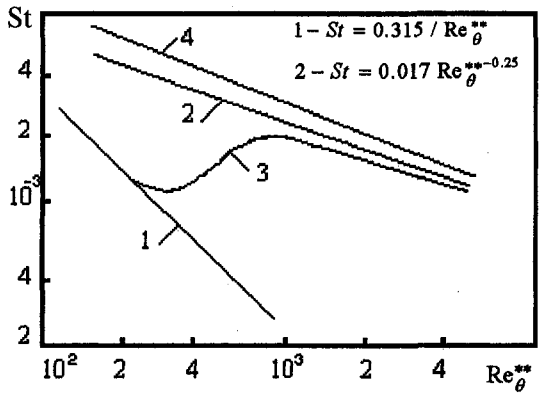

Fig. 4 Variation of the Stanton number in laminar (1), turbulent (2), transitional (3) boundary layers with zero free-stream turbulence and in turbulent boundary layer with nonzero free stream turbulence (4—ν_{T_δ}/ν = 300)

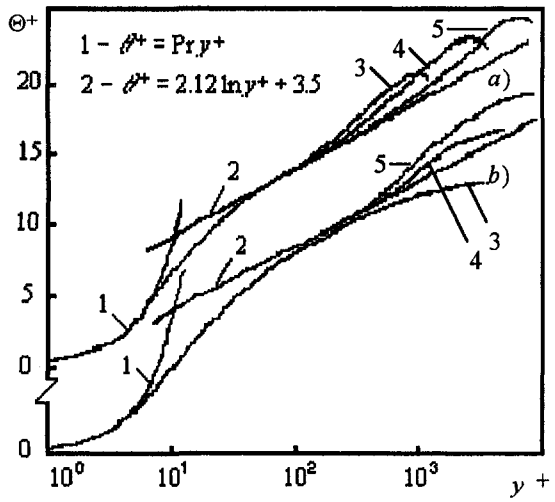

Fig. 5 Temperature profiles in the turbulent boundary layer (*a*) zero and (*b*) nonzero free-stream turbulence; 3—Re** = 2000; ν_{T_δ}/ν_{T_0} = 10; 4—4000; 5.5; 5—10,000; 1.3

Results and Discussions

Turbulent Boundary Layer (Flat Plate). The results of calculations of the Stanton number on a flat plate with respect to the Reynolds number Re_θ^{**} are presented in Fig. 4. As one can see, the results for laminar and turbulent boundary layers with zero free-stream turbulence (Fig. 4, lines 1 and 2) follow well-known relations (Kutateladze and Leontiev, 1990) for laminar and turbulent boundary layers, respectively:

$$St = \frac{0.2205}{Re_\Theta^{**}Pr}$$

$$St = 0.0128\ Pr^{-0.75}(Re_\Theta^{**})^{-0.25}.$$

(all calculations were performed for air Pr = 0.7 and Pr_T = 0.85).

When a free stream contains turbulent fluctuations, enhancement of heat transfer takes place and the transition point moves to the lower Reynolds numbers (Fig. 4, line 3, $Re_{tr}^{**} = 200$). The heat transfer enhancement over the zero free-stream turbulence case is about ~35 percent when parameter $\nu_{T_\delta}/\nu_{T_0} = 10$ (Fig. 4, line 4).

Figure 5 represents temperature profiles for different values of Reynolds number. A temperature profile in the turbulent boundary layer could be described in a similar way as the velocity profile

$$\Theta^+ = Pry^+; \quad \Theta^+ = \frac{1}{K_\theta}\ln y^+ + C_\theta + \frac{\Pi_\theta}{K_\theta}\omega_\theta, \quad (28)$$

where, according to the Kader and Yaglom (1980) recommendations, $K_\theta = K/Pr_T = 0.47$, $Pr_T = 0.85$, $C_\theta = 3.5$; $\Pi_\theta \sim 0.3$ (Cebeci and Bradshaw, 1984).

Under the influence of free-stream turbulence, the temperature profile changes in such a way that profile parameter Π_θ decreases and in some cases even becomes negative (Fig. 5, profile 3(*b*)).

Figure 6 shows the intensification of the heat and momentum transfer under the influence of free-stream turbulence. The friction coefficient and Stanton number both increase with the parameter ν_{T_δ}/ν_{T_0}, which corresponds to the level of turbulence in the free stream. The heat transfer process is more affected by the free-stream turbulence than is momentum transfer (Fig. 6). The latter leads to the violation of the Reynolds analogy and to the growth of the ratio $2St/c_f$. This result is in agreement

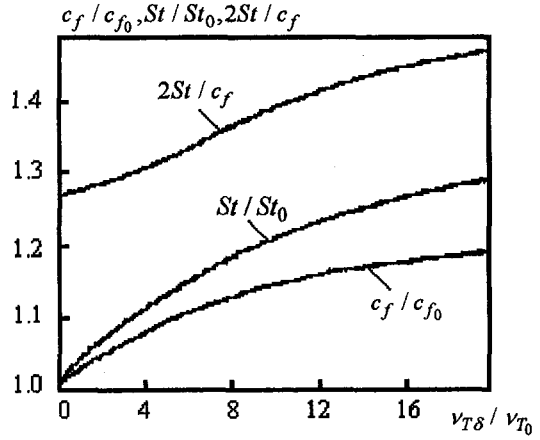

Fig. 6 Enhancement of the transfer processes under the influence of the free-stream turbulence in the flat-plate turbulent boundary layer

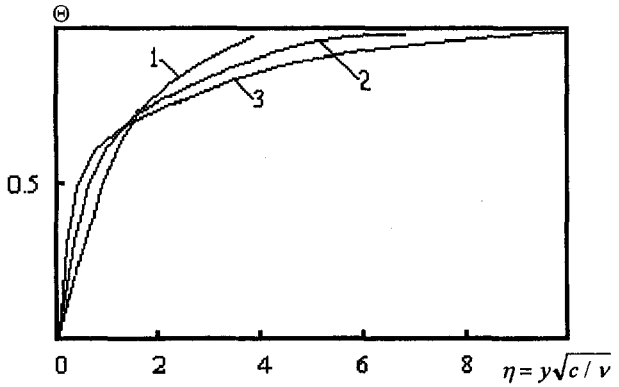

Fig. 8 Temperature profiles in the vicinity of the forward stagnation point of the circular cylinder: $Re_D = 2 \times 10^4$; 1—$Re_{ef_\delta} = 1$; 2—5.1; 3—17.9

with experimental data obtained by Dyban and Epik (1985), and qualitatively corresponds with the experimental data obtained by Maciejewski and Moffat (1992).

There is another flow pattern that can be modeled by the proposed approach. For the plate with an unheated starting length, the thermal boundary layer develops inside the momentum boundary layer. For such a thermal boundary layer, there are turbulent fluctuations in the free stream and, therefore, there is turbulent heat flux q_{ef_δ} at the outer boundary of the layer. This situation is similar to the one that occurs when a turbulent boundary layer with free-stream turbulence develops along a flat plate without an unheated starting length.

"Pseudolaminar" Boundary Layer (Flat Plate, Forward Stagnation Point of a Circular Cylinder). The free-stream turbulence changes the laminar boundary layer in such a way that velocity and temperature gradients increase in the near wall region. Due to these changes, the heat transfer and friction coefficients increase in the "pseudolaminar" boundary layer (laminar boundary layer with nonzero free-stream turbulence). Figure 7 presents the results of the simulation of the Stanton number at different levels of free-stream turbulence along a flat plate. The results of calculations show that the intensification of the heat transfer increases as the flow moves closer to the transition region. The effective Reynolds number

$$\mathrm{Re}_{ef_\delta} = 1 + \frac{\nu_{T_\delta}}{\nu} f(\mathrm{Re}_{T_\delta}) \tag{29}$$

represents the level of the turbulence in the free stream (Dyban and Epik, 1978).

Under the influence of the free-stream turbulence, not only do velocity and temperature gradients increase, but the thicknesses of the momentum and thermal boundary layers increase as well. Because of these changes, the velocity and temperature profiles are different in the "pseudolaminar" boundary layer. Figure 8 shows the changes of the temperature profiles under the influence of the free-stream turbulence near the stagnation point of a circular cylinder. As one can see, the principle of similarity of temperature profiles is not valid in the "pseudolaminar" boundary layer. The last conclusion applies to the velocity profiles as well.

Figure 9 presents the calculations results and the experimental data for the heat transfer coefficients near the stagnation point of a circular cylinder at different levels of turbulence. Calculations were performed for Reynolds number $10^3 \le \mathrm{Re}_D \le 2*10^4$

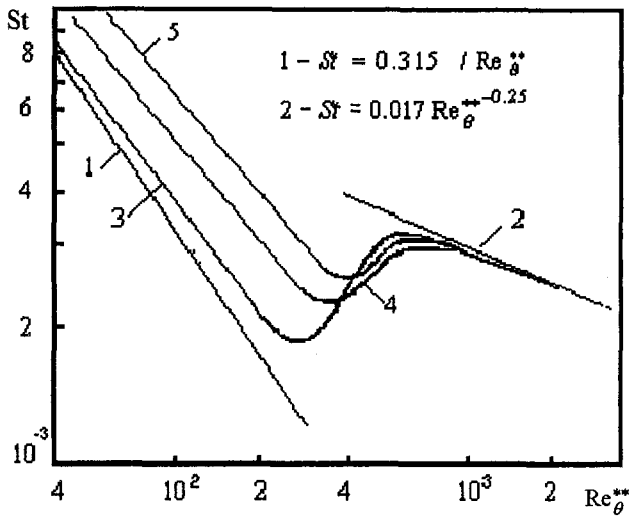

Fig. 7 Variation of the Stanton number in a "pseudolaminar" boundary layer along a flat plate: 3—$Re_{ef_\delta} = 1.5$; 4—3; 5—6

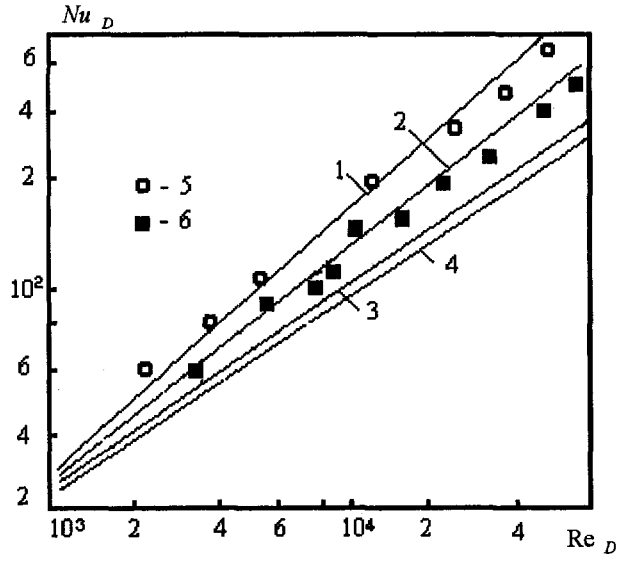

Fig. 9 The influence of the free-stream turbulence on heat transfer in the vicinity of the forward stagnation point of the circular cylinder; present calculations: 1—Tu_∞ = 23 percent; 2—12.2 percent; 3—6.7 percent; 4—1.5 percent; experiment (Dyban et al., 1975); 5—Tu_∞ = 23 percent; 6—12.2 percent

and the free-stream turbulence level $0 \le Tu_\infty \le 23$ percent, which corresponds to $1 \le \mathrm{Re}_{ef_\delta} \le 18$. The results show that heat transfer enhancement increases with Re_D at a fixed value of Tu_∞. Indeed, the exponents n in equations such as $\mathrm{Nu}_D = k\,\mathrm{Re}_D^n$ turn out to be functions of the free-stream turbulence: The value of n increases from 0.5 at $Tu_\infty = 2.5$ percent to 0.7 at $Tu_\infty = 23$ percent.

The free-stream turbulence affects heat transfer more than it does friction. This effect shows up in the increasing of the Reynolds analogy coefficient $2\mathrm{St}/c_f$. From our calculations for the flow near the stagnation point of a circular cylinder the following approximation formula was derived:

$$\frac{2\mathrm{St}}{c_f} = \frac{2\mathrm{St}_0}{c_{f_0}}\{1 + 0.27\tanh[0.3\,(\mathrm{Re}_{ef_\delta} - 1)]\}, \quad (30)$$

where $2\mathrm{St}_0/c_{f_0} = 2.057/\sqrt{\mathrm{Re}_x \mathrm{Pr}^{0.6}} = 0.573$ is determined for the nonturbulent air flow (Cebeci and Bradshaw, 1984). Equation (30) could be also rearranged as

$$\frac{\mathrm{St}}{\mathrm{St}_0} = \frac{c_f}{c_{f_0}}\{1 + 0.27\tanh[0.3(\mathrm{Re}_{ef_\delta} - 1)]\}. \quad (31)$$

The following expression correlates the enhancement of heat transfer in the "pseudolaminar" boundary layer on a flat plate and near the stagnation point of a circular cylinder over the range of $0 < \mathrm{Re}_{ef_\delta} < 1$

$$\frac{\mathrm{St}}{\mathrm{St}_0} = 1 + \frac{1 + 0.6m}{2}\varphi\left(\frac{\mathrm{Re}^{**}}{\mathrm{Re}^{**}_{tr}}\right) \times \{\tanh[0.075(\mathrm{Re}_{ef_\delta} - 1)]\}^{0.5}, \quad (32)$$

where $m = 0$ corresponds to the flow over a flat plate, and $m = 1$ to the flow near the stagnation point of a circular cylinder. The value of the function φ in Eq. (32) depends on the location of the point under consideration with respect to the transition point

$$\varphi\left(\frac{\mathrm{Re}^{**}}{\mathrm{Re}^{**}_{tr}}\right) = 1 + 1.5\left(\frac{\mathrm{Re}^{**}}{\mathrm{Re}^{**}_{tr}}\right). \quad (33)$$

As experiment has shown (Dyban and Epik, 1985), in the case of the flow in the vicinity of the stagnation point of a circular cylinder ratio $\mathrm{Re}_{**}/\mathrm{Re}^{**}_{tr} \approx 0.05 \div 0.01$, where $\mathrm{Re}^{**}_{tr} = 3200$. Thus for this case the function given by Eq. (33) is virtually equal to unity.

Figure 10 represents the comparison of the derived Eq. (32) with corresponding experimental data.

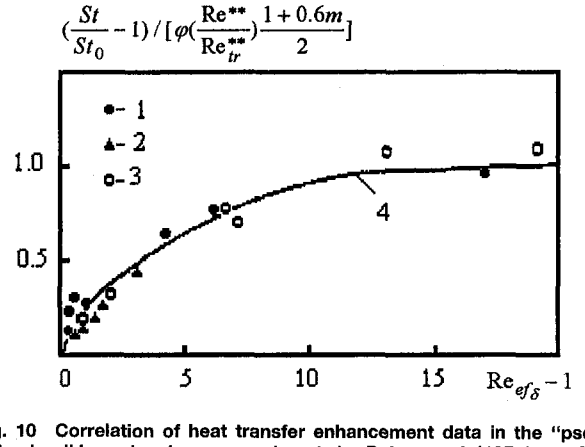

Fig. 10 Correlation of heat transfer enhancement data in the "pseudolaminar" boundary layer; experiment: 1—Dyban et al. (1975), 2—Sikmanovic et al. (1974), Suprun (1988); 4—present calculations Eq. (32)

Conclusion

In the study presented, the relaxation model is applied to simulate the momentum and thermal boundary layers for laminar, transitional, and turbulent flows when turbulent fluctuations are present in the free stream. The relaxation formulas (7) and (8) account for nonzero Reynolds stresses and nonzero heat flux in the region close to the outer edge of the boundary layer. By using these formulas, it becomes possible to predict the velocity and temperature profiles with negative parameters Π_0 and Π_θ that take place in many cases with nonzero free-stream turbulence. The usually employed Boussinesq hypothesis does not allow for such results.

The approach presented in this paper could be used for modeling thermal boundary layer along the flat plate with the unheated starting length, with the local flow separation in the leading edge of the plate, or in other circumstances that can cause nonsimilar development of the momentum and thermal boundary layers.

The calculational results for heat transfer and friction coefficients, for velocity and temperature profiles, for Reynolds stresses and turbulent heat fluxes are in agreement with corresponding experimental data for turbulent boundary layers as well as for "pseudolaminar" boundary layers. The method and results could be used for predicting the heat transfer rates to turbine blades.

References

Blair, M. F., 1983, "Influence of Free-Stream Turbulence on Turbulent Boundary Layer Heat Transfer and Mean Profile Development, Parts I and II," ASME *Journal of Heat Transfer,* Vol. 105, pp. 33–47.

Bradshaw, P., Ferriss, D. H., and Atwell, N. P., 1967, "Calculation of Boundary-Layer Development Using the Turbulent Energy Equation," *J. Fluid Mech.,* Vol. 28, pp. 593–616.

Cebeci, T., and Bradshaw, P., 1984, *Physical and Computational Aspects of Convective Heat Transfer,* Springer Verlag.

Charnay, G., Mathien, J., and Comte-Bellot, G., 1976, "Response of a Turbulent Boundary Layer to Random Fluctuations in the External Stream," *The Physics of Fluids,* Vol. 19, No. 9, pp. 1261–1272.

Consigny, H., and Richards, B. E., 1982, "Short-Duration Measurments of Heat Transfer Rate to a Gas Turbine Rotor Blade," ASME *Journal of Engineering for Power,* Vol. 104, p. 542.

Dyban, Ye.P., Epick, E. Ya., and Kozlova, L. G., 1975, "Heat Transfer in the Vicinity of the Front Stagnation Point of a Cylinder in the Transverse Flow," *Heat Transfer—Soviet Research,* Vol. 7, No. 2, pp. 70–73.

Dyban, Ye.P., and Epik E.Ya., 1978, "Heat Transfer in a Boundary Layer in Turbulized Air Flow," *Heat Transfer,* Vol. 2, Toronto, Canada, FC(a)-4, pp. 507–512.

Dyban, Ye.P., and Epik, E. Ya., 1985, *Teplomassoobmen i Gidrodinamika Turbulizirovannykh Potokov* (*Heat and Mass Transfer and Hydrodynamics in Turbulent Flow*), Naukova Dumka Press, Kiev.

Dyban, Ye.P., and Fridman, E. A., 1987, "Relaksatsionnaya Model' Perenosa Teploty i Impulsa v Pristennykh Pogranichnykh Sloyakh Turbulizirovannykh Potokov," (The Relaxation Model of Heat and Momentum Transfer in Boundary Layers with Nonzero Free Stream Turbulence), *Prom. Teplotechnika,* Vol. 9, No. 4, pp. 16–27.

Fridman E., 1989, "Numerical Simulation of Heat and Momentum Transfer in Boundary Layers With Nonzero Free Stream Turbulence," Ph.D. Thesis, Thermophysics Institute, Kiev, Ukraine.

Hinze, J. O., 1976, "Gedachtniseffekte in der Turbulenz," *ZAMM,* Vol. 56, pp. 403–415.

Junkhan, G. H., and Serovy, G. K., 1967, "Effects of Free-Stream Turbulence and Pressure gradient on Flat-Plate Boundary-Layer Velocity Profiles and on Heat Transfer," ASME *Journal of Heat Transfer,* Vol. 89, pp. 169–176.

Kader, B. A., and Yaglom, A. M., 1980, "Zakony podobiya dlya pristennykh turbulentnykh techeniy," (The Similarity in Near Wall Turbulent Flows), *Itogy Nauki i Techniki, Mechanika Zidkosty i Gasa,* Vol. 15, pp. 81–155.

Kestin, J., 1966, "The Effect of Free Stream Turbulence on Heat Transfer Rates," *Advances in Heat Transfer,* Academic Press, N.Y.–London, Vol. 3, pp. 1–32.

Kutateladze, S. S., and Leontiev, A. I., 1990, *Heat Transfer, Mass Transfer, and Friction in Turbulent Boundary Layers* (translation from Russian), Hemisphere Publishing Corporation.

Loytsyanskiy, L. G., 1970, *Mechanika Zidkosty i Gasa* (Liquid and Gas Mechanics), Nauka, Miscow.

Loytsyanskiy, L. G., 1982, "Nasledstvennye Yavleniya v Turbylentnykh Potokakh," (Memory Effects in Turbulent Flows), *Isv. AN SSSR, Mechanika Zidkosty i Gasa,* No. 2, pp. 5–19.

Maciejewski, P. K., and Moffat R. J., 1992, "Heat Transfer With Very High Free-Stream Turbulence, Parts I and II," ASME *Journal of Heat Transfer,* Vol. 114, pp. 827–839.

McDonald, H., and Kreskovsky, J. P., 1974, "Effect of Free Stream Turbulence on the Turbulent Boundary Layer," *Int. J. Heat and Mass Transfer,* Vol. 17, No. 7, pp. 705–716.

Mehendale, A. B., Han, J. C., and Ou, S., 1991, "Influence of High Mainstream Turbulence on Leading Edge Heat Transfer," ASME *Journal of Heat Transfer,* Vol. 113, pp. 843–850.

Miyazaki, H., and Sparrow E. M., 1977, "Analysis of Effects of Free-Stream Turbulence on Heat Transfer and Skin Friction," ASME *Journal of Heat Transfer,* Vol. 99, pp. 614–619.

O'Brien, J. E., and VanFossen, G. J., 1985, "The Influence of Jet-Grid Turbulence on Heat Transfer From the Stagnation Region of a Cylinder in Crossflow," ASME Paper No. 85-HT-58.

Pedisius, A. A., Kazimekas, P.-V. A., and Slanciauskas, A. A., 1979, "Heat Transfer From a Plate to a High-Turbulence Air Flow," *Heat Transfer—Soviet Research,* Vol. 11, No. 5, p. 125.

Sikmanovic, S., Oka, S., and Djurevic S. K., 1974, "Influence of the Structure of Turbulent Flow on Heat Transfer From a Single Cylinder in a Cross Flow," *Proc. 5th Int. Heat Transf. Conference,* Vol. II, pp. 320–324, AIChE, New York.

Simonich, J. C., and Bradshaw, P., 1978, "Effect of Free-Stream Turbulence on Heat Transfer Through a Turbulent Boundary Layer," ASME *Journal of Heat Transfer,* Vol. 100, pp. 6–13.

Smith, M. C., and Kuethe, A. M., 1966, "Effects of Turbulence on Laminar Skin Friction and Heat Transfer," *The Physics of Fluids,* Vol. 9, pp. 2337–2344.

Suprun, T. T., 1988, "Heat Transfer and Friction Coefficients in the Boundary Layer of a Plate in Turbulent Flow," Ph.D. Thesis, Thermophysics Institute, Kiev, Ukraine.

Traci, R. M., and Wilcox D. C., 1975, "Freestream Turbulence Effects on Stagnation Point Heat Transfer," *AIAA Journal,* Vol. 13, No. 7, pp. 890–896.

Wang, J. H., Jen, H. F., and Hartel, X. X., 1985, "Airfoil Heat Transfer Calculation Using a Low Reynolds Number Version of a Two-Equation Turbulence Model," ASME *Journal of Heat Transfer,* Vol. 107, pp. 60–69.

Effect of Periodic Wake Passing on Film Effectiveness of Discrete Cooling Holes Around the Leading Edge of a Blunt Body

K. Funazaki

M. Yokota

Department of Mechanical Engineering,
Iwate University,
Morioka, Japan

S. Yamawaki

Aero-Engine & Space Operations,
Ishikawajima-Harima Heavy Industries,
Nishitama-gun, Tokyo, Japan

Detailed studies are conducted on film effectiveness of discrete cooling holes around the leading edge of a blunt body that is subjected to periodically incoming wakes as well as free-stream turbulence with various levels of intensity. The cooling holes have a configuration similar to that of typical turbine blades except for the spanwise inclination angle. Secondary air is heated so that the temperature difference between the mainstream and secondary air is about 20 K. In this case, the air density ratio of the mainstream and secondary air becomes less than unity, therefore the flow condition encountered in an actual aero-engine cannot be simulated in terms of the density ratio. A spoke-wheel type wake generator is used in this study. In addition, three types of turbulence grids are used to elevate the free-stream turbulence intensity. We adopt three blowing ratios of the secondary air to the mainstream. For each of the blowing ratios, wall temperatures around the surface of the test model are measured by thermocouples situated inside the model. The temperature is visualized using liquid crystals in order to obtain qualitative information of film effectiveness distribution.

Introduction

To improve the performance of gas turbines, the specifications for turbine inlet temperature continue to increase while cooling air flow is kept to a minimum. For this reason, turbine cooling techniques must be improved not only for blades in the first stage but also for blades in the subsequent stages. Furthermore, those blade metal temperatures must be predicted more accurately.

Film cooling is an effective method for protecting blade surfaces from high temperature combustion gas. There have been many investigations to study film cooling on flat and curved surfaces for low mainstream turbulence intensities.

The leading edge of turbine blades is a prime area of concern in this study because the surface heat transfer coefficient around it is inherently high. In addition, since the boundary-layer thickness on the leading edge is thin, the free-stream turbulence and the periodic wake affect heat transfer very much.

Recently, Mehendale and Han (1992), using a blunt body with a circular leading edge as a test model, studied the effect of free-stream turbulence on film cooling effectiveness and the surface heat transfer coefficient, where secondary air was injected through two rows of inclined holes locating at ± 15 and ± 40 deg from the stagnation. Passive and jet grids generated several turbulence levels in the range of $Tu = 5.07 - 12.9$ percent. The leading edge Reynolds number was 100,000. They found that the leading edge film effectiveness for blowing ratio of 0.4 was significantly reduced by high free-stream turbulence. For blowing ratios of 0.8 and 1.2, the free-stream turbulence effect diminished at the leading edge but still existed on the flat sidewall region. They also pointed out that the effect of free-stream turbulence was more pronounced for ± 15 deg one row injection than ± 40 deg one row injection.

Abhari and Epstein (1994) studied heat transfer on a film cooled rotor blade, under simulated nondimensional engine conditions, with time-resolved measurements. They found that film cooling reduced the time-averaged heat transfer by as much as 60 percent on the suction side, but the effect on the pressure side was relatively limited one. Takeishi et al. (1992) compared the film effectiveness for a rotor blade with that for the corresponding stationary cascade under 4 percent free-stream turbulence intensity, using the heat-mass transfer analogy. They reported that in the leading edge region and on the suction surface, the film effectiveness for the cascade and rotor blade matched well, whereas on the pressure surface the cascade film effectiveness was higher. Although these two studies are useful, the effect of wakes and centrifugal force could not be isolated.

Mehendale et al. (1994) studied the effect of periodic wakes on film effectiveness and heat transfer on a model turbine blade with air or CO_2 film injection through three rows of film holes in the leading edge region and two rows each on the pressure and suction surfaces. They found that an increase in wake Strouhal number caused a decrease in film effectiveness values over most of the blade surface for both density ratios and at all blowing ratios. Since they used a model blade, they could not focus on the leading edge, which had the highest heat load.

Recently, Funazaki (1996) studied the influence of periodically passing wakes on the heat transfer over the leading edge as well as the flat plate. Local heat transfer distributions along the test surface were measured under the several unsteady conditions of bar-passing Strouhal number for four inlet Reynolds numbers. He found that the heat transfer along the surface of the test model was enhanced by the wakes with increasing Strouhal number. He derived a correlation and compared it with other experimental data. Using this correlation, his study yielded similar results to those of the previous studies concerning the wake effect, despite the large difference in the geometrical conditions.

Contributed by the International Gas Turbine Institute and presented at the 40th International Gas Turbine and Aeroengine Congress and Exhibition; Houston, Texas, June 5–8, 1995. Manuscript received by the International Gas Turbine Institute February 3, 1995. Paper No. 95-GT-183. Associate Technical Editor: C. J. Russo.

This study focuses on the effect of periodic passing wakes on the leading edge film cooling under several free-stream turbulence conditions using a blunt body with semi-circular leading edge and flat afterbody, which is similar to that of Mehendale et al. (1992) or Funazaki (1996). The present study is aimed at the investigation of the leading edge cooling effectiveness for turbine rotor blades or for stationary blades in the second or subsequent stages. The configurations of film holes are adopted from that of typical turbine blades, except for the spanwise inclination angle. All holes have their axes normal to the test model surface in consideration of applying the present results to the stationary blade case. This somewhat simplified configuration also helps us understand the effect of periodic wakes on film cooling, compared to the cases of spanwise inclined cooling holes. However, since we are aware of the necessity for investigation of more realistic cases, the succeeding study is now under way to examine the wake-affected film cooling effectiveness of 30 deg spanwise inclined cooling holes, which will be compared with the present results to examine the dependency of the unsteady effects on the inclination. The upstream periodic wake is produced by a spoke-wheel type wake generator like those used by Dullenkopf et al. (1991). The free-stream turbulence is generated by turbulence grids. We adopt three blowing ratios of the secondary air to the mainstream. For each of the blowing ratios, adiabatic wall temperature around the test surface subjected to the wakes as well as the free-stream turbulence is measured by thermocouples situated inside the test model. The effect of elevated free-stream turbulence on the wake-affected film effectiveness is also investigated. The temperature is visualized using liquid crystals in order to obtain qualitative information on the film effectiveness distribution.

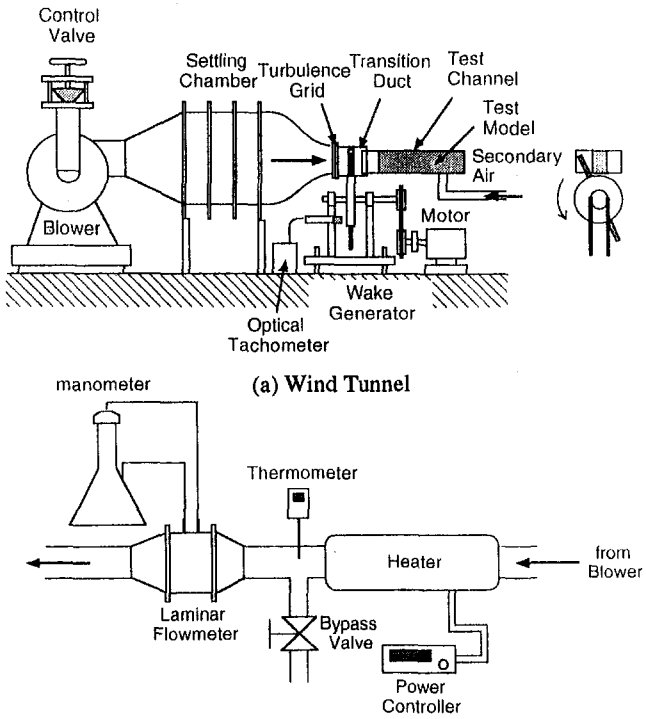

Fig. 1 Schematic layout of the test apparatus

Test Apparatus and Instrument

A schematic layout of the test apparatus is shown in Fig. 1. This apparatus is almost the same with one used in previous heat transfer test by Funazaki (1996), except for the secondary air supply system. The main flow rate is adjusted by the inlet valve of the blower. Air from the blower passes through a settling chamber to the contraction nozzle with the exit cross section of 240 mm × 350 mm. The test channel containing the test model is inserted into the transition duct, which is attached to the contraction nozzle. To remove the upstream boundary layer, the front portion of the test channel has a sharp-edged and 10 mm clearance with the transition duct. It also has a slot, through which the wake-generating bars can pass. The wake-generating bars, of 5 mm diameter and 250 mm length, are mounted on a disk rim. The rotational speed of the disk is controlled by transmission gear box connected to an induction motor. The rotational speed, ranging from 900 through 1500 rpm, is monitored by an optical tachometer and a stroboscope is also used to check the fluctuation of the rotation. Although the inertia of the disk is large enough to maintain a nearly constant rotational speed, a slight vibration of the cylinder bar and some structural vibration was observed. It didn't seem to drastically alter the wake, however. A turbulence grid is attached to the contraction nozzle exit, which is 300 mm upstream of the test model leading edge and 100 mm upstream of the wake generator. Three types of grid are used and details

Nomenclature

B = mean blowing ratio = $\rho_2 U_2 / \rho_\infty U_\infty$
B_{15}, B_{40} = local blowing ratio
D = leading edge diameter
d = cooling hole diameter
d_g = diameter of the turbulence grid wire
f = wake passing frequency = $nn_c/60$
L = axial gap between the turbulence grid and the model leading edge
L_e, $L_{e,w}$ = streamwise dissipation length of free-stream turbulence and wake turbulence
M = grid mesh size of the turbulence grid
M_{15}, M_{40} = local momentum ratio
Nu_D = Nusselt number based on the leading edge diameter
n, n_c = rotating speed and the number of wake generating bars
R = radius of the leading edge
Re_D = Reynolds number based on the diameter of the leading edge and the inlet velocity = $U_\infty D/\nu$
S = Strouhal number = fD/U_∞
T, T_{aw} = temperature, adiabatic wall temperature
$Tu(t)$ = turbulence intensity
Tu_b = background turbulence intensity
U_{local} = local flow velocity around the model surface
U_∞ = inlet velocity
u' = streamwise velocity fluctuation
V_{out} = outlet velocity
v = velocity on the model surface
$v_j(t)$, $\tilde{v}(t)$ = unsteady velocity, ensemble-averaged velocity
X = streamwise distance measured from the wake generating bar
X_G = streamwise distance measured from the turbulence grid
x = axial distance measured from the leading edge
x_{surf} = distance along the surface from the stagnation on the leading edge
η = film effectiveness = $(T_{aw} - T_\infty)/(T_2 - T_\infty)$

Subscripts

∞, 2 = mainstream, secondary air
15, 40 = first row, second row

Table 1 Configurations of turbulence grids characteristics

	Grid 1	Grid 2	Grid 3
Wire Diameter(dg)	0.8 mm	1.9 mm	5.0 mm
Mesh Width (M)	5.0 mm	10.0 mm	30.0 mm
Degree of Openness	0.70	0.66	0.69
M/dg	6.25	5.26	6.00
Tu_b (Eq.(7))	1.5%	2.2%	4.0%

of the grid configurations are shown in Table 1. Although the turbulence intensity attainable with these "passive type" grids at the test model location is at most 4 percent as demonstrated later, it appears high enough to simulate the inlet flow condition to a turbine rotor blade. This can be justified for the first-stage rotor considerating the flow acceleration through the first-stage nozzle, and a corresponding inlet turbulence intensity to the first stage nozzle of about 10 percent.

The secondary air, which is supplied to the film hole on the leading edge of the test model, is heated before a laminar flow meter. Accordingly, the film air temperature is higher than the free-stream temperature, so that we cannot completely simulate the situation in an actual engine.

The cross section of the test channel is 200 mm high and 300 mm wide and its length is 1000 mm. The test model consists of a semi-circular leading edge of 100 mm diameter and a flat afterbody, shown in Fig. 2. The test model is assembled with acrylic-resin parts of 10 mm thickness and 200 mm height. Two rows of holes of d = 10 mm diameter and 40 mm ($4d$) pitch, located at ±15 and ±40 deg angled with the test model centerline. The ratio of the leading edge diameter and the cooling hole diameter, D/d is 10, We will refer to the film holes at ±15 and ±40 deg as "the first row" and "the second row," respectively.

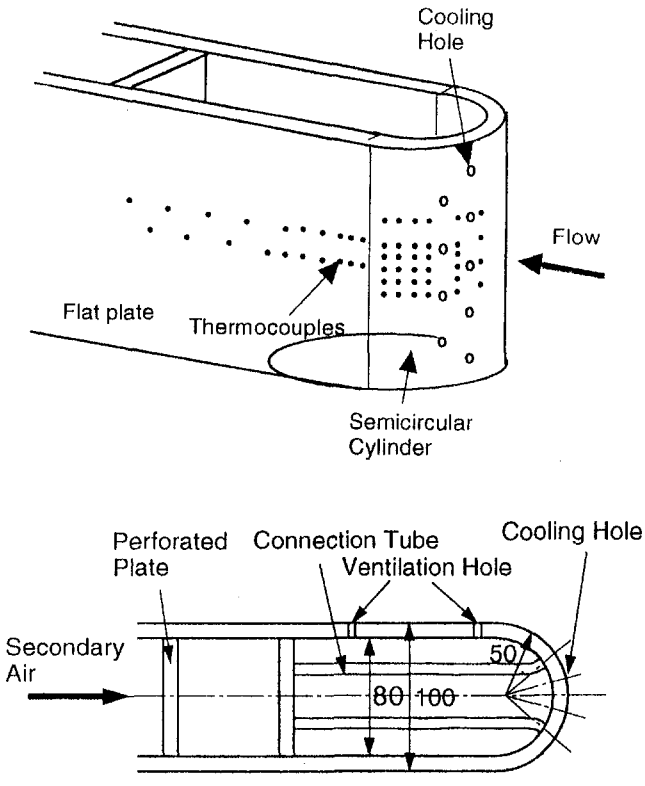

Fig. 2 Test model

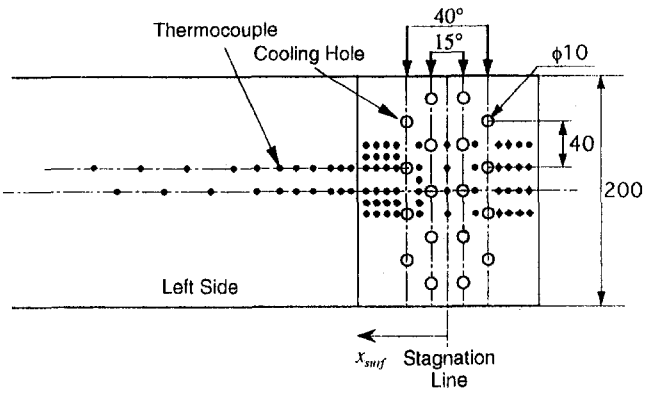

Fig. 3 Layout of thermocouples and film holes (unfolded surface view)

The secondary air is supplied from the flow distribution chamber inside the model to the holes through vinyl tubes. The vinyl tubes are insulated to prevent heat loss. Figure 3 shows the location of thermocouples and film holes. To measure an adiabatic surface temperature distribution, 74 thermocouples are embedded on the model surface. The secondary air temperature is measured near the hole exit. The surrounding temperature around the tubes is also measured. Free-stream temperature is measured near the lower end of the leading edge stagnation line. To prevent temperature increase inside the model, two ventilation holes are located on the flat plate of the model opposite to the test surface. All thermocouples are connected to a datalogger controlled by a personal computer.

These temperature data are then averaged over 10 samples acquired within a few minites to calculate time-averaged wall temperature distributions. To visualize the temperature distribution, liquid crystal sheets of 0.1 mm thickness (RW3040; Nippon Capsule Products) are attached to the model surface after the measurements with the thermocouples. The color changes in a temperature range of 30 ~ 40°C.

Pressure distributions around the test model are obtained using the test model of the same dimensions with the present one except for cooling holes, as had been employed by Funazaki (1996). Local flow velocity U_{local} is then determined from those data.

Experiment

In the present study, normalized parameters adopted in this study, except for Mach number, compare with those encountered in a real turbomachine as shown in Appendix A.

The inlet free-stream velocity was 20 m/s and the Reynolds number Re_D was 141,000. The rotational speeds of the wake generator were 900, 1260, and 1500 rpm. The corresponding Strouhal numbers, defined as

$$S = \frac{(nn_c/60)D}{U_\infty}, \tag{1}$$

were 0.22, 0.31 and 0.37.

Unsteady velocity measurements were conducted using a hot-wire anemometer. Several series of unsteady velocity data $v_j(t)\{j = 1, \ldots, m\}$ are processed to calculate the ensemble-averaged velocity $\tilde{v}(t)$

$$\tilde{v}(t) = \frac{1}{m}\sum_{j=1}^{m} v_j(t) \tag{2}$$

where m = 256. The time-resolved turbulence intensity used in this study is defined as the ensemble-averaged variance and calculated by

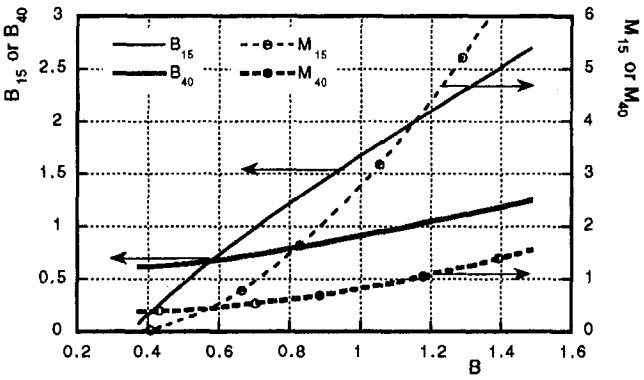

Fig. 4 Relationship of local and mean blowing ratio

$$Tu(t) = \frac{\frac{1}{m-1}\sum_{j=1}^{m}(v_j(t) - \bar{v}(t))^2}{U_{\text{local}}} \tag{3}$$

The blowing ratio B, the dominant parameter for film cooling, is defined as

$$B = \frac{\rho_2 U_2}{\rho_\infty U_\infty}. \tag{4}$$

B is based on the mean secondary air and the inlet flow mass flux. All experiments were conducted at the mean blowing ratios, $B = 0.4$, 0.8, or 1.2. Although this blowing ratio is a convenient parameter for this type of experiment, local blowing ratio at each row is more useful for understanding the local film cooling performance. The local blowing ratio is defined as

$$B_{15} = \frac{\rho_{2,15}U_{2,15}}{\rho_{\infty,15}U_{\infty,15}}, \quad B_{40} = \frac{\rho_{2,40}U_{2,40}}{\rho_{\infty,40}U_{\infty,40}}. \tag{5}$$

Figure 4 shows the analytical result of the relationship between the local and mean blowing ratios, as well as the relationship between the local momentum ratio and mean blowing ratios. Readers can refer to Appendix B for more detail. Notice that these relationships differ for each row. For instance, for B_{15}, the slope of the curve is about 2.5 and $B_{15} \geqslant 1$ when $B \geq 0.8$. In contrast, for B_{40}, the slope is about 0.5 and $B_{40} \leq 1$ even when $B \leq 1.2$.

Film effectiveness η is defined as

$$\eta = \frac{T_{aw} - T_\infty}{T_2 - T_\infty}, \tag{6}$$

where T_{aw} is the adiabatic wall temperature, T_2 is the secondary air temperature, and T_∞ is mainstream temperature. During the experiment, the temperature difference $T_{aw} - T_w$ was maintained about 20 K. To give the model a sufficiently adiabatic condition, a temperature increase inside the model was limited by two ventilation holes described previously. The temperature inside the model was therefore maintained only 5–6 K higher than mainstream temperature, which was nearly equal to the average temperature around the outer surface of the model. It can be consequently expected that such a small difference in temperature between both sides of the plate yielded almost adiabatic condition of the model surface except near the film holes.

An uncertainty analysis based on the method of Kline and McClintock (1953) was carried out for the film effectiveness. The uncertainty of film effectiveness is about 4.5 percent near the film holes and less than 9.7 percent for downstream.

Results and Discussion

Velocity Distribution. Figure 5 shows the velocity distribution around the leading edge of the test model. In this figure, the results of a potential flow analysis by use of BEM (Boundary Element Method) are compared with the measurement data. The heat transfer distribution ($Nu_D/Re_D^{0.5}$) is also plotted (Funazaki, 1996). Velocity distributions are the same on both sides of the leading edge, showing the symmetry of the flow field with respect the model center line. These data show that there was a separation bubble around the junction of leading edge and flat plate. The separation began at $X_{surf}/R \cong 1$ and reattached at $X_{surf}/R \cong 2$. Velocity fluctuations were not discernible even under the influence of the wakes, since these distributions were measured by a slow response Betz manometer. It does not seem from this figure that the velocity distributions change drastically even when periodic wakes exist in the mainstream. However, we are aware of the importance of unsteady effects on the separated flow structure and the next projects concerning the unsteady effects are under way, but this is beyond the scope of the present study.

Free-Stream Turbulence. Figure 6 shows the free-stream turbulence measured at 200 mm upstream of the leading edge by use of a hot-wire anemometer. In order to avoid the influence of the model-disturbed flow field during this measurement as well as wake measurements described next, the test model was moved downstream by 200 mm from the nominal position so that the distance from the turbulence grid to the leading edge of the model was 500 mm. Note that streamwise traversing of the hot-wire probe could not be conducted due to a structural restriction of the test section. Therefore, only three data points are plotted in this figure against the streamwise distance normalized on the mesh width of the turbulence grid, X_G/M. Also cited are some of the results of Kestin and Wood (1971) for $M/d_g = 3.0$.

Although larger M/d_g in the present case provides lower turbulence intensities compared to those of Kestin and Wood, the present data tend to align along a line on the logarithmic diagram like the data of Kestin and Wood, where this line can be expressed by

$$Tu_b = 10.64(X_G/M)^{-0.559}, \quad M/d_g = 6 \tag{7}$$

Considering that the turbulence grids adopted here have almost the same values of M/d_g ($\cong$6), it seems possible to use Eq. (7) to predict the streamwise decay of the turbulence from each of the grids.

On the other hand, as pointed out by Kestin and Wood (1971) or Mehendale and Han (1992), the free-stream turbulence intensity rapidly increases near the stagnation of the test model. For the purpose of determining a reference turbulence intensity to the test model, Funazaki et al. (1995) derived the following expression for describing the behavior of turbulence intensity along the stagnation streamline, combining Eq. (7) with the solution of the potential flow field near the stagnation:

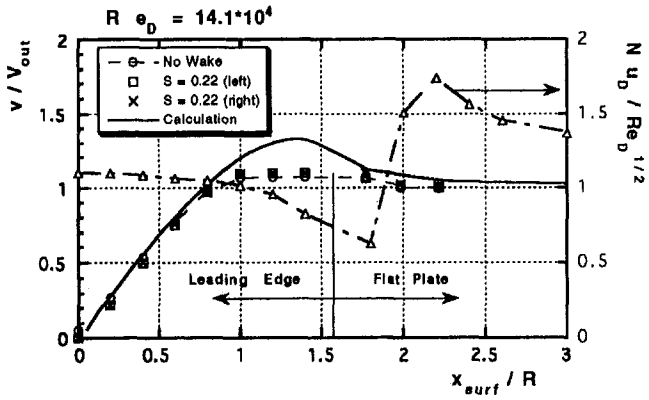

Fig. 5 Velocity and heat transfer distribution around the leading edge

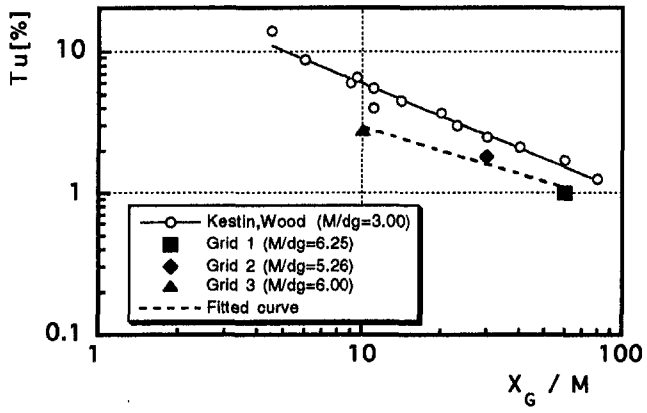

(a) The decay of free stream-turbulence

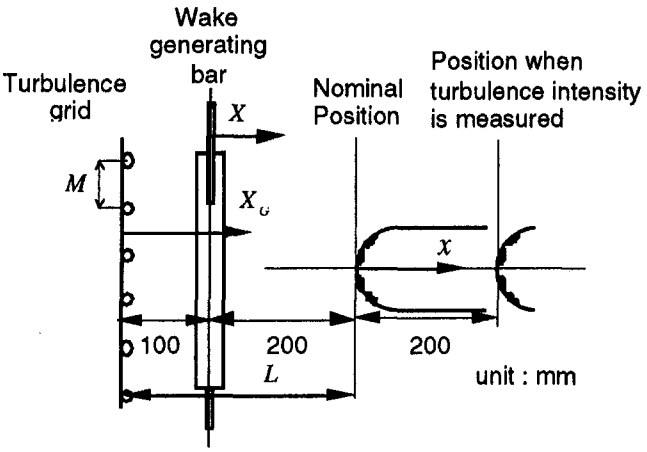

(b) Nomenclature

Fig. 6 The decay of free-stream turbulence

$$Tu_b(x) = 10.64\left(\frac{L - |x|}{M}\right)^{-0.559} \times \frac{1}{1 - (R/(x - R))^2} \quad (8)$$

In the nominal setting of the test model L was 300 mm, from which the minimum free-stream turbulence intensity was estimated as shown in Table 1. Like Mehendale et al. (1991), we hereafter use these minimum values as reference turbulence intensity.

As for length scale of the free-stream turbulence, a streamwise turbulence dissipation scale L_e, defined as (Hancock and Bradshaw, 1983)

$$L_e = -\frac{(\bar{u}'^2)^{3/2}}{Ud\bar{u}'^2/dx} \quad (9)$$

was calculated by Eq. (7). As a result, at X_G = 300 mm we have L_e = 2.8 mm, 4.2 mm, and 7.8 mm for Grid 1, Grid 2, and Grid 3, respectively.

Wake Measurements. The measurement of unsteady velocity fluctuation were carried out using a hot wire anemometer, the details being described by Funazaki et al. (1995). Figure 7 shows some of the results about velocity and turbulence intensity measured 5 mm upstream of the leading edge stagnation with and without grid. The periodic wakes provide periodic increases of turbulence intensity. Care must be paid to more than 20 percent turbulence intensities occurring within the wakes, which are due to the reduced free-stream velocity near the model leading edge. Upstream of the test model, maximum turbulence intensity in the wake was 8 percent at most. The ensemble-averaged velocity increased slightly when the wakes were passing, probably due to the wake deformation near the blunt leading edge. Random peaks of Tu after the wake passed also appeared. Even when the turbulence grid was inserted in the upstream, the maximum value of Tu did not change but the amplitude of Tu decreased.

From these measurements, Funazaki et al. (1995) derived the following correlation for streamwise decay of turbulence intensity in the wake,

$$Tu_{\max} = 73.58\left(\frac{X}{d}\right)^{-0.67} \quad (10)$$

Although this correlation, irrespective of wake passing Strouhal number, actually contains some amount of scatter, it is useful to understand the generic trend of the wake turbulence decay.

For convenience in the later discussion, we determine a streamwise turbulence dissipation length scale of the wake turbulence, $L_{e,w}$ from Eq. (9) in conjunction with Eq. (10) likewise in the case for free-stream turbulence. It follows that $L_{e,w}$ = 9.2 mm at X = 200 mm, which corresponds to X_G = 300 mm.

Film Effectiveness

The Wake Effect With No Turbulence Grid. Figures 8, 9 and 10 show spanwise averaged film effectiveness distributions for three wake Strouhal numbers as well as "no wake" condition with low free-stream turbulence (no grid). These figures

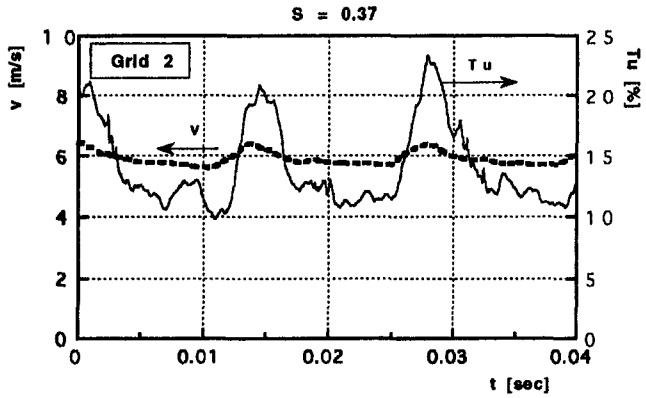

(a) No grid

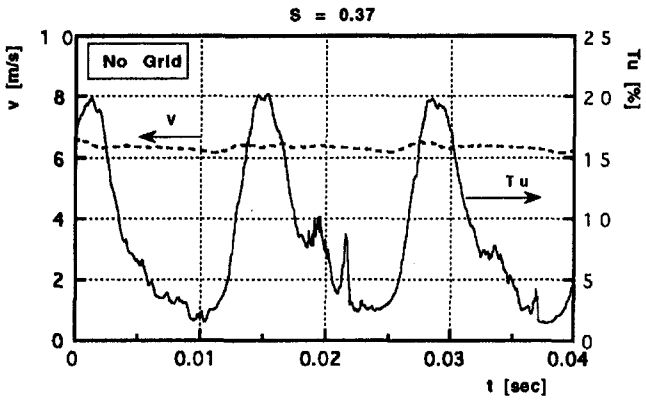

(b) With grid

Fig. 7 Unsteady velocity and turbulence profiles at 5 mm upstream of the leading edge with and without grids

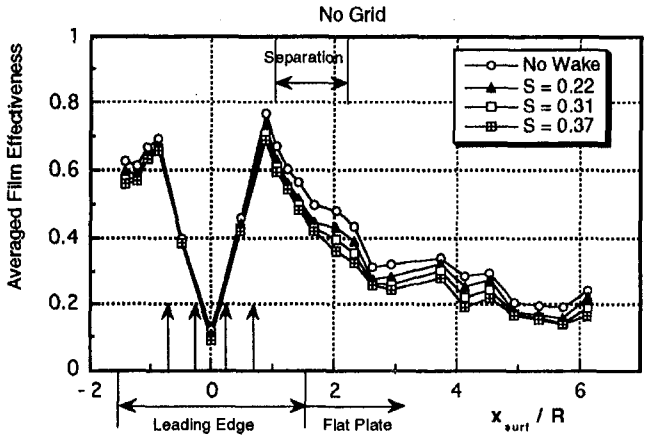

Fig. 8 Averaged film effectiveness without turbulence grid (B = 0.4)

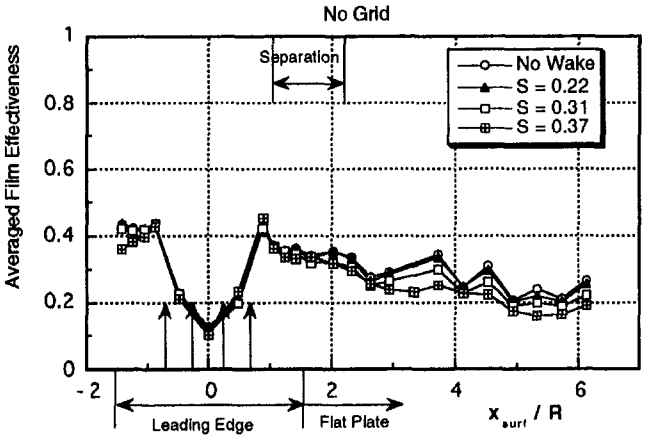

Fig. 9 Averaged film effectiveness without turbulence grid (B = 0.8)

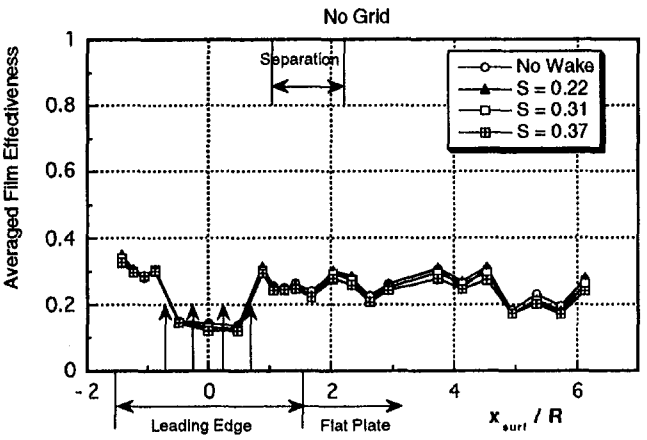

Fig. 10 Averaged film effectiveness without turbulence grid (B = 1.2)

differ by the mean blowing ratio, B, which is 0.4, 0.8, and 1.2, respectively. The position of the first row of film holes is at $X_{surf}/R = 0.262$ and at 0.698 for the second row. In these figures, the location of the separation bubble is also indicated on a basis of the "no wake" and "no grid" heat transfer data. In each case, film effectiveness has a peak value just after the second row of film holes. In $X_{surf}/R > 3$, all data show a slight fluctuation, because thermocouples are staggered as shown in Fig. 2.

The maximum film effectiveness appeared at B = 0.4, but its film effectiveness decreased rapidly downstream thereafter.

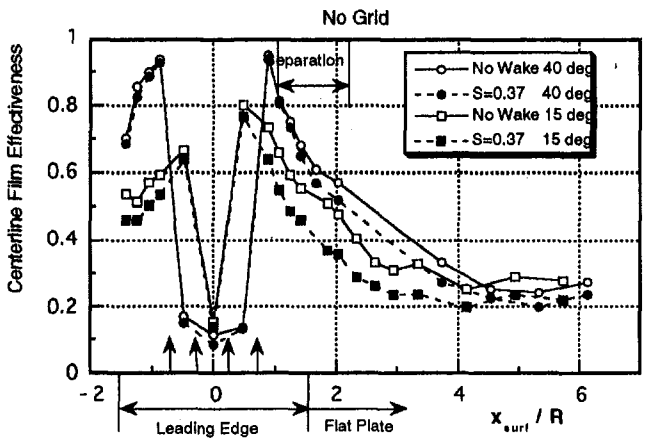

(a) B=0.4

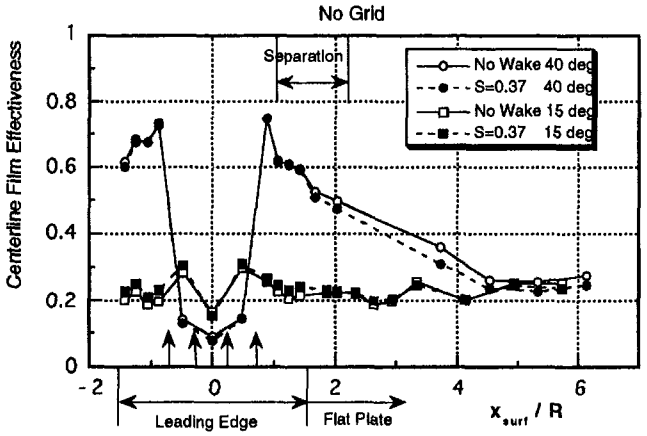

Fig. 11 Local film effectiveness without the turbulence grid

At B = 1.2, film effectiveness distribution was nearly flat (η = 0.2 to 0.3). Far downstream, $X_{surf}/R > 4$, film effectiveness was almost same for all blowing ratios.

The effect of periodic wakes on film effectiveness was larger for the lower blowing ratio cases. For example, at B = 0.4 the maximum decrease of film effectiveness by the wake was more than 0.1, while at B = 1.2 the effect of wakes was indistinguishable.

Figure 11(a, b) shows local film effectiveness distributions in the low and middle blowing ratio cases, respectively. In these figures, centerline film effectiveness distributions for each row are plotted with and without wakes. For B = 0.4, the effect of wakes for the first row caused a decrease of spanwise-averaged effectiveness as was also seen in Fig. 8. For B = 0.8, the effectiveness of the first row was low everywhere. In contrast, for the second row, a decrease of film effectiveness appeared only for $x_{surf}/R > 2$ in both blowing ratio cases.

There is a reasonable explanation why the first row centerline film effectiveness was significantly affected by the periodic wakes and blowing ratio. When B = 0.4, the local blowing ratio, B_{15}, was about 0.2 (refer to Fig. 4). At this very low local blowing ratio, film air easily attached to the surface; therefore, the film effectiveness was high. However, the film air also had quite low momentum and low turbulence compared to the surrounding air flow, which made it easy for the turbulence of periodic wakes to interact with the film air. In the case of B = 0.8, on the contrary, the local blowing ratio for the first row was $B_{15} \cong 1.2$ so that blow-off occurred, which resulted in low effectiveness. On the other hand, the local blowing ratio of the

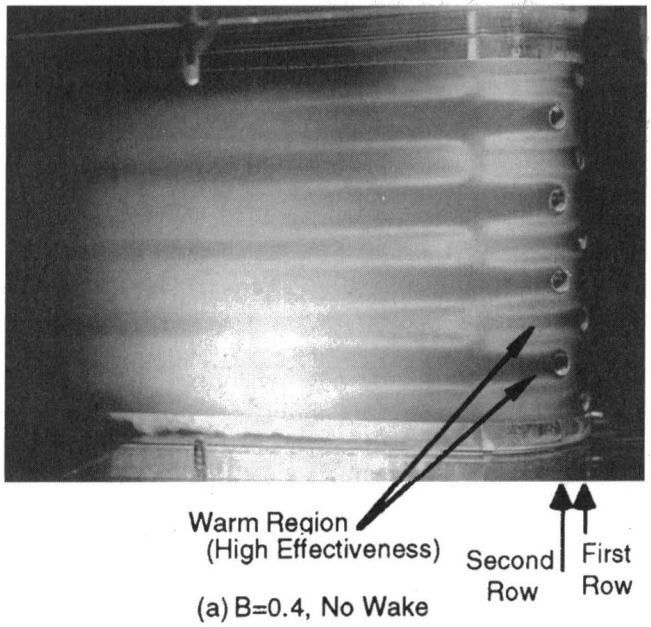

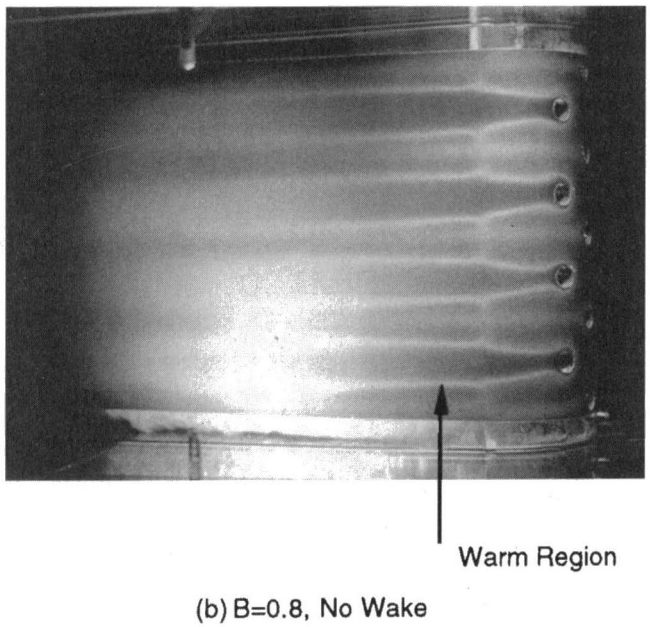

Fig. 12 Detailed temperature distribution around film holes

second row, B_{40}, changed slowly from 0.6 to 0.8 when B changed from 0.4 to 0.8 as shown in Fig. 4. Since B_{40} remained sufficiently low, the film air attached to the surface. The momentum of the second row air was also high enough that the turbulence from the periodic wakes could not affect the film air, especially near the film holes.

Figure 12 shows detailed temperature distribution around film holes through which heated secondary air was injected. Remember that the air was supplied to all the holes at the same time. There were high-temperature regions (high film effectiveness) downstream of both the first and second rows at $B = 0.4$. For higher blowing ratio, no warm regions downstream of the first row were confirmed because of the blow-off.

The Effect of Free-Stream Turbulence and Wakes. Figures 13, 14, and 15 show the spanwise-averaged film effectiveness obtained for three cases of free-stream turbulence intensity with three blowing ratios, respectively. There were no wakes in these cases. The manner in which the film effectiveness changed with

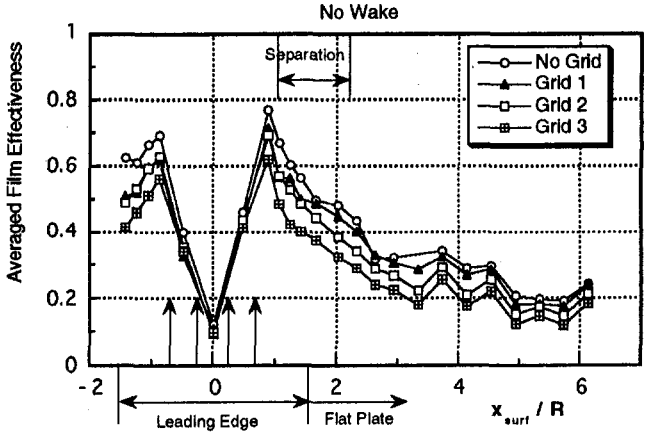

Fig. 13 Averaged film effectiveness without the wake effect (B = 0.4)

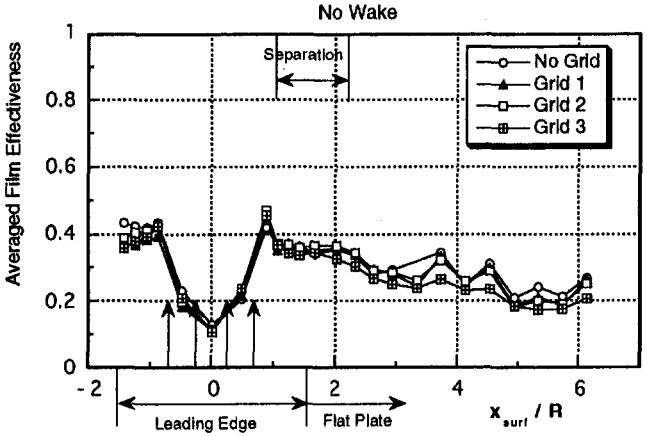

Fig. 14 Averaged film effectiveness without the wake effect (B = 0.8)

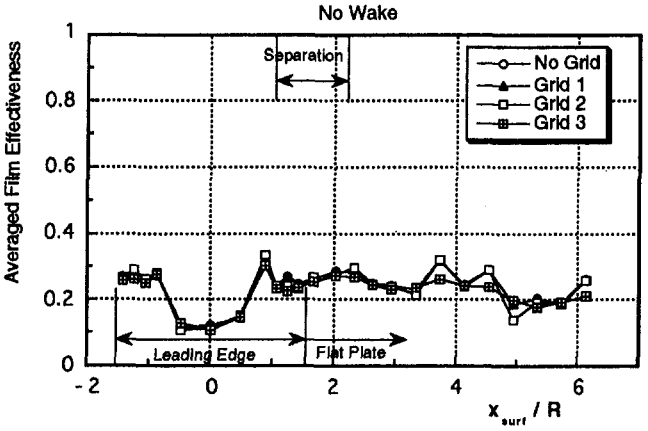

Fig. 15 Averaged film effectiveness without the wake effect (B = 1.2)

increase in free-stream turbulence resembles that of increasing the wake Strouhal number. At the lower blowing ratio, B = 0.4, the effect of free-stream turbulence on the film effectiveness was evident. The maximum reduction of effectiveness was about 0.2. For the case of no grid in Fig. 13, there appeared a region where the effectiveness distribution somewhat plateaued at about $x_{surf}/R = 3$ in the neighborhood of reattachment. This flat distribution disappeared as the turbulence intensity increased. It is not clear at this moment how the separation affected the film air flow; however, it is conceivable that some fraction of the secondary air was caught in the separation bubble

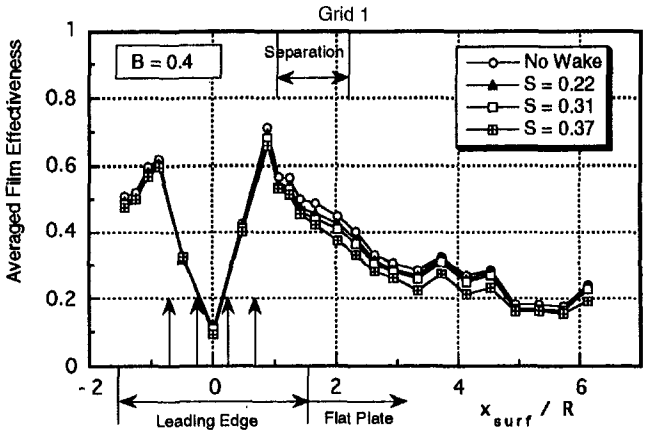

Fig. 16 Averaged film effectiveness with wake and free-stream turbulence effect (B = 0.4, Grid 1)

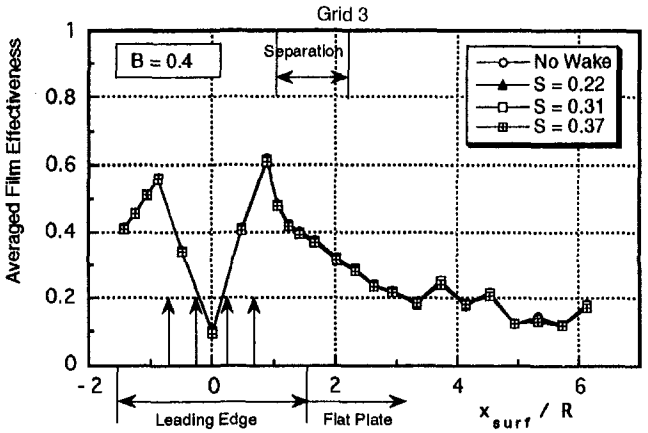

Fig. 18 Averaged film effectiveness with wake and free-stream turbulence effect (B = 0.4, Grid 3)

in the low free-stream turbulence case (no grid) and warm air stayed there for a relatively longer time.

Mehendale and Han (1992) conducted their study at almost the same conditions. Under low free-stream turbulence, the present film effectiveness for low blowing ratio, B = 0.4, agrees with their results well. Although the trend of decrease in film effectiveness with increasing blowing ratio also agrees, the present data shows lower effectiveness for high blowing ratio. This difference may be attributed to the difference in hole inclination angle. Their angle was 30 deg, while the holes in this study were normal to the surface. They also indicated that the film effectiveness for low blowing ratio (B = 0.4) decreased dramatically with increasing free-stream turbulence. Although this trend agrees with the present study, their data showed a more rapid decrease at higher blowing ratios.

The effects of periodic wakes on film effectiveness under the enhanced free-stream turbulences are shown in Figs. 16, 17, and 18, respectively. Only the results for the low blowing ratio case are shown here because they clearly show the effect of wake and turbulence. Although effectiveness decreased as wake Strouhal number increased, there was no wake effect at the highest free-stream turbulence. One might wonder why the periodic wakes of over 20 percent turbulence intensity as seen in Fig. 7 had almost no further impact on the film effectiveness in Fig. 18. One reason for this phenomenon is that the corresponding maximum turbulence intensity in the wake at the upstream was actually 8 percent at most. The other reason is that the observed wake duration relatively decreased compared to one wake passing period under the enhanced background turbulence, which weakened the wake effect. Furthermore, the effect of turbulence length scale cannot be dismissed. As shown previously, the streamwise turbulence dissipation length scale of the free-stream turbulence generated by Grid 3 (L_e/D = 0.078) was comparable to that of the wake turbulence (L_e/D = 0.092), which could be another possible reason for the reduction of the wake effect by the enhanced free-stream turbulence.

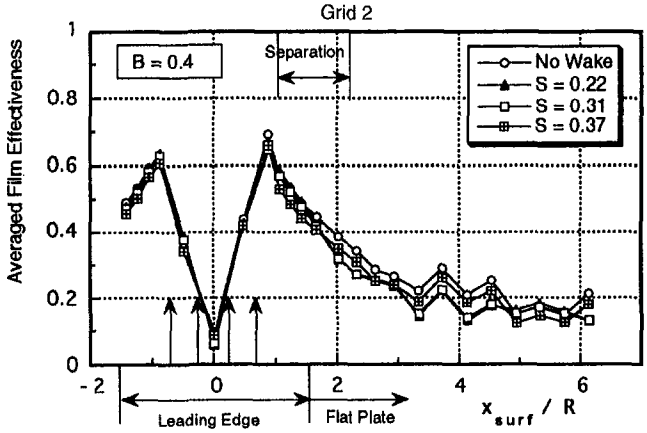

Fig. 17 Averaged film effectiveness with wake and free-stream turbulence effect (B = 0.4, Grid 2)

Conclusions

Detailed studies were conducted on film effectiveness of discrete film holes around the leading edge of a blunt body that was subjected to periodically incoming wakes as well as free-stream turbulence with various levels of intensity. Several important findings, useful for designing film-cooled turbine blades, were then obtained through the studies. The findings are summarized as follows:

1 In the range of this experiment, spanwise-averaged film effectiveness became highest at the blowing ratio of 0.4, because injected air from both the first and second rows attached to the surface.

2 For $B > 0.8$, the local blowing ratio for the first row was so high that the injected air blew off. This resulted in low film effectiveness downstream of the first row and deteriorated spanwise-averaged film effectiveness.

3 When a periodic wake impinged on the blunt body, film effectiveness decreased with increase of wake Strouhal number. The film effectiveness decreased most at the lowest mean blowing ratio, B = 0.4, because very low-momentum air injected from the first row was considerably susceptive to the wake.

4 Film effectiveness decreased with increase in free-stream turbulence, which diminished the effect of periodic wakes. This phenomenon could be attributed to the roles of the turbulence intensity as well as the turbulence length scale.

Acknowledgments

The authors are greatly indebted to Mr. K. Koizumi of Iwate University for his effort in executing the experiment and Dr. R. Henk of IHI for his review of this paper.

References

Abhari, R. S., and Epstein, A. H., 1994, "An Experimental Study of Film Cooling in a Rotating Transonic Turbine," ASME JOURNAL OF TURBOMACHINERY, Vol. 116, pp. 63–70.

Dullenkopf, K., Schulz, A., and Wittig, S., 1991, "The Effect of Incident Wake Conditions on the Mean Heat Transfer of an Airfoil," ASME JOURNAL OF TURBOMACHINERY, Vol. 113, pp. 412--418.

Funazaki, K., Yamawaki, S., and Maya, T., 1995, "Studies on Wake-Affected Heat Transfer Around the Leading Edge a Blunt Body," to be published in *Proc. 4th ASME–JSME Thermal Engineering Joint Conference.*

Funazaki, K., 1996, "Studies on Wake-Affected Heat Transfer Around the Circular Leading Edge of Blunt Body," ASME JOURNAL OF TURBOMACHINERY, Vol. 118, pp. 452–460.

Goebel, S. G., Abuaf, N., Lovett, J. A., and Lee, C. P., 1993, "Measurement of Combustor Velocity and Turbulence Profiles," ASME Paper No. 93-GT-228.

Hancock, P. E., and Bradshaw, P., 1983, "The Effect of Free-Stream Turbulence on Turbulent Boundary Layers," ASME *Journal of Fluids Engineering,* Vol. 105, pp. 284–289.

Kestin, J., and Wood, R., 1971, "The Influence of Turbulence on Mass Transfer From Cylinders," ASME *Journal of Heat Transfer,* Vol. 93, pp. 321–327.

Kline, S. J., and McClintock, F. A., 1953, "Describing Uncertainties in Single Sample Experiments," *Mechanical Engineering,* Vol. 75, pp. 3–8.

Mehendale, A. B., Han, J. C., and Ou, S., 1991, "Influence of High Mainstream Turbulence on Leading Edge Heat Transfer," ASME JOURNAL OF TURBOMACHINERY, Vol. 113, pp. 843–850.

Mehendale, A. B., and Han, J. C., 1992, "Influence of High Mainstream Turbulence on Leading Edge Film Cooling Heat Transfer," ASME JOURNAL OF TURBOMACHINERY, Vol. 114, pp. 707–715.

Mehendale, A. B., Han, J. C., Ou, S., and Lee., C. P., 1994, "Unsteady Wake Over a Linear Turbine Blade Cascade With Air and CO_2 Film Injection: Part II—Effect on Film Effectiveness and Heat Transfer Distributions," ASME JOURNAL OF TURBOMACHINERY, Vol. 116, pp. 730–737.

Ou, S., Mehendale, A. B., and Han, J. C., 1992, "Influence of High Mainstream Turbulence on Leading Edge Film Cooling Heat Transfer: Effect of Film Hole Row Location," ASME JOURNAL OF TURBOMACHINERY, Vol. 114, pp. 716–723.

Ou, S., Han, J. C., Mehendale, A. B., and Lee., C. P., 1994, "Unsteady Wake Over a Linear Turbine Blade Cascade With Air and CO_2 Film Injection: Part I—Effect on Heat Transfer Coefficients," ASME JOURNAL OF TURBOMACHINERY, Vol. 116, pp. 721–729.

Takeishi, K., Aoki, S., Sato, T, and Tsukagoshi, K., 1992, "Film Cooling on a Gas Turbine Rotor Blade," ASME JOURNAL OF TURBOMACHINERY, Vol. 114, pp. 828–834.

APPENDIX A

In this appendix, we show that the parameters adopted in this study almost match those encountered in a real turbomachine.

Table A.1 shows comparisons between several normalized parameters for a real turbomachine and the present study. As for an incident turbulence intensity to turbine rotor blades, the analytical approach is as follows.

Along a steady streamline away from the blade surfaces, turbulence kinetic energy k is governed by

$$\frac{Dk}{Dt} = -\epsilon, \tag{A.1}$$

where ϵ is the dissipation rate and can be calculated from the relationship $\epsilon = k^{3/2}/L_\epsilon$, prescribing the mixing length L_ϵ. Assuming steady flow and isotropic turbulence, we have

$$\frac{D}{Dt} = U_s \frac{\partial}{\partial x_s}, \tag{A.2}$$

$$k = 1.5(U_s \cdot Tu)^2, \tag{A.3}$$

where U_s represents the streamwise velocity along the streamline. Equation (A.1) can be integrated between nozzle inlet (x_{so}) and nozzle exit (x_s) to yield the turbulence intensity at the nozzle exit as follows,

Table A.1 Comparison between several normalized parameter for a real turbomachine and the present study

	Real turbomachine	Present study
Reynolds number Re_D	$10^4 \sim 10^6$	14.1×10^4
Strouhal number S	0.2 ~ 0.4	0.22 ~ 0.37
Turbulence intensity Tu	3 ~ 5%	1.5 ~ 4 %

$$k(x_s) = k(x_{s0}) - \int_{x_{s0}}^{x_s} \frac{\epsilon dx'}{U(x')}. \tag{A.4}$$

Taking account of the experimental finding by Goebel et al. (1993) that the turbulence intensity at the exit of combustor was around 10–15 percent on the average, we can roughly estimate the turbulence intensity at nozzle exit from Eq. (A.4), which is easily converted into the value in the coordinate system fixed to the rotor blade as presented in Table A.1. This shows the test conditions almost match the real case.

APPENDIX B

Applying the Bernoulli equation to a streamtube between the plenum chamber within the model and the exit of a cooling hole, we have the generic expression as follows:

$$P_2 = p_{out} + \frac{\rho}{2} v_{out}^2 + \left(\zeta_{in} + \lambda \frac{l}{d}\right) \frac{\rho}{2} v_{out}^2, \tag{B.1}$$

where P_2 = total pressure in the chamber, p_{out} = hole exit static pressure, v_{out} = mean velocity in the tube, ζ_{in} = inlet loss coefficient, λ = friction coefficient, l = tube length, d = tube inner diameter. From this equation, mean injection velocities from the cooling holes of the first and second rows are calculated by

$$v_{15} = \sqrt{\frac{2(P_2 - p_{15})}{\rho\left(1 + \zeta_{in} + \lambda \frac{l_{15}}{d}\right)}} = \sqrt{\frac{2(P_2 - p_\infty + p_\infty - p_{15})}{\rho\left(1 + \zeta + \lambda \frac{l_{15}}{d}\right)}}, \tag{B.2}$$

$$v_{40} = \sqrt{\frac{2(P_2 - p_{15})}{\rho\left(1 + \zeta_{in} + \lambda \frac{l_{40}}{d}\right)}} = \sqrt{\frac{2(P_2 - p_\infty + p_\infty - p_{15})}{\rho\left(1 + \zeta_{in} + \lambda \frac{l_{40}}{d}\right)}}. \tag{B.3}$$

From the experiment by Funazaki (1996), it was found that the velocity distribution near the stagnation could be approximated by that of the potential flow around the circular cylinder. Consequently, p_{15} and p_{40} can be given by

$$p_\infty - p_{15} = -0.732 \frac{\rho}{2} U_\infty^2, \tag{B.4}$$

$$p_\infty - p_{40} = 0.653 \frac{\rho}{2} U_\infty^2, \tag{B.5}$$

where p_∞ is the free-stream static pressure upstream of the test model. From Eqs. (B.2) ~ (B.5),

$$\frac{v_{15}}{U_\infty} = -\frac{\sqrt{C_{p2} - 0.732}}{\sqrt{1 + \zeta_{in} + \lambda \frac{l_{15}}{d}}}, \tag{B.6}$$

$$\frac{v_{40}}{U_\infty} = \frac{\sqrt{C_{p2} - 0.653}}{\sqrt{1 + \zeta_{in} + \lambda \frac{l_{40}}{d}}}, \tag{B.7}$$

$$C_p = \frac{P_2 - p_\infty}{\frac{\rho}{2} U_\infty^2}. \quad \text{(B.8)}$$

From the definition of the blowing ratio B, also considering that the air density ratio of the mainstream and secondary air is about unity, we have

$$B = \frac{\rho_2 U_2}{\rho_\infty U_\infty} = \frac{U_2}{U_\infty} = \frac{1}{U_\infty}\left\{\frac{n_{15} v_{15} + n_{40} v_{40}}{n_{15} + n_{40}}\right\}. \quad \text{(B.9)}$$

where n_{15} and n_{40} are numbers of cooling holes of the first and second rows. Accordingly, B is expressed by the following equation:

$$B = \frac{\sqrt{C_p}}{(n_{15} + n_{40})\sqrt{1 + \zeta_{in} + \lambda \frac{l}{d}}} \times \left\{ n_{15} \sqrt{1 - \frac{0.732}{C_p}} + n_{40} \sqrt{1 + \frac{0.653}{C_p}} \right\}. \quad \text{(B.10)}$$

Local blowing ratio $\bar{B}$, defined as

$$\bar{B} = \frac{\rho_2 v_{out}}{\rho_\infty U_{local}} = \frac{v_{out}}{U_{local}} = \frac{v_{out}}{U_\infty} \cdot \frac{U_\infty}{U_{local}}, \quad \text{(B.11)}$$

can be finally obtained as a function of B, from Eq. (B.6) or (B.7) and Eq. (B.10) (using C_p as a parameter B).

Heat Transfer and Film Cooling Effectiveness in a Linear Airfoil Cascade

N. Abuaf

R. Bunker

Corporate Research & Development,
General Electric Company,
Schenectady, NY 12301

C. P. Lee

GE Aircraft Engines,
General Electric Company,
Cincinnati, OH

A warm (315°C) wind tunnel test facility equipped with a linear cascade of film cooled vane airfoils was used in the simultaneous determination of the local gas side heat transfer coefficients and the adiabatic film cooling effectiveness. The test rig can be operated in either a steady-state or a transient mode. The steady-state operation provides adiabatic film cooling effectiveness values while the transient mode generates data for the determination of the local heat transfer coefficients from the temperature–time variations and of the film effectiveness from the steady wall temperatures within the same aerothermal environment. The linear cascade consists of five airfoils. The 14 percent cascade inlet free-stream turbulence intensity is generated by a perforated plate, positioned upstream of the airfoil leading edge. For the first transient tests, five cylinders having roughly the same blockage as the initial 20 percent axial chord of the airfoils were used. The cylinder stagnation point heat transfer coefficients compare well with values calculated from correlations. Static pressure distributions measured over an instrumented airfoil agree with inviscid predictions. Heat transfer coefficients and adiabatic film cooling effectiveness results were obtained with a smooth airfoil having three separate film injection locations, two along the suction side, and the third one covering the leading edge showerhead region. Near the film injection locations, the heat transfer coefficients increase with the blowing film. At the termination of the film cooled airfoil tests, the film holes were plugged and heat transfer tests were conducted with non-film cooled airfoils. These results agree with boundary layer code predictions.

1 Introduction

Advances in turbine performance over the past few decades have resulted from acquiring detailed information in each of the multi-disciplined efforts required for efficient turbine design and operation. With respect to the thermal design of turbines, and particularly the hot gas path components of the high-pressure turbine, researchers have steadily obtained increased knowledge of both external and internal heat transfer. Aided by advances in instrumentation, data acquisition, computational capabilities, and new experimental methodologies, more and more of the specific factors affecting the thermophysics are being investigated. This applies to localized regions of the turbine, such as interaction of film cooling jets with the mainstream gas and the surfaces as well as to the more global situations of passage and interstage flow and heat transfer. As designs approach stoichiometric turbine inlet conditions, obtaining such information under conditions that properly model the appropriate nondimensional operating parameters becomes of increasing importance.

In lieu of the extreme expense and difficulty of experimentation under actual turbine operating conditions, most research has utilized wind tunnels, cascades, and turbine rigs that operate with reduced pressures and temperatures, and nonreacting gases. In the case of vane and blade heat transfer, a significant level of effort has been expended over the past 25 years by many researchers. This effort has increased in the last several years, such that many facilities are now operating to determine heat transfer distributions on airfoils with various conditions of film cooling, coolant-to-gas density ratios, blowing parameters, inlet flow turbulence intensities, Reynolds numbers, unsteadiness, etc. These facilities incorporate several differing methodologies, most of which result in a few limitations being imposed on the character and usefulness of the information obtained. For film cooled airfoils, it is desired to obtain both local heat transfer coefficients, and local adiabatic wall temperatures, within the same aerothermal fluid and surface conditions.

Airfoil cascades generally operate under either steady-state or transient conditions. Steady-state cascades have been reported in recent experiments, which use a number of different methods. The cascades of Nirmalan and Hylton (1990) and Dullenkopf et al. (1991) utilized internally cooled airfoils, sufficiently instrumented with thermocouples, to determine the external heat transfer coefficients by finite element analysis. While this method is capable of obtaining heat transfer coefficients, under conditions of film cooling (e.g., Nirmalan and Hylton), to obtain the adiabatic film effectiveness, several experiments have to be run at different coolant temperatures. Cascade tests of Takeishi et al. (1990), Mehendale and Han (1992), and Ou et al. (1994) have used airfoils made of insulator materials, with surface-mounted thin-foil heaters, having thermocouples embedded or tack-welded behind the heaters. This method is capable of obtaining both heat transfer coefficients and film effectiveness, but must utilize two separate tests to do so, with differing thermal boundary conditions. Also, due to the materials typically used, such tests generally are limited in the operation temperatures (coolant-to-gas density ratio) and pressure (Reynolds numbers) levels of the coolant and gas sides. In similar tests, liquid crystals have been used by Schobeiri et al. (1991), and Ou and Han (1992), to provide the surface temperature indication. Here also, the liquid crystals limit the range of temperatures that may be investigated and thus cannot model the engine coolant-to-gas density ratios of around 2 unless a heavy gas is used as the coolant medium. The methodology employed by Liu and Rodi (1992) seeks to obtain a constant

Contributed by the International Gas Turbine Institute and presented at the 40th International Gas Turbine and Aeroengine Congress and Exhibition, Houston, Texas, June 5–8, 1995. Manuscript received by the International Gas Turbine Institute February 4, 1995. Paper No. 95-GT-3. Associate Technical Editor: C. J. Russo.

temperature surface via controlled heaters and temperature sensor feedback, and uses "hot-film" sensors to determine the local heat transfer coefficients without film cooling. Takeishi et al. (1992) used the mass transfer analogy with CO_2 injectant, under both stationary and rotational conditions, to determine film effectiveness locally. Thin-walled airfoils of metal, with imbedded thermocouples and internal insulation have been used by Takeishi et al. (1990), and in earlier tests of Lander et al. (1972), to obtain film effectiveness distributions for various film cooling configurations.

Several transient methodologies have been used to obtain heat transfer characteristics, with the particularly attractive feature of reducing costly experimental test times associated with the many hours of steady-state operation, especially for larger turbine rigs. Many researchers are now using Isentropic Light Piston Compression Tube facilities, including Camci and Arts (1990, 1991), Arts and Lapidus (1992), Jones et al. (1978), Harasgama and Wedlake (1991). In these test rigs, airfoils made of machinable ceramic (Macor), or coated with a layer of ceramic, are instrumented with thin-film gages on the exterior surface. The short duration of the test obtains a period of steady conditions as the compressed gas is expanded through the rig. Employing one-dimensional, semi-infinite conduction analysis of the surface yields the heat transfer coefficients. Short-duration blow-down facilities, such as those of Guenette et al. (1989), Haldeman et al. (1992), and Abhari and Epstein (1994) are designed for the testing of entire turbine stages, or even high-pressure and low-pressure turbines together. Running to fully scaled engine parameters, these rigs must utilize actual or slave engine hardware. Fast response surface heat flux gages are used to determine the heat transfer coefficients, both instantaneous and averaged quantities locally. A method using very short duration tests has been demonstrated by Dunn and Stoddard (1979), and used for many turbine rig experiments such as those of Dunn et al. (1994). This method employs a shock tube facility to provide compressed gas with negligible heating of the turbine, thus reducing conduction effects. Here too, fast response surface gages determine the instantaneous heat transfer coefficients, all based upon turbine inlet temperature. The methodology of Vedula and Metzger (1991) requires two indications of surface temperature at the same point in space, but at differing times within one transient test (or two indications from two tests of essentially identical conditions). These researchers utilized Plexiglas substrates coated with liquid crystals, and one-dimensional semi-infinite conduction modeling, to simultaneously determine both heat transfer coefficients and film effectiveness values locally, based upon the local reference temperatures. This method is limited in the test pressure and temperature levels, imposed by substrate material and by liquid crystals, and thus cannot fully model engine dimensionless parameters. Finally, the cascade experiments by Lander et al. (1972) determined heat transfer coefficients from the transient heating of airfoils suddenly exposed to a convecting fluid of known conditions. These tests utilized two cascades, one to set flow conditions, and one to quickly shuttle into the flow. Thin-walled metal airfoils with imbedded thermocouples were used to obtain the temperature–time history of the surface at many locations.

The objectives of the present work were to build a transient test facility, similar to that of Lander et al., which will be able to provide both heat transfer coefficients and film cooling effectiveness values in linear airfoil cascades under pressure and temperature conditions that can simulate engine nondimensional parameters.

2 Test Facility

Apparatus. The transient facility presented in Fig. 1 consists of the inlet components: the main air feed line, the inlet flow straightening section, and the containment box with an elevator carrying two identical cascade sections. The first cascade section (the dummy) is used to set the flow rates and the second cascade section has airfoils instrumented with pressure taps or imbedded thermocouples. The exit components consist of the exhaust section with a back pressure control valve, the system bypass piping, the secondary film air cooling lines, and the auxiliary air cooling lines for the elevator bearing and the containment box. The primary air is supplied by a Joy rotary compressor capable of providing air flow rates up to 4.53 kg/s at pressures up to 30 atm and maximum preheat temperatures of 510°C. The flow straightening components upstream of the cascade consist of several sections transitioning the 15.24-cm-dia circular feed line into a rectangular inlet section for the linear cascade. Perforated plates are placed between the interconnecting flanges at several sections of the test rig. The flow inlet section to the linear cascade included a flow converging section with elliptically shaped walls. The fiberglass-insulated flow straightening section was enclosed in a 60.9 cm pipe. This enclosure, which is kept at a pressure close to the flow pressure, prevents the straightening section from experiencing large pressure differentials across its side walls. The containment box is 99.6 cm long, 24.6 cm wide, and 96.5 cm high, and is manufactured from six heavy plates that can withstand the test pressures. The top wall of the box was used to provide all the penetrations for the cooling air feed lines. The secondary cooling air is supplied by a second compressor (the Worthington), which is capable of supplying 1.8 kg/s at pressures up to 30 atms. A chiller installed between the film cooling cavity supply lines and the box permitted the control of the cooling air temperatures to perform tests with coolant-to-main air density ratios of around 2. Three secondary air feed lines were provided to supply

Nomenclature

a = constant = $h_f/\rho l c_p$
c_p = stainless steel specific heat
h_f = local heat transfer coefficient
l = airfoil wall thickness
m = blowing ratio = $\rho_c U_c/\rho_g U_g$
$\mathrm{Nu_{cyl}}$ = Nusselt number based on cylinder diameter; cylinder stagnation point Nusselt number (Eq. (4))
P = Local static pressure
Pr = Prandtl number
P_{stag} = Cascade inlet stagnation pressure
$\mathrm{Re_D}$ = Reynolds number based on cylinder diameter
Re = Reynolds number based on cascade inlet conditions and airfoil chord length
t = time
T_{aw} = adiabatic wall temperature
T_{cav} = coolant feed cavity temperature
T_{co} = coolant hole exit temperature
T_{rec} = recovery temperature
Tu = turbulence intensity
T_w(steady-state) = wall steady-state temperature reached at end of transient
T_w(initial) = initial wall temperature at onset of transient
$T_w(t)$ = wall temperature at time (t) of transient
U_c = local film coolant hole exit velocity
U_g = local air side velocity at film injection point
V_g = free-stream air inlet velocity
η = film cooling effectiveness
ρ = stainless steel density
ρ_c = local film coolant hole exit density
ρ_g = local air side density at film injection location
ρ_c/ρ_g = density ratio

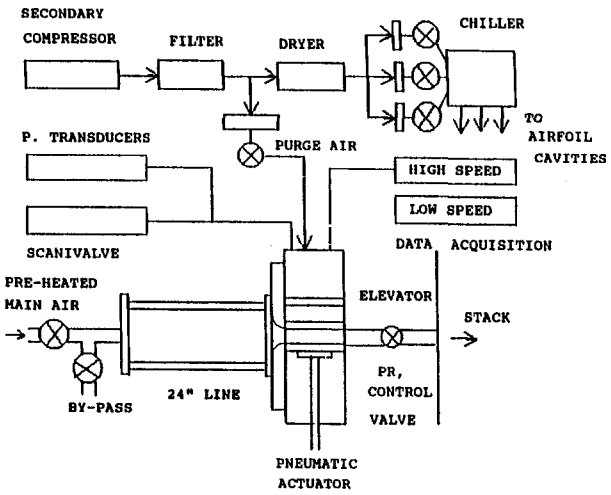

Fig. 1 Schematic of test facility

air to three airfoil film cooling cavities. The film cooling air was first passed through a filter and a drier before going into the air chiller. All the relevant air flow rates were measured with instrumented thin-plate orifices. The elevator was connected to the shaft of a pneumatic cylinder, at the bottom box wall, which was used for raising and lowering the elevator, thus controlling the air flow to pass through the dummy or the instrumented cascade section.

The test rig instrumentation consists of flow temperature and pressure monitoring devices and the data acquisition system. For the present facility, there were two different sets of data acquisition requirements. For static tests, the data were collected at a slow pace over a relatively long period of time (every ten seconds over many hours). For dynamic tests, in addition to the steady-state flow information, data were collected quickly over a short time period. Thirteen hundred data points for each of 40 thermocouples were recorded during the initial 60 seconds of the transient. During the first 10 seconds the scan rate is set to 50 readings per second, during the next 20 seconds the scan rate is 25 readings per second, and during the last 30 seconds the scan rate is 10 readings per second.

Procedure. For the transient tests performed to obtain the heat transfer and film cooling effectiveness results, the following procedure was followed: (*i*) with the elevator in the lower position, the main air flow conditions were set with the instrumented cascade in the flow field, (*ii*) the auxiliary cooling air flows were adjusted, (*iii*) the elevator was moved to the up position, transferring the flow to the "dummy cascade," (*iv*) the secondary film cooling flows were adjusted for each active film cavity, (*v*) the data acquisition was programmed for a dynamic test, (*vi*) a transient test was initiated and conducted by actuating the pneumatic cylinder, moving the elevator down and exposing the instrumented cascade to the main air flow, (*vii*) the transient data were transferred to the main computer for future analysis, (*viii*) steady-state data were collected before and after the transient test to check the flow conditions.

To analyze the transient data and convert the temperature information into a local heat transfer coefficient, the lumped parameter equation derived by Lander et al. (1972) was used. This equation represents a thin-walled section energy balance having negligible radiation and conduction losses, including the net lateral conduction within the wall and the conduction through the thermocouple leads. The lumped parameter approximation is usually valid for small values of the Biot number, defined as $\mathrm{Bi} = h_f l/k$. A curve-fitting program was used to fit an exponential curve to the data:

$$\frac{T_w(\text{steady-state}) - T_w(t)}{T_w(\text{steady-state}) - T_w(\text{initial})} = e^{-at} \tag{1}$$

Here T_w(steady-state) corresponds to the local steady-state temperature of the metal wall at the end of the transient, T_w(initial) is the metal wall temperature at time zero and $T_w(t)$ is the temperature data recorded by the high-speed data acquisition system at time t. The exponential constant a calculated by a curve fitting program was then used to calculate the local heat transfer coefficient, h_f, based on the temperature difference between the final and initial values of the temperatures:

$$a = \frac{h_f}{\rho l c_p} \tag{2}$$

In this expression ρ is the stainless steel density, c_p is the specific heat, and l is the wall thickness (0.165 cm).

The film effectiveness was calculated from

$$\eta = \frac{T_{\text{rec}} - T_{aw}}{T_{\text{rec}} - T_{co}} \tag{3}$$

In this equation T_{aw} is the wall temperature measured at the end of the transient test when steady conditions are reached, T_{co} is the coolant exit temperature. The local recovery temperature, T_{rec}, is calculated using a typical Mach number distribution taken from the cascade static pressure distribution results with a recovery factor of 0.88. Since one Mach number distribution was used for each series of tests having a given air flow rate, there may be slight errors in T_{rec}, near the trailing edge, due to variations in test-to-test pressure ratios and varying coolant addition amounts.

Using the method of Kline and McClintock (1953) for single-sample experimental uncertainties, and considering the data acquisition standard deviations for the performed tests, the single-sample uncertainties of the inlet gas, film coolant cavity, and adiabatic wall temperatures were estimated to be 1.5, 1.1, and 1.7°C, respectively. The free-stream velocity ranges from 0 to 274 m/s. Using one percent as the uncertainty in the free-stream velocity, the recovery temperature uncertainty is about 1.6°C. Then, taking the coolant exit temperature to be the cavity temperature, and using representative worst case temperature differences, the uncertainty in film effectiveness is ±0.01. Depending upon the film effectiveness local level, this represents from 1.5 percent to 17 percent uncertainty. The temperature difference between the recovery and coolant exit temperature is the controlling factor in this uncertainty. The uncertainty in the heat transfer coefficients measured with the transient method was calculated to be 8 percent for a typical test condition.

3 Preliminary Tests

For the transient tests, it was important to determine the elevator moving times between the up and down positions and compare the time scales involved with the thermal transient response time of the airfoil wall thermocouples. The travel time of the elevator under its own weight is around 0.2 seconds. The drop times are reduced to 0.1 seconds and to 0.07 seconds when the pneumatic cylinder is driven by 3.4 or 6.8 atm pressures. This time scale of 0.1 second related to the motion of the elevator is small when compared to the thermal transient test time, which is usually of the order of tens of seconds.

Air velocity distributions were measured at five locations at the flow area in the flange downstream of the smooth elliptic converging section. The five traverse locations were chosen to be symmetric with respect to the centerline of the passage. The velocity distributions were measured with a traversing Cobra probe while the flow discharged directly to atmosphere. The air flow was set to 0.47 kg/s, which provided a Reynolds number of 146,150 based on the cascade inlet conditions and the airfoil chord length. The average mass velocity was 22.6 m/s. The

averages of the velocity distributions, measured at each one of the five traverse locations, were within 5 percent of the mass flow velocity.

Axial velocity profiles, head loss coefficients, and streamwise turbulence intensities and their decay downstream of a perforated plate, similar to the one used in the present tests upstream of the cascade inlet, were experimentally determined in a separate wind tunnel with hot-wire anemometry. The perforated plate used had 0.63-cm-dia holes on 0.95 cm centers and a plate thickness of 0.32 cm, providing an open flow area of 42 percent. The results showed that (*i*) this specific perforated plate produced high turbulence intensities that decayed as a function of distance downstream of the plate, (*ii*) the turbulence decayed to a constant value as a function of inlet Reynolds number. For the Reynolds numbers range of 90,000 to 180,000, a 14 percent turbulence occurred at about 5 cm from the plate, which is typical of the distance between the perforated plate and the airfoil leading edge.

4 Cylinder in Crossflow

Tests were first conducted with cylinders in crossflow to record data with a basic configuration that has been studied extensively. A schematic of the test section with the cylinders in crossflow is presented in Fig. 2. The test rig consisted of three hollow cylinders, shown as 2, 3, and 4 (1.587 cm in diameter, 0.165 cm wall thickness), and two half-solid cylinders (1 and 5) forming a portion of the two side walls. The dimensions are representative of the airfoil leading edge flow blockage and wall thicknesses. The cylinders were positioned at a distance of 7.11 cm center-to-center. The side walls turning the flow at the exit region were straight. To divide the flow evenly between the four passages, side walls made out thin sheet metal were added downstream of each cylinder.

Two hollow center cylinders were prepared for data recording. The first one had a pressure tap at the stagnation point. The second instrumented one had a 0.051 cm thermocouple embedded into a groove along the stagnation line. Both the pressure tap and the sensing point of the thermocouple were located at the center of the flow passage.

Flow velocity distributions were measured at the center of each of the four flow passages designated as 1 to 4 in Fig. 2. The flow velocities at the center of each passage were measured by means of a cobra probe with the local static pressure for each passage being measured through a tap hole located 2.2 cm upstream of the probe. On the average the ratio of the cobra probe velocities to the mass-averaged flow velocities is 1.03 and shows a standard deviation of ± 10 percent. These velocity distributions showed that the inlet air flow was uniformly distributed among the four flow passages.

The transient heat transfer tests were conducted with the cylinder at air flow rates varying from 0.53 to 1.81 kg/s. Figure 3(*a*) depicts the transient temperature data (solid line) as a function of time for a period of 60 seconds at the air flow rate of 0.53 kg/s, corresponding to a cylinder Reynolds number of 20,700. The initial cylinder wall temperature was 66°C and the final steady-state temperature was 132.8°C, which corresponds to the air temperature. Figure 3(*b*) represents the transient temperature data (solid line) recorded at the higher flow rate of 1.81 kg/s, corresponding to a cylinder Reynolds number of 66,530. The cylinder initial temperature in this case was 68°C and the final steady-state temperature was 174°C. The open squares connected with a dashed line presented in Figs. 3(*a*) and 3(*b*) correspond to the data fit obtained with the curve fit program.

The Nusselt numbers (based on cylinder diameter) calculated from the stagnation point heat transfer results are plotted as solid squares in Fig. 4 as a function of the cylinder Reynolds numbers. On the same figure we have also plotted as a solid line the classical cylinder in crossflow stagnation point correlation (Kreith, 1966)

$$\mathrm{Nu}_{\mathrm{cyl}} = 1.14\ \mathrm{Re}_{\mathrm{D}}^{0.5}\ \mathrm{Pr}^{0.4} \tag{4}$$

The dashed line depicted in the same figure represents the stagnation point heat transfer correlation presented by Lowery and Vachon (1975), which includes the effect of the free-stream turbulence intensity:

$$\frac{\mathrm{Nu}}{\sqrt{\mathrm{Re}_{\mathrm{D}}}} = 1.01 + 2.624\left[\frac{Tu\sqrt{\mathrm{Re}_{\mathrm{D}}}}{100}\right] - 3.07\left[\frac{Tu\sqrt{\mathrm{Re}_{\mathrm{D}}}}{100}\right]^2 \tag{5}$$

The experimental results agree quite satisfactorily with the cylinder stagnation point Nusselt number predictions with a free-stream turbulence intensity of 14 percent.

5 Linear Airfoil Cascade Tests

The schematic of the cascade geometry is shown in Fig. 5. The cascade has four flow passages and five smooth airfoils, counting the contoured side walls. The three center airfoils are removable and interchangeable, and are the instrumented ones. The lower end wall has seven static pressure taps as indicated, to monitor cascade inlet and exit pressures. The upper end wall has eight taps, which may be used for pressure or temperature instrumentation rakes. The cascade inlet was provided with a turbulence generation grid providing a turbulence intensity of 14 percent at the leading edge plane. The flow path is convergent to simulate real nozzle passage geometries and the contraction is depicted in the insert of Fig. 5. Three airfoils were instrumented with static pressure taps. One had static pressure taps all along the suction and pressure surfaces while the other two had pressure taps only along the suction or the pressure sides. During pressure distribution testing, the three airfoils were in-

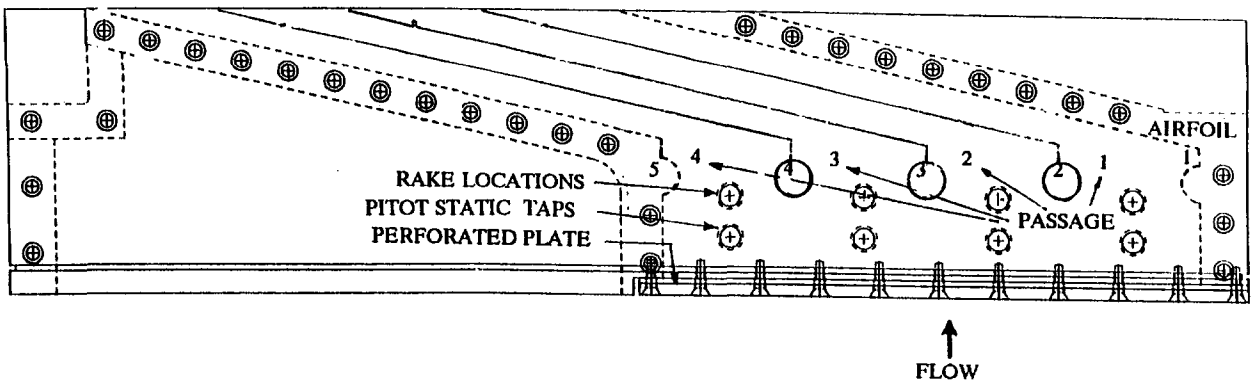

Fig. 2 Schematic of the test section with cylinders in crossflow

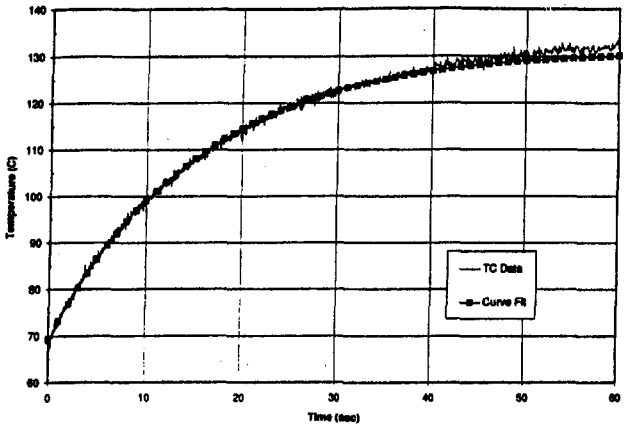

Fig. 3(*a*) Variation of stagnation point temperature with time for a transient test conducted at an air flow rate of 0.53 kg/s, comparison with curve fit (squares)

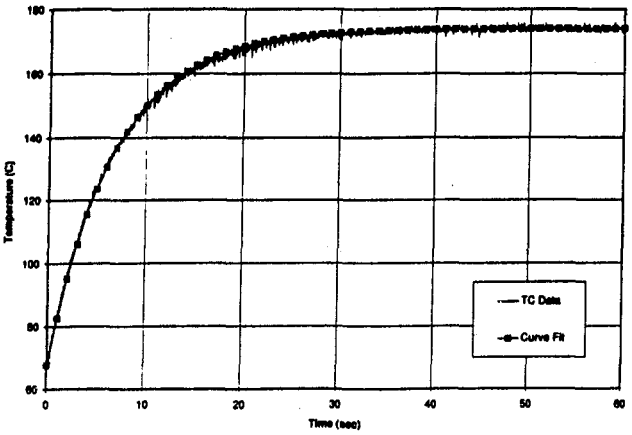

Fig. 3(*b*) Variation of stagnation point temperature with time for a transient test conducted at an air flow rate of 1.81 kg/s, comparison with curve fit (squares)

stalled, providing static pressures for the middle two flow passages. The static pressure taps are spaced 0.63 cm apart, beginning at the stagnation point of each airfoil. Airfoils 2 and 4 remain in the cascade for all testing. Figure 5 also shows the thermocouple locations for the specific airfoil configuration with three film cavities feeding fourteen rows of film cooling holes, nine in the showerhead region plus five along the suction side.

First velocity distributions were measured at the center of each of the four cascade passages by a rake of seven Pitot tubes, which were positioned at a distance of 6.35 cm upstream of the leading edge of the airfoils and at the center of each passage. With an air flow rate of 4.4 kg/s, an inlet pressure of 8.43 atm, and temperature of 207°C, the average flow velocities of passages 1, 2, 3, and 4 were measured to be 30.2, 39.0, 36.9, and 42.3 m/s respectively. The average flow velocity corresponds to 40.5 m/s. Passage 1 has a lower flow than 4, while passages 2 and 3, which surround the test airfoil, appear to have flows close to the average. The throat widths of each passage were measured with a telescope gage and found that passage 1 had a smaller throat than passage 4. The air temperature distributions at the same four center passage locations were also measured with seven sensor thermocouple probes and found to be uniform with a maximum deviation of 0.8 percent.

To calculate the Mach number distributions along the centerline airfoil, static pressure distribution measurements were performed with the pressure instrumented airfoil for two flow rates. Static pressure distributions were also measured along the pressure side of Airfoil 2 and suction side of Airfoil 4, during the tests and found to agree with the center airfoil distributions. The Mach number distributions calculated from the pressure distributions for two Reynolds numbers of 338,000 and 517,000 (mass flow 1.9 and 2.8 kg/s) are presented in Fig. 6. In the same figure the calculated Mach numbers are compared with the predicted Mach number distributions for two cascade pressure ratios of 1.36 and 1.57. These pressure ratios correspond to the pressure ratios expected without and with film addition. The measured Mach number values are scattered within the two expected limits. The objective of these static pressure measurements was to show that all tests were performed under similar flow conditions, i.e., different Reynolds numbers but similar Mach number distributions.

The center airfoil was then replaced with the thermocouple instrumented one to conduct transient heat transfer tests. At the completion of the runs with film injection, a series of tests was conducted to measure the local heat transfer coefficient distributions with no film injection and closed film holes. For these experiments all the film cooling holes were plugged with silicon RTV and the surface wiped as smooth as possible. Figures 7 and 8 depict the local heat transfer coefficients obtained for the pressure and suction sides (plugged holes) as a function of two Reynolds numbers, 338,000 and 517,000 (mass flow rates 1.9 and 2.8 kg/s) with an inlet turbulence intensity of 14 percent. The heat transfer coefficients calculated from a cylinder in crossflow and turbulent flat plate correlations for the specific flow conditions and Mach number distributions are also presented. On the same figures, we also present the heat transfer coefficients calculated from a boundary layer code with a $k-\epsilon$ turbulence model (KEP) for the same flow conditions and the Mach number distributions (Zerkle and Lounsbury, 1989). The KEP program is a modified version of the original STANX code. KEP uses a low-Reynolds-number $k-\epsilon$ turbulence model while STANX solved the boundary layer equations using a hybrid turbulence model (mixing length model coupled with a one-equation turbulence model). The KEP code was tested by Zerkle and Lounsbury (1989) for the prediction of laminar and turbulent heat transfer and transition in flat plates. The same authors used the KEP program to predict heat transfer for vanes in a linear cascade and for rotating blades in a turbine test facility. In addition to the free-stream turbulence intensity and flow acceleration, KEP also models the effect of surface curvature and surface roughness. The comparison shows that the heat transfer coefficients measured along the pressure side are lower than the predictions for a dimensionless distance larger than 0.5 and lie between the two predictions for shorter distances. On the other hand, the suction side heat transfer coefficients are relatively flat along the surface, and lower than the turbulent flat plate predictions but closer to the boundary layer code calculations. Since the present film cooling row configuration had most of the film cooling holes along the leading edge showerhead region and along the suction side of the airfoil, the

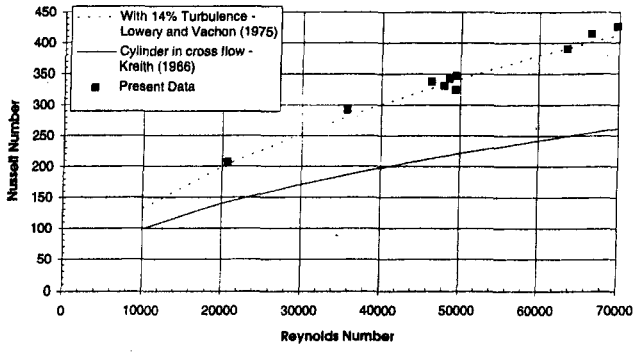

Fig. 4 Comparison of cylinder stagnation point Nusselt number data (solid diamonds) with cylinder in crossflow correlation (Kreith, 1966) and Lowery and Vachon's correlation (1975) accounting for turbulence effects

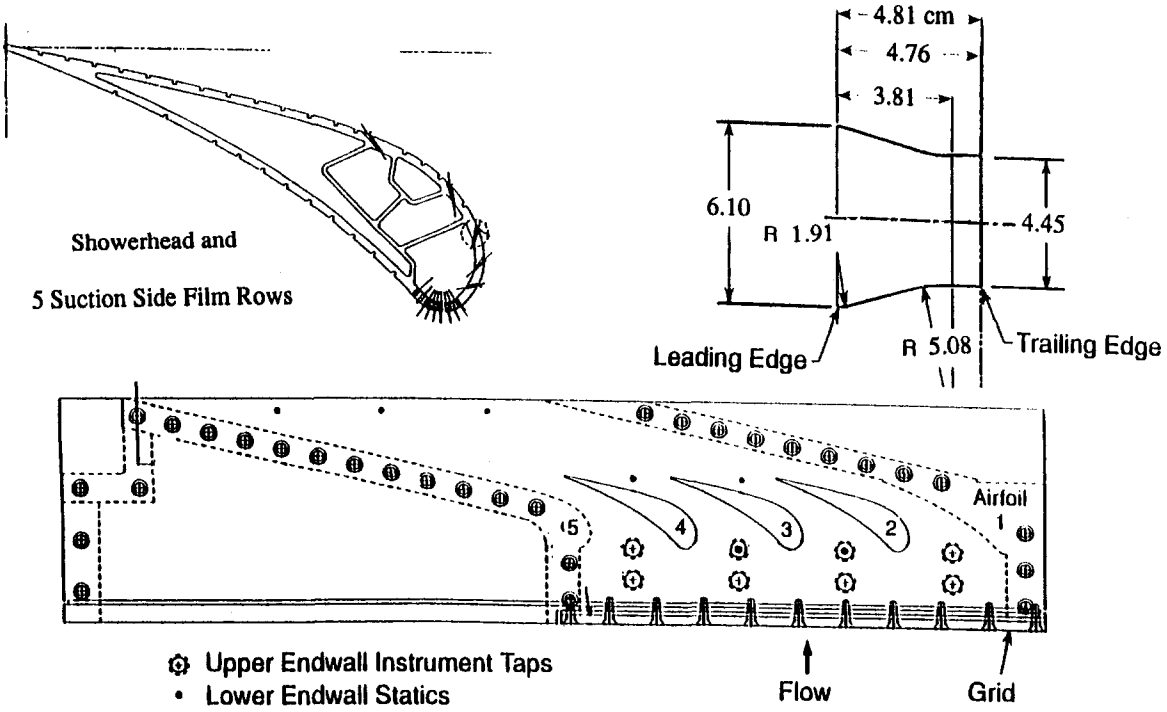

Fig. 5 Schematic of the cascade test section, and Instrumented cascade airfoil configuration with thermocouple locations, film cooling holes, and three film feed cavities

disturbance of the RTV plugged film cooling rows on the measured heat transfer coefficients is not known. The dip in the heat transfer coefficients observed near the fourth thermocouple (located at 4.09 cm from the leading edge stagnation point along the suction side), we believe is due to such an effect since this region is where the last row of film cooling holes are positioned, in addition to conduction losses due to the cavity ribs near this specific thermocouple.

Figure 8 also presents the heat transfer coefficients obtained with the transient method at a flow rate of 2.8 kg/s and an inlet turbulence intensity of 14 percent with film injection through all three film cavities. The showerhead film had density ratios of around 2.0 and blowing ratios of 1.5 to 2.7 based on approach gas velocity and density, while suction side film rows had density ratios of 1.8 to 2.0 with blowing ratios of 1.2 to 1.4 based on local gas velocities and densities. The heat transfer coefficients along the pressure side show an increase in the local values due to the film injection at the leading edge, which is being swept toward the pressure surface. The suction side heat transfer coefficients also show significant increases due to the film injection. The largest enhancement in the heat transfer coefficients is observed at the first thermocouple locations along the suction side. For the heat transfer coefficients investigated, the wall Biot numbers ranged between 0.06 and 0.23.

The steady-state wall temperature distributions obtained at the end of the transient are plotted in Fig. 9. Since the walls are not truly adiabatic, conduction corrections were required to adjust the measured wall temperatures. In regions where the walls are essentially one dimensional and well insulated, these corrections are minor. But in more complex regions, such as near film holes, these corrections required more detailed analysis.

The individual coolant film row blowing ratios were calculated by using measurements of the cavity mass flow rates, cavity air pressures and temperatures, measured exit static pressures (Mach number distribution), and film hole discharge coefficients. The hole mass flow rates were used to estimate the coolant temperature rise through the film holes, taking into ac-

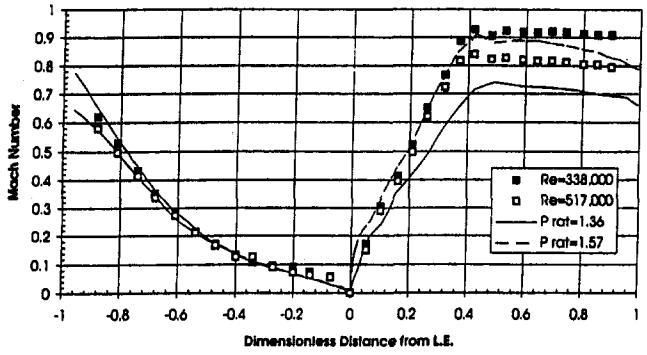

Fig. 6 Plot of Mach number distributions as a function of distance from leading edge. Pressure side (negative *x* axis), suction side (positive *x* axis). Comparison with inviscid code Mach number predictions for two cascade pressure ratios of 1.36 and 1.57.

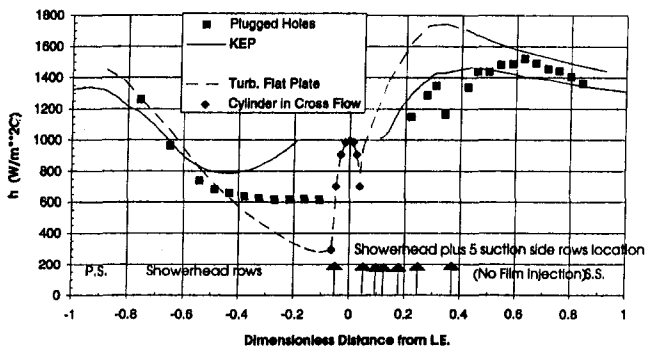

Fig. 7 Comparison of heat transfer coefficients measured with the transient technique at an air Reynolds number of 338,000 with plugged film holes versus the cylinder in cross flow and turbulent flat plate predictions and the boundary layer code (KEP) calculations

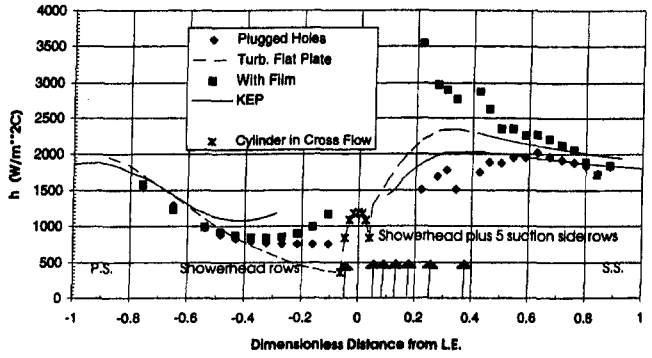

Fig. 8 Comparison of heat transfer coefficients at an air Reynolds number of 517,000 with plugged film holes and with film injection through all three film cavities versus the cylinder in crossflow and turbulent flat plate predictions and the boundary layer code (KEP) calculations with no film

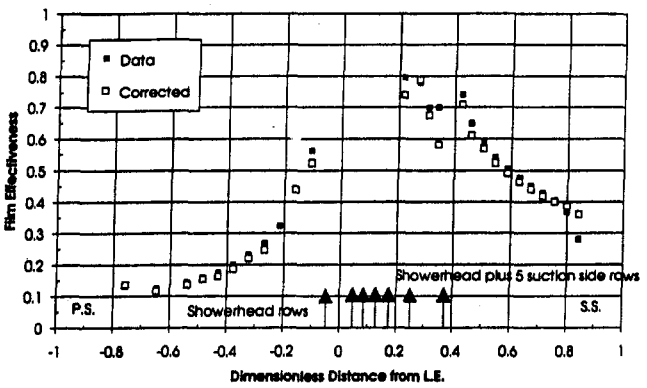

Fig. 10 Film cooling effectiveness distributions calculated at the end of the transient test at an air Reynolds number of 517,000, with film injection through all three film cavities

count entry and roughness effects on internal hole heat transfer. The resulting film exit temperatures were generally 11 to 28°C greater than the cavity temperature, depending upon the flow rate and the wall temperature in the vicinity of the film hole. Considering the airfoil configuration and thermocouple locations, the coolant exit temperature associated with the nearest upstream film row was used when determining the film effectiveness at each measurement locations. No attempt has been made to predict a mixed film coolant exit temperature due to multiple upstream film rows.

Figure 10 shows the accumulated pressure and suction side raw film effectiveness results with the three film cavities active, for the flow conditions specified above during the transient test. In the same figure the corrected film cooling effectiveness values are also plotted. The corrections to the measured adiabatic wall temperatures included, conduction corrections calculated on a one-dimensional basis, and the measured local heat transfer coefficients.

6 Summary and Conclusions

A transient test facility has been built for the purpose of determining both heat transfer coefficient and film cooling effectiveness distributions in a linear airfoil cascade. The cascade is capable of operation in either the steady-state mode, to obtain local adiabatic film effectiveness values, or in the transient mode, to obtain both heat transfer coefficients and film effectiveness values. The transient operation is of particular importance, in that the relevant heat transfer characteristics are determined within the same aerothermal environment.

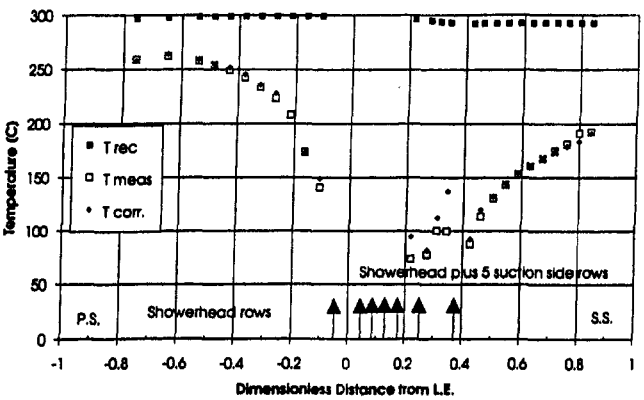

Fig. 9 Recovery temperature distributions calculated and the steady wall temperatures measured at the end of the transient test at an air Reynolds number of 517,000, with film injection through all three film cavities

A test cascade of cylinders in crossflow has been used to verify the experimental methodology. Stagnation point heat transfer coefficients obtained agree with the established correlation for a cylinder in crossflow including turbulence effects.

Heat transfer coefficient and film cooling effectiveness distributions were obtained for a linear airfoil cascade, with and without film coolant injection at two flow numbers. For the particular airfoil used in these tests, the findings include: (*i*) The pressure and suction side heat transfer coefficients obtained with 14 percent inlet turbulence and plugged film holes follow the boundary layer code (KEP) predictions, (*ii*) the film injection increases the heat transfer coefficient levels both on the pressure and suction sides.

References

Abhari, R. S., and Epstein, A. H., 1994, "An Experimental Study of Film Cooling in a Rotating Transonic Turbine," ASME JOURNAL OF TURBOMACHINERY, Vol. 116, pp. 63–70.

Arts, T., and Lapidus, I., 1992, "Thermal Effects of a Coolant Film Along the Suction Side of a High Pressure Turbine Nozzle Guide Vane," AGARD 80th Symposium of Propulsion and Energetics Panel, Antalya, Turkey, Oct., AGARD-CP-527.

Camci, C., and Arts, T., 1990, "An Experimental Convective Heat Transfer Investigation Around a Film-Cooled Gas Turbine Blade," ASME JOURNAL OF TURBOMACHINERY, Vol. 112, pp. 497–503.

Camci, C., and Arts, T., 1991, "Effect of Incidence on Wall Heating Rates and Aerodynamics on a Film-Cooled Transonic Turbine Blade," ASME JOURNAL OF TURBOMACHINERY, Vol. 113, pp. 493–501.

Dullenkopf, K., Schulz, A., and Wittig, S., 1991, "The Effect of Incident Wake Conditions on the Mean Heat Transfer of an Airfoil," ASME JOURNAL OF TURBOMACHINERY, Vol. 113, pp. 412–418.

Dunn, M. G., and Stoddard, F. J., 1979, "Measurement of Heat-Transfer Rate to a Gas Turbine Stator," ASME *Journal of Engineering for Power,* Vol. 101, pp. 275–280.

Dunn, M. G., Kim, J., Civinskas, K. C., and Boyle, R. J., 1994, "Time-Averaged Heat Transfer and Pressure Measurements and Comparison With Prediction for a Two-Stage Turbine," ASME JOURNAL OF TURBOMACHINERY, Vol. 116, pp. 14–22.

Guenette, G. R., Epstein, A. H., Giles, M. B., Haimes, R., and Norton, R. J. G., 1989, "Fully Scaled Transonic Turbine Rotor Heat Transfer Measurements," ASME JOURNAL OF TURBOMACHINERY, Vol. 111, pp. 1–7.

Haldeman, C. W., Dunn, M. G., MacArthur, C. D., and Murawski, C. G., 1992, "The USAF Advanced Turbine Aerothermal Research Rig (ATARR)," AGARD 80th Symposium of Propulsion and Energetics Panel, Antalya, Turkey, Oct., AGARD-CP-527.

Harasgama, S. P., and Wedlake, E. T., 1991, "Heat Transfer and Aerodynamics of a High Rim Speed Turbine Nozzle Guide Vane Tested in the RAE Isentropic Light Piston Cascade (ILPC)," ASME JOURNAL OF TURBOMACHINERY, Vol. 113, pp. 384–391.

Jones, T. V., Schultz, D. L., Oldfield, M. L. G., and Daniels, L. C., 1978, "Measurement of Heat Transfer Rate to Turbine Blades and Nozzle Guide Vanes in a Transient Cascade," *Proc. 6th International Heat Transfer Conference,* Toronto, Canada, pp. 73–78.

Kreith, F., 1966, *Principles of Heat Transfer,* International Textbook Co., Scranton, PA, p. 408.

Lander, R. D., Fish, R. W., and Suo, M., 1972, "External Heat-Transfer Distribution on Film Cooled Turbine Vane," *J. Aircraft,* Vol. 9, No. 10, pp. 707–714.

Liu, X., and Rodi, W., 1992, "Measurement of Unsteady Flow and Heat Transfer in a Linear Turbine Cascade," ASME Paper No. 92-GT-323.

Lowery, G. W., and Vachon, R. I., 1975, "The Effect of Turbulence on Heat Transfer From Heated Cylinders," *Int. J. Heat Mass Transfer,* Vol. 18, pp. 1229–1242.

Mehendale, A. B., and Han, J. C., 1992, "Influence of High Mainstream Turbulence on Leading Edge Film Cooling Heat Transfer," ASME JOURNAL OF TURBOMACHINERY, Vol. 114, No. 4, pp. 707–715.

Mehendale, A. B., Han, J. C., and Ou, S., 1991, "Influence of High Mainstream Turbulence on Leading Edge Heat Transfer," ASME *Journal of Heat Transfer,* Vol. 113, pp. 843–850.

Nirmalan, N. V., and Hylton, L. D., 1990, "An Experimental Study of Turbine Vane Heat Transfer With Leading Edge and Downstream Film Cooling," ASME JOURNAL OF TURBOMACHINERY, Vol. 112, pp. 477–487.

Ou, S., and Han, J. C., 1992, "Influence of Mainstream Turbulence on Leading Edge Film Cooling Heat Transfer Through Two Rows of Inclined Film Slots," ASME JOURNAL OF TURBOMACHINERY, Vol. 114, pp. 724–733.

Ou, S., Han, J. C., Mehendale, A. B., and Lee, C. P., 1994, "Unsteady Wake Over a Linear Turbine Blade Cascade With Air and CO_2 Film Injection: Part I—Effect on Heat Transfer Coefficients," ASME JOURNAL OF TURBOMACHINERY, Vol. 116, pp. 721–729.

Schobeiri, T., McFarland, E., and Yeh, F., 1991, "Aerodynamics and Heat Transfer Investigations on a High Reynolds Number Turbine Cascade," ASME Paper No. 91-GT-157.

Takeishi, K., Matsuura, M., Aoki, S., and Sato, T., 1990, "An Experimental Study of Heat Transfer and Film Cooling on Low Aspect Ratio Turbine Nozzles," ASME JOURNAL OF TURBOMACHINERY, Vol. 112, pp. 488–496.

Takeishi, K., Aoki, S., Sato, T., and Tsukagoshi, K., 1992, "Film Cooling on a Gas Turbine Rotor Blade," ASME JOURNAL OF TURBOMACHINERY, Vol. 114, pp. 828–834.

Vedula, R. J., and Metzger, D. E., 1991, "A Method for the Simultaneous Determination of Local Effectiveness and Heat Transfer Distributions in Three-Temperature Convection Situations," ASME Paper No. 91-GT-345.

Zerkle, R. D., and Lounsbury, R. J., 1989, "Freestream Turbulence Effect on Turbine Airfoil Heat Transfer," *J. Propulsion,* Vol. 5, No. 1, pp. 82–88.

Flow Characteristics and Aerodynamic Losses of Film-Cooling Jets With Compound Angle Orientations

Sang Woo Lee

Yong Beom Kim[1]

Department of Mechanical Engineering,
Kum-Oh National University of Technology,
Kumi, Kyungbook,
Republic of Korea

Joon Sik Lee

Department of Mechanical Engineering,
Seoul National University,
Seoul, Republic of Korea

Oil-film flow visualizations and three-dimensional flow measurements using a five-hole probe have been conducted to investigate the flow characteristics and aerodynamic loss distributions of film-cooling jets with compound angle orientations. For a fixed inclination angle of the injection hole, measurements are performed at various orientation angles to the direction of the mainstream in the case of three velocity ratios of 0.5, 1.0, and 2.0. Flow visualizations for the velocity ratio of 2.0 show that the increase in the orientation angle furnishes better film coverage on the test surface, but gives rise to large flow disturbances in the mainstream. A near-wall flow model has been proposed based on the surface flow visualizations. It has also been found from the flow measurements that as the orientation angle increases, a pair of counter-rotating vortices turn to a single strong one, and the aerodynamic loss field is closely related to the secondary flow. Even in the case of the velocity ratio of 2.0, aerodynamic loss is produced within the jet region when the orientation angle is large. Regardless of the velocity ratio, the mass-averaged aerodynamic loss increases with increasing orientation angle, the effect of which on aerodynamic loss is pronounced when the velocity ratio is large.

Introduction

Film-cooling has been one of the most extensively studied cooling methods over the last two decades due to its wide variety of practical applications in such high-temperature systems as turbine blades, combustors, and after-burners. A lot of studies have been performed to enhance film-cooling effectiveness for various injection systems, among which film-cooling with compound angle orientation has recently been recognized as one of the most effective cooling arrangements. This compound angle orientation can also be encountered in blade film-cooling with a strong vortical mainflow like a passage vortex and in film-cooling at the turbine endwall where the main flow is not usually parallel to the turbine axial direction.

Most of studies on flow characteristics of coolant jets in mainstream (Pietrzyk et al., 1989; Sinha et al., 1991; Lee et al., 1994; Leylek and Zerkle, 1994) were concerned with jets injected in a parallel direction with mainstream. Only a few studies have been investigated on the compound angle orientations. Ligrani and Mitchell (1994) reported the effect of longitudinal embedded vortices on the flow field and heat transfer over a plate with rows of film-cooling holes with compound angle orientations. Honami et al. (1994) studied the behavior of laterally injected film-cooling jets at low mass flux ratios, which can be regarded as the limiting case of the compound film-cooling with $\beta = 90$ deg. They found by a liquid crystal technique and a double-wire probe that the laterally injected jets showed an asymmetric behavior with a large scale of vortex motion. Generally, introduction of jets into a mainstream at compound angles inevitably produces vigorous interaction and mixing of the two fluids, which may result in a considerable aerodynamic loss. Yamamoto et al. (1991) investigated the flow and aerodynamic loss field in a linear cascade passage with film-cooling air jets injected through various slits, and found that the cascade overall loss decreased when the air was injected along the mainstream, but increased when the air was injected against the mainstream at certain locations from the blade leading edge. Mayle and Anderson (1991) reported aerodynamic loss data for stagnation film-cooling in the spanwise direction ($\beta = 90$ deg). They found that the aerodynamic loss caused by injection increased linearly with the increment of the mass injected. Recently, Cho and Goldstein (1993) investigated heat (mass) transfer and film cooling effectiveness within the film-cooling holes and on the backside surface, using the naphthalene sublimation technique.

Understanding of complete three-dimensional flow structure and aerodynamic loss field associated with film-cooling jets with compound angle orientations is essential to the optimal thermal design of gas turbine hot components. In this study, flow characteristics and aerodynamic loss distributions of the compound film-cooling jets have been investigated with orientation angle variations through oil-film flow visualization and three-dimensional flow measurements.

Experimental Apparatus and Procedure

The wind tunnel used in this study was an open-circuit type with a cross section of 0.8 m × 0.4 m. At a mean velocity of 15 m/s, uniformity of the mean velocity and turbulence level were 1.0 and 0.5 percent, respectively. The uniform flow coming out from the wind tunnel contraction body is developing to the turbulent boundary-layer flow on the floor of the test section after a trip wire of 1.8 mm in diameter, which is located 60 mm downstream of the wind tunnel exit. A rotatable circular injection plate made of plexiglass, as shown in Fig. 1, was placed on the floor of 20 mm in thickness, and its center was located 740 mm downstream of the trip wire.

In order to simulate the injection air flow as a fully developed one, the injection tube with inner diameter, D, of 30 mm was

[1] Present address: Design Department, TOP Eng. Co., Orori 60-3 Koa-myon, Kumi, Kyongbuk, 730-810 Korea.

Contributed by the International Gas Turbine Institute and presented at the 40th International Gas Turbine and Aeroengine Congress and Exhibition, Houston, Texas, June 5–8, 1995. Manuscript received by the International Gas Turbine Institute February 27, 1995. Paper No. 95-GT-38. Associate Technical Editor: C. J. Russo.

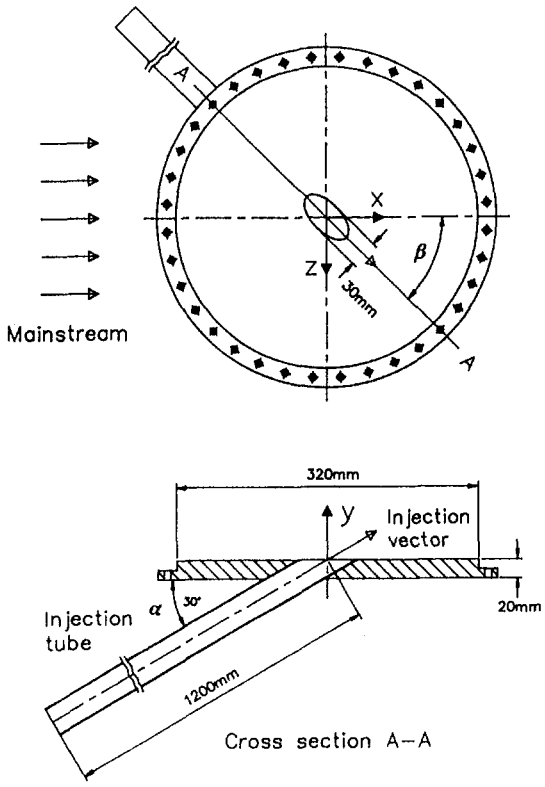

Fig. 1 Rotatable injection plate and coordinate system

made 1200 mm long. The injection tube was attached at the center of the rotatable injection plate so that the center of the injection hole always lay at the same position regardless of orientation variations. The x, y, and z are streamwise, normal, and spanwise coordinates, respectively, with respect to the mainstream direction.

The compound angle orientation can be identified by two injection angles, the inclination angle, α, and the orientation angle, β, as depicted in Fig. 1. The inclination angle is defined as the angle between the injection vector and its projection on $x-z$ plane, and the orientation angle as the angle between the streamwise direction and projection of the injection vector on $x-z$ plane. The inclination angle was fixed at 30 deg throughout the experiments; meanwhile, the orientation angle was varied by 5 deg. The injection hole has an elliptical shape. The major axis of the ellipse is 60 mm long and its minor axis is 30 mm long. The injection air from a centrifugal blower (AEG, AM132-SP2) was supplied to the injection tube via a bypass valve, a heat exchanger, an orifice, and a flow control valve in sequence. The present study employed a corner-tapping orifice based on ISO 5167 (1991).

A five-hole probe (United Electric Controls, DC-125-24-F-22-CD) of 0.125 in. in tip diameter, which has a "cobra" configuration, was used to measure three-dimensional velocity components. The automatic probe traverse system was equipped with a pair of linear motion guides (Samik, SAR1615T), stepping motors (Oriental Motor, UPH599-A), and stepping motor drivers (Oriental Motor, UDX5114). Probe traversing and pressure measurement were controlled by a personal computer (IBM, AT 486) equipped with plug-in boards such as Multi-Function DI/O Board (National Instruments, AT-MIO-16D-H-9) and GPIB adapter (National Instruments, AT-GPIB). The automatic probe traverse system and pressure scanning box (Furness Controls, FC091-6) for switching the pressure holes from the five-hole probe in sequence were controlled by digital-out signals from the Multi-Function DI/O Board. Measured pressures were transformed into DC voltages by a high-accuracy differential pressure transducer (MKS, Type 120AD-00010RAB) and power-supply readout (MKS, Type 510B), in which an electric heater was installed to keep the transducer at constant temperature of 45°C. The electric signals were sampled by a 12-bit A-D converter in the Multi-Function DI/O Board, and transferred into the computer. The temperatures of mainstream and jet flow were measured by T-type thermocouples connected to a temperature scanner (Keithley, Model 2001 TSCAN), which was also controlled by the computer through the GPIB. The whole measurement system was controlled in a proper sequence by a stand-alone C-language program developed with an instrument software, LabWindows (National Instruments, ver.2.3).

In this study, a non-nulling calibration program based on Treaster and Yocum (1979) was developed to determine flow angles, total pressure, and static pressure from calibration charts. The calibration was carried out for pitch and yaw angles in range between −40 deg and 40 deg with an increment of 5 deg.

Experimental Conditions and Uncertainties

During flow visualization and velocity measurement, free-stream velocity, U_∞, measured at $x = -500$ mm was maintained at 15 m/s. At the center of the injection plate, the boundary-

Nomenclature

$C_{Pt,bas}$ = base total pressure loss coefficient without injection, Eq. (1)
$C_{Pt,inj}$ = total pressure loss coefficient with injection, Eq. (2)
$C_{Pt,net}$ = net total pressure loss coefficient due to injection, Eq. (3)
$\bar{C}_{Pt,bas}$ = mass-averaged base total pressure loss coefficient, Eq. (4)
$\bar{C}_{Pt,inj}$ = mass-averaged total pressure loss coefficient with injection, Eq. (5)
$\bar{C}_{Pt,net}$ = mass-averaged net total pressure loss coefficient, Eq. (6)
D = inner diameter of injection tube
J = momentum flux ratio = $\rho_j U_j^2/\rho_\infty U_\infty^2$
$P_{t,bas}$ = total pressure measured without injection
$P_{t,inj}$ = total pressure measured with injection
$P_{t,\infty}$ = free-stream total pressure
R = velocity ratio = U_j/U_∞
Re_D = Reynolds number = $U_j D/\nu_\infty$
Re_{δ_2} = Reynolds number = $U_\infty \delta_2/\nu_\infty$
U = x-directional velocity
U_b = x-directional velocity without injection
U_j = spatially averaged velocity across injection tube
U_∞ = free-stream velocity
V = y-directional velocity
W = z-directional velocity
x = coordinate in streamwise direction, Fig. 1
y = coordinate in normal direction, Fig. 1
z = coordinate in spanwise direction, Fig. 1
α = inclination angle, defined as the angle between injection vector and its projection on $x-z$ plane, Fig. 1
β = orientation angle, defined as the angle between x axis and projection of injection vector on $x-z$ plane, Fig. 1
δ_2 = momentum boundary layer thickness at the hole site
ν_∞ = kinematic viscosity of mainstream
ρ_j = density of injected fluid
ρ_∞ = density of mainstream fluid
Ω_x = dimensionless vorticity in x direction = $(D/U_\infty)[(\partial W/\partial y) - (\partial V/\partial z)]$

Table 1 Experimental conditions

	U_∞ (m/s)	D (mm)	α (deg)	β (deg)	R (J)
Oil-film visualization	15	30	30	30, 60, 90	2.0(4.0)
Flow measurement	15	30	30	30, 60, 90	0.5(0.25), 1.0(1.0)
				0, 15, 30, 45, 60, 75, 90	2.0(4.0)

layer thickness was about 17.5 mm and the displacement and momentum thicknesses were 2.29 mm and 1.81 mm, respectively. The two dimensionality of the mainstream boundary layer was assured by measuring velocity profiles at four spanwise positions. The Reynolds number based on the free-stream velocity and momentum boundary layer thickness, Re_{δ_2}, was 1.80×10^3 and the Reynolds number defined using the spatially averaged injection velocity and diameter of the injection tube, Re_D, was 5.97×10^4, when the velocity ratio is 2.0. The temperature difference between the mainstream and jet was controlled within 0.5°C, so that the density ratio of the two fluids, ρ_j/ρ_∞, was safely assumed to be unity. During the flow visualizations, the velocity ratio, $R = U_j/U_\infty$, and the momentum flux ratio, $J = \rho_j U_j^2/\rho_\infty U_\infty^2$, were fixed as 2.0 and 4.0, respectively. In the case of flow measurements, the velocity ratio is changed to be $R = 0.5$, 1.0, and 2.0, which are equivalent to $J = 0.25$, 1.0, and 4.0, respectively. For the inclination angle of 30 deg, the orientation angle was varied as in Table 1. The three-dimensional flow measurements using the five-hole probe were conducted in the y–z plane where $x/D = 8$, with an interval of $D/6$ in both y and z directions. Flow measurements in the z direction were carried out at 37 points for all cases, but the measuring locations were different from one case to another. In the y direction, measurements were performed at 18 points for $R = 0.5$ and 1.0, and at 24 points for $R = 2.0$, starting from $y = D/6$. The experimental conditions are summarized in Table 1.

The uncertainty intervals presented in this study were evaluated with 95 percent confidence. Uncertainties associated with the probe location were given to be ±0.1 mm in the x direction and ±0.05 mm in both y and z directions, and uncertainty in pressure measurement was estimated to be ±0.7 percent of the free-stream dynamic pressure. The uncertainty in the injection flow measurements based on the uncertainty analysis of the ISO 5167 (1991) was ±0.5 percent of mass flow rate. The orifice measurement also showed a good agreement within 1 percent, compared with the result using a total-head probe. In the five-hole probe measurement, uncertainty intervals based on Kline and McClintock (1953) were calculated to be ±1.1 deg in flow angles and ±1.4 percent in velocity magnitude with the same approach employed by Shepherd (1981). After completion of the present experiments, mass balance and repeatability were checked when $R = 2.0$ and $\beta = 60$ deg. The results showed that the net mass flux calculated at six boundary surfaces of measuring control volume between the planes with $x/D = 8$ and 12 was balanced to within 0.4 percent of total inlet mass flux. The uncertainties from the repeatability test were found to be ±1.5 deg for flow angles and ±1.9 percent of free-stream velocity for velocity magnitude.

Results and Discussion

Surface Flow Visualization. Surface flow visualization using oil film is considered as one of the most effective ways to understand the near-wall flow pattern (Goldstein and Chen, 1985). In this study, two different approaches for oil-film visualizations were employed using a mixture of carbon-black and kerosine. In the first approach (referred to as Method 1 hereafter), only the surface 100 mm upstream of the injection-hole site was initially coated with the oil film. In this method, the oil film on the surface flows along only with the mainstream fluid in the downstream direction. Accordingly, the oil-film trace on the surface clearly distinguished the mainstream from the jet region. In order to move the mixture easily with the mainflow, kerosine was spread on the whole test surface before the upstream coating of the mixture. In the second approach (Method 2), the whole test surface was initially covered with the oil film.

Based on the observation from the flow visualizations, a unique surface flow model has been suggested for $R = 2.0$, as shown in Fig. 2. This flow map was depicted specifically based on the visualization when $\beta = 60$ deg in Fig. 3(b); however, the overall flow patterns were similar for various orientation angles. The dotted lines in Fig. 2 are streamlines drawn selectively after the surface impressions of Fig. 3(b), and the solid lines denote boundaries among different flow regions. The lines AB, BD, BE, EF, and GI are obtained from Method 1, and the lines EH and GJ from Method 2. The line DBE is considered as a three-dimensional separation line, along which the oncoming boundary layer flow separates from the surface, and point B is a so-called saddle point. All streamlines near the line ABC are found to be parallel with the line, which means that there is no near-wall flow crossing the line ABC. In the hatched areas near the injection hole, which is drawn from Method 2 in Fig. 3(b), the mixture accumulates without moving out of the areas, and the kerosine is finally evaporated there. Therefore, the areas may be considered as flow recirculation zones.

The present flow model comprises five flow regions. Regions 1 and 2, bounded by the lines ABEF and ABDGI, respectively, are occupied only by the mainstream fluid. The overall flow structure in Region 1 shows that moving downstream, the mainstream is pushed outward in the positive z direction by the jet injection, and streamline curvatures are relatively small exclusive of those near the saddle point B. In Region 2, however, the streamlines show large curvatures, which result from strong inward motion of the mainstream fluid toward the wake formed behind the jet. Region 3 is bounded by the closed line BEHCDB. Generally, the oncoming mainflow is obstructed by the jet near the injection hole, just like a near-wall flow around a cylinder protruded in the boundary-layer flow and consequently very complicated secondary flows are generated. Along the line DBE, the oncoming mainstream is separated from the wall and the separated flow is developed into several vortical motions such as horseshoe vortices, separation vortices, countervortices, and corner vortices, as proposed by Ishii and Honami (1986). In addition to the mutual deflection of the jet and mainstream, the jet entrains the mainstream fluid with a vigorous turbulent

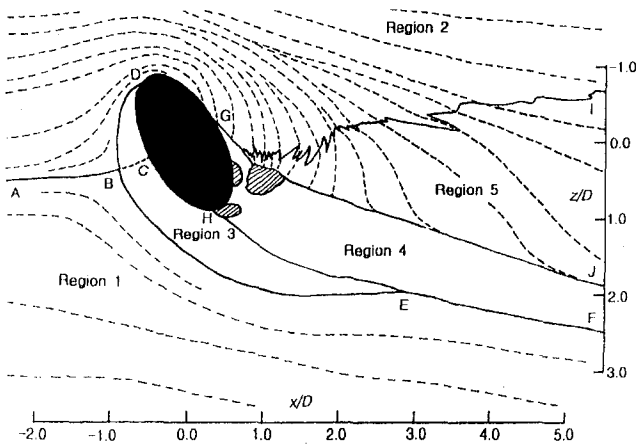

Fig. 2 Surface flow model based on oil-film visualization for $\beta = 60$ deg in the case of $R = 2.0$

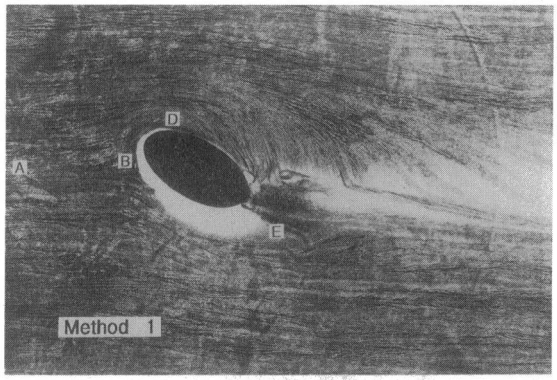

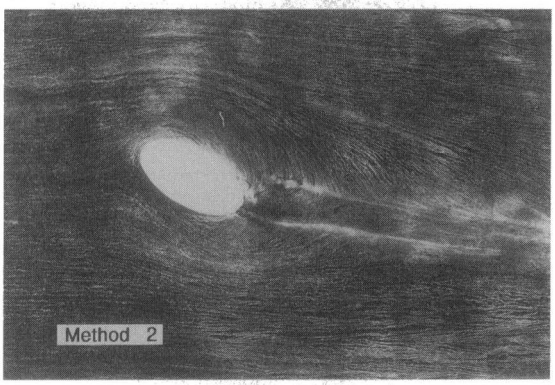

(a) β = 30 deg

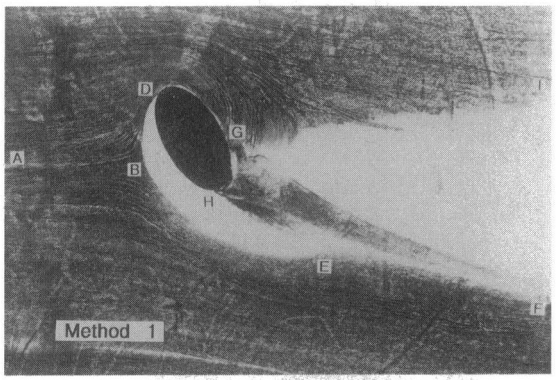

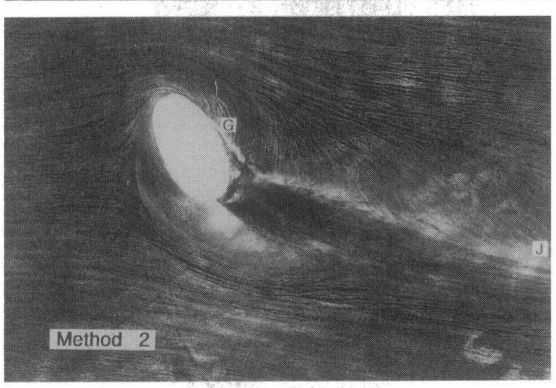

(b) β = 60 deg

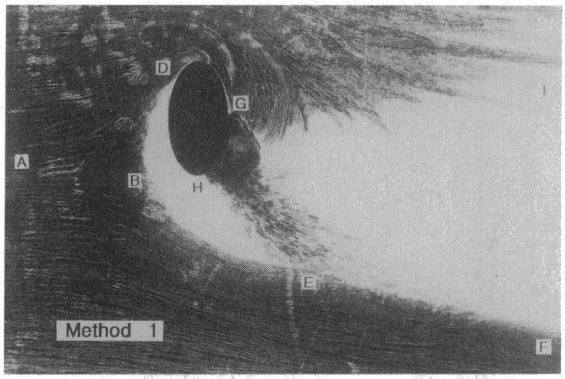

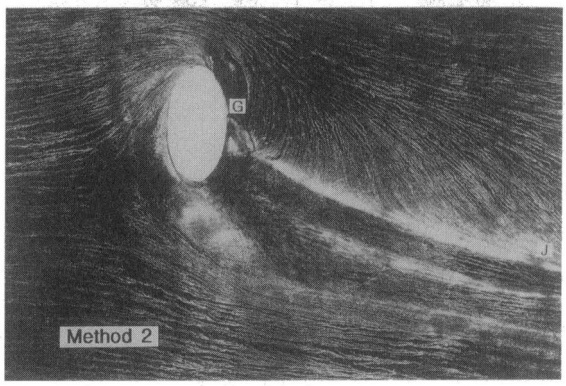

(c) β = 90 deg

Fig. 3 Surface flow visualization for R = 2.0

mixing. Examining the flow visualizations in Figs. 3(b) and 3(c), the streamlines on the surface from Method 2 are nearly parallel with the line EF, which was obtained from Method 1, and near the line GI, the surface streamlines from Method 2 always cross the line GI drawn after Method 1. In the oil-film visualization using the carbon-black and kerosine mixture, the kerosine is continuously evaporating during moving downstream. Thus, especially in the case of Method 1, the mixture can cease to move with the mainstream, without overcoming friction, in the areas where near-wall flow is slowed down. The line GI originates from this fact. Accordingly, different from other solid lines, the line GI is neither a separation line nor a boundary between the mainstream and jet regions. The region between the lines GJ and HEF, which is defined as Region 4, is the one occupied by the injected jet. The film-cooling effectiveness in Region 4 is expected to be the highest among the five regions. These discussions on the line GI show that the flow pattern in Region 5, lying between Regions 2 and 4, is very similar to that in Region 2, because the dotted lines always pass across the line GI. However, there is a strong streamwise vortex above Region 5, which will be shown later from the three-dimensional flow data.

Figure 3 shows the surface flow visualizations when β = 30, 60, and 90 deg. For β = 30 deg (Fig. 3(a)), streamline deflections due to the presence of the jet are relatively small and the whole test area in Method 1 is covered with the mixture, except for the narrow area classified as Region 3 in the surface flow model. Region 4, where jet fluid touchs the wall, is not apparent at this orientation angle. The area between the two nearly parallel lines running downstream, starting from the downstream edge of the injection hole in Method 2, could be identified as a wake region lying underneath the jet trajectory. The mainstream fluid near the wall in the wake is attributed to the inward motion due to the pressure drop in this region. Just like the flow map in Fig. 2, there exist three recirculating zones downstream of the injection hole in an asymmetric manner. As the orientation angle increases to 60 deg, the flow pattern is significantly altered. First of all, the near-field and downstream of the injection hole are clearly classified into five regions as in Fig. 2 and the injected jet influences very large area. With the increment of the orientation angle, the area of Region 4 is significantly extended, which means that large orientation angle results in wide film coverage, especially in the spanwise direction.

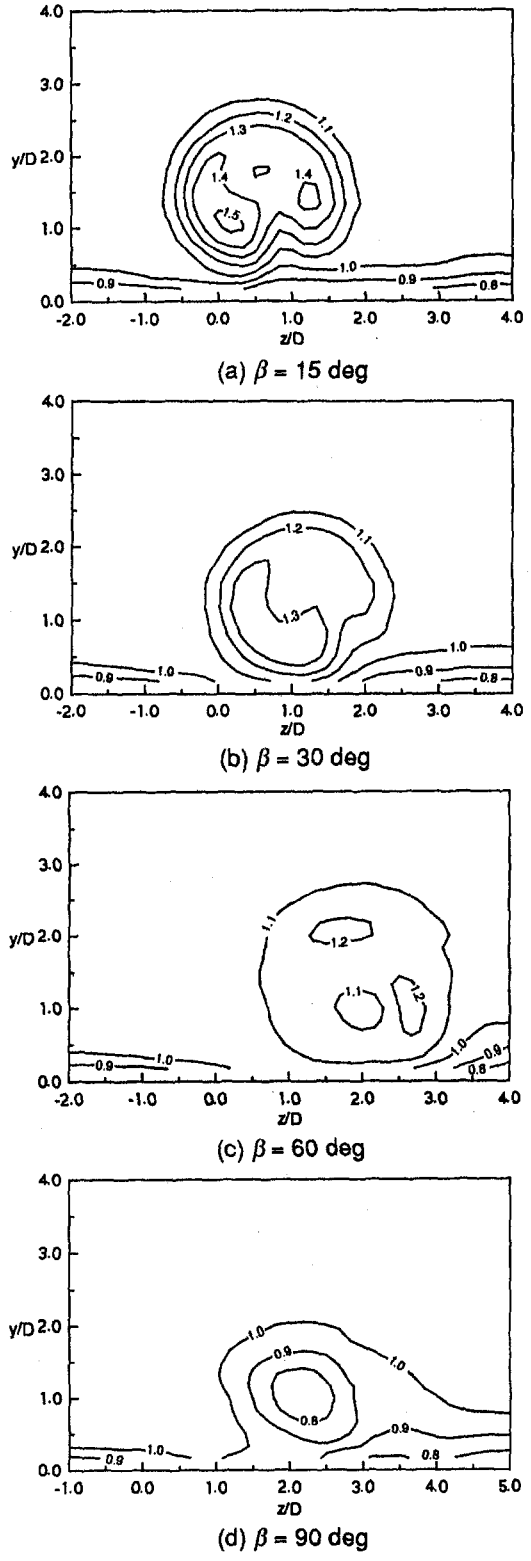

Fig. 4 Contours of dimensionless x-directional velocity, U/U_∞, at x/D = 8 for R = 2.0

Interestingly, the areas where the mixture is accumulated, just like the hatched areas in Fig. 2, are incorporated into a single large one when $\beta = 90$ deg (Fig. 3(c)), which implies that the flow disturbance in the case of $\beta = 90$ deg is much larger than that when $\beta = 60$ deg. In Figs. 3(b) and 3(c), the flow reversal is apparently observed near point G and the streamlines in the reverse-flow region head toward the hatched areas. From these flow visualizations, it is found that with the increase of the orientation angle, the areas of Regions 3, 4, and 5 are widely extended and the streamlines on the surface are greatly curved with a large deviation from flow symmetry. Moreover, the flow disturbances including flow reversal and flow recirculation in-

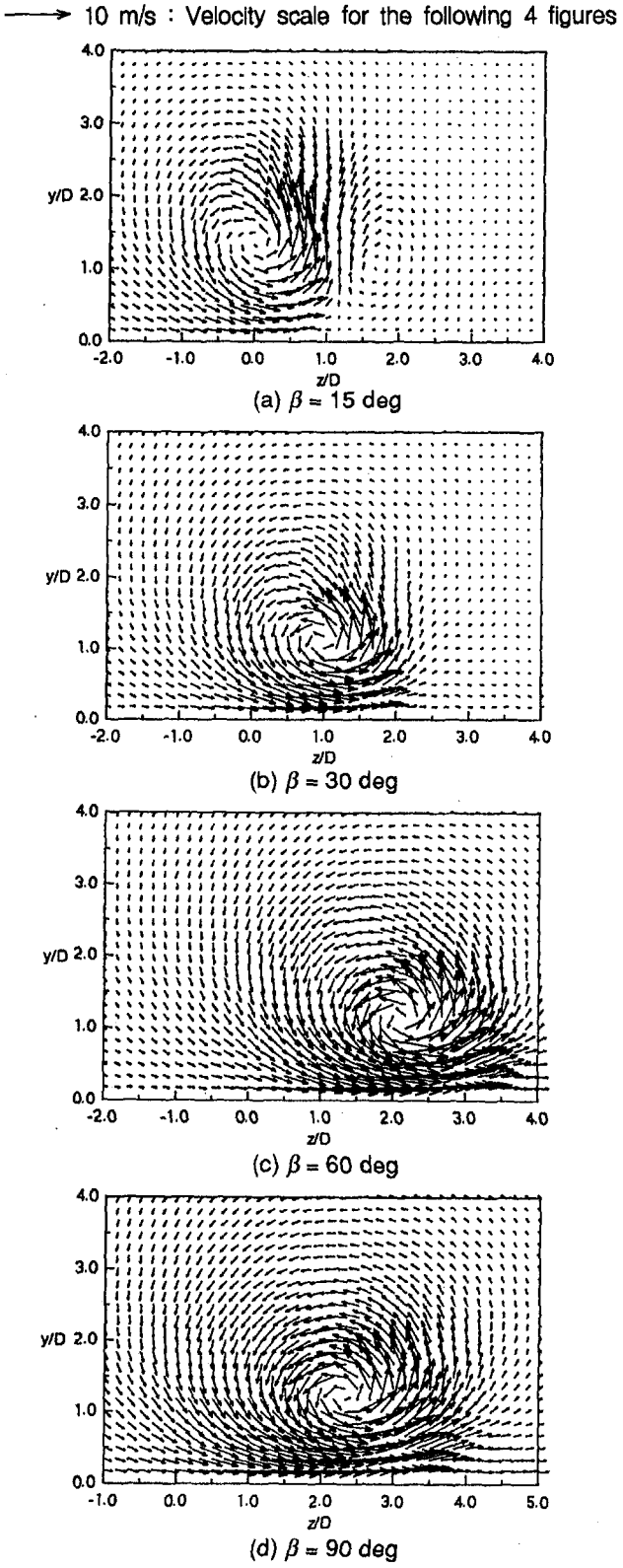

Fig. 5 Projection of velocity vectors on y–z plane at x/D = 8 for R = 2.0

crease remarkably with the orientation angle. These facts indicate that large orientation angle may result in large aerodynamic loss as well as high film-cooling effectiveness.

Three-Dimensional Flow Fields. The downstream flow of the streamwise injected jet in a mainstream is characterized by a pair of counterrotating vortices with flow symmetry (Lee et al., 1994; Leylek and Zerkle, 1994). Film-cooling jets with an orientation angle other than 0 deg show very different flow structure, losing the flow symmetry. Distributions of x-directional velocity component, U_j/U_∞, secondary flows in y–z plane, and dimensionless vorticity in x direction, Ω_x, for β = 15, 30, 60, and 90 deg in the case of R = 2.0 are presented in Figs. 4, 5, and 6, respectively. All the measurements were carried out in y–z plane at x/D = 8. As can be seen in the figures, flow symmetry with respect to the jet symmetry plane is no longer existent even when β = 15 deg. The streamwise velocity contours in Fig. 4 show that the velocity gradients decrease with an increase in the orientation angle and eventually the velocity deficit in the jet core is found in the case of β = 90 deg.

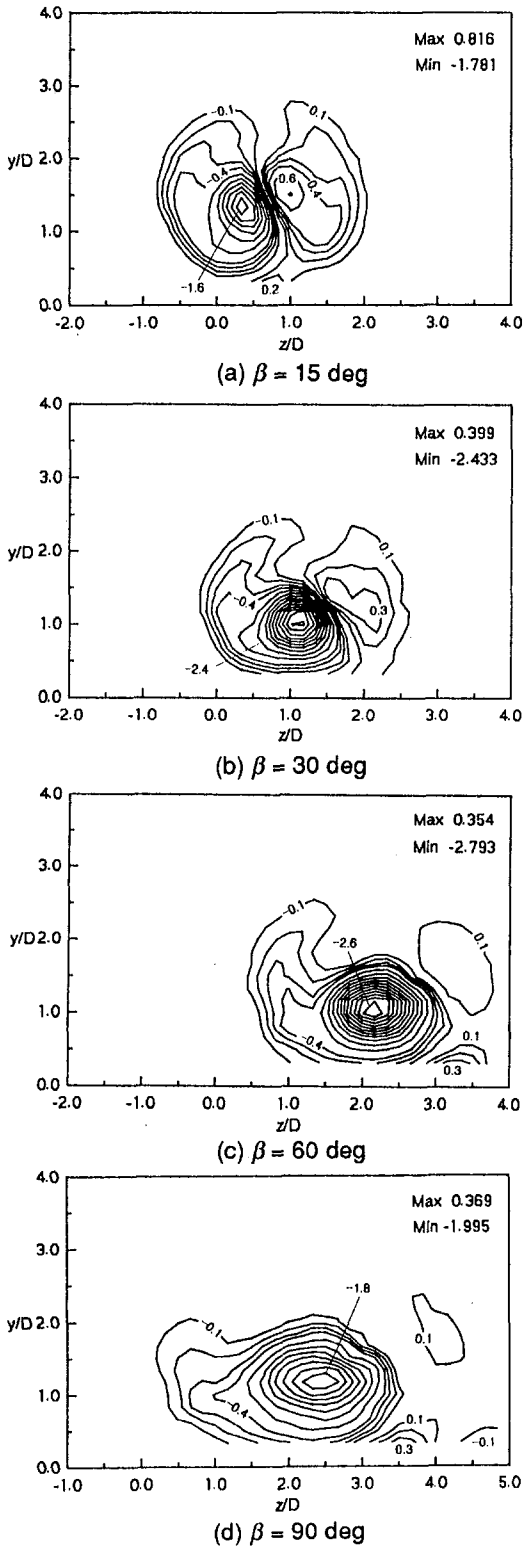

Fig. 6 Contours of dimensionless vorticity in x-direction, Ω_x, at x/D = 8 for R = 2.0

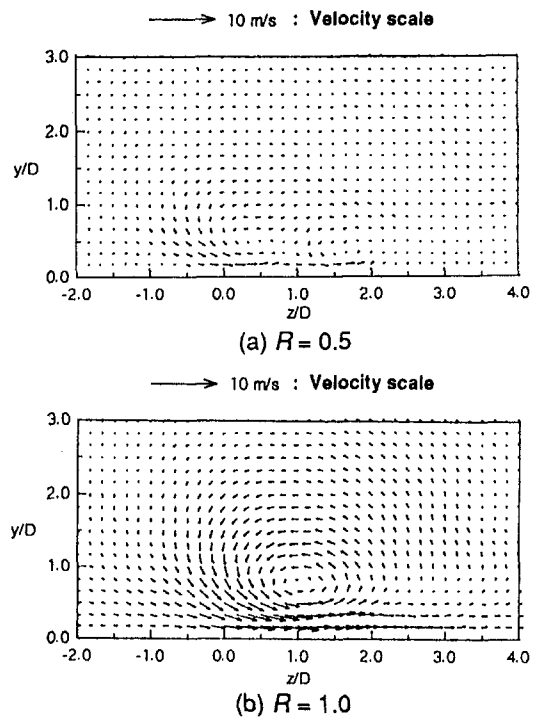

Fig. 7 Projection of velocity vectors on y–z plane at x/D = 8 for β = 90 deg

The projections of the velocity vectors on the y–z plane (Fig. 5) show that when β = 15 deg, secondary flow has a pair of counterrotating vortices. However, as the orientation angle increases, the vortex rotating in counterclockwise direction becomes stronger, while the vortex in a clockwise sense is rapidly weakened. For β = 30 deg, the clockwise vortex seems to be extinct (Fig. 5(b)), and a strong counterclockwise vortex occupies the whole measurement area. In the case of β = 90 deg, the single counterclockwise rotating vortex structure is maintained. When the orientation angle increases from 15 deg to 30 deg and from 30 deg to 60 deg, the location of the vortex center migrates by about 1D in the positive z direction. On the other hand, the change in the vortex center is only 0.25D from 60 deg to 90 deg. It is inferred from these facts that the z-directional momentum of the jet persists far downstream in the case of small orientation angles; meanwhile in the case of large orientation angles, the jet loses the z-momentum strength right after being injected from the hole because of a strong collision with the mainstream.

As in Fig. 6, the regions of positive and negative vorticities are observed regardless of the orientation angle. The negative-vorticity region expands with the increase in the orientation angle, and occupies all the measurement domain at last. The peak value of absolute vorticity in the counterclockwise vortex, which is usually larger than that in the clockwise vortex, has

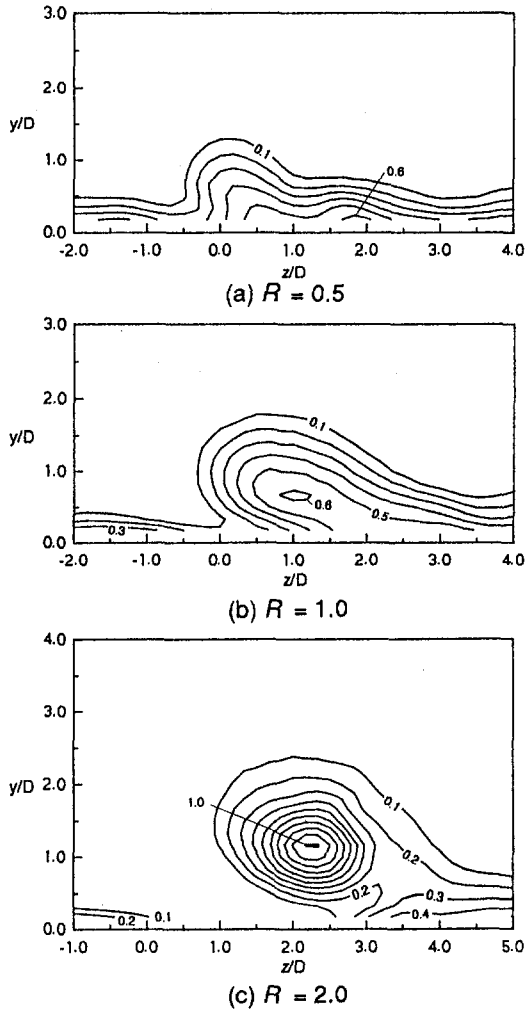

Fig. 8 Contours of total pressure loss coefficient with injection, $C_{Pt,inj}$, at $x/D = 8$ for $\beta = 90$ deg

its maximum when $\beta = 60$ deg, and then decreases when $\beta = 90$ deg. It is noticeable that the peak value for $\beta = 90$ deg, which is much less than those for $\beta = 30$ deg and 60 deg, is found to be nearly the same as that for $\beta = 15$ deg.

The secondary flows at $x/D = 8$ in the case of $R = 0.5$ and 1.0 for $\beta = 90$ are presented in Fig. 7. Comparison of these figures with Fig. 5(d) shows that the strength of the downstream secondary flow strongly depends on the velocity ratio. When the velocity ratio is 0.5, the secondary flow seems to have two vortices, but their strengths are negligibly small. In the case of $R = 1.0$, however, there exists only single vortex in the counterclockwise direction as in Fig. 5(d). Examining the whole three-dimensional flow data in this study, it is concluded that independent of the velocity ratio, there always exists a single vortex system at large orientation angles except for the case of $R = 0.5$.

Aerodynamic Loss Distributions. Aerodynamic loss in the flow field of film-cooling consists of the loss generation from the jet injection as well as the aerodynamic loss due to total pressure deficit in the boundary layer. Thus, two total pressure loss coefficients can be defined as follows:

$$C_{Pt,bas} = \frac{P_{t,\infty} - P_{t,bas}}{\frac{1}{2}\rho U_\infty^2} \quad (1)$$

$$C_{Pt,inj} = \frac{P_{t,\infty} - P_{t,inj}}{\frac{1}{2}\rho U_\infty^2} \quad (2)$$

In these equations, $P_{t,\infty}$ represents the free-stream total pressure measured at $x = -500$ mm, $P_{t,inj}$ denotes the total pressure measured in the whole y–z plane at $x/D = 8.0$ with the jet injection, whereas $P_{t,bas}$ stands for the measured total pressure at the same location without the injection. Therefore, the base total pressure loss coefficient defined as Eq. (1), $C_{Pt,bas}$, represents the base flow loss associated with total pressure deficit in the boundary layer when jet is not injected; meanwhile the second loss coefficient, $C_{Pt,inj}$, defined as Eq. (2), is the total pressure loss coefficient measured in the presence of film-cooling jet. In the discussion of the aerodynamic loss in the film-cooled region, it would be meaningful to introduce another loss coefficient, which stands for the total pressure deficit due solely to the jet injection. The third net total pressure loss coefficient can be defined as below:

$$C_{Pt,net} = C_{Pt,inj} - C_{Pt,bas} \quad (3)$$

The typical total pressure loss coefficients with injection, $C_{Pt,inj}$, for $\beta = 90$ deg are introduced in Fig. 8 as a reference to the comparison with the sole effect of the jet injection on aerodynamic loss. The net total pressure loss coefficient distributions in y–z plane at $x/D = 8.0$ for $R = 0.5$, 1.0 and 2.0 are presented in Figs. 9, 10, and 11 in turn. Distributions of $C_{Pt,net}$ shown in Figs. 9(c), 10(c), and 11(d) are obtained by subtracting $C_{Pt,bas}$ from $C_{Pt,inj}$ shown in Figs. 8(a), 8(b), and 8(c), respectively. Comparisons of $C_{Pt,net}$ when $\beta = 90$ deg with $C_{Pt,inj}$ in Fig. 8 provide some insights on the relation between $C_{Pt,net}$ and $C_{Pt,inj}$. The positive value of $C_{Pt,net}$ implies total pressure deficit arising from the presence of the jet, while the negative

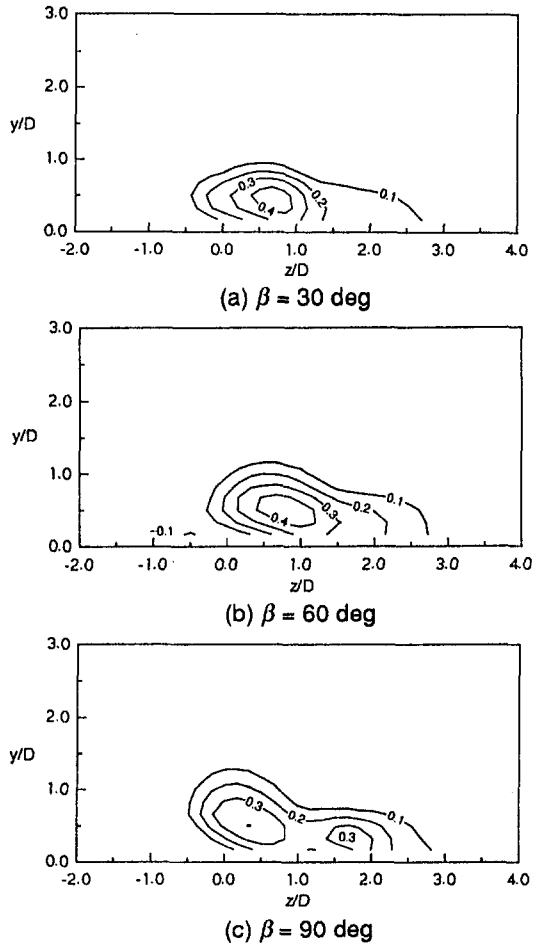

Fig. 9 Contours of net total pressure loss coefficient, $C_{Pt,net}$, at $x/D = 8$ for $R = 0.5$

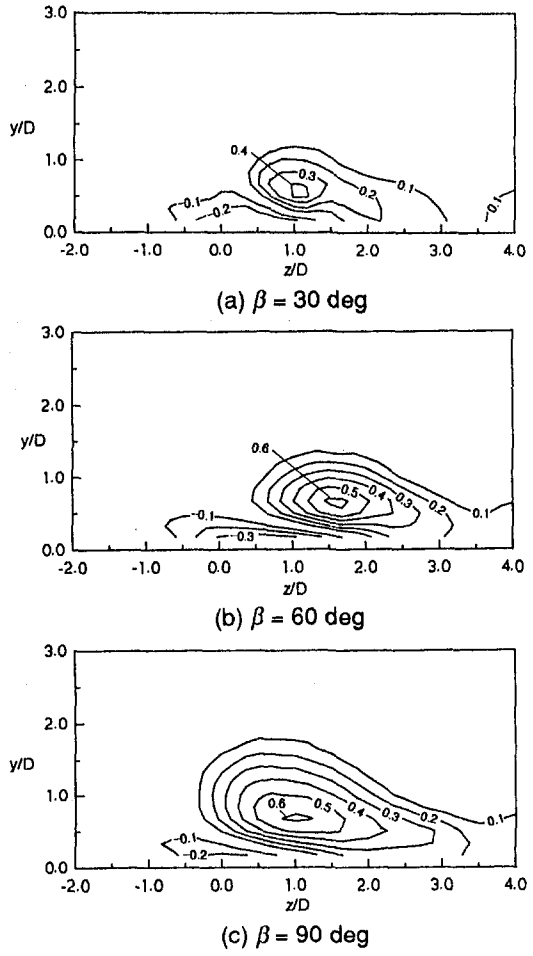

Fig. 10 Contours of net total pressure loss coefficient, $C_{Pt,net}$, at x/D = 8 for R = 1.0

value of $C_{Pt,net}$ represents total pressure surplus contributed by the jet injection. Actually, $C_{Pt,net}$ does not deliver actual net aerodynamic loss on the film-cooled surface because total pressure from the jet is not accounted for in $C_{Pt,net}$. However, present $C_{Pt,net}$ data can provide information on the aerodynamic penalties of compound-angle film cooling as a function of the orientation angle and velocity ratio. When the velocity ratio is 0.5 (Fig. 9), there always exists positive $C_{Pt,net}$ all over the measurement planes for all orientation angles, but the changes in distribution of $C_{Pt,net}$ are minute with the orientation angle variations. In particular, two peak values of $C_{Pt,net}$ are observed in the case of β = 90 deg, which results from two vortices as can be seen in Fig. 7(a). This fact implies that the loss distribution is strongly related to the secondary flow. It is noted that when the velocity ratio is 1.0 (Fig. 10), the region with negative net total pressure loss coefficient can be seen near the wall boundary. The region with the positive net total pressure loss coefficient expands with increasing orientation angle. When the velocity ratio becomes 2.0 (Fig. 11), the trend of aerodynamic loss is changed remarkably. There is no region with positive net total pressure loss coefficients in the case that the orientation angle is less than 60 deg, because the injection velocity is twice as large as the free-stream velocity. When β = 60 deg, a small confined region with positive net total pressure loss coefficient appears near the jet core, which is surrounded by the region with negative net total pressure loss coefficient. The positive net total pressure loss coefficients are also found near the wall on the right corner of the measurement domain, where the mainstream is retarded by the jet. Examining the contours of net total pressure loss coefficient for R = 2.0, it is realized when β is larger than 60 deg that positive value of $C_{Pt,net}$ appears inside the jet and its area tends to expand toward the outer region, and finally positive net total pressure loss coefficient spreads over the whole jet region as in Fig. 11(d). Generally, large aerodynamic loss may be produced for large orientation angle. This is because for the large orientation angle, the mainstream is widely blocked by the jet with strong flow disturbances such as flow reversal and

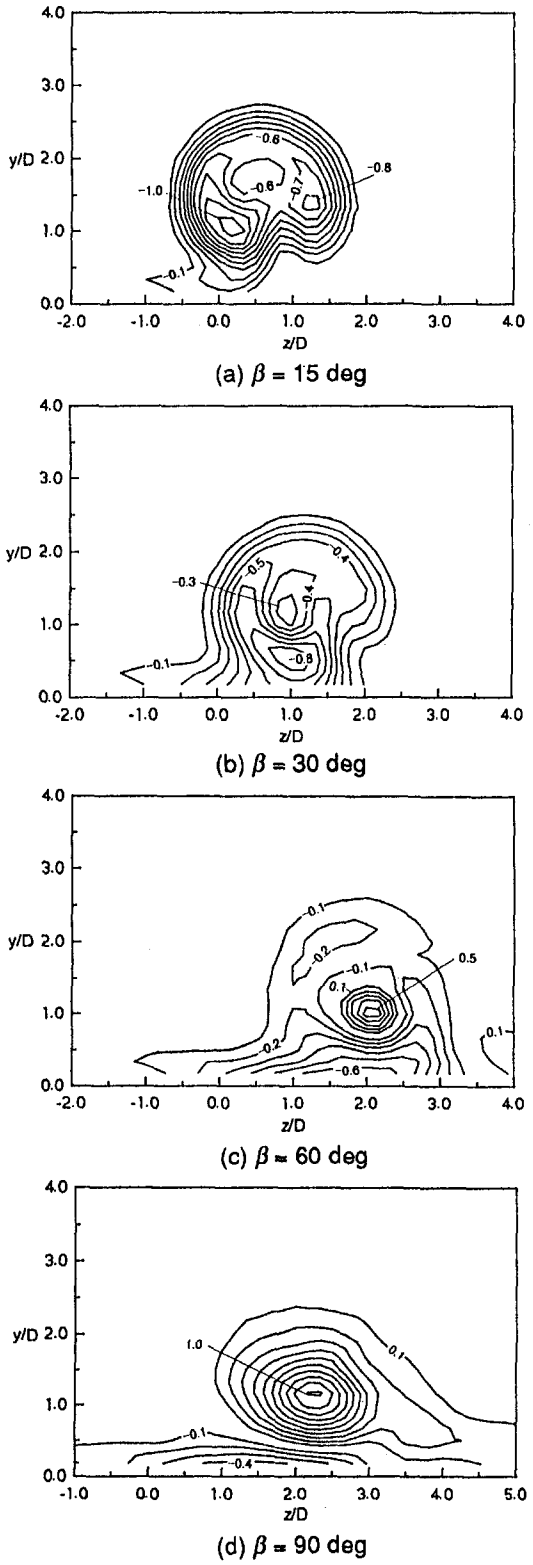

Fig. 11 Contours of net total pressure loss coefficient, $C_{Pt,net}$, at x/D = 8 for R = 2.0

recirculation, which may cause a vigorous mixing between the two flows as shown by the flow visualization (Fig. 3). The negative net total pressure loss coefficient near the wall in the case of $\beta = 90$ deg seems to result from the increase in total pressure contributed by large W as can be seen in Fig. 5(d). In comparison of the net total pressure loss coefficients (Figs. 11(c) and 11(d)) with the secondary flows (Figs. 5(c) and 5(d)), the vortex center coincides approximately with the location of the peak net total pressure loss coefficient. This reveals that the aerodynamic loss is associated with the strong secondary vortical motion and this seems to be the key mechanism in the generation of aerodynamic loss of the film-cooling jets with compound angle orientations.

The mass-averaged total pressure loss coefficients can be defined as follows:

$$\bar{C}_{Pt,bas} = \frac{\int_{z^-}^{z^+}\int_{y^-}^{y^+} C_{Pt,bas}U_b\,dydz}{\int_{z^-}^{z^+}\int_{y^-}^{y^+} U_b\,dydz} \tag{4}$$

$$\bar{C}_{Pt,inj} = \frac{\int_{z^-}^{z^+}\int_{y^-}^{y^+} C_{Pt,inj}U\,dydz}{\int_{z^-}^{z^+}\int_{y^-}^{y^+} U\,dydz} \tag{5}$$

$$\bar{C}_{Pt,net} = \bar{C}_{Pt,inj} - \bar{C}_{Pt,bas} \tag{6}$$

In Eqs. (4) and (5), U is x-directional velocity measured at each measurement location in the y–z plane with $x/D = 8$, and U_b is x-directional velocity measured with $P_{t,bas}$ at the same location without injection. For all the cases, y^- and y^+ in the equations are fixed at 0 and $3D$, respectively. The integration in z direction is performed over the measurement interval of $6D$, but z^+ and z^- may have different values, depending on each measurement case. In this study, $\bar{C}_{Pt,bas}$, defined in Eq. (4), is calculated to be about 0.029. The mass-averaged net total pressure loss coefficient, $\bar{C}_{Pt,net}$, is presented in Fig. 12 as a function of the orientation angle. $\bar{C}_{Pt,net}$ is strongly dependent on the velocity ratio and tends to increase with the increment of the orientation angle regardless of the velocity ratio. This tendency is pronounced in the case of $R = 2.0$. When $R = 0.5$, there is very small change in $\bar{C}_{Pt,net}$ with the orientation angle compared with that for $R = 2.0$, and for the velocity ratios of 0.5 and 1.0, all the mass-averaged net total pressure loss

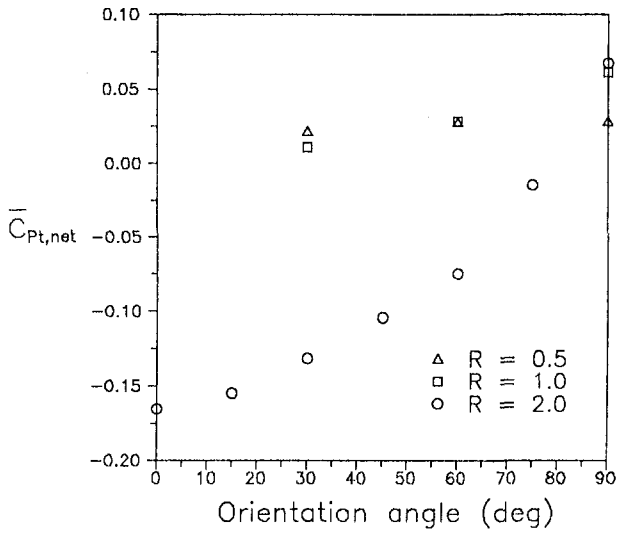

Fig. 12 Mass-averaged net total pressure loss coefficient at $x/D = 8$ as a function of orientation angle

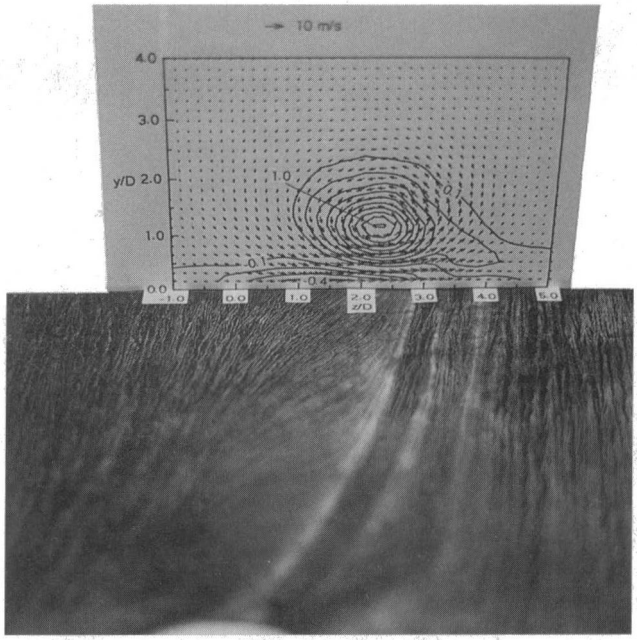

Fig. 13 Surface flow visualization compared with measured flow data at $x/D = 8$ for $\beta = 90$ deg in the case of $R = 2.0$

coefficients have positive values. Therefore, it is noted that when the velocity ratio is not larger than unity, there always exists the mass-averaged aerodynamic loss due to the jet injection. However, the results for $R = 2.0$ show a totally different trend. The mass-averaged net total pressure loss coefficient for $R = 2.0$ has negative value in most cases except for $\beta = 90$ deg and increases very steeply with the orientation angle. Thus, when the velocity ratio is larger than unity, there exists considerable total pressure surplus in the film-cooled area for small orientation angles; whereas, if the orientation angle is 90 deg with velocity ratios larger than unity, the advantage of the total pressure gain in the case of the small orientation angles can be lost. When $\beta = 90$ deg, the mass-averaged net total pressure loss coefficient for $R = 2.0$, which has positive value, is not so serious compared with that for $R = 1.0$.

To obtain high-performance film cooling, aerodynamic loss should be minimized for the required film cooling effectiveness. In the case that the velocity ratio is less than unity, aerodynamic loss is weakly dependent on the orientation angle. On the other hand, aerodynamic loss is significantly changed with the orientation angle variations, when the velocity ratio is larger than unity. From the present surface flow visualizations for $R = 2.0$, the area of Region 4 expanded with the increment of orientation angle (Fig. 3). These facts imply that when the velocity ratio is larger than unity, the high film-cooling effectiveness obtained for large orientation angles inevitably accompanies considerable increase in the aerodynamic loss, compared with the case of small orientation angle. Therefore, there might be an optimal orientation angle for the velocity ratios larger than unity, compromising the trend of the film-cooling coverage and the aerodynamic loss.

Comparison of Flow Visualization With Flow Measurement Data. Figure 13 shows the comparison of the surface flow visualization for $\beta = 90$ deg (Fig. 3(c), Method 2) with the flow data at $x/D = 8.0$ when $R = 2.0$. In the photograph, velocity vectors and contours of the net total pressure loss coefficient are drawn in the same scale as in the visualization. The line GJ in the visualization passes approximately through $z/D = 3.0$ at $x/D = 8.0$, and the line EF is extended downstream to the point of about $z/D = 4.0$ at $x/D = 8.0$. Thus, at $x/D = 8.0$, Region 4, proposed in Fig. 2, lies between $z/D = 3.0$ and 4.0. From Fig. 13, it is noted that the location of maximum

loss, which nearly coincides with the vortex center, lies just above Region 5. Therefore, it is concluded that a large portion of the jet flows over Region 5, being separated from the wall, and the remainder touches the wall in Region 4.

Conclusion

Flow visualizations and detailed flow measurements for film cooling jets with compound angle orientations have been performed for a simulated large-scale film cooling hole. For three velocity ratios of 0.5, 1.0, and 2.0, three-dimensional flow data and aerodynamic losses are reported with the variation of the orientation angle. The results in this study are summarized as follows.

Surface flow visualizations show that the increase in the orientation angle results in better film coverage, especially in the spanwise direction, but produces more flow disturbances such as flow reversal and recirculation. A near-wall flow model for the velocity ratio of 2.0 has been proposed from the visualizations. In this flow model, the near-field of the injection hole comprises five regions, and various flow phenomena in each region are discussed in detail.

There exist very complex three-dimensional flows in the film-cooled area with compound angle orientations. In the case of small orientation angle, the downstream flow is characterized by a pair of counterrotating vortices. As the orientation angle increases, however, the counterrotating vortices turn to a single strong vortex, except for the case of the velocity ratio of 0.5, and the strength of downstream secondary flow strongly depends on the velocity ratio.

When the velocity ratio is 0.5 and 1.0, there is always aerodynamic loss as a result of the jet injection regardless of the orientation angle, but the loss increase with the increment of the orientation angle is relatively small. For the velocity ratio of 2.0, a large amount of total pressure surplus occurred in the film-cooled area when the orientation angle was small. In the case that the orientation angle is larger than 60 deg, the aerodynamic loss is produced within the jet region even for the velocity ratio of 2.0. For this large velocity ratio, the largest aerodynamic loss is generated when the orientation angle is 90 deg.

Acknowledgments

The research herein was conducted with the support of the Korea Science and Engineering Foundation (KOSEF Grant No. 931-1000-002-2).

References

Cho, H. H., and Goldstein, R. J., 1993, "Heat (Mass) Transfer and Film Cooling Effectiveness With Injection Through Discrete Holes. Part 1: Within Holes and on the Back Surface," ASME Paper No. 93-WA/HT-58.

Goldstein, R. J., and Chen, H. P., 1985, "Film Cooling on a Gas Turbine Blade Near the End Wall," ASME JOURNAL OF TURBOMACHINERY, Vol. 107, pp. 117–122.

Honami, S., Shizawa, T., and Uchiyama, A., 1994, "Behavior of the Laterally Injected Jet in Film Cooling: Measurements of Surface Temperature and Velocity/Temperature Field Within the Jet," ASME JOURNAL OF TURBOMACHINERY, Vol. 116, pp. 106–112.

Ishii, J., and Honami, S., 1986, "A Three-Dimensional Turbulent Detached Flow With a Horseshoe Vortex," ASME *Journal of Engineering for Gas Turbines and Power*, Vol. 108, pp. 125–130.

ISO 5167-1:1991(E), 1991, "Measurement of Fluid Flow by Means of Pressure Differential Devices—Part 1: Orifice Plates, Nozzles and Venturi Tubes Inserted in Circular Cross-Section Conduits Running Full," International Organization for Standardization.

Kline, S. J., and McClintock, F. A., 1953, "Describing Uncertainties in Single Sample Experiments," *Mechanical Engineering*, Jan., pp. 3–8.

Lee, S. W., Lee, J. S., and Ro, S. T., 1994, "Experimental Study on the Flow Characteristics of Streamwise Inclined Jets in Crossflow on Flat Plate," ASME JOURNAL OF TURBOMACHINERY, Vol. 116, pp. 97–105.

Leylek, J. H., and Zerkle, R. D., 1994, "Discrete-Jet Film Cooling: A Comparison of Computational Results With Experiments," ASME JOURNAL OF TURBOMACHINERY, Vol. 116, pp. 358–368.

Ligrani, P. M., and Mitchell, S. W., 1994, "Interactions Between Embedded Vortices and Injectant From Film Cooling Holes With Compound Angle Orientations in a Turbulent Boundary Layer," ASME JOURNAL OF TURBOMACHINERY, Vol. 116, pp. 80–91.

Mayle, R. E., and Anderson, A., 1991, "Velocity and Temperature Profiles for Stagnation Film Cooling," ASME JOURNAL OF TURBOMACHINERY, Vol. 113, pp. 457–463.

Pietrzyk, J. R., Bogard, D. G., and Crawford, M. E., 1989, "Hydrodynamic Measurements of Jets in Crossflow for Gas Turbine Film Cooling Applications," ASME JOURNAL OF TURBOMACHINERY, Vol. 111, pp. 139–145.

Shepherd, I. C., 1981, "A Four Hole Pressure Probe for Fluid Flow Measurements in Three Dimensions," ASME *Journal of Fluids Engineering*, Vol. 103, pp. 590–594.

Sinha, A. K., Bogard, D. G., and Crawford, M. E., 1991, "Gas Turbine Film Cooling: Flowfield Due to a Second Row of Holes," ASME JOURNAL OF TURBOMACHINERY, Vol. 113, pp. 450–456.

Treaster, A. L., and Yocum, A. M., 1979, "The Calibration and Application of Five-Hole Probes," *ISA Transactions*, Vol. 18, pp. 23–34.

Yamamoto, A., Kondo, Y., and Murao, R., 1991, "Cooling-Air Injection Into Secondary Flow and Loss Fields Within a Linear Turbine Cascade," ASME JOURNAL OF TURBOMACHINERY, Vol. 113, pp. 375–383.

Total-Coverage Discrete Hole Wall Cooling

H. H. Cho
Department of Mechanical Engineering,
Yonsei University,
Seoul, Korea 120-749

R. J. Goldstein
Department of Mechanical Engineering,
University of Minnesota,
Minneapolis, MN 55455

The present study investigates heat/mass transfer for flow through perforated plates for application to combustor wall and turbine blade film cooling. The experiments are conducted for hole length-to-diameter ratios of 0.68 to 1.5, for hole pitch-to-diameter ratios of 1.5 and 3.0, for gap distance between two parallel perforated plates of 0 to 3 hole diameters, and for Reynolds numbers of 60 to 13,700. Local heat/mass transfer coefficients near and inside the cooling holes are obtained using a naphthalene sublimation technique. Detailed knowledge of the local transfer coefficients is essential to analyze thermal stress in turbine components. The results indicate that the heat/mass transfer coefficients inside the hole surface vary significantly due to flow separation and reattachment. The transfer coefficient near the reattachment point is about four and half times that for a fully developed circular tube flow. The heat/mass transfer coefficient on the leeward surface has the same order as that on the windward surface because of a strong recirculation flow between neighboring jets from the array of holes. For flow through two in-line layers, the transfer coefficient affected by the gap spacing is approximately 100 percent higher on the windward surface of the second wall and is about 20 percent lower on the inside hole surface than that with a single layer. The transfer coefficient on the leeward surface is not affected by upstream flow conditions due probably to strong recirculation in the wake flow.

Introduction

The thermal efficiency of gas turbine systems depends strongly on turbine inlet temperature. Inlet temperature is limited by the structural failure of the engine components, mainly attributable to high thermal stresses and reductions in material strength due to high wall temperature. Wall temperature can be reduced by various cooling techniques including transpiration and film cooling. Porous materials produce near-uniform heat/mass transfer rates on their surface with flow through the plate. These characteristics are desirable to protect the surface from hot gases in components of high-performance gas turbine engines. However, transpiration (porous) material usually has a clogging problem from internal oxidation and particles, and is structurally weak. To alleviate clogging and improve the strength of the transpiration material in combustor walls, laminated plates with perforations have been developed. The laminates (pseudo-transpiration material) still produce the high efficiency of transpiration cooling and sustain the structural strength [e.g., Lamilloy from Detroit Diesel Allison (Nealy and Reider, 1980) and Transply from Rolls Royce Ltd. (Wassell and Bhangu, 1980)] though problems are encountered in clogging by contaminant particles for small pore sizes. Total coverage film-cooled blades, which are covered with a single perforated metal sheet, were tested in high-temperature conditions by Hempel et al. (1980). This cooling scheme helps to prevent thermal stresses and permit increased efficiency.

The present study investigates heat/mass transfer characteristics for flow through laminated plates with hole perforations. The laminated plates, or porous plates, are modeled using plates with circular holes in a square array. With total coverage cooling for flow through the laminated plate, the analysis of overall heat transfer requires heat transfer coefficients around the hole entrance and inside the hole surfaces as well as adiabatic wall temperature (film cooling effectiveness) and heat transfer on the exposed surfaces. A mass transfer technique is used to measure transfer rates on the inside hole surface and on the plate around the hole entrance and the hole exit. This technique also eliminates the conduction error inherent in heat transfer experiments. The surface boundary condition is analogous to an isothermal surface in a corresponding heat transfer problem. The time-averaged local mass transfer rates are obtained with surface measurements from the change in thickness of the subliming material. The mass transfer coefficients can be converted to the heat transfer coefficients using the heat and mass transfer analogy.

The flow pattern through an array of holes at small hole-to-hole spacing is different from the flow through a single hole. The flow is confined by its neighboring holes and the entire flow field is divided into an assembly of cells bounded by the stagnation lines on the windward surface. Within the holes, the flow pattern is expected to be similar to that in a single hole. For the leeward surface, the ejected flows from the holes induce recirculating flows between the jets. This increases the heat transfer on the leeward surface due to the high turbulence level with an impingement effect at the midplane.

Ortiz (1981) measured the average mass transfer rates on a windward surface with a staggered hole array using a weighing method. The ratios of pitch to hole diameter were 2.0 and 2.5 and Reynolds number was between 2000 and 20,000. He found that Sherwood number was proportional to $Re^{0.476}$.

Andrews et al. (1984–1989) extensively investigated the average heat transfer rates for arrays of holes drilled through a plate. They studied the influence of plate thicknesses (hole length) from about 0.8 to 9.9 hole diameters, with a pitch of about 1.9 to 21.4 hole diameters, and for Re = 500 to 43,000. They argue that the heat transfer on the windward surface and inside the hole is dominant, but the leeward surface is ignored. However, as shown in the present study, the heat transfer on the leeward surface should be included for spacings (pitch) between holes as small as three hole diameters.

The present study deals with the local transfer coefficients. The results will help to develop an optimal hole configuration in laminate materials.

Flow through laminated plates (or a porous medium) is better simulated using multiple layers than with a single plate. Two

Contributed by the International Gas Turbine Institute and presented at the 40th International Gas Turbine and Aeroengine Congress and Exhibition, Houston, Texas, June 5–8, 1995. Manuscript received by the International Gas Turbine Institute February 4, 1995. Paper No. 95-GT-12. Associate Technical Editor: C. J. Russo.

parallel perforated plates are also studied with an in-line hole arrangement to investigate effects of upstream perforated plates. There are few studies for multiple layered plates and generally average heat (or mass) transfer was measured. To improve efficiency and prevent hot spots, both overall heat transfer coefficient and its local variation must be studied.

Experimental Apparatus and Procedure

1 Experimental Apparatus. The apparatus is similar to that used by Cho et al. (1997) in their single hole measurements. A plenum chamber with a square section (572 mm by 572 mm) and a height of 1400 mm is used. The upper wall of the large square plenum chamber has an array of holes. The mass transfer active area is positioned at the center of the upper wall to eliminate side wall effects. Room air drawn into a settling baffle passes through the perforated test plate into the plenum chamber, through an orifice plate (flow measuring device) and a blower, and then is discharged outside the building. The settling baffle around the chamber effectively eliminates the random motion of room air.

The experimental facility enables measurement of the local/average naphthalene sublimation rates on the inside hole surface and on the surfaces near the hole exposed to the air flow. The test plates are cast with a thin naphthalene layer for sublimation prior to being exposed to the air stream. Two different types of test specimen are used in the present experiments: one for average (weighing) measurements and local values on windward and leeward surfaces; the other for local measurements inside the hole. Two parallel perforated plates are also investigated with various gap spacings.

For average (weighing) measurements, small test plates are employed as shown in Fig. 1. These test plates are positioned in the center of plenum top plate. The perforated plates have 3 by 3 (9) or 5 by 5 (25) holes cast with naphthalene in an overall array of 7 by 7 holes (Table 1). Local measurements on the windward and leeward surfaces are conducted on the small test plates. In addition, to accommodate a mass limitation of 200 gm for the laboratory balance, the test plates are machined thin to reduce the total mass. The short time needed for the weighing measurement, reduces extraneous natural convection effects. This average (weighing) measurement is also compared with numerical integration of the local measurement results.

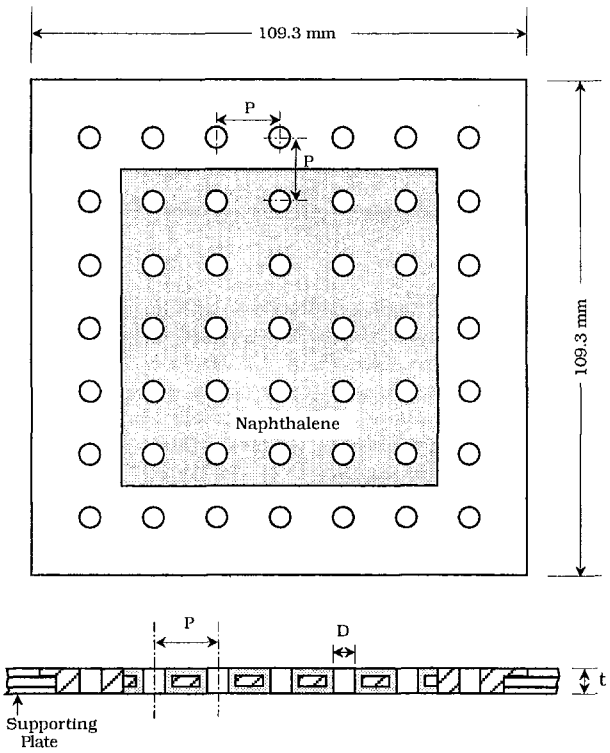

Fig. 1 Test plate of an array of holes for weighing measurements

For local mass transfer rate measurements in a hole, the entire top plate (572 × 572 mm) of the plenum chamber is perforated

Nomenclature

D = hole diameter; 4.76 mm $\leq D \leq$ 25.4 mm in present study
d_e = area equivalent diameter in an array of holes; $\pi d_e^2/4 = P^2$
d_o = diameter of active boundary on windward and leeward surfaces
D_{naph} = mass diffusion coefficient of naphthalene vapor in air
F_s = conversion factor in Fig. 11 = $5.31\ \mathrm{Re}^{-0.196}$
G = gap distance between two parallel perforated plates; 0 to 3D in the present study
h_m = local mass transfer coefficient, Eq. (1)
$\dot{m}$ = local naphthalene mass transfer per unit area and time
$\mathrm{Nu_h}$ = Nusselt number based on inside hole surface area
Pr = Prandtl number
P = pitch of an array of holes (cf. Fig. 1)
r = radius
Re = Reynolds number based on the hole diameter and the average velocity in the hole
r_i = radius of hole
r_o = radius of active surface on windward and leeward surface; $r_o(\theta) = r_o(0°)/\cos\theta$ for $0° \leq \theta \leq 45°$
Sc = Schmidt number for naphthalene in air = ν/D_{naph}; about 2.28 at 298 K and 0.1 MPa
Sh = Sherwood number based on the hole diameter, Eq. (2)
$\mathrm{Sh_{dc}}$ = Sherwood number based on characteristic length $d_e = h_m d_e/D_{naph}$
$\mathrm{Sh_{do}}$ = Sherwood number based on characteristic length $d_o = h_m d_o/D_{naph}$
$\mathrm{Sh_L}$ = piecewise-averaged Sh (averaged from the hole entrance to the position, L)
$\mathrm{Sh_{peak}}$ = peak Sh at the reattachment point in hole
Sh_∞ = reference Sherwood number of a fully developed circular tube flow
$\overline{\mathrm{Sh}}$ = average Sherwood number
$\overline{\overline{\mathrm{Sh}}}$ = overall averaged Sherwood number
t = hole length ($0.68 \leq t/D \leq 1.5$)
T_w = local wall temperature
X, Z = distance from the center of a hole (Cartesian coordinates in Fig. 2)
Y = coordinates and direction along the hole axis
Y_{peak} = peak Sh location inside the hole (at or near reattachment point)
$\delta\tau$ = test duration
δz = local sublimation depth of naphthalene
ρ_s = density of solid naphthalene
$\rho_{v,w}$ = naphthalene vapor density on the surface
$\rho_{v,\infty}$ = naphthalene vapor density of the approaching flow ($\rho_{v,\infty} = 0$ in the present study)
σ = standard deviation
θ = angle around hole (Fig. 2)

Table 1 Configurations of the test plates (total number of holes = 7 × 7)

D (mm)	4.76	4.76	4.76	9.51	25.4
P/D	3.0	3.0	3.0	1.5	3.0
t/D	1.36	0.95	0.95	0.68	1.48
No. of active holes	5 x 5	3 x 3	5 x 5	5 x 5	1

in an array of 7 by 7 holes (49 holes), whose centers form an square pattern (in-line array). The array of holes maintains a ratio of hole-pitch-to-diameter of 3:1 with a hole diameter of 25.4 mm. The center of the plenum top is an aperture whose edges are one half diameter bigger than the symmetry region boundaries. This square cavity matches with the hole measurement test plate, which is cast with naphthalene. The square cast areas ($4D \times 4D$) on the top and bottom are one half diameter bigger on each edge than the one square symmetry region ($3D \times 3D$) (Fig. 2). This gives a boundary condition without a discontinuity in mass transfer at the symmetry lines. The hole (25.4 mm diameter) in the test plate is recessed about 3.2 mm. After casting, this recess is filled with naphthalene and the 25.4 mm diameter circular hole is formed. The hole has metal annular rims at the top and the bottom. The rims of the hole, which are nonsubliming surfaces, are used as reference points for measuring inside the hole. Cho et al. (1997) describe in detail the experimental apparatus used here.

For parallel perforated plate tests, two plates, which have the same hole size and pattern, are positioned in an in-line arrangement with various gap spacings. The first plate is fabricated using a Plexiglas sheet and the second plate is the mass transfer measurement plate used in the single layer experiment. The gap between the two plates is varied between 0 and $3D$ (76.2 mm).

All active mass transfer surfaces employed in the experiments are cast. Molten naphthalene poured into a mold solidifies, and the mold is separated from the test plate. The mold consists of the test plate, a highly polished aluminum flat plate, and a circular cylinder. The smoothness of the exposed naphthalene surface is comparable to that of the polished aluminum adjacent to it in the mold.

2 Data Acquisition System and Measurements. A computer-controlled measurement system is used to scan the profile of the naphthalene surface. This system satisfies many requirements to obtain useful local sublimation depths of a naphthalene surface; these include precise positioning of the plates, accurate depth measuring, and rapid data acquisition to minimize the natural convection losses. The measurement systems consist of a depth gage, a linear signal conditioner, a digital multimeter, stepper-motor driven positioners, a motor controller, and a microcomputer. The depth gage (a linear variation differential transformer; LVDT) has 0.5 mm linear range and 25.4 nm (1.0 μin.) resolution. To measure inside hole mass transfer rates, an extended stylus is used to reach deep inside the hole (Cho, 1992). The measurement errors of the LVDT are about 0.15 μm (6 μin.; 2σ) for the flat plate measurement and about 0.45 μm (18 μin.) for the inside hole measurement at a 95 percent confidence level.

The profile of the naphthalene surface elevation is measured on the measurement tables before and after each test run. The difference between the two sets of surface elevations (with respect to a reference level on the nonsubliming metal surface) is a measure of the sublimation depth. Each test run time is selected so that the average sublimation depth of the naphthalene surface will be about 0.05 mm (0.002 in.). The sublimation depth is two or three orders of magnitude higher than the measurement error.

For small-hole plates, a weighing method is used to determine the overall average mass transfer coefficient. This weighing method, with a precision balance, has smaller measurement error and little natural convection loss during the measurement, because it can be conducted quickly.

Because the vapor pressure of naphthalene is quite sensitive to temperature (about 10 percent change per °C), the naphthalene surface temperature is measured using T-type (copper-constantan) thermocouples installed within the naphthalene, as close as possible to the surface. During the run, the temperature variation of the naphthalene surface is maintained within about 0.2°C.

The local mass transfer coefficient,

$$h_m = \frac{\dot{m}}{\rho_{v,w} - \rho_{v,\infty}} = \frac{\rho_s(\delta z/\delta\tau)}{\rho_{v,w}} \tag{1}$$

since $\rho_{v,\infty} = 0$ in the present study. The Sherwood number can be expressed as:

$$\mathrm{Sh} = \frac{h_m D}{D_{\mathrm{naph}}} \tag{2}$$

D_{naph} is determined from a correlation recommended by Goldstein and Cho (1995). During the experiment, extraneous sublimation losses by natural convection are corrected from the total sublimation rate based on a natural convection rate and the measurement duration.

Uncertainty of the Sherwood numbers is within 7.1 percent for the entire operating range of the measurement based on a 95 percent confidence interval. This uncertainty is mainly attributed to the uncertainty of the properties of naphthalene, such as the naphthalene saturated vapor pressure (3.77 percent) and diffusion coefficient of naphthalene vapor in air (5.1 percent). In contrast, the error due to the depth measurement is only 0.9 percent. The other uncertainties are 0.1, 1.1, and 4.9 percent for T_w, ρ_s, and h_m, respectively.

Results and Discussion

The heat/mass transfer coefficient for flow through a thin perforated plate of an in-line array of holes is examined in this study. The flow pattern with small hole-to-hole spacing is

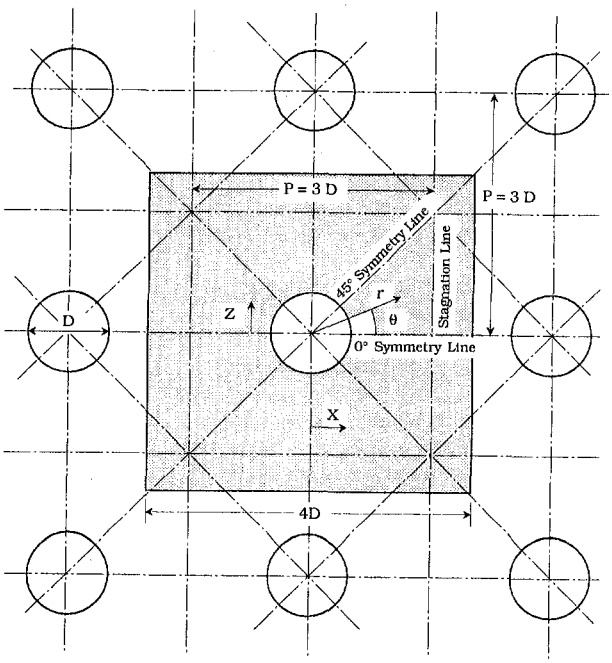

Fig. 2 Symmetry lines and coordinate system at an in-line array of holes

different from the flow through a single hole. The flow through a hole is confined by neighboring hole flows, as shown in Fig. 3. The flow on the windward surface has stagnation lines, which occur at the symmetry lines between holes (Fig. 2). The entire flow field is divided into an assembly of square cells bounded by the stagnation lines (symmetry lines). The flow in each subdivided cell has the same pattern. The flow symmetry lines (stagnation lines) are also symmetry lines for the concentration field because the concentration boundary condition is uniform. Thus, mass transfer does not occur across the symmetry lines. The flow pattern inside the hole will be similar to that in a single hole. The transfer coefficient is low within the separation region due to the low wall velocity and because fluid is trapped in the recirculation bubble. The mass transfer increases quickly and has a maximum value in the reattachment region. Then, the mass transfer coefficient decreases gradually downstream, as in developing tube flow. On the leeward surface, the ejected flows induce recirculation between the jets. The recirculation flow, which includes impingement between the holes, increases the heat transfer on the leeward surface.

1 Windward and Leeward Surfaces. Figure 4 shows the local mass transfer coefficients on windward and leeward surfaces of the small test plate at a Reynolds number of 1460. The active area is 5 by 5 holes out of 7 by 7 entire holes with hole-to-hole pitch $P = 3D$ and plate thickness, $t = 0.95D$. The 5 by 5 active holes have surfaces coated with naphthalene and have a constant temperature condition in the analogous heat transfer situation. The two dotted vertical lines at $X/D = 1$ and 2, 4 and 5, 7 and 8, 10 and 11, and 13 and 14 mark the edge of the hole for $Z/D = 0$. On the windward surfaces, the mass transfer rates are symmetric for each subdomain (from the center of the hole to the symmetry line between holes; Fig. 3) except at the extreme ends of the active surface. The pattern of transfer coefficients is similar for different Reynolds numbers, minimum values at the stagnation lines and highest values around the holes. On the leeward surface, the results show that the mass transfer coefficient is affected more at the extreme ends of the active surface than for the windward surface. This is caused by the entrainment flow from the outside. Around the center holes, the mass transfer rate is to be free from these edge effects. The mass transfer rates are fairly uniform on the leeward surface due to good mixing in the wake region.

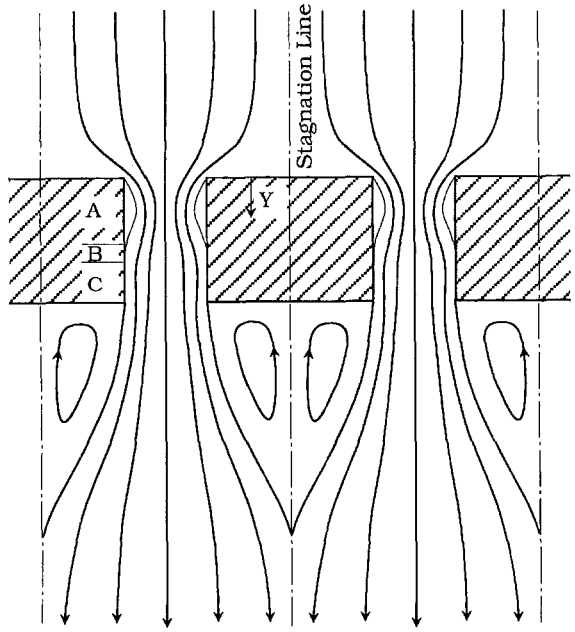

A : Separation Region
B : Reattachment Region
C : Developing Region

Fig. 3 Schematic flow pattern through an array of holes

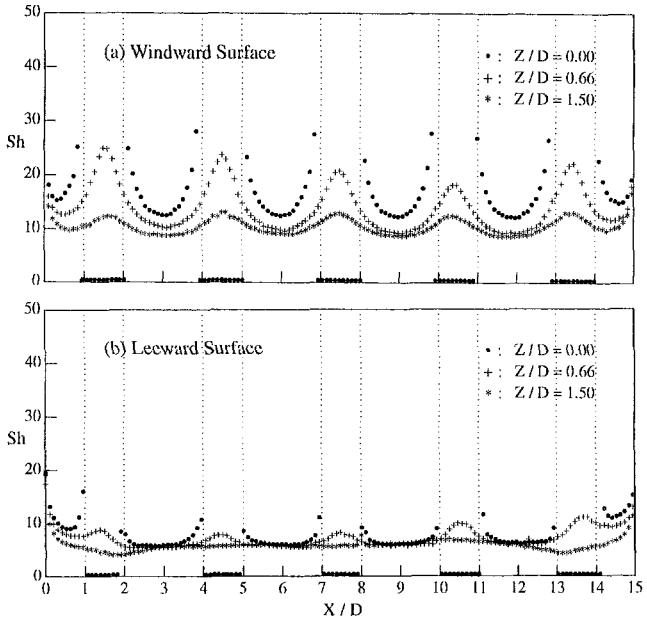

Fig. 4 Local Sherwood number of an array of holes at Re = 1460

The investigation of 5 by 5 (or 3 by 3) active holes among a 7 by 7 hole array indicates that the mass transfer rate at center holes is not sensitive to the edge effect. The result from the center hole in 7 by 7 hole array simulates the results in infinite array of holes. Experiments conducted with a large test specimen to measure transfer coefficients in the hole will not be affected by the edge boundary discontinuity.

Figure 5 presents the mass transfer coefficients on the windward and leeward surfaces in cylindrical coordinates at Re = 11,800 and is compared with that at flow through a single hole (only at $\theta = 0$ deg; Cho et al., 1997). The test plate is the same for both multihole and single hole configurations. The angle indicated in the figures is measured from the line connecting adjacent holes, while the line at $\theta = 45$ deg is a diagonal (Fig. 2). On the windward surface, the transfer rate increases about 50 percent from the single hole case. The multihole causes stagnation of the approach flow on symmetry lines between the holes. Consequently the flow has a shorter path to the hole inlet, which results in higher mass transfer coefficients. On the leeward surface, the transfer rate is very uniform and much higher than for a single hole in the entire domain except near the outer boundary. The magnitude of the transfer coefficients is almost the same on both the windward and leeward surfaces and is approximately three times that of the leeward surface for flow through a single hole. This high and uniform transfer rate is caused by turbulent transfer within the wake and recirculating flow.

Figure 6 presents a contour plot from the local data at Re = 11,800 for the windward surface. The contour lines (constant transfer coefficient lines) are symmetric about the centerline and have a diamond shape rather than circular. The highest transfer rate occurs along the shortest path from the stagnation line to the hole.

Figure 7 shows that the local Sh at $\theta = 0$ deg divided by $Re^{0.5}$ collapses the data onto a single curve for each surface as Reynolds number varies. Note that the exponent of 0.5 matches that of a laminar stagnation flow on a flat plate. This means that the local $Sh/Re^{0.5}$ values on the windward and leeward surfaces are invariant of Reynolds numbers.

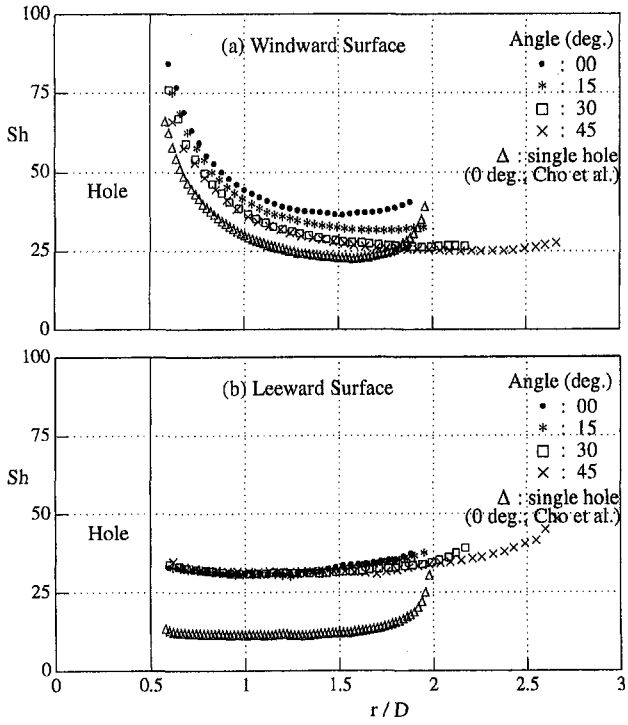

Fig. 5 Local Sherwood number at Re = 11,800 (compared with that of a single hole flow; Cho et al., 1997)

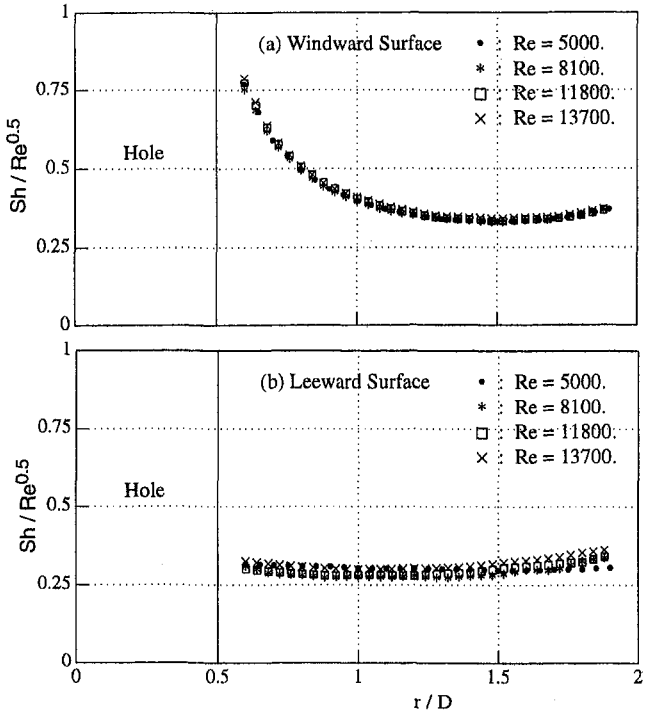

Fig. 7 Normalized Sherwood number at θ = 0 deg

For various angles from θ = 0 to 45 deg, the data collapse reasonably well for Sh based on d_o ($Sh_{do} = Sh*d_o/D$) versus a dimensionless length scale of $(r - r_i)/(r_o - r_i)$ (Fig. 8). At a given angle, d_o and r_o represent a diameter and a radius of the circle, which intersects the stagnation line centered at the hole. Thus, d_o and r_o are functions of θ and the stagnation line is on $(r - r_i)/(r_o - r_i) = 1.0$. Therefore, the transfer rates on the windward surface can be correlated in a single curve for an in-line array of holes.

2 Inside Hole Surfaces. The overall pattern of the Sherwood number distribution on inner hole surfaces is similar to the case of a single hole flow (Cho et al., 1997). According to the mass transfer pattern, the inside hole can be modeled by three different regions whose approximate boundaries are shown in Fig. 3. They are:

(A) the recirculation (or separation) region at the inlet of the hole
(B) the reattachment region
(C) the developing region.

The flow and concentration fields at the inlet of the hole may not be axisymmetric due to the square subdomain on the windward surface. Results indicate a small variation with the angle around the hole at the lowest Reynolds number of 2000 in the present study. However, the Sherwood numbers change little in the circumferential direction inside the hole surface for Re ≥ 3200. The results imply that the flow and mass field is axisymmetric inside the hole for Re ≥ 3200.

Figure 9 shows the local Sherwood number profiles for different Reynolds numbers in the range 2000 ≤ Re ≤ 12,000 and the results are compared with single hole data (Cho et al., 1997). The reattachment points (actually the peak points of Sh) occur closer to the hole entrance than those of the single hole flow (Fig. 10(*a*)). The reason is that for the array of holes

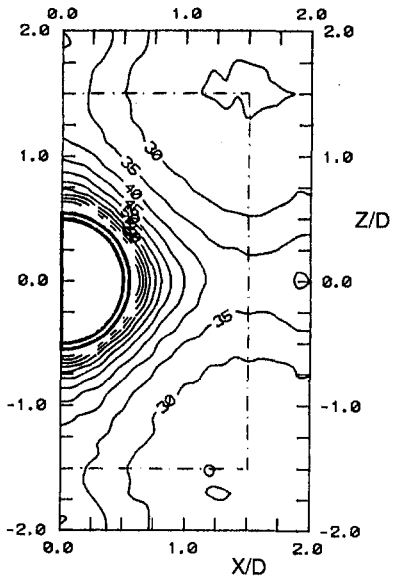

Fig. 6 Contour plot on the windward surface at Re = 11,800

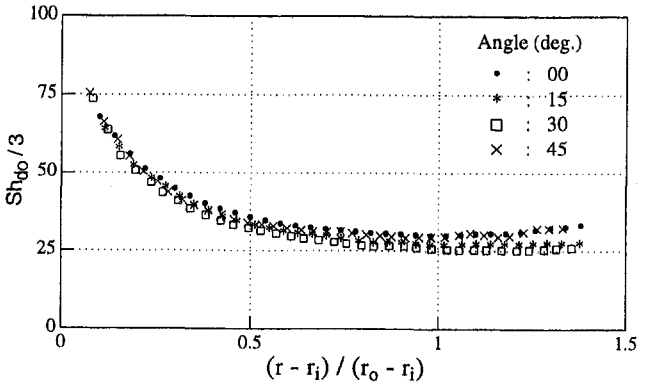

Fig. 8 Local Sh_{do} on the windward surface at Re = 8100

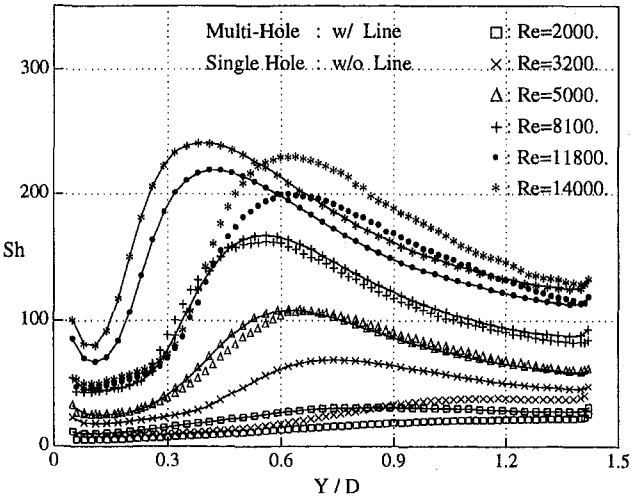

Fig. 9 Comparison of Sh inside the holes for an array of holes and a single hole flow (Cho et al., 1997)

there is less lateral momentum at the hole inlet due to the confined approaching flow. The approaching flow is also more disturbed after stagnation on the multihole windward surface. This greater disturbance will induce turbulence earlier, and result in a shorter reattachment. Turbulent flow has a shorter separation region with higher Sh values. The separation length has a minimum value (~0.5) at Re = 7000, increases slightly around Re = 8,000, and drops to a value of $Y_{peak}/D \cong 0.4$, which is shorter than $Y_{peak}/D \cong 0.56$ for a single hole flow. Again this is attributable to less lateral momentum at the inlet of the hole as explained before.

The peak Sherwood number variation with Reynolds number changes slope at Re ≅ 4000 (Fig. 10(*b*)). This critical Reynolds number is lower than for a single hole flow. The peak Sh value is little different for Re ≥ 5000, as both flows have turbulent reattachment. The average values of Sherwood number inside the hole, which are integrated numerically from the local data, increase the same as the peak values. The correlation equations, determined from least-squares fits, are;

$$Sh_{peak} = 0.07\ Re^{0.861} \quad (Re \geq 4{,}000) \tag{3}$$

$$\overline{Sh} = 0.04\ Re^{0.878} \quad (Re \geq 4{,}000) \tag{4}$$

for $t/D = 1.48$.

The normalized Sherwood numbers with respect to a fully developed circular tube flow, using Mills' correlation (1962), do not collapse to a single curve. The values at the peak point are around $Sh/Sh_\infty = 4.5$ (4.0 for a single hole flow), which means that the local maximum rate of mass transfer is approximately four and half times the mass transfer rate in a fully developed circular tube flow.

A piecewise-averaged Sherwood number, which is the average from the entrance to the point of interest, is investigated for various Reynolds numbers (Fig. 11). For a thin plate, less than $t/D = 0.5$, the piecewise-averaged mass transfer coefficient will be different due to no reattachment in the hole and a recirculating zone extending to the leeward side. The piecewise-averaged values are normalized by the fully developed coefficients. The normalized peak values increase slightly with Reynolds number. Note that the single hole peak values remain independent of Reynolds number. However, the results can be collapsed to a single curve and the single hole flow data with a factor, which will be a function of Reynolds number and hole-to-hole spacing. The factor $F_s = 5.31\ Re^{-0.196}$ is obtained for Re = 5000 to 14,000 but only one spacing has been investigated in the present study. Figure 11 shows the data as a single curve (except at Re = 6900) and the curve is fitted by the correlation from single hole flow (Cho et al., 1997).

The local variation on the surfaces is compared for different Reynolds numbers in Fig. 12. The transfer coefficient inside the hole is dominant and the rates on the windward and the leeward surfaces are similar in magnitude. For the single hole flow, the transfer rate on the leeward surface was quite small. For the multihole case, the surface area inside the hole is 22 percent of the total active area, but the mass transfer from it is about 50 percent which increases slightly with Re, in the present hole

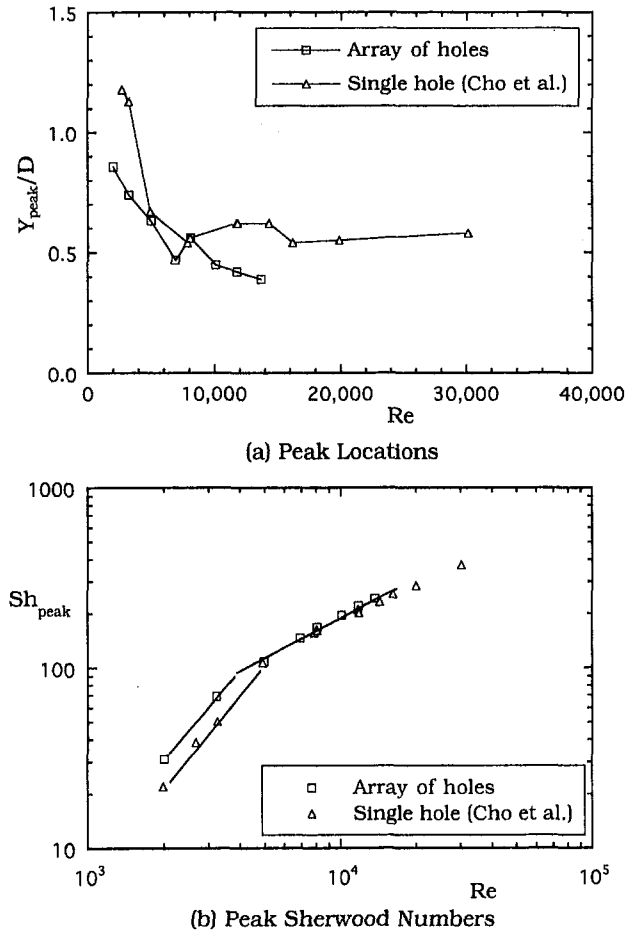

Fig. 10 Peak Sh locations and values at the inside hole surface (compared with those of a single hole flow; Cho et al., 1997)

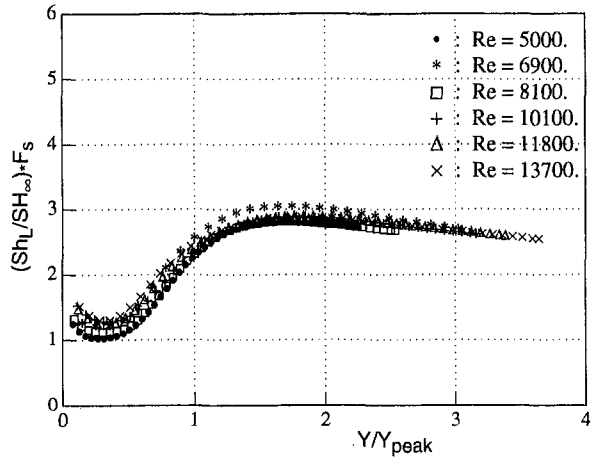

Fig. 11 Normalized piecewise-average Sh inside the hole surface

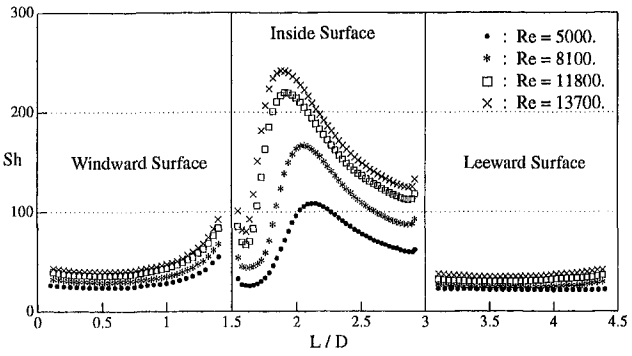

Fig. 12 Comparison of local Sh for an array of holes

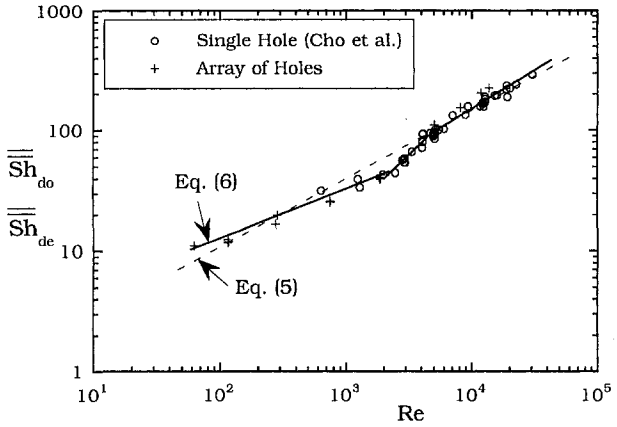

Fig. 14 Overall averaged Sh (compared with a single-hole flow; Cho et al., 1997)

configuration. It can be concluded that about half of the heat/mass transfer for an array of perforated holes will be from the inner hole surfaces themselves.

Figure 13 represents the average transfer coefficients at the individual surfaces for an extended range of Re = 270 to 14,000 at two different hole diameters with the hole-to-hole spacing $P = 3D$. On the windward surface, the average Sh has the same slope for the two hole diameters. However, the slopes of the average Sh on the inside and leeward surfaces decrease at around Re ≅ 3500 because the flow moves to the turbulent regime after separation at the inlet of the holes.

Figure 14 shows the overall (three surfaces) mass transfer coefficients for different hole diameters and plate thicknesses. The overall average Sh (for all three surfaces) is based on the outer active boundary diameter for single holes and on the equivalent diameter, d_e, for arrays of holes. The equivalent diameter, d_e, is a function of the pitch, P, and the relation is obtained by an equivalent area, $\pi d_e^2/4 = P^2$. Recall d_o is the active boundary diameter for a single-hole case (Cho et al., 1997). The Sherwood numbers, averaged over the respective areas, are plotted in a single curve and it is somewhat linear for Re = 60 to 30,000:

$$\overline{\overline{Sh}}_{de} = 0.644\ Re^{0.582} \tag{5}$$

As with the single hole results, the correlation equation can be subdivided into three parts, which correspond to laminar, transition, and turbulence zones (for $1.5 \le P/D \le 3$ and $0.68 \le t/D \le 1.5$).

$$\overline{\overline{Sh}}_{de} = 1.678\ Re^{0.426} \quad (60 \le Re \le 2000) \tag{6a}$$

$$\overline{\overline{Sh}}_{de} = 0.0388\ Re^{0.915} \quad (2000 < Re \le 5000) \tag{6b}$$

$$\overline{\overline{Sh}}_{de} = 0.433\ Re^{0.633} \quad (5000 < Re \le 30{,}000) \tag{6c}$$

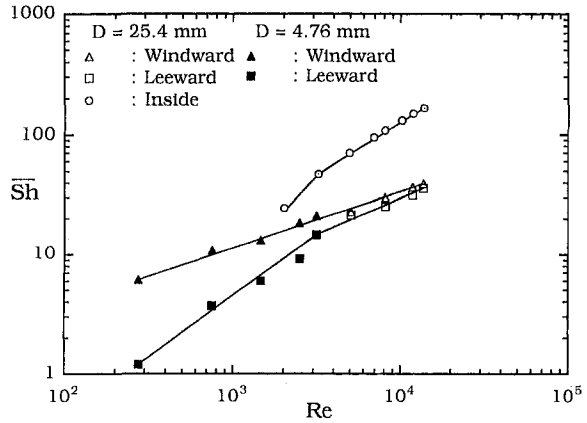

Fig. 13 Averaged Sh on the individual surface

Andrews and Bazdidi-Tehrani (1989) measured average heat transfer coefficients of arrays of holes for various hole spacings. They correlated the data based on the inside hole surface area

$$\overline{\overline{Nu}}_h = 0.147\left(\frac{P}{D}\right)^{0.72} Re^{0.55}\ Pr^{0.33} \tag{7}$$

However, this equation is only good for $P/D = 11$ and $t/D = 4.5$ and the data for other cases are scattered from the equation. The equation (data) for the case $P/D = 11$ and $t/D = 4.5$ is converted to Sh based on the characteristic length, d_e, in the present correlation via heat and mass transfer analogy; $\overline{\overline{Sh}}/Nu = (Sc/Pr)^{0.4}$. The converted equation is given by $\overline{\overline{Sh}}_{de} = 0.812\ Re^{0.55}$. When this equation and Eq. (5) are compared numerically, the resulting average Sherwood numbers are shown in Table 2. The difference between two data is small at the low Reynolds number and increases with Reynolds number. The reason may be that the transfer rate on the leeward surface is not negligible at high Reynolds numbers. Thus, the present correlations can be applied to a large hole spacing $P = 11D$ and a thick plate $t = 4.5D$.

3 Flow Through Two Parallel Perforated Plates. Flow through laminated plates or a porous medium is better simulated using multiple layers than with a single perforated plate. Two perforated plates are studied with an in-line layer arrangement and compared with the single plate data.

3.1 Windward and Leeward Surfaces of the Second Plate. Measurements are made only on the second plate as the mass/heat transfer coefficients on the first plate should be the same as those for a single plate except on leeward surface. The main jet stream goes directly through the holes of the second plate. But, some air washes the windward surface and collides with the flow from the adjacent jets, resulting in a mild peak in Sh number on the second plate (Fig. 15).

Figure 16 presents the radial variations of Sh for gap size, $G = 2D$, and Re = 8,100. A small peak occurs at $r/D = \pm 1.5$ due to the secondary vortices from two adjacent jets. The local

Table 2 Comparison of Andrews' (1989) correlation and Eq. (5)

Re	Andrews'	Eq. (5)	difference
1,000	36.3	36.0	1.0%
2,000	53.1	53.8	1.3%
5,000	87.9	91.8	4.2%
10,000	128.7	137.5	6.4%
20,000	188.4	205.8	8.4%

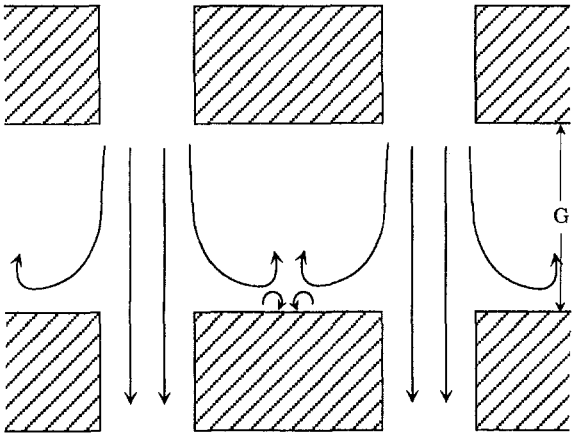

Fig. 15 Schematic flow pattern through two parallel perforated plates (in-line arrangement)

Sh distribution is axisymmetric and the local Sh is about twice that of the single layer near the hole but about equal near the symmetry line. At $\theta = 45$ deg line (diagonal of the holes), there is no peak at the middle and the Sh value is lower than along the $\theta = 0$ deg line. It is caused by the longer path of the wall jet and its weak collision with adjacent jets.

The contour plot is presented in Fig. 16(b) and shows good symmetry. The two concentric circles in the contour plot are

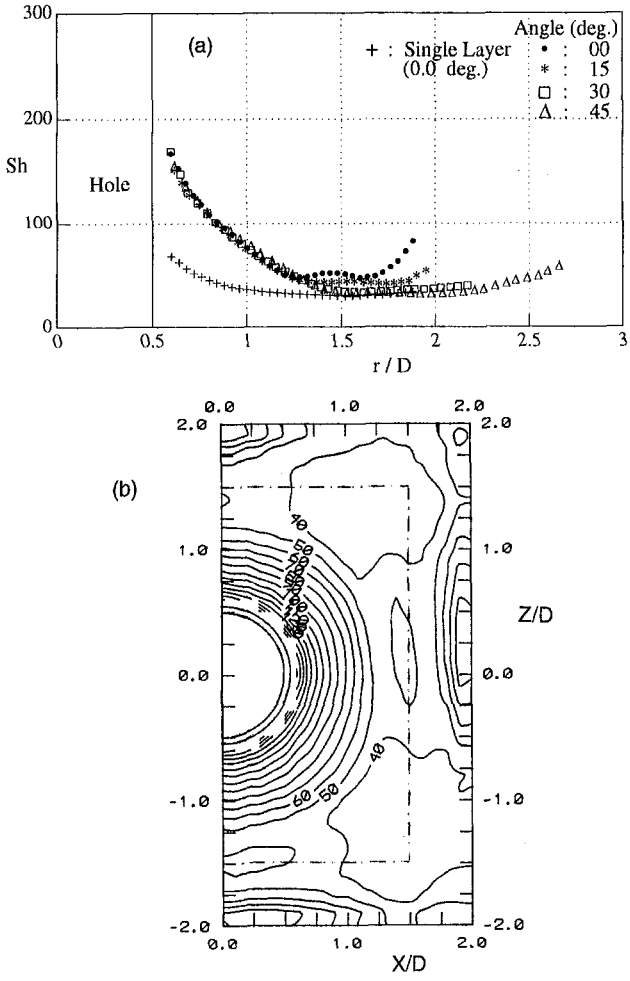

Fig. 16 Local Sh on the windward surface of the second plate at $G = 2D$ and Re = 8,100: (a) along radial direction; (b) contour plot

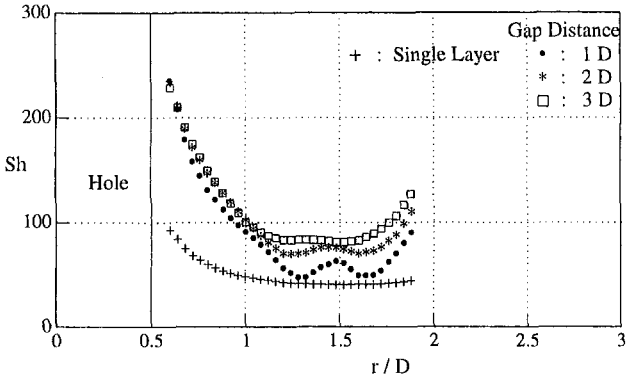

Fig. 17 Comparison of Sh on the windward surface for various gap distances at Re = 13,700 and $\theta = 0$ deg

the outline of the aluminum rim used as a reference in mass transfer measurements. The Sh values change rapidly near the hole and show the mild peak only at the middle of the axes ($\theta = 0$ deg line) that connect the holes.

The effects of gap distance between two perforated plates are presented in Fig. 17 at Re = 13,700 and $\theta = 0$ deg and compared with results from a single plate. In general, the Sh increases with gap distance, especially in the middle region (at the symmetry line; $r/D = \pm 1.5$). At higher gap distance, more of the jet stream is expected to wash the windward surface of the second plate rather than escape directly through the hole.

Figure 18 presents the Sh values at different Reynolds numbers for $G = 2D$. The magnitude of Sh increases continuously with Reynolds number and the patterns are similar for all Reynolds numbers. When the local Sh values are compared with those of a single plate, they show values about two times higher.

Sh on the leeward surface of the second plate is, as expected, fairly uniform over the entire domain and the same as that on the leeward surface of a single layer flow.

3.2 Inside Hole Surface of the Second Plate. Figure 19 presents a comparison of Sh values at various gap distances at Re = 13,700. The results show no peak point (no reattachment as no separation) at $G = 1D$. As gap distance is increased, separation at the hole entrance appears and its length increases with increasing gap distance. The Sh values in the recirculating region of the second plate hole entrance also increase with gap distance.

Figure 20 presents the local Sh inside the hole at $G = 2D$ for Re = 5000 to 13,700. The Sh values indicate that separation

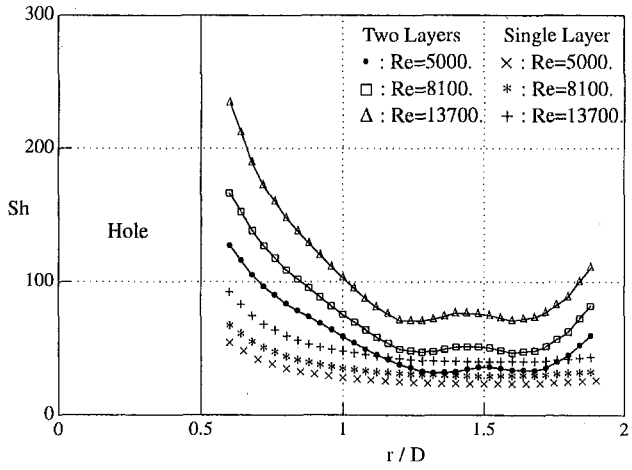

Fig. 18 Comparison of Sh on the windward surface for different Reynolds numbers at $G = 2D$ and $\theta = 0$ deg

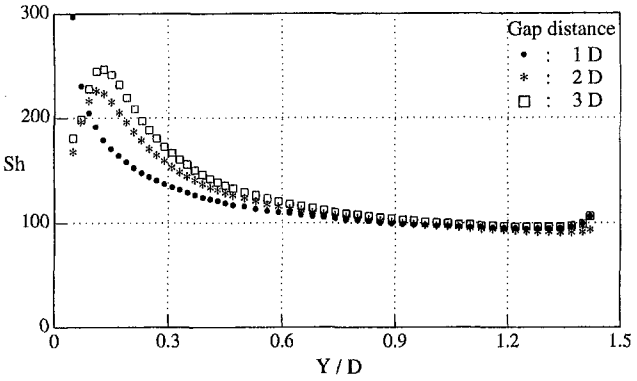

Fig. 19 Local Sh inside the hole of the second plate for various gap distances at Re = 13,700

occurs only at the high Reynolds number Re = 13,700 with a short separation length. The overall Sh values are lower than for a single layer flow due to the development of a jet core (low velocity near the hole surface) from the first plate, analogous to using a thicker plate which will be discussed later. The magnitude of Sh on the second plate is approximately 20 percent lower than that of the single layer flow.

3.3 Double Thickness Plate With Starting Active Area at the Middle of the Hole. One layer of perforated plate with double thickness ($t \cong 3D$) is conducted to compare the mass transfer coefficient inside the hole of two parallel perforated plates. The mass active area starts halfway through the hole (zero gap distance between two perforated plates), such that the mass active field starts later than the flow field in a circular tube flow. The Sh has a high value around $Y/D = 0$ as the mass boundary layer starts. A comparison of Sh with two perforated layers shows greater agreement at lower Reynolds number and at smaller gap distances, Fig. 21. At a small gap distance (less than $1D$ with Re = 13,700), it appears that the hole flow at the second plate of the two layers resembles a circular tube flow without a gap. Thus, the transfer rate at the second plate of the two perforated layers can be simulated by a double thickness plate with the mass active area starting at the middle of the hole.

3.4 Average Sherwood Numbers. The average Sherwood numbers are compared with the one-layer case for each surface in Tables 3 and 4. The average Sh on the windward surface of the second plate is about twice that of the single layer case and

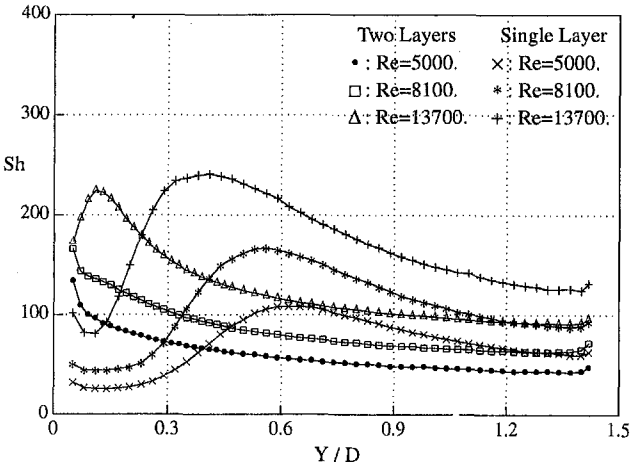

Fig. 20 Comparison of Sh in hole for different Reynolds numbers at *G* = 2*D*

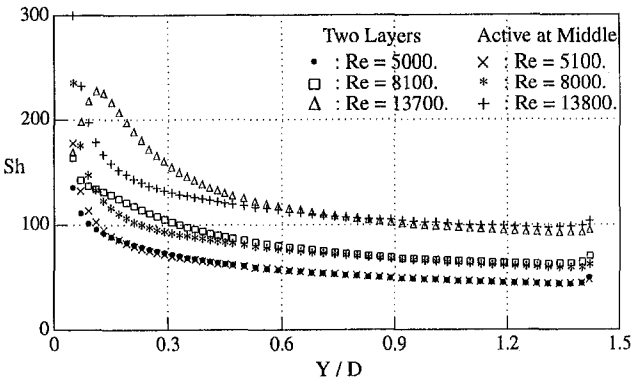

(a) Various Reynolds Numbers (G = 2D for Two Layers)

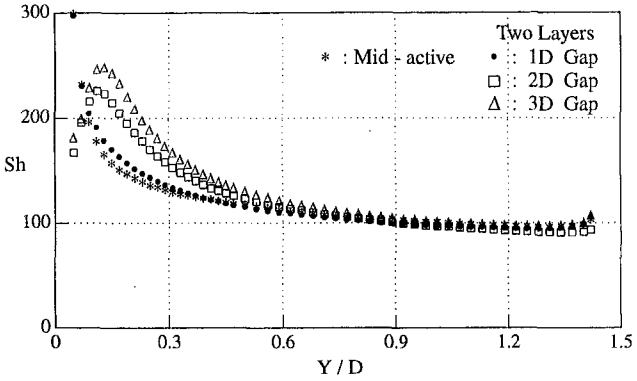

(b) Various Gap Distances for Two Layers at Re = 13,700

Fig. 21 Local Sh inside the hole of mass active at midhole (compared with two perforated layers)

the ratio increases slightly with Reynolds number. At the inside hole surface, the average Sh of the second plate is about 16 percent lower at Re = 5000 than for the one layer case, but the ratio increases and is 25 percent lower at Re = 13,700. At the leeward surface, the difference between two layers and single layer is negligible.

For Re = 5000 to 14,000, an overall averaged Sh at the second plate is correlated by:

$$\overline{\overline{Sh}}_{de} = 0.176\ Re^{0.635} \tag{8}$$

The overall averaged Sh is compared with the value for the single layer case in Table 5. It shows that the overall averaged Sh at the second plate of two perforated layers increases approximately 15 ~ 20 percent from that for the single layer.

3.5 Flow and Mass/Heat Transfer Models in Two Perforated Plate Layers. For in-line layer arrangements, the central portion of the jet from each hole of the first plate goes directly into the holes of the second plate. As the gap distance increases, however, some of the jet stream washes the windward surface of the second plate (Fig. 15). The flow outside the central portion of the jet develops on the windward surface. This flow is similar to the wall-jet from an impinging jet on a solid plate.

Table 3 The average Sh on the windward surface of the second plate for *P/D* = 3 (various gap distances)

	Two layers			Single layer
Re G	1D	2D	3D	
5000		47.0		22.9
8100		62.6		30.2
13700	69.9	86.4	95.1	39.3

When the wall-jets collide, the primary vortices upwash with the counter secondary vortices impinging on the midline. The secondary vortex impingement increases the mass/heat transfer in the midregion between the holes, as shown in Fig. 17. However, the peak Sh is relatively small because the secondary vortices are suppressed by the upwash main wall-flows in a confined space.

The velocity profile of the main jet stream leaving a hole of the first plate does not change significantly as it passes through the gap. When the flow enters a hole of the second plate, the velocity distribution is similar to the exit flow of the first plates for small gaps. For a small gap distance (less than $1D$), therefore, it appears that the hole flow at the second plate of the two layers resembles a circular tube flow without a gap. Thus, the mass/heat transfer in a hole of the second plate of the two perforated layers can be simulated from a tube flow with double thickness (Fig. 21).

Conclusions

Flow Through a Single Perforated Plate

(*i*) Mass transfer coefficients on the windward surface for $P/D = 3$ increases approximately 50 percent from that for single hole flow due to flow stagnation centered between holes. The transfer rate increases with Reynolds number to 0.5 power as with a laminar stagnation flow on a flat plate.

(*ii*) On the leeward surface, the transfer rate is much higher (about three times) than for the single hole flow case due to strong recirculation between neighboring jets. This recirculation results from impingement on the surface. Also, the distribution of the transfer rates is relatively uniform and the magnitude is the same as that on the windward surface for high Re ($\geq \sim 5{,}000$).

(*iii*) Inside the hole, separation flow becomes turbulent at a lower Re and has a shorter separation length ($0.4D$) than for a single-hole flow because the upstream flow is more disturbed due to the stagnation.

(*iv*) The value of peak Sh (about 4.5 Sh_∞) near reattachment in the holes is slightly higher than for a single hole flow. The overall transfer rate is dominated by the inside hole surface.

(*v*) For both flows through a single hole and arrays of holes, the overall averaged Sh is correlated well with the characteristic length of d_o (outer boundary of the active area) for a single hole and d_e (an area equivalent diameter) for arrays of holes.

Flow Through Two Parallel Perforated Plates

(*i*) On the windward surface of the second plate, the transfer coefficient distribution is axisymmetric around the hole except for the stagnation region between holes. The transfer rate increases with the gap distance because the jet flow spreads wider for the larger gap. The transfer rate is about twice that of a single layer case.

Table 4 The average Sh on the inside hole surface of the second plate for $t/D = 1.48$ (various gap distances)

	Two layers			Mid-active	Single layer
Re G	1D	2D	3D		
5000		59.0		60.1	70.4
8100		83.1		80.7	108.9
13700	117.0	123.7	131.2	118.3	167.8

Table 5 Comparison of overall averaged Sh at the second plate of two layers and at single layer for $P/D = 3$ and $t/D = 1.48$

Re	Two layers	Single layer	Increment
5000	39.6	32.9	21%
8100	52.5	45.7	15%
13700	74.8	66.3	13%

(*ii*) Inside the hole of the second plate, no separation at the hole entrance is observed for a small gap distance ($G = 1D$) with a low Re. The separation zone, although it is small, increases slightly with higher gap distances and higher Reynolds numbers. The transfer coefficient is approximately 20 percent lower than for a single plate.

(*iii*) The transfer coefficient in a double-thickness plate (zero gap distance), with the active area starting halfway through the hole (a thermal entry problem), is very close to the two perforated plates with a low Re and a small gap distance. One can infer that the transfer coefficient inside the hole of two perforated plates can be determined from that of a single layer with double thickness.

Acknowledgments

Support from the Air Force Office of Scientific Research and through the Engineering Research Program of the Department of Energy aided greatly in the conduct of this study.

References

Andrews, G. E., and Mkpadi, M. C., 1984, "Full-Coverage Discrete Hole Wall Cooling: Discharge Coefficients," ASME *Journal of Engineering for Gas Turbines and Power,* Vol. 106, pp. 183–192.

Andrews, G. E., Asere, A. A., Gupta, M. L., and Mkpadi, M. C., 1985, "Full Coverage Discrete Hole Film Cooling; The Influence of Hole Size," ASME Paper No. 85-GT-47.

Andrews, G. E., Alikhanizadeh, M., Asere, A. A., Hussain, C. I., Khoshkbar Azari, M. S., and Mkpadi, M. C., 1986a, "Small Diameter Film Cooling Holes: Wall Convective Heat Transfer," ASME JOURNAL OF TURBOMACHINERY, Vol. 108, pp. 283–289.

Andrews, G. E., Asere, A. A., Mkpadi, M. C., and Tirmahi, A., 1986b, "Transpiration Cooling: Contribution of Film Cooling to the Overall Cooling Effectiveness," ASME Paper No. 86-GT-136.

Andrews, G. E., Alikhanizadeh, M., Bazdini Tehrani, F., Hussain, C. I., and Khoshkbar Azari, M. S., 1987, "Small Diameter Film Cooling Holes: The Influence of Hole Size and Pitch," ASME Paper No. 87-GT-28.

Andrews, G. E., and Bazdidi-Tehrani, F., 1989, "Small Diameter Film Cooling Hole Heat Transfer: The Influence of the Number of Holes," ASME Paper No. 89-GT-7.

Cho, H. H., 1992, "Heat/Mass Transfer Flow Through an Array of Holes and Slits," Ph.D. Thesis, Univ. of Minnesota.

Cho, H. H., Jabbari, M. Y., and Goldstein, R. J., 1997, "Experimental Mass (Heat) Transfer in and Near a Circular Hole in a Flat Plate," *Int. J. Heat Mass Transfer,* Vol. 40, pp. 2431–2443.

Goldstein, R. J., and Cho, H. H., 1995, "A Review of Mass (Heat) Transfer Measurements Using Naphthalene Sublimation," *Exp. Thermal and Fluid Science,* Vol. 10, pp. 416–434.

Hempel, H., Friedrich, R., and Wittig, S., 1980, "Full Coverage Film-Cooled Blading in High Temperature Gas Turbines: Cooling Effectiveness, Profile Loss and Thermal Efficiency," ASME *Journal of Engineering for Power,* Vol. 102, No. 4.

Mills, A. F., 1962, "Experimental Investigation of Turbulent Heat Transfer in the Entrance Region of a Circular Conduit," *J. Mech. Eng. Sci.,* Vol. 4, pp. 63–77.

Nealy, D. A., and Reider, S. B., 1980, "Evaluation of Laminated Porous Wall Materials for Combustor Liner Cooling," ASME *Journal of Engineering for Power,* Vol. 102, pp. 268–276.

Ortiz, C., 1981, "Heat Transfer Coefficients for the Upstream Face of a Perforated Plate Positioned Normal to an Oncoming Flow," M.S. Thesis, Univ. of Minnesota.

Wassell, A. B., and Bhangu, J. K., 1980, "The Development and Application of Improved Combustor Wall Cooling Techniques," ASME Paper No. 80-GT-66.

Multiple Jets in a Crossflow: Detailed Measurements and Numerical Simulations

P. Ajersch

J.-M. Zhou

S. Ketler

M. Salcudean

I. S. Gartshore

Department of Mechanical Engineering,
University of British Columbia,
Vancouver, British Columbia, Canada

The fluid mechanics and heat transfer characteristics of film cooling are three-dimensional and highly complex. To understand this problem better, an experimental study was conducted in a low-speed wind tunnel on a row of six rectangular jets injected at 90 deg to the crossflow (mainstream flow). The jet-to-crossflow velocity ratios (blowing ratios) examined were 0.5, 1.0, and 1.5, and the jet spacing-to-jet width ratio was 3.0. No significant temperature difference between jet and crossflow air was introduced. Mean velocities and six flow stresses were measured using a three-component laser-Doppler velocimeter operating in coincidence mode. Seeding of both jet and cross-stream air was achieved with a commercially available smoke generator. Flow statistics are reported in the form of vector plots, contours, and x–y graphs, showing velocity, turbulence intensity, and Reynolds stresses. To complement the detailed measurements, flow visualization was accomplished by transmitting the laser beam through a cylindrical lens, thereby generating a narrow, intense sheet of light. Jet air only was seeded with smoke, which was illuminated in the plane of the light sheet. Therefore, it was possible to record on video tape the trajectory and penetration of the jets in the crossflow. Selected still images from the recordings are presented. Numerical simulations of the observed flow field were made by using a multigrid, segmented, $k-\epsilon$ CFD code. Special near-wall treatment included a nonisotropic formulation for the effective viscosity, a low-Re model for k, and an algebraic model for the length scale. Comparisons between the measured and computed velocities show good agreement for the nonuniform mean flow at the jet exit plane. Velocities and stresses on the jet centerline downstream of the orifice are less well predicted, probably because of inadequate turbulence modeling, while values off the centerline match those of the experiments much more closely.

Introduction

There exist several engineering applications for which the study of jets issuing into a crossflow is of primary relevance. These include dispersion of pollutants, gas injection in combustors, V/STOL transition flight aerodynamics, and film cooling of gas turbine blades. A number of parameters may be used to describe uniquely the fluid mechanics associated with a given application, one being the jet-to-crossflow velocity ratio R. For this study, which examines the multiple jet film cooling of gas turbine blades, applicable values of R are relatively low, near unity.

For a single strong jet (i.e., $R \gg 1.0$) in a crossflow, the flow field is typified by a jet core deflected by the crossflow, penetrating the free-stream boundary layer. The jet centerline curves most strongly in the near jet region and flattens out downstream. As fluid from the free stream is diverted to either side of the obstructing jet, shear stresses induce a rotating motion, which develops into a pair of counterrotating vortices. Fric and Roshko (1989) describe the other primary vortices in the flow. One is a ring vortex, which circumscribes the jet as it exits the jet channel. Another is a horseshoe vortex in the near field upstream of the jet exit—a result of the deceleration of free-stream fluid as it approaches the obstructing jet. The third is a wake vortex pair, which has the appearance of a von Karman vortex street, though it is thought to be generated not at the jet/crossflow interface, but at the wall in the near jet region. According to Andreopoulos (1985), the near field of strong jets is controlled largely by complex inviscid dynamics, as opposed to that of a weak jet, which is turbulence dominated. Therefore, a weak jet (e.g., $R = 1.0$) may not exhibit all the characteristics described above.

A configuration involving a row of jets introduces a new parameter: the spacing-to-diameter ratio s/D. For the extreme case of $s/D = 1.0$ (i.e., a two-dimensional slot), jet penetration is strongest. As the spacing increases toward an intermediate value somewhere between 3 to 5 diameters, the jet penetration decreases, partly due to the increasing entrainment of free-stream fluid (Sterland and Hollingsworth, 1975). As spacing increases, further free-stream fluid begins to flow between the jets, thereby elevating the lee side pressure and causing the jets to penetrate deeper into the crossflow. The single jet marks the other extreme case of $s/D = \infty$ where penetration is high. In the application of turbine blade cooling by discrete hole injection, typical design spacing corresponds to that of weak jet penetration.

This study is primarily concerned with multiple jets and low velocity ratios. Previous literature concerning single jets is still relevant and some examples of work involving such jets are cited below. A description of some of the literature involving multiple jets and relevant numerical work is also made.

A number of experimental studies have been performed for the single jet: Andreopoulos and Rodi (1984), and Perry et al. (1993), for example. The former was one of the most detailed works wherein mean velocities and six flow stresses were measured with a three-component hot-wire probe. The authors were able to describe the flow field thoroughly for $R = 0.5$, 1.0, and 2.0, and to evaluate the usefulness of the eddy-viscosity model based on their findings.

Contributed by the International Gas Turbine Institute and presented at the 40th International Gas Turbine and Aeroengine Congress and Exhibition, Houston, Texas, June 5–8, 1995. Manuscript received by the International Gas Turbine Institute February 4, 1995. Paper No. 95-GT-9. Associate Technical Editor: C. J. Russo.

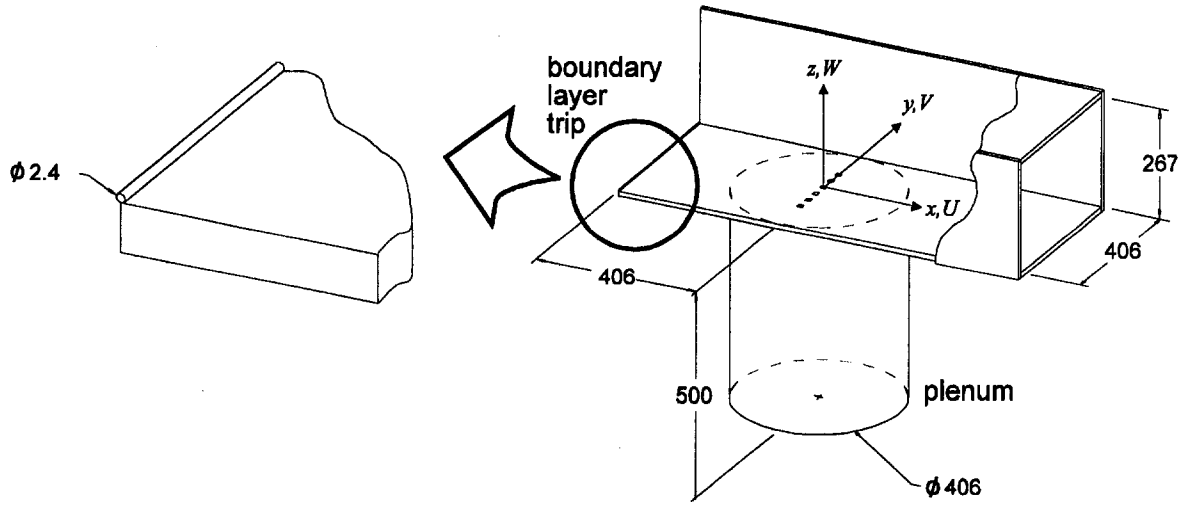

Fig. 1 Test section geometry; all dimensions in mm

Weak multiple jets issuing normally into a crossflow have been studied experimentally by Sugiyama and Usami (1979) who reported pressures and mean velocities for a row of nine jets spaced at 3-D and exiting at $R = 2.0$. Khan et al. (1982) reported jet concentration and mean velocities for $s/D = 2$ and $s/D = 4$ with $R = 2.3$, and compared their results to a coarse-grid numerical simulation. Isaac and Jakubowski (1985) used hot-wire probes to measure mean velocities and five flow stresses in the region about tandem jets exiting at $R = 2$. Studies involving even lower velocity ratios, which better represent the application of the turbine blade cooling, are less common. Peña and Arts (1992) reported two-component laser-Doppler velocimetry (LDV) measurements for velocity ratios as low as 0.5. They also varied the spacing from 3D to 5D, and varied the jet density from $1.0\rho_{cf}$ to $2.0\rho_{cf}$. Their primary interest was in the flow several diameters downstream of the injection hole.

The case of multiple jets issuing into a crossflow at an angle of less than 90 deg to the surface is also of great relevance to the application of turbine blade cooling, as this configuration induces less aerodynamic mixing between injected and free-stream fluids. Kadotani and Goldstein (1979) examined the effects of boundary layer thickness, Reynolds number, and free-stream turbulence intensity on film cooling effectiveness, and velocity and temperature distribution. They used a row of jets inclined at 35 deg to the mainstream direction, issuing into the crossflow with velocity ratios between $R = 0.2$ and $R = 1.5$. Two-component LDV velocity measurements were reported by Foucault et al. (1992) on a row of 45 deg inclined jets exiting at $R = 0.6$ and $R = 1.6$. Distributions of temperature and temperature fluctuations were also reported in this paper.

Some studies have examined the flow field in the region about a jet exiting a scaled model of a turbine blade (Beeck et al., 1992; Benz et al., 1993). The geometry was simplified to a slot jet exiting a two-dimensional blade in both papers. Both experimental measurements and numerical simulations were performed by these authors.

Normal jets in a crossflow have also been represented by numerical simulations. Demuren (1993) examined a single jet issuing into a crossflow at $R = 0.5$ and $R = 2.0$ with a finite-volume multigrid method, and compared the results with those of Andreopoulos and Rodi (1984). Kim and Benson (1993) used a multiple-time-scale model to calculate the flow field of a row of jets for $R = 2.3$, and captured some interesting structures in the near-jet region.

The focus of this paper is on the flow field about a row of 90 deg jets in a crossflow. Mean velocities and six flow stresses were measured using a three-component LDV operating in coincidence-mode, a technique which, to the best of the authors' knowledge, has previously not been applied to jets in a crossflow. The importance of this measurement method is explained later in the paper. The results are reported in the form of vector plots, contour plots, and xy-profiles, and trends with changing R are compared. Low velocity ratios were used (i.e., $R = 0.5$, 1.0, and 1.5) to best represent the conditions of a cooling jet in a turbine blade. Although the $R = 1.5$ value may be somewhat high for film cooling, the set of data for this case was useful for comparison with the numerical simulation.

A modified multigrid finite-difference (MGFD) numerical simulation is compared with the experimental results and discrepancies between the two are discussed.

Nomenclature

D = jet diameter (= jet width)
F.S. = denotes full scale
J = jet-to-crossflow momentum ratio
N = number of data points in a record
R = jet-to-crossflow velocity ratio
U, V, W = mean velocity component with respect to axes x, y, and z, respectively
$U(t), V(t), W(t)$, = instantaneous velocity with respect to axes x, y, and z, respectively
V_{cf} = crossflow velocity
V_{jet} = bulk jet velocity
$\bar{V}$ = three-dimensional velocity vector
cf = denotes crossflow
fs = denotes free stream
i = denotes ith data point in a record
k = turbulence kinetic energy
s = general flow statistic
u, v, w = fluctuating velocity component with respect to axes x, y, and z, respectively
u', v', w' = normal stresses with respect to axes x, y, and z, respectively
$\overline{vw}, \overline{uw}, \overline{uv}$ = shear stresses
x, y, z = axes of the tunnel coordinate system

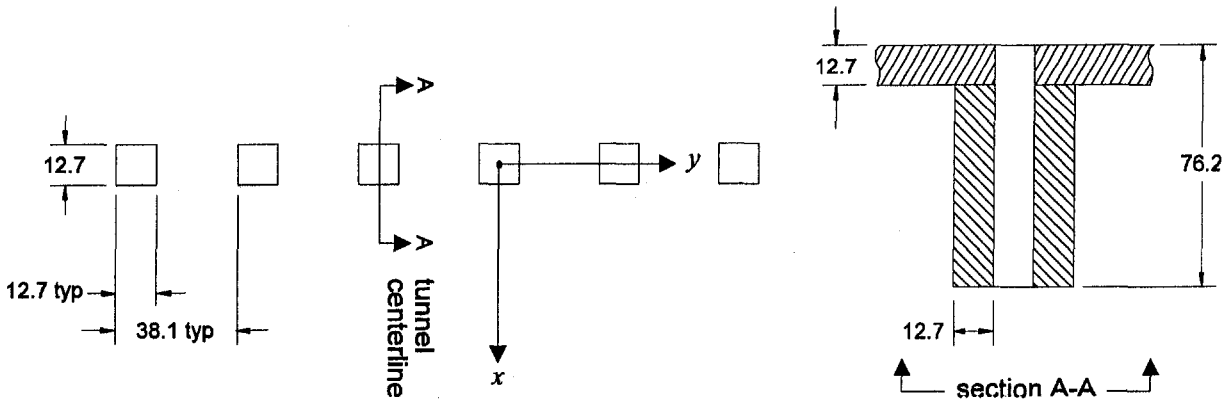

Fig. 2 Detail of the jet exit; all dimensions in mm

Square jets were used in this study because (1) the rectangular grid used in the numerical simulation imposed difficulty in modeling a round jet, and (2) such jets increase the practicality of changing the jet spacing and jet aspect ratio in future experiments. Throughout this paper, references are made to the "diameter" of the jet. This terminology is rooted in the past study of jets, as well as in the practical machining of cooling holes, where round jets are customarily used. The term "diameter" is to be equated here to "jet width."

Experimental Arrangements

The wind tunnel used to generate the crossflow was a 267 mm × 406 mm open-loop forced-draft tunnel with a maximum air speed of 12 m/s. The test section was 1016 mm long and located just downstream of a 4:1 area contraction section. Flow uniformity was achieved with five screens and a 50-mm-thick section of honeycomb between the inlet and the test section. To ensure that a fully turbulent boundary layer was present in the test section, a 2.4 mm rod was affixed to the tunnel floor at the test section entry. Details of the test section geometry are shown in Fig. 1.

A row of six square jets was arranged on the tunnel floor 406 mm downstream of the boundary layer trip. The row was oriented perpendicular to the direction of the crossflow and the jets issued into the crossflow at an angle of 90 deg to the plane of the tunnel floor. Each jet measured 12.7 mm × 12.7 mm in cross-section and had an entry length of 6 diameters (Fig. 2). Spacing between jet centerlines was 3 diameters. The entries to the jet channels were sharp-edged, as opposed to nozzle-shaped. Air flow for the jets was supplied by a 400 kPa (static) compressed air line and was regulated by two flow regulators configured in series. A 0.918 m^3/min (F.S.) rotometer was used to measure the volume flow. A 406 mm diameter by 500 mm tall plenum—or settling chamber—was positioned below the tunnel floor between the air line and the jet channels.

The coordinate system used in this experiment is shown in Fig. 1. The origin corresponds to the center of one of the middle two jets designated EAST1.

Flow field characteristics of jets in a crossflow are strongly dependent on the momentum ratio as defined by

$$J = \frac{\rho_{\text{jet}} V_{\text{jet}}^2}{\rho_{cf} V_{cf}^2} \tag{1}$$

(Holdeman and Walker, 1977). In this low-speed isothermal experiment, the densities in Eq. (1) cancel, and the relevant parameter becomes the velocity ratio R. Three cases of R were examined: 0.5, 1.0, and 1.5 (i.e., $J = 0.25$, 1.0, and 2.25, respectively). Throughout the experiment, the bulk jet velocity was maintained at 5.5 m/s; therefore, the crossflow velocities used were 3.67 m/s, 5.5 m/s, and 11.0 m/s. Based on the jet diameter of 12.7 mm and the viscosity of air at standard pressure and temperature, the jet Reynolds number was constant at approximately 4700.

Data Collection. Flow statistics for this experiment were obtained by LDV. A Coherent Innova 7.0 W argon-ion laser paired with a TSI Colorburst model 9201 multicolor beam sepa-

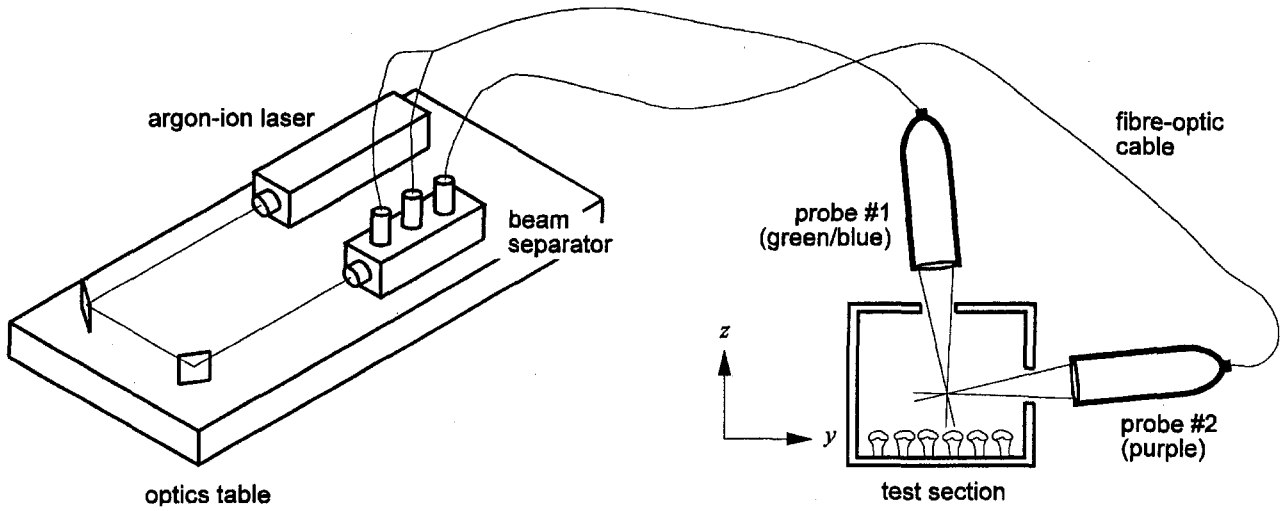

Fig. 3 Laser setup and arrangement of probes with respect to test section

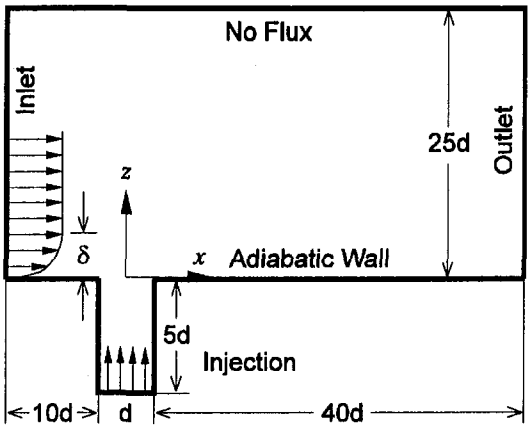

Fig. 4 Computational domain; not to scale

rator were used as the source for the three pairs of beams (Fig. 3). These beams were coupled through fiber optic cables to two probes (TSI models 9831 and 9832), and were focused to a single measurement volume in the test section. The probes also acted to retrieve the Doppler signals, which were transmitted through fiber optic cable to a TSI Colorlink model 9230 photomultiplier, and then to three TSI IFA550 processors. A TSI software package controlled the acquisition and storage of raw data.

Flow was seeded by smoke generation. A Rocso 1500 unit was used at the wind tunnel inlet to generate seed particles in the crossflow. The second device was a Genie machine arranged in-line with the compressed air source to generate seed particles in the jet flow. Particles sizes were estimated to lie between 5 μm and 60 μm.

The LDV system was operated in three-component coincidence mode, which allows for the calculation of three mean velocities and six flow stresses.

One difficulty associated with acquiring vector measurements is that of accurately aligning the measurement probe with the desired reference axes. This is particularly important when a weak velocity component is being measured in the presence of a large one. For example, consider velocity in a boundary layer, where the streamwise velocity component is dominant. If one seeks the velocity component perpendicular to the wall, the probe must be aligned accurately. Otherwise, the dominant streamwise velocity will map onto the component being measured. Errors introduced by this type of angular misalignment may be corrected if (1) the angle of misalignment is accurately known, and (2) an assumption or accurate estimate can be made regarding the magnitudes of the two other velocities. In the case of multiple jets issuing into a crossflow, accurate estimates of the complex flow field are not available a priori.

Table 1 Uncertainty in measured values (20 to 1)

Quantity	Uncertainty (standardized method)	Uncertainty (including velocity bias)
angle of misalignment	±0.15°	
measurement position	±0.1 mm	
mean velocity	$\pm 0.01 V_{jet}$	$\pm 0.1 V_{jet}$
normal stress	$\pm 0.001 V_{jet}^2$	$\pm 0.01 V_{jet}^2$
shear stress	$\pm 0.0002 V_{jet}^2$	$\pm 0.002 V_{jet}^2$

The problem is compounded when cross-correlated terms like shear stresses are sought. If the three probes cannot be aligned precisely normal to one another, a correction needs to be made to each measured velocity component at each time for a given measurement position.

Since the two LDV probes in this study were angled at approximately 6 deg to the tunnel floor (Fig. 3) to allow near-wall measurements, corrections were required and were applied to the time traces of raw data following the acquisition process. It was therefore necessary to measure the three angles by which each probe was misaligned with respect to the reference axes. The magnitudes of the corrections are apparent in the velocity transformation matrix below, which was used to recalculate each data measurement accepted by the LDV processor:

$$\begin{bmatrix} U(t) \\ V(t) \\ W(t) \end{bmatrix} = \begin{bmatrix} 0.9999 & 0.0121 & 0.0024 \\ -0.0099 & 0.9946 & -0.1091 \\ -0.0176 & 0.1036 & 0.9941 \end{bmatrix} \begin{bmatrix} U_m(t) \\ V_m(t) \\ W_m(t) \end{bmatrix}$$

$U(t)$, $V(t)$, and $W(t)$ refer to three components of velocity aligned to the reference axes at time t, and the subscript m denotes the three measured components of velocity.

If flow statistics in turbulent flow are simply calculated by using arithmetic averages, a bias will exist in the statistics (Edwards, 1987). A variety of weighted averaging techniques can be applied to correct this error (McLaughlin and Tiederman, 1973), each with its own set of advantages. The technique selected here was inverse velocity weighting.

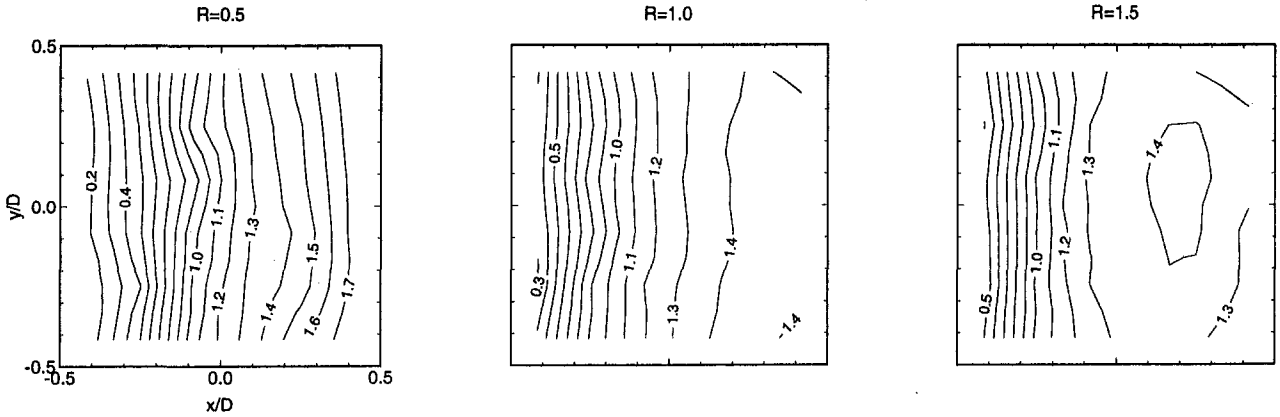

Fig. 5 Vertical velocity at the jet exit (W/V_{jet}). z/D = 0.0

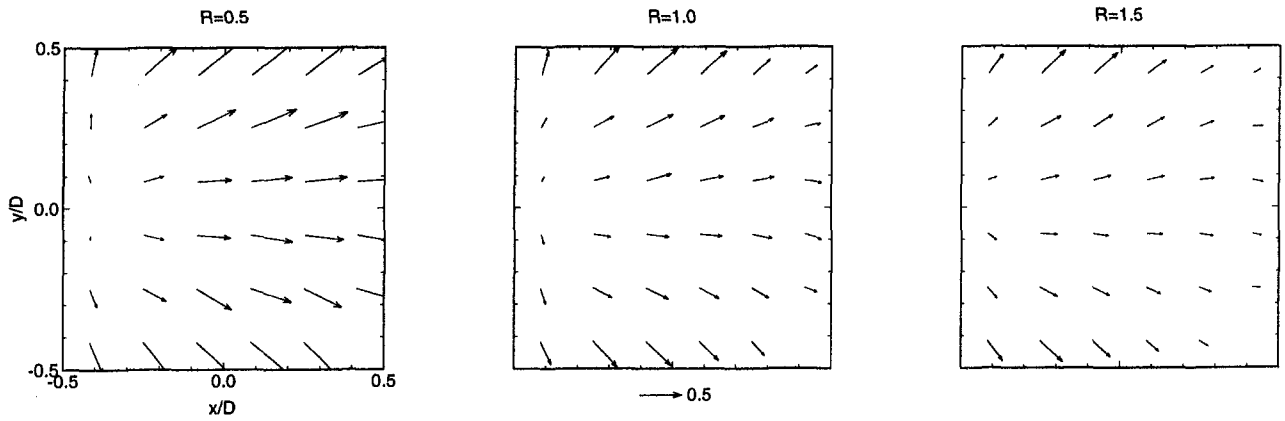

Fig. 6 Velocity in the plane of the jet exit ($\bar{V}/V_{jet}$); $z/D = 0.0$

The expected value of a general flow statistic s is then calculated by

$$\langle s \rangle = \frac{\sum_i^N s_i \frac{1}{|\bar{V}_i|}}{\sum_i^N \frac{1}{|\bar{V}_i|}}$$

where s_i is the contribution to the statistic s from the ith data point and $\bar{V}_i$ is the velocity for that same point.

The level of uncertainty in the LDV measurements was a function of all measured or sampled quantities, namely (1) the angles by which each probe was misaligned with respect to the tunnel coordinate system, (2) the position of the measurement volume, (3) the time count used by the LDV processor, and (4) other LDV system parameters. The last two items are considered to be highly accurate, as their contribution to the uncertainty in mean velocity is smaller than the contribution of the other measured quantities, by an order of magnitude. Table 1 lists the uncertainty in the measured quantities and the resultant uncertainty in the mean velocities and Reynolds stresses, as determined by the standardized method of Kline and McClintock (1953). The uncertainty in the flow quantities however, is highly dependent on the flow field, which is not known a priori; the values listed represent a conservative estimate. The standardized method yields relatively low values of uncertainty, but does not account for the turbulence-induced bias noted above. Although the bias is corrected here by inverse velocity weighting, the corrections are not complete and a significant level of uncertainty remains. In effect, there exists a level of uncertainty in the bias; therefore, the bias cannot be thoroughly eliminated. The third column of Table 1 lists more realistic estimates of uncertainty, which account for the bias.

Flow Visualization. Flow visualization was accomplished by transmitting the original laser beam through a cylindrical lens to generate a narrow, intense sheet of light. Jet air was mixed with smoke, while crossflow air remained unseeded. The light sheet was directed into the tunnel from above and oriented perpendicular to the direction of the crossflow. A S-VHS video camera operating at 30 frames/s was used to film the motion of the jet in yz-planes at various downstream positions. Although the resolution of the video camera was less than that of a print film, the advantage of recording a time trace of the jet motion proved to be useful.

The flow conditions investigated were the same as for the LDV measurements, with the addition of set of video frames corresponding to a jet Reynolds number of 900.

Computational Method

The experimental conditions described above were numerically simulated using a $k-\epsilon$ turbulence model and a three-dimensional MGFD solution technique (Nowak, 1991) with the following modifications: (1) a low-Re k model, and (2) a simplified algebraic length scale and a nonisotropic extension to the effective viscosity for near-wall turbulence.

Figure 4 shows the computational domain. Symmetric boundaries were imposed at $y/D = -1.5$ and $y/D = 1.5$. The boundary layer thickness was set to 2.0 diameters to match that of the experiment. Approximately 200,000 cells in a nonuniform rectangular grid were used to represent the flow field. Grid indepen-

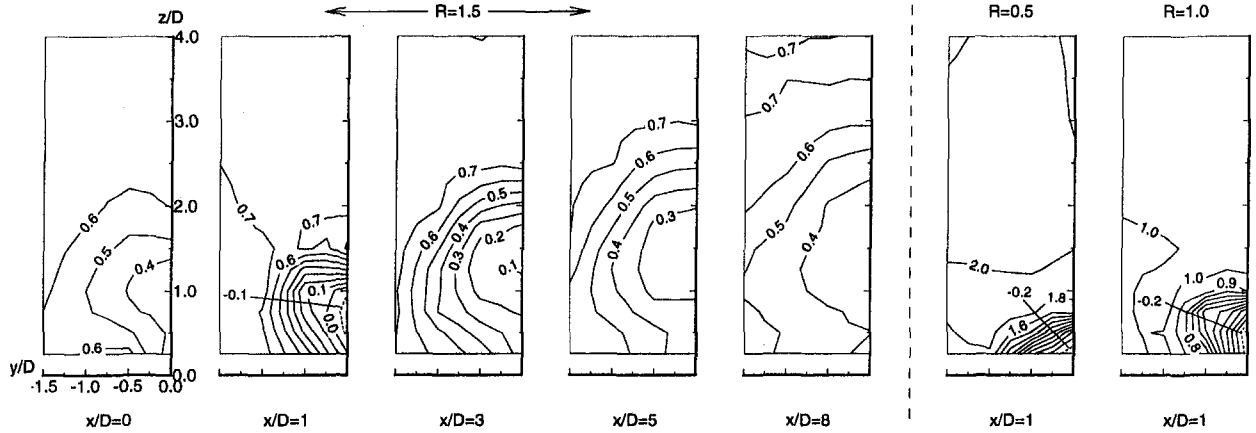

Fig. 7 Streamwise velocity in cross-tunnel planes (U/V_{jet})

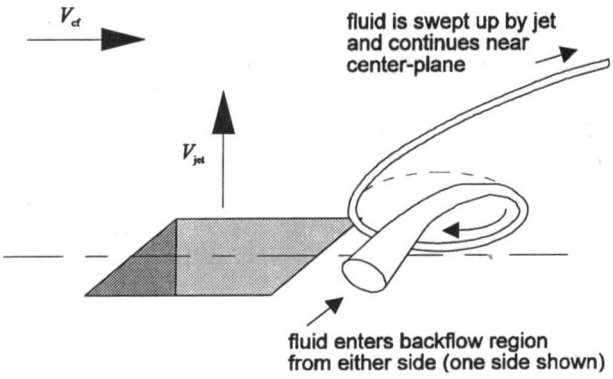

Fig. 8 Trajectory of fluid in the backflow region

dence was established by comparing a solution for the grid described above with that for a more refined grid. It was found that minimal differences existed between the solutions. The cell width in the plane of the jet exit was $D/12$, and the cell height next to the adiabatic wall was $D/48$. The jet entry length used was 5.0 diameters—1.0 diameter less than the experimental value. Uniform velocity and kinetic energy were imposed at the jet entrance.

Further details regarding the computational method are given by Zhou (1994) and Zhou et al. (1993), in which solutions were obtained for similar geometric configurations and slightly different boundary conditions.

Discussion of Results

Measurements were made at $x/D = -5$ in order to determine the crossflow characteristics. It was found that the free-stream turbulence kinetic energy k as defined by

$$k = 0.5(\overline{uu} + \overline{vv} + \overline{ww})$$

was approximately 2 percent of V_{cf} in the cases of $R = 1.5$ and $R = 1.0$, and 1.2 percent of V_{cf} in the case of $R = 0.5$. The boundary layer thickness was approximately $2.0D$, and the maximum turbulence kinetic energy in the boundary layer was on the order of 10 percent of V_{cf}. Turbulence was nonisotropic with the magnitude of u' being approximately twice that of either v' or w'.

Jet Exit Condition. The flow field at the level of the jet exit is strongly dependent on the jet-to-crossflow velocity ratio R. Figure 5 shows the normalized vertical velocity contours in this plane for the three cases. As expected, the relatively stronger jet ($R = 1.5$) is least affected by the crossflow while the weak jet ($R = 0.5$) is the most deflected. For $R = 0.5$, W/V_{jet} on the upstream side is less than 0.2, and on the downstream side rises above 1.7. The profile shape is wedgelike, with a steeper gradient on the upstream half. As the jet strength increases, the flow becomes slightly more uniform, but still exhibits the characteristics described above. The normalized velocity components in the jet exit plane are shown in the vector plot of Fig. 6. The streamwise deflection of the jet is made readily apparent, and appears to be most pronounced for $R = 0.5$. Lateral deflection also exists, and increases in magnitude with distance away from the jet centerline. The patterns of Figs. 5 and 6 should be perfectly symmetric about the centerline $y = 0$. From these and other measured results, the symmetry is found to be quite good.

Mean Velocity Field. A series of contours showing the streamwise component of velocity in several yz-planes is shown in Fig. 7. The first five plots correspond to the $R = 1.5$ case at positions of $x/D = \{0, 1, 3, 5, 8\}$. The two on the right are for the other velocity ratios at a position of $x/D = 1$. In the far field of the jet, a wake structure appears. The size of the wake—as defined by the velocity isoline $U = 90\%\ V_{cf}\ (U/V_{jet} = 0.6)$—increases between 3 and 8 diameters downstream. Fluid in this region accelerates from $0.1V_{jet}$ to over $0.3V_{jet}$ over this same distance. What differentiates this flow from a case with a higher velocity ratio (i.e., $R \gg 1.5$) is that there exists no local maximum in U/V_{jet}. Customarily, the location of the maximum is used to quantify the penetration of a jet; however, here this is inapplicable. What is observed in Fig. 7 are local *minima* in U/V_{jet}, which correspond more closely to a wake centerline than any form of jet centerline.

In the case of $R = 1.5$, a small zone of negative flow appears in the near region downstream of the jet, indicating the presence of three-dimensional separation. One must not equate this flow field to that of a two-dimensional jet by labeling this as recirculation, for the flow in this region probably travels the circular path only once. According to Andreopoulos and Rodi (1984), a streamline here follows a spiral path as it approaches the jet center-plane from either side as illustrated in Fig. 8. It then curves toward the floor, and follows a path upstream. As it rises to return to the beginning of the loop, it is swept upward into the crossflow by the jet. The backflow in the $R = 1.0$ case is localized much closer to the tunnel floor. This is due to the stronger deflection of the jet, which reduces the size of the low-pressure region. There is evidence of the same in the case of $R = 0.5$, but more resolved measurements would be necessary to comment further on the size and structure.

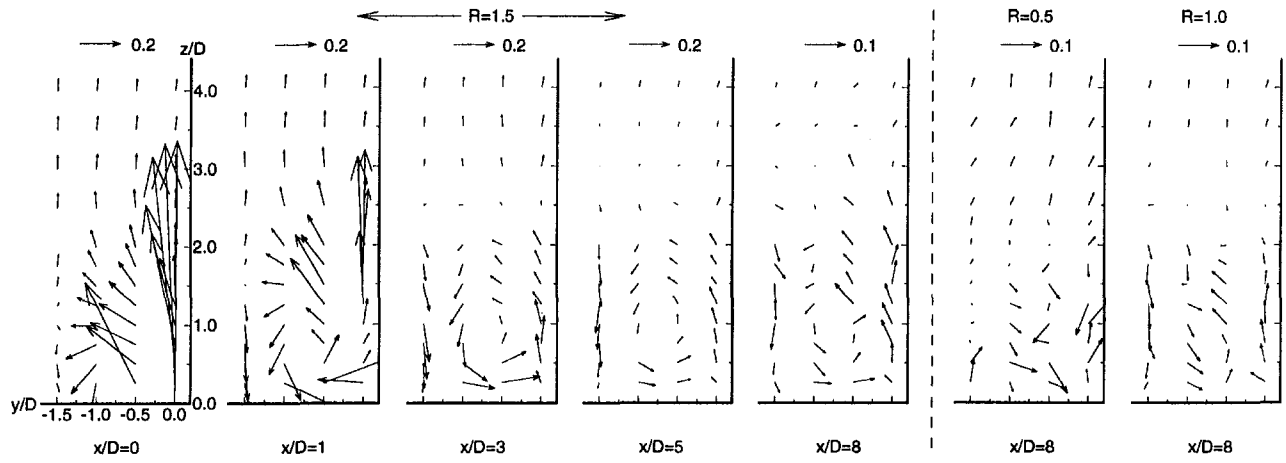

Fig. 9 Velocity normal to the mainstream velocity in cross-tunnel planes nondimensionalized by V_{jet}

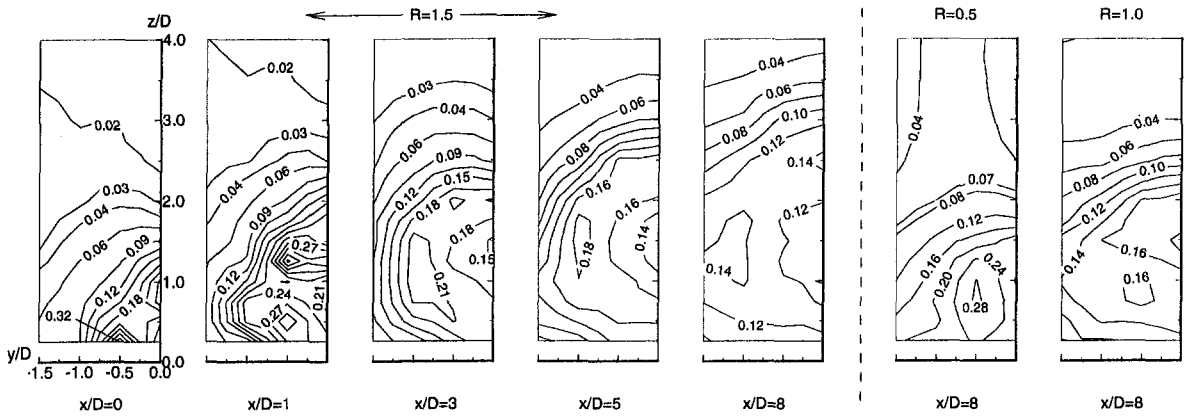

Fig. 10 Turbulence kinetic energy in cross-tunnel planes ($\sqrt{k}/V_{jet}$)

The three-dimensional nature of the flow field is illustrated by the vector plots in Fig. 9. The five plots on the left show the mean velocity components in the same yz-planes pictured in Fig. 7. The two plots on the right correspond to $R = 1.0$ and $R = 0.5$ at $x/D = 8$. At $x/D = 0$, the jet is seen to exit at a normalized velocity greater than unity, which is expected from the jet exit condition discussed earlier. A fairly strong lateral component of velocity at positions away from the center-plane shows how the crossflow bends around the jet. By $x/D = 1$, one half of the counterrotating vortex pair (CRVP) is apparent, its strength decreasing with downstream position. At $x/D = 8$, the vortex shape is still visible. In searching for an indication of the stability of the CRVP, at least between 0 and 8 diameters downstream, one must keep in mind that each measurement point was sampled for 30 to 90 seconds, and that variations in the vortex shape and position may occur within this time span. For the smaller velocity ratios, at $x/D = 8$, the CRVP appears to be weaker. In fact for $R = 0.5$, there seems to be no large-scale vortex structure this far downstream. Since the jet in this case does not penetrate the boundary layer, the turbulence in this region possibly acts to destroy the large-scale but weak vortex structure.

Turbulence Kinetic Energy. Contours of normalized turbulence kinetic energy, $\sqrt{k}/V_{jet}$, are shown for several yz-planes in Fig. 10. The layout of the plots is similar to that of Fig. 9. Up to $x/D = 1$ in the case of $R = 1.5$, turbulence levels near $z/D = 4.0$ are close to those measured in the free stream at $x/D = -5$. Nevertheless, the influence of the jet is considerable, as one can see by following the penetration of the contour line denoting 300 percent $\sqrt{k_{fs}}$, or $\sqrt{k}/V_{jet} = 0.04$. This turbulence level is higher than that of the undisturbed free-stream level, but still far from that seen at the jet exit. It is used here to determine the extent of the jet's penetration. By $x/D = 8$, the jet reaches a height of $3.8D$, which is deeper than one might note by examining contours of U/V_{jet} or vector plots in the yz-plane.

A local minimum of turbulence kinetic energy occurs along the jet center-plane, and approximately coincides with the minima in U/V_{jet} from Fig. 7. As one would expect in a wake, the turbulence level here decreases with position downstream, dropping from 0.15 to 0.10 between $x/D = 3$ and $x/D = 8$.

A peak in turbulence kinetic energy occurs at approximately $y/D = -1.0$ beyond 1 diameter downstream. A comparison of the $\sqrt{k}/V_{jet}$ contours with the $V-W$ vector plots of Fig. 9 shows that the peaks in $\sqrt{k}/V_{jet}$ occur close to the edge of the vortex. The shear generated at the edge of the vortex promotes considerable mixing in this region. Also, any instability or unsteadiness in the position of the vortex would appear as an increase in turbulence kinetic energy at its edge, because of the shear layer moving through a fixed measurement point.

Another local maximum first appears in the near-wake region, occurring 1.25 diameters above the tunnel floor at $x/D = 1$, where $\sqrt{k}/V_{jet}$ reaches 0.36. This region is one where the jet and crossflow directly interact and may be characterized by instability and significant shear, thus explaining the presence of high turbulence. This spot of maximum turbulence decays at downstream positions, but still persists and penetrates 2.5 diameters by $x/D = 8$.

Turbulence seems to spread well in the lateral direction. From $x/D = 0$ to $x/D = 3$, strong gradients in $\sqrt{k}$ with respect to y are evident, which suggests that turbulence has not yet spread to the plane of symmetry between jets. Downstream of this point, however, levels of higher turbulence do reach $y/D = -1.5$, which suggests that adjacent jets have merged.

The distribution of turbulence kinetic energy is similar for the $R = 1.0$ jet at $x/D = 8$; however, it differs for the case of $R = 0.5$. For this weak jet case, the turbulence levels in the plane of symmetry between jets are very close to those found upstream in the boundary layer. It would seem that the jets have not spread far beyond 1.0 diameter in the lateral direction, and that adjacent jets have therefore not merged. A second observation for the $R = 0.5$ jet is that the contour line denoting 300 percent $\sqrt{k_{fs}}$, or $\sqrt{k}/V_{jet} = 0.07$, rises only slightly above the $2.0D$ thick boundary layer, thus indicating that this jet interacts primarily with the turbulent boundary layer, where inviscid dynamics are less important than they would be in the free stream. Above $z/D = 3.0$, there is a noticeable spanwise variation in $\sqrt{k}/V_{jet}$. A final observation is that the spot of high turbulence

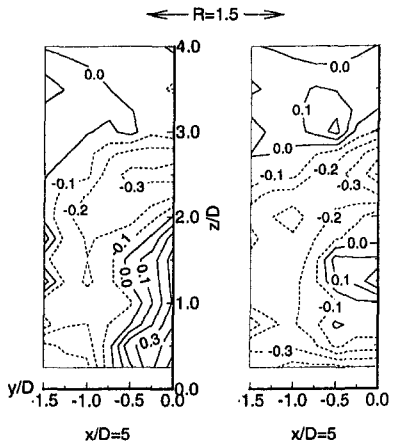

Fig. 11 Normal stress ratio in cross-tunnel planes: left: $(v' - u')/u'$; right: $(w' - u')/u'$

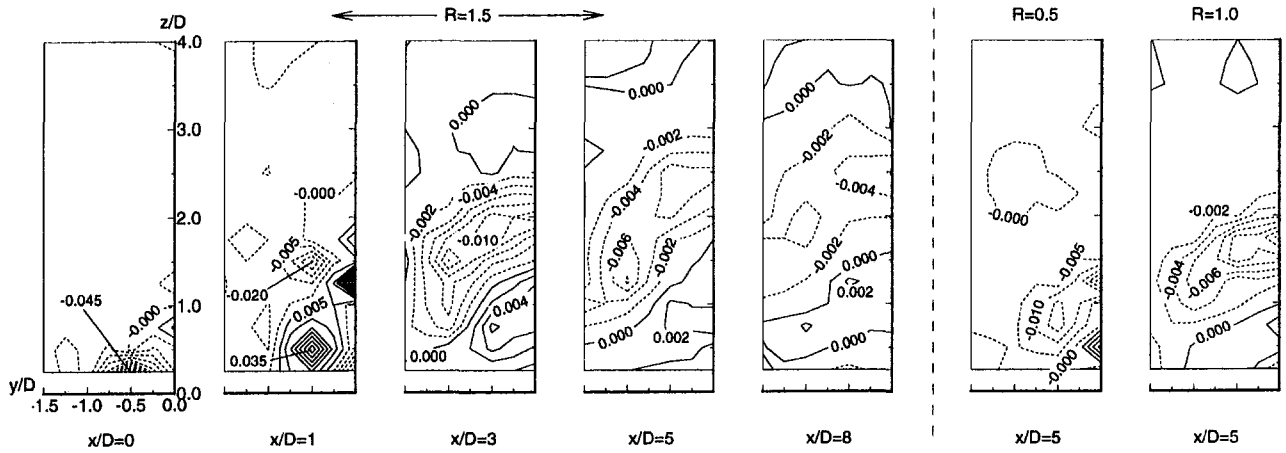

Fig. 12 Shear stress in cross-tunnel planes ($\overline{uw}/V_{jet}^2$)

kinetic energy occurs not in the jet center-plane, but at $y/D = -0.5$. It appears as early as $x/D = 1$ (not shown for $R = 0.5$) and decreases in intensity with position downstream. Interestingly, at $x/D = 8$ where the vortex structure is no longer distinct (see Fig. 9), the maximum still appears as a result of advective transport of turbulence from upstream positions.

Isotropy. An examination of turbulence kinetic energy provides valuable information about the turbulent nature of the flow; however, additional information is contained in the individual normal stress terms, which are not always equal. The numerical simulation assumes isotropic turbulence except near the wall, where a simplified algebraic turbulence model for near-wall nonisotropic turbulence is used. The effects of this assumption, however, are not entirely clear.

For the purpose of this discussion, only the case of $R = 1.5$ is considered. Figure 11 shows contour plots of two normal stress ratios, hereafter called the v' ratio and the w' ratio, defined as

$$\frac{v' - u'}{u'} \quad \text{and} \quad \frac{w' - u'}{u'}$$

respectively. Both plots correspond to the yz-plane at $x/D = 5$. A zero value of both ratios indicates that the flow is isotropic. In the wake region of the jet, the v' ratio is seen to rise to 0.5, and is representative of the flow at other downstream positions. This indicates that v' can exceed u' by 50 percent in the wake, where turbulence in the lateral direction is dominant. In the region of shear on the top side of the jet, the ratio drops to -0.3. In this region, the velocity gradient $\partial U/\partial z$ is dominant, and contributes to the production of u'. Here, v' is 30 percent lower than u', as expected.

Contours of the w' ratio are mostly negative, but rise above zero in a small region in the wake. A minimum value of -0.4 is found close to the floor, typical of near wall flow.

Shear Stresses. Shear stresses are often left unmeasured and unreported because of the lack of available tools. Three-component coincidence-mode laser-Doppler velocimetry, as used here, does allow for these measurements. The results are discussed below.

An Examination of $\overline{uw}$. Figure 12 shows a series of contours of the shear stress $\overline{uw}$ normalized by V_{jet}^2. The five plots on the left correspond to $R = 1.5$ at $x/D = \{0, 1, 3, 5, 8\}$, while the two on the right are for $R = 1.0$ and $R = 0.5$ at $x/D = 5$. First consider the case of $R = 1.5$. In the near-jet region of $x/D \leq 1$, there seems to be little large-scale organization in the flow. A refined measurement grid is needed to reveal more information here. At downstream positions, one observes that $\overline{uw}/V_{jet}^2$ reaches a negative peak far from the tunnel floor. The negative contours define a shape not unlike a crescent above the jet with the concave side facing downward. Negative values occur here since the crossflow far from the wall ($z/D \geq 1.5$) exhibits the characteristics of a boundary layer with positive $\partial U/\partial z$ and turbulence kinetic energy dropping from a high near $z/D = 2.0$ to its free-stream value farther away. Positive peaks of $\overline{uw}/V_{jet}^2$ appear on the lower bound of the jet, but are weaker in magnitude. Based on Fig. 7, $\partial U/\partial z$ is negative in this region.

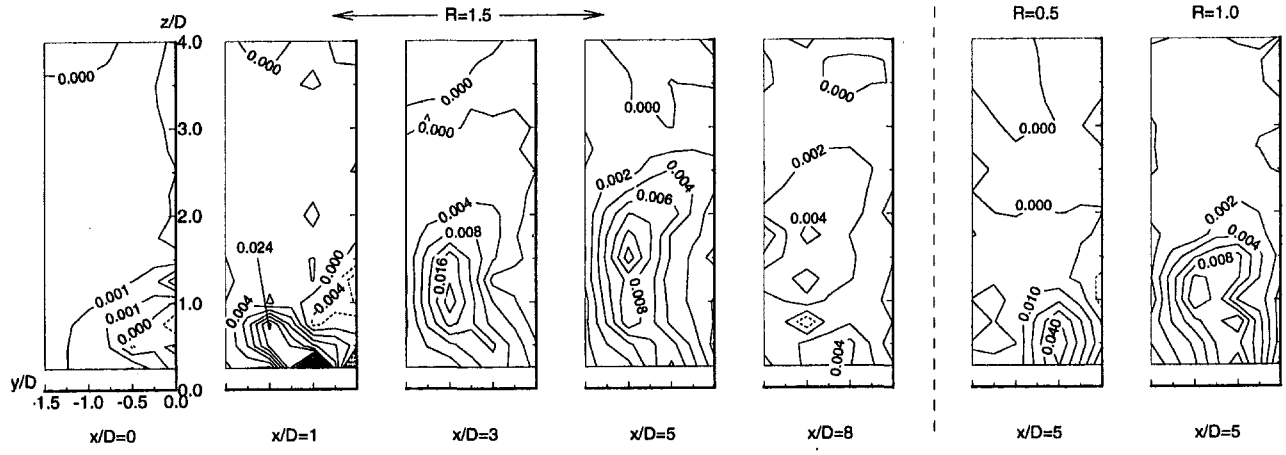

Fig. 13 Shear stress in cross-tunnel planes ($\overline{uv}/V_{jet}^2$)

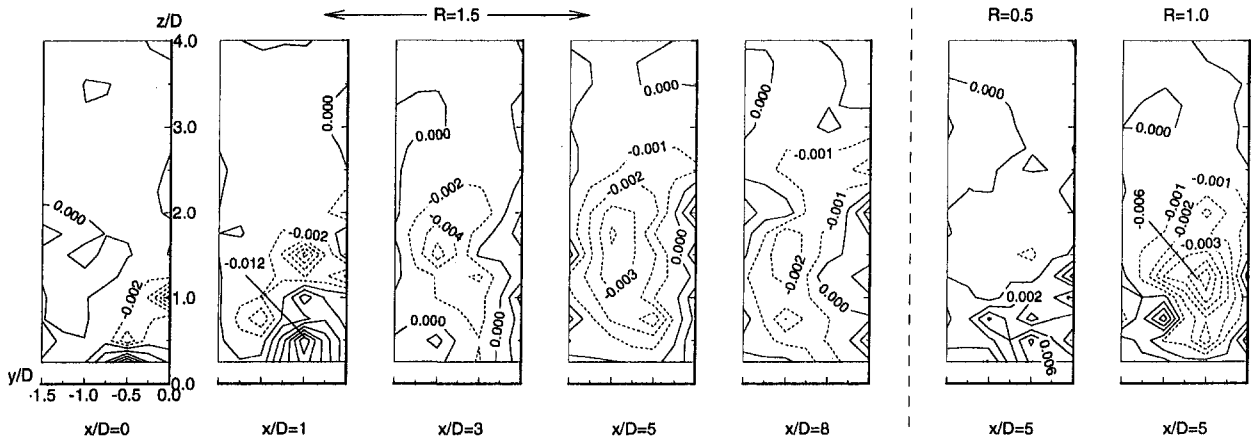

Fig. 14 Shear stress in cross-tunnel planes ($\overline{vw}/V_{jet}^2$)

The weaker jet cases show the same trends as above. The crescent shape is evident, and the regions of negative and positive $\overline{uw}$ are both observed. In the case of $R = 0.5$, this shear stress is virtually zero above $z/D = 2.0$, confirming that the structures of the weak jet do not penetrate through the boundary layer.

An Examination of $\overline{uv}$. Contours of $\overline{uv}/V_{jet}^2$ are shown in Fig. 13 for various downstream positions. The layout of these plots is the same as for Fig. 12. Some organization of this shear stress appears to exist by $x/D = 1$, and is clearly apparent at all subsequent positions downstream. Again, the contours form a crescent-shaped region; however, here it is located beside the jet, the plotted values are positive, and the concave side faces inward.

Andreopoulos and Rodi (1984) state that the shear stress $\overline{uv}$ is an indication of lateral turbulent mixing. One should then expect to see a correlation between $\overline{uv}$ and the side bounds of the jet. The reason for this is rooted in the wall jet, which expands in the axial direction. The shear layer circumscribes the jet, and the spread of turbulence is primarily normal to this. Therefore, the spread of turbulence in a deflected jet should occur radially from the jet centerline, with *lateral* spread occurring near the left and right edges of the jet. In Fig. 13, indication of this is apparent where the contours define the crescent shape noted above.

The $\overline{uv}/V_{jet}^2$ contours for the two weaker jet cases outline less of a crescent shape at $x/D = 5$, but still define a vertically elongated positive peak to the side of the jet. For $R = 0.5$, there is minimal variation in this shear stress above $z/D = 1.5$, suggesting again that the jet has not penetrated the boundary layer.

As a check of the experimental technique and the symmetry of the jet injection, measured values of $\overline{uv}/V_{jet}^2$ in the jet center-plane, as well as in the between-jet plane, should by symmetry drop to zero. One can see in Fig. 13 that this is generally the case, although slight variations in $\overline{uv}/V_{jet}^2$ do occur at these boundaries. The exception is at $x/D = 1$ for $R = 1.5$, where $\overline{uv}/V_{jet}^2$ drops as low as -0.008. This is likely to be a fault of the experimental technique, which decreases in accuracy with elevated levels of turbulence and unsteadiness in the mean flow. At this position $\sqrt{k}/V_{jet} = 0.32$.

An Examination of $\overline{vw}$. Contour plots showing the measured values of $\overline{vw}/V_{jet}^2$ are displayed in Fig. 14 and are laid out as in Fig. 12. In the case of $R = 1.5$, in particular for $x/D \geq 3$, a region of primarily negative shear stress rises in magnitude to a peak at approximately $y/D = -1.0$. Values of $\overline{vw}/V_{jet}^2$ are generally somewhat less that the other shear stresses at the same locations. This is partly due to the magnitude of the terms contributing to the production of this stress. Andreopoulos and Rodi (1984) state that the shear stress $\overline{vw}$ acts to damp the secondary-vortex motion, and that it is the gradients $\partial V/\partial z$ and $\partial W/\partial y$ that generate this shear stress. These gradients, however, are weaker than those involved in the production of $\overline{uw}$ and $\overline{uv}$, which are $\partial U/\partial z$ and $\partial U/\partial y$, respectively.

The contour plot for the case of $R = 1.0$ shows that the values of $\overline{vw}/V_{jet}^2$ are again primarily negative at $x/D = 5$ with a peak in magnitude occurring closer to the jet center-plane at $y/D = -0.5$. The contours of $\overline{vw}/V_{jet}^2$ for the weakest jet do not seem to capture any large-scale trends in this shear stress. For this case, the resolution of the measurement field is not sufficiently refined, given that the structures of the jet lie much closer to the tunnel floor.

Flow Visualization. General features observed in the flow visualization experiment are described below. Due to limited space, only one sequence of still images is shown in this paper.

It was found that the penetration was deepest and lateral spread widest for the $R = 1.5$ jets as expected. By $x/D = 8$, individual jets were nearly indistinguishable. The case of $R = 1.0$ was similar, but jets did not show signs of merging until $x/D = 5$. Individual jets could still be recognized at $x/D = 8$. As for the $R = 0.5$ jets, vertical penetration only slightly exceeded 2.0 diameters. Nowhere were the jets seen to merge except possibly close to the floor at $x/D = 8$.

A sequence of five images is presented in Fig. 15. These are for the case of $R = 0.5$ and $Re_{jet} = 900$. The position of the cutting plane is $x/D = 0.5$—the downstream edge of the jet exit. The CRVP appears in these images, but with an interesting

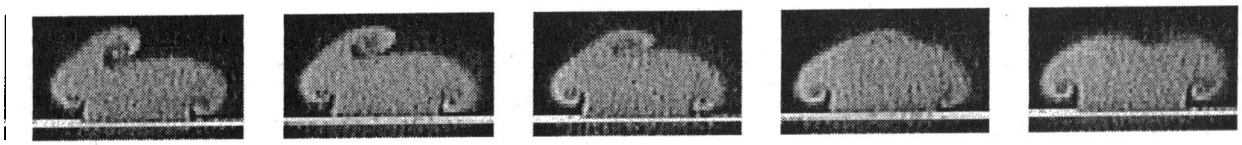

Fig. 15 Image sequence of $R = 0.5$ jet at $x/D = 0.5$, time increasing by 1/30 s for each frame from left to right

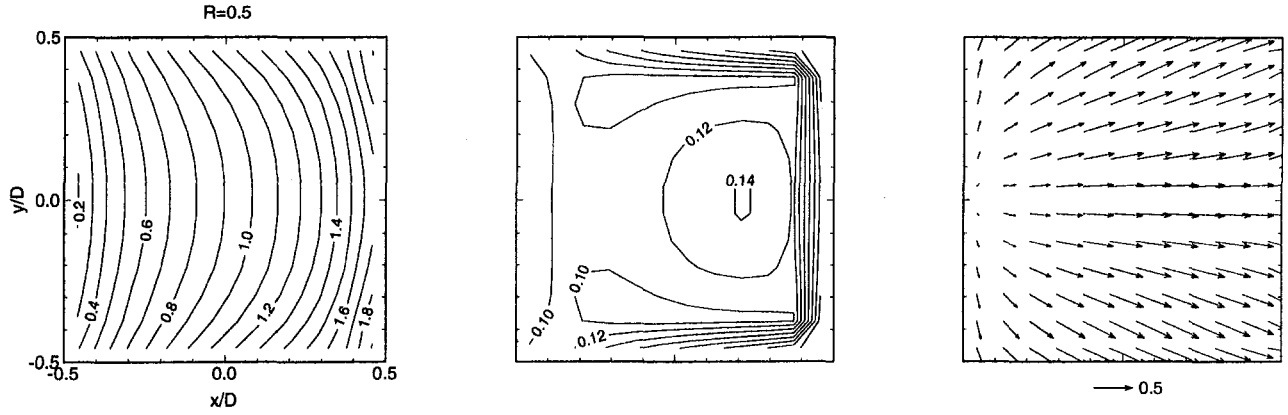

Fig. 16 Jet exit condition from numerical simulation of $R = 0.5$ jet; left: (W/V_{jet}); middle: $(\sqrt{k}/V_{jet})$; right: $(\bar{V}/V_{jet})$; $z/D = 0.0$

variation. On the left side of the jet, a secondary pair of vortices is visible. This structure disappears by the fourth frame, at which point the jet has a standard appearance. In the last frame, the jet seems to split in half, a trend that persists for five more frames (not shown). After this, a secondary pair of vortices materializes on the right side of the jet. The process continues indefinitely. For the cases of $Re_{jet} = 4700$, there was evidence of the same, but with greater frame-to-frame variation. This difference may be attributed to (1) higher turbulence levels in the jet, or (2) a smaller characteristic time scale caused by a higher convection speed.

These interesting structures, which endure for several frames, are too large to be considered turbulent fluctuations. Their time scale is on the order of 5 frames or 0.167 s. In comparison, the characteristic turbulent time scale of the system is approximated by dividing the jet exit diameter by the free-stream convection speed of 2.2 m/s, and is found to be 0.006 s—a value approximately 30 times smaller than the time scale of the structures. Therefore, what is observed is best described as large-scale unsteady flow structures, possibly Görtler vortices associated with flow curvature.

Computational Results. Simulations were performed for the three velocity ratios. In the results below, only the two extremes, $R = 0.5$ and $R = 1.5$, are considered.

The jet exit condition for $R = 0.5$ is shown in Fig. 16. Plotted contours are for the normalized vertical velocity W/V_{jet} and for the turbulence kinetic energy $\sqrt{k}/V_{jet}$ in the plane of the jet exit. The vector plot shows the velocities in the exit plane. The trends in mean velocity are similar to those seen in Figs. 5 and 6. The jet is deflected in the crossflow direction, especially near the upstream side of the exit. Lateral deflection is also apparent. Although the velocities at the level of the jet exit approximate the experimental condition, the turbulence does not. Computed turbulence kinetic energy is nearly uniform across the exit, and moderately elevated at the walls. Experimental values are generally higher, especially near the upstream third of the exit. This difference is certainly a function of the jet inlet boundary condition where uniform velocity and uniform turbulence kinetic energy are imposed in the computations. Experimentally, quiescent fluid in the plenum accelerates around the sharp edges of the inlet into the jet channel, so that turbulence kinetic energy is already nonuniform. This emphasizes the importance of modeling the jet channel in such simulations.

Profiles of streamwise velocity at $x/D = \{0, 1, 3, 5, 8\}$ are shown in Fig. 17. Computational results are compared with experimental data for $R = 0.5$ and $R = 1.5$. In all cases, the streamwise velocity in the jet wake is overpredicted. This is particularly noticeable at $x/D = 3$. The simulation does capture a region of backflow at $x/D = 1$, which is smaller and closer to the floor than that observed in the measurements.

Figure 18 shows the lateral component of velocity at $y/D = -0.5$, a plane that crosses the structures of the CRVP. Here, the agreement is much better.

Figure 19 shows vertical velocity profiles at $y/D = -1.0$. These plots show the downflow that exists on the outer edge of the CRVP. In terms of general trends, the simulations are in fairly good agreement with the experiments. The magnitude of the downflow, however, is underpredicted.

Profiles of turbulence kinetic energy in the jet center-plane are shown in Fig. 20. For large x/D, the local minimum in

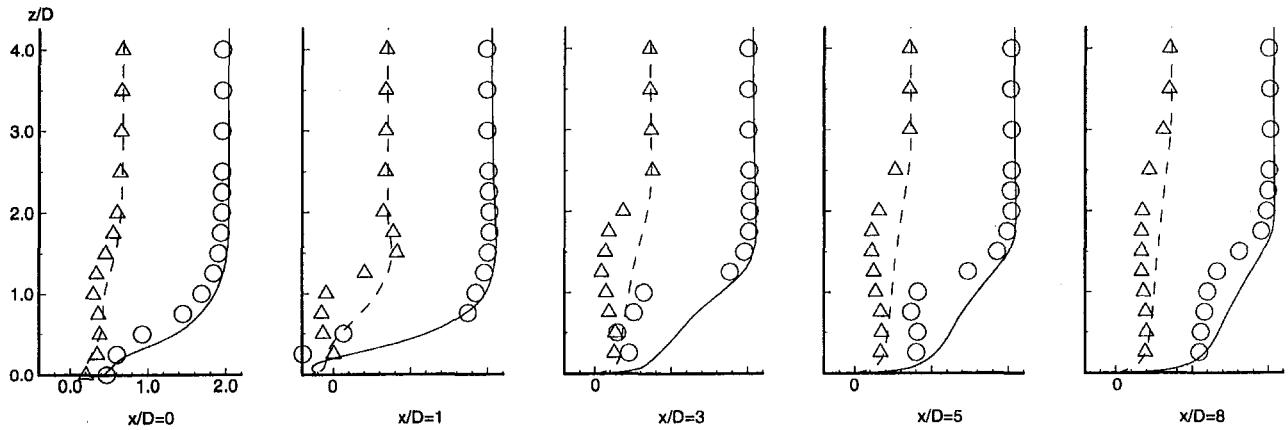

Fig. 17 Comparison of streamwise velocity (U/V_{jet}) for $y/D = 0$; measured: $\Delta R = 1.5$, $\circ$ $R = 0.5$; computed: – – – $R = 1.5$, —— $R = 0.5$

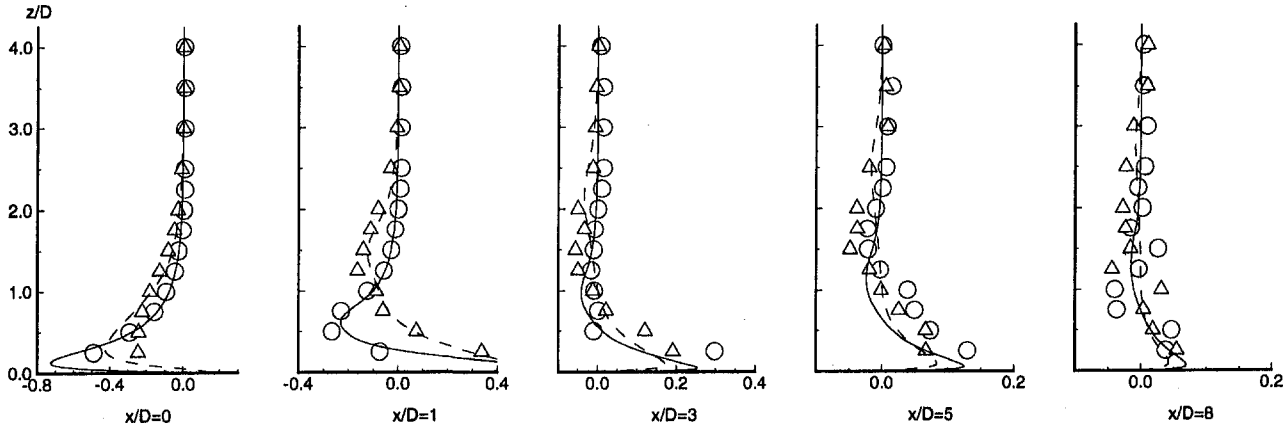

Fig. 18 Comparison of cross-tunnel velocity (V/V_{jet}) for $y/D = -0.5$; measured: △ $R = 1.5$, ○ $R = 0.5$; computed: – – – $R = 1.5$, —— $R = 0.5$

$\sqrt{k}/V_{jet}$ that was measured in the wake region of the jet is not captured by the simulation, which shows a smooth distribution of turbulence kinetic energy, which rises to a peak away from the floor. The location of this peak decreases in magnitude and penetrates deeper with position downstream. Although the profile shape differs from that of the experiments, the characteristic turbulence levels—e.g., $\sqrt{k_{max}}/V_{jet}$—do not. In the near field, agreement varies. The weak jet simulation represents the flow well at $x/D = 0$, but overpredicts values of $\sqrt{k}/V_{jet}$ at $x/D = 1$. The strong jet simulation underpredicts turbulence kinetic energy at $x/D = 0$.

Finally, a comparison of the shear stress $\overline{uw}$ is made. Figure 21 shows profiles of this stress in the jet center-plane. Dramatic differences occur between simulation and experiment, especially at $x/D = 3$ and $x/D = 5$, where the extent of the region of negative shear stress is overpredicted. In the near field, the largest difference occurs for the weak jet at $x/D = 1$, where computed $\overline{uw}$ drops below -0.20. At this location, the velocity gradient $\partial U/\partial z$ is overpredicted (see Fig. 17), as is k (see Fig. 20), which is used in the calculation of eddy viscosity. Andreopoulos and Rodi state that eddy viscosity models should in principle be able to represent the shear stress distribution in flow where $\overline{uw}$ and $\partial U/\partial z$ are generally of opposite sign, but that no simple model can be expected to work well. One case when the model fails is when streamlines converge/diverge and the influence of the gradient $\partial V/\partial y$ becomes significant. This certainly occurs in the near field where free-stream fluid accelerates around the jet.

It is evident from the comparison given above that the numerical simulations were unable to predict all velocities and flow stresses accurately throughout the computational domain. The solution technique (Nowak, 1991) is considered to be sound and dependable, and is used extensively by the CFD group at the author's institution. Furthermore, grid independence was established as the final solutions did not change significantly from the results of a coarser grid structure. The discrepancies, therefore, are most probably attributed to the $k-\epsilon$ turbulence model and the near-wall treatment of turbulence. These methods were devised with two-dimensional cases in mind, and work well for simple flows; however, the flow about a row of jets in a crossflow is very three dimensional, and presents a severe test to the turbulence models used. It is clear that further refinements are necessary.

Conclusions

Three-dimensional coincident mode LDV, flow visualization, and $k-\epsilon$ numerical simulations have been used to investigate the complex flow created by a row of six square jets blowing at 90 deg into a crossflow. Jet-to-crossflow velocity ratios between 0.5 and 1.5 have been considered, to cover a range pertinent to many film cooling applications.

The vertical velocity at the jet exit plane is nonuniform, particularly at low values of R, as expected. Present numerical calculations, which include the entrance duct, represent the observed mean velocities reasonably well, but a computational domain that includes the entrance to the duct, and some part of the plenum, is necessary to predict the mean velocity and kinetic energy fields at the exit plane with better accuracy.

The counterrotating vortex pair, characteristic of most jets injected into a crossflow, is observed in the present results for

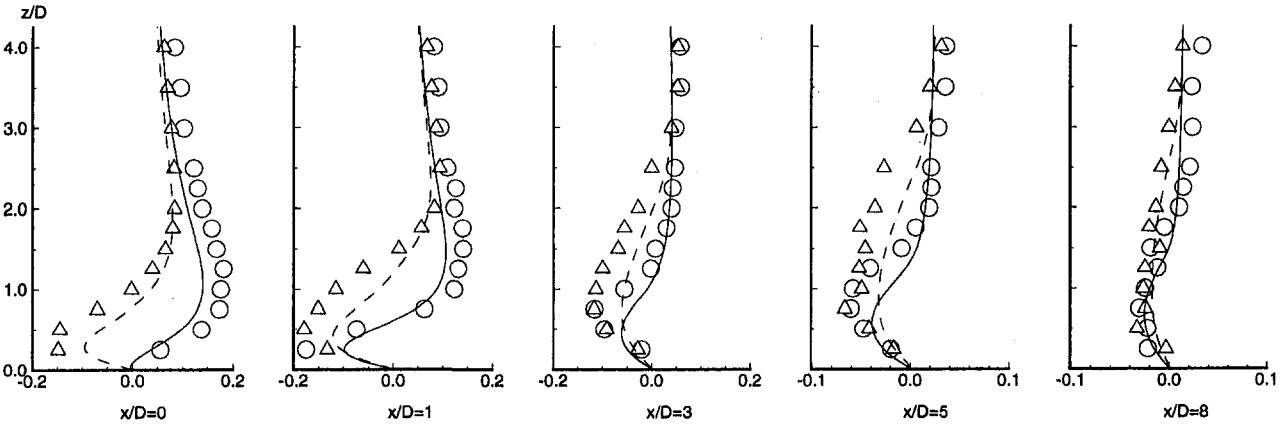

Fig. 19 Comparison of vertical velocity (W/V_{jet}) for $y/D = -1.0$; measured: △ $R = 1.5$, ○ $R = 0.5$; computed: – – – $R = 1.5$, —— $R = 0.5$

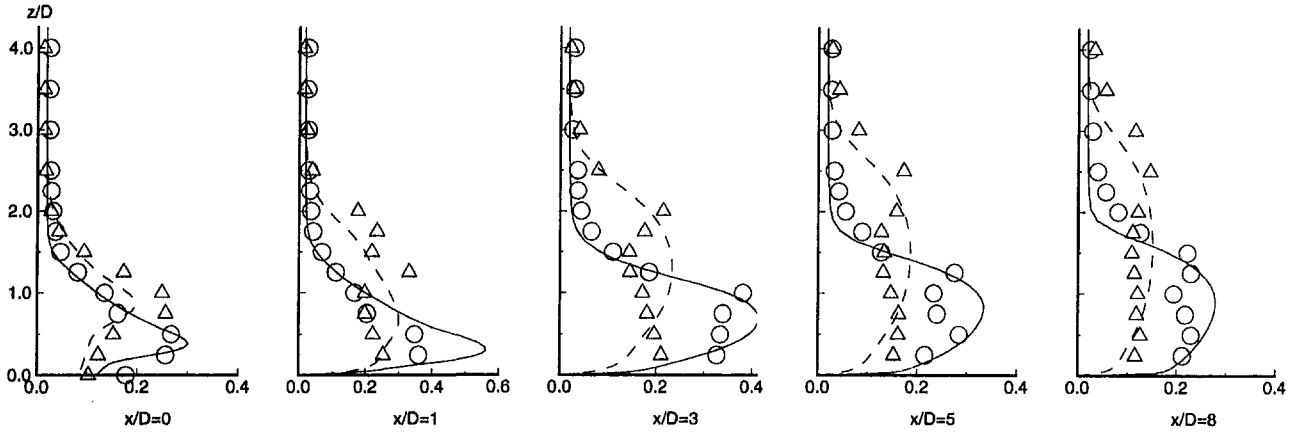

Fig. 20 Comparison of turbulence kinetic energy ($\sqrt{k}/V_{jet}$) for $y/D = 0$; measured: △ $R = 1.5$, ○ $R = 0.5$; computed: – – – $R = 1.5$, —— $R = 0.5$

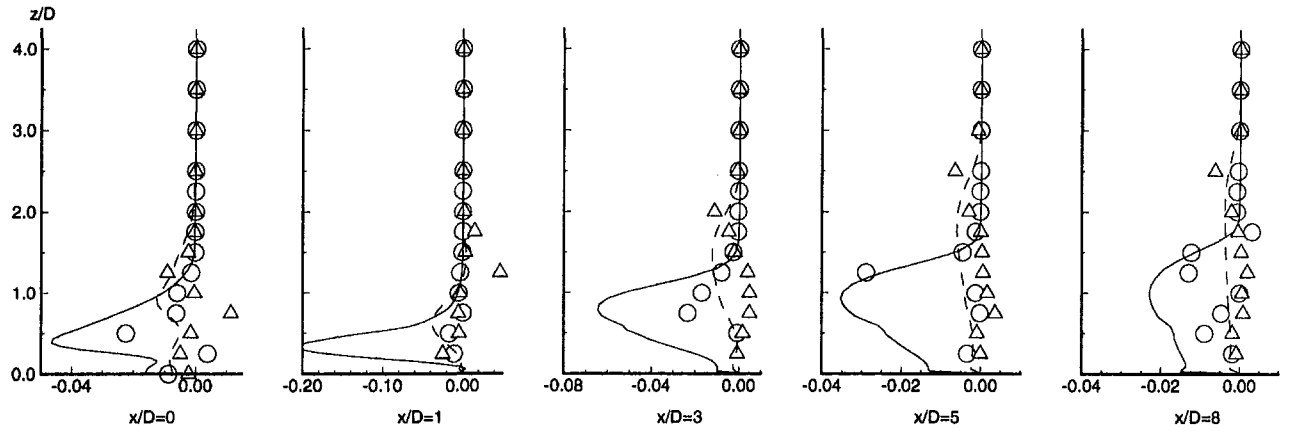

Fig. 21 Comparison of shear stress ($\overline{uw}/V_{jet}^2$) for $y/D = 0$; measured: △ $R = 1.5$, ○ $R = 0.5$; computed: – – – $R = 1.5$, —— $R = 0.5$

$R = 1.5$ and $R = 1.0$, but is less distinct for $R = 0.5$ where the jet is too weak to penetrate through the turbulent boundary layer formed upstream of injection. Adjacent jets appear to interact only for $R = 1.5$ and $R = 1.0$. When $R = 0.5$, the jet structures are eroded by the boundary layer before this interaction is possible. Small backflow regions are observed just downstream of the jet in all cases; these are present in the numerical results as well.

The turbulence is highly nonisotropic near the injection point, as expected. In the "wake" region downstream of injection, the turbulence differs strongly from that of an undisturbed boundary layer. Computational results using the $k-\epsilon$ method do not represent this isotropy, and are "tuned" to predict simpler cases such as boundary layer flows. Shear stresses are therefore not well predicted by the computations, particularly for the strong jet ($R = 1.5$) near the jet exit.

Calculations predict the main features of the observed flow field but are inaccurate in the center-plane close to the injection hole. Agreement between computed and measured results is far better in a streamwise plane through the edge of the jet ($y/D = 0.5$) than in the center-plane ($y/D = 0.0$). Inability to predict center-plane values accurately may not be critical if spanwise averages of film cooling effectiveness, for example, are computed.

An unsteady, low-frequency, asymmetric vortex pair observed by the flow visualization, may represent instability arising from streamline curvature. It is not captured in any way by the calculations, nor explicitly by the measurements.

Acknowledgments

This work was supported by the Natural Sciences and Engineering Research Council of Canada and by Pratt and Whitney Canada.

References

Andreopoulos, J., 1985, "On the Structure of Jets in a Cross Flow," *Journal of Fluid Mechanics,* Vol. 138, pp. 93–127.

Andreopoulos, J., and Rodi, W., 1984, "Experimental Investigation of Jets in a Crossflow," *Journal of Fluid Mechanics,* Vol. 138, pp. 93–127.

Beeck, A., Fottner, L., Benz, E., and Wittig, S., 1992, "The Aerodynamic Effect of Coolant Ejection in the Leading Edge Region of a Film-Cooled Turbine Blade," *Heat Transfer and Cooling in Gas Turbines,* AGARD-CP-527, Paper No. 35.

Benz, E., Wittig, S., Beeck, A., and Fottner, L., 1993, "Analysis of Cooling Jets Near the Leading Edge of Turbine Blades," *Computational and Experimental Assessment of Jets in Cross Flow,* AGARD-CP-534, Paper No. 37.

Demuren, A. O., 1993, "Characteristics of Three-Dimensional Turbulent Jets in Crossflow," *International Journal of Engineering Science,* Vol. 31, No. 6, pp. 899–913.

Edwards, R. V., ed., 1987, "Report of the Special Panel on Statistical Particle Bias Problems in Laser Anemometry," ASME *Journal of Fluids Engineering,* Vol. 109, pp. 89–93.

Foucault, E., Deniboire, P., and Bousgarbiès, J.-L., 1992, "Etude Experimentale du Transfert de Chaleur Près d'une Paroi Plane Chauffée en Présence d'Injections Multiples (Ecoulement Subsonique)," *Heat Transfer and Cooling in Gas Turbines,* AGARD-CP-527, Paper No. 4.

Fric, T. F., and Roshko, A., 1989, "Structure in the Near Field of the Transverse Jet," *Proc. 7th Symposium of Turbulent Shear Flows,* pp. 6.4.1–6.4.6.

Holdeman, J. D., and Walker, R. E., 1977, "Mixing of a Row of Jets With a Confined Crossflow," *AIAA Journal,* Vol. 15, pp. 243–249.

Isaac, K. M., and Jakubowski, A. K., 1985, "Experimental Study of the Interaction of Multiple Jets in a Crossflow," *AIAA Journal,* Vol. 23, No. 11, pp. 1679–1683.

Kadotani, K., and Goldstein, R. J., 1979, "On the Nature of Jets Entering a Turbulent Flow," ASME *Journal of Engineering for Power,* Vol. 101, pp. 459–465.

Khan, Z. A., McGuirk, J. J., and Whitelaw, J. H., 1982, "A Row of Jets in Crossflow," *Fluid Dynamics of Jets With Application to V/STOL,* AGARD-CP-308, Paper No. 10.

Kim, S.-W., and Benson, T. J., 1993, "Fluid Flow of a Row of Jets in Crossflow—A Numerical Study," *AIAA Journal,* Vol. 31, No. 5, pp. 806–811.

Kline, S. J., and McClintock, F. A., 1953, "Describing Uncertainties in Single-Sample Experiments," *Mechanical Engineering,* Jan., pp. 3–8.

McLaughlin, D. K., and Tiederman, W. G., 1973, "Biasing Correction for Individual Realization of Laser Anemometer Measurements in Turbulent Flows," *Physics of Fluids,* Vol. 16, pp. 2082–2088.

Nowak, P., 1991, "3-D Segmented Multi-Grid Computing Code," Technical Report, Department of Mechanical Engineering, University of British Columbia, Vancouver, Canada.

Peña, F. López, and Arts, T., 1992, "On the Development of a Film Cooling Layer," *Heat Transfer and Cooling in Gas Turbines,* AGARD-CP-527, Paper No. 36.

Perry, A. E., Kelso, R. M., and Lim, T. T., 1993, "Topological Structure of a Jet in a Cross Flow," *Computational and Experimental Assessment of Jets in Cross Flow,* AGARD-CP-534, Paper No. 12.

Sterland, P. R., and Hollingsworth, M. A., 1975, "An Experimental Study of Multiple Jets Directed Normally to a Cross-Flow," *Journal of Mechanical Engineering Science,* Vol. 17, No. 3, pp. 117–124.

Sugiyama, Y., and Usami, Y., 1979, "Experiments on the Flow in and Around Jets Directed Normal to a Crossflow," *Bulletin JSME,* Vol. 22, pp. 1736–1795.

Zhou, J.-M., Salcudean, M., and Gartshore, I., 1993, "Prediction of Film Cooling by Discrete-Hole Injection," ASME Paper No. 93-GT-75.

Zhou, J.-M., 1994, "A Computational and Experimental Investigation of Gas Turbine Blade Film Cooling," Ph.D. Thesis, University of British Columbia, Vancouver, Canada.

Effect of Velocity and Temperature Distribution at the Hole Exit on Film Cooling of Turbine Blades

V. K. Garg
AYT Corporation.

R. E. Gaugler
Turbine Branch,
Turbomachinery & Propulsion
Systems Division.

NASA Lewis Research Center,
Mail Stop 5-11,
Cleveland, OH 44135

An existing three-dimensional Navier–Stokes code (Arnone et al., 1991), modified to include film cooling considerations (Garg and Gaugler, 1994), has been used to study the effect of coolant velocity and temperature distribution at the hole exit on the heat transfer coefficient on three film-cooled turbine blades, namely, the C3X vane, the VKI rotor, and the ACE rotor. Results are also compared with the experimental data for all the blades. Moreover, Mayle's transition criterion (1991), Forest's model for augmentation of leading edge heat transfer due to free-stream turbulence (1977), and Crawford's model for augmentation of eddy viscosity due to film cooling (Crawford et al., 1980) are used. Use of Mayle's and Forest's models is relevant only for the ACE rotor due to the absence of showerhead cooling on this rotor. It is found that, in some cases, the effect of distribution of coolant velocity and temperature at the hole exit can be as much as 60 percent on the heat transfer coefficient at the blade suction surface, and 50 percent at the pressure surface. Also, different effects are observed on the pressure and suction surface depending upon the blade as well as upon the hole shape, conical or cylindrical.

1 Introduction

There is a growing tendency these days to use higher and higher temperatures at the inlet to a turbine since it yields higher thermal efficiency. Modern gas turbine engines are designed to operate at inlet temperatures of 1800–2000 K, which are far beyond the allowable metal temperatures. Thus, to maintain acceptable life and safety standards, the structural elements need to be protected against the severe thermal loads. This calls for an efficient cooling system. One such cooling technique currently used for high-temperature turbines is film cooling. In this technique, cooler air is injected into the high-temperature boundary layer on the blade surface. Since the cooler air is bled directly from the compressor before it passes through the combustion chamber, it represents a loss in the total power output. The designer's goal is therefore to minimize the coolant necessary to insure adequate turbine life.

To this end, considerable effort has been devoted to understanding the coolant film behavior and its interaction with the mainstream flow. The film cooling performance is influenced by the wall curvature, three-dimensional external flow structure, free-stream turbulence, compressibility, flow unsteadiness, the hole size, shape and location, and the angle of injection. Many studies on film cooling have been confined to simple geometries, for example, two-dimensional flat and curved plates in steady, incompressible flow. A survey of work up to 1971 has been provided by Goldstein (1971). While several further studies in this field have been summarized by Garg and Gaugler (1993, 1994, 1996), we will discuss some relevant ones here from the point of view of the present study.

Bergeles et al. (1980) devised a finite-difference code with a semi-elliptic treatment of the flow field in the neighborhood of the injection holes. The comparison of predicted results with experimental data on a flat plate showed poor agreement in the vicinity of the hole partly due to the assumption of a uniform coolant velocity at the hole exit. Schönung and Rodi (1987) presented a two-dimensional boundary layer model with a modification for three-dimensional elliptic flow for simulating the effects of film cooling by a single row of holes. The region near the injection was leapt over and new profiles were prescribed at a certain distance behind the blowing region. Later, Haas et al. (1992) extended Schönung and Rodi's (1987) model to account for density differences between the hot gas and the injected coolant gas. However, both the models did not account for the effects of curvature and multiple rows of holes. Tafti and Yavuzkurt (1990) developed a two-dimensional injection model for use with a two-dimensional low-Reynolds-number $k-\epsilon$ model boundary layer code for film-cooling applications. They specified a uniform coolant temperature but nonuniform velocity profile at the hole exit. Dibelius et al. (1990) developed an elliptic procedure near the injection area but a partially parabolic procedure far downstream for film cooling on a flat plate. They prescribed a uniform coolant velocity but slightly nonuniform coolant temperature at the hole exit.

Vogel (1991) described a three-dimensional Navier–Stokes code for film-cooled gas turbine blades that couples the flow problem over the blade with the three-dimensional heat conduction problem within the blade. Using a uniform coolant velocity at the hole exit, Vogel compared the heat transfer coefficients with experimental data for injection on a flat plate. He could not get reliable results on a turbine blade due to the computer storage limitations that did not allow more than four to six mesh cells within the hole opening on the blade surface. Benz and Wittig (1992) analyzed the elliptic interaction of film-cooling air with the main flow by simultaneously computing the coolant and main flows for film cooling at the leading edge of a turbine blade. They prescribed a uniform coolant flow at entry to the injection pipe, and found a nonuniform velocity profile at the hole exit. They did not provide any information about the temperature field. Amer et al. (1992) compared two forms each of the $k-\epsilon$ and $k-\omega$ family of turbulence models for film cooling,

Contributed by the International Gas Turbine Institute and presented at the 40th International Gas Turbine and Aeroengine Congress and Exhibition, Houston, Texas, June 5–8, 1995. Manuscript received by the International Gas Turbine Institute February 4, 1995. Paper No. 95-GT-2. Associate Technical Editor: C. J. Russo.

and found all of them to be inappropriate. Realizing the importance of coolant distribution at the hole exit, they tried a linear, a parabolic, and the $\frac{1}{7}$th power-law velocity profile for the coolant at the hole exit. Finding only small differences due to the parabolic and power-law profiles, they provided most results using the latter profile.

Dorney and Davis (1993) analyzed the film-cooling effectiveness from one and two rows of holes on a turbine vane, using Rai's (1989) numerical technique. They carried out both two- and three-dimensional simulations, but represented each hole by just two grid points, and specified uniform velocity and temperature of the coolant at the hole exit. Choi (1993) developed a multizone code for film cooling with a fine mesh near the coolant hole and injection pipe overlapped on the global coarse grid. He specified uniform conditions for the coolant at entry to the injection pipe but provided no details for the coolant profiles at the hole exit. Leylek and Zerkle (1994) analyzed the coupled problem of flow in the plenum, film-hole, and crossstream region for film cooling on a flat plate using the $k-\epsilon$ model of turbulence in a three-dimensional Navier–Stokes code. They found the flow within the film-hole to be extremely complex, containing counterrotating vortices and local jetting effects that make the flow field in this region highly elliptic. The distribution of dependent variables at the hole exit plane resulted from the interaction of three competing mechanisms, namely, counterrotating structure and local jetting effects within the film-hole, and crossflow blockage.

Fougeres and Heider (1994) solved the unsteady three-dimensional Navier–Stokes equations, completed by a mixing-length turbulence model, using a finite volume technique. They presented two applications of the multidomain code: one for a single row of hot jets injected into a flat-plate turbulent boundary layer, and another for a plane nozzle guide vane with two rows of staggered holes on the pressure as well as suction side of the vane. They specified uniform conditions for the coolant at entry to the injection pipe but provided no details for the coolant profiles at the hole exit. Weigand and Harasgama (1994) carried out a numerical investigation of film cooling on a turbine rotor blade using the Dawes (1993) code that utilizes an unstructured solution adaptive grid methodology for solving three-dimensional Navier–Stokes equations. They discretized the plenum chamber and the injection pipe. However, a rather academic case of blowing in the tangential direction was studied due to limitations of the code. As such, comparison with experimental data was not possible.

Hall et al. (1994) analyzed the showerhead film cooling on the C3X vane with a multiblock, three-dimensional Navier–Stokes code using the Baldwin–Lomax turbulence model. Taking advantage of the spanwise periodicity of the planar C3X vane, the computational span was restricted to just one spanwise pitch of the showerhead holes. The final airfoil C-grid had over 2.1 million grid points with a 17 × 17 grid patch on each of the five holes. Such a grid refinement cannot be handled by present-day computers if the vane were annular, requiring the whole span to be analyzed, not just a slice of it. The computational domain included the injection pipe but not the plenum chamber. They specified uniform coolant conditions at entry to the injection pipe but provided no details of the coolant distribution at the hole exit.

This survey indicates that the effect of coolant distribution at the hole exit, though important, has not yet been investigated on real turbine blades. This is precisely the objective of the present study. Herein, an existing three-dimensional Navier–Stokes code (Arnone et al., 1991), modified to include film-cooling considerations (Garg and Gaugler, 1994), has been used to study the effect of coolant velocity and temperature profiles at the hole exit on the heat transfer characteristics of film-cooled turbine blades. Comparison with experimental data for a C3X vane with nine rows of film cooling holes (Hylton et al., 1988), for a VKI rotor with six rows of holes (Camci and Arts, 1990), and for the ACE rotor with three rows of holes (Norton et al., 1990), is provided.

2 Analysis

The three-dimensional Navier–Stokes code of Arnone et al. (1991) for the analysis of turbomachinery flows was modified by Garg and Gaugler (1994) to include film-cooling effects and Mayle's transition criterion (Mayle, 1991). It was further modified to include Forest's model for augmentation of leading edge heat transfer due to free-stream turbulence (Forest, 1977), and Crawford's model for augmentation of eddy viscosity due to film cooling (Crawford et al., 1980). Briefly, the code is an explicit, multigrid, cell-centered, finite volume code with an algebraic turbulence model. The Navier–Stokes equations in a rotating Cartesian coordinate system are mapped onto a general body-fitted coordinate system using standard techniques. Viscous effects in the streamwise direction are neglected in comparison to those in the other two directions. Justification for this assumption is provided by Garg and Gaugler (1994). The multistage Runge–Kutta scheme developed by Jameson et al. (1981) is used to advance the flow solution in time from an initial guess to the steady state. A spatially varying time step along with a CFL number of 5 was used to speed convergence

Nomenclature

a, b = semi-axes of the ellipse describing the hole exit on the blade surface
a_o–a_3 = coefficients in Eq. (1)
B_r = blowing ratio = $(\rho_c V_c)/(\rho_\infty U_\infty)$
c = true chord of the blade
C_F = coefficient in Eq. (2)
d = coolant hole diameter
h = heat transfer coefficient based on $(T_o - T_w)$
h_o = standard value = 1135.6 W/m^2-K = 200 Btu/hr-ft^2-R
k = von Karman constant
l = mixing length
L = length of the injection pipe
M = Mach number
p = pressure
PD = penetration distance (Crawford's model)
r = coolant hole radius = $d/2$
Re = Reynolds number based on the true chord length
s = distance from the leading edge along the pressure or suction surface
s_o, z_o = coordinates of the center of hole exit on the blade surface
T = temperature
Tu = turbulent intensity
U = main-flow velocity
V = coolant velocity at any point within the hole exit
x = streamwise distance from the point of injection
y^+ = dimensionless distance of the first point off the blade surface
z = distance along the span
δ = boundary layer thickness
ϵ_M = eddy diffusivity for momentum
γ = ratio of specific heats
η, ζ = coordinates from the center of hole exit (see Eq. (1))
θ = momentum thickness
ν = kinematic viscosity
ρ = density

Subscripts

1 = at inlet
2 = at exit
c = for coolant (average value)
e = edge of boundary layer
m = maximum value
n = corresponding to uncooled blade
o = stagnation value
w = at the blade surface
∞ = local free-stream value

to the steady state. Eigenvalue-scaled artificial dissipation and variable-coefficient implicit residual smoothing are used along with a full-multigrid method.

The effects of film cooling have been incorporated into the code in the form of appropriate boundary conditions at the hole locations on the blade surface. Each hole exit (generally an ellipse with semi-axes a and b in the plane of the blade surface) is represented by several control volumes (about 20) having a total area equal to the area of the hole exit, and passing the same coolant mass flow. Different velocity and temperature profiles for the injected gas can be specified at the hole exit. Earlier studies indicate that typical gas turbine film cooling situations involve steep polynomial profiles with their maxima shifted in upstream or downstream direction from the jet centerline. Based on a detailed computation through the plenum chamber and injection pipe, Leylek and Zerkle (1994) found that for high L/d ($\geq$3.0) and high blowing ratio ($\geq$1.0) or for low L/d and low blowing ratio, the exit velocity profile is very much like a fully developed turbulent pipe flow profile. For other combinations of L/d and blowing ratio, Leylek and Zerkle (1994) found that the exit velocity profile is polynomial with shifted maxima. For the cases reported here, turbulent ($\frac{1}{7}$th power-law) and polynomial profiles of the form

$$\frac{V}{V_c} = a_3 \frac{T - T_w}{T_c - T_w} = (1 - \eta^2 - \zeta^2)(a_o + a_1\eta + a_2\eta^2) \quad (1)$$

where

$$\eta = (s - s_o)/a, \quad \zeta = (z - z_o)/b$$

were specified, in order to study their effect on the heat transfer coefficient at the blade surface. Note that Eq. (1) automatically satisfies $V = 0$ condition on the boundary of the hole exit, and in it (s_o, z_o) denotes the center of hole exit, and η and ζ are interchangeable. Using the coolant mass conservation condition, coefficients a_o, a_1, a_2 can be related to V_m, the maximum value of V and its location, V_l. Then using the coolant energy conservation, a_3 can be related to the other coefficients. These relations are

$$a_2 = \frac{1}{1 + 6V_l^2}\left[12 - \frac{6V_m(1 - 3V_l^2)}{(1 - V_l^2)^2}\right],$$

$$a_1 = \frac{2V_lV_m}{(1 - V_l^2)^2} - 2a_2V_l, \quad a_o = 2 - a_2/6,$$

$$a_3 = a_o^2/3 + (a_1^2 + 2a_oa_2)/24 + a_2^2/80$$

For all three blades analyzed here, the experimentally determined temperatures were specified at the blade surface, and wall heat flux was calculated. The algebraic mixing length turbulence model of Baldwin and Lomax (1978) was used. This model has been used satisfactorily by Boyle and Giel (1992), Ameri and Arnone (1994, 1996), and Boyle and Ameri (1997) for heat transfer calculations on turbine blades without film cooling, and by Hall et al. (1994), and Garg and Gaugler (1994) with film cooling. In fact, Ameri and Arnone (1994) compared the Baldwin–Lomax model and Coakley's $q-\omega$ model against experimental data of Graziani et al. (1980), and found that the algebraic model was able to produce many of the flow features better than the two-equation model. They further state that this conclusion is strengthened when one takes into account the relative economy of computations with the algebraic model.

Moreover, Mayle's transition criterion (1991) has been implemented in the code. The incoming flow in the experimental tests on the ACE rotor (Norton et al., 1990) had a turbulence intensity of 4.0 percent, and it is assumed constant for application of Mayle's model. For the C3X vane and the VKI rotor, Mayle's criterion is immaterial since the flow turns turbulent at the leading edge itself due to showerhead injection.

2.1 Forest's Model. The strong favorable free-stream pressure gradients near the leading edge result in laminar flow, even with high free-stream turbulence. The laminar heat transfer at the leading edge is, however, increased by the free-stream turbulence. The model of Forest (1977) was incorporated in order to account for this increase. According to this model

$$\epsilon_M = C_F l T u_\infty U_\infty \quad (2)$$

where the mixing length, l, is defined as

$$l = \min(ky, 0.08\delta)$$

While several ways to calculate the boundary layer thickness were tried following Davis et al. (1988), it was found that the best method was to relate it to the momentum thickness whose calculation is described later on. The coefficient C_F is found from

$$C_F = \frac{0.75}{1 + 0.04/|\lambda|}$$

where

$$\lambda = \frac{\theta^2}{\nu}\frac{dU_e}{ds}$$

The momentum thickness is calculated using Thwaites' method, as given by White (1974). According to this, the momentum thickness at a location s_1 along the blade surface is given by

$$\theta^2(s_1) = \frac{0.45\nu}{U_e^6(s_1)}\int_0^{s_1} U_e^5 ds$$

The origin in this calculation is taken as the geometric stagnation point. This calculation of ϵ_M due to free-stream turbulence was carried out only when the flow was laminar. Otherwise, the analysis would give significantly increased heat transfer for fully turbulent flow (Boyle, 1991). For the cases analyzed here, it implies that Forest's model is used only for the ACE rotor since for both the VKI rotor and the C3X vane, the flow is turbulent at the leading edge itself due to the shower-head injection.

2.2 Crawford's Model. Crawford's model for augmentation of eddy viscosity due to film cooling (Crawford et al., 1980) was developed for use in a two-dimensional boundary layer code to predict heat transfer in full-coverage film cooling situations on flat surfaces. Though not really applicable to the situation, it was used by Stepka and Gaugler (1983) to compare the predicted Stanton numbers with the experimental data for rows of film-cooling holes around the circumference of a cylinder in crossflow. In the absence of a better model, we adopted it also for the present calculations. According to this model, the eddy diffusivity for momentum in the presence of film cooling is modeled by algebraically augmenting the Prandtl mixing length using

$$\frac{l}{\delta} = \left(\frac{l}{\delta}\right)_{3\text{-D}} + \left(\frac{l}{\delta}\right)_a \quad (3)$$

where the "3-D" subscript refers to the three-dimensional mixing length from the Baldwin and Lomax model, and the "a" denotes the departure due to jet-boundary layer interaction, given by

$$\left(\frac{l}{\delta}\right)_a = \lambda_{\max,a} \cdot F \cdot f,$$

$$F = 2.718\left(\frac{y}{PD}\right)^2 \exp\left[-\left(\frac{y}{PD}\right)^2\right],$$

$$f = \exp[-(x/\delta)/2],$$

$$\lambda_{\max,a} = 0.0353 \exp(2.65B_r) \quad \text{for slant angled injection}$$

$$\lambda_{\max,a} = 0.0177 \exp(2.64B_r) \quad \text{for compound angled injection}$$

$$\lambda_{\max,a} = 0.0601 \exp(3.46B_r) \quad \text{for normal injection}$$

where x is the streamwise distance measured from the point of injection, and PD is the penetration distance. While Crawford's model is essentially two dimensional, we extended it to three dimensions by linearly augmenting the eddy viscosity in the spanwise direction between holes.

3 Blades and Experimental Details

The experimental data on the C3X vane have been provided by Hylton et al. (1988). Figure 1 shows the C3X vane with the film-cooling hole details. The test vane was internally cooled by an array of ten radial cooling holes (not shown in Fig. 1) in the active part of the vane. No heat transfer measurements were made in the actual film-cooled nose piece of the vane as it was thermally isolated from the rest of the vane. In addition to the details available in Fig. 1, the two rows of holes on the pressure surface were located at $s/s_m = 0.197$, 0.225, and on the suction surface at $s/s_m = 0.254$, 0.276. One row of showerhead holes was located at the geometric leading edge, with one row on the suction side and three on the pressure side. The active part of the test vane surface was instrumented with 123 0.51-mm-dia sheathed CA thermocouples to measure the temperature at the blade surface. The thermocouple junctions were located in a plane 2.54 mm off midspan. The heat transfer coefficient for each radial cooling hole was calculated from the hole diameter, measured coolant flow rate, and coolant temperature with a correction applied for thermal entry region effects. The internal temperature field of the test vane was obtained from a finite element solution of the steady-state heat conduction equation, using the measured surface temperatures as boundary conditions. Experimental values of the heat flux at the blade surface were then obtained from the normal temperature gradient at the blade surface, and these were used to derive the local heat transfer coefficient at a spanwise location 2.54 mm off the midspan of the blade. More details are available from Hylton et al. (1988).

The experimental data on the VKI rotor have been provided by Camci and Arts (1990), using the short-duration VKI Isentropic Compression Tube facility. Figure 2 shows the VKI rotor geometry along with cooling hole details. Three staggered rows of cylindrical cooling holes ($d = 0.8$ mm; $s/c = -0.0285$, 0, 0.0285) were located around the leading edge. The row and hole spacings were both 2.48 mm. These holes were spanwise angled at 30 deg from the tangential direction and drilled in a plane perpendicular to the blade surface. Two staggered rows of conical holes ($d = 0.8$ mm; $s/c = 0.206$, 0.237) were located on the suction side. The row and hole spacings were respectively 2.48 and 2.64 mm. These holes were inclined at 37 and 43 deg with respect to the local blade surface and drilled in a plane perpendicular to the span. One row of conical holes ($d = 0.8$ mm; $s/c = -0.315$) was located along the pressure side. The hole spacing was 2.64 mm. These holes were inclined at 35 deg with respect to the local blade surface and drilled in a plane perpendicular to the span. The blade instrumented for heat flux measurements was milled from "Macor" glass ceramic and 45 platinum thin films were applied on its surface. Three independent cavities were drilled along the blade height to act as plenum chambers. The local wall convective heat flux was deduced from the corresponding time-dependent surface temperature evolution, provided by the platinum thin-film gages. The wall temperature/wall heat flux conversion was obtained from an electrical analogy, simulating a one-dimensional semi-infinite body configuration. More details are available from Camci and Arts (1990).

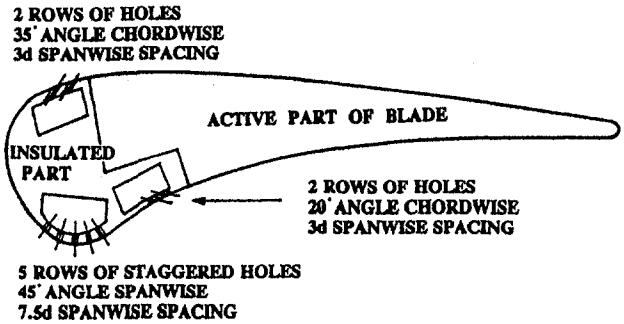

Fig. 1 C3X vane and cooling hole details

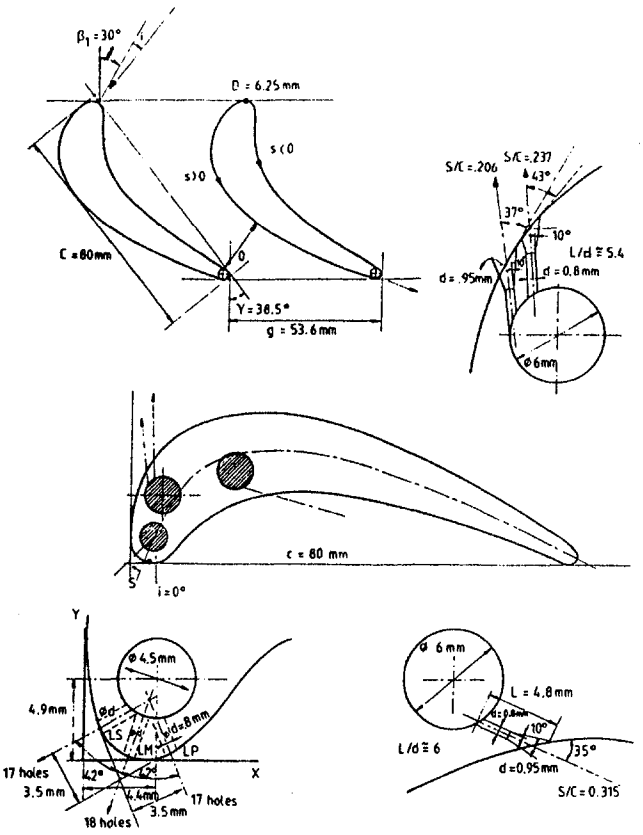

Fig. 2 VKI rotor and cooling hole details

The experimental data on the ACE rotor have been provided by Norton et al. (1990), using the Isentropic Light Piston Tunnel at Oxford University. The blade profile tested was the midheight streamline section of a highly loaded, transonic, research turbine rotor. Build X of the ACE rotor, shown in Fig. 3, was used for comparison purposes. In this, one row of cylindrical holes ($d = 0.65$ mm; $s/s_m = 0.7$) was located on the suction surface, with a hole spacing of $4d$. Two staggered rows of cylindrical holes ($d = 0.65$ mm; $s/s_m = 0.5$, 0.56) were located on the pressure surface, with a row and hole spacing of $4d$ each. All holes were inclined 30 deg to the local blade surface and drilled in a plane perpendicular to the span. The instrumented blades were manufactured from "Macor" glass ceramic onto which were placed thin film platinum resistance thermometers and pads. The heat transfer measurement technique is simi-

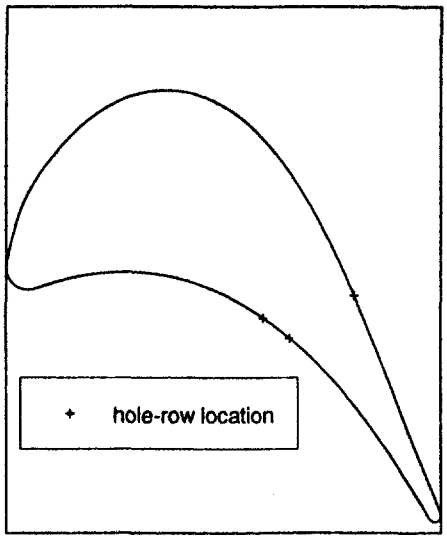

Fig. 3 ACE rotor and cooling hole locations

Table 1 Parameter values for the cases analyzed

Main Flow Parameters (Experimental)

Blade	Case	p_o (kN/m^2)	T_o (K)	M_1	Re_1	M_2	Re_2	Tu
C3X	44135	281.55	705	0.20	6.2×10^5	0.90	2.0×10^6	6.5%
C3X	44155	280.95	705	0.19	6.0×10^5	0.90	2.0×10^6	6.5%
C3X	44355	284.02	702	0.18	5.6×10^5	0.90	2.02×10^6	6.5%
VKI	all	290.00	415	0.25	-	0.925	2.32×10^6	5.2%
ACE	6115	286.22	463	0.396	5.5×10^5	1.196	1.01×10^6	4.0%
ACE	6109	238.83	402	0.39	5.4×10^5	1.182	1.01×10^6	4.0%

Film Cooling Parameters (Derived)

Blade	Case	$(\rho_c V_c \gamma^{1/2})/(\rho_o c_o)$			T_c/T_o		
		Shower Head	Suction Surface	Pressure Surface	Shower Head	Suction Surface	Pressure Surface
C3X	44135	0.20	0.634	0.426	0.745	0.558	0.668
C3X	44155	0.411	0.639	0.427	0.7	0.55	0.667
C3X	44355	0.366	0.564	0.387	0.826	0.7	0.803
VKI	2.07%	.092-.13	.176,.182	0.231	.657-.666	0.645	0.623
VKI	3.09%	.166-.237	.224,.233	0.314	.609-.618	0.623	0.584
VKI	3.32%	.175-.249	.239,.248	0.352	.491-.499	0.497	0.449
ACE	6115	0.0	0.314	.18,.20	-	0.514	0.62
ACE	6109	0.0	0.635	.37,.41	-	0.595	.695,.7

lar to that used by Camci and Arts (1990). More details are available from Norton et al. (1990).

4 Computational Details

For all the blades, the computational span, shown in Fig. 4, is different from the real span. The ordinate in each part of Fig. 4 denotes the distance along the blade surface in the spanwise direction, while the abscissa denotes the distance along the blade surface in the chordwise direction, both normalized by the hole radius, r. For the VKI rotor, the hole spacing in the span direction was assumed to be 2.56 mm ($=6.4r$) for all holes, representing a deviation of ±3 percent from the actual values of 2.48 and 2.64 mm. It may be noted that the abscissa in Fig. 4 has breaks so as to accommodate all the rows of holes. The shape and orientation of the hole openings in Fig. 4 are a direct consequence of the angles the holes make with the spanwise or chordwise direction. For all the blades, the pattern of holes shown in Fig. 4 is repeated in the spanwise direction. For the C3X vane and the VKI rotor, periodic boundary conditions are imposed due to showerhead injection, while for the ACE rotor, symmetry conditions are imposed on the ends of the computational span.

Since the hole diameter on all the blades is less than 1 mm, the grid size has to be varied along the blade chord. For computational accuracy, the ratio of two adjacent grid sizes in any direction was kept within 0.76 to 1.3. A periodic C-grid with up to one million grid points was used. For the C3X vane, the grid used was $281 \times 45 \times 81$, while for the VKI and ACE rotors, it was $353 \times 53 \times 17$ and $313 \times 53 \times 17$, respectively, where the first number represents the number of grid points along the main flow direction, the second in the blade-to-blade direction, and the third in the span direction. Normal to the blade surface is the dense viscous grid, with $y^+ < 1$ for the first

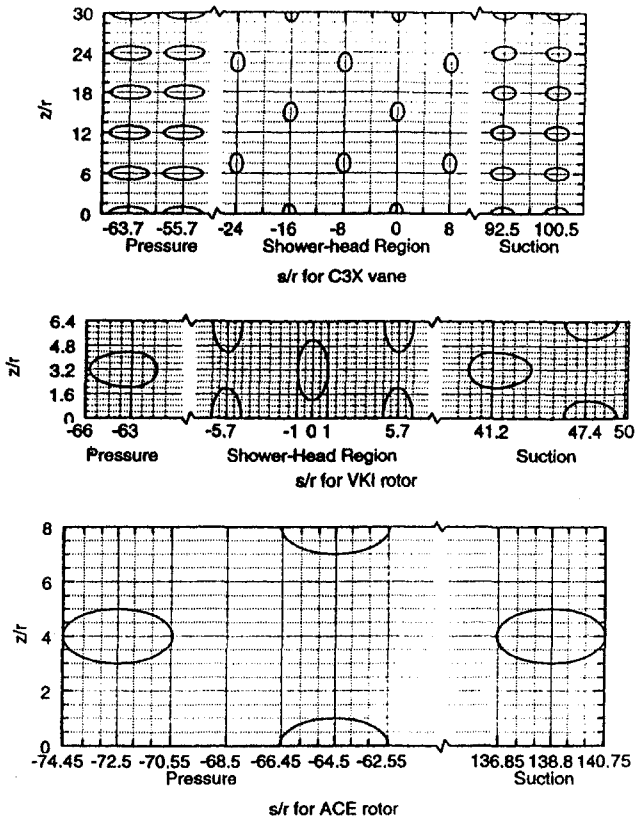

Fig. 4 Computational span for the C3X vane, VKI rotor, and the ACE rotor

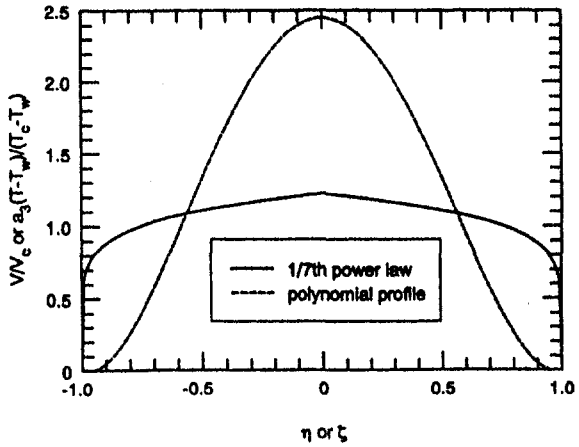

Fig. 5 Coolant velocity and temperature profiles at the hole exit

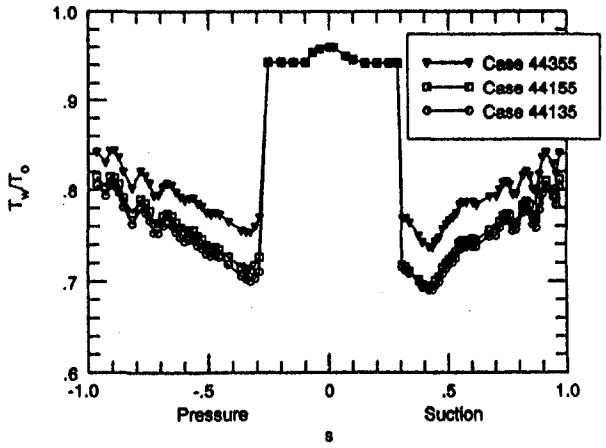

Fig. 6 Blade surface temperature for various cases (C3X vane)

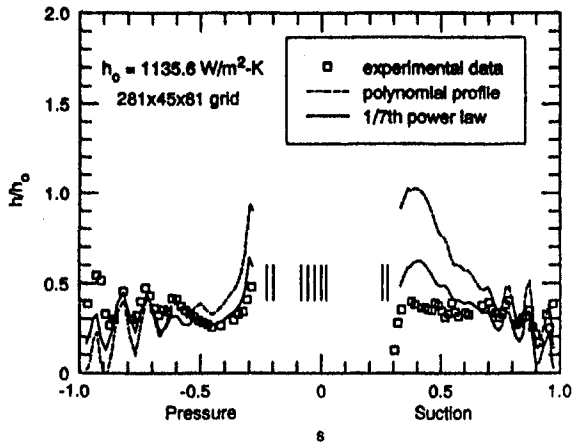

Fig. 8 Effect of coolant velocity and temperature profiles on the normalized heat transfer coefficient at the C3X vane surface (case 44155)

point off the blade surface, following Boyle and Giel (1992). Computations were run on the 8-processor Cray Y-MP supercomputer at the NASA Lewis Research Center, and on the 16-processor C-90 supercomputer at NASA Ames Research Center. The code requires about 60 million words (Mw) of storage and takes about 20 seconds per iteration (full-multigrid) on the C-90 machine for one million grid points. For a given grid the first case requires about 1100 iterations to converge, while subsequent cases for the same grid require about 300 iterations starting with the solution for the previous case.

5 Results and Discussion

Three experimental cases for the C3X vane, three for the VKI rotor, and two for the ACE rotor were analyzed for comparison. The values of various parameters for these cases are given in Table 1. In this table, the derived film-cooling parameters are based upon the assumption of one-dimensional compressible flow through the hole. For the C3X vane, cases 44135 and 44155 represent the minimum and maximum blowing ratio, respectively, for the showerhead holes, while case 44355 represents the warmest coolant. For the VKI rotor, case number is designated by the ratio of coolant mass to the main-flow mass; the main difference between the 3.09 and 3.32 percent cases being the colder coolant for the latter. For the ACE rotor, case 6115 represents about half the blowing ratio for the case 6109. In all cases except case 6115 for the ACE rotor, the blowing ratio is high ($B_r \geq 1.0$).

Figure 5 shows the coolant velocity and temperature profiles at the hole exit, the effect of which was studied on the heat transfer coefficient at various blade surfaces. The profiles shown in Fig. 5 are at the centerline through the hole, with the abscissa covering the hole. Clearly, the $\frac{1}{7}$th power law profile does not satisfy the zero gradient condition at the centerline. The polynomial profile shown is for V_m = 2.449 = twice the maximum velocity for the $\frac{1}{7}$th power law profile, and $V_l = 0$. It was found, however, that results for the heat transfer coefficient corresponding to the polynomial profile did not change more than ~5 percent for $-0.4 \leq V_l \leq 0.4$.

We now present results for the three blades separately. Figure 6 shows the nonuniform experimentally determined temperature on the C3X vane surface for the three cases. These temperature values were specified as the boundary condition for the blade surface temperature in the code as well. In this and later figures, except Figs. 10–12, s represents the normalized distance along the pressure or suction surface of the blade. Besides the somewhat erratic temperature variation over $|s| > 0.25$, caused by the internal cooling holes (not shown in Fig. 1) in the active part of the blade, there is a sharp drop in temperature at each end of the insulated portion of the blade ($|s| \approx 0.25$).

Figures 7–9 provide the effect of coolant velocity and temperature distribution at the hole exit on the normalized heat transfer coefficient (solid and dash curves) at the blade surface in comparison with experimental data (Hylton et al., 1988), denoted by □, for the cases 44135, 44155, and 44355, respectively, at a spanwise location (near midspan) where the experi-

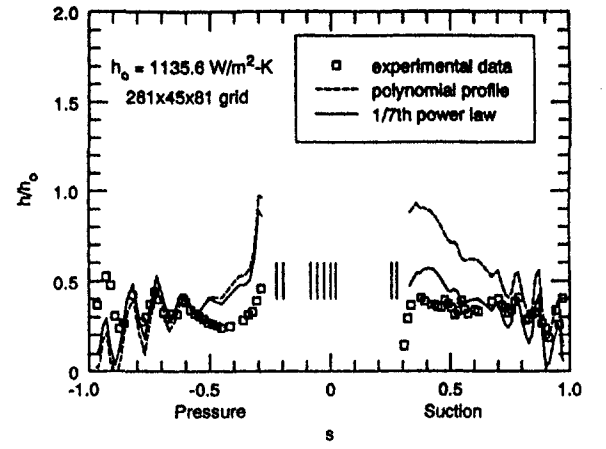

Fig. 7 Effect of coolant velocity and temperature profiles on the normalized heat transfer coefficient at the C3X vane surface (case 44135)

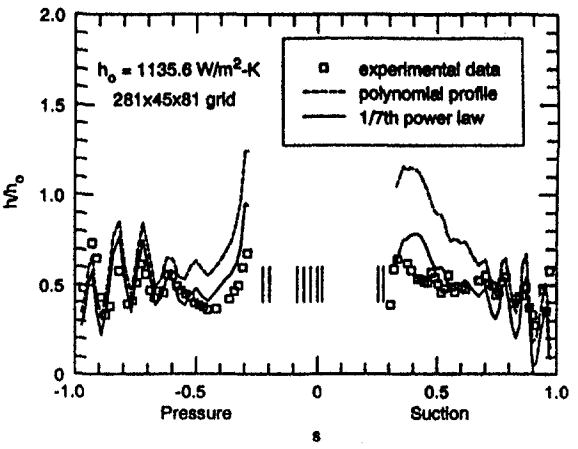

Fig. 9 Effect of coolant velocity and temperature profiles on the normalized heat transfer coefficient at the C3X vane surface (case 44355)

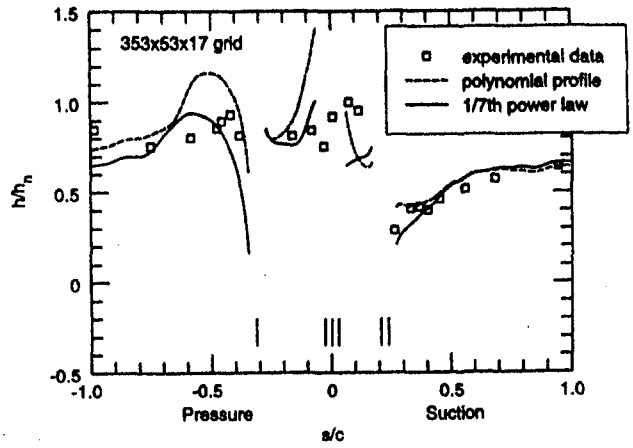

Fig. 10 Effect of coolant velocity and temperature profiles on the normalized heat transfer coefficient at the VKI rotor surface (2.07 percent coolant case)

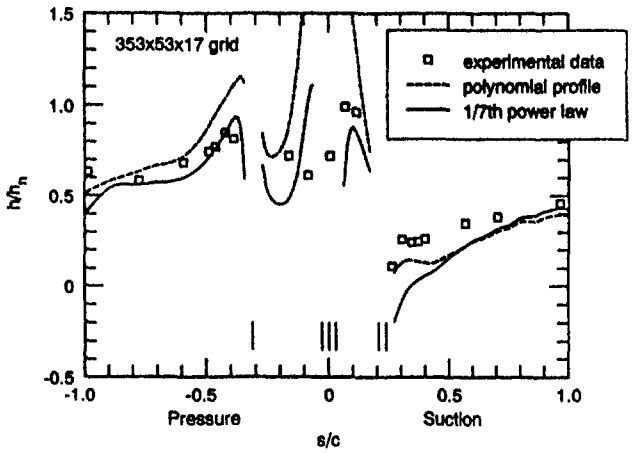

Fig. 12 Effect of coolant velocity and temperature profiles on the normalized heat transfer coefficient at the VKI rotor surface (3.32 percent coolant case)

mental data were taken. The heat transfer coefficient values in these figures have been normalized with respect to an arbitrary value, h_o = 1135.6 kW/m^2-K, as per Hylton et al. (1988). There are no data given for about 25 percent of surface length on either side of the leading edge since this portion contained the plenum chambers for injection of the colder gas and was insulated from the rest of the blade in the experimental tests (cf. Fig. 1). The fluctuations in the data are due to the nonuniform blade surface temperature in the experimental data. The nine short vertical lines near the center-bottom of these figures denote the location of film cooling rows. For all three cases the normalized heat transfer coefficient corresponding to the polynomial profiles of coolant velocity and temperature at the hole exit is about 50–60 percent higher than that corresponding to the $\frac{1}{7}$th power law over most of the suction surface. However, the difference over the pressure surface is only about ±10 percent for the case 44135 (Fig. 7), about ±20 percent for the case 44155 (Fig. 8), and about 35 percent for the case 44355 (Fig. 9). Also, the $\frac{1}{7}$th power law profile results seem to match better with the experimental data than the polynomial profile results for all the cases.

For the C3X vane, we may point out that experimentally, the heat flux on the blade (inner) surface was calculated from a finite element analysis of conduction within the blade, and the heat transfer coefficient was then found by dividing this heat flux by $(T_o - T_w)$. The present study computes the heat transfer coefficients on the blade (outer) surface from the three-dimensional Navier–Stokes analysis. Also, the uncertainty in the heat transfer coefficient measurement varies from about 10 percent near $|s| \approx 0.3$ to about 22 percent near $|s| \approx 0.95$ (Hylton et al., 1988).

Let us now turn to the comparison of results for the VKI rotor. For this rotor, the blade was specified to be isothermal with $T_w/T_o = 0.7$. Figures 10–12 display the effect of coolant velocity and temperature distribution at the hole exit on the normalized heat transfer coefficient (solid and dash curves) at the blade surface in comparison with experimental data (Camci and Arts, 1990), denoted by □, for the three cases at midspan. In these figures, h_n corresponds to the heat transfer coefficient at an uncooled blade surface. Also, the abscissa represents the surface distance along the blade normalized by the true chord, in conformity with the available experimental data (Camci and Arts, 1990). The six short vertical lines in the center-bottom of these figures denote the location of film-cooling rows. From these figures we find, in contrast to the results for the C3X vane, that the differences in h/h_n values corresponding to the two coolant profiles at the hole exit are negligible over most of the suction surface and considerable (about 30 percent) over the pressure surface. The heat transfer coefficient corresponding to the polynomial profiles of coolant injection is generally larger than that corresponding to the $\frac{1}{7}$th power law profiles. Also, comparison with experimental data is fair for either of the coolant profiles results. The experimental uncertainty in the measurement of heat transfer coefficient is about 5 percent except

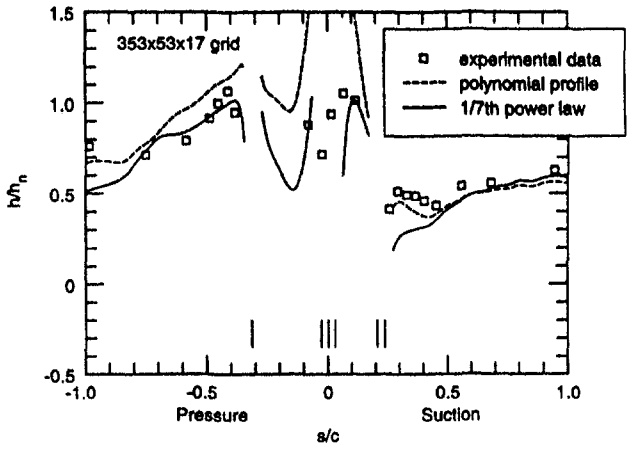

Fig. 11 Effect of coolant velocity and temperature profiles on the normalized heat transfer coefficient at the VKI rotor surface (3.09 percent coolant case)

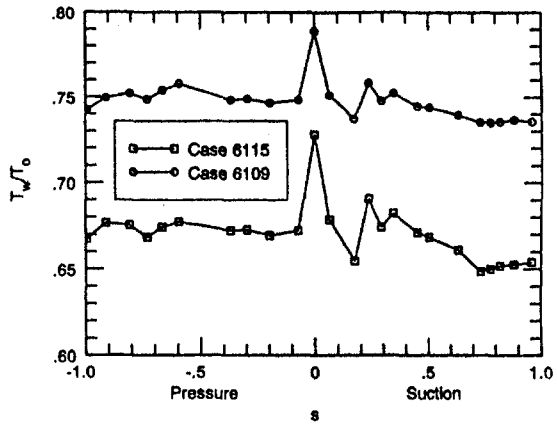

Fig. 13 Blade surface temperature for the two cases (ACE rotor)

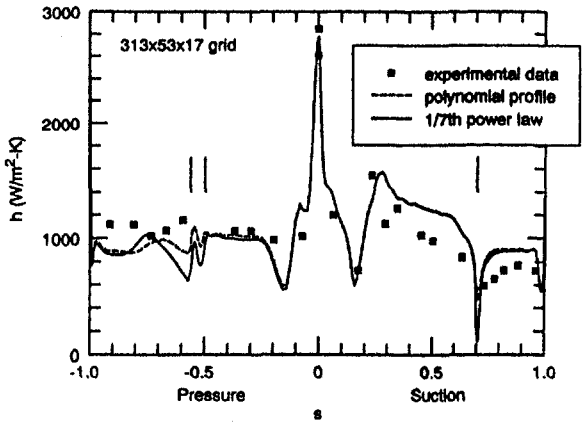

Fig. 14 Effect of coolant velocity and temperature profiles on the heat transfer coefficient at the ACE rotor surface (case 6115)

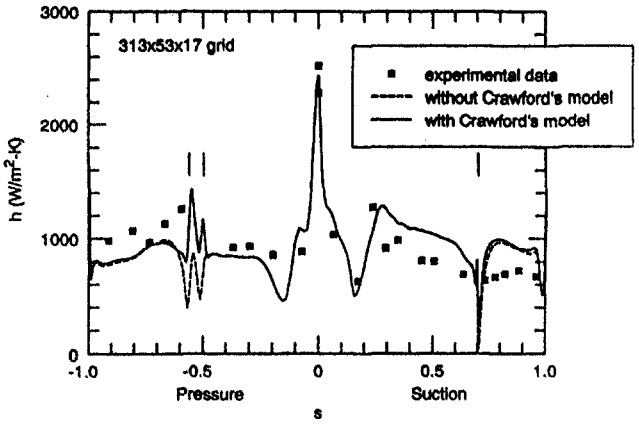

Fig. 16 Effect of Crawford's model on the heat transfer coefficient at the ACE rotor surface (case 6109)

in the shower-head region where it is estimated to be as high as 10–15 percent (Camci and Arts, 1990). Due to normalization with respect to h_n, however, each experimental data point represents two measurements, one for the cooled and another for the uncooled blade. The same is true for the computations as well, and may be the reason for the relatively good comparison with the experimental data for the VKI rotor in contrast to that for the C3X vane in Figs. 7–9. We may also point out that the suction and pressure surface holes on the VKI rotor are conical while the showerhead holes on the VKI rotor as well as all holes on the C3X vane are cylindrical. This may account for the relatively smaller effect of coolant velocity and temperature distribution at the hole exit on the heat transfer coefficient at the VKI rotor surface in contrast to that for the C3X vane.

We now turn to the discussion of results for the ACE rotor. Figure 13 shows the nonuniform experimentally determined temperature on the ACE rotor surface for the two cases analyzed. These temperature values were specified as the boundary condition for the blade surface temperature in the code as well. Figures 14 and 15 show the effect of coolant velocity and temperature distribution at the hole exit on the heat transfer coefficient (solid and dash curves) at the blade surface in comparison with experimental data (Norton et al., 1990), denoted by ■, for the two cases at midspan. The short vertical lines in these figures as well as Fig. 16 denote the location of film cooling rows. Due to the absence of showerhead cooling, this is the only case where Mayle's transition criterion and Forest's model for augmentation of laminar heat transfer at the leading edge due to free-stream turbulence are useful. Clearly, both models seem to be effective in yielding results that compare well with the experimental data. While the effect of coolant profiles at the hole exit is negligible for the low blowing ratio case 6115 in Fig. 14, it is considerable (as much as 50 percent higher h corresponding to the polynomial profile) over the pressure surface for the high blowing ratio case 6109 in Fig. 15. For both cases, however, the effect on the suction surface is negligible, in conformity with the results for the VKI rotor but in direct contrast to those for the C3X vane. The polynomial profile for the coolant velocity and temperature distribution at the hole exit results in a very good comparison with the experimental data downstream of the cooling holes on the pressure surface in Fig. 15. Norton et al. (1990) could not get such a good comparison on the pressure surface; their prediction is similar to ours for the $\frac{1}{7}$th power law profile.

Figure 16 shows the effect of Crawford's model on the heat transfer coefficient at the ACE rotor surface for the case 6109. The results in Fig. 16 correspond to the polynomial profiles for coolant velocity and temperature at the hole exit. Clearly, the effect of Crawford's model is felt only within the region of holes; it is negligible downstream of the holes. We may note that due to the absence of showerhead cooling, the flow upstream of the holes is essentially two dimensional (no spanwise variation) for the ACE rotor.

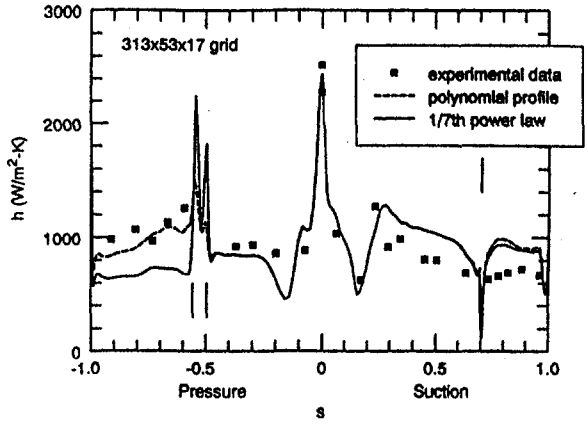

Fig. 15 Effect of coolant velocity and temperature profiles on the heat transfer coefficient at the ACE rotor surface (case 6109)

6 Conclusions

A three-dimensional Navier–Stokes code has been used to study the effect of coolant velocity and temperature distribution at the hole exit on the heat transfer coefficient on three film-cooled turbine blades, namely, the C3X vane, the VKI rotor, and the ACE rotor. Results are also compared with the experimental data for all the blades. Moreover, Mayle's transition criterion (Mayle, 1991), Forest's model for augmentation of leading edge heat transfer due to free-stream turbulence (Forest, 1977), and Crawford's model for augmentation of eddy viscosity due to film cooling (Crawford et al., 1980) are used. It is found that different velocity and temperature distributions of coolant at the hole exit can lead to as much as a 60 percent change in the heat transfer coefficient at the blade surface in some cases. Also, different effects are observed on the pressure and suction surface depending upon the blade as well as upon the hole shape, conical or cylindrical. Thus specification of proper conditions at the hole exit is important in film-cooling applications. This calls for a detailed analysis of the in-hole and near-hole physics under conditions relevant to the gas turbine.

Acknowledgments

This work was done when the first author held a National Research Council–NASA Research Associateship at the NASA

Lewis Research Center. Helpful discussions with A. A. Ameri and R. J. Boyle of the NASA Lewis Research Center are gratefully acknowledged.

References

Amer, A. A., Jubran, B. A., and Hamdan, M. A., 1992, "Comparison of Different Two-Equation Turbulence Models for Prediction of Film Cooling From Two Rows of Holes," *Numer. Heat Transfer,* Vol. 21, Part A, pp. 143–162.

Ameri, A. A., and Arnone, A., 1994, "Prediction of Turbine Blade Passage Heat Transfer Using a Zero and a Two-Equation Turbulence Model," ASME Paper No. 94-GT-122.

Ameri, A. A., and Arnone, A., 1996, "Transition Modeling Effects on Turbine Rotor Blade Heat Transfer Predictions," ASME JOURNAL OF TURBOMACHINERY, Vol. 118, pp. 307–314.

Arnone, A., Liou, M.-S., and Povinelli, L. A., 1991, "Multigrid Calculation of Three-Dimensional Viscous Cascade Flows," AIAA Paper No. 91-3238.

Baldwin, B. S., and Lomax, H., 1978, "Thin-Layer Approximation and Algebraic Model for Separated Turbulent Flows," AIAA Paper No. 78-257.

Benz, E., and Wittig, S., 1992, "Prediction of the Interaction of Coolant Ejection With the Main Stream at the Leading Edge of a Turbine Blade: Attached Grid Application," *Proc. Intl. Symp. Heat Transfer in Turbomachinery,* Athens, Greece.

Bergeles, G., Gosman, A. D., and Launder, B. E., 1980, "Double-Row Discrete-Hole Cooling: an Experimental and Numerical Study," ASME *Journal of Engineering for Power,* Vol. 102, pp. 498–503.

Boyle, R. J., 1991, "Navier–Stokes Analysis of Turbine Blade Heat Transfer," ASME JOURNAL OF TURBOMACHINERY, Vol. 113, pp. 392–403.

Boyle, R. J., and Ameri, A. A., 1997, "Grid Orthogonality Effects on Predicted Turbine Midspan Heat Transfer and Performance," ASME JOURNAL OF TURBOMACHINERY, Vol. 119, pp. 31–38.

Boyle, R. J., and Giel, P., 1992, "Three-Dimensional Navier–Stokes Heat Transfer Predictions for Turbine Blade Rows," AIAA Paper No. 92-3068.

Camci, C., and Arts, T., 1990, "An Experimental Convective Heat Transfer Investigation Around a Film-Cooled Gas Turbine Blade," ASME JOURNAL OF TURBOMACHINERY, Vol. 112, pp. 497–503.

Choi, D., 1993, "A Navier–Stokes Analysis of Film Cooling in a Turbine Blade," AIAA Paper No. 93-0158.

Crawford, M. E., Kays, W. M., and Moffat, R. J., 1980, "Full-Coverage Film Cooling on Flat, Isothermal Surfaces: A Summary Report on Data and Predictions," NASA CR 3219.

Davis, R. L., Hobbs, D. E., and Weingold, H. D., 1988, "Prediction of Compressor Cascade Performance Using a Navier–Stokes Technique," ASME JOURNAL OF TURBOMACHINERY, Vol. 110, pp. 520–531.

Dawes, W. N., 1993, "The Extension of a Solution-Adaptive Three-Dimensional Navier–Stokes Solver Toward Geometries of Arbitrary Complexity," ASME JOURNAL OF TURBOMACHINERY, Vol. 115, pp. 283–295.

Dibelius, G. H., Pitt, R., and Wen, B., 1990, "Numerical Prediction of Film Cooling Effectiveness and the Associated Aerodynamic Losses With a Three-Dimensional Calculation Procedure," ASME Paper No. 90-GT-226.

Dorney, D. J., and Davis, R. L., 1993, "Numerical Simulation of Turbine Hot Spot Alleviation Using Film Cooling," *J. Propul. Power,* Vol. 9, pp. 329–336.

Forest, A. E., 1977, "Engineering Predictions of Transitional Boundary Layers," AGARD-CP-224.

Fougeres, J. M., and Heider, R., 1994, "Three-Dimensional Navier–Stokes Prediction of Heat Transfer with Film Cooling," ASME Paper No. 94-GT-14.

Garg, V. K., and Gaugler, R. E., 1993, "Heat Transfer in Film-Cooled Turbine Blades," ASME Paper No. 93-GT-81.

Garg, V. K., and Gaugler, R. E., 1994, "Prediction of Film Cooling on Gas Turbine Airfoils," ASME Paper No. 94-GT-16.

Garg, V. K., and Gaugler, R. E., 1996, "Leading Edge Film Cooling Effects on Turbine Blade Heat Transfer," *Numer. Heat Transfer,* Vol. 30, Part A, pp. 165–187.

Goldstein, R. J., 1971, "Film Cooling," *Advances in Heat Transfer,* Vol. 7, pp. 321–379.

Graziani, R. A., Blair, M. F., Taylor, J. R., and Mayle, R. E., 1980, "An Experimental Study of Endwall and Airfoil Surface Heat Transfer in a Large Scale Turbine Blade Cascade," ASME *Journal of Engineering for Power,* Vol. 102, pp. 257–267.

Haas, W., Rodi, W., and Schönung, B., 1992, "The Influence of Density Difference Between Hot and Coolant Gas on Film Cooling by a Row of Holes: Predictions and Experiments," ASME JOURNAL OF TURBOMACHINERY, Vol. 114, pp. 747–755.

Hall, E. J., Topp, D. A., and Delaney, R. A., 1994, "Aerodynamic/Heat Transfer Analysis of Discrete Site Film-Cooled Turbine Airfoils," AIAA Paper No. 94-3070.

Hylton, L. D., Nirmalan, V., Sultanian, B. K., and Kaufman, R. M., 1988, "The Effects of Leading Edge and Downstream Film Cooling on Turbine Vane Heat Transfer," NASA CR 182133.

Jameson, A., Schmidt, W., and Turkel, E., 1981, "Numerical Solutions of the Euler Equations by Finite Volume Methods Using Runge–Kutta Time-Stepping Schemes," AIAA Paper No. 81-1259.

Leylek, J. H., and Zerkle, R. D., 1994, "Discrete-Jet Film Cooling: A Comparison of Computational Results With Experiments," ASME JOURNAL OF TURBOMACHINERY, Vol. 116, pp. 358–368.

Mayle, R. E., 1991, "The Role of Laminar–Turbulent Transition in Gas Turbine Engines," ASME JOURNAL OF TURBOMACHINERY, Vol. 113, pp. 509–537.

Norton, R. J. G., Forest, A. E., White, A. J., Henshaw, D. G., Epstein, A. H., Schultz, D. L., and Oldfield, M. L. G., 1990, "Turbine Cooling System Design, Vol. I and III," WRDC-TR-89-2109.

Rai, M. M., 1989, "Three-Dimensional Navier–Stokes Simulations of Turbine Rotor-Stator Interaction; Part I—Methodology," *AIAA J. Propul. & Power,* Vol. 5, pp. 305–311.

Schönung, B., and Rodi, W., 1987, "Prediction of Film Cooling by a Row of Holes With a Two-Dimensional Boundary-Layer Procedure," ASME JOURNAL OF TURBOMACHINERY, Vol. 109, pp. 579–587.

Stepka, F. S., and Gaugler, R. E., 1983, "Comparison of Predicted and Experimental External Heat Transfer Around a Film Cooled Cylinder in Crossflow," ASME Paper No. 83-GT-47.

Tafti, D. K., and Yavuzkurt, S., 1990, "Prediction of Heat Transfer Characteristics for Discrete Hole Film Cooling for Turbine Blade Applications," ASME JOURNAL OF TURBOMACHINERY, Vol. 112, pp. 504–511.

Vogel, T., 1991, "Computation of 3-D Viscous Flow and Heat Transfer for the Application to Film Cooled Gas Turbine Blades," Paper No. 7, AGARD-CP-510.

Weigand, B., and Harasgama, S. P., 1994, "Computations of a Film Cooled Turbine Rotor Blade With Non-uniform Inlet Temperature Distribution Using a Three-Dimensional Viscous Procedure," ASME Paper No. 94-GT-15.

White, F. M., 1974, *Viscous Fluid Flow,* McGraw-Hill, New York.

Adiabatic Effectiveness, Thermal Fields, and Velocity Fields for Film Cooling With Large Angle Injection

A. Kohli

D. G. Bogard

Mechanical Engineering Department,
University of Texas at Austin,
Austin, TX 78712

The film cooling performance and velocity field were investigated for discrete round holes inclined at an injection angle of 55 deg. Results are compared to typical round film cooling holes, with an injection angle of 35 deg. All experiments in this study were performed at a density ratio of DR = 1.6, using cryogenic cooling of the injected air. Centerline and lateral distributions of effectiveness were obtained for a range of momentum flux ratios. Thermal field and two component mean velocity and turbulence intensity measurements were made at a momentum flux ratio that was within the range of maximum spatially averaged effectiveness. Compared to round holes with 35 deg injection angle, the 55 deg holes showed only a slight degradation in centerline effectiveness for low momentum flux ratios, while a significant reduction in effectiveness was seen at high momentum flux ratios. The thermal field for the 55 deg round holes indicated a faster decay of cooling capacity for the 55 deg round holes. The high turbulence levels for the 55 deg round hole coincided with the sharp velocity gradients between the jet and free stream, and the decay of turbulence levels with downstream distance was found to be similar to those for a 35 deg hole.

Introduction

Film cooling of gas turbine blades is generally achieved through discrete holes inclined at shallow angles to the blade surface. As film cooling research has mainly focused on studying holes with injection angles of about 30 deg, there is a dearth of studies investigating large injection angles. The motivation for this study was to determine the sensitivity to injection angle and to ascertain whether adequate film cooling performance could be achieved with injection at large angles. Currently large angle injection is used near the leading edge of airfoils due to geometric considerations. However, large angle injection could be used more generally across the airfoil if the performance penalty is not too severe. This study presents detailed effectiveness, thermal, and velocity field measurements for round holes with an injection angle of 35 and 55 deg.

The only previous study of film cooling effectiveness that included holes with a large injection angle was that by Foster and Lampard (1980). Laterally averaged effectiveness for long injection tubes spaced $3D$ apart and inclined at 35, 55, and 90 deg were measured. Foreign gas injection was used to obtain a density ratio of DR = 2, and results were presented for two blowing ratios, $M = 0.5$ and 1.4 ($I = 0.125$ and 0.98). Based on the results of Thole et al. (1992), who found that complete detachment of the cooling jets occurs at $I = 0.8$ for holes inclined at 35 deg, the higher blowing ratio used by Foster and Lampard would have resulted in detached cooling jets. This is consistent with the low effectiveness values they found at the higher blowing ratio. Consequently, with effectiveness measurements at only one low blowing ratio for which the cooling jets remain attached, the results of Foster and Lampard do not establish the momentum flux ratio for maximum effectiveness when using 55 deg angled holes.

Foster and Lampard also measured profiles of the mean streamwise velocity component at the jet centerline at four streamwise positions for a blowing ratio of $M = 1.4$. Their results show a distinct velocity defect behind the jet, which is consistent with a detached jet expected for this high blowing ratio. Four profiles of foreign gas concentration were also measured, and these too indicated jet lift-off. In the present study, we have made much more detailed velocity and thermal field measurements, and we performed these measurements at the blowing conditions that provide maximum effectiveness. Moreover, the present study provides lateral thermal field measurements, which are essential to obtain full field information about the jets.

The only study that has detailed measurements of mean and turbulence quantities for film cooling jets was done by Pietrzyk et al. (1990). The hydrodynamics of film cooling jets, inclined at 35 deg and for density ratios of DR = 1 and 2, were evaluated in terms of mean velocity profiles and contours of turbulence intensities, turbulent shear stresses, and correlation coefficients. Similar measurements have been made in this study for round holes inclined at 55 deg.

In this study centerline, laterally averaged, and spatially averaged effectivenesses were measured over a range of blowing conditions for round holes inclined at 55 deg. To allow comparison with data in literature, effectiveness measurements at two momentum flux ratios were done for 35 deg round holes. All flow conditions were matched for measurements with the 35 deg holes and the 55 deg holes. In addition to the effectiveness measurements, thermal field and two-component mean velocity and turbulence levels were recorded at a momentum flux ratio within the optimum operating range for the 55 deg round holes.

Experimental Facilities and Techniques

Experiments were carried out in a closed-loop wind tunnel with a secondary cryogenic injection system. Liquid nitrogen was used to cool the injected air to −85°C, with $T_\infty \sim 25$°C; this resulted in a density ratio of DR = 1.6. Details of the facility shown in Fig. 1 can be found from Pietrzyk et al. (1990). For

Contributed by the International Gas Turbine Institute and presented at the 40th International Gas Turbine and Aeroengine Congress and Exhibition, Houston, Texas, June 5–8, 1995. Manuscript received by the International Gas Turbine Institute February 5, 1995. Paper No. 95-GT-219. Associate Technical Editor: C. J. Russo.

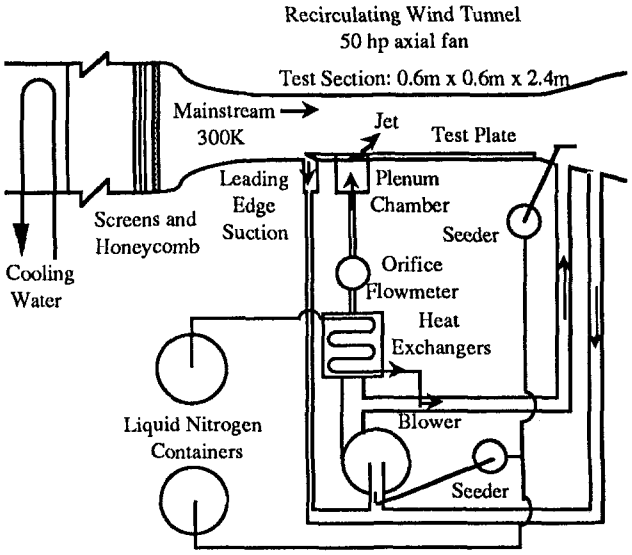

Fig. 1 Film cooling test facility

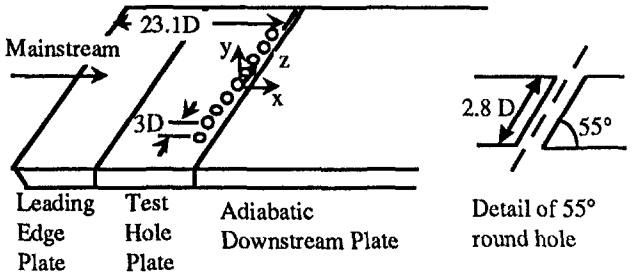

Fig. 2 Test section geometry

all the experiments in this study, the jet velocity was held constant at $U_j = 6.25$ m/s. Different momentum flux ratios were obtained by varying the free-stream velocity over the range $U_\infty = 10$ to 30 m/s. The momentum flux ratios investigated in this study were between $I = 0.08$ and 0.63 ($M = 0.35$ and 1.0). For a free-stream velocity of $U_\infty = 20$ m/s, the approaching boundary layer was turbulent at the leading edge of the holes and the boundary layer parameters were $\mathrm{Re}_{\delta 2} = 1100$, $\delta_1/D = 0.12$, and $H = 1.48$. The variation of free-stream velocity in both spanwise and streamwise directions was ±0.5 percent, and the free-stream turbulence level was about Tu = 0.2 percent. Detailed documentation of the free-stream and turbulent boundary layer quality can be found from Pietrzyk et al. (1990).

The test plate (see Fig. 2) consisted of three separate sections: a leading edge plate, followed by a film cooling hole plate, downstream of which was an adiabatic plate instrumented with thermocouples. For this study a single row of nine round holes inclined at 55 deg was used. The holes had a diameter of $D = 11.1$ mm, were spaced $P/D = 3$ apart, and had a length, $L/D = 2.8$, representative of actual gas turbines. The hole inlets and exits were sharp edged, and the interiors were aerodynamically smooth. To minimize conduction losses, the film cooling hole plate was made out of extruded polystyrene foam (Styrofoam), which had a thickness of 2.5 cm. The adiabatic plate comprised of 1.3-cm-thick Styrofoam glued on to a 1.3 cm fiberglass composite (Extren) sheet for structural rigidity. A 15 cm layer of Corning fiberglass insulation was installed below the adiabatic plate to reduce backside conduction losses. Sinha et al. (1991) used a three-dimensional conduction heat transfer code to determine that the conduction errors were minimal for this configuration.

All temperature measurements in this study were made using E-type thermocouples. The jet temperature, T_j, was measured inside the plenum chamber, three diameters below the hole entrance. Wall temperature measurements were made with ribbon-type thermocouples glued to the surface of the adiabatic plate. The thickness of a ribbon thermocouple junction was less than 0.09 mm (which ensured that the surface was aerodynamically smooth) and the junction surface area was 0.4 mm square. These thermocouples were located on the centerline of the central hole at $x/D = 2$, 3, 5, 6, 8, 10, 15, 22, 30, and 50. In addition to the above, four spanwise arrays of thermocouples were located at $x/D = 3$, 6, 10, and 15. Each spanwise array consisted of seven thermocouples equally spaced between $-1.5 \le z/D \le 1.5$, giving the surface temperature (adiabatic wall temperature, T_{aw}) distribution across one hole pitch. The laterally averaged effectivenesses ($\overline{\eta}$) were determined by integrating the measured lateral distribution of η and dividing by the span between holes. This calculation, done using trapezoidal integration was found to be within 1 percent of the result obtained by integrating a Gaussian curve fit through the data. Therefore, in all the results presented in this study, trapezoidal integration was used to calculate $\overline{\eta}$. The spatially averaged effectivenesses ($\overline{\overline{\eta}}$) were determined by integrating $\overline{\eta}$ over $3 \le x/D \le 15$ and dividing by the streamwise distance. As $\overline{\eta}$ followed a very monotonic trend over this streamwise range, $\overline{\overline{\eta}}$ was also calculated using trapezoidal integration.

The thermal field measurements were made with a thermocouple probe with a 50-μm-dia sensor. In order to get full field information about the jet, lateral planes of temperature data were recorded at $x/D = -1.2$, −0.6, 0, 3, 6, 10, 15, and 30. The typical array of measurement positions for a lateral profile

Nomenclature

D = diameter of film cooling hole
DR = density ratio of jet to free stream $= \rho_j/\rho_\infty$
H = shape factor $= \delta_1/\delta_2$
I = momentum flux ratio of jet to free stream $= \rho_j U_j^2/\rho_\infty U_\infty^2$
L = hole length
M = mass flux (blowing) ratio of jet to free stream $= \rho_j U_j/\rho_\infty U_\infty$
P = hole spacing
$\mathrm{Re}_{\delta 2}$ = Reynolds number $= U_\infty \delta_2/\nu$
T = temperature
Tu = free-stream turbulence level
TL = two-dimensional turbulence level $= (u_{\mathrm{rms}}^2 + V_{\mathrm{rms}}^2)^{1/2}/U_\infty$
U = mean velocity, x direction
u_{rms} = rms velocity, x direction
V = mean velocity, y direction
VR = velocity ratio of jet to free stream $= U_j/U_\infty$
v_{rms} = rms velocity, y direction
x = streamwise distance measured from the downstream edge of holes
y = wall normal distance
z = spanwise distance measured from the centerline of holes
δ_1 = displacement thickness
δ_2 = momentum thickness
η = adiabatic wall effectiveness $= (T_{aw} - T_\infty)/(T_j - T_\infty)$
ρ = density
θ = normalized temperature $= (T - T_\infty)/(T_j - T_\infty)$

Subscripts

aw = adiabatic wall
cl = centerline
j = jet
rms = root mean square
∞ = free stream

Superscripts

$-$ = lateral average
$=$ = spatial average

had 15 measurements in the spanwise direction and 12 in the vertical direction, for a total of 180 measurement points. In addition to the above, temperature profiles were measured on the centerline of the jet at x/D = 0.5, 1, 2, 5, 8, 22, and 50, with typically 12 measurement positions in each profile. For these thermal field measurements, the temperature at each measurement position was obtained by using a sample size of 100 points over a duration of 100 ms. While recording the data, the mean temperature at each measurement position was verified to be steady within $\Delta\theta = \pm 0.01$.

A back-scatter LDV system, TSI model 9100-10, was operated as a two-component system for the velocity measurements. The LDV system used a 2W argon ion laser, a 3.75X beam expander, a 450 mm focusing lens, frequency shifters, and TSI 1990 counter signal processors. The LDV was mounted on a traverse system, which allowed travel in three directions with a resolution of 2 μm. The LDV was tilted at an angle of 9 deg to allow measurement of the vertical component of the velocity near the wall. This does not affect measurement of the streamwise component of velocity, but the vertical velocities are 9 deg off the normal to the wall. The velocity data were acquired using a Macintosh II computer with a digital input board, National Instruments model NB-DIO-32F.

Mean streamwise and wall normal components of velocity and turbulence intensities were measured along the jet centerline at x/D = −2, −1.2, −0.6, 0, 0.5, 1, 2, 3, 6, 10, 15, 22, 30, and 50. The locations for these velocity profiles, with a larger concentration near the hole, were chosen to resolve the steep gradients expected near the hole exit. Each profile had 14 or more measurement positions with closer spacing of measurements in regions of high turbulence. Velocity bias correction was applied to the measurements by using the residence time weighting. Titanium dioxide particles generated by using dry

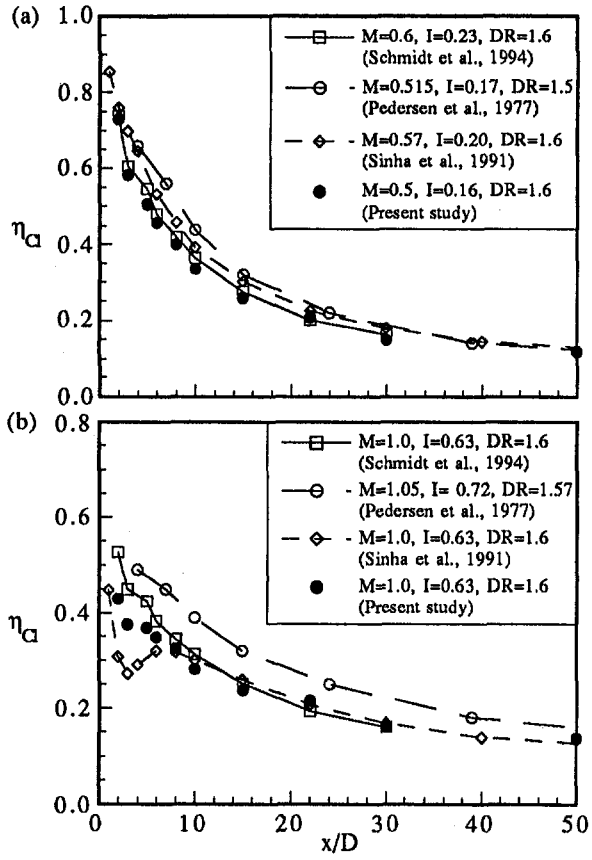

Fig. 3 Comparison of centerline effectiveness for the 35 deg round hole to published data at (*a*) low and (*b*) high momentum flux ratios

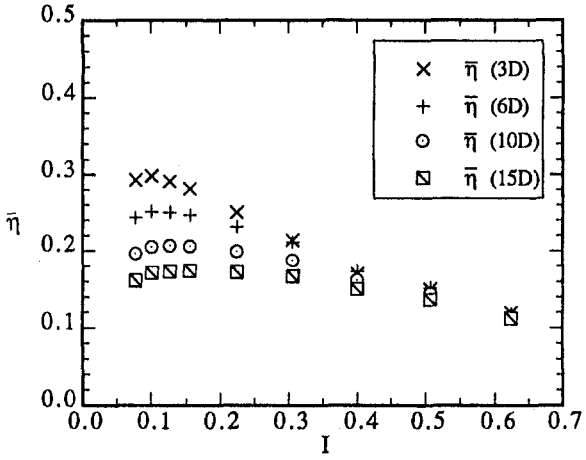

Fig. 4(*a*) Laterally averaged effectiveness at different momentum flux ratios, I, for the 55 deg round hole.

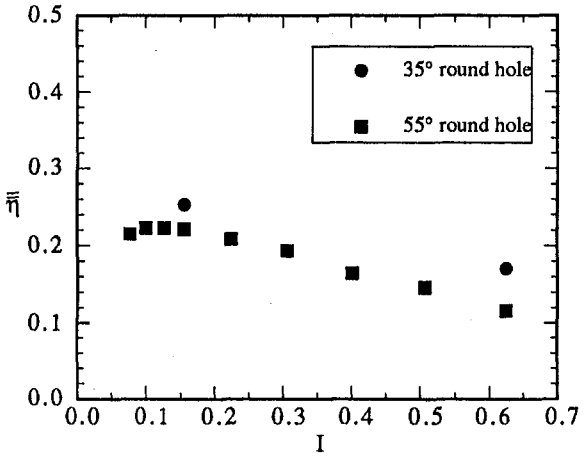

Fig. 4(*b*) Spatially averaged effectiveness over 3 ≤ x/D ≤ 15 for the 55 and 35 deg round holes

particle generators were used as seed for the velocity measurements. To avoid non-uniform seeding, the free-stream and film cooling loops were seeded independently. Details of the design of these dry particle generators can be found from Pietrzyk (1989).

The variation of mean velocity between individual film cooling jets as reported by Pietrzyk et al. (1990) was $\delta U_j = \pm 2.6$ percent. For the experiments conducted in this study, the mass flux ratio for each jet was held constant within $\delta M = \pm 5$ percent. This includes variations in the overall secondary flow loop and variations between individual jet velocities. The variation in density ratio due to changes in the jet and free-stream temperatures was estimated as δDR = ±2.5 percent. The uncertainties in local, laterally averaged, and spatially averaged effectiveness measurements, based on the statistical analysis of a number of previous experiments conducted in our facilities, were $\delta\eta$ = 0.03, $\delta\bar{\eta}$ = 0.03, and $\delta\bar{\bar{\eta}}$ = 0.02, respectively. Repeatability tests were conducted at I = 0.1 in this study, and the variation in local, laterally averaged, and spatially averaged effectiveness obtained from multiple sets and different runs was less than ±0.01. The uncertainty in thermal field results at a nominal value of θ = 0.5 due to variation in the free-stream and jet temperatures, and the uncertainty in the temperature measurement was $\delta\theta = \pm 2.5$ percent. Repeatability tests were used to establish precision uncertainties for the LDV velocity measurements near the wall of ±1 percent for U and V, and ±3 percent for u_{rms} and v_{rms}, where the percentages are based on the free-stream velocity for the mean velocities and the maximum level

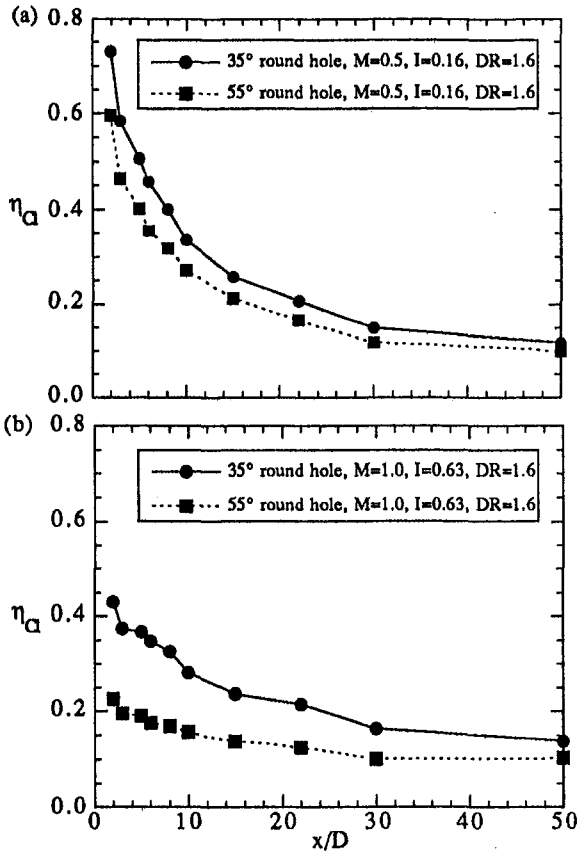

Fig. 5 Comparison of centerline effectiveness for the 35 and 55 deg round holes at (*a*) low and (*b*) high momentum flux ratio

for the rms measurements. Farther away from the wall precision uncertainties were less. The bias errors in the velocity measurements were mainly due to the error in calculating the beam angle, and were estimated to be less than 0.5 percent.

Results and Discussion

As mentioned earlier, in order to allow comparison with data available in literature, centerline effectiveness measurements were made for 35 deg round holes at two momentum flux ratios. In Fig. 3, these results are shown along with those from: Pedersen et al. (1977), Sinha et al. (1991), and Schmidt et al. (1996). For low I as shown in Fig. 3(a), there is good agreement between results of the present study and data from literature. Figure 3(b) shows the results for high I, for which jet lift-off occurs in the near hole region. The present results show some deviation from the data of Pedersen et al. and Sinha et al. near the injection location. This deviation can be attributed to the different length-to-diameter ratio used in these studies. While Pedersen et al. used long tubes for injection, Sinha et al. used a hole length of $L/D = 1.75$.

Effectiveness measurements were made for the 55 deg round holes, at nine momentum flux ratios over the range from I = 0.08 to 0.63 (M = 0.35 to 1.0). Results from these tests are presented in terms of laterally averaged effectiveness in Fig. 4(a). As expected, the peak in lateral effectiveness shifts to higher momentum flux ratios with increasing downstream distance. Figure 4(b) shows variation of the spatially averaged effectiveness with momentum flux ratio for the 55 and 35 deg holes. For the 55 deg holes, the spatially averaged effectiveness stays relatively constant for momentum flux ratios $0.08 \le I \le 0.2$, and decreases for $I > 0.2$. This is similar to results reported by Schmidt et al. (1996) for holes inclined at 35 deg where the spatially averaged effectiveness was relatively constant for $0.1 \le I \le 0.4$ and decreased for $I > 0.4$. This decrease in spatially averaged effectiveness occurs at a lower momentum flux ratio for the 55 deg holes because the jets have a higher trajectory and detach from the wall at lower I compared to the 35 deg holes. At the low momentum flux ratio (I = 0.16), the spatially averaged effectiveness for the 55 deg holes is about 90 percent of that for the 35 deg holes, but at the high momentum flux ratio (I = 0.63) this reduces to 70 percent.

Centerline effectiveness as a function of streamwise distance for the 35 and 55 deg holes at low and high momentum flux ratio are presented in Fig. 5. At I = 0.16, the centerline effectiveness of the 55 deg holes is only slightly inferior to the 35 deg holes, but at I = 0.63 there is a significant reduction in centerline effectiveness for the 55 deg holes. Figure 6 shows results for laterally averaged effectiveness at low and high momentum flux ratios from this study along with data from literature. Note that the data from Pedersen et al. (1977) at similar momentum flux ratios is for 35 deg round holes. Data for both 35 and 55 deg round holes from Foster and Lampard (1980) were available only at the low momentum flux ratio. At both low and high momentum flux ratios, there is good agreement between data for the 35 deg round holes from Pedersen et al. and the present study. At the low momentum flux ratio, while the effectiveness results of Foster and Lampard are much higher, they show a similar decrease in effectiveness at the higher injection angle as indicated by this study. It should be noted that, for M = 1.4 (I = 0.96) Foster and Lampard found the laterally averaged effectiveness for the 55 deg hole to be greater than that of the 35 deg hole. Though such high momentum flux ratios were not investigated in this study, the trend of significantly reduced effectiveness for the higher injection angle at I = 0.63 contradicts the result of Foster and Lampard.

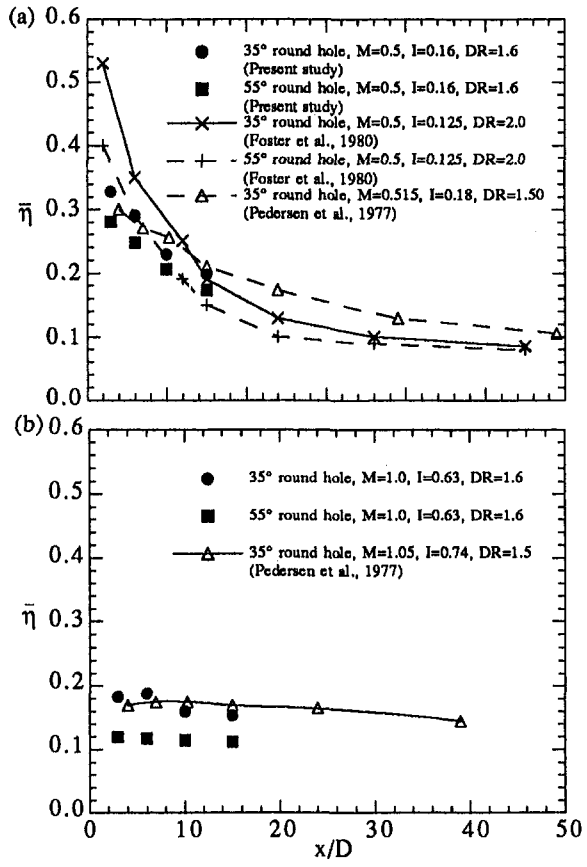

Fig. 6 Comparison of laterally averaged effectiveness for the 35 and 55 deg round holes at (*a*) low and (*b*) high momentum flux ratio

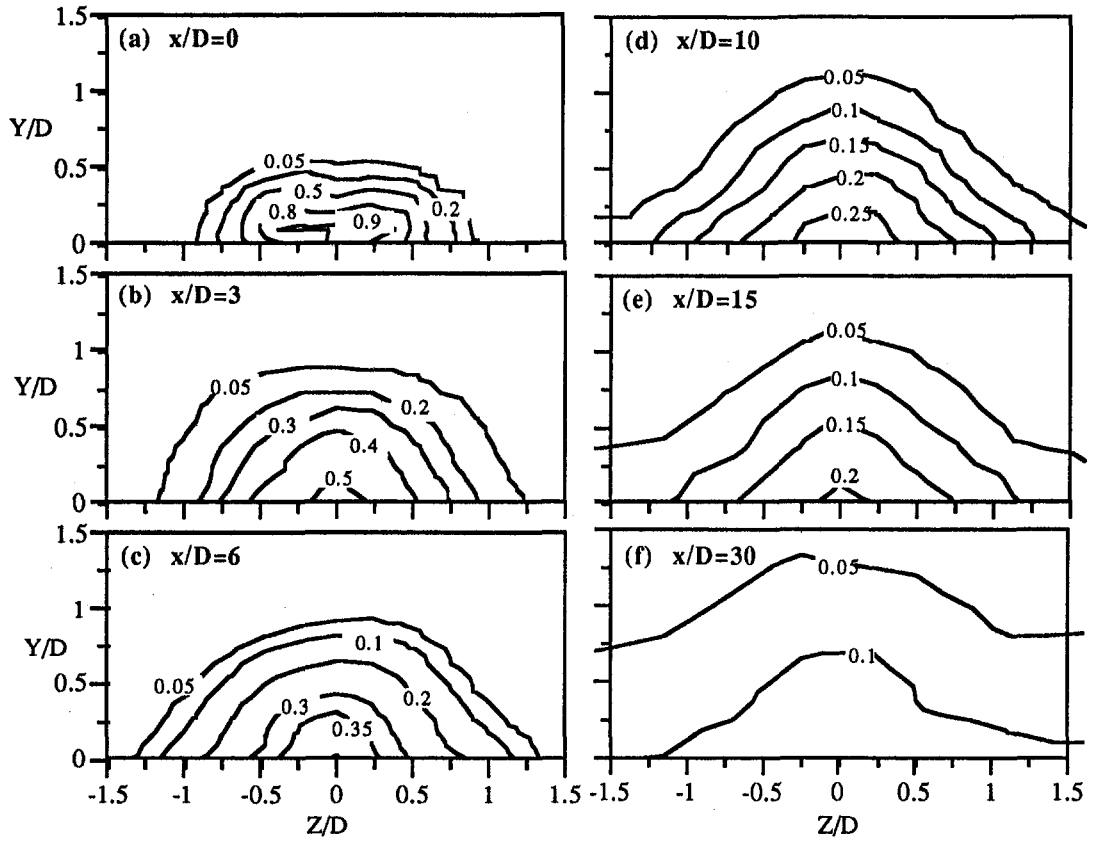

Fig. 7 Lateral temperature contours for the 55 deg round hole at various streamwise locations: M = 0.4, I = 0.1, DR = 1.6

Thermal field measurements for the 55 deg round holes were done at a momentum flux ratio of $I = 0.1$ ($M = 0.4$), which is within the range of maximum spatially averaged effectiveness. Normalized temperature contours, θ, of the film cooling jet in the lateral plane at $x/D = 0$, 3, 6, 10, 15, and 30 are shown in Fig. 7. At $x/D = 0$, the jet is already diffuse because of interaction with the mainstream. This is illustrated by the $\theta = 0.9$ contour, which is limited to a very small region at the core of the jet, and the edge of the jet, which extends well beyond the hole. The reduction in contour levels indicates the drop in effectiveness that occurs as the jet moves downstream. At $x/D = 10$, nonzero values of θ at the half pitch line indicate that the jets from adjacent holes begin to merge.

Figure 8(a) shows the thermal field for the 55 deg holes at the jet centerline near the injection location. The temperature contours over the hole indicate that at this low momentum flux ratio, the jet is pushed toward the trailing edge of the hole by the free stream. The temperature contours for $\theta = 0.7$ curve back near the hole exit, suggesting that there is a slight separation region. The effectiveness of the jet decays rapidly with downstream distance; for example, there are no levels higher than $\theta = 0.6$ beyond $x/D = 2$. For comparison, Fig. 8(b) shows the centerline temperature contours for a 35 deg round hole at a similar momentum flux ratio. The most distinctive difference between the 55 and 35 deg holes is the significantly greater diffusion of the cooling jet near the hole for the 55 deg holes. For example, the centerline θ levels have decreased below $\theta = 0.7$ by $1D$ downstream of the hole for the 55 deg holes, but θ is above $\theta = 0.8$ at this same position for the 35 deg holes. These results are consistent with the centerline effectiveness results, which showed lower values for the 55 deg round hole. Although the 55 deg holes show greater penetration of the cooling jets initially, by $x/D = 5$ the height of the cooling jets is essentially the same for the 55 and 35 deg holes.

Figure 9 shows the mean velocity vectors near and far away from the injection location for the 55 deg round holes at its

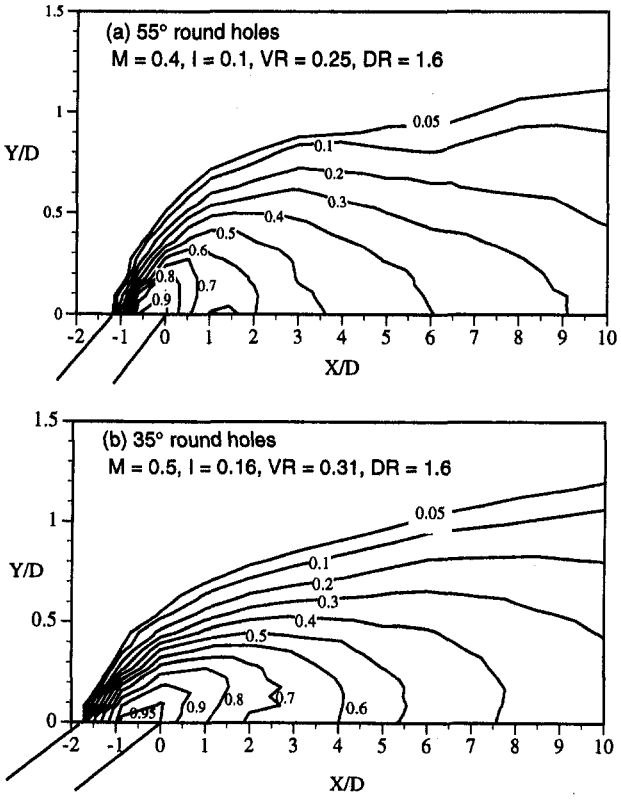

Fig. 8 Centerline temperature contours for the (*a*) 55 deg and (*b*) 35 deg round hole

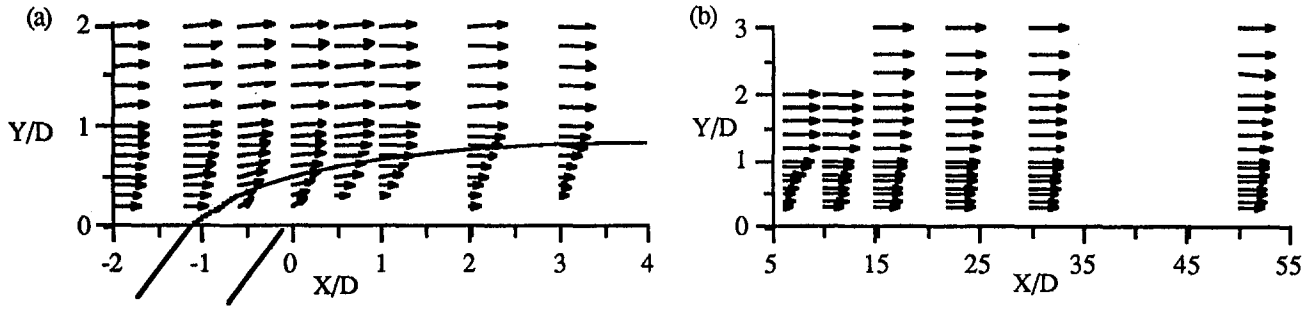

Fig. 9 Mean velocity vectors, (*a*) near and (*b*) away from the injection location for the 55 deg round hole: M = 0.4, I = 0.1, VR = 0.25, DR = 1.6

optimum momentum flux ratio of $I = 0.1$, which corresponds to a blowing ratio of $M = 0.4$ and a velocity ratio of VR = 0.25. The small velocity ratio results in a large shear layer between the jet and mainstream, which is evident in Fig. 9. The edge of the jet indicated in Fig. 9 is based on the thermal field measurements described earlier. There is good agreement between the location of shear layers from velocity data and the edge of the jet from thermal field measurements. Strong shear layers extend from the hole to beyond $x/D = 5$ and generate high turbulence levels (discussed later). The free stream pushes the jet toward the wall, bending the jet over completely by $x/D = 2$, clear from the velocity vectors, which are nearly parallel with the free stream. This behavior of the velocity vectors suggests that there is slight separation region at $x/D \sim 1$. This is consistent with the results of the thermal field measurements as discussed earlier. The sharp gradients between the jet and the free stream are smeared out by $x/D = 10$, and farther downstream the flow slowly relaxes to a boundary layer flow.

The turbulence levels, TL, in terms of percentage of the free-stream velocity, near and away from the injection location are presented in Figs. 10 and 11. These results are compared with those of Pietrzyk et al. (1990) for jets with density ratio of DR = 2, injected through 35 deg round holes at a velocity ratio VR = 0.25. Note that in the results of Pietrzyk et al., the streamwise distance is measured from the upstream edge of the hole. It is clear that qualitatively the turbulence levels are very similar for the two holes. Both show formation of a region with very high turbulence levels generated by the shear layer between the jet and free stream. Over the hole, as shown in Fig. 10, turbulence levels of TL = 14 to 16 percent occurred for the 55 deg hole, while the 35 deg hole shows turbulence levels between TL = 10 to 12 percent. The same trend continues immediately downstream of the hole, where the 55 deg hole shows higher turbulence levels compared to the 35 deg hole. The higher turbulence levels for the 55 deg hole are consistent with a shorter hole length and/or higher trajectory of jets. Away from the injection location, as shown in Fig. 11, a maximum turbulence level of TL = 20 percent occurred with the 55 deg holes as compared to a maximum of TL = 16 percent for the 35 deg holes. The turbulence levels begin to decay beyond $x/D = 6$, which is consistent with the reduction in the sharp velocity gradients between the jet and free stream, as indicated by the mean velocity profiles. The decay of the turbulence levels with downstream distance is very similar for the two angles.

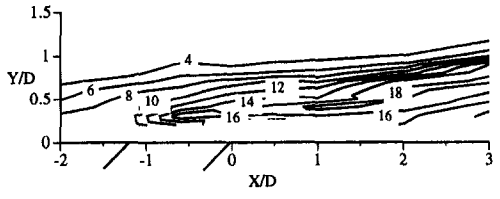

Fig. 10(*a*) Turbulence levels near the injection location for the 55 deg round hole: $M = 0.4$, $I = 0.1$, VR = 0.25, DR = 1.6

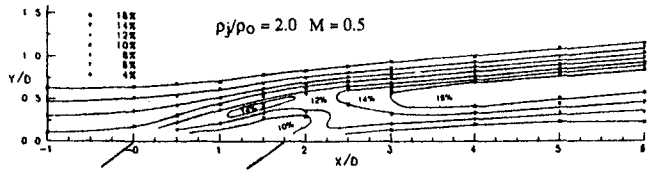

Fig. 10(*b*) Turbulence levels near the injection location for the 35 round hole: $M = 0.5$, $I = 0.125$, VR = 0.25, DR = 2.0 (From Pietrzyk et al., 1990)

Conclusions

Overall the adiabatic film cooling effectiveness with holes inclined at 55 deg is similar to that with holes inclined at 35 deg. Maximum effectiveness for the 55 deg holes occurs at momentum flux ratios of $I \sim 0.1$, which is similar to 35 deg holes. Moreover, the average effectiveness for the 55 deg holes at this low momentum flux ratio is only 10 percent lower than that for the 35 deg holes. Therefore, at low momentum flux ratios, the turbine blade designer has the flexibility to choose injection angles greater than 35 deg, resulting in stronger blades with minimal reduction in the film cooling performance. With increasing momentum flux ratio, however, the average effectiveness decreases more rapidly with the 55 deg holes so that by $I \sim 0.6$ the average effectiveness for the 55 deg holes is 30 percent less than for 35 deg holes.

Thermal field measurements revealed that the 55 deg holes have considerably greater diffusion of the cooling jets near the holes (within $1D$ of the trailing edge of the hole) as compared to the 35 deg holes. This initial greater diffusion appears to be

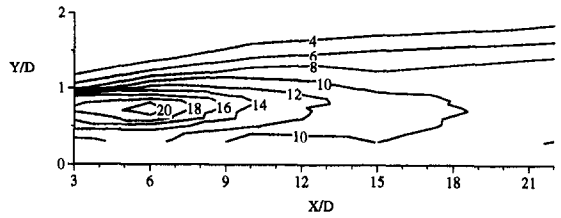

Fig. 11(*a*) Turbulence levels away from the injection location for the 55 deg round hole: $M = 0.4$, $I = 0.1$, VR = 0.25, DR = 1.6

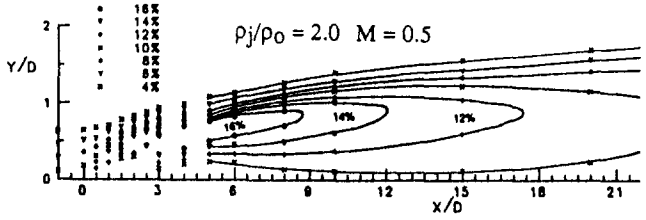

Fig. 11(*b*) Turbulence levels away from the injection location for the 35 deg round hole: $M = 0.5$, $I = 0.125$, VR = 0.25, DR = 2.0 (From Pietrzyk et al. 1990)

the primary cause of the decreased effectiveness for the 55 deg holes. Lateral thermal profiles show the lateral spread of the jets and indicates that the jets spaced $3D$ apart begin to merge by $x/D = 10$ downstream. Turbulence field measurements show higher turbulence levels within and above the hole and immediately downstream for 55 deg holes compared to 35 deg holes. These higher turbulence levels indicate a more vigorous interaction and mixing of the jet with the mainstream, which results in the greater diffusion of the cooling jet.

Acknowledgments

The authors gratefully acknowledge Garrett Engine Division of the Allied-Signal Aerospace Company for support of this research. We would also like to thank Mr. Donald Schmidt and Mr. Basav Sen for providing the thermal field data for the 35 deg round hole, and Mr. Donald Schmidt for his assistance during thermal field measurements.

References

Foster, N. W., and Lampard, D., 1980, "The Flow and Film Cooling Effectiveness Following Injection Through a Row of Holes," ASME *Journal of Engineering for Power,* Vol 102, pp. 584–588.

Pedersen, D. R., Eckert, E. R. G., and Goldstein, R. J., 1977, "Film Cooling With Large Density Differences Between the Mainstream and the Secondary Fluid Measured by the Heat–Mass Transfer Analogy," ASME *Journal of Heat Transfer,* Vol. 99, pp. 620–627.

Pietrzyk, J. R., 1989, "Experimental Study of the Interaction of Dense Jets with a Crossflow for Gas Turbine Applications," Ph. D Thesis, University of Texas at Austin.

Pietrzyk, J. R., Bogard, D. G., and Crawford, M. E., 1990, "Effects of Density Ratio on the Hydrodynamics of Film Cooling," ASME JOURNAL OF TURBOMACHINERY, Vol. 112, pp. 437–443.

Schmidt, D. L., Sen, B., and Bogard, D. G., 1996, "Film Cooling With Compound Angle Holes: Adiabatic Effectiveness," ASME JOURNAL OF TURBOMACHINERY, Vol. 118, pp. 807–813.

Sinha, A. K., Bogard, D. G., and Crawford, M. E., 1991, "Film Cooling Effectiveness Downstream of a Single Row of Holes With Variable Density Ratio," ASME JOURNAL OF TURBOMACHINERY, Vol. 113, pp. 442–449.

Thole, K. A., Sinha, A. K., Bogard, D. G., and Crawford, M. E., 1992, "Mean Temperature Measurements of Jets With a Crossflow for Gas Turbine Film Cooling Application," in: *Rotating Machinery Transport Phenomena,* J. H. Kim and W. J. Yang, eds., Hemisphere Pub. Corp., New York.

Effects of Free-Stream Turbulence on the Instantaneous Heat Transfer in a Wall Jet Flow

S. Yavuzkurt
Associate Professor,
Department of Mechanical Engineering,
Center for Gas Turbines and Power,
The Pennsylvania State University,
University Park, PA 16802

This is a preliminary study in order to understand how free-stream turbulence increases heat transfer. Effects of free-stream turbulence on instantaneous heat transfer were investigated in a wall jet flow. Heat transfer traces obtained by a hot-film probe flush-mounted with the surface showed an intermittent structure with definite peaks at certain time intervals. The number of peaks per unit time increased with increasing turbulence intensity. A wall jet test rig was designed and built. The initial thickness and the velocity of the wall jet were 10 cm and 24.4 m/s, respectively. The hot-film probe, which was flush with the surfaces, was positioned at 10 cm intervals on the surface in the flow direction. The profiles of mean velocity and axial component of the Reynolds stress were measured with a horizontal hot-wire probe. Space correlation coefficients for u' and q' were obtained in the vertical direction to the wall. This paper concentrates on the effects of turbulence level on instantaneous heat transfer at the wall. It is speculated that the intermittent structures of the heat transfer traces are related to burst phenomena and increase in heat transfer is due to increased ejections (bursts) at the wall with increasing turbulence levels.

Introduction

Free-stream turbulence (FST) is the turbulence in the approach stream. It is experienced in many applications. For example, nozzle guide vanes and the rotor blades in a gas turbine are exposed to high levels of FST.

FST has an important influence on surface heat transfer. Under high levels of turbulence (10–20 percent), there is an appreciable increase in the heat transfer rate regardless of the character of the boundary layer.

Some representative results in this area can be found in the studies by Kestin (1966), Kearney et al. (1970), Brown and Burton (1978), Bradshaw and Simonich (1978), and Blair (1983). A detailed review of this literature is given by Moffat and turbulence levels up to 10 percent cause a proportional increase in heat transfer for constant velocity and accelerating turbulent boundary layers. It is indicated that large effects on the average values may result if the turbulence affects the location of the transition and if the heat transfer data are compared at constant x-Reynolds number, i.e., at the same axial location for constant free-stream velocity.

One of the important observations from the literature in this area is that under the same levels of turbulence, different researchers found different enhancement of heat transfer rates. This leads to the speculation that not only the velocity scale but also the length scale of the turbulence is important. In fact, Moffat and Maciejewski (1984) relate to this fact and suggest that the effect of the length scale should be investigated.

Most of the studies used, one way or another, grid-generated turbulence in their experiments where the length and velocity scales are usually small. More recently, the flow fields of jets and wall jets have been used in order to simulate high free-stream turbulence encountered in turbomachinery. Moffat and Maciejewski (1985) used a circular wall jet in order to obtain free-stream turbulence intensities up to 48 percent. They measured Stanton numbers as much as 350 percent above the standard values for zero free-stream velocity gradient turbulent boundary layer correlations. Ames and Moffat (1990) have investigated the effects of free-stream turbulence created by 6.4-cm-dia jet injection into a main flow in a plenum chamber followed by a wind tunnel test section on the heat transfer to a flat plate boundary layer. This study used autocorrelations to measure the length scales. In another recent study, MacMullin et al. (1989) investigated the effects of free-stream turbulence from a circular wall jet on a flat plate boundary layer heat and momentum transfer with turbulence intensities 7–18 percent. They also observed increased Stanton numbers and skin friction coefficient with increasing turbulence intensities. They used autocorrelations for the determination of length scales. The influence of length scale on the Stanton numbers was not conclusive. Rivir et al. (1992) studied the heat transfer in a two-dimensional planar wall jet up to FST intensities of 20 percent and observed up to 100 percent increases in heat transfer compared to standard correlations. However, no general correlation could be found that would represent the data from all these studies.

The present belief of the author is that the length scales in the cross-stream direction to the wall and in the transverse (cross-span) direction to the flow are more important in determining the scales within the boundary layer which affect the heat transfer. Yavuzkurt (1990, 1993) carried out experiments on the experimental setup used by Ames and Moffat (1990). In these experiments length scales of turbulence were measured in all three coordinate directions, both in the free stream and within the boundary layer using two triple hot-wire probes. An FST number was defined using all the velocity and length scales of the normal stresses in the free stream normalized by the boundary layer thickness and free-stream velocity. This quantity correlated the heat transfer data very well.

A detailed discussion on the free-stream turbulence distortion for flows approaching stagnation and its effects on heat transfer can be found from Tafti (1989). It was seen from these investigations that there is a need to understand the fundamental mechanisms through which FST affects heat transfer. A fundamental study of near-wall layers of the flow under the effects of FST might be helpful in clarifying these issues.

Contributed by the International Gas Turbine Institute and presented at the 40th International Gas Turbine and Aeroengine Congress and Exhibition, Houston, Texas, June 5–8, 1995. Manuscript received by the International Gas Turbine Institute February 5, 1995. Paper No. 95-GT-43. Associate Technical Editor: C. J. Russo.

Research on structure of turbulent flows has shown that they contain considerable structure. The presence of near-wall "streaks" and "bursts" is well documented. These are the structures that are found in the viscous sublayer and that differentiate turbulent flows from laminar flows. One means of investigating the flow structures is called "quadrant analysis" (Wallace et al., 1972; Willmarth and Lu, 1972). The technique involves partitioning the flow signal into four quadrants based on the instantaneous signs of the fluctuating velocity components u' and v'. As explained by Volino and Simon (1994), in a boundary layer type flow when the wall is heated, a turbulent parcel of fluid moving away from the wall ($v' > 0$) would most likely be of relatively low velocity ($u' < 0$) and high temperature ($t' > 0$). Such a motion would be classified as a "hot ejection." The present author's opinion is that this hot ejection is related to the burst phenomena and will increase the heat transfer at the wall. Therefore, there is a strong correlation between the instantaneous increase in heat transfer and ejections. It is postulated that FST leads to increases in ejection events at the wall thereby increasing the heat transfer. The main objective of this research is to test this hypothesis. The preliminary indications of this fact will be discussed in this paper.

Experimental Procedures

The experiments were carried out in a wall-jet flow as shown in Fig. 1. The rationale in using wall-jet flows for FST is explained by Moffat and Maciejewski (1985), MacMullin et al. (1989), and River et al. (1992). A centrifugal blower with a flow rate of 2000 scfm is connected to a transition section containing a honeycomb. Honeycomb was used to even out the disturbances in the blower flow. Even with these precautions, the inlet velocity profile was only flat up to 6 cm from the bottom wall. From 6 to 10 cm there was a 10 percent increase in the inlet mean velocity profile. The spanwise uniformity was measured. The mean velocity profiles were within 2–3 percent of each other at ±5 cm from the centerline. The turbulence level at the inlet was 5 percent. A sheet metal nozzle was built with an exit 10 cm high and 30 cm wide, giving it an aspect ratio of 3. The initial jet velocity at the centerline was about 24.4 m/s. To the nozzle exit a test section made of plexiglass was attached. The test surface was 1.8 m long and 30 cm wide. The side walls were 30 cm in height in order to prevent external disturbances. The top of the test section was open to facilitate a wall-jet flow. However, a top wall was also built to be used later for boundary layer type flows.

The velocity data were taken with a TSI 1210-T1.5 horizontal hot-wire probe. A universal traverse mechanism was built, which allowed the probe to be moved in the "y" and the "z" directions. The probe can also be moved in the "x" (axial) direction with a slider mechanism riding on the side wall of the test section. The slider mechanism was 1 ft high from the test surface and did not effect the flow. A TSI 1237 hot-film probe flush-mounted on the surface was used to measure instantaneous heat transfer, to identify the ejections of turbulent fluid from the wall. Constant-temperature hot-film operates on the same principle as the hot wire. It responds to heat transfer from its surface. Therefore, with a simple analysis it can be shown that the instantaneous heat transfer can be related to fluctuating and mean voltage output of the anemometer. In fact, the ratios of fluctuating (q') and time-averaged ($\overline{Q}$) heat transfer rates $q'/\overline{Q} = (2e'E + e'^2 - \overline{e'^2})/(E^2 + \overline{e'^2})$ where E and e' are the time-averaged and fluctuating voltage outputs of the constant-temperature anemometer. The test surface had 1.27 cm holes located at 10 cm centers for the positioning of the plug that held the hot-film probe. The hot-wire and hot-film probes were connected to a TSI IFA 100 flow analyzer operating in constant-temperature anemometry mode. The hot-wire probes were calibrated using a 486 computer and a calibration program utilizing modified King's law. The same computer was also used for data acquisition and partial data reduction. A DT2829, 8-channel simultaneous A/D board with 30 kHz response for each channel was used as an interface between the analog signals and the computer. The 486 computer calculated the instantaneous values of streamwise velocity u' for both hot-wire probes and also a value proportional to q' (instantaneous heat flux rate) for the hot-film probe. These quantities were stored on magnetic disks and later were ana-

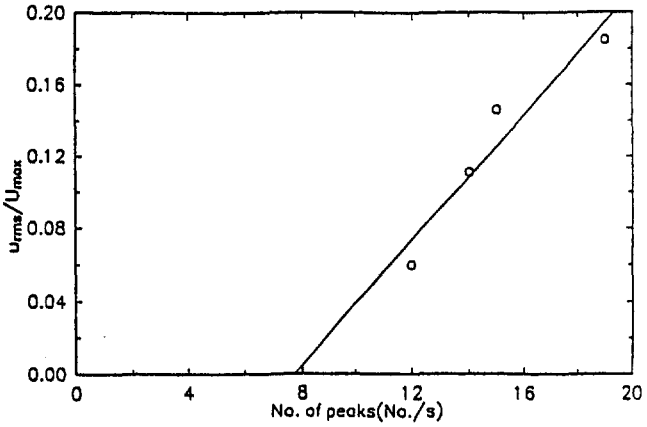

Fig. 2 Increase in the number of peaks per unit time in the instantaneous heat transfer as a function of turbulence intensity

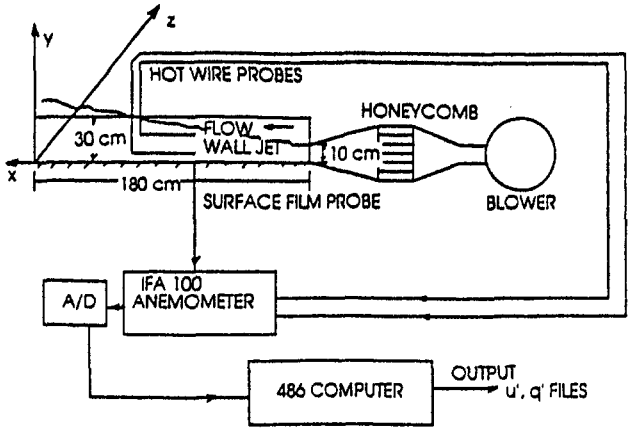

Fig. 1 Wall jet test rig and data acquisition system

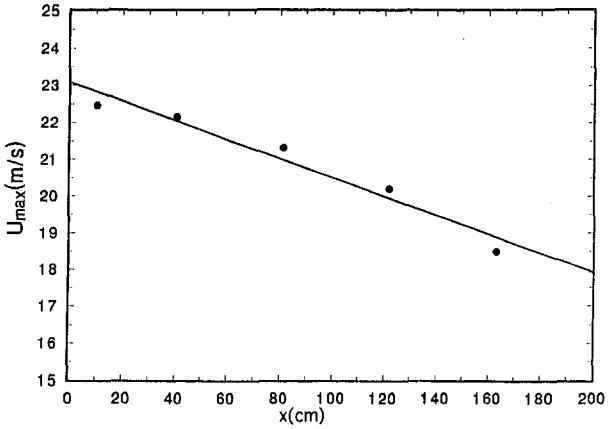

Fig. 3 Maximum velocity in the wall jet as a function of axial distance

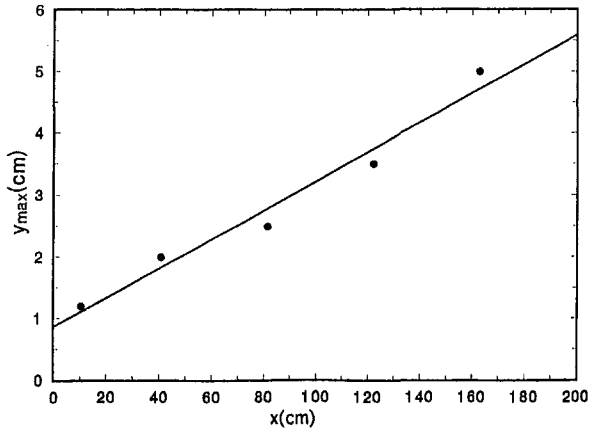

Fig. 4 Location of maximum velocity in the wall jet as a function of axial distance

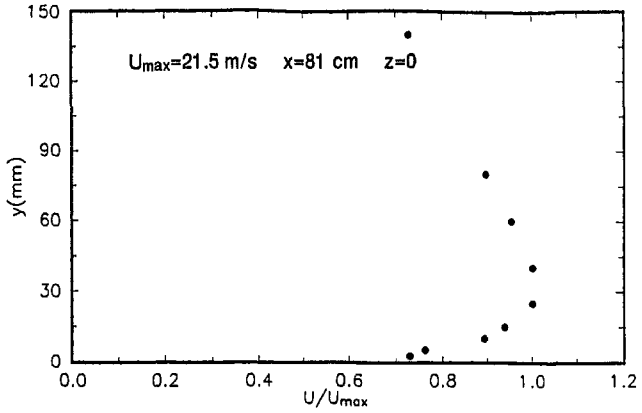

Fig. 6 Dimensionless mean velocity profile of developed wall jet

lyzed with a main frame computer to obtain, mean velocities, rms values of u', and autocorrelations of u' and q'. The u' and q' space correlation was defined as follows:

Space correlation of u' and q' in the y direction

$$R_{uq} = \frac{\overline{u'(x, \Delta y, 0, t)q'(x, 0, 0, t)}}{\sqrt{\overline{u'^2}\,\overline{q'^2}}}$$

The data were taken at 4000 Hz with a sample size of 40,960 points, resulting in 10.2 seconds of real time data for all quantities measured at every measurement location. The measurements were made under isothermal conditions. Uncertainties in the measurements were calculated following the procedure described by Yavuzkurt (1984). They were 1 percent for mean velocity, 1.5 percent for u_{rms}, and about 5 percent for the correlations except very near the wall ($y \simeq$ for 2.5 mm) when the probe is in contact with the wall.

Results and Discussion

The main goal was to show that the number of ejections as indicated by the peaks in the instantaneous heat transfer rate increases as the FST increases. This goal was partly achieved. Figure 2 shows the axial Reynolds stress normalized by maximum value of the mean velocity defined as turbulence intensity at the y location at which the maximum mean velocity occurs (y_{max}) as a function of number of peaks per unit time in the instantaneous heat transfer traces, obtained from the hot-film probe. The peaks in the instantaneous q traces will be discussed later. This figure shows that as hypothesized, there is a definite increase in the number of peaks with increasing FST level.

Figures 3 and 4 show important mean parameters of the wall jet. As expected, the maximum mean velocity decreases linearly and the y_{max} (location at which the maximum mean velocity occurs) increases linearly in the axial direction. The axial distance was measured from the end of the nozzle or the start of the test section. These figures indicate the presence of a well-behaved wall jet (Launder, 1983). However, the objective of this study is not to explore a wall jet and its properties, but rather to use the wall jet flow as a source of high free-stream turbulence.

Figure 5 shows instantaneous traces of q' at the wall (y = 0) indicated by the hot-film probe as a function of time. The values of q' were normalized with the mean value of the heat transfer rate Q. The traces are shown at two axial stations of

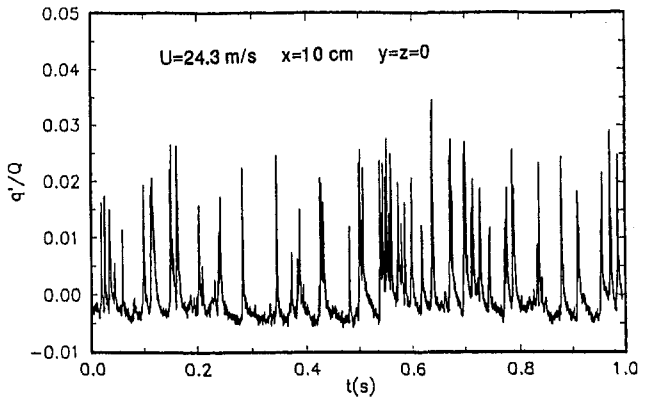

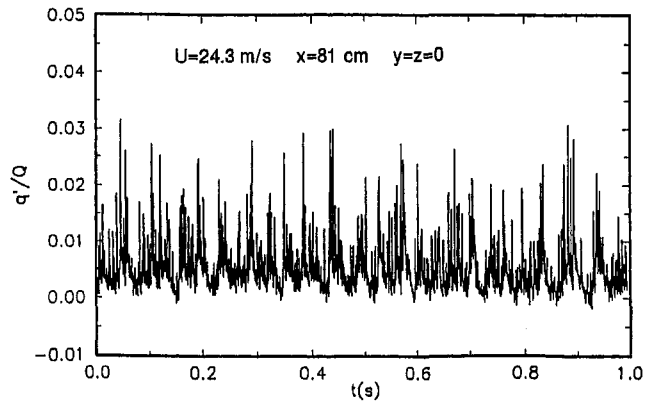

Fig. 5 Dimensionless fluctuating heat transfer rate as a function of time at two axial locations

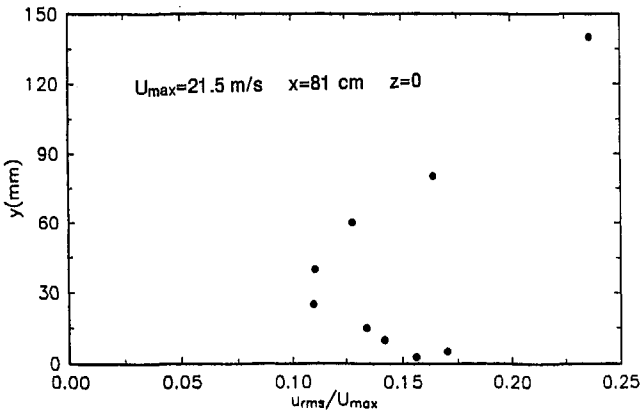

Fig. 7 Dimensionless axial Reynolds stress profile in the wall jet

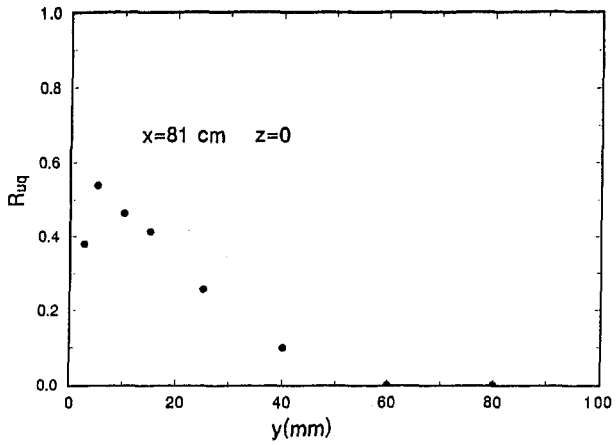

Fig. 8 Space correlation coefficient of u' and q' at X = 81 cm in the wall jet

10 cm and 81 cm along the centerline ($z = 0$) of the test surface as examples. As can be seen, there are definite peaks in heat transfer traces. It was suggested that these peaks were related to ejections that are associated with a burst event (Clark et al., 1992; Volina and Simon, 1994). In calculating number of peaks per unit time, the signals were conditioned in order to reduce the uncertainty such that values of $q'/Q < 0.02$ were discarded. The value 0.02 was determined by looking at the figures and choosing the highest peaks. Then the number of peaks per second were calculated for time intervals of 1 s, 2 s, 3 s, up to 10 s. It was seen that in all axial locations number of peaks per unit time reached a constant within a 10 s time interval, meaning number of peaks counted was the same for 9 s and 10 s intervals. Similar results are obtained if the signal is conditioned such that values of $q'/Q < 0.01$ were rejected but the number of peaks considered increased accordingly.

Figure 6 shows a normalized mean velocity profile at $x = 81$ cm as an example. After some initial nonuniformities the profiles take a well-known shape (Launder, 1983) for a wall jet and the maximum in the mean velocity near the wall starts becoming noticeable at this location.

Figure 7 shows a typical normalized turbulence intensity profile at $x = 81$ cm. The turbulence intensity far away from the wall at about $y = 100$ mm is high due to high shear between the outer edges of the wall jet and the surrounding stationary air. However, the intensity, which is defined as the intensity of FST at $y = y_{max}$, increased from 5 to 18 percent from $x = 40.6$ cm to $x = 163$ cm. This is the intensity used in plotting Fig. 2.

Figure 8 gives an example of the space correlation of u' and q' at $x = 81$ cm. As can be seen from this figure the values of R_{uq} near $y = 0$ are quite high; they are in the order of 0.5 in the developed wall jet. The drop very near the wall ($y = 2.5$ mm) is due to probe interference with the flow, since at this position the probe touches the wall. It is apparent from this figure that the effect of fluctuations far from the wall (at $y \simeq 60$ mm for a 100 mm initial wall jet height) is felt at the wall, indicating high levels of FST strongly influence the events near the wall. The value of correlation at $y = y_{max} = 25$ mm for this axial location is 0.22.

Conclusions

- Experiments were carried out in a wall jet to explore the effects of high FST on the instantaneous heat transfer at the wall.
- It was found that number of ejections identified by the number of peaks in the instantaneous q' traces increases as the FST intensity increases.
- Space correlation between u' and q' in the vertical direction shows that the effects of fluctuations as far as 60 mm from the wall are felt at the wall, suggesting that one of the mechanisms through which FST affects heat transfer is its long length scales in the cross-stream direction.

Future Work

The work here is by no means complete. The large amount of data stored in disks will be analyzed further in order to explore the relationship between the length scales of FST and the burst phenomena. The same experiments will be repeated using two triple probes for the measurement of length scales of u', v', and w' components in all three coordinate directions. It is possible that v' and w' components of FST have more important effects on the events near the wall. Variable-Interval Time Averaging (VITA) techniques such as explained by Bogard and Tiederman (1986) will also be used to identify the burst events. Results of this technique will be compared with the results obtained from the peak counting technique used here.

Acknowledgments

The author expresses his deep appreciation to AFOSR Summer Faculty Research Program for supplying this opportunity to carry out this research at WPAFB. His sincere thanks go to Dr. Richard Rivir of WL/POTC, WPAFB for his help and guidance during this research. Last but not least, the cooperation of Greg Cala, David Pestian, and John Schmoll is greatly appreciated; their help made it possible to get so many results in a two month period.

References

Ames, A. E., and Moffat, R. J., 1990, "Heat Transfer With High Intensity, Large Scale Turbulence: The Flat Plate Turbulent Boundary Layer and Cylindrical Stagnation Point," Report No. HMT-44, Mech. Engr. Dept., Stanford University, CA.

Blair, M. F., 1983, "Influence of Free Stream Turbulence on Turbulent Boundary Layer Heat Transfer: Parts I and II," ASME *Journal of Heat Transfer*, Vol. 105.

Bogard, D. G., and Tiederman, W. G., 1986, "Burst Detection With Single-Point Velocity Measurements," *J. Fluid Mech.*, Vol. 169, pp. 389–413.

Bradshaw, P., and Simonich, P., 1978, "Effect of Free Stream Turbulence on Heat Transfer Through a Turbulent Boundary Layer," ASME *Journal of Heat Transfer*, Vol. 100, No. 4.

Brown, A., and Burton, R. C., 1978, "The Effects of Free Stream Turbulence Intensity and Velocity Distribution on Heat Transfer to Curved Surfaces," ASME *Journal of Engineering for Power*, Vol. 100, pp. 159–168.

Clark, J. P., LaGraff, J. E., Magari, P. J., and Jones, T. V., 1992, "Measurement of Turbulent Spots and Intermittency Modelling at Gas Turbine Conditions," *Proc. 80th Symp. of NATO/AGARD, Propulsion and Energetics Panel, Heat Transfer and Cooling in Gas Turbines*, Antalya, Turkey, Oct. 12–16.

Kearney, D. W., Kays, W. M., and Moffat, R. J., 1970, "The Effect of Free Stream Turbulence on Heat Transfer to a Strongly Accelerated Turbulent Boundary Layer," *Proc. 1970 Heat Transfer and Fluid Mechanics Institute*, T. Sarpkaya, ed.

Kestin, J., 1966, "The Effect of Free Stream Turbulence on Heat Transfer Rates," *Advances in Heat Transfer*, Vol. 3, Academic Press.

Launder, B. E., 1983, "The Turbulent Wall Jet—Measurements and Modeling," *Ann. Rev. Fluid Mech.*, pp. 429–459.

MacMullin, R., Elrod, W., and Rivir, R., 1989, "Free Stream Turbulence From a Circular Wall Jet on a Flat Plate Heat Transfer and Boundary Layer Flow," ASME JOURNAL OF TURBOMACHINERY, Vol. 111, pp. 78–86.

Moffat, R. J., and Maciejewski, P. K., 1984, "Effects of Very High Turbulence on Convective Heat Transfer," *Proc. HOST Conference*, NASA Conference Publication 2339, NASA Lerc, pp. 381–388.

Moffat, R. J., and Maciejewski, P. K., 1985, "Heat Transfer With Very High Free Stream Turbulence," *Proc. HOST Conference*, NASA Conference Publication 2405, NASA Lerc, pp. 203–215.

Rivir, R. B., Troha, W. T., Eckele, W. A., and Schmoll, W. J., 1992, "Heat Transfer in High Turbulence Flows—A 2D Planar Wall Jet," *Proc. NATO/AGARD 80th Symposium of the Propulsion and Energetics Panel*, Antalya, Turkey, Oct. 12–16.

Tafti, D., 1989, "Prediction of Heat Transfer Characteristics for Discrete Hole Film Cooling on Flat Plate and Turbine Blades," Ph.D. Dissertation, Penn State University, Department of Mechanical Engineering.

Volino, R. J., and Simon, T. W., 1994, "An Application of Octant Analysis to Turbulent and Transitional Flow Data," ASME JOURNAL OF TURBOMACHINERY, Vol. 116, pp. 752–758.

Wallace, J. M., Eckelmann, H., and Brodkey, R. S., 1972, "The Wall Region in Turbulent Shear Flow," *J. Fluid Mech.,* Vol. 54, part 1, pp. 39–48.

Willmarth, W. W., and Lu, S. S., 1972, "Structure of the Reynolds Stress Near the Wall," *J. Fluid Mech.,* Vol. 55, part 1, pp. 65–92.

Yavuzkurt, S., 1984, "A Guide to Uncertainty Analysis of Hot-Wire Data," ASME *Journal of Fluids Engineering,* Vol. 106, pp. 181–186.

Yavuzkurt, S., 1990, "Characterization of Length and Velocity Scales of Free Stream Turbulence and Investigation of their Effects on Surface Heat Transfer," Center for Turbulence Research, Stanford University, Annual Research Briefs 1990, pp. 253–262.

Yavuzkurt, S., and Batchelder, X. X., 1993, "A Correlation for Heat Transfer Under High Free Stream Turbulence Conditions," *Proc. 9th Symposium on Turbulent Shear Flows,* Kyoto, Japan, Aug. 10–18.

Flow and Heat Transfer in a Preswirl Rotor–Stator System

M. Wilson

R. Pilbrow

J. M. Owen

School of Mechanical Engineering,
University of Bath,
Bath, United Kingdom

Conditions in the internal-air system of a high-pressure turbine stage are modeled using a rig comprising an outer preswirl chamber separated by a seal from an inner rotor–stator system. Preswirl nozzles in the stator supply the "blade-cooling" air, which leaves the system via holes in the rotor, and disk-cooling air enters at the center of the system and leaves through clearances in the peripheral seals. The experimental rig is instrumented with thermocouples, fluxmeters, pitot tubes, and pressure taps, enabling temperatures, heat fluxes, velocities, and pressures to be measured at a number of radial locations. For rotational Reynolds numbers of $Re_\phi \simeq 1.2 \times 10^6$*, the swirl ratio and the ratios of disk-cooling and blade-cooling flow rates are chosen to be representative of those found inside gas turbines. Measured radial distributions of velocity, temperature, and Nusselt number are compared with computations obtained from an axisymmetric elliptic solver, featuring a low-Reynolds-number* $k-\epsilon$ *turbulence model. For the inner rotor–stator system, the computed core temperatures and velocities are in good agreement with measured values, but the Nusselt numbers are underpredicted. For the outer preswirl chamber, it was possible to make comparisons between the measured and computed values for cooling-air temperatures but not for the Nusselt numbers. As expected, the temperature of the blade-cooling air decreases as the inlet swirl ratio increases, but the computed air temperatures are significantly lower than the measured ones. Overall, the results give valuable insight into some of the heat transfer characteristics of this complex system.*

1 Introduction

In many gas turbines, the high-pressure blade-cooling air is supplied through preswirl nozzles, as illustrated in Fig. 1. The stationary nozzles swirl the cooling air up to a speed close to that of the rotating blade-cooling entry holes, thereby reducing the air temperature relative to the blades. The cooling air swirls across the wheel-space into the entry holes at the roots of the blades and then flows radially outward through the internal blade-cooling passages.

This internal-air system is sometimes referred to as the blade-cooling-air transfer system. In some "direct-transfer systems," as shown in Fig. 1, the preswirl nozzles are located at a similar radius to the blade-cooling entry holes in the rotor. In "cover-plate systems," the preswirl nozzles are located at a smaller radius, and the air flows radially outward in the clearance between the turbine disk and a cover plate attached to it.

In addition to the preswirl air, disk-cooling air enters near the center of the wheel-space and flows radially outward over the turbine disk, removing heat generated by windage and heat conducted into the disk from the turbine blades. Cooling air leaves the wheel-space via the rim seal preventing, or at least reducing, the ingress of hot mainstream gas. There are therefore two air inlets (for the disk-cooling and preswirl flows) and two outlets (for the sealing and blade-cooling flows).

The designer of a direct-transfer system could specify that the mass flow rate of the disk-cooling air, $\dot{m}_d$, equals that of the sealing air, $\dot{m}_s$, and that the mass flow rate of the preswirl air, $\dot{m}_p$, equals that of the blade-cooling air, $\dot{m}_b$. The designer could not, however, guarantee that disk-cooling air (and perhaps ingested mainstream gas) does not end up in the blade-cooling passages or that some of the preswirl air does not pass through the rim seals. The temperature and destination of the cooling air, and the heat transfer between the air and the disk, depend on the thermal boundary conditions and on the turbulent flow processes that occur inside the wheel-space.

The essential features of this complex flow can be modeled, computationally and experimentally, by using a simple rotor–stator system in which plane rotating and stationary disks are used to represent the more complex geometries that occur inside a gas turbine. Heat transfer in rotor–stator systems without preswirl flow has been studied extensively (see, for example, Owen and Rogers, 1989; Dibelius and Heinen, 1990; Bunker et al., 1992a, b; Chen et al., 1994). Some attention has also been paid to the preswirl system: Meierhofer and Franklin (1981) measured the performance of an engine preswirl system, El-Oun and Owen (1989) produced a simple theoretical model to determine the blade-cooling air temperature for an adiabatic system, Staub (1992) made thermal measurements in a model of a turbine wheel-space, and Chen et al. (1993a, b) used both axisymmetric and three-dimensional (3D) elliptic solvers to study the flow and heat transfer in rotor–stator systems, with and without preswirl flow. An important finding by Chen et al. was that the axisymmetric code appeared to reproduce many of the important features of the computed 3D flow structure.

For an adiabatic rotor–stator system, where heat transfer is negligible, El-Oun and Owen (1989) used the Reynolds analogy (see Owen and Rogers, 1989) to estimate the temperature difference between the preswirl air and the blade-cooling air. In their "unmixed theory," the disk-cooling air does not mix with the preswirl air; and, if the total temperature of the preswirl air, $T_{p,T}$, is known, the theory predicts the total temperature of the blade-cooling air, $T_{b,T}$. In gas turbines, and in the experiments described below, mixing and heat transfer can cause a significant increase in $T_{b,T}$: the authors took account of this in their "mixed theory." The "unmixed theory" of El-Oun and Owen for an adiabatic system, where heat transfer is negligible, gives

Contributed by the International Gas Turbine Institute and presented at the 40th International Gas Turbine and Aeroengine Congress and Exhibition, Houston, Texas, June 5–8, 1995. Manuscript received by the International Gas Turbine Institute February 27, 1995. Paper No. 95-GT-239. Associate Technical Editor: C. J. Russo.

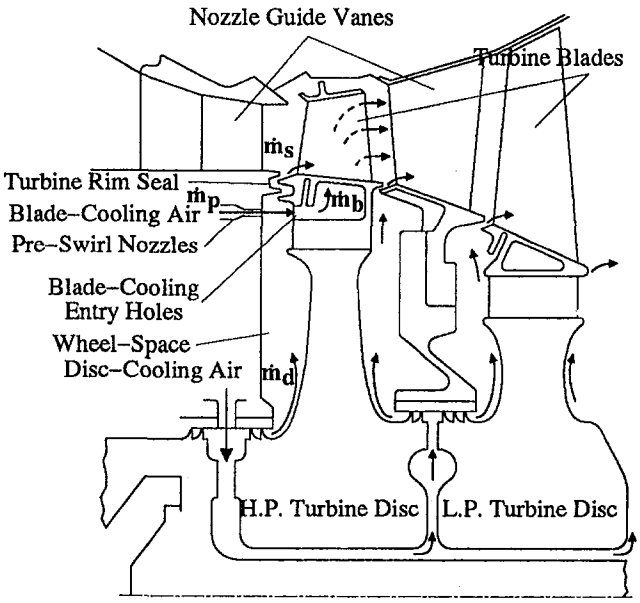

Fig. 1 Typical internal-air system for an industrial gas turbine

$$\frac{C_p(T_{b,T} - T_{p,T})}{1/2\Omega^2 r_p^2} = R(1 - S_r)^2 - S_r^2 \qquad (1.1)$$

where S_r is the swirl ratio and R is the recovery factor, which can be estimated from

$$R = \mathrm{Pr}^{1/3} \qquad (1.2)$$

where Pr is the Prandtl number of the air. It follows that $T_{b,T} \leq T_{p,T}$ when

$$S_r \geq (1 + R^{-1/2})^{-1} \qquad (1.3)$$

For example, for Pr = 0.71, $T_{b,T} \leq T_{p,T}$ when $S_r \geq 0.49$. The air temperatures measured by El-Oun and Owen were in mainly good agreement with the "unmixed theory" for the case of a preswirl system with a radial inflow of disk-cooling air (where mixing between the two flows does not occur) and with the "mixed theory" for the case where there was a radial outflow (where mixing does occur).

The turbine designer needs to calculate the heat transfer from the rotating and stationary surfaces to the cooling air and to estimate the temperature of the air that enters the blade-cooling holes. The use of separate preswirl nozzles in the stator and discrete blade-cooling holes in the rotor makes the resulting flow three dimensional and unsteady. The axisymmetric, steady computations described below were carried out to provide insight into the complicated turbulent mixing between the superposed flows and to assess the effects of modeling simplifications. Future work, using 3D time-dependent codes, may be necessary to identify limitations of the relatively fast axisymmetric procedures for design applications.

In the work described below, heat transfer measurements are made in a preswirl rotor–stator rig, similar to the "adiabatic rig" used by El-Oun and Owen, and the measurements are compared with computations obtained from an axisymmetric elliptic solver. The experimental rig and instrumentation are described in Section 2, free-disk heat transfer tests in Section 3, the computational method in Section 4, and comparisons between measurements and computations in Section 5.

2 Experimental Apparatus

2.1 Operating Range. For rotating-disk systems, the magnitude of the turbulent flow parameter, λ_T (where $\lambda_T = C_{w,d}\mathrm{Re}_\phi^{-0.8}$, $C_{w,d}$ being the nondimensional disk-cooling flow rate and Re_ϕ the rotational Reynolds number), has a strong influence on the flow structure. A value of $\lambda_T = 0.22$ is associated with the free-disk entrainment rate (that is, the flow rate entrained by a disk rotating in a quiescent environment), and for most engine applications, λ_T and Re_ϕ are of the order of 10^{-1} and 10^7, respectively. In typical turbines, the ratio of the nondimensional disk-cooling to blade-cooling flows ($C_{w,d}/C_{w,b}$) is of the order of 10^{-1}, the nondimensional preswirl and blade-cooling flows are approximately equal ($C_{w,p} \simeq C_{w,b}$), and the swirl ratio, S_r, is approximately unity. For the rig described below, the maximum value of Re_ϕ was around 2×10^6, and the values of λ_T and the ratios of flow rates were chosen to match those found in turbines.

Axisymmetric computations, using the method described in Section 4, have shown that the flow structures computed at

Nomenclature

a = inner radius of disk
b = outer radius of disk
C_p = specific heat at constant pressure
C_w = nondimensional mass flow rate = $\dot{m}/\mu b$
G = gap ratio = s/b
G_c = shroud-clearance ratio = s_c/b
h = enthalpy
k = turbulent kinetic energy; thermal conductivity
$\dot{m}$ = mass flow rate
Nu* = local Nusselt number = $q_o r/k(T_o - T_{\mathrm{ref}})$
p = static pressure
P = production rate of turbulent kinetic energy
Pr = Prandtl number = $\mu C_p/k$
Pr_t = turbulent Prandtl number
q_o = convective heat flux from disk to air
r = radial coordinate
R = recovery factor
Re_ϕ = rotational Reynolds number = $\rho\Omega b^2/\mu$
s = axial gap between disks
s_c = axial clearance between shroud and disk
S_r = swirl ratio = $V_{\phi,p}/\Omega r_p$
T = temperature
U_τ = friction velocity = $\sqrt{\tau_w/\rho}$
V_r, V_ϕ, V_z = time-averaged velocity components in r, ϕ, z directions
x = nondimensional radius = r/b
y = distance normal to wall
y^+ = wall-distance Reynolds number = $\rho U_\tau y/\mu$
z = axial coordinate measured from stator
ϵ = turbulent energy dissipation rate
λ_T = turbulent flow parameter = $C_{w,d}\,\mathrm{Re}_\phi^{-0.8}$
μ = dynamic viscosity
ρ = density
ϕ = tangential coordinate; dummy variable
τ_w = total wall shear stress
Ω = angular speed of disk

Subscripts

ad = adiabatic value
b = blade-cooling flow
d = disk-cooling flow
e = effective value
o = surface of rotating disk
p = preswirl flow
ref = reference value
s = sealing flow
t = turbulent value
T = total value
∞ = value outside the boundary layer

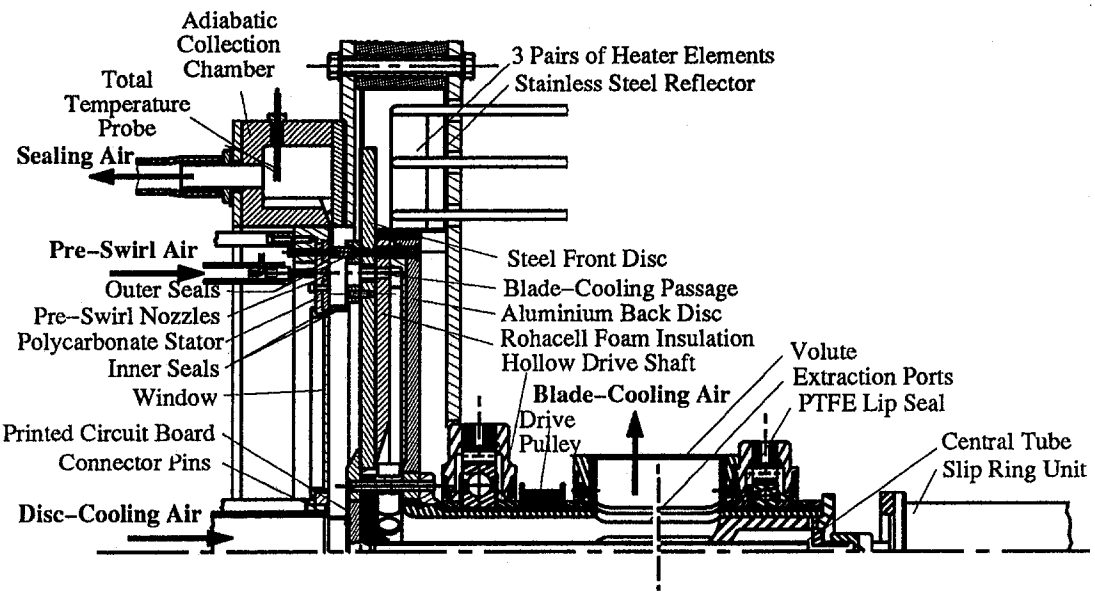

Fig. 2 Preswirl rotor-stator rig

$Re_\phi \simeq 2 \times 10^6$ are similar to those computed (for the same values of λ_T, S_r, and $C_{w,p}/C_{w,d}$) at $Re_\phi = 8 \times 10^6$. This does not prove that the computed flow is the same as that occurring in *turbines* operating at high values of Re_ϕ, but it does confirm the importance of modeling the appropriate nondimensional quantities. Further computational and experimental evidence, obtained at engine operating conditions, will be required to test the validity of the authors' results.

In summary, experimental measurements were made over the following ranges of nondimensional parameters:

$$6 \times 10^5 < Re_\phi < 2.4 \times 10^6$$
$$5 \times 10^3 < C_{w,p} < 2 \times 10^4,\ 10^3 < C_{w,d} < 7.5 \times 10^3$$
$$0.8 < C_{w,p}/C_{w,d} < 16,\ 0.03 < \lambda_T < 0.06$$
$$\text{and } 0.5 < S_r < 3.7.$$

For the experiments reported in this paper, the Reynolds number was fixed at $Re_\phi \simeq 1.2 \times 10^6$ and the ranges of the other parameters were altered accordingly.

2.2 Rotor-Stator Rig. A sectioned view of the rig is shown in Fig 2, and details of the preswirl chamber and seal geometry are shown in Fig 3.

The composite *rotor* comprised a front disk of 580 mm diameter, made from steel, and a back disk of 450 mm diameter, made from aluminum, the two disks being separated by a 22 mm layer of Rohacell foam insulation ($k \simeq 0.03$ W/m K). Sixty blade-cooling holes, of 12 mm diameter, located at a radius of 200 mm, were drilled axially through the steel disk, which was 9.4 mm thick, into the Rohacell foam. Rohacell bushes, with an inside diameter of 7.7 mm, were inserted into these holes to reduce heat transfer to the cooling air. Passages in the foam layer between the disks allowed the "blade-cooling" air to be transferred radially inward to a hollow drive shaft. The air left the rig through a volute, and PTFE lip seals between the stationary volute and the rotating shaft minimized air leakage.

The *stator* was made from 10-mm-thick polycarbonate sheet ($k \simeq 0.2$ W/mK) supported by a steel frame. A removable window, of 120 mm diameter and made from 4-mm-thick calcium aluminate glass, provided optical access for infrared and visible radiation. Sixty nozzles, 2.9 mm diameter and inclined at 20 deg to the tangential direction, were located at a radius of 200 mm. Stationary and rotating sealing rings, made from steel, were located either side of the preswirl nozzles, as shown in Fig. 3, and the rotating seals were bolted and dowelled to the steel disk. Disk-cooling air could be supplied through a tube of 52.5 mm internal diameter attached to the center of the stator, and the sealing air left the periphery of the system through an adiabatic collection chamber, made from Rohacell foam, attached to the outside of the stator.

The rotor could be rotated up to 7000 rpm by a variable-speed electric motor and a belt and pulley system, with the drive pulley located between the two bearings on the hollow drive shaft. The periphery of the steel disk could be heated up to 160°C by six stationary, thyristor-controlled, electric heaters with a total power output of 9.5 kW. The radiant heater elements were located inside a thermally insulated enclosure, lined with stainless-steel reflectors, to reduce heat loss.

For the dimensionless groups x, G, Re_ϕ, and C_w, the outer radius of the disk was taken as $b = 215$ mm (the centerline of

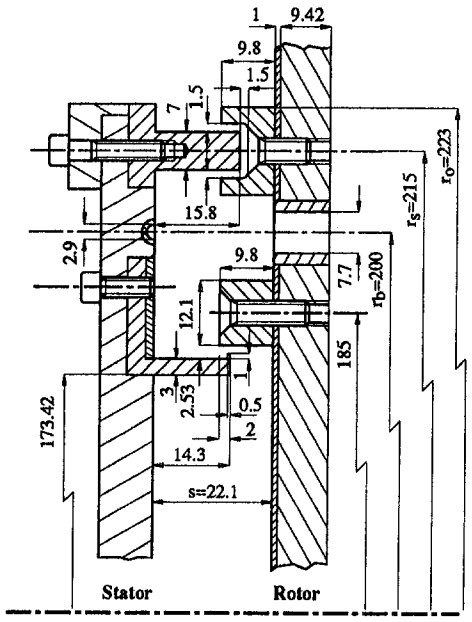

Fig. 3 Details of preswirl chamber and seal geometry (dimensions in mm)

the outer seal). The gap between the disks was $s = 22.1$ mm (Fig. 3).

2.3 Cooling-Air Supply. For some of the tests described below, the disk-cooling and preswirl air was supplied from separate centrifugal compressors, and the blade-cooling and sealing air was extracted by Rootes blowers. For other tests, the air was supplied from a Bellis and Morecombe reciprocating compressor capable of delivering up to 0.5 kg/s of air at an absolute pressure of up to 5 bar. Each of the four flow rates was measured, with an uncertainty of ±3 percent, using an orifice plate made and fitted in accordance with British Standards (BS 1042). For the preswirl flow, a system of manifolds was used to distribute the flow to each of the 60 nozzles.

The total temperature of the inlet air was controlled by a heat exchanger, and for the experiments described below it was in the range 20–30°C. The air supply was adjusted to ensure, within the uncertainty limits, equal flow rates of the preswirl and blade-cooling air and of the disk-cooling and sealing air ($C_{w,p} = C_{w,b}$ and $C_{w,d} = C_{w,s}$). (For some tests, the air was admitted to only 30 of the 60 preswirl nozzles; this enabled the swirl ratio, S_r, to be altered independently of the preswirl flow rate.)

2.4 Instrumentation. Details of the instrumented rotor and stator are shown in Fig 4. The front face of the steel disk was covered with a 1-mm-thick glass-fiber epoxy-resin "mat" ($k = 0.3$ W/mK) in which six fluxmeters and 12 thermocouples were embedded at various radial locations: The mat reduced thermal-disturbance errors and avoided the need to cut slots in the highly stressed disk. The fluxmeters (RDF Model No 27036-3) were made from a thermopile of chromel–alumel foil on a film of Kapton ($k = 0.2$ W/mK) 0.3 mm thick. The active size of the thermopile was 4 mm × 2 mm, with the longer side located tangentially on the disk. The thermocouples were made of copper and constantan wires of 0.125 mm diameter and, in addition to the thermocouples on the disk, total-temperature probes were located in two of the blade-cooling holes (to measure $T_{b,T}$). The fluxmeter and thermocouple wires were soldered to pins mounted in a printed-circuit board (PCB) at the center of the disk (as shown in Fig. 2).

As the fluxmeters and thermocouples were electrically isolated in the glass-fiber mat, it was possible to make some wires common so as to take all the signals out through a 24-way silver slipring assembly (IDM PM24). The rotating pins on the PCB were connected to the sliprings by copper wire, passed through a tube in the center of the drive shaft, and the effective "cold junction" temperature was determined by measuring the temperature of the disk-cooling air that impinged on the pins.

The glass-fiber mat was sprayed with matt black paint, with an emissivity of 0.94, and six segments of the mat were then coated with thermochromic liquid crystals, with a band-width of around 1°C at 56°C. It was therefore possible to measure the surface temperature of the mat using thermocouples, liquid crystals and infrared thermal imaging. In the latter case, an Agema IR imager with a resolution of 0.2°C was used. When two or more methods were used to measure the surface temperature, the agreement was typically better than ±1°C.

The stator (see Fig. 4(b)) was instrumented with static pressure taps, pitot tubes, thermocouples, and total-temperature probes located at eight radial positions. The pitot tubes and total-temperature probes, which were aligned with the tangential direction, were located at the same radial position in the midplane ($z/s = \frac{1}{2}$) of the wheel-space. Using the static and total pressures, the tangential component of velocity, V_ϕ, could be measured in the midplane. In addition, a total-temperature probe was located in the central tube (feeding the disk-cooling air to the wheel-space), two were located immediately upstream of the preswirl nozzles (to measure $T_{p,T}$), and four were located in the adiabatic collection chamber. It was therefore possible to measure the total temperature of the cooling air at both inlets and both outlets of the system.

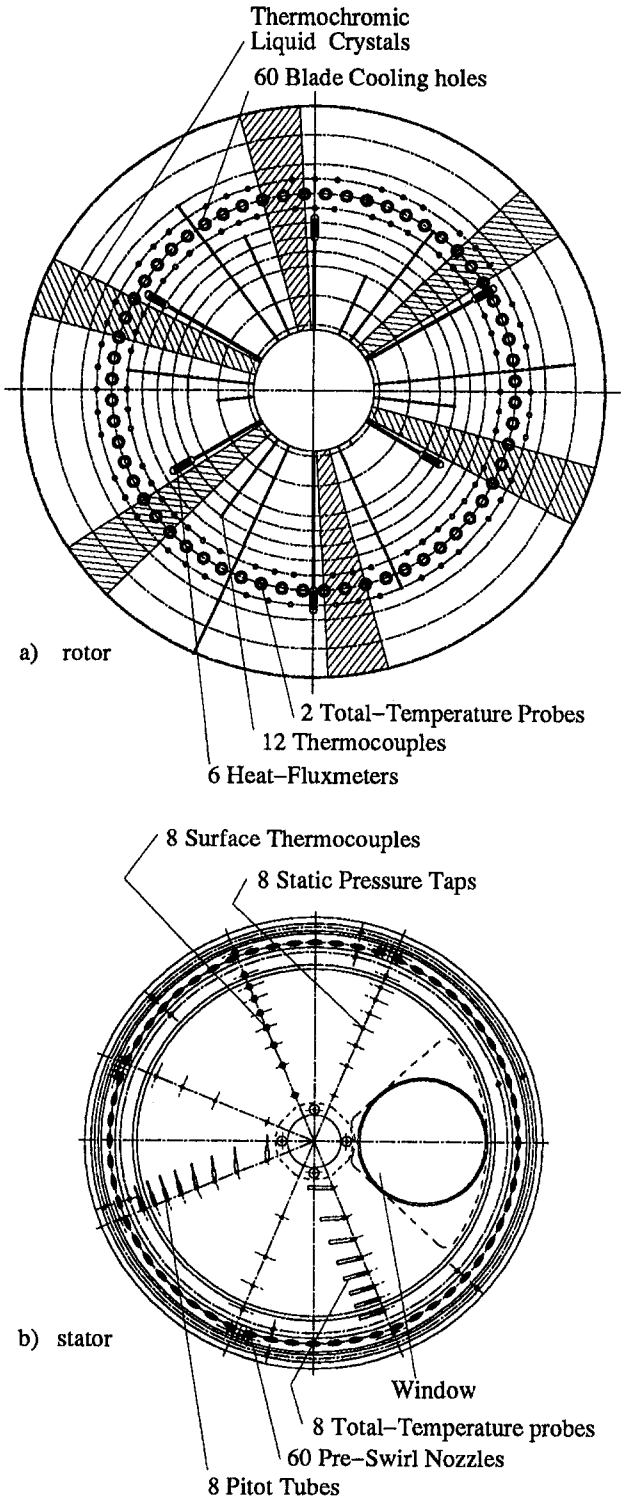

Fig. 4 Instrumented rotor and stator

The pressure readings, which were obtained from a Scanivalve system, and the thermocouple and fluxmeter signals were measured using a computer-controlled Schlumberger data logger. The Scanivalve pressure transducer had a specified range of 0.17 bar and the manufacturer's specified accuracy was ±0.06 percent of the calibrated range. However, for each test the transducer was calibrated using a water-filled manometer with an uncertainty of better than ±0.5 mm W.G (0.05 mbar). Thus

for a typical test, the uncertainty in the pressure measurements was estimated to be ±0.07 mbar. Details of the fluxmeter calibration are given below.

3 Free-Disk Tests and Fluxmeter Calibration

Previous experience with fluxmeters has shown that in situ calibration is essential, and the method described by Long (1991) was used for the tests described below. In essence, this method uses a simple theoretical model for the thermopile involving three empirical constants related to the thermoelectric characteristics and thermal resistance of the fluxmeter. From experiments, in which the heat fluxes are known and the fluxmeter voltages are measured, a regression analysis can be used to determine the "best" three constants for each fluxmeter.

The free-disk case is reasonably well understood and the heat transfer can be computed with good accuracy (see Ong and Owen, 1991). Farthing (1988) carried out free-disk tests to calibrate the fluxmeters on his rig, and the values of the three constants were chosen to provide the best fit to the computations of Ong; a similar procedure was carried out recently by Chen et al. (1996). It should be pointed out that although there are correlations for Nusselt numbers for the free disk (see, for example, Owen and Rogers, 1989), the Nusselt numbers depend strongly on the radial distribution of temperature on the disk, and individual computations of the Nusselt numbers are necessary if accurate values are required.

The rig described in Section 2 was converted to a "free disk" by removing the stator and the rotating seals and by blanking-off the blade-cooling holes. The holes were covered with a 0.105-mm-thick layer of Kapton tape extending from a radius of $r = 175$ mm to $r = 223$ mm. A total of 28 free-disk tests was then conducted for rotational speeds between 1000 and 5750 rpm with the disk heated to a maximum temperature of 130°C.

The radial distribution of Nusselt number for each test was computed using a version of the elliptic solver described in Section 4; the code had previously been checked using the free-disk data of Northrop and Owen (1988). For the current free-disk computations, the measured surface temperatures provided thermal boundary conditions for the front face of the disk. Using the computed fluxes and measured voltages for each fluxmeter, the three fluxmeter constants were "optimised" using a regression analysis based on the data for all tests.

For the tests described below, the local Nusselt number, Nu*, is defined as

$$\mathrm{Nu}^* = q_o r/k(T_o - T_{\mathrm{ref}}) \tag{3.1}$$

where q_o is the local heat flux (measured in the experiments by a fluxmeter), T_o is the local surface temperature (measured by a thermocouple), and T_{ref} is a reference temperature. For the free-disk tests, the *adiabatic-disk temperature*, $T_{o,ad}$, (see Owen and Rogers, 1989) was used such that

$$T_{\mathrm{ref}} = T_{o,ad} = T_\infty + \frac{R\Omega^2 r^2}{2Cp} \tag{3.2}$$

where R is the recovery factor calculated from Eq. (1.2). For these tests, T_∞ was the measured ambient air temperature outside the boundary layer on the disk.

Figure 5 shows the radial variaton of Nu*, calculated as described above, for a number of rotational speeds (2744, 3756, 4750, 5758 rpm). The agreement between the six fluxmeter measurements (using the optimized constants) and the computations is mainly good. Having effectively "calibrated" the fluxmeters using the free-disk tests, they can be used with some confidence for the rotor–stator tests described below. (Although sceptics may consider the good agreement between the measured and computed Nusselt numbers to be an example of a self-fulfilling prophecy, it should be remembered that, even with three arbitrary constants, the typical regression had around 20 degrees of freedom: There were more ways to get it wrong than to get it right!)

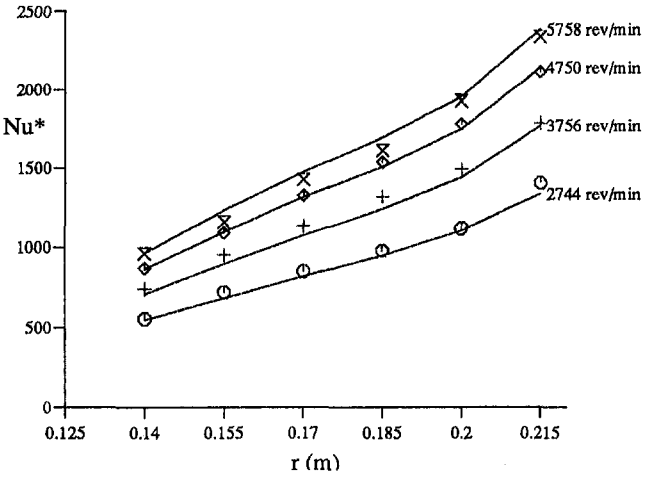

Fig. 5 Radial distribution of Nusselt numbers for free-disk tests; — computations, symbols refer to experimental data

For the rotor–stator tests discussed below, T_∞ was arbitrarily chosen to be the temperature of the disk-cooling air at inlet to the system. It is realized that the chosen values of T_∞ and T_{ref} are almost certainly inappropriate for the preswirl system, even though the difference between inlet total temperatures of the preswirl and disk-cooling air was kept as small as was practicable. (The preswirl problem, involving two air inlets, is an example of the so-called "three-temperature problem," for which the "driving temperature difference" is unknown in theory and is probably immeasurable in practice.)

It should also be pointed out that the measured heat fluxes represented the total flux (including radiation and convection) from the disk. No corrections for radiation were made to the measured Nusselt numbers presented below.

4 Computational Method

4.1 Outline of Method. The axisymmetric, elliptic, multigrid finite-volume solver used here is described by Kilic et al. (1994). The current work extends the preswirl applications described by Chen et al. (1993a, b), Wilson et al. (1994), and Wilson and Owen (1994), who used a parallel version of the same code. Details of the equations solved are given in the appendix.

In summary, the numerical method solves discretized forms of the axisymmetric, steady, incompressible, Reynolds-averaged Navier–Stokes and energy equations in primitive variables, using hybrid upwind differencing for the convective terms on a cylindrical-polar mesh with staggered storage locations for velocity components. A fixed V-cycle multigrid implementation of the SIMPLEC pressure-correction solution procedure is used, following that described by Vaughan et al. (1989), including the use of a Gosman damping factor to stabilize the coupling between the radial and tangential momentum equations. The averaged turbulent flow equations are closed using the low-Reynolds-number $k-\epsilon$ turbulence model of Launder and Sharma (1974).

Recent computations by Kilic et al. (1994) and Chen et al. (1996) show good predictions of flow and heat transfer using low-Reynolds-number turbulence models for contrarotating disks, free disks, and rotor–stator systems where thin boundary layers remain attached to the disks. The accuracy of the model depends upon the use of a sufficiently fine grid close to the wall, and computational tests using the present code indicate that a dimensionless distance of $y+ < 0.5$ is required for the

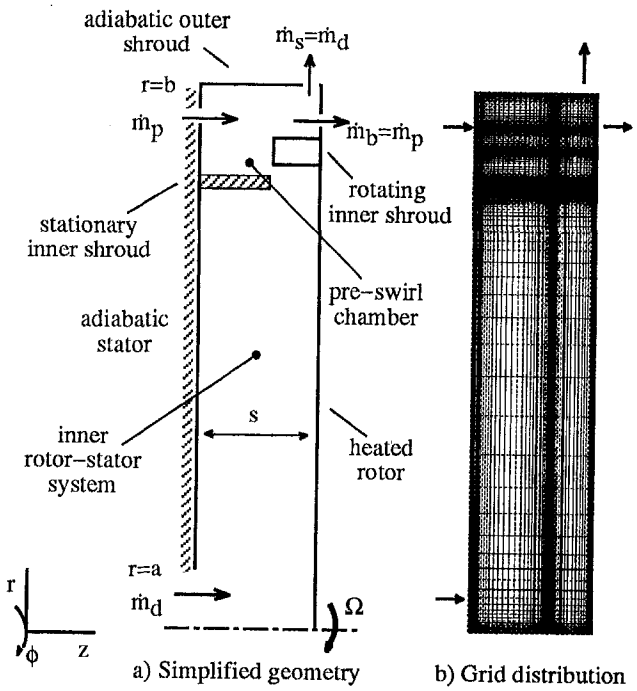

Fig. 6 Simplified geometry and grid distribution for preswirl computations

near-wall grid point for reliable application; this is in agreement with observations made by Morse (1988) for a different low-Reynolds-number turbulence model. The Launder–Sharma model is preferred here as the turbulent-viscosity damping function does not depend explicitly on the geometric term $y+$, simplifying computation of the flow near the inner seal (see Fig. 3). The turbulence-model equations are solved only on the finest grid, and the turbulence quantities derived by restriction are used directly on the coarser grids in the multigrid sequence. Modifications to the Launder–Sharma model (Iacovides and Toumpanakis, 1993) may be desirable for rotor–stator flows, but the original model has been used for the results presented below.

4.2 Computational Grid and Boundary Conditions. Referring to the rig geometry shown in Fig. 3, a computational grid was developed with the following simplifications for the axisymmetric studies: (*i*) The discrete preswirl nozzles and blade-cooling holes are modeled by equivalent-area annular slots (see Chen et al. 1993a, b); (*ii*) the radial faces of the stationary and rotating shrouds, forming the inner seal, coincide at z = 14.3 mm, and the lip on the stationary shroud is not modeled (reducing the total number of grid-points required); (*iii*) the outer seal is modeled as a rotating shroud at 215 mm radius with clearance of 1.88 mm at the rotor (for computational economy).

Figure 6 shows the boundary conditions and the 115 × 323 (axial × radial) grid used for the computations described below. The geometric expansion factors used for the grid generation did not exceed 1.2. The inner shrouds were modeled as solid obstructions within the grid, and the shroud surfaces were treated in the same way as the other domain boundaries within the multigrid sequence. Inlet boundary conditions, for the disk flow entering at the axis and for the preswirl flow, could be specified directly from flow rate and temperature measurements in a particular experiment. The two flows were respectively balanced by the blade-cooling and sealing flows in the experiment, as indicated in Fig. 6(*a*). Where measurements were available, static temperatures on the rotor and stator were supplied as polynomial approximations to the data: The stator surface in the preswirl chamber and the stationary inner shroud were assumed adiabatic. The heat flux measured underneath the rotating inner shroud was evenly distributed over its surface in the computational model, and the simplified outer shroud was assumed adiabatic.

The three-level multigrid computations occupied 30MB memory, requiring 230 full iterations and around 13 hours on a Silicon Graphics R4400 workstation; at this stage the root-mean-square change in each variable between iterations was below 2×10^{-5}, and the solution did not change appreciably in the next 50 iterations. It is likely that computing times could be reduced by re-optimization of relaxation parameters, but this was not attempted.

4.3 Computed Flow Structure. Figure 7(*a*) illustrates the computed flow structure inside the preswirl chamber for $\mathrm{Re}_\phi = 1.23 \times 10^6$, $C_{w,d} = 4580$, $C_{w,p} = 9980$ ($\lambda_T = 0.0615$, $C_{w,p}/C_{w,d} = 2.18$, $S_r = 0.99$). The fluid in the disk boundary layer flows around the rotating inner shroud and leaves through the blade-cooling slot in the rotor. The preswirl crossflow causes recirculations to be set up inside the preswirl chamber, above and below the preswirl centerline at $x = 0.93$. The fluid impinging on the disk above the centerline forms the sealing flow at the outer shroud clearance, adjacent to the rotor in the computational model. Below the centerline, fluid from the outer edge of the disk boundary layer is taken up in the clockwise recirculation, flowing toward the stator before being entrained into the crossflow and leaving through the blade-cooling slot. This "indirect" path of the disk-cooling air influences the temperature of the blade-cooling air, as noted by Chen et al. (1993a, b) from laminar-flow computations and by El-Oun and Owen (1989) from their "mixed theory." The disk-cooling flow is sufficient to prevent any ingress of fluid from the preswirl chamber into the inner rotor–stator system.

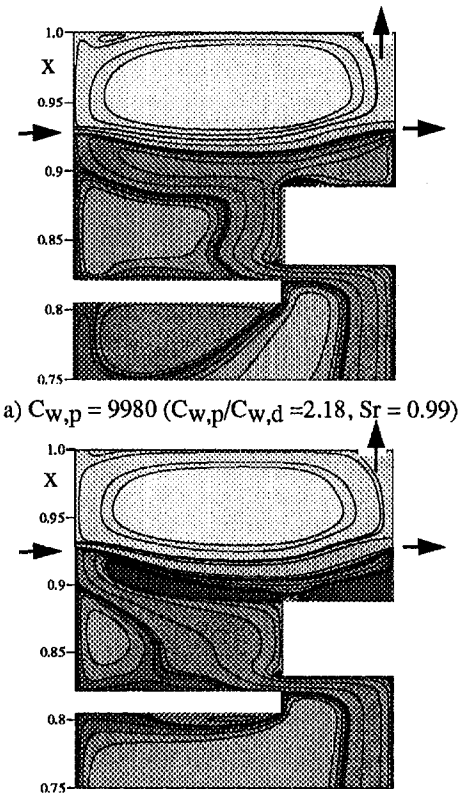

Fig. 7 Computed streamlines for $\mathrm{Re}_\phi = 1.23 \times 10^6$ and $\lambda_T \simeq 0.06$ (not to scale)

Table 1 Nondimensional parameters for the four test cases

Case	Re_ϕ	$C_{w,d}$	$C_{w,p}$	λ_T	$C_{w,p}/C_{w,d}$	S_r
1	1.27×10^6	2280	9960	0.0298	4.37	0.99
2	1.27×10^6	2250	20300	0.0294	9.02	1.98
3	1.23×10^6	4580	9980	0.0615	2.18	0.99
4	1.23×10^6	4450	20100	0.0598	4.52	1.98

Figure 7(*b*) shows the predicted streamlines when the preswirl crossflow is double that for the case in Fig. 7(*a*). In this case, the disk boundary layer separates at the top of the inner shroud due to the more powerful clockwise recirculation, and all the disk-cooling flow follows the "indirect" path described above. There is again no reverse flow at the inner seal, and consequently no effect of the crossflow on heat transfer in the inner system.

Comparisons between computations and measurements are described in Section 5.

5 Comparison Between Computed and Measured Results

Computations were performed for comparison with selected tests carried out at a speed of 4000 rpm (corresponding to $Re_\phi \simeq 1.25 \times 10^6$). Computations at higher rotational speeds require a finer grid to satisfy the $y+ < 0.5$ criterion for the near-wall grid point, incurring longer computing times, while numerical studies at a fixed speed allow the response of the model to changes in superposed flow rates to be assessed.

Computations were conducted at four conditions, common to both the single-seal and double-seal experiments but, to simplify the discussion, only the results for the double-seal tests are described here. For each computed case, boundary conditions were supplied using experimental data as described in Section 4.2. The test conditions for the four double-seal cases are given in Table 1, and comparisons between the predictions and experimental data are given in Figs. 8–11.

Figure 8 shows the comparison between computations and data for case 1. Figure 8(*a*) shows the fitted static temperature boundary conditions for the rotor and stator surfaces, and the computed midplane ($z/s = 0.5$) temperature. The stator surface was assumed adiabatic radially outward of the last measurement point, which explains the increase in temperature on the stator inside the preswirl chamber. The midplane temperature is well predicted in the inner rotor–stator system, but appears to be overpredicted just outward of the stationary shroud.

Figure 8(*b*) shows that the measured tangential velocities in the midplane ($z/s = 0.5$) are well predicted; it should be noted that the zero velocities for $0.807 < x < 0.82$ correspond to the presence of the stationary shroud. The comparison with static pressures, measured on the stator but not shown here, was also good.

It should be remembered that the velocity measurements were made using the total pressure obtained from a pitot tube, aligned with the circumferential direction, and the static pressure obtained from a pressure tap in the stator. In the rotating core of the inner rotor–stator system ($x < 0.8$), where there is no radial flow and the axial flow is very weak, the measurement of V_ϕ should have only a small uncertainty (<3 percent). In the preswirl chamber ($x \geq 0.83$), the flow can be three dimensional and unsteady; the resulting total pressure will be higher, and the pitot tube is likely to give an overestimate of V_ϕ. This overestimate will increase as $C_{w,p}$ increases, but it is difficult to quantify the error.

Figure 8(*c*) shows the comparison between measured and predicted values for Nusselt numbers on the rotor. There is some underprediction of the data in the inner system. In the preswirl chamber, impinging flow above and below the crossflow centerline ($x = 0.93$) gives rise to very high predicted Nusselt numbers as the edges of the blade-cooling slot are approached; this is a region where the low-Reynolds-number turbulence model may be inappropriate. The Nusselt number at $x = 0.93$ was measured on the rotor surface between the blade-cooling holes; this region corresponds to the slot in the axisymmetric model.

Figure 9 shows comparisons between the measured and computed results for case 2; the value of λ_T is the same as for case 1 but the preswirl flow rate, and hence the swirl ratio, is approximately double. The agreement between the computed midplane temperatures and velocities is mainly good but the Nusselt numbers in the inner rotor–stator system are significantly underpredicted. The apparent underprediction of V_ϕ at $x = 0.84$, in the preswirl chamber, may be due, in part at least, to the overestimate in the measured total pressure referred to above. (A similar discrepancy can be seen in Fig. 11(*b*), which was also obtained at the higher value of $C_{w,p}$.)

Comparison between Figs. 9(*c*) and 8(*c*) shows that the computed Nusselt numbers in the inner system are virtually the same, which is consistent with λ_T being unchanged, but the measured values in Fig. 9(*c*) are much higher. This implies that, in the experiment, the increased values of $C_{w,p}$ and S_r in the preswirl chamber caused conditions to change in the inner

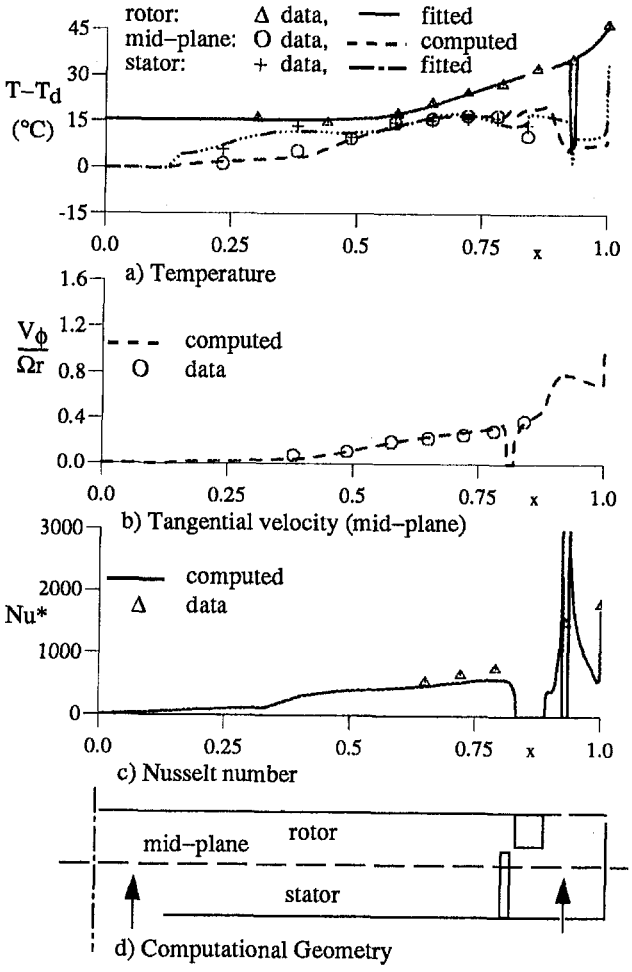

Fig. 8 Comparison between computations and measurements for case 1: $Re_\phi = 1.27 \times 10^6$, $C_{w,d} = 2280$, $C_{w,p} = 9960$ ($\lambda_T = 0.0298$, $C_{w,p}/C_{w,d} = 4.37$, $S_r = 0.99$)

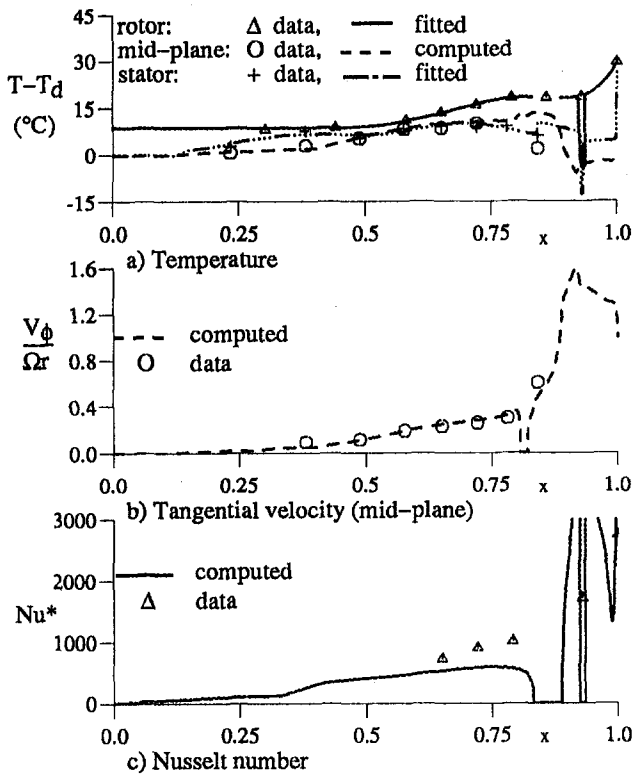

Fig. 9 Comparison between computations and measurements for case 2: $Re_\phi = 1.27 \times 10^6$, $C_{w,d} = 2250$, $C_{w,p} = 20{,}300$ ($\lambda_T = 0.0294$, $C_{w,p}/C_{w,d} = 9.02$, $S_r = 1.98$)

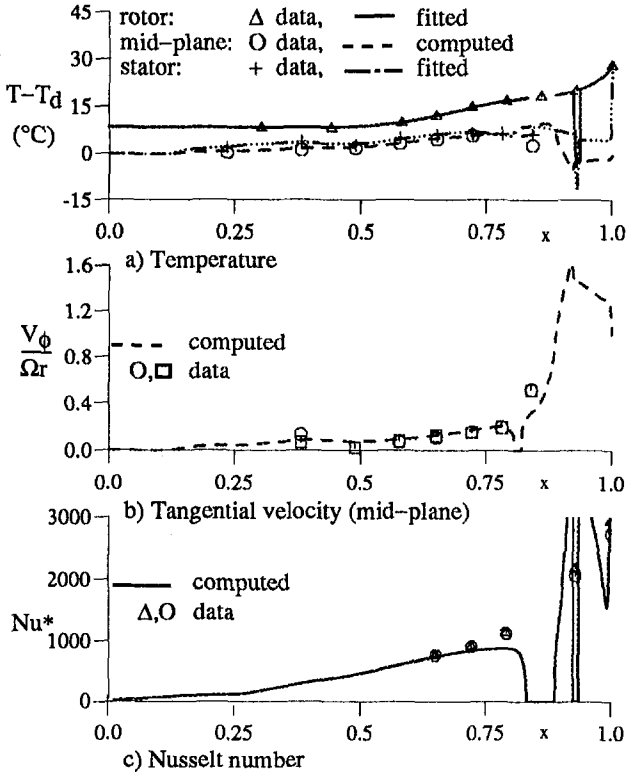

Fig. 11 Comparison between computations and measurements for case 4: $Re_\phi = 1.23 \times 10^6$, $C_{w,d} = 4450$, $C_{w,p} = 20100$ ($\lambda_T = 0.0598$, $C_{w,p}/C_{w,d} = 4.52$, $S_r = 1.98$)

rotor–stator system. It is possible that ingress of preswirl air into the inner system occurred in the experiment, but no evidence of this was found in the computations. (For the experiment, $C_{w,d}$ = 2250 is less than the value required to prevent ingress in a rotor–stator system with a radial-clearance seal, according to the results of Phadke and Owen, 1988.)

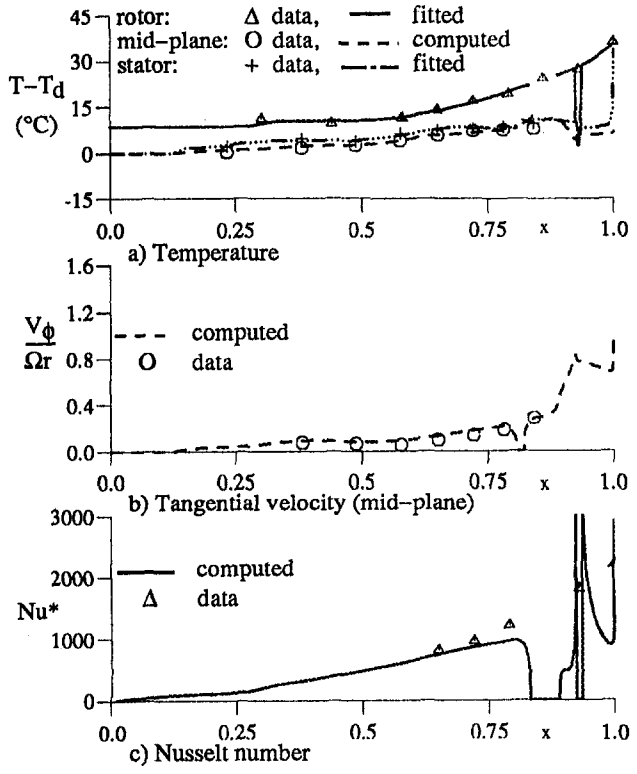

Fig. 10 Comparison between computations and measurements for case 3: $Re_\phi = 1.23 \times 10^6$, $C_{w,d} = 4580$, $C_{w,p} = 9980$ ($\lambda_T = 0.0615$, $C_{w,p}/C_{w,d} = 2.18$, $S_r = 0.99$)

Figures 10 and 11 show the results for cases 3 and 4: These correspond to cases 1 and 2, respectively, but with the value of $C_{w,d}$ doubled. It should be noted that there are two sets of experimental Nusselt numbers in Fig. 11; the two sets of data show the good repeatability of these experiments.

Referring to Fig. 10, the midplane temperature and velocity are well predicted in both the inner rotor–stator system and the preswirl chamber. The Nusselt numbers in the inner system are slightly underpredicted.

Figure 11 shows similar results to Fig. 10 although the midplane temperature in the preswirl chamber is slightly overpredicted and the midplane velocity underpredicted. An interesting point is that both the computed and measured Nusselt numbers in the inner system in Fig. 11 are virtually the same as those in Fig. 10. This contrasts with the results for Figs. 8 and 9, at the lower value of $C_{w,d}$, and suggests that if ingress had occurred in the experiments for case 2 then it did not occur at the higher value of $C_{w,d}$. Comparison between Figs. 10(c) and 11(c) (and also between Figs. 8(c) and 9(c)) shows that the measured Nusselt number at $x = 0.93$ (between the blade-cooling holes) increases as $C_{w,p}$ (and, consequently, S_r) increases.

Table 2 shows comparisons between the measured and computed values of $T_{b,T} - T_{p,T}$, the difference between the total temperatures of the cooling air at inlet to the blade-cooling holes and outlet from the preswirl nozzles. Also shown in Table 2 are the values calculated from Eq. (1.1), the "unmixed theory" of El-Oun and Owen (1989) for an adiabatic preswirl system. A negative value of $T_{b,T} - T_{p,T}$ indicates that, despite heat transfer from the disk, the preswirl effect has still managed to reduce the temperature of the blade-cooling air.

The experiments, the computations and the "unmixed theory" all confirm that the temperature of the blade-cooling air is lowest when the swirl ratio is highest. In fact, for $S_r = 1.98$

Table 2 Comparison between measured and computed values of $T_{b,T} - T_{p,T}$ for $Re_\phi \simeq 1.2 \times 10^6$

Case	λ_T	$C_{w,p}/C_{w,d}$	S_r	$T_{b,T} - T_{p,T}$ (°C)		
				Experiment	Computation	"Unmixed theory"
1	0.030	4.4	0.99	8.7	6.5	- 3.4
2	0.029	9.0	1.98	- 1.7	-3.4	- 10.6
3	0.062	2.2	0.99	6.0	2.9	- 3.4
4	0.060	4.5	1.98	- 1.4	-2.8	- 10.6

(cases 2 and 4), all three sets of results show that $T_{b,T} - T_{p,T}$ is negative. In all four cases, the computed values of $T_{b,T} - T_{p,T}$ are intermediate between the values from the "unmixed theory" and the experiments: The computed temperatures are much closer to the latter values than to the former ones. Although the computations show the correct trends, they consistently underestimate the (relatively small) measured values of $T_{b,T} - T_{p,T}$: The average discrepancy being 2.1°C, and the estimated experimental uncertainty being around 1°C.

The difference between the computations of $T_{b,T} - T_{p,T}$ and the "unmixed theory" is caused partly by the mixing processes (an adiabatic phenomenon) but mainly by heat transfer, which is unaccounted for in the adiabatic theory. The difference between the computations and the measurements could be caused by a number of factors including the steady, axisymmetric assumptions, the simplified computational geometry, inaccurate or indeterminate thermal boundary conditions, an inappropriate turbulence model, and experimental errors: The list is long. However despite (or perhaps because of!) these factors, the level of agreement between the computations and the measurements is encouraging.

Although experimental data were obtained at other conditions, these have still to be analyzed and the findings will be reported elsewhere. It can be said, however, that without the computations it would be difficult to interpret the experimental data. Conversely, without the data, designers would not believe the computations!

6 Conclusions

A comparison between measured and computed velocities, temperatures and Nusselt numbers has been made for a preswirl rotor–stator system for $Re_\phi \simeq 1.2 \times 10^6$, $\lambda_T \simeq 0.03$ and 0.06, $S_r \simeq 1$ and 2, and $2.2 < C_{w,p}/C_{w,d} < 9.0$. The measurements were made on a rig comprising an outer preswirl chamber separated by a seal from an inner rotor–stator system. The computations were carried out using an axisymmetric elliptic solver incorporating a low-Reynolds-number $k-\epsilon$ turbulence model. The principal conclusions are listed below.

For the inner rotor–stator system, the computed midplane temperatures and velocities were in mainly good agreement with the measured values, but the computed Nusselt numbers for the rotor tended to underpredict the measured values. For one particular case ($Re_\phi = 1.27 \times 10^6$, $\lambda_T = 0.03$, $C_{w,p}/C_{w,d} = 9$), the measured Nusselt numbers were significantly higher than the computed values; it was speculated that ingress from the preswirl chamber had occurred in the experiment but not in the computations.

For the preswirl chamber, there was less instrumentation and comparisons were difficult to make. As expected, the midplane velocity increased as S_r increased, but the computations tended to underestimate the measured velocities. The measured Nusselt number between the blade-cooling holes in the rotor increased as $C_{w,p}$ (and, consequently, S_r) increased, but the axisymmetric code made direct comparisons inappropriate here.

Measurements made of $T_{b,T} - T_{p,T}$ (the difference between the total temperatures of the blade-cooling and preswirl air) were compared with computed values and with values obtained from the "unmixed theory" of El-Oun and Owen (1989) for an adiabatic preswirl system. All three sets of values (experimental, computational, theoretical) show that the blade-cooling temperatures were lowest when the swirl ratio was highest, and the computed values were intermediate between the other two. The magnitudes of the measured values of $T_{b,T} - T_{p,T}$ were small, between −1.7°C and +8.7°C, but the difference between the computed and measured values was greater than the estimated experimental uncertainty. Although this difference is significant, the computed blade-cooling air temperatures show the correct trend.

Experimental measurements obtained at other conditions have still to be analyzed, and it certainly should not be suggested that the axisymmetric computations can accurately model all the features of an actual gas turbine preswirl system. However, the results obtained are encouraging, and they have given insight into the heat transfer characteristics of an extremely complex three-dimensional, unsteady flow system.

Acknowledgments

The authors wish to thank the UK Engineering and Physical Sciences Research Council, European Gas Turbines Ltd., and Motoren- und Turbinen-Union GmbH for supporting the work described in this paper.

References

Bunker, R. S., Metzger, D. E., and Wittig, S., 1992a, "Local Heat Transfer in Turbine Disk Cavities. Part I: Rotor and Stator Cooling With Hub Injection of Coolant," ASME JOURNAL OF TURBOMACHINERY, Vol. 114, pp. 211–220.

Bunker, R. S., Metzger, D. E., and Wittig, S., 1992b, "Local Heat Transfer in Turbine Disk Cavities. Part II: Rotor Cooling With Radial Injection of Coolant," ASME JOURNAL OF TURBOMACHINERY, Vol. 114, pp. 221–228.

Chen, J.-X., Gan, X., and Owen, J. M., 1996, "Heat Transfer in an Air-Cooled Rotor–Stator System," ASME JOURNAL OF TURBOMACHINERY, Vol. 118, pp. 444–451.

Chen, J.-X., Owen, J. M., and Wilson, M., 1993a, "Parallel-Computing Techniques Applied to Rotor–Stator Systems: Fluid Dynamics Computations," *Proc. 8th Intl. Conf. Numer. Meth. Laminar Turbulent Flow,* Swansea, Pineridge Press, pp. 899–911.

Chen, J.-X., Owen, J. M., and Wilson, M., 1993b, "Parallel-Computing Techniques Applied to Rotor–Stator Systems: Thermal Computations," *Proc. 8th Int. Conf. Numer. Meth. Thermal Problems,* Swansea, Pineridge Press, pp. 1212–1226.

Dibelius, G. H., and Heinen, M., 1990, "Heat Transfer From a Rotating Disc," ASME Paper No. 90-GT-219.

El-Oun, Z., and Owen, J. M., 1989, "Pre-swirl Blade-Cooling Effectiveness in an Adiabatic Rotor–Stator System," ASME JOURNAL OF TURBOMACHINERY, Vol. 111, pp. 522–529.

Farthing, P. R., 1988, "The Effect of Geometry on Flow and Heat Transfer in a Rotating Cavity," DPhil thesis, University of Sussex, United Kingdom.

Iacovides, H., and Toumpanakis, P., 1993, "Turbulence Modelling of Flow in Axisymmetric Rotor–Stator Systems," *Proc. 5th Int. Symp. Refined Flow Modelling and Turbulence Measurements,* Paris, Sept.

Kilic, M., Gan, X., and Owen, J. M., 1994, "Transitional Flow Between Contra-rotating Discs," *J. Fluid Mech.,* Vol. 281, pp. 119–135.

Launder, B. E., and Sharma, B. I., 1974, "Application of the Energy-Dissipation Model of Turbulence to the Calculation of Flow Near a Spinning Disc," *Letters in Heat and Mass Transfer,* Vol. 1, pp. 131–138.

Long, C. A., 1991, "A Calibration Technique for Thermopile Heat-Flux Gauges," *Proc. 5th Int. Exhibition and Congress for Sensors and Systems Technology,* Nuremberg.

Meierhofer, B., and Franklin, C. J., 1981, "An Investigation of the Preswirled Cooling Airflow to a Turbine Disc by Measuring the Air Temperature in the Rotating Channels," ASME Paper No. 81-GT-132.

Morse, A. P., 1988, "Numerical Prediction of Turbulent Flow in Rotating Cavities," ASME JOURNAL OF TURBOMACHINERY, Vol. 110, pp. 202–215.

Northrop, A., and Owen, J. M., 1988, "Heat Transfer Measurements in Rotating-Disc Systems. Part I: The Free Disc," *Int. J. Heat Fluid Flow,* Vol. 9, pp. 19–26.

Ong, C. L., and Owen, J. M., 1991, "Computation of the Flow and Heat Transfer Due to a Rotating Disc," *Int. J. Heat Fluid Flow,* Vol. 12, pp. 106–115.

Owen, J. M., and Rogers, R. H., 1989, *Flow and Heat Transfer in Rotating-Disc Systems, Vol. 1: Rotor-Stator Systems,* Research Studies Press, Taunton; Wiley, New York.

Phadke, U. P., and Owen, J. M., 1988, "Aerodynamic Aspects of the Sealing of Gas Turbine Rotor–Stator Systems. Part I: The Behaviour of Simple Shrouded Rotating-Disc Systems in a Quiescent Environment," *Int. J. Heat Fluid Flow,* Vol. 9, pp. 98–105.

Staub, F. W., 1992, "Rotor Cavity Flow and Heat Transfer With Inlet Swirl and Radial Outflows of Cooling Air," ASME Paper No. 92-GT-378.

Vaughan, C. M., Gilham, S., and Chew, J. W., 1989, "Numerical Solutions of Rotating Disc Flows Using a Non-linear Multigrid Algorithm," *Proc. 6th Intl. Conf. Numer. Meth. Laminar Turbulent Flow,* Swansea, Pineridge Press, pp. 66–73.

Wilson, M., Chen, J. X., Pilbrow, R. G., and Owen, J. M., 1994, "Computations of Flow and Heat Transfer in Pre-swirl Rotor–Stator Systems," *ICHMT Int. Symp. Turbulence, Heat and Mass Transfer,* Lisbon, Aug.

Wilson, M., and Owen, J. M., 1994, "Axisymmetric Computations of Flow and Heat Transfer in a Pre-swirl Rotor–Stator system," *Proc. 1st Int. Conf. Flow Interaction,* Hong Kong, pp. 447–450.

APPENDIX

Conservation Equations and Low-Reynolds-Number $k-\epsilon$ Turbulence Model

The axisymmetric equations for conservation of momentum, mass, energy, and turbulence quantities k and ϵ can be written in the following form using a cylindrical-polar coordinate system (r, ϕ, z) with velocity components (v_r, v_ϕ, v_z):

$$\frac{\partial}{\partial z}(\rho v_z \phi) + \frac{1}{r}\frac{\partial}{\partial r}(r\rho v_r \phi) = \frac{\partial}{\partial z}\left[\Gamma_z \frac{\partial \phi}{\partial z}\right] + \frac{1}{r}\frac{\partial}{\partial r}\left[r\Gamma_r \frac{\partial \phi}{\partial r}\right] + S_\phi$$

where the dummy variable ϕ represents the transported variables v_r, v_ϕ, v_z, k, ϵ, or h, and the continuity equation is recovered by setting $\phi = 1$ and $S_\phi = 0$. S_ϕ contains all source terms (Table A.1). Γ_z and Γ_r are the effective diffusivities comprising both laminar and turbulent components: $k_\epsilon = \mu/\mathrm{Pr} + \mu_t/\mathrm{Pr}_t$ is the effective thermal diffusivity, and the effective viscosity is $\mu_e = \mu + \mu_t$, where μ_t is determined from the computed turbulence quantities k and ϵ:

$$\mu_t = C_\mu f_\mu \rho k^2/\epsilon$$

where f_μ is a near-wall damping function:

$$f_\mu = \exp\{-3.4/[1 + \mathrm{Re}_t/50)]^2\}$$

which forms part of the LR $k-\epsilon$ model described by Launder and Sharma (1974). In Table A.2, D and E are the extra terms added to the high-Reynolds-number form of the model, to represent near-wall behavior. The production rate P of turbulent kinetic energy (k) is given by:

$$P = \mu_t\left[2\left\{\left(\frac{\partial v_z}{\partial z}\right)^2 + \left(\frac{\partial v_r}{\partial r}\right)^2 + \left(\frac{v_r}{r}\right)^2\right\} + \left\{\frac{\partial v_z}{\partial r} + \frac{\partial v_r}{\partial z}\right\}^2 + \left(\frac{\partial v_\phi}{\partial z}\right)^2 + \left\{\frac{r\partial}{\partial r}\left(\frac{v_\phi}{r}\right)\right\}^2\right]$$

The empirical coefficients appearing in the model are given by:

$c_\mu = 0.09$; $c_{\epsilon 1} = 1.44$;
$c_{\epsilon 2} = 1.92\ (1 - 0.3\exp(-\mathrm{Re}_t^2))$
$\sigma_k = 1.0$; $\sigma_\epsilon = 1.3$; $\mathrm{Pr}_t = 0.9$

where $\mathrm{Re}_t = k^2/\nu\epsilon$ is the local turbulent Reynolds number.

Table A.1 Source terms

ϕ	Γ_z	Γ_r	S_ϕ
v_z	$2\mu_e - \mu$	μ_e	$-\frac{\partial}{\partial z}(p+\frac{2}{3}\rho k) + \frac{1}{r}\frac{\partial}{\partial r}(r\mu_t\frac{\partial v_r}{\partial z})$
v_r	μ_e	$2\mu_e-\mu$	$-\frac{\partial}{\partial r}(p+\frac{2}{3}\rho k) -(2\mu_e-\mu)\frac{v_r}{r^2} + \frac{\rho v_\phi^2}{r} + \frac{\partial}{\partial z}(\mu_t\frac{\partial v_z}{\partial r})$
v_ϕ	μ_e	μ_e	$-\frac{\rho v_r v_\phi}{r} - \mu_e\frac{v_\phi}{r^2} - \frac{v_\phi}{r}\frac{\partial \mu_t}{\partial r}$
k	$\mu + \mu_t/\sigma_k$	$\mu + \mu_t/\sigma_k$	$P - \rho\varepsilon - D$
ε	$\mu + \mu_t/\sigma_\varepsilon$	$\mu + \mu_t/\sigma_\varepsilon$	$\varepsilon/k(c_{\varepsilon 1}P - c_{\varepsilon 2}\rho\varepsilon) + E$
h	k_e/Cp	k_e/Cp	$\frac{1}{r}\frac{\partial}{\partial r}\left[(\mu_e - k_e/Cp)r\frac{\partial}{\partial r}\left(\frac{v_r^2+v_z^2+v_\phi^2}{2}\right)\right]$ $+ \frac{\partial}{\partial z}\left[(\mu_e - k_e/Cp)\frac{\partial}{\partial z}\left(\frac{v_r^2+v_z^2+v_\phi^2}{2}\right)\right]$ $+ \frac{1}{r}\frac{\partial}{\partial r}\left[\mu_e r\left(\frac{1}{3}v_r\frac{\partial v_r}{\partial r} - \frac{2}{3}\frac{v_r^2}{r} - \frac{2}{3}v_r\frac{\partial v_z}{\partial z} - \frac{v_\phi^2}{r} + v_z\frac{\partial v_r}{\partial z}\right)\right]$ $+ \frac{\partial}{\partial z}\left[\mu_e\left(v_r\frac{\partial v_r}{\partial r} + \frac{1}{3}v_z\frac{\partial v_z}{\partial r} - \frac{2}{3}v_r\frac{\partial}{r\partial r}(rv_r)\right)\right]$

Table A.2 Extra terms *D* and *E* appearing in Table A.1

$D = 2\mu\left[\left(\frac{\partial\sqrt{k}}{\partial z}\right)^2 + \left(\frac{\partial\sqrt{k}}{\partial r}\right)^2\right]$
$E = \frac{2\mu\mu_t}{\rho}\left[\left(\frac{\partial^2 v_r}{\partial z^2}\right)^2 + \left(\frac{\partial^2 v_\phi}{\partial z^2}\right)^2 + \left(\frac{\partial^2 v_z}{\partial r^2}\right)^2 + \left(\frac{\partial^2 v_\phi}{\partial r^2}\right)^2\right]$

Turbulent Flow Heat Transfer and Friction in a Rectangular Channel With Varying Numbers of Ribbed Walls

P. R. Chandra

M. E. Niland

Mechanical Engineering Department,
McNeese State University,
Lake Charles, LA 70609

J. C. Han

Mechanical Engineering Department,
Texas A&M University,
College Station, TX 77843

An experimental study of wall heat transfer and friction characteristics of a fully developed turbulent air flow in a rectangular channel with transverse ribs on one, two, and four walls is reported. Tests were performed for Reynolds numbers ranging from 10,000 to 80,000. The pitch-to-rib height ratio, P/e, was kept at 8 and rib height-to-channel hydraulic diameter ratio, e/D_h, was kept at 0.0625. The channel length-to-hydraulic diameter ratio, L/D_h, was 15. The heat transfer coefficient and friction factor values were enhanced with the increase in the number of ribbed walls. The friction roughness function, $R(e^+)$, was almost constant over the entire range of tests performed and was within comparable limits of the previously published data. The heat transfer roughness function, $G(e^+)$, decreased with additional ribbed walls and compared well with previous work in this area. Friction data obtained experimentally for the case with four ribbed walls compared well with the values predicted by the assumed theoretical relationship used in the present study and past publications. Results of this investigation could be used in various applications of internal channel turbulent flows involving different numbers of roughened walls.

Introduction

Repeated ribs or protuberances have been used as promoters of turbulence to enhance the heat transfer to the flow of coolants in channels. These roughness elements break the laminar sublayer of the flow and thus enhance the heat transfer as well as the pressure drop, which is an important parameter in the analysis of the overall performance of such flows. Investigations have been conducted to predict the effect of the number of ribbed walls on heat transfer and friction characteristics. In applications such as cooling of gas turbine airfoils, rib turbulators are cast only on two opposite sides of the cooling channel, since the heat transfer takes place from the inner walls of the pressure and the suction sides of the blades. While turbine blade internal cooling has been widely studied in the past, other applications such as electronic equipment, heat exchangers, scramjet engine inlets, and nuclear waste processes utilize the results of enhanced internal cooling in channels with one, two, three, or all four rib-roughened walls. The present results with four ribbed-wall channels are used to validate the assumptions made in the past to develop semi-empirical correlations for friction and heat transfer roughness functions.

Several publications have addressed the comprehensive review of turbine blade cooling and the analysis of heat transfer and friction characteristics of flow in channels with two opposite rib-roughened walls. Effects of flow Reynolds number and rib geometry (rib height, spacing, angle-of-attack, and configuration) on heat transfer and pressure drop in the fully developed region of a uniformly heated square and rectangular channels have been investigated (Han et al., 1978, 1985; Han, 1984). Further studies of these effects on the local values of heat transfer and pressure drop have also been reported (Han, 1988; Han and Park, 1988; Han et al., 1989; Park et al., 1992). Results show that the angled ribs provide a better heat transfer enhancement than the transverse ribs, and the lower aspect ratio channels perform better than the higher aspect ratio channels. The heat/mass transfer analogy has been applied to study local heat transfer distribution in two-pass and three-pass ribbed channels (Han et al., 1988; Chandra et al., 1988; Chandra and Han, 1989; Han and Zhang, 1991; Chyu and Natarajan, 1995). High-performance heat transfer ducts with parallel broken and V-shaped broken ribs have been reported (Han et al., 1991; Han and Zhang, 1992; Kukreja et al., 1993; Taslim et al., 1996). Wedge-shaped and delta-shaped turbulence promoters have been used in square channel study (Han et al., 1993). All the above-mentioned studies are for turbine blade cooling channels with two opposite ribbed walls. Heat transfer enhancement in triangular ducts with rib turbulators has also been investigated (Metzger and Vedula, 1987; Zhang et al., 1994). Experiments with one ribbed-wall channel have also been reported (Liou and Hwang, 1992; Acharya et al., 1993). No study of the internal cooling channels with three and four ribbed walls has been reported.

Semi-empirical correlations over a wide range of rib geometries for the friction and heat transfer design calculations are derived from the law-of-the-wall similarity for flow over rough surfaces. The similarity law concept was first developed by Nikuradse (1950), who applied it successfully to correlate the friction data for fully developed turbulent flow in tubes with sand roughness. Based on the heat-momentum transfer analogy, Dipprey and Sabersky (1963) developed the heat transfer similarity law for fully developed turbulent flow in tubes with sand roughness. Further work in this regard was reported by Webb et al. (1971) and Han et al. (1978). A detailed analysis of the application of the similarity laws in the case of rectangular channels is presented by Han (1984, 1988).

The objective of this experimental study is to investigate the effect of the number of ribbed walls on wall friction and the heat transfer coefficient. In the past, most heat transfer and friction loss experiments have been related to turbine blade cooling channels with two ribbed walls. The present study ex-

Contributed by the International Gas Turbine Institute and presented at the 40th International Gas Turbine and Aeroengine Congress and Exhibition, Houston, Texas, June 5–8, 1995. Manuscript received by the International Gas Turbine Institute February 4, 1995. Paper No. 95-GT-13. Associate Technical Editor: C. J. Russo.

tends its base to provide experimental data for cooling channels with one, two, three, or four ribbed walls. Also, the semi-empirical correlations developed in the past were based on the assumption that the values of the friction and heat transfer coefficients in a duct with two smooth and two ribbed walls can be calculated by combining their respective values obtained from geometrically similar ducts with four smooth walls and four ribbed walls. Values from four-sided smooth and four-sided ribbed wall cases are weighed proportionally to the widths of the smooth and the ribbed walls. There were no experimental verification of this assumption. The other objectives of the present research are to validate the assumption used in the past as well as to develop correlations not only for channels with two opposite ribbed walls but also for channels with one, three, or four ribbed walls.

Experimental Apparatus and Procedure

Figure 1(a) shows the cross section of the channel with heaters and insulation. The rectangular channel is of 7.62 cm × 3.81 cm (3.0 in. × 1.5 in.) cross-section and is 76.2 cm (30 in.) long. The test section is made of ten 7.62 cm (3.0 in.) long sections of 0.64 cm (0.25 in.) thick aluminum plates separated by 0.08 cm thick balsa wood to reduce both the streamwise and circumferential heat conduction and to obtain the regional average values of the heat transfer coefficient. Square sharp-edged brass ribs with a height of 0.318 cm ($e/D_h = 0.0625$) and equally spaced at 2.54 cm ($P/e = 8$) as shown in Fig. 1(b) are glued with silicone adhesive onto the walls of the channel in configurations described in Fig. 1(c). The channel walls are heated individually with electric strip heaters, which are embedded and flatly placed between the aluminum and wood plates to insure good contact (Fig. 1(a)). Heaters are independently controlled by a transformer and provide a constant heat flux to the channel walls. The entire test section is enclosed by an additional 3.81 cm (1.5 in.) thick styrofoam insulation.

Measurement of the channel wall regional temperature is accomplished by 40 copper constantan thermocouples, which are installed along the axial centerlines of the four walls of the channel. A streamwise temperature distribution is recorded for all the ribbed and smooth walls. Temperatures of the air entering and leaving the test channel are also recorded. The measured average exit air temperature is used to check the calculated value based on the energy balance.

Two pressure taps are drilled 45.7 cm (18.0 in.) apart, X/D_h = 2.25–11.25, along the axial centerline of one of the smooth walls to determine the pressure drop. An inclined manometer is used to measure the pressure differential over the specified

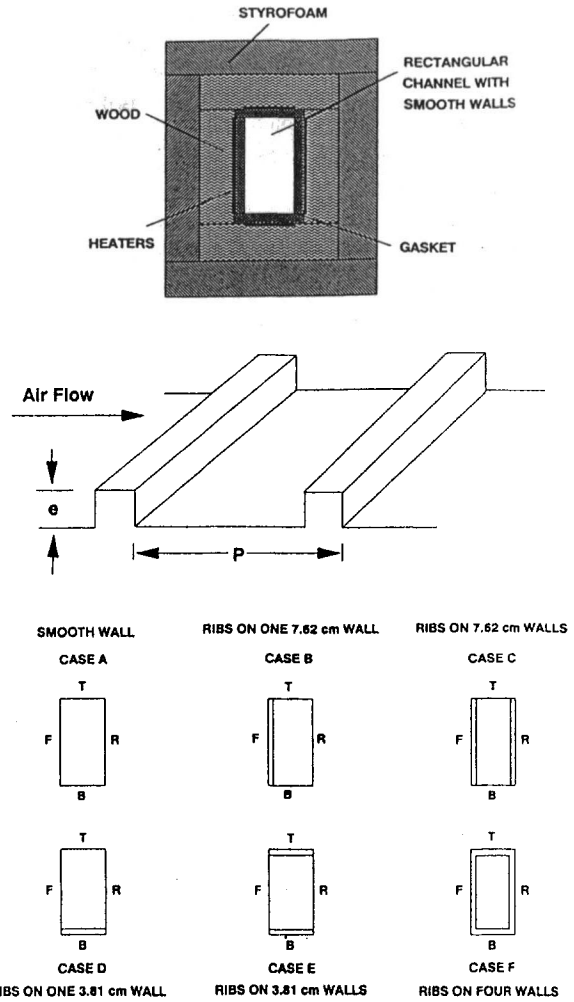

Fig. 1 (*a*) Cross section of the test channel [7.62 cm × 3.81 cm]; (*b*) ribbed wall geometry; (*c*) cases with varying number of ribbed walls

channel length. Air flow is adjusted to obtain the desired Reynolds number. Power to the heaters is adjusted so that the temperatures of the four walls at a cross-sectional location are about the same and the difference between the last section wall temperature and the exit air temperature is about 15°C (27°F). When thermal steady state is reached, air inlet and exit tempera-

Nomenclature

A_s = heat transfer surface area
D_h = channel hydraulic diameter
e = rib height
e^+ = roughness Reynolds number
f = friction factor
f_o = friction factor in fully developed smooth pipe turbulent flow
f_{rr} = friction factor in a four ribbed wall channel
f_{ss} = friction factor in a smooth channel
$G(e^+)$ = heat transfer roughness function
g_c = conversion factor
H = channel height = 1.5 in or 3.81 cm
h = heat transfer coefficient
k = thermal conductivity of air
L = channel length
Nu = Nusselt number = hD_h/k
$\mathrm{Nu_o}$ = Nusselt number in fully developed smooth pipe turbulent flow
$\mathrm{Nu_r}$ = ribbed wall Nusselt number
$\mathrm{Nu_s}$ = smooth wall Nusselt number
P = rib pitch
Pr = Prandtl number of air
Δp = pressure drop across the test section
q = heat generation rate from the heaters
q_{loss} = heat loss rate through insulation
Q = flow mass velocity = ρV
Re = Reynolds number = $\rho D_h V/\mu$
$R(e^+)$ = friction roughness function
$\mathrm{St_r}$ = ribbed wall Stanton number = $\mathrm{Nu_r}/(\mathrm{Re}\cdot\mathrm{Pr})$
T_b = bulk mean temperature
T_w = local wall temperature
V = air mean velocity
W = flow channel width = 3.0 in. or 7.62 cm
Wr = ribbed wall width at a cross section
Ws = smooth wall width at a cross section
Wt = width of the channel at a cross section
X = axial distance from the channel inlet
μ = air viscosity
ρ = air density

tures, atmospheric temperature, and temperatures along the channel walls are recorded. Upstream pressure and the pressure drop across the orifice, atmospheric pressure, and the pressure drop over a specified channel length are also recorded. Voltages supplied to the heaters are noted. The same procedure is repeated for the range of the Reynolds numbers and for all the rib configurations.

Data Reduction

The friction factor can be defined in terms of the pressure drop and the air mass velocity and can be calculated for a fully developed flow from

$$f = \Delta p/(4(L/D_h)(Q^2/2\rho g_c)) \quad (1)$$

The friction factor is normalized by the friction factor for fully developed turbulent flow in a smooth circular tube ($10^4 < \mathrm{Re} < 10^6$) proposed by Blasius (Kays and Crawford, 1989) as:

$$f/f_o = f/(0.046\ \mathrm{Re}^{-0.2}) \quad (2)$$

The local heat transfer coefficient is calculated from the local net heat transfer rate per unit area to the cooling air, the local wall temperature, and the local bulk mean air temperature as:

$$h = (q - q_{\mathrm{loss}})/(A_s(T_w - T_b)) \quad (3)$$

The local net heat transfer rate for the smooth and ribbed walls is the power supplied to the respective wall heaters minus the heat loss from the test duct to the atmosphere and the streamwise heat conduction loss along the channel walls. Power generated from the heaters is calculated from the heater resistance and the voltage supplied. Distribution of the bulk temperature is evaluated from the energy balance in conjunction with the sum of the net rates of heat transfer from the four channel walls to the air, the air mass flow rate, and the inlet air bulk temperature. The heaters provide a nearly uniform heat flux to the walls of the test duct.

Local Nusselt numbers are normalized by the Nusselt number for fully developed turbulent flow in a smooth circular tube correlated by Dittus–Boelter as given in Eq. (4). The computer program accounts for the effect of the bulk air temperature in the calculations of various properties needed in the data analysis.

$$\mathrm{Nu}/\mathrm{Nu}_o = (hD_h/k)/(0.023\ \mathrm{Re}^{0.8}\ \mathrm{Pr}^{0.4}) \quad (4)$$

The maximum uncertainties in the heat transfer coefficient and friction factor are estimated to be ±7 percent and ±8 percent, respectively, by using the uncertainty estimation method of Kline and McClintock (1953). The maximum heat loss to the atmosphere is about 6 percent of the total heat supplied to the channel walls. No flow experiments were conducted to estimate heat losses through the insulation.

Theoretical Analysis

Developed by combining the concepts of Nikuradse (1950) and Dipprey and Sabersky (1963), and the laws of the wall in fully developed turbulent flow, the friction and heat transfer similarity laws imply that the friction and the heat transfer data for any geometrically similar roughness family (repeated-ribs) may be correlated by the roughness functions, $R(e^+)$ or dimensionless velocity at the tip of the ribs and $G(e^+)$ or dimensionless temperature at the tip of the ribs, respectively. According to Han (1988), the laws of the wall can also be applied to fully developed turbulent flow in rectangular channels with repeated-rib rougheners and with different channel aspect ratios. Thus, the friction and heat transfer similarity laws in rectangular channels with four-sided ribbed walls can be expressed by

$$R(e^+) = (f_{rr}/2)^{-1/2} + 2.5\ \ln((2e/D_h)(Z)) + 2.5 \quad (5)$$

$$G(e^+) = ((f_{rr}/2)^{1/2})/\mathrm{St}_r + 2.5\ \ln((2e/D_h)(Z)) + 2.5 \quad (6)$$

$$e^+ = (e/D_h)\ \mathrm{Re}(f_{rr}/2)^{1/2} \quad (7)$$

where

$$Z = 2W/(W + H)$$

For turbulent flow in rectangular channels with varying numbers of ribbed walls, the friction factor, f, can be expressed as a weighted average of the four-side smooth channel friction factor, f_{ss}, and the four-sided ribbed channel friction factor, f_{rr}. These friction factors are weighted by the total smooth wall width at a cross section, Ws, and the total ribbed wall width at a cross section, Wr. On the basis of this assumption, the relationship between three friction factors, f, f_{ss}, and f_{rr}, is given by

$$f_{rr} = f + (Ws/Wr)(f - f_{ss}) \quad (8)$$

The friction roughness function, $R(e^+)$, and heat transfer roughness function, $G(e^+)$, can be experimentally determined and correlated by friction factor, f, and ribbed wall Stanton number, St_r, for fully developed turbulent flow in a rectangular channel with different number of ribbed walls.

Results and Discussion

Regionally Averaged Heat Transfer. Figures 2–7 represent regionally averaged heat transfer coefficients, which are computed and plotted as normalized Nusselt number ratio versus normalized axial distance from the channel entrance. In these figures, rib placement on specific channel walls is shown in the frame. Letters F, T, R, and B represent front, top, rear, and bottom walls, respectively. Figure 2 represents the regionally averaged Nusselt number distributions for the smooth case. The Nusselt number ratio decreases with increasing axial distance and reaching a constant value in the fully developed region for a given Reynolds number. The results are as expected and compare well with the Dittus–Boelter correlation, Eq. (4).

Figures 3–7 are the results of the cases with one, two, and four ribbed channel walls. These figures show the regionally averaged ribbed-side and smooth-side Nusselt number ratio distributions for full transverse ribs versus normalized axial distance. The results show that for all cases, local Nusselt number ratios on ribbed as well as on smooth walls decrease with increasing Reynolds number. The Nusselt number ratio reaches almost a constant value in the fully developed region. Local smooth and ribbed wall Nusselt number ratios increase with each additional ribbed wall.

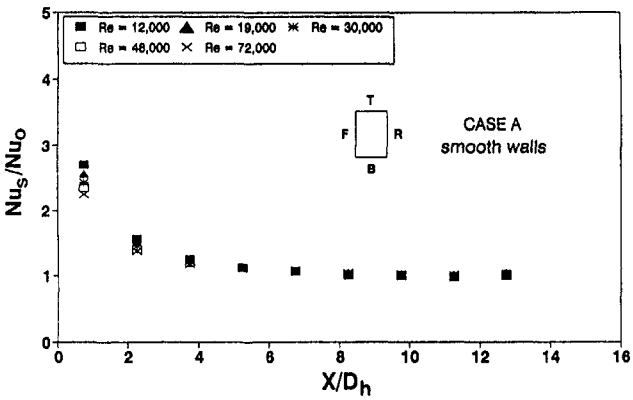

Fig. 2 Axial heat transfer distributions—smooth channel

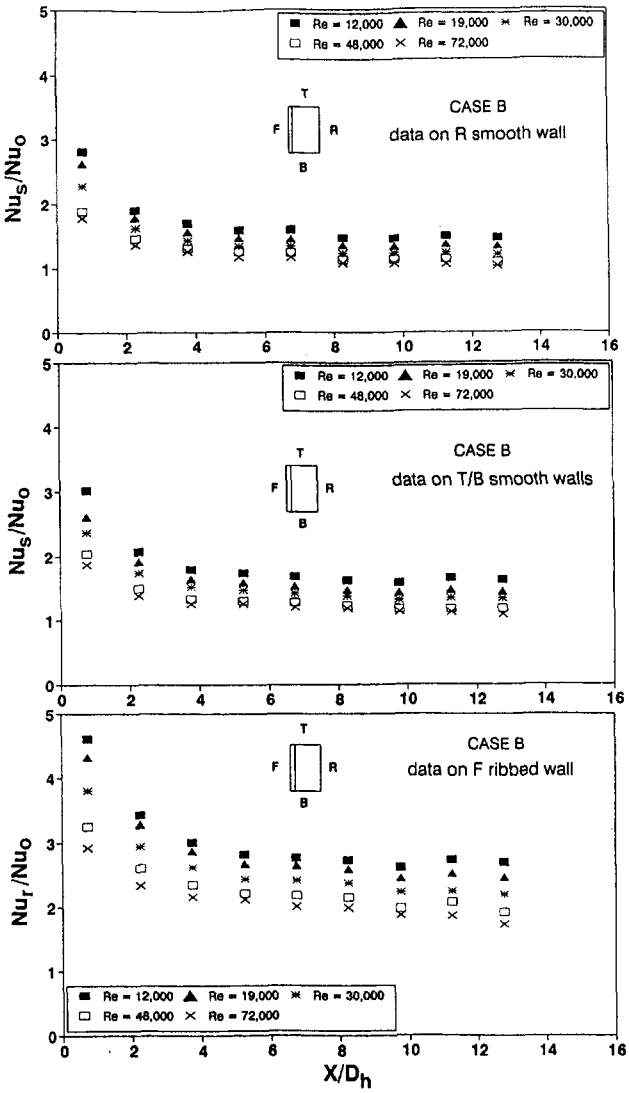

Fig. 3 Axial heat transfer distributions—one long wall ribbed channel

Channel Averaged Heat Transfer and Pressure Drop. Figure 8 shows Nu_r/Nu_o and Nu_s/Nu_o, the Nusselt number ratio versus Reynolds number for cases A–F. The ribbed-side and smooth-side Nusselt number ratios are the average values of the regional ribbed wall and smooth wall Nusselt number ratios for the fully developed heated channel length (X/D_h = 5.25 to X/D_h = 12.75), respectively. It is evident from the results that the channel Nusselt number ratio decreases as Reynolds number increases.

Case B with one 7.62 cm ribbed wall shows a heat transfer enhancement of 2.72 to 1.92 times over the range of Reynold numbers from 11,000 to 72,000. Nusselt number ratios on adjacent and opposite smooth sides are in the range of 1.64 to 1.15 (about 40 percent decrease from that of the ribbed side) and 1.50 to 1.08 (about 45 percent decrease from that of the ribbed side), respectively. The channel with two opposite 7.62 cm ribbed walls, Case C, exhibits an enhancement of 2.96 to 2.04 on ribbed walls and of 1.91 to 1.38 on smooth walls. This constitutes an increase in ribbed wall heat transfer of about 10 percent over Case B. Ribs on one 3.81 cm wall, Case D, give about 12 percent lower ribbed-wall heat transfer (2.39 to 1.76) than that of the case with ribs on one 7.62 cm wall. On the adjacent smooth walls, the Nusselt number ratios are about 7 percent lower (1.43 to 1.06) and on the opposite smooth wall the ratios are about 15 percent lower (1.2 to 1.02) compared to the corresponding values of Case B. Ribs on two opposite 3.81 cm walls, Case E, show a reduction of 15 percent in the ribbed wall and 23 percent in the smooth wall heat transfer values compared to the corresponding values of Case C, channel with ribs on two 7.62 cm walls. The fully ribbed channel, Case F, exhibits the highest heat transfer enhancement of 3.24 to 2.17 over the range of Reynolds numbers (about 6 percent higher than Case C with two ribbed walls. This trend of heat transfer enhancement with increase in the number of ribbed walls is apparently due to the increase in the level of turbulence generated in the channel.

Figure 9 compares the friction factor ratio for all the cases studied. The results show that the friction factor ratio increases with increasing Reynolds number. Ribs on all four walls of the channel, Case F, create maximum pressure-drop/friction-factor that is about 12.14 times f_o for the Reynolds number of 30,000. The flow encounters greater resistance with each additional ribbed wall and thus experiences higher friction. The friction factor ratio, f/f_o, for the smooth channel is slightly higher when compared to the calculated Blasius values for a smooth circular pipe. For comparison at Reynolds number of 30,000, the friction ratio is 2.85, 4.76, 4.93, and 8.38 for cases D, E, B, and C, respectively. There is a 67 percent increase in the friction values with ribs on two 3.81 cm walls than with ribs on one 3.81 cm wall, and a 70 percent increase with ribs on two 7.62 cm walls compared to that with ribs on one 7.62 cm wall.

Heat Transfer Performance. Figure 10 represents the ribbed-wall Nusselt number ratio and the smooth-wall Nusselt number ratio versus the friction factor ratio for the cases B to F. Results show that the Nusselt number ratio decreases while the friction factor ratio increases with increasing Reynolds number as discussed in the previous section. This means that the heat transfer performance decreases with increasing Reynolds numbers. Case D with ribs on one 3.81 cm wall shows 2.39 to 1.76 times rib side heat transfer enhancement for a corresponding friction factor ratio increase of 2.44 to 3.31. Case C with ribs on two 7.62 cm walls provides 2.96 to 2.04 times rib side

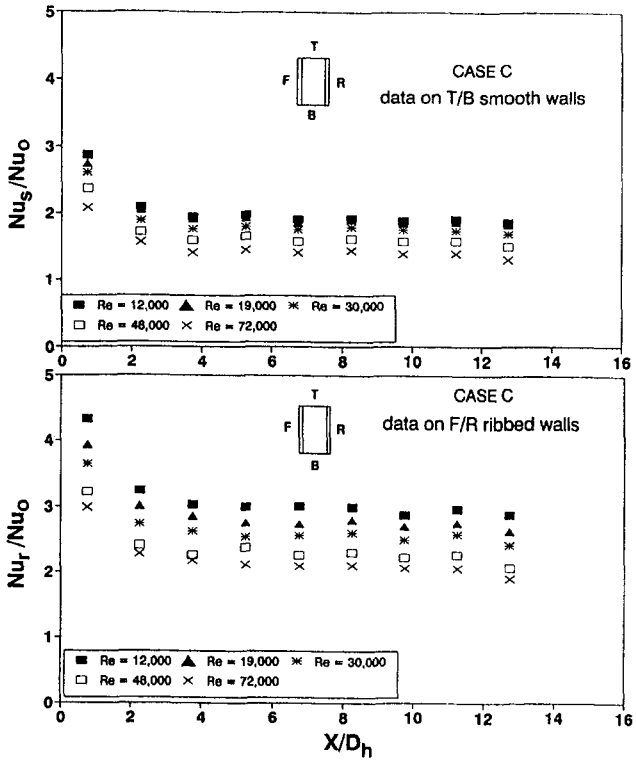

Fig. 4 Axial heat transfer distributions—two long wall ribbed channel

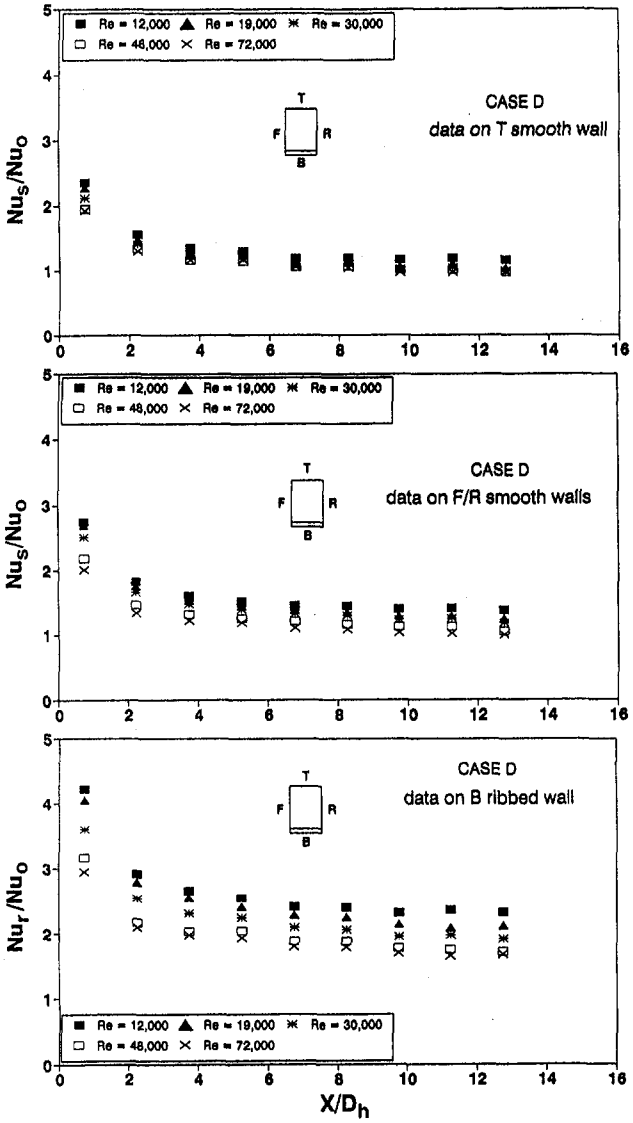

Fig. 5 Axial heat transfer distributions—one short wall ribbed channel

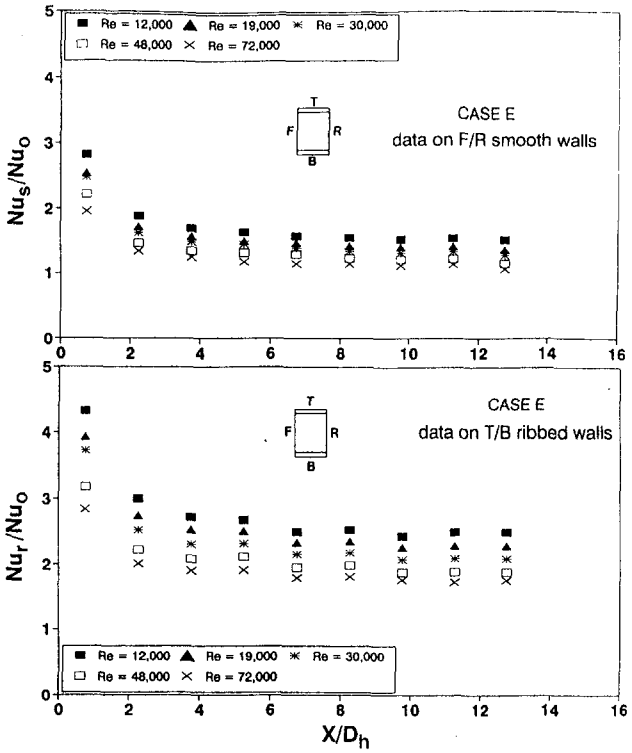

Fig. 6 Axial heat transfer distributions—two short wall ribbed channel

heat transfer enhancement and 6.68 to 9.95 times corresponding pressure drop penalty with increasing Reynolds number from 12,000 to 72,000. On the other hand, Case F with four ribbed walls enhances the rib side heat transfer by 3.28 to 2.08 times but also increases the pressure drop by 9.55 to 14.33 times, with increasing Reynolds number.

Friction and Heat Transfer Correlations. As discussed earlier, the wall similarity laws were employed to correlate the friction and heat transfer data for fully developed turbulent flow in rectangular channel with one, two, and four ribbed walls. According to the friction similarity law, the measured friction factor, f, the ribbed and smooth wall widths, Wr and Ws, channel width and height, W and H, the rib height-to-hydraulic diameter ratio, e/D_h, and the Reynolds number are correlated with friction roughness function, $R(e^+)$, given in Eq. (5). The plot of $R(e^+)$ versus the roughness Reynolds number, e^+, is shown in Fig. 11(a). The friction roughness function correlation of the present investigation is given by Eq. (9) with a deviation of ±4 percent:

$$R(e^+) = 3.41, \quad 836 \geq e^+ \geq 130 \tag{9}$$

It is evident that the friction roughness function is independent of the roughness Reynolds number for all the cases studied. From the experimental values of $R(e^+)$, the friction factor, f, can be predicted by Eqs. (5) and (8) for channels with different aspect ratios used in applications requiring different number of ribbed walls. The correlated value of the function $R(e^+)$ of the present study with one, two, and four ribbed walls for $P/e = 8$ is about 7 percent higher than the correlated value of Han (1988) with two ribbed walls for $P/e = 10$.

According to the heat transfer similarity law, the measured Stanton number on the ribbed walls, St_r, the friction factor, f, the ribbed and smooth wall widths, Wr and Ws, and $R(e^+)$ are correlated with the heat transfer roughness function, $G(e^+)$, given in Eq. (6). $G(e^+)$ versus the roughness Reynolds number, e^+, is plotted in Fig. 11(b). The heat transfer roughness function increases with increasing roughness Reynolds number for all the rib configurations. On the other hand, the value of $G(e^+)$ decreases with additional ribbed walls. The correlation of $G(e^+)$ for the present investigation is given by Eq. (10) with a deviation of ±4 percent. These results for $P/e = 8$ compare reasonably well with Han (1988) with two ribbed walls for $P/e = 10$. For a given rib configuration, number of ribbed walls,

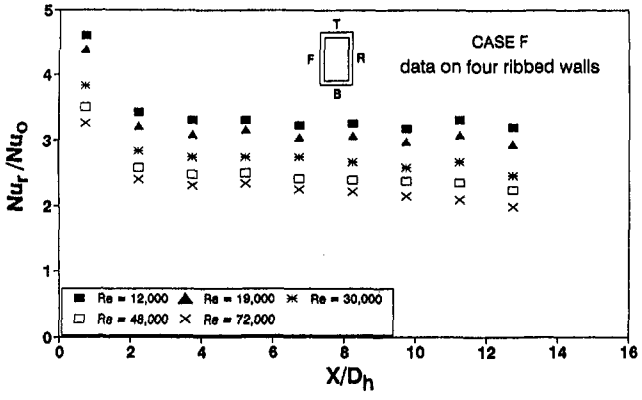

Fig. 7 Axial heat transfer distributions—four wall ribbed channel

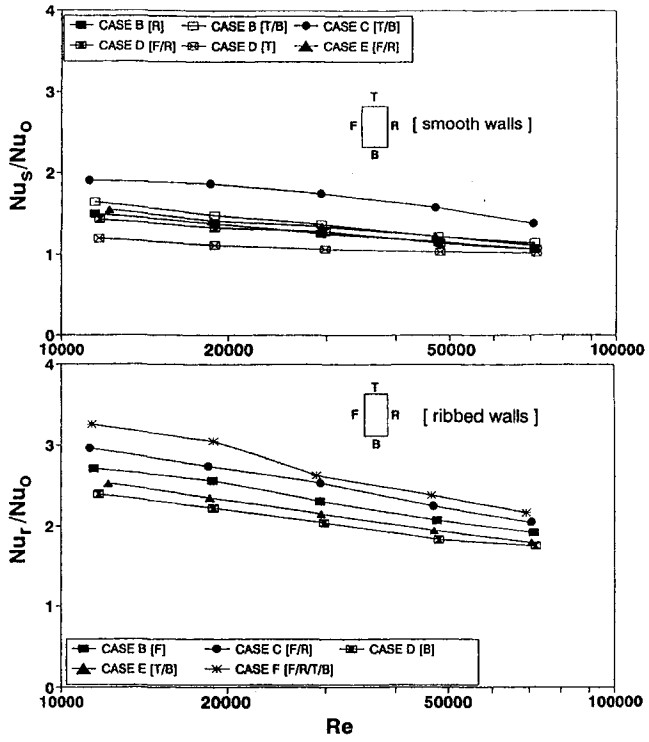

Fig. 8 Nusselt number ratio versus Reynolds number

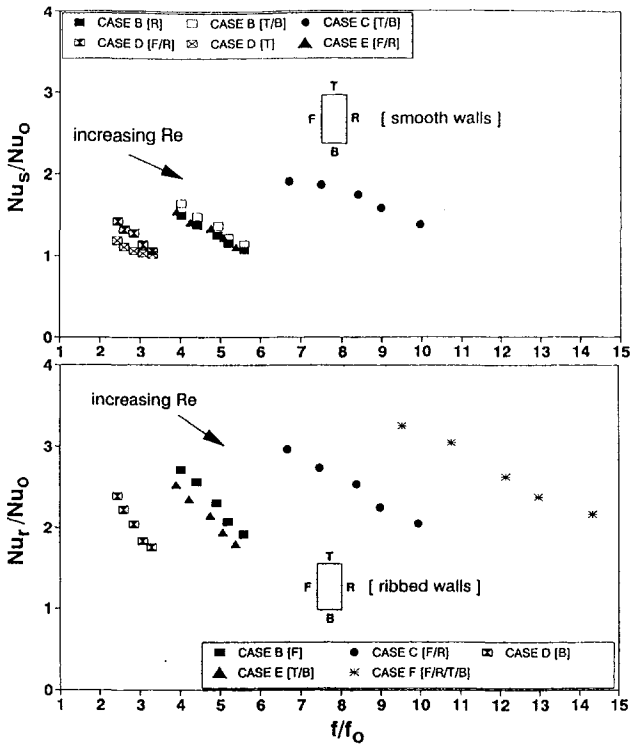

Fig. 10 Nusselt number ratio versus friction factor ratio

and flow Reynolds number, the heat transfer coefficient can be predicted from the experimental values of heat transfer roughness function, $G(e^+)$ and Eqs. (5)–(8).

$$G(e^+) = 1.427(e^+)^{0.435}(Wr/Wt)^{-0.156},$$

$$836 \geq e^+ \geq 130 \quad (10)$$

One of the goals of the present investigation is to confirm the validity of the method used in the past (Han, 1984, 1988) to predict the friction factor in four-sided ribbed wall channels. Experiments conducted in the past have involved channels with two opposite rib-roughened walls. The friction factor for a four-sided ribbed duct is needed to correlate the friction roughness and heat transfer roughness functions. As explained earlier, in the present study, the four-sided friction factor, f_{rr}, is calculated by Eq. (8) for channels with one and two ribbed walls. These values are then compared with the experimental values of Case F, the channel with four-ribbed walls. The present predictions of four-sided ribbed channel friction factor to be used for cases with fewer ribbed walls agree with the experimental results. The present experimental study strongly verifies the validity of the prediction method used to calculate friction factor for four-sided ribbed-wall channels.

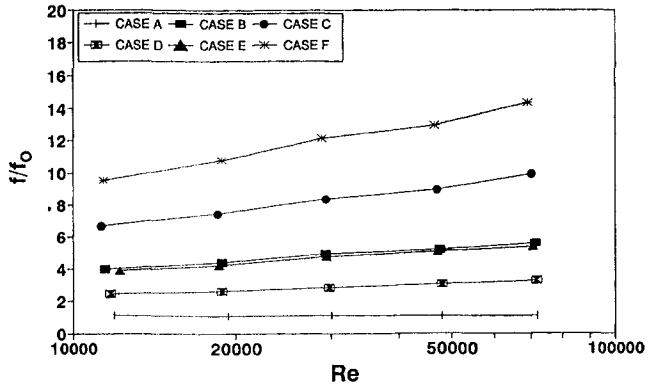

Fig. 9 Friction factor ratio versus Reynolds number

Conclusions

- The regionally averaged Nusselt number ratio decreases with increasing Reynolds number for the range of the test data. Local regional Nusselt number ratio reaches almost a constant value in the fully developed region of the channel.
- Relative to a smooth circular pipe, the heat transfer enhancement increases with the increase in the number of ribbed channel walls and ranges from 2.04 for one ribbed wall case to 2.63 (30 percent increase) for four ribbed wall case, for Re = 30,000.
- The channel with two 7.62 cm ribbed walls shows a 10 percent increase in heat transfer enhancement over the one 7.62 cm ribbed wall case. The case with two 3.81 cm ribbed walls shows a 5 percent increase in heat transfer enhancement over the case with one 3.81 cm ribbed wall, for Re = 30,000. The four ribbed wall case shows an increase of 29 percent over the case with ribs on one 3.81 cm wall and 4 percent increase over the case with ribs on two 7.62 cm walls, respectively, for Re = 30,000.
- Friction factor ratios increase with increasing Reynolds number. The lowest friction factor occurs for the case with minimum total ribbed wall width at a cross section, Wr. The friction ratio is highest in the four ribbed wall case. The heat transfer performance decreases with increasing Reynolds number.
- The friction roughness function, $R(e^+)$, is independent of the roughness Reynolds number (e^+) for all the cases studied ($P/e = 8$), and is equal to 3.41, which is about 7 percent higher than that of Han (1988) with two ribbed walls ($P/e = 10$).
- The heat transfer roughness function, $G(e^+)$, increases with increasing roughness Reynolds number (e^+) and decreases with additional ribbed walls in the channel. The correlation of the function for the present study ($P/e =$

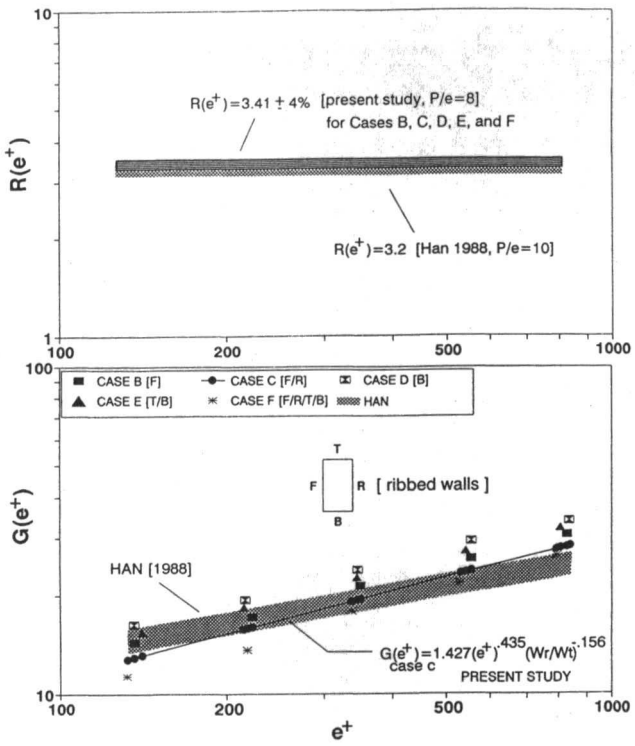

Fig. 11 (*a*) **Ribbed channel friction correlation;** (*b*) **ribbed channel heat transfer correlation**

8) compares reasonably well with Han (1988) with two ribbed walls ($P/e = 10$).

- The friction factor can be determined by a weighted average of the four-sided smooth duct friction factor and the four-sided ribbed duct friction factor as indicated in Eq. (8). Experimental results agree with the past prediction studies for cases with fewer ribbed walls. The prediction method and the experimental data may be applied to the design of equipment that requires internal cooling channels with one, two, three, or four ribbed walls.

Acknowledgments

This material is based upon work supported by the National Science Foundation under Grant No. CTS-9116489. The research was conducted at McNeese State University.

References

Acharya, S., Dutta, S., Myrum, T. A., and Baker, R. S., 1993, "Periodically Developed Flow and Heat Transfer in a Ribbed Duct," *Int. J. Heat Mass Transfer,* Vol. 36, pp. 2069–2082.

Chandra, P. R., Han, J. C., and Lau, S. C., 1988, "Effect of Rib Angle on Local Heat/Mass Transfer Distribution in a Two-Pass Rib Roughened Channel," ASME JOURNAL OF TURBOMACHINERY, Vol. 110, pp. 233–241.

Chandra, P. R., and Han, J. C., 1989, "Pressure Drop and Mass Transfer in Two-Pass Ribbed Channels," *J. of Thermophysics and Heat Transfer,* Vol. 3, pp. 315–320.

Chyu, M. K., and Natarajan, V., 1995, "Surface Heat Transfer From a Three-Pass Blade Cooling Passage Simulator," ASME JOURNAL OF TURBOMACHINERY, Vol. 117, pp. 650–656.

Dipprey, D. F., and Sabersky, R. H., 1963, "Heat and Momentum Transfer in Smooth and Rough Tubes in Various Prandtl Number," *Int. J. Heat Mass Transfer,* Vol. 6, pp. 329–353.

Han, J. C., Glicksman, L. R., and Rohsenow, W. M., 1978, "An Investigation of Heat Transfer and Friction for Rib-Roughened Surfaces," *Int. J. Heat Mass Transfer,* Vol. 21, pp. 1143–1156.

Han, J. C., 1984, "Heat Transfer and Friction in Channels With Two Opposite Rib-Roughened Walls," ASME *Journal of Heat Transfer,* Vol. 106, pp. 774–781.

Han, J. C., Park, J. S., and Lei, C. K., 1985, "Heat Transfer Enhancement in Channels With Turbulence Promoters," ASME *Journal of Engineering for Gas Turbines and Power,* Vol. 107, pp. 629–635.

Han, J. C., 1988, "Heat Transfer and Friction Characteristics in Rectangular Channels With Rib Turbulators," ASME *Journal of Heat Transfer,* Vol. 110, pp. 321–328.

Han, J. C., and Park, J. S., 1988, "Developing Heat Transfer in Rectangular Channels With Rib Turbulators," *Int. J. Heat Mass Transfer,* Vol. 31, pp. 183–195.

Han, J. C., Ou, S., Park, J. S., and Lei, C. K., 1989, "Augmented Heat Transfer in Rectangular Channels of Narrow Aspect Ratios With Rib Turbulators," *Int. J. Heat Mass Transfer,* Vol. 32, pp. 1619–1630.

Han, J. C., Chandra, P. R., and Lau, S. C., 1988, "Local Heat/Mass Transfer Distributions Around Sharp 180° Turns in Two-Pass Smooth and Rib-Roughened Channels," ASME *Journal of Heat Transfer,* Vol. 110, pp. 91–98.

Han, J. C., and Zhang, P., 1991, "Effect of Rib-Angle Orientation on Local Mass Transfer Distribution in a Three-Pass Rib-Roughened Channel," ASME JOURNAL OF TURBOMACHINERY, Vol. 113, pp. 123–130.

Han, J. C., Zhang, Y. M., and Lee, C. P., 1991, "Augmented Heat Transfer in Square Channels With Parallel, Crossed, and V-Shaped Angled Ribs," ASME *Journal of Heat Transfer,* Vol. 113, pp. 590–596.

Han, J. C., and Zhang, Y. M., 1992, "High Performance Heat Transfer Ducts With Parallel Broken and V-Shaped Broken Ribs," *Int. J. Heat Mass Transfer,* Vol. 35, pp. 513–523.

Han, J. C., Huang, J. J., and Lee, C. P., 1993, "Augmented Heat Transfer in Square Channels With Wedge-Shaped and Delta-Shaped Turbulence Promoters," *J. of Enhanced Heat Transfer,* Vol. 1, pp. 37–52.

Kays, W. M., and Crawford, M. E., 1989, *Convective Heat and Mass Transfer,* 2nd ed., McGraw-Hill, New York.

Kline, S. J., and McClintock, F. A., 1953, "Describing Uncertainties in Single Sample Experiments," *Mechanical Engineering,* Vol. 75, Jan., pp. 3–8.

Kukreja, R. T., Lau, S. C., and McMillin, R. D., 1993, "Local Heat/Mass Transfer Distribution in a Square Channel with Full and V-Shaped Ribs," *Int. J. Heat Mass Transfer,* Vol. 36, pp. 2013–2020.

Liou, T. M., and Hwang, J. J., 1992, "Turbulent Heat Transfer Augmentation and Friction in Periodic Fully Developed Channel Flows," ASME *Journal of Heat Transfer,* Vol. 114, pp. 56–64.

Metzger, D. E., and Vedula, R. P., 1987, "Heat Transfer in Triangular Channels With Angled Roughness Ribs on Two Walls," *Experimental Heat Transfer,* Vol. 1, pp. 31–44.

Nikuradse, J., 1950, "Laws for Flow in Rough Pipes," NACA TM 1292.

Park, J. S., Han, J. C., Huang, Y., and Ou, S., 1992, "Heat Transfer Performance Comparisons of Five Different Rectangular Channels with Parallel Angled Ribs," *Int. J. Heat Mass Transfer,* Vol. 35, pp. 2891–2903.

Taslim, M. E., Li, T., and Kercher, D. M., 1996, "Experimental Heat Transfer and Friction in Channels Roughened With Angled, V-Shaped, and Discrete Ribs on Two Opposite Walls," ASME JOURNAL OF TURBOMACHINERY, Vol. 118, pp. 20–28.

Webb, R. L., Eckert, E. R. G., and Goldstein, R. J., 1971, "Heat Transfer and Friction in Tubes With Repeated-Rib Roughness," *Int. J. Heat Mass Transfer,* Vol. 14, pp. 601–617.

Zhang, Y. M., Gu, W. Z., and Han, J. C., 1994, "Augmented Heat Transfer in Triangular Ducts With Full and Partial Ribbed Walls," *J. of Thermophysics and Heat Transfer,* Vol. 8, pp. 574–579.

An Experimental Investigation of the Rib Surface-Averaged Heat Transfer Coefficient in a Rib-Roughened Square Passage

M. E. Taslim

C. M. Wadsworth

Department of Mechanical Engineering,
Northeastern University,
Boston, MA 02115

Turbine blade cooling, a common practice in modern aircraft engines, is accomplished, among other methods, by passing the cooling air through an often serpentine passage in the core of the blade. Furthermore, to enhance the heat transfer coefficient, these passages are roughened with rib-shaped turbulence promoters (turbulators). Considerable data are available on the heat transfer coefficient on the passage surface between the ribs. However, the heat transfer coefficients on the surface of the ribs themselves have not been investigated to the same extent. In small aircraft engines with small cooling passages and relatively large ribs, the rib surfaces comprise a large portion of the passage heat transfer area. Therefore, an accurate account of the heat transfer coefficient on the rib surfaces is critical in the overall design of the blade cooling system. The objective of this experimental investigation was to conduct a series of 13 tests to measure the rib surface-averaged heat transfer coefficient, h_{rib}, in a square duct roughened with staggered 90 deg ribs. To investigate the effects that blockage ratio, e/D_h, and pitch-to-height ratio, S/e, have on h_{rib} and passage friction factor, three rib geometries corresponding to blockage ratios of 0.133, 0.167, and 0.25 were tested for pitch-to-height ratios of 5, 7, 8.5, and 10. Comparisons were made between the rib average heat transfer coefficient and that on the wall surface between two ribs, h_{floor}, reported previously. Heat transfer coefficients of the upstream-most rib and that of a typical rib located in the middle of the rib-roughened region of the passage wall were also compared. It is concluded that:

1 The rib average heat transfer coefficient is much higher than that for the area between the ribs;

2 similar to the heat transfer coefficient on the surface between the ribs, the average rib heat transfer coefficient increases with the blockage ratio;

3 a pitch-to-height ratios of 8.5 consistently produced the highest rib average heat transfer coefficients amongst all tested;

4 under otherwise identical conditions, ribs in upstream-most position produced lower heat transfer coefficients than the midchannel positions,

5 the upstream-most rib average heat transfer coefficients decreased with the blockage ratio; and

6 thermal performance decreased with increased blockage ratio. While a pitch-to-height ratio of 8.5 and 10 had the highest thermal performance for the smallest rib geometry, thermal performance of high blockage ribs did not change significantly with the pitch-to-height ratio.

Introduction

Various cooling methods have been developed over the years to ensure that the turbine blade metal temperatures are maintained at a level consistent with airfoil design life. The objective in turbine blade cooling is to achieve maximum internal heat transfer coefficients while minimizing the coolant flow rate. One such method is to route coolant air through rib-roughened serpentine channels within the airfoil and convectively remove heat from the blade. The coolant is then ejected either at the tip of the blade, through the cooling slots along the trailing edge, or through the film holes along the airfoil surface.

Geometric parameters such as channel aspect ratio (AR), rib height-to-passage hydraulic diameter (e/D_h) or blockage ratio, rib angle of attack (α), the manner in which the ribs are positioned relative to one another (in-line, staggered, criss-cross, etc.), rib pitch-to-height ratio (S/e) and rib shape (round versus sharp corners, fillets, rib aspect ratio (AR_r), and skewness toward the flow direction) have pronounced effects on both local and overall heat transfer coefficients. Some of these effects were studied by different investigators, such as Abuaf et al. (1986), Burggraf (1970), Chandra et al. (1988, 1989), Han et al. (1978, 1984, 1985, 1992), Metzger et al. (1983, 1990), Taslim et al. (1988a, b, 1991a, b, c), Webb et al. (1971). A great majority of these studies, however, measure the heat transfer coefficients on the surface between the ribs and a few measured the overall average heat transfer coefficient for the combined ribs and area between them.

The objective of this investigation was, while isolating the ribs from the wall surface thermally, to measure the overall heat transfer coefficient on the rib surface and to study the effects pitch-to-height ratio (S/e), blockage ratio (e/D_h), and rib orientation (upstream-most position or in the middle of channel rib-

Contributed by the International Gas Turbine Institute and presented at the 39th International Gas Turbine and Aeroengine Congress and Exposition, The Hague, The Netherlands, June 13–16, 1994. Manuscript received by the International Gas Turbine Institute February 15, 1994. Paper No. 94-GT-162. Associate Technical Editor: E. M. Greitzer.

roughened portion) have on the rib surface heat transfer coefficient for a channel aspect ratio (AR) of one.

Among those investigations dealing with the measurement of heat transfer coefficients on the ribs are the following. Solntsev et al. (1973) experimentally investigated heat transfer in the vicinity of sudden two and three-dimensional steps of circular and square cross-sectional areas mounted on a flat surface in an open channel. Enhancement in heat transfer coefficient is reported for a range of Reynolds number between 10^4 to 10^5.

Berger and Hau (1979) did an experimental study of flow over square ribs in a pipe using an electrochemical analogue technique to measure mass/heat transfer on the ribs as well as on the wall surface between them. For a blockage ratio (e/d) of 0.0364, they varied the rib pitch-to-height ratio from 3 to 10 for a range of Reynolds number between 10,000 and 25,000. At a Reynolds number of 10^4, they showed enhancements, compared to smooth channels, in mass (heat) transfer on the ribs in the order of 4.4 and 5.2 for pitch-to-height ratios of 10 and 7, respectively.

Metzger et al. (1988) used a thermal transient technique to examine the contribution of the rib heat transfer to the overall heat transfer of a rib-roughened wall with variations in rib angle of attack and pitch. Square ribs representing a blockage ratio of 0.14 were mounted on only one wider side of a 0.154 aspect ratio rectangular channel. Main conclusions were that heat transfer on the rib surface significantly contributed to the overall rib-roughened wall heat transfer and this contribution was mainly dependent on rib pitch-to-height spacing, with very little effect of rib angle.

Lockett and Collins (1990) used a holographic interferometry technique to measure heat transfer coefficient in a 0.25 aspect ratio rectangular channel. Square ribs with sharp as well as round top corners representing a blockage ratio, e/D_h, of 0.067 and a pitch-to-height ratio of 7.2 were mounted on one of the wider sides of the channel perpendicular to the flow direction. They reported overall enhancements in heat transfer of up to 2.24 at a Reynolds number of 7400.

Liou et al. (1991) performed both numerical and experimental investigation of turbulent flow in a 4:1 aspect ratio rectangular channel roughened on two opposite wider sides with square ribs in an in-line arrangement perpendicular to the flow direction. The rib blockage ratio, e/D_h, was 0.081 and four pitch-to-height ratios of 5, 10, 15, and 20 were examined at a fixed Reynolds number of 33,000. Two-dimensional Navier–Stokes equations in elliptic form in conjunction with the $k-\epsilon$ turbulence model were solved numerically and holographic interferometry technique was used in the experimental part. They reported an enhancement in heat transfer on the rib surface of 3.1.

Sato et al. (1992) investigated the flow characteristics and heat transfer in a rectangular channel with a total of 20 square ribs on two opposite walls in staggered, in-line, and quarter-pitch-shift arrangements. The channel aspect ratio was 0.2 and the ribs, mounted on the two wider sides of the channel, had a blockage ratio of 0.12. Details of the flow and heat transfer over a typical rib-roughened section (including the rib surface) well downstream of the first rib were presented. They concluded that the staggered arrangement had a better heat transfer performance than the other two arrangements.

Dawes (1994) solved the three-dimensional Navier–Stokes equations in a rotating serpentine coolant passage of cylindrical geometry roughened with square ribs. Rib blockage, e/d, and pitch-to-height ratios were 0.2 and 10, respectively. Results of this work were compared with other numerical and experimental works.

Liou and Hwang (1993) also used the holographic interferometry technique to measure heat transfer coefficient and friction factor in a 0.25 aspect ratio rectangular channel with three rib shapes, including a square rib geometry mounted on two opposite wider sides in an in-line arrangement perpendicular to the flow direction. For one blockage ratio of 0.08, they tested four rib pitch-to-height ratios of 8, 10, 15, and 20 in a range of Reynolds number between 7800 and 50,000. Heat transfer coefficient was measured over the ribs as well as the wall surfaces between the ribs. They reported overall enhancements in heat transfer of 2.2 and 2.7 for semi-cylindrical and square ribs for the range of Reynolds number tested, respectively.

Test Sections

Figure 1 shows schematically the layout and cross-sectional area of a typical test section and rib geometry details are shown in Table 1. All test sections, with a length of 116.84 cm, had a square 3.81 cm by 3.81 cm cross-sectional area. Three walls of these channels were made of 1.27-cm-thick clear acrylic plastic. The fourth wall, on which the surface heaters and instrumented copper rib were mounted and all measurements were taken, was made of a 10.16-cm-thick machineable polyurethane slab. Eighteen ribs of square cross section with sharp corners were symmetrically staggered on the polyurethane and opposite acrylic walls (nine on each wall) at 90 deg angle of attack to the air flow. The entrance region of all test sections was left unturbulated to simulate the cooling passage in the dovetail region of a gas turbine blade. All ribs but one were machined out of acrylic plastic and were mounted on the walls using a special double-stick 0.05-mm-thick tape with minimal temperature deformation characteristics. The instrumented rib on which

Nomenclature

a = channel height (Fig. 1)
b = channel width (Fig. 1)
A = nonturbulated channel cross-sectional area = ab
A_{floor} = wall heat transfer area between two ribs
A_{rib} = rib total heat transfer area (three sides)
A_{total} = total heat transfer area = $A_{\text{rib}} + A_{\text{floor}}$
AR = channel aspect ratio = b/a
AR_r = rib aspect ratio = e/w
D_h = hydraulic diameter based on nonturbulated cross section = $4A/P = a$
e = rib height
$\bar{f}$ = Darcy friction factor = $(\Delta P(D_h/L))/(\frac{1}{2}\rho U_m^2)$
$\bar{f}_s$ = Darcy friction factor in an all-smooth-wall channel
h_{floor} = average heat transfer coefficient on the wall surface between a pair of ribs
h_{overall} = overall average heat transfer coefficient on a rib and the wall surface between a pair of ribs
h_{rib} = rib average heat transfer coefficient
k = air thermal conductivity
L = length of the rib-roughened portion of the test section
$\dot{m}$ = air mass flow rate
$\overline{\text{Nu}}$ = rib average Nusselt number = $h_{\text{rib}}D_h/k$
$\overline{\text{Nu}}_s$ = average Nusselt number in a smooth channel
P = unturbulated passage perimeter
Pr = Prandtl number
Re = Reynolds number
S = rib pitch (center-to-center)
T_f = film temperature = $0.5(T_s + T_m)$
T_m = air mixed mean temperature
T_s = surface temperature
U_m = air mean velocity
w = turbulator width
X = distance between the instrumented rib and test section entrance (Fig. 1)
α = angle of attack
μ = air dynamic viscosity
ΔP = pressure drop across the rib-roughened portion of the test section
ρ = air density

all measurements were taken was machined out of copper. Inside this copper rib, as centrally as possible, was installed a 60 Ohm cylindrical electric heater running the full length using a highly conductive silver glue. Also installed in the copper rib were three calibrated thermocouples to measure the surface temperature. These three thermocouples were equally spaced over the length of the rib with their beads close to the rib surface. Their temperature readings were found to be the same within a fraction of a degree. For data reduction, the average of the three temperatures was used. Copper rib surfaces were polished to minimize the radiational heat losses from the copper rib to the unheated wall. Rib heat transfer coefficient measurements were performed for two distinct rib locations. First, the copper rib was mounted in the middle of the rib-roughened portion of the channel (fifth rib) and the other eight acrylic plastic ribs were arranged on each side with the desired rib pitch-to-height ratio. Second, the copper rib was moved to the upstream-most position and the other eight ribs were mounted downstream of it. Table 1 shows the rib location from the channel entrance, X, for each geometry.

Two 3.81 cm by 27.94 cm custom-made etched-foil heaters with a thickness of 0.15 mm were placed on the polyurethane wall abutting both sides of the copper rib using the same special double-stick tape. The test sections were covered on all sides by 5-cm-thick styrofoam sheets to minimize heat losses to the environment. Surface heat flux in the test section was generated by the heaters through a custom-designed power supply unit. Each heater was individually controlled by a variable transformer.

Before testing, thermocouples were calibrated using ice water and boiling water reference points and calibration curves were constructed for minor deviations (within a fraction of a degree). For a typical test run, the Reynolds number was set by precisely fixing the mass flow rate. The heat flux was induced by adjusting heater power until the copper rib reached the desired temperature. Enough time was given so that the system came to thermal equilibrium, at which time data were recorded. Power to the copper rib was then increased to gather data at a higher surface temperature. This procedure was repeated for all copper temperatures and flow rates.

Static pressure taps were mounted on all three acrylic plastic walls of each test section to measure the pressure drop across

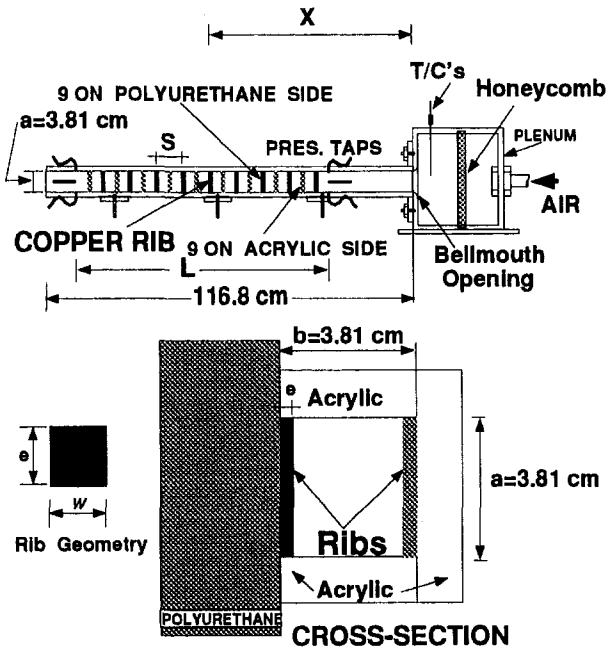

Fig. 1 Schematic of a typical test section

Table 1 Specifications

TESTS	e (mm)	e/D_h	S/e	X (cm)	X/D_h	Remarks
1	9.525	0.25	10	72.39	19.	Middle Position
2	9.525	0.25	8.5	72.39	19.	Middle Position
3	9.525	0.25	7	72.39	19.	Middle Position
4	9.525	0.25	5	72.39	19.	Middle Position
5	9.525	0.167	8.5	40.	10.5	Upstream-most Position
6	6.35	0.167	10	57.15	15.	Middle Position
7	6.35	0.167	8.5	57.31	15.04	Middle Position
8	6.35	0.167	5	57.31	15.04	Middle Position
9	6.35	0.167	8.5	35.72	9.375	Upstream-most Position
10	5.08	0.133	10	57.15	15.	Middle Position
11	5.08	0.133	8.5	57.15	15.	Middle Position
12	5.08	0.133	5	57.15	15.	Middle Position
13	5.08	0.133	8.5	39.88	10.47	Upstream-most Position

AR=1, AR_t = e/w = 1, $\alpha = 90^0$ Staggered for all geometries

the rib-roughened portion of the test section. A contact micromanometer with an accuracy of 0.025 mm of water column measured the pressure differences between the static pressure taps. A critical venturimeter, with choked flow for all cases tested, measured the total mass flow rate entering the test section. The reported friction factor is the overall passage average, $\bar{f}$, and not just the for rib-roughened surfaces. Details of the experimental apparatus and test procedures are reported by Wadsworth (1994).

The radiational heat loss from the heated rib (and wall) to the unheated walls as well as losses to ambient air were taken into consideration when heat transfer coefficients were calculated. The reported heat transfer coefficients are the averages over the rib surfaces and not that of wall surfaces between the ribs. The heat transfer coefficients on the roughened walls for various geometries are reported by those investigators mentioned in the Introduction section. Experimental uncertainties, following the method of Kline and McClintock (1953), were determined to be ±6 percent and ±8 percent for the heat transfer coefficient and friction factor, respectively.

Results and Discussion

Average rib heat transfer results for the 13 rib geometries are compared with the all-smooth-wall channel Dittus–Boelter (1930) correlation ($\overline{Nu}_s = 0.023\ Re^{0.8}\ Pr^{0.4}$) in Figs. 2, 3, 5, 7, 8, 10, 11, 13, and 15. With this correlation, the enhancement (relative to smooth walls) in rib-roughened heat transfer coefficients is readily evaluated. The thermal performance based on the same pumping power is given by $(\overline{Nu}/\overline{Nu}_s)/(\bar{f}/\bar{f}_s)^{1/3}$ (Han et al., 1985), where $\bar{f}_s$ is the all-smooth-wall friction factor from Moody (1944). Air properties for Nusselt and Reynolds number calculations are based on the local film temperature, T_f, for all cases.

Figure 2 shows the Nusselt versus Reynolds numbers for the first rib geometry corresponding to a blockage ratio, e/D_h, of 0.25 and pitch-to-height ratio, S/e, of 10. Copper rib temperature is varied from 43.3°C to 82.2°C with no change in the measured heat transfer coefficient. This lack of effect of copper surface temperature on heat transfer coefficient continued for all geometries and temperatures examined. Furthermore, this insensitivity of the measured heat transfer coefficient to the rib surface temperature supports the accuracy of our accounting for the heat losses to the ambient air and radiational losses from the heated copper rib to the unheated surrounding walls.

To investigate the effects pitch-to-height ratio have on rib heat transfer and channel overall friction factor, the same rib geometry was tested for four pitch-to-height ratios of 5, 7, 8.5, and 10 (geometries 1–4 in Table 1), the results of which are

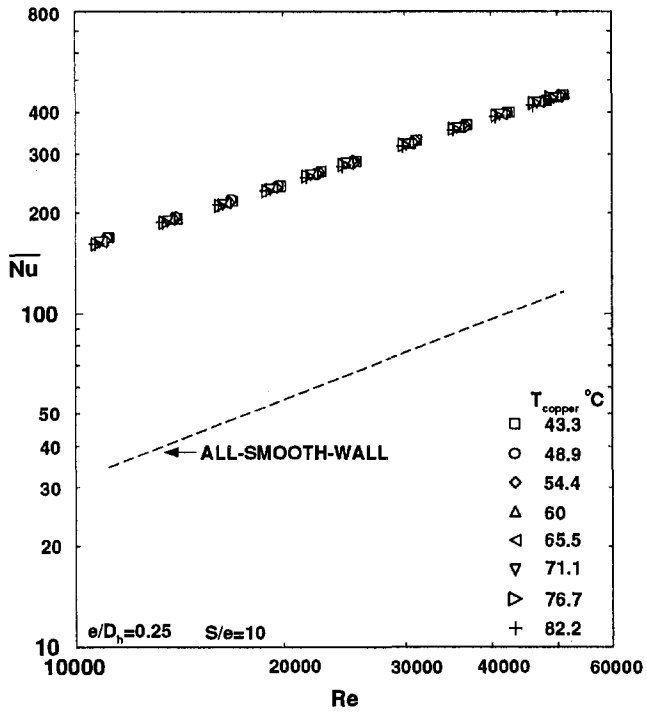

Fig. 2 Rib-averaged Nusselt number for a range of rib surface temperatures

shown in Fig. 3. Also shown in Fig. 3 are the rib heat transfer results for an S/e of 8.5 when the instrumented copper rib was mounted in the upstream-most position (geometry 5 in Table 1). The middle position Nusselt numbers did not change significantly with the pitch-to-height ratio, but were consistently higher for an S/e of 8.5. The heat transfer enhancement for the upstream-most rib was considerably lower than for those in the middle of the rib-roughened region, indicating that upstream ribs and those staggered on the opposite wall contribute significantly to the very high level of heat transfer enhancement of downstream ribs by interrupting the flow and diverting its direction, thus promoting high levels of mixing. Friction factors for these geometries are shown in Fig. 4. Higher friction factors for S/e of 10 and 8.5, compared to 5, are in line with the Colburn (1933) analogy between heat transfer coefficient and friction factor.

Also shown in Fig. 3 are the heat transfer results for the area between the ribs (called floor heat transfer by some investigators) reported by Taslim et al. (1991b). It can be seen that, for the midstream ribs, the rib average heat transfer coefficients are much higher than those for the area between the ribs (h_{floor}). Therefore, the contribution of the ribs to the overall heat transfer in a rib-roughened passage is significant. A simple area-weighted averaging analysis leads to the following relation:

$$\frac{h_{rib}A_{rib}}{h_{overall}A_{overall}} = \left\{1 + \frac{h_{floor}}{h_{rib}}\left[\frac{1}{3}\left(\frac{S}{e} - 1\right)\right]\right\}^{-1}$$

where $h_{overall} = (h_{rib}A_{rib} + h_{floor}A_{floor})/(A_{rib} + A_{floor})$ and $A_{total} = A_{rib} + A_{floor}$. For example, at a typical value of

$$\frac{h_{floor}}{h_{rib}} = \frac{2}{3}$$

and at $S/e = 10$ and 5, the $h_{rib}A_{rib}$ can be as high as 33 to 53 percent of $h_{overall}A_{total}$, respectively.

The next series of four tests, shown in Fig. 5, correspond to a rib blockage ratio of 0.167, three of which (geometries 6–8 in Table 1) were performed for pitch-to-height ratios of 10, 8.5, and 5 with the instrumented copper rib mounted in the middle of the rib-roughened region. The fourth test represents the heat transfer results when copper rib was mounted in upstream-most position (geometry 9 in Table 1). Again, the rib-averaged heat transfer results for the pitch-to-height ratio of 8.5 were slightly higher than those of 10 and significantly higher than those of $S/e = 5$. Also, heat transfer enhancement for the upstream-most rib was lower than that for midpoint ribs, although not as much

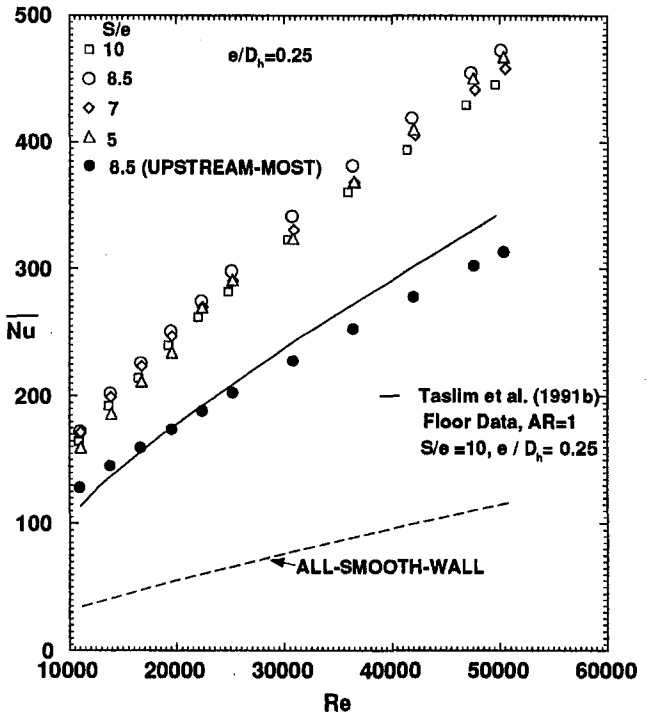

Fig. 3 Rib-averaged Nusselt number for a range of pitch-to-height ratios, $e/D_h = 0.25$

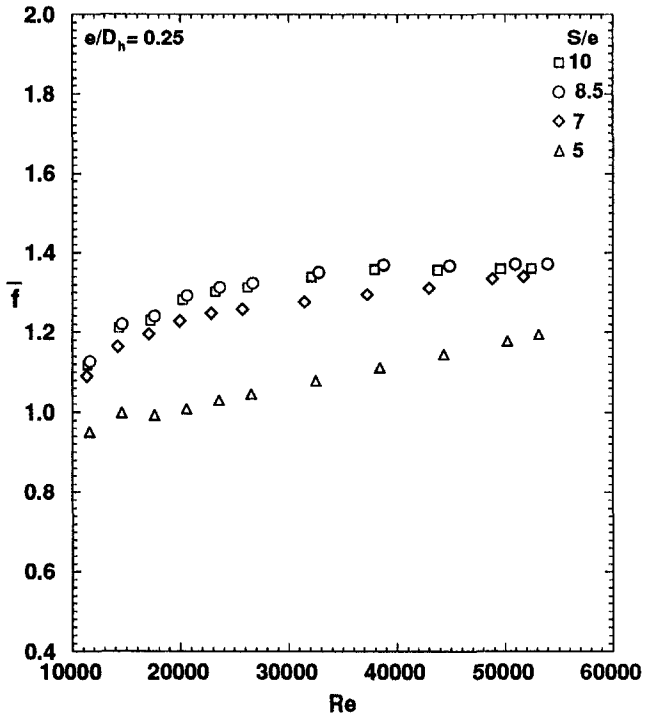

Fig. 4 Channel-averaged friction factor for a range of pitch-to-height ratios, $e/D_h = 0.25$

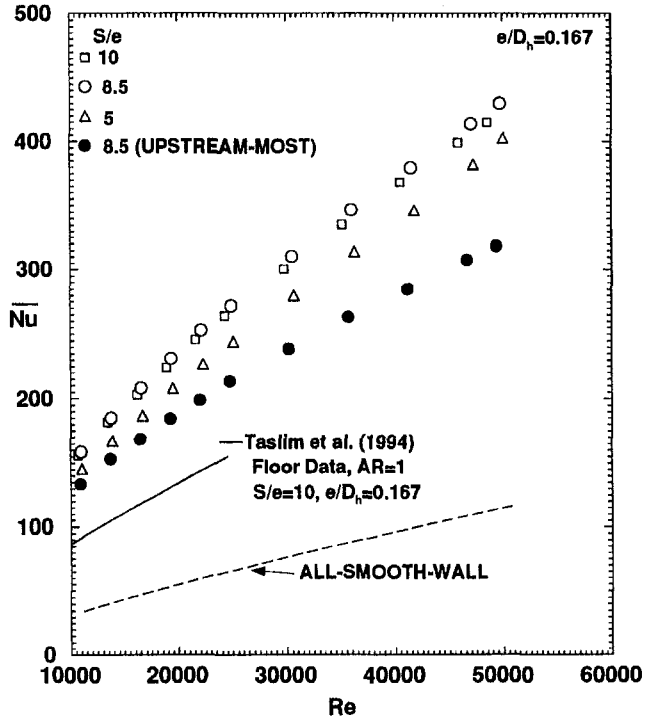

Fig. 5 Rib-averaged Nusselt number for a range of pitch-to-height ratios, $e/D_h = 0.167$

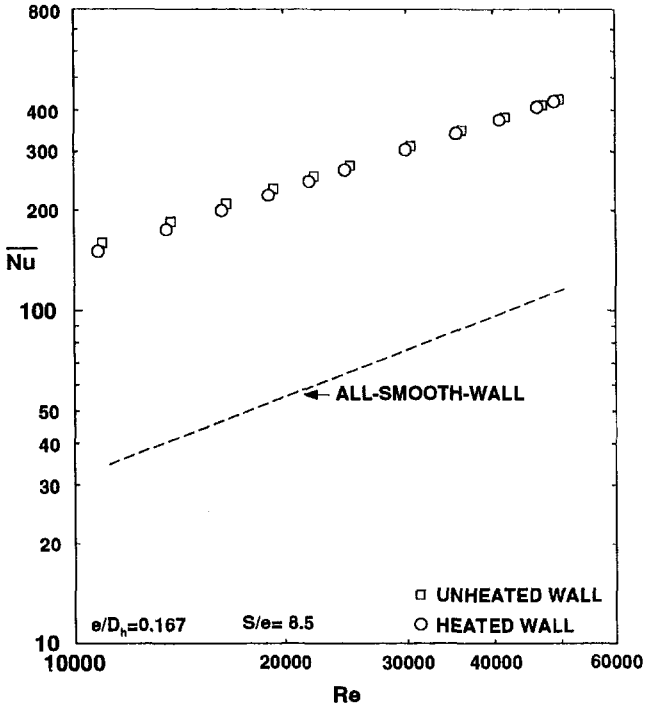

Fig. 7 Comparison of rib-averaged Nusselt number for heated and unheated walls

lower as it was for the blockage ratio of 0.25 as seen in Fig. 3 (we will see that this difference further decreases for a still lower blockage ratio test). Note also that the rib average heat transfer coefficients are much higher than those on the floor, represented by the solid line (Taslim et al., 1996). The friction factors for these tests are shown in Fig. 6, and the trend is similar to that of Fig. 4, i.e., $S/e = 8.5$, showing a slightly higher friction factor.

Figure 7 shows the results of two tests of identical geometries for which the foil heaters were on and off, respectively. No difference, beyond experimental uncertainties, was observed between the two sets of results, indicating that the thermal boundary layer, being interrupted repeatedly by the ribs, did not affect

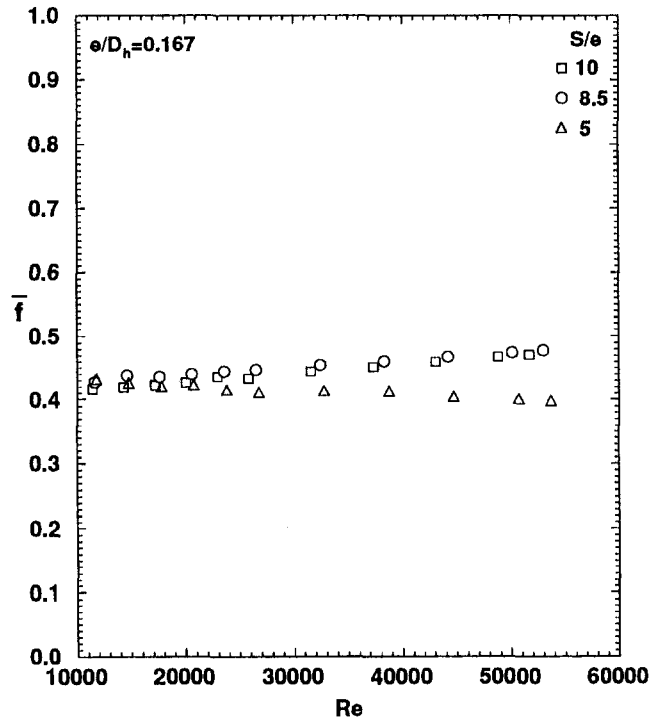

Fig. 6 Channel-averaged friction factor for a range of pitch-to-height ratios, $e/D_h = 0.167$

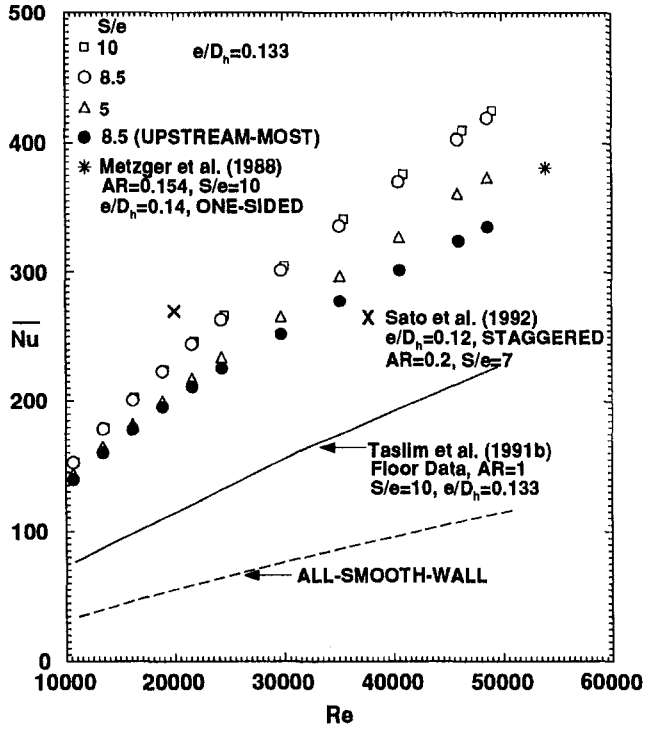

Fig. 8 Rib-averaged Nusselt number for a range of pitch-to-height ratios, $e/D_h = 0.133$

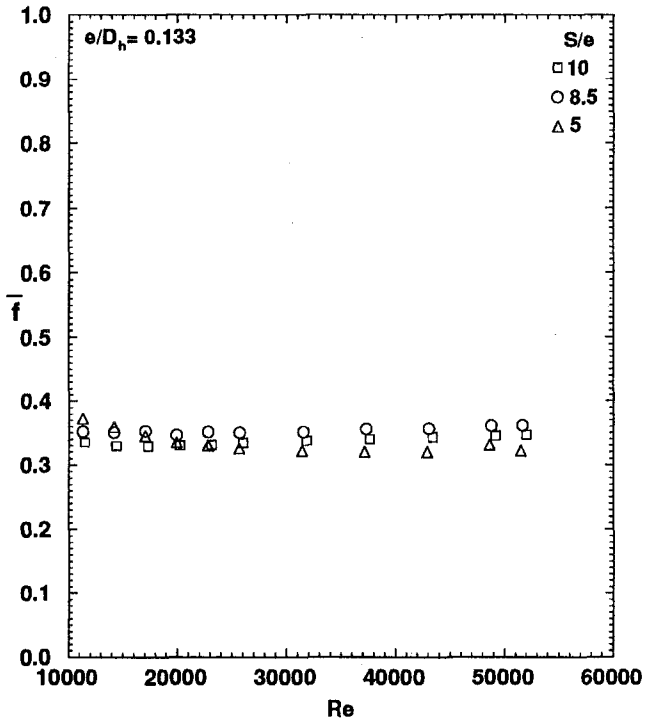

Fig. 9 Channel-averaged friction factor for a range of pitch-to-height ratios, $e/D_h = 0.133$

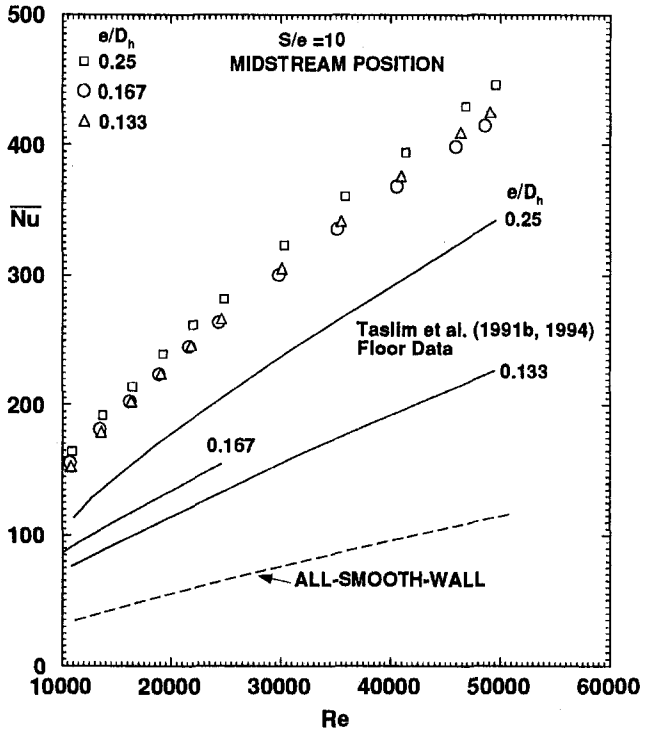

Fig. 11 Rib-averaged Nusselt number for a range of blockage ratios, $S/e = 10$

the heat transfer. It would appear that the mixing phenomenon was the dominant driving force for the high levels of heat transfer coefficient.

The next four tests, shown in Fig. 8, correspond to a yet smaller rib blockage ratio of 0.133. The first three tests (geometries 10–12 in Table 1) were performed for pitch-to-height ratios of 10, 8.5, and 5 with the instrumented copper rib mounted in the middle of the rib-roughened region. The fourth test represents the heat transfer results for the copper rib mounted in the upstream-most position (geometry 13 in Table 1). Floor heat transfer results (Taslim et al., 1991b) are also shown for comparison. Again, heat transfer results for the pitch-to-height ratio of 8.5 were slightly higher than those for 10 and significantly higher than those for $S/e = 5$. In contrast to the above-men-

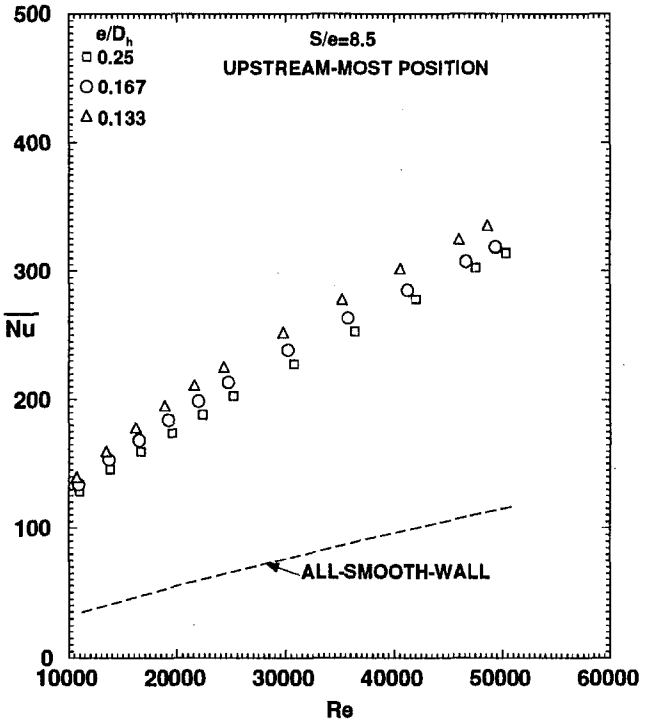

Fig. 10 Average Nusselt number of the upstream-most ribs for a range of blockage ratios

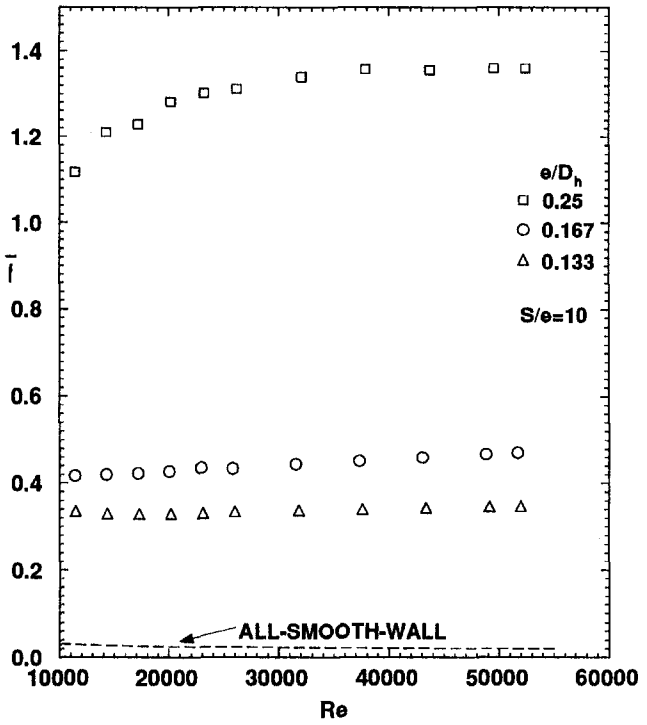

Fig. 12 Channel-averaged friction factor for a range of blockage ratios, $S/e = 10$

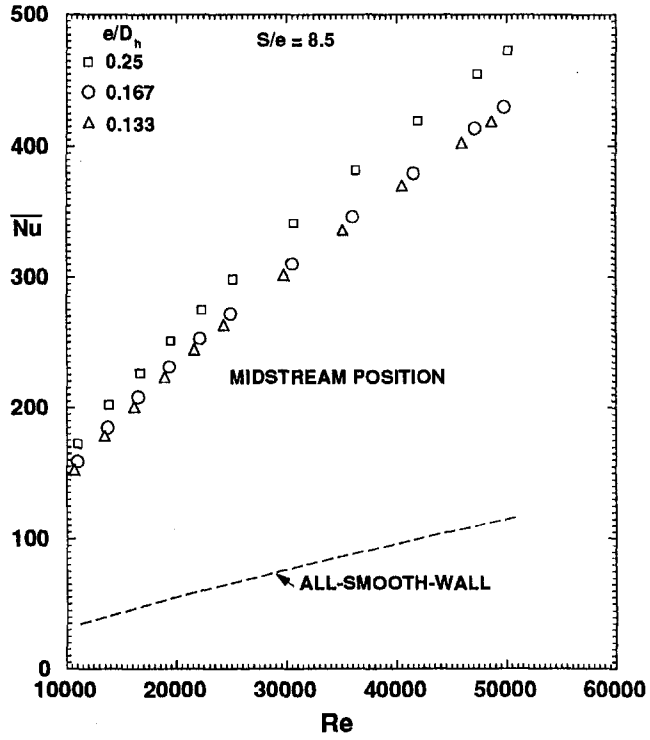

Fig. 13 Rib-averaged Nusselt number for a range of blockage ratios, $S/e = 8.5$

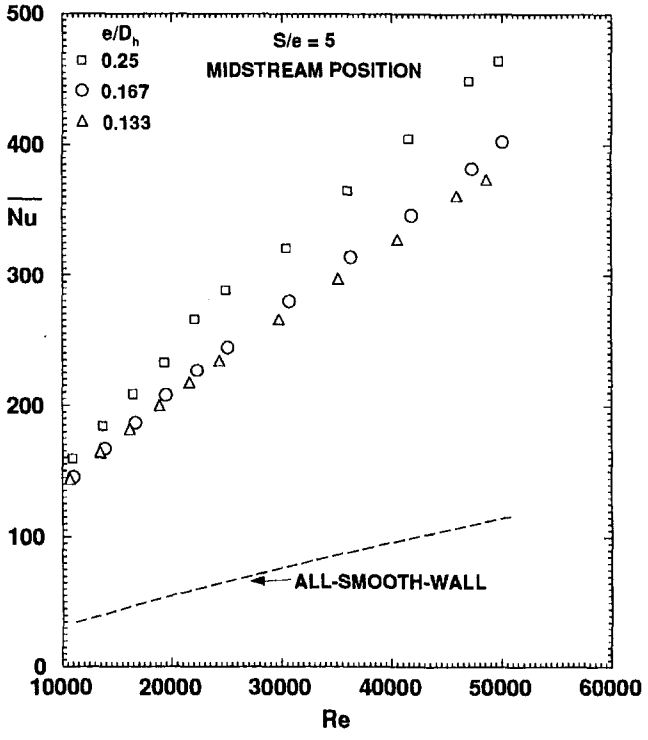

Fig. 15 Rib-averaged Nusselt number for a range of blockage ratios, $S/e = 5$

tioned cases of higher blockage ratios, the heat transfer enhancements for the upstream-most rib were comparable to those of midpoint ribs at low Reynolds numbers, and only at higher Reynolds numbers did they start to deviate. This is an indication that the contribution of the staggered ribs on the opposite wall to the copper rib heat transfer coefficient, caused by the diversion of flow toward the ribs on opposite wall, is more significant for higher blockage ratios and at higher Reynolds number. The two closest geometries found in the open literature are also shown in that figure. The data point from Metzger et al. (1988) is for a one-side-roughened channel, and the data point from Sato et al. (1992) is for a staggered arrangement, both in very

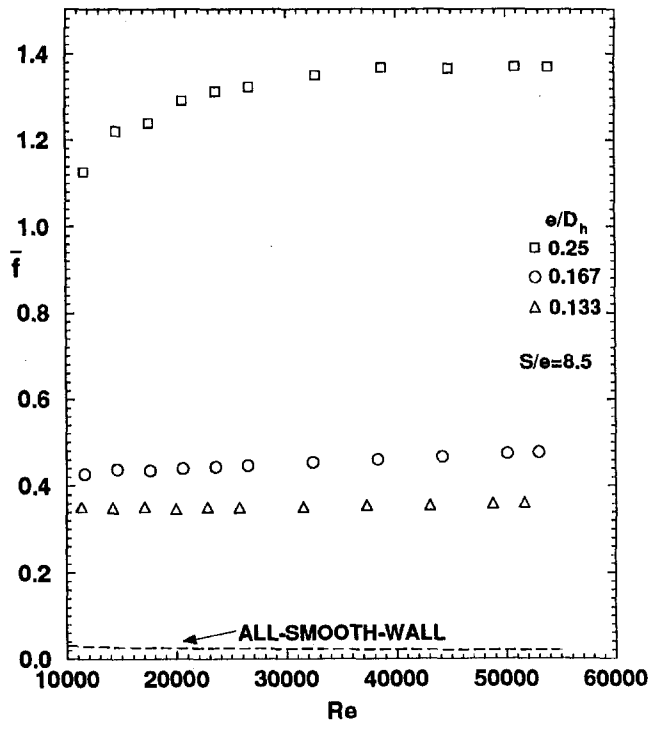

Fig. 14 Channel-averaged friction factor for a range of blockage ratios, $S/e = 8.5$

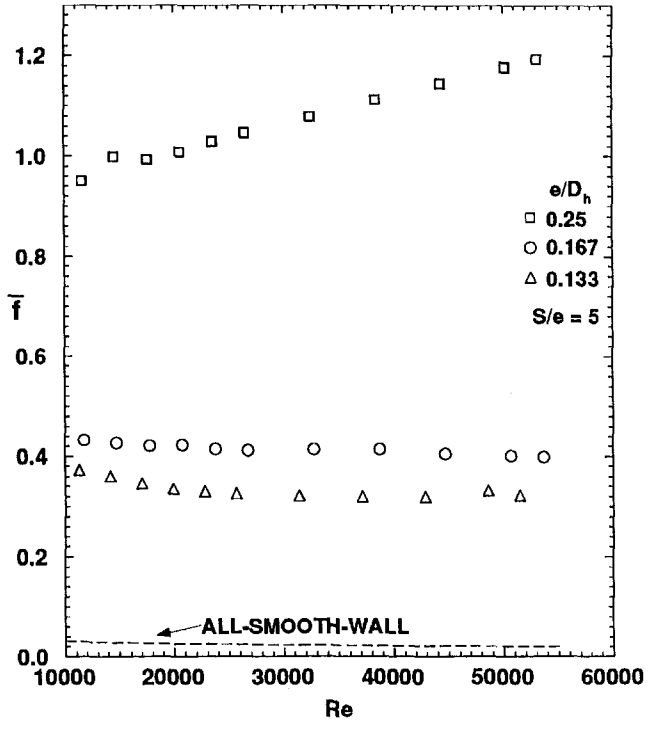

Fig. 16 Channel-averaged friction factor for a range of blockage ratios, $S/e = 5$

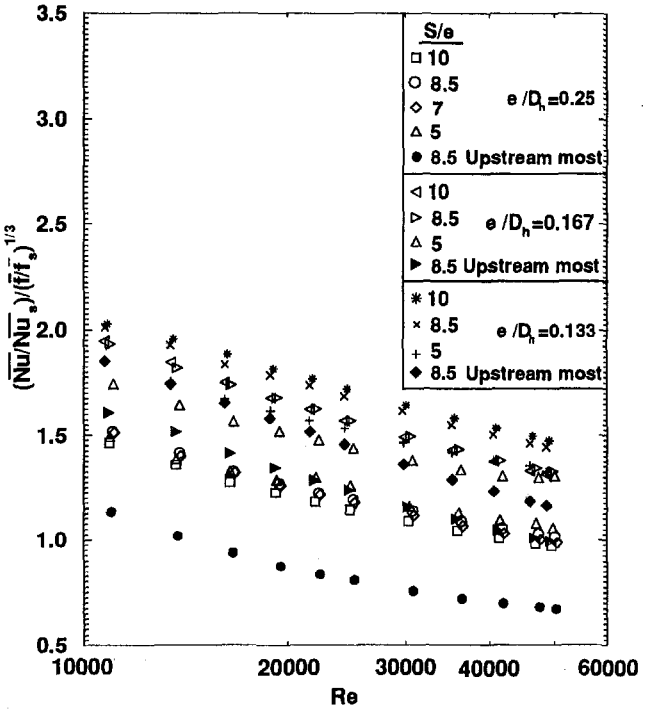

Fig. 17 Thermal performances of the geometries

low-aspect-ratio channels. The differences between those blockage ratios ($e/b = 0.243$, one-wall, and $2e/b = 0.4$, respectively) and present geometries ($2e/b = 0.266$) would appear to explain the differences in heat transfer. The friction factors for the present tests are shown in Fig. 9. The pitch-to-height ratio shows significantly less effect on the friction factor than the other two higher blockage ratios tested.

Figure 10 combines the results of all three geometries of the rib in the upstream-most position at S/e of 8.5. It is seen that smaller ribs produce higher heat transfer coefficients. Not benefiting from effects of ribs on the opposite wall, it is speculated that this behavior is due to the change of flow pattern over different ribs. In other words, in the extreme case, recirculating bubbles may form on both the back and top of the big rib, reducing the contribution of the rib top surface to heat transfer, known to be major for square ribs with sharp corners by all investigators mentioned above. For the smaller ribs, however, the top surface is in contact with core air; thus, higher heat transfer coefficients are produced.

Figures 11 and 12 compare the mid-channel rib heat transfer coefficient and channel friction factors for three blockage ratios at one pitch-to-height ratio of 10. In contrast with the heat transfer coefficient on the area between a pair of ribs, which is highly affected by the blockage ratio, the rib heat transfer coefficient does not show as strong of a dependence on blockage ratio for $S/e = 10$. However, as ribs are brought closer to each other by reducing pitch-to-height ratios, rib heat transfer coefficient is more and more affected by the blockage ratio (Figs. 13 and 15). The corresponding friction factors for S/e of 8.5 and 5 are shown in Figs. 14 and 16.

Finally, the thermal performances of all geometries tested are compared in Fig. 17. It is seen that as the blockage ratio increases, the rib thermal performance decreases and thermal performance of high blockage ribs does not change significantly with the pitch-to-height ratio. For each rib geometry, the upstream-most rib has the lowest thermal performance. This was expected since those ribs had lower heat transfer coefficient than those in the middle of the rib-roughened region.

Conclusions

A total of 13 rib geometries representing three blockage ratios in a practical range for small aircraft engines and at three pitch-to-height ratios were tested for heat transfer and pressure loss variations. From this study, it is concluded that:

1 For the geometries tested, the rib-averaged heat transfer coefficient is much higher than that for the area between the ribs. For high blockage ribs with large heat transfer areas, commonly used in small gas turbines, the rib heat transfer is a significant portion of the overall heat transfer in the cooling passages. As for the area between the ribs, rib-averaged heat transfer coefficient increases with blockage ratio.

2 Among all tested pitch-to-height ratios, a ratio of 8.5 consistently produced higher heat transfer coefficients.

3 Under otherwise identical conditions, ribs in the upstream-most position produced lower heat transfer coefficients. In that position, for the three rib geometries tested, the rib-averaged heat transfer coefficients decreased with the blockage ratio.

4 Thermal performance decreased with increased blockage ratio. While pitch-to-height ratios of 8.5 and 10 had the highest thermal performance for the smallest rib geometry, thermal performance of high blockage ribs did not change significantly with the pitch-to-height ratio.

Acknowledgments

The authors wish to express gratitude to Mr. James E. Hinds for his professional advice in preparing the final manuscript.

References

Abuaf, N., Gibbs, R., and Baum, R., 1986, "Pressure Drop and Heat Transfer Coefficient Distributions in Serpentine Passages With and Without Turbulence Promoters," *The Eighth International Heat Transfer Conference,* C. L. Tien, V. P. Carey, and J. K. Ferrel, eds., pp. 2837–2845.

Berger, F. P., and Hau, K. F., 1979, "Local Mass/Heat Transfer Distribution on Surfaces Roughened With Small Square Ribs," *International Journal of Heat Mass Transfer,* Vol. 22, pp. 1645–1656.

Burggraf, F., 1970, "Experimental Heat Transfer and Pressure Drop With Two Dimensional Turbulence Promoters Applied to Two Opposite Walls of a Square Tube," *Augmentation of Convective Heat and Mass Transfer,* A. E. Bergles and R. L. Webb, eds., ASME, New York, pp. 70–79.

Chandra, P. R., Han, J. C., and Lau, S. C., 1988, "Effect of Rib Angle on Local Heat/Mass Transfer Distribution in a Two Pass Rib-Roughened Channel," ASME JOURNAL OF TURBOMACHINERY, Vol. 110, pp. 233–241.

Chandra, P. R., and Han, J. C., 1989, "Pressure Drop and Mass Transfer in Two-Pass Ribbed Channels," AIAA *Journal of Thermophysics,* Vol. 3, No. 3, pp. 315–319.

Colburn, A. P., 1933, "A Method of Correlating Forced Convection Heat Transfer Data and a Comparison With Fluid Friction," *Trans. AIChE,* Vol. 29, pp. 174–210.

Dawes, W. N., 1994, "The Solution-Adaptive Numerical Simulation of the Three-Dimensional Viscous Flow in the Serpentine Coolant Passage of a Radial Inflow Turbine Blade," ASME JOURNAL OF TURBOMACHINERY, Vol. 116, pp. 141–148.

Dittus, F. W., and Boelter, L. M. K., 1930, *Publications in Engineering,* University of California, Berkeley, CA, Vol. 2, p. 443.

Han, J. C., Glicksman, L. R., and Rohsenow, W. M., 1978, "An Investigation of Heat Transfer and Friction for Rib Roughened Surfaces," *International Journal of Heat Mass Transfer,* Vol. 21, pp. 1143–1156.

Han, J. C., 1984, "Heat Transfer and Friction in Channels With Two Opposite Rib-Roughened Walls," ASME *Journal of Heat Transfer,* Vol. 106, pp. 774–781.

Han, J. C., Park, J. S., and Lei, C. K., 1985, "Heat Transfer Enhancement in Channels With Turbulence Promoters," ASME *Journal of Engineering for Gas Turbines and Power,* Vol. 107, pp. 628–635.

Han, J. C., Zhang, Y. M., and Lee, C. P., 1992, "Influence of Surface Heat Flux Ratio on Heat Transfer Augmentation in Square Channels With Parallel, Crossed, and V-Shaped Angled Ribs," ASME JOURNAL OF TURBOMACHINERY, Vol. 114, pp. 872–880.

Kline, S. J., and McClintock, F. A., 1953, "Describing Uncertainty in Single-Sample Experiments," *Mechanical Engineering,* Vol. 75, Jan., pp. 3–8.

Liou, T. M., Hwang, J. J., and Chen, S. H., 1991, "Turbulent Heat Transfer and Fluid Flow in a Channel With Repeated Rib Pairs," *Proc. ASME/JSME Thermal Eng.,* Vol. 3, pp. 205–212.

Liou, T. M., and Hwang, J. J., 1993, "Effects of Ridge Shapes on Turbulent Heat Transfer and Friction in a Rectangular Channel," *International Journal of Heat Mass Transfer,* Vol. 36, pp. 931–940.

Lockett, J. F., and Collins, M. W., 1990, "Holographic Interferometry Applied to Rib-Roughness Heat Transfer in Turbulent Flow," *International Journal of Heat and Mass Transfer,* Vol. 33, pp. 2439–2449.

Metzger, D. E., Fan, C. S., and Pennington, J. W., 1983, "Heat Transfer and Flow Friction Characteristics of Very Rough Transverse Ribbed Surfaces With and Without Pin Fins," *Proc. ASME–JSME Thermal Engineering Joint Conference,* Vol. 1, pp. 429–436.

Metzger, D. E., Chyu, M. K., and Bunker, R. S., 1988, "The Contribution of On-Rib Heat Transfer Coefficients to Total Heat Transfer from Rib-Roughened Surfaces," *Transport Phenomena in Rotating Machinery,* J. H. Kim, ed., Hemisphere Publishing Co.

Metzger, D. E., Fan, C. S., and Yu, Y., 1990, "Effects of Rib Angle and Orientation on Local Heat Transfer in Square Channels With Angled Roughness Ribs," *Compact Heat Exchangers: A Festschrift for A. L. London,* Hemisphere Publishing Co., pp. 151–167.

Moody, L. F., 1944, "Friction Factors for Pipe Flow," *Transactions of ASME,* Vol. 66, p. 671.

Sato, H., Hishida, K., and Maeda, M., 1992, "Characteristics of Turbulent Flow and Heat Transfer in a Rectangular Channel With Repeated Rib Roughness," *Exp. Heat Transfer,* Vol. 5, pp. 1–16.

Solntsev, V. P., Luzhanskii, B. E., and Kryukov, V. N., 1973, "An Investigation of Heat Transfer in the Turbulent Separation Zones in the Vicinity of Sudden Steps," *Heat Transfer—Soviet Research,* Vol. 5, No. 2, pp. 122–128.

Taslim, M. E., and Spring, S. D., 1988a, "An Experimental Investigation of Heat Transfer Coefficients and Friction Factors in Passages of Different Aspect Ratio Roughened With 45° Turbulators," *Proc. ASME National Heat Conference,* Houston, TX.

Taslim, M. E., and Spring, S. D., 1988b, "Experimental Heat Transfer and Friction Factors in Turbulated Cooling Passages of Different Aspect Ratios, Where Turbulators Are Staggered," Paper No. AIAA-88-3014.

Taslim, M. E., and Spring, S. D., 1991a, "An Experimental Investigation Into the Effects Turbulator Profile and Spacing Have on Heat Transfer Coefficients and Friction Factors in Small Cooled Turbine Airfoils," Paper No. AIAA-91-2033.

Taslim, M. E., Rahman, A., and Spring, S. D., 1991b, "An Experimental Investigation of Heat Transfer Coefficients in a Spanwise Rotating Channel With Two Opposite Rib-Roughened Walls," ASME JOURNAL OF TURBOMACHINERY, Vol. 113, pp. 75–82.

Taslim, M. E., Bondi, L. A., and Kercher, D. M., 1991c, "An Experimental Investigation of Heat Transfer in an Orthogonally Rotating Channel Roughened With 45 deg Criss-Cross Ribs on Two Opposite Walls," ASME JOURNAL OF TURBOMACHINERY, Vol. 113, pp. 346–353.

Taslim, M. E., Li, T., and Kercher, D. M., 1996, "Experimental Heat Transfer and Friction in Channels Roughened With Angled, V-Shape and Discrete Ribs on Two Opposite Walls," ASME JOURNAL OF TURBOMACHINERY, Vol. 118, pp. 20–28.

Wadsworth, C. M., 1997, "An Experimental Investigation of the Rib Surface-Averaged Heat Transfer in a Rib-Roughened Square Passage," MS Thesis, Mechanical Engineering Dept., Northeastern University, Boston, MA.

Webb, R. L., Eckert, E. R. G., and Goldstein, R. J., 1971, "Heat Transfer and Friction in Tubes With Repeated-Rib-Roughness," *International Journal of Heat Mass Transfer,* Vol. 14, pp. 601–617.

Prediction and Measurement of the Total Pressure Loss in an Engine Representative Diffuser System

A. R. Little

P. A. Denman

A. P. Manners

Department of Aeronautical and Automotive Engineering and Transport Studies, Loughborough University of Technology, Loughborough, Leicestershire, United Kingdom

An experimental and computational investigation of the flow in an engine representative diffuser system has been performed. Many parametric changes to the system were considered including inlet conditions, prediffuser geometry, cowl geometry and prediffuser strut position. The focus of this paper is an overview of the results from the twelve configurations that were both predicted and experimentally tested. It was shown that the CFD predictions contained a high degree of numerical error and that to reduce this to a low level would currently be impractical for a parametric study of this type. However, by carefully maintaining approximately the same degree of numerical error in the predictions, it was shown that a valid parametric study could be performed to the extent that the same conclusions about the parametric changes can be drawn equally from the predictions or measurements with one small exception. It was recognized that the level of agreement between the predicted and measured losses was to a degree fortuitous and that the $k-\epsilon$ turbulence model performs poorly for this type of flow.

Introduction

The diffuser system of a gas turbine combustion system is the region between the last stage of the compressor and the entry to the combustion chamber. The role of this region is primarily to guide the flow to the various features of the combustion chamber with a minimum loss in mechanical energy and a maximum rise in static pressure (LeFebvre, 1983). Despite a performance penalty, the majority of modern diffuser systems use a dump rather than a fully faired design due to its relative stability, insensitivity to flow distortion, and thermal distortion of the walls.

Until recently, the design of the diffuser system has been largely based on measured correlations obtained from parametric studies of typical diffuser systems (e.g., Fishenden and Stevens, 1977) followed by extensive experimental testing. This is an expensive and time-consuming process, which is complicated further by the interest in more modern designs to which existing correlations may not be applicable: for example, features such as double annular combustion chambers, passing a large proportion of the air through the cowl and the addition of substantial load-bearing radial struts.

Computational Fluid Dynamics (CFD) potentially offers a considerable improvement to this design process by replacing the existing correlations with a method that can be applied to designs that differ substantially from current practice. It can perform parametric studies more rapidly and cheaply given the initial investment in CFD methods, expertise, and computational facilities. In addition, it provides an important and new piece of information, which is the reason for the difference in performance of various designs. Although this information tends to be underutilized at present, it should eventually lead to a much better understanding of the flow and a consequent reduction in the number of modifications to be evaluated either computationally or experimentally. However, this is all subject to the CFD method producing sufficiently accurate predictions.

A number of experimental investigations of diffuser systems have been performed. Fishenden and Stevens (1977) investigated the effect of prediffuser geometry, dump gap, and flow split between the inner and outer annuli for a model dump diffuser system using a fully annular test rig and a solid combustor. Srinivasan et al. (1990) also investigated the effect of varying the flow splits between the inner and outer annuli but included the effect of cowl porosity. Hestermann et al. (1991) investigated the performance of a diffuser system with a solid cowl in order to establish the effects of prediffuser geometry on the overall performance. More recent investigations have used slightly more realistic geometries. Studies carried out by Carrotte et al. (1994) have investigated the magnitude and location of the loss of total pressure within the diffuser system of current engine designs.

Computationally, several investigations have been performed, although most of the early contributions to the open literature have involved two-dimensional planar or axisymmetric predictions such as Shyy (1985) and Koutmos and McGuirk (1989). These investigations have used a finite volume scheme, body-fitted meshes, and the $k-\epsilon$ turbulence model. More recently, several papers have been published that include both CFD and experimental results. Srinivasan et al. (1990) and Carrotte et al. (1994) both showed good agreement for the mean flow field but less favorable agreement for the turbulence quantities and the various performance parameters such as static pressure recovery and total pressure loss. Both of the experimental investigations employed sector rigs. At present there are few contributions in which three-dimensional calculations have been performed. Karki et al. (1992) modeled a 45 deg sector rig in which burner feed arms and struts were included and highlighted the strong three-dimensional nature of the flow within the sector.

This paper presents an overview of some of the results from an experimental and computational investigation of the flow in an engine realistic diffuser system. Several parametric changes were made to the system, such as inlet conditions, prediffuser

Contributed by the International Gas Turbine Institute and presented at the 40th International Gas Turbine and Aeroengine Congress and Exhibition, Houston, Texas, June 5–8, 1995. Manuscript received by the International Gas Turbine Institute February 10, 1995. Paper No. 95-GT-110. Associate Technical Editor: C. J. Russo.

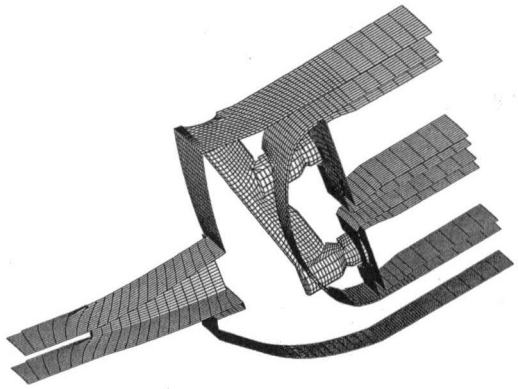

Fig. 1 Surface grid for the datum geometry

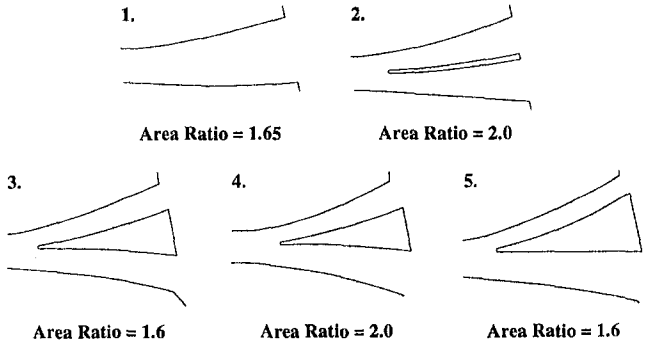

Fig. 2 Prediffuser geometries

geometry, cowl geometry, and position of prediffuser strut relative to the burner feed arm. Over 40 experimental tests were conducted in a period of 15 months and over 40 three-dimensional predictions were generated on a small parallel processing computer in a period of about three months. The focus of this paper is an overview of the results from the 12 configurations that have been both experimentally tested and predicted.

Geometry

The diffuser system considered was for a double annular combustion chamber, which is being increasingly adopted by aeroengine manufacturers in order to satisfy future pollutant emissions regulations. The primary focus of this research was to minimize the total pressure loss, particularly to the inner and outer annuli, although there were several other secondary considerations such as the air feed to the fuel injectors. The experimental investigation was conducted using a perspex model of the diffuser system in which burner feed arms were included but combustor primary ports and cooling rings were omitted. Several geometric variations of the diffuser system were considered such as alternative prediffuser designs, alternative cowl designs, and the position of the prediffuser struts relative to the burner. These are briefly described below.

Five different prediffusers were tested. The first design of area ratio 1.6 was made up of curved walls that turned the flow outward to a cant angle of 11.5 deg at the exit. The second design was of a similar shape but with an increased area ratio of 2.0 and a thin vane along the center. The three remaining designs split and turned the flow by varying amounts toward the inner and outer annuli. The area ratios of these designs varied between 1.6 and 2.0. Outlines of all the prediffuser designs are shown in Fig. 2. A thick load bearing radial strut was present in all the prediffuser designs and was placed either directly in-line with or midway between the burners.

Two cowl configurations were tested. The first comprised a single cowl covering both sections of the combustor with a plunged elliptical slot cut out for the burner arm. The second consisted of separate cowls for each section of the combustor with round plunged holes for the injectors. Outlines of both cowl configurations are shown in Fig. 3.

Figure 1 shows the first prediffuser with the strut in line with the burner and the single cowl. This was the datum configuration.

CFD Method

With the exception of the grid generation and parallelization, the CFD methods used for this set of predictions can be viewed as currently "standard" methods, which are available in several commercial codes. They are very briefly summarized below.

The fluid motion was governed by the incompressible, constant density, isothermal, time-averaged form of the Navier–Stokes equations. The coordinates of the differential operators were expressed in general nonorthogonal coordinates while the velocity and stress components were expressed in Cartesian coordinates. The equations were discretized using a collocated finite volume method. Pressure/velocity decoupling was prevented by introducing "pressure smoothing" in the manner of Rhie and Chow (1982). All terms were evaluated using centered differencing, except for the convection terms, which were evaluated using either hybrid differencing (Spalding, 1972) or QUICK differencing (Leonard, 1979). The algebraic equations were solved using the SIMPLE algorithm of Patankar and Spalding (1972). The turbulence was modeled with the $k-\epsilon$ model of Jones and Launder (1973) using the standard set of empirical constants as optimized by Jones (1980). The code has been

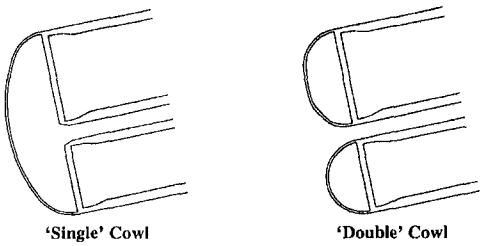

Fig. 3 Cowl geometries

Nomenclature

A = area
K = calibration factor
k = turbulent kinetic energy
P = total pressure
$\bar{P}$ = mass-weighted total pressure
p = static pressure
$\bar{p}$ = mass-weighted static pressure
p_{ps} = measured pseudostatic pressure
r = radial distance from engine centerline
U = magnitude of mean velocity component
U_i = mean velocity component
U_n = mean velocity component normal to surface
u_i = fluctuating velocity component
V = volume
ϵ = dissipation rate of turbulent kinetic energy
λ = total pressure loss coefficient
μ = coefficient of viscosity
ρ = density

adapted to run in a fully implicit manner on distributed memory parallel processing computers.

The mesh used by the CFD code was generated as follows. Firstly, a CAD solid model of the diffuser system was specified from a set of engineering drawings. A mesh was algebraically generated on the surface of the solid model and subsequently smoothed by solving a set of elliptic partial differential equations. Figure 1 shows an example of the grid on the solid surfaces within the solution domain. The internal mesh was then generated by using the surface mesh as boundary conditions for a set of Poisson equations as described by Thompson et al. (1985). Further details on the grid generation are given by Manners and King (1991).

The CFD predictions were of the tested geometry and not an equivalent engine configuration. Two simplifications were made: The circular rings of holes in the fuel injectors were replaced with an annular gap of equivalent area and the plunging on the cowl was omitted. The first was due to lack of grid resolution. The second was due to ambiguities in the mathematical representation of plunged holes in general and, furthermore, it was believed unnecessary to represent this region fully, given that the primary interest of the study was in the losses to the inner and outer annuli. The flow splits would not be affected by the change in discharge coefficient because they are imposed by the exit boundary conditions.

For the predictions, two sets of inlet conditions were used: fully developed and a set based on some measurements at the inlet. The early predictions all used fully developed inlet conditions because measurements at the inlet had not been taken. In order not to invalidate the various parametric studies, many of the later predictions also used fully developed inlet conditions. The set of fully developed conditions was obtained by performing a separate upstream prediction. The measured data at the inlet consisted of the axial velocity component shown in Fig. 4 plus a free-stream turbulence intensity measurement of 4 percent. Again, a separate upstream prediction was performed in order to approximately match the measured inlet data and obtain reasonable values for the solution variables not measured.

The downstream boundary conditions were specified as zero gradient normal to the exit for all solution variables except pressure which was extrapolated from internal values. The mass flow splits imposed on the five downstream annuli were those used experimentally and are shown in Fig. 5.

Since there was no swirl in the model fuel injector, symmetry conditions could be used on a half sector width as shown in Fig. 1. Wall functions were used to impose "law of the wall" conditions for cells adjacent to walls as described by Manners (1988).

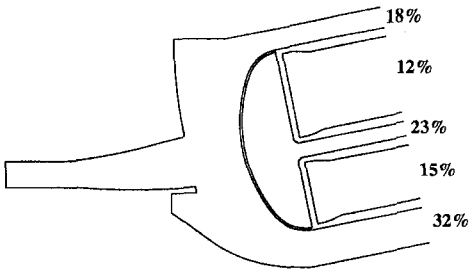

Fig. 5 Mass flow splits

Experimental Method

The experimental data were recorded under cold conditions from a 48 deg, four-burner sector perspex model of a double annular combustor system. The test rig shown in Fig. 6 was vertically mounted and supplied with air from a centrifugal fan via an underfloor plenum. Air entered the rig through a flared intake section containing a total of 19 thin uncambered blades positioned immediately upstream of the model working section. The blade thickness/chord and space/chord ratios were 0.08 and 0.38, respectively, and the trailing edge of each was located at traverse plane A. Although the vanes were aerodynamically unloaded, their presence generated modest blade wakes that were allowed to pass freely into the model working section. The normalized contours of axial velocity recorded at the inlet reference plane A are shown in Fig. 4. Turbulence grids could also be added to the inlet section in order to generate higher levels of turbulence intensity at the inlet reference plane. The turbulence intensity at the midpassage position immediately upstream of the vanes could be increased from approximately 1 to 4 percent of the mean inlet velocity. Although the grid-generated turbulence was unrepresentative of that present immediately downstream of a compressor, its inclusion allowed the effect of a change of turbulence to be determined.

The test rig working section consisted of a prediffuser followed by a double annular combustor system, comprising main and pilot combustors surrounded by inner, outer, and splitter annuli. The system was outwardly canted and the modular nature of the working section allowed easy installation of alternative prediffuser and combustor cowl configurations. Four burner feed arms were also included in the combustor test section. However, the burner rings (i.e., swirlers and fuel injectors) to which these were mounted were not engine representative but served only to provide the correct combustor backplate porosity.

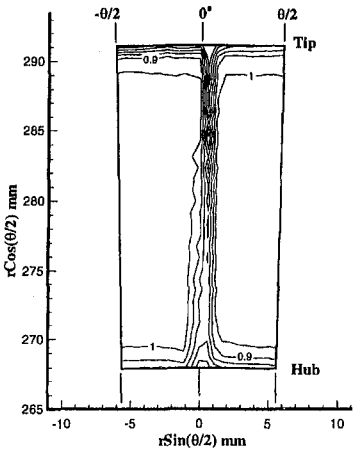

Fig. 4 Normalized axial velocity at traverse plane A

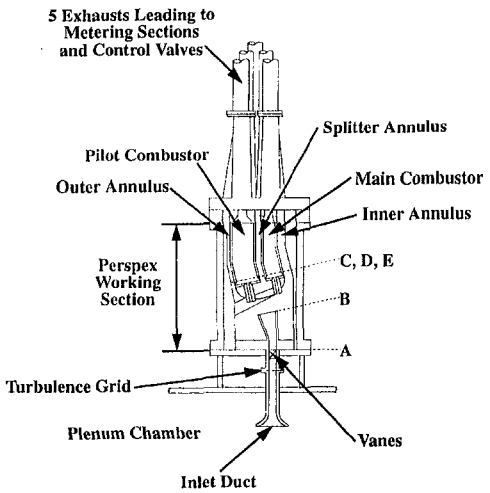

Fig. 6 Experimental test facility

All of the experimental data were recorded at an inlet Mach number of 0.26 ± 0.2 percent and this operating condition corresponded to a blade chord Reynolds number of 2.1×10^5. The mass flow rate through each combustor system element was controlled by butterfly valves located in the exhaust pipes approximately 30 pipe diameters downstream of the test section. Using these devices, the mass flow rate through each annulus could be controlled to within ±0.1 percent of the total mass of air passing through the test rig.

The performance of the diffuser system was derived for each configuration from time-averaged pressure measurements recorded at the five traverse planes shown in Fig. 6. The data were measured relative to the wall static pressure present in the intake section upstream and recorded using Furness FCO 44 differential pressure transducers. Full area traverses were performed using a "button hook" probe (see Fig. 7) at prediffuser inlet (plane A), prediffuser exit (plane B) and at entry to both the inner (plane C) and outer (plane E) annuli. The axial location of planes C and E coincided with that of the primary port admission holes that would be present in an engine. The splitter annulus (plane D), however, could not be traversed in the same way. Instead, total pressure data were recorded by means of six fixed pitot rakes, equally distributed across the central burner sector of the model. Each pitot rake was made up of six pitot tubes and the static pressure distribution was inferred from static tappings placed in the walls of the splitter annulus.

At prediffuser entry, an area traverse was performed across a single blade space in order to define the experimental inlet conditions. The result is presented in Fig. 4 in terms of contours of axial velocity. Area traverses were also conducted for each configuration at planes B, C, and E but were confined to the central burner sector (i.e., ±6 deg) of the four-burner sector model in order to minimize the influence of the side walls. The adverse effects of sector endwall mass flow displacements were recognized and have previously been addressed experimentally by Carrote et al. (1994) and computationally by Little and Manners (1993).

The area traverses at planes A, B, C, and E were conducted using a "button hook" probe, the principle of which is indicated in Fig. 7.

The technique was adopted by Carrotte et al. (1994) to evaluate the relative performance of dump and short faired combustor diffuser systems. The device is operated in two modes. The first as a conventional pitot probe to record the upstream total pressure and the second to obtain a "pseudo" static pressure, with the probe head rotated through 180 deg to face the downstream direction. Using a suitable calibration factor K (assumed constant), the true local flow field static pressure can be deduced from:

$$K = \frac{P - p_{ps}}{P - p}$$

where P and p_{ps} are the measured total and "pseudo" static pressures respectively and p is the true local static pressure. Probe calibration was performed over the desired velocity range in a low-turbulence environment in which the conditions could be accurately defined. As a result, the calibration constant, K, could be determined to within ±1 percent of the mean value. After calibration, a probe of this type can be used to investigate flow fields in which the presence of flow curvature prohibits the use of pitot tubes and wall static tappings only.

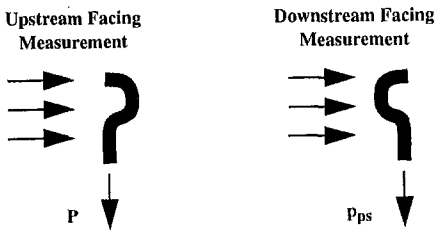

Fig. 7 Button hook probe operation

The mass-weighted total pressures recorded using the button hook probe at traverse planes A, B, C, and E could be repeated to within ±1 mm H_2O, a variation of less than ±0.25 percent of the dynamic head measured at the inlet reference plane A. This translates to an error of ±0.003 in the derived mass-weighted total pressure loss coefficient at each traverse plane.

Loss Parameters

The loss between two stations 1 and 2 can be determined by integrating the mass-weighted total and static pressures:

$$\lambda = \frac{\tilde{P}_1 - \tilde{P}_2}{\tilde{P}_1 - \tilde{p}_1}$$

where

$$\tilde{P} = \frac{\int (p + \frac{1}{2}\rho U^2)\rho U_n dA}{\int \rho U_n dA} \quad \text{and} \quad \tilde{p} = \frac{\int (p)\rho U_n dA}{\int \rho U_n dA}$$

This is subsequently referred to as the "flux" method and was used for both the measurements and the predictions.

The predictions can also evaluate the loss by integrating throughout the volume of interest the work done by the mean flow against the viscous and turbulent stresses:

$$\lambda = \frac{\int \left(-\left(\overline{\rho u_i u_j} + \mu \left(\frac{\partial U_i}{\partial x_j} + \frac{\partial U_j}{\partial x_i} \right) \right) \frac{\partial U_i}{\partial x_j} \right) dV}{\int_{\text{inlet}} (\frac{1}{2}\rho U^2) U_n dA}$$

This is subsequently referred to as the "volume" method. The difference between the two methods of loss evaluation is a sensitive measure of the numerical error in the solution. Further discussion is given by Little and Manners (1993).

Results

Grid Refinement. Predictions were performed for the datum geometry (i.e., prediffuser 1, single cowl, and strut in-line with the burner) shown in Fig. 1 with fully developed inlet conditions for two levels of grid refinement: a coarse grid of approximately 70,000 grid points and a medium grid of approximately 450,000 grid points. The main flow features for both predictions were similar, although the medium grid had significantly better resolved shear layers.

The level of numerical error present in the predictions was estimated by comparing the overall loss coefficients evaluated by the two alternative methods described and is shown in Fig. 8.

For the coarse mesh, the overall loss evaluated by the "flux" method is approximately double that of the "volume" method, indicating a large level of numerical error. The level of agreement is better for the medium grid density, but the prediction clearly cannot be considered to be approaching grid independence. A further doubling of the grid density would require nearly 4 million grid points, but was not possible with the small parallel processing computer available for the predictions. Subject to the flow pattern remaining unchanged, such a prediction would enable a good estimate of the grid independent overall loss to be made. See Little and Manners (1993) for further discussion.

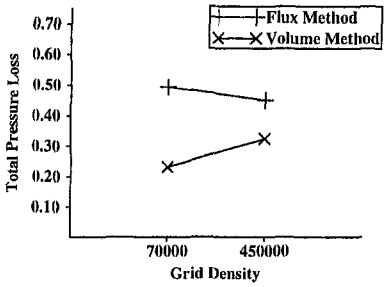

Fig. 8 The effect of grid refinement

All the predictions reported below used the coarse grid density in order to perform a parametric study in a reasonable time. Care was taken to maintain approximately the same grid density for all geometries in an effort to have similar levels of numerical error in all the predictions.

Measurements and Predictions for the First Set of Inlet Conditions. The measurements were taken without an upstream turbulence grid giving a free-stream turbulence intensity of 1 percent and an inlet axial velocity profile similar to that shown in Fig. 4. The predictions were performed before the inlet conditions were measured and in their absence fully developed conditions were specified. Given this consistent difference between the measurements and predictions, seven configurations can be compared and are summarised in Table 1.

Figure 9 shows a comparison between the predicted and measured total pressure loss in the outer, splitter, and inner annuli (planes C, D, and E, respectively in Fig. 6) with respect to the inlet plane A. The predicted and measured losses were evaluated using the "flux" method.

Given the high levels of numerical error, there is surprisingly good agreement between the measurements and predictions and the trends, briefly discussed below, have been well predicted. This suggests that the CFD method is successfully modeling the relative change in the balance of the dominant loss generating processes.

The overall level, rather than the trends, is fortuitously close to the measurements. For example, if it were possible to split the overall loss evaluated using the "volume" method into components in Fig. 9, then the level of the predicted loss curves would be roughly halved. There are several known deficiencies in the predictions that have combined to bring about the close agreement in the level. The fully developed profile has increased the loss in the inner and outer annuli relative to that in the splitter due to the relative change in total pressure at the inlet feeding the annuli. The high levels of diffusive numerical error have raised the predicted losses (Little and Manners, 1993). The $k-\epsilon$ turbulence model has two significant failings for this type of flow. First, it overpredicts loss in impingement regions (Craft and Launder 1991) and, secondly, it cannot predict the large increase in loss due to streamline curvature of the flow

Table 1 Configurations for first set of inlet conditions

Configuration	Pre-Diffuser	Cowl	Strut/Burner
B1	2	single	in-line
B2	2	double	in-line
B3	4	single	in-line
B4	4	double	in-line
B5	4	double	out-of-line

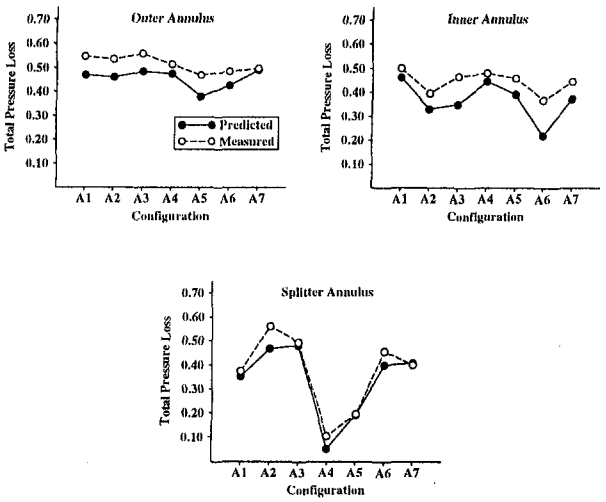

Fig. 9 Losses for the first set of inlet conditions

over the head of the combustor (Bradshaw, 1973). The second failing is almost certainly the larger and leads to an underprediction of the loss in the inner and outer annuli for a fully resolved prediction.

Both the predicted and measured results show the beneficial effects of increasing prediffuser area ratio provided that the flow in the prediffuser remains attached. The prediffusers with the larger area ratios (i.e., 2 and 4 in Fig. 2) both have reduced losses to the inner and outer annuli. For these two geometries, the velocity of the flow in the dump region has reduced, reducing the generation of turbulence and hence the losses. This can be seen in Fig. 10, which compares the levels of turbulent kinetic energy in the outer dump region for configurations A3 and A6.

The low loss in the inner annulus for configuration A6 was caused by the faired nature of the geometry effectively extending the diffusion length and eliminating the dump recirculation as shown in Fig. 11.

The loss between the inlet and the splitter annulus is dominated by the blockages present. There is no blockage present for prediffuser 1 with the double cowl (configuration A4) and the loss is consequently small. The boundary layers on the vane of prediffuser 2 introduce a significant loss (configuration A5) although this is less than that introduced by the single cowl (configuration A1). The largest loss is caused by splitting and turning the prediffuser flow toward the inner and outer annuli (configurations A2, A3, A6, and A7).

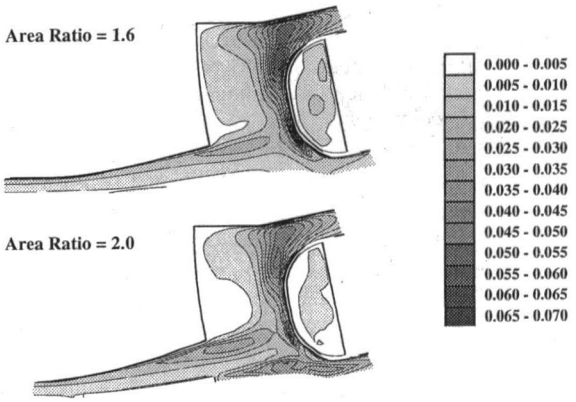

Fig. 10 Turbulence levels in upper dump region for different area ratios (normalized by U_1^2)

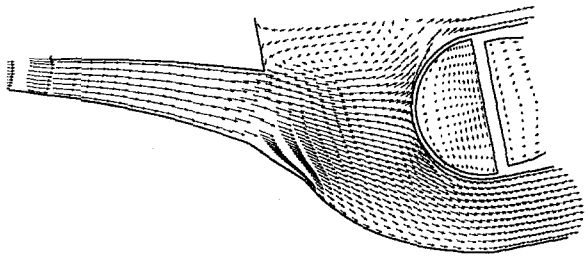

Fig. 11 Velocity vectors in inner dump region for configuration A6

When this comparison was initially performed, configuration A7 stood out because the predicted losses were significantly larger than the measured losses. An investigation of the predicted flow field revealed a separation on the outer wall at the inlet to the prediffuser. This was caused by the coarse grid creating a sharp corner in place of the smooth but tightly radiused corner shown in Fig. 2. A few additional axial grid lines eliminated the problem by improving the definition of the prediffuser wall curvature. This is an example of one of the main concerns in a computational exercise using coarse grids, namely, if the flow pattern changes significantly with increased grid resolution, trends will not be properly predicted. In all of the other predictions and measurements, no separation was present in the prediffuser.

Measurements and Predictions for the Second Set of Inlet Conditions. The measurements were taken with an upstream turbulence grid giving a free-stream turbulence intensity of 4 percent and the inlet axial velocity profile shown in Fig. 4. The predictions were performed with a set of inlet profiles approximating the measured inlet conditions. The predictions and measurements can be compared for the five configurations given in Table 2.

Figure 12 shows a comparison between the predicted and measured total pressure loss in the outer, splitter, and inner annuli (planes C, D, and E, respectively, in Fig. 6) with respect to inlet plane A. Again, the trends have been reasonably well predicted. The effects of cowl and prediffuser geometry on the splitter loss are well predicted and similar to the previous set of tests. The effect of changing the prediffuser geometry is also well predicted for the inner and outer annuli. The small increase in loss due to moving the strut and burner out of line is not well predicted for the inner and outer annuli although the sign is correct. The relatively small change in loss in the inner and outer annulus caused by changing the cowl is incorrect in the predictions. Although the reason is uncertain without further experimental data, the likely causes are the missing plunging since there is a small amount of spillage out of the elliptical hole in the single cowl and/or the problems with the $k-\epsilon$ turbulence model in impingement regions.

By comparing the measured losses for configurations A5/B2 and A6/B5 it can be seen that increasing the free-stream

Table 2 Configurations for second set of inlet conditions

Configuration	Pre-Diffuser	Cowl	Strut/Burner
B1	2	single	in-line
B2	2	double	in-line
B3	4	single	in-line
B4	4	double	in-line
B5	4	double	out-of-line

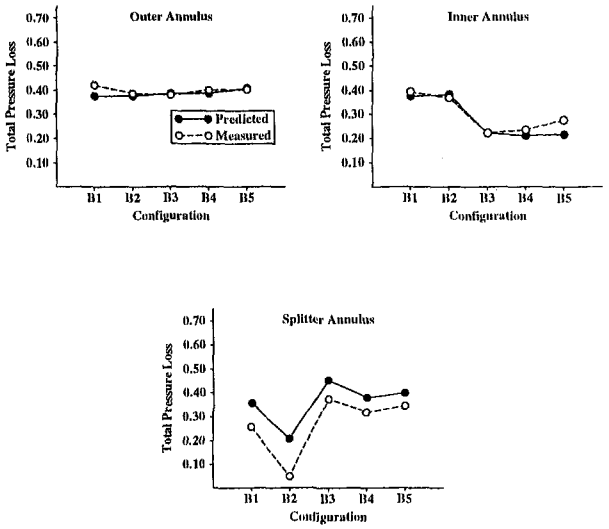

Fig. 12 Losses for the second set of inlet conditions

turbulence from 1 to 4 percent has significantly reduced the losses in the diffuser system (see Fig. 13). This is caused by the increased levels of turbulence in the prediffuser improving the shape of the boundary layers and consequently improving the performance of the prediffuser (i.e., flatter exit velocity profile and higher pressure recovery) leading to reduced velocity gradients in the dump region and lower losses. This is in agreement with previous experimental investigations (see Stevens and Williams, 1980).

For the predictions, the comparison between configurations A5/B2 and A6/B5 is more complex. In changing from the fully developed to the experimental inlet profile, the velocity profile has changed from being significantly peaked to being largely flat and the overall level of turbulence at the inlet has reduced for the flow entering the inner and outer annuli instead of increasing as in the measurements. The effect of the velocity profile is to decrease the loss in the inner and outer annuli and increase the loss in the splitter annulus due to the increased total pressure at the inlet for the flow entering the inner and outer annuli at the expense of that for the splitter annulus. The effect of the reduced level of turbulence in the inner and outer annuli, as shown by the measurements, is to increase the loss. These two effects combine to leave the predicted loss in the annuli largely unchanged, as shown in Fig. 13.

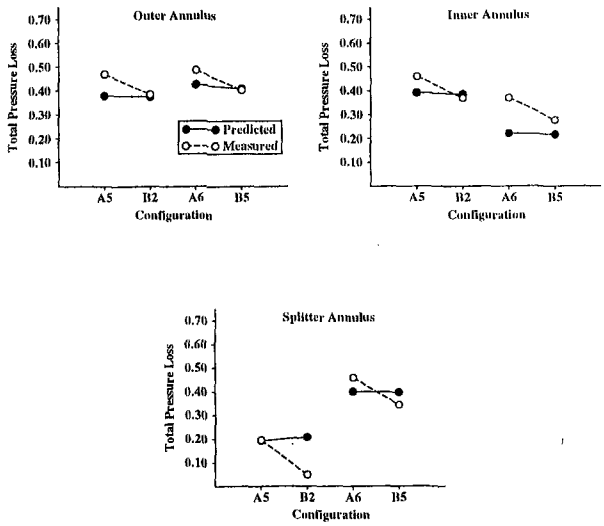

Fig. 13 The effect of changing the inlet conditions

Conclusions

The CFD predictions were shown to have a high level of numerical error and that using a sufficiently refined grid to reduce this to a low level would currently be impractical for a parametric study.

By carefully maintaining approximately the same degree of numerical error in the set of predictions, it was shown that a valid parametric study could be performed to the extent that the same conclusions about the parametric changes can be drawn equally from the predictions or measurements with one small exception. The small effect on loss of changing the cowl was incorrectly predicted for the inner and outer annuli and is believed to be caused by the missing plunging of the elliptical hole in the single cowl and/or the deficiencies in the $k-\epsilon$ turbulence model.

It was recognized that the level of agreement between the predicted and measured losses was to a degree fortuitous. Refining the grid would decrease the predicted loss and increase the difference between the predictions and measurements. The turbulence model is the cause of this discrepancy and, along with methods of efficiently increasing the grid resolution, is the subject of further study.

Acknowledgments

The work described in this paper was carried out within the Rolls-Royce University Technology Centre at the Department of Aeronautical and Automotive Engineering and Transport Studies, Loughborough University. The authors would like to acknowledge the financial support of Rolls-Royce plc. and the Defence Research Agency (Pyestock) under contracts B1F1-309DC and B1F1-291DC.

References

Bradshaw, P., 1973, "Effects of Streamline Curvature on Turbulent Flow," AGARDograph No. 169.

Carrotte, J. F., Denman, P. A., Wray, A. P., and Fry, P., 1994, "Detailed Performance Comparison of a Dump and Short Faired Combustor Diffuser System," ASME *Journal of Engineering for Gas Turbine and Power,* Vol. 116, pp. 517–526.

Craft, T. M., and Launder, B. E., 1991, "Computation of Impinging Flows Using Second Moment Closures," Eighth Symposium on Turbulent Shear Flows, Technical University of Munich, Paper No. 8-5.

Fishenden, C. R., and Stevens, S. J., 1977, "Performance of Annular Combustor Dump Diffusers," *Journal of Aircraft,* Vol. 14, pp. 60–67.

Hestermann, R., Kim, S., and Wittig, S., 1991, "Geometrical Dependence of the Fluid Dynamic Performance Parameters of Plane Combustor Model Diffusers," ISABE 91-7105, pp. 995–1001.

Jones, W. P., 1980, "Models for Turbulent Flows With Variable Density and Combustion," *Prediction Methods for Turbulent Flows,* W. Kollman, ed., Hemisphere Publishing Company.

Jones, W. P., and Launder, B. E., 1973, "Calculation of Low Reynolds Number Phenomena With a Two Equation Model of Turbulence," *International Journal of Heat and Mass Transfer,* Vol. 16, pp. 1189–1130.

Karki, K. C., Oechsle, V. L., and Mongia, H. C., 1992, "A Computational Procedure for Diffuser-Combustor Flow Interaction Analysis," ASME *Journal of Engineering for Gas Turbines and Power,* Vol. 114, pp. 1–7.

Koutmos, P., and McGuirk, J. J., 1989, "Numerical Calculations of the Flow in Annular Combustor Dump Diffuser Geometries," *Proceedings of the IMechE,* Vol. 20, pp. 319–331.

Lefebvre, A. H., 1983, *Gas Turbine Combustion,* Hemisphere.

Little, A. R., and Manners, A. P., 1993, "Predictions of the Pressure Losses in 2D Model Dump Diffusers," ASME Paper No. GT-93-184.

Manners, A. P., 1988, "The Calculation of the Flows in Gas Turbine Combustion Systems," Ph.D. Thesis, University of London.

Manners, A. P., and King, R. A., 1991, "Grid Generation and Flow Calculation for Complex Gas Turbine Combustion Systems," *Proc. New Techniques in Mathematics and Computational Modelling of Turbulent Diffusion and Mixing in Industrial and Environmental Problems,* Loughborough, 26–28 Mar.

Patankar, S. V., and Spalding, D. B., 1972, "A Calculation Procedure for Heat, Mass and Momentum Transfer in Three-Dimensional Parabolic Flows," *International Journal of Heat and Mass Transfer,* Vol. 15, pp. 1787–1806.

Rhie, C. M., and Chow, W. L., 1982, "A Numerical Study of the Turbulent Flow Past an Isolated Airfoil," *AIAA Journal,* Vol. 21, No. 11, pp. 1525–1532.

Shyy, W., 1985, "A Numerical Study of Annular Dump Diffuser Flows," *Computer Methods in Applied Mechanics and Engineering,* Vol. 53, pp. 47–65.

Spalding, D. B., 1972, "A Novel Finite-Difference Formulation for Differential Expressions Involving Both First and Second Derivatives," *Int. Journal of Numerical Methods in Engineering,* Vol. 4, pp. 551–559.

Srinivasan, R., Freeman, G., Grahmann, J., and Coleman, E., 1990, "Parametric Evaluation of the Aerodynamic Performance of an Annular Combustor Diffuser System," Paper No. AIAA-90-2163.

Stevens, S. J., and Williams, G. J., 1980, "The Influence of Inlet Conditions on the Performance of Annular Diffusers," ASME *Journal of Fluids Engineering,* Vol. 102, pp. 357–363.

Thompson, J. F., Warsi, Z. U. A., and Mastin, C. W., 1985, *Numerical Grid Generation. Foundations and Applications,* North-Holland.

Journal of Turbomachinery

Technical Briefs

A Remote Surface Pressure Measurement Technique for Rotating Elements

J. P. Hubner,[1] J. D. Abbitt,[1] B. F. Carroll,[1] and K. S. Schanze[2]

Introduction

This technical note describes a photoluminescent paint technique developed to measure the steady-state surface pressure distributions on rotating elements. The application of pressure-sensitive paints (PSPs) as a means of measuring surface pressure has emerged in recent years as a viable alternative to conventional transducers, yielding accurate quantitative results (Morris et al., 1993; McLachlan et al., 1993; Morris, 1995). Current techniques for PSP measurements on wind-tunnel models involve measuring the ratio of luminescence intensity between images of the model acquired during wind-on and wind-off conditions to account for lighting conditions and paint uniformity. The application of this type of technique to rotating elements presents difficulties due to element deformation between wind-on and wind-off testing conditions as well as limited or often unavailable static pressure taps necessary for the intensity-pressure calibration.

Alternatively, a lifetime measurement technique is insensitive to lighting conditions and paint uniformity. Thus, wind-on to wind-off image ratios are not necessary, eliminating associated difficulties due to model deformation. Additionally, by characterizing the relationship between the PSP lifetimes and pressure prior to testing, the need for in situ pressure measurements and corresponding conventional pressure tap instrumentation is eliminated. Burns and Sullivan (1995) describe a lifetime-based technique to measure pressure on rotating machinery with tip speeds exceeding 200 m/s. Their method measures the phase shift that occurs between a modulated excitation source and the corresponding emission response of the paint. The technique performed in this paper uses an unmodulated light source and measures the actual intensity decay with respect to time. The corresponding lifetimes of decay are then calibrated with the steady-state pressure.

[1] Department of Aerospace Engineering, Mechanics, and Engineering Science, University of Florida, Gainesville, FL 32611-6250.

[2] Department of Chemistry, University of Florida, Gainesville, FL 32611.

Contributed by the Turbomachinery Division for publication in the JOURNAL OF TURBOMACHINERY. Manuscript received by the Turbomachinery Division March 11, 1996. Associate Technical Editor: R. A. Delaney

Theoretical Background

The principle of PSP is based on the inducement of photoluminescence of the paint via an external light source and the subsequent dynamic quenching of the process due to the presence of oxygen. The paint is composed of probe molecules doped into a binder material on the surface of interest. After external stimulation of the molecules, the energy in the excited electronic states is dissipated back down to the ground state by radiative (fluorescence and phosphorescence) and nonradiative transitions. The lifetimes for fluorescence and phosphorescence are inversely related to the various deactivation rates. Dynamic quenching, a form of nonradiative decay, involves deactivation of the excited state of the luminescent molecule by collisions with other molecules—in this case oxygen molecules. The quenching process, isolated from the other forms of nonradiative decay, is proportional to the diffused oxygen concentration in the paint layer when self-quenching is negligible, and in turn, is directly related to the air pressure above the layer. The radiative decay rates, however, are independent of oxygen concentration. In application, the quenching will decrease the luminescence of the paint and provide the means of measuring pressure. The excited states are often deactivated by first-order processes (Ingle and Crouch, 1988) and the luminescence decay intensity over short time periods can be modeled by a simple exponential decay equation,

$$I(t) = A \exp(-t/\tau), \tag{1}$$

where I is the intensity, A is the pre-exponential constant, t is time, and τ is the luminescence lifetime.

Experimental Procedure

Figure 1 shows a schematic of the experimental luminescence decay on a spinning flat disk. The 118-mm-dia disk was coated with a proprietary platinum octaethylporphyrin (PtOEP) paint supplied by McDonnell Douglas. The temperature sensitivity of the paint is approximately 1 percent de-

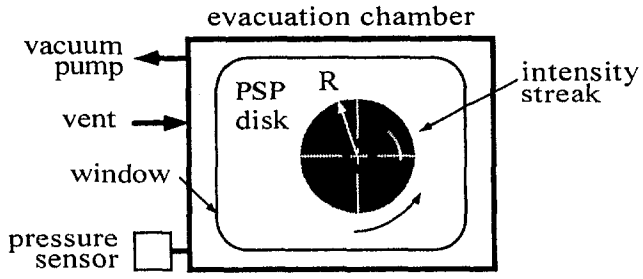

Fig. 1 Schematic of the spinning disk experimental setup

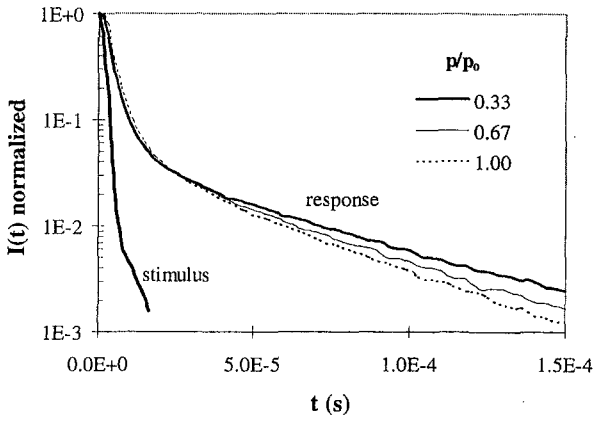

Fig. 2 Normalized emission intensity decay versus time for various chamber pressures (r/R = 0.92)

Table 1 Measured lifetime ratios for various excitation intensities and radial positions

I/I_{max}	r/R	$\tau/\tau_{o,max}$	Data Points
1.00	0.92	1.11	60
0.93	0.92	1.10	61
0.72	0.92	1.11	61
0.55	0.92	1.10	60
0.32	0.92	1.09	61
0.10	0.92	0.97	61
1.00	0.81	1.12	54
1.00	0.70	1.12	47
1.00	0.54	1.13	36
1.00	0.31	1.09	21

$p/p_0 = 0.67$

crease in luminescence per 1°C. The disk was spun up to speeds of 300 Hz (18,000 rpm) using a variable-speed motor, and both the disk and motor were enclosed in an evacuation chamber in order to vary the pressure acting on the disk while maintaining a constant temperature (25°C). The painted surface of the disk was excited by the beam spot of an attenuated, unmodulated argon-ion laser source (λ = 488 nm). The intensity decay at various radial positions was measured by the pixel registration of the luminescence streak on a 14-bit, cooled CCD camera. Further details regarding the testing procedure as well as experimental uncertainty are listed in Hubner et al. (1996).

Results and Discussions

Figure 2 shows typical intensity traces for the spinning disk at three pressure levels. Initially, the measured decay process is relatively insensitive to pressure ($t < 10^{-5}$ s); however, on the time scale associated with phosphorescence, an expected dependency with pressure is visible. As illustrated in Fig. 2, when a larger concentration of oxygen is present (higher pressures), the dynamic quenching process inhibits the phosphorescence, and the intensity of luminescence decreases faster resulting in shorter measured lifetimes.

A calibration of measured lifetimes versus pressure is shown in Fig. 3. Equation (2) shows the expected form of a referenced lifetime-pressure calibration,

$$\tau_0/\tau = C_1 + C_2 p/p_0, \qquad (2)$$

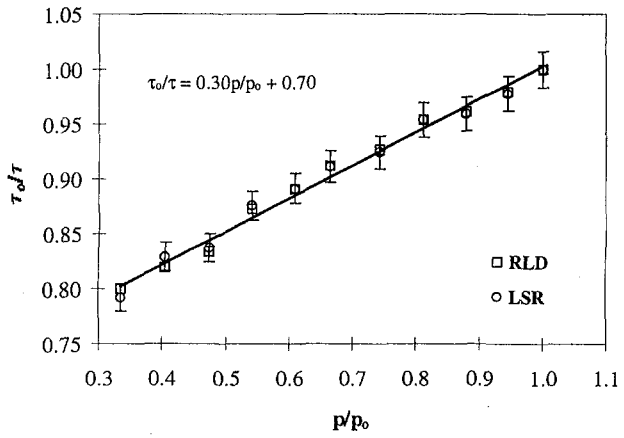

Fig. 3 Calibration of lifetime decay with pressure

where C_1 and C_2 are calibration constants (temperature dependent) and the subscript, 0, is the reference atmospheric state. A least-square regression (LSR) fit was first used to calculate the decay lifetimes over a 100 μs period. Precision uncertainty bounds of the calculations for each pressure were determined from uncertainties associated with the rotation speed and intensity shot noise. An alternative lifetime calculation was performed using a rapid lifetime determination (RLD) technique (Ballew and Demas, 1989). This technique calculates the corresponding lifetime from the ratio of integrated intensity over equal time increments. The results in Fig. 3 show slightly less scatter for the RLD calculations than the LSR calculations: correlation coefficients of 0.989 and 0.986, respectively. Further reduction in the scatter could be achieved by masking the registration of the high-intensity fluorescent decay and increasing the exposure time of the camera, more fully utilizing the full-well capacity of the camera to provide greater dynamic range. The need to eliminate the experimental scatter in the data is illustrated when considering the paint's pressure sensitivity. The influence coefficient, $\tau/p(\partial p/\partial \tau)$, is 3.1 at atmospheric conditions; this high value amplifies lifetime measurement errors when converting to pressure.

Table 1 lists lifetime calculations for various excitation intensities and radial locations. Because the technique is insensitive to the excitation energy and the pressure is radially independent over the disk, the lifetime measurements were expected to be constant. The tabulated results show this to be the case until errors due to low emission levels and poor temporal resolution corrupted the data.

Conclusions

The technique demonstrated has been extended to measure the lifetime ratios and pressure contours on a more complex element with a radial and azimuthal gradients and varying surface inclinations (Hubner et al., 1996). In order to increase the pressure-lifetime sensitivity and increase the system dynamic range, additional research regarding the various probe molecules and binders needs to be conducted. Dual lumiphor coatings, a hybrid temperature-pressure sensitive paint, would allow the compensation of temperature effects without introducing conventional temperature transducers. Due to the breakdown of the organic dyes at high temperatures (<200°C), the technique is limited to cold flow environments.

References

Ballew, R. M., and Demas, J. N., 1989, "An Error Analysis of the Rapid Lifetime Determination Method for the Evaluation of Single Exponential Decays," *Analytical Chemistry*, Vol. 61, pp. 30–33.

Burns, S. P., and Sullivan, J. P., 1995, "The Use of Pressure Sensitive Paints on Rotating Machinery," *16th ICIASF Record,* IEEE-CH34827-95, pp. 32.1–32.14.

Hubner, J. P., Abbitt, J. D., and Carroll, B. F., 1996, "Pressure Measurements on Rotating Machinery Using Lifetime Imaging of Pressure Sensitive Paint," AIAA Paper No. 96-2934.

Ingle, J. D., and Crouch, S. R., 1988, *Spectrochemical Analysis,* Prentice Hall, Englewood Cliffs, NJ, pp. 338–349.

McLachlan, B. G., Kavandi, J. L., Callis, J. B., Gouterman, M., Green, E., Khalil, G., and Burns, D., 1993, "Surface Pressure Field Mapping Using Luminescent Coatings," *Experiments in Fluids,* Vol. 14, pp. 33–41.

Morris, M. J., Donovan, J. F., Kegelman, J. T., Schwab, S. D., Levy, R. L., and Crites, R. C., 1993, "Aerodynamic Applications of Pressure Sensitive Paint," *Journal of Aircraft,* Vol. 31(3), pp. 419–425.

Morris, M. J., 1995, "Use of Pressure-Sensitive Paints in Low-Speed Flows," *16th ICIASF Record,* IEEE-CH34827-95, pp. 31.1–31.10.

Improvement of Tip Leakage Loss Model for Axial Turbines

Byung Nam Kim [1,3] **and Myung Kyoon Chung** [2,3]

Introduction

Tip leakage has a significant effect on the aerodynamic and thermal performance of gas turbines. Losses from the leakage flow often account for as much as one third of the total loss through a turbine stage. Among the recent experimental studies, Bindon (1989) measured the flow field in the tip gap and the subsequent mixing region in a linear cascade of turbine blades. He suggested that the tip leakage loss consists of two components, i.e., the internal gap loss and the mixing loss. In addition, he demonstrated that the fluid of low total pressure contributes significantly to the mixing loss after the flow leaves the gap. Based on the above-mentioned experimental observation and the three-dimensional N–S calculation of Storer and Cumpsty (1994), the present study is aimed at improving a tip leakage loss model that is consistent with the physics of the real leakage flows.

Development of a Tip Leakage Loss Model

The kinetic energy associated with the gap velocity normal to the blade chord, defined by $\Delta E = \int_{\dot{m}_g} 0.5 V_N^2 d\dot{m}_g$, is not recovered downstream and thus constitutes the major portion of the tip leakage loss. Assuming that the fluid is accelerated normal to the chord entirely by the pressure difference between the suction side and the pressure side, V_N may be estimated by $V_N = [2\lambda(P_{PS} - P_{SS})/\rho]^{1/2}$.

The tip unloading factor, λ, takes account of the flow resistance in the gap. Then, the following tip clearance loss coefficient can be obtained by the same derivation procedure as used by Yaras and Sjolander (1992):

$$Y_{\text{gap}} = 2K_E\sigma \frac{\tau}{h} C_D \lambda^{1.5} \frac{\cos^2(\alpha_2)}{\cos^3(\alpha_m)} C_L^{1.5}, \quad (1)$$

Note that the factor $\lambda^{1.5}$ does not appear in the work of Yaras and Sjolander (1992). Here, σ is the solidity (σ = blade chord/spacing), τ the tip gap height, h the blade span, C_D the discharge coefficient, and C_L is the lift coefficient.

The discharge coefficient is a measure of the area blocked by the tip separation bubble and the tip-wall boundary layer. Yaras et al. (1989) found that C_D of 0.577 gives a very satisfactory distribution of the leakage flow along the blade chord for 2.8 percent axial chord clearance. Dishart and Moore (1990) obtained C_D of about 0.7 from their experiment. However, from our semi-three-dimensional flow calculations (Kim, 1996), we found that an average value for a flat tip configuration is 0.67.

Now, consider the kinetic energy loss in the mixing region between the clearance discharge and the mainstream. A simplification of the theory is made by a method similar to that of Denton (1993) for the case when the flow rate of one of the streams is small. Consider a case where the fluid is injected with a small mass flow rate, $\dot{m}_c$, at an angle ζ and with velocity V_c into a mainstream flow, which has a mass flow rate $\dot{m}_m$ and velocity V_m (see Fig. 7 of Denton, 1993). When the flow is assumed incompressible and the pressure of the injected fluid is the same as that of the mainstream, the following formula for the total entropy creation, or pressure loss over the whole flow, can be obtained from the governing equations in Denton (1993):

$$T\dot{S} = -\dot{m}_2 \frac{\Delta p_0}{\rho} = V_2^2 \dot{m}_2 \cdot \left(\frac{\dot{m}_c}{\dot{m}_2} \sin\zeta\right) \cdot \left[2 - \frac{V_c}{V_2}\cos\zeta - \frac{\dot{m}_c}{\dot{m}_2}\sin\zeta\right], \quad (2)$$

where $\dot{m}_c = 0.3\rho V_c \cdot \tau \cdot c$ and $\dot{m}_2 = \rho V_2 \cdot h \cdot s \cdot \cos\alpha_2$. Here, c is the blade chord and s is the blade spacing.

According to Yaras and Sjolander (1992), the normal component of tip leakage jet speed in the suction side of a blade, V_c, is $C_D V_2 \sqrt{\lambda C_L}$. The factor 0.3 is introduced in the expression for $\dot{m}_c$ since the mixing loss starts to rise significantly at 70 percent chord (Bindon, 1989). Then the mixed-out loss of tip leakage jet, Y_{mix}, is obtained from Eq. (2) by the definition, $Y = 2\Delta p_0/\rho V_2^2$ as follows:

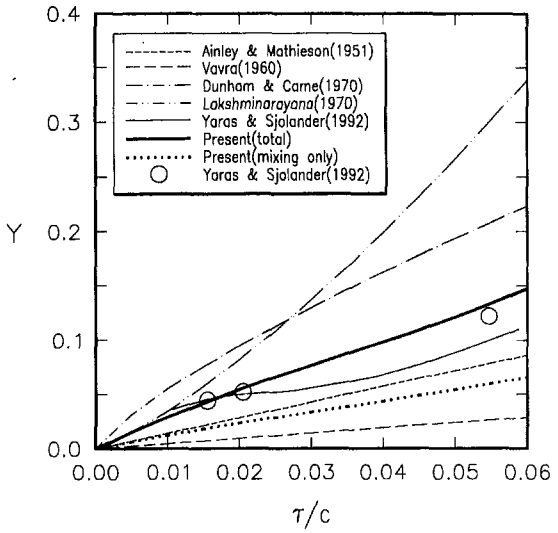

Fig. 1 Comparison between tip leakage loss predictions and measurements

[1] Graduate research assistant.

[2] Professor, to whom communication should be addressed: telephone: 82-42-869-3210, 5210; Fax: 82-42-861-1694; e-mail: mkchung@convex.kaist.ac.kr.

[3] Department of Mechanical Engineering, Korea Advanced Institute of Science and Technology, Yusong-ku, Taejon, 305-701, Korea.

Contributed by the Turbomachinery Committee of THE AMERICAN SOCIETY OF MECHANICAL ENGINEERS. Manuscript received by the Turbomachinery Committee March 15, 1996. Associate Technical Editor: R. A. Delaney.

Burns, S. P., and Sullivan, J. P., 1995, "The Use of Pressure Sensitive Paints on Rotating Machinery," *16th ICIASF Record,* IEEE-CH34827-95, pp. 32.1–32.14.

Hubner, J. P., Abbitt, J. D., and Carroll, B. F., 1996, "Pressure Measurements on Rotating Machinery Using Lifetime Imaging of Pressure Sensitive Paint," AIAA Paper No. 96-2934.

Ingle, J. D., and Crouch, S. R., 1988, *Spectrochemical Analysis,* Prentice Hall, Englewood Cliffs, NJ, pp. 338–349.

McLachlan, B. G., Kavandi, J. L., Callis, J. B., Gouterman, M., Green, E., Khalil, G., and Burns, D., 1993, "Surface Pressure Field Mapping Using Luminescent Coatings," *Experiments in Fluids,* Vol. 14, pp. 33–41.

Morris, M. J., Donovan, J. F., Kegelman, J. T., Schwab, S. D., Levy, R. L., and Crites, R. C., 1993, "Aerodynamic Applications of Pressure Sensitive Paint," *Journal of Aircraft,* Vol. 31(3), pp. 419–425.

Morris, M. J., 1995, "Use of Pressure-Sensitive Paints in Low-Speed Flows," *16th ICIASF Record,* IEEE-CH34827-95, pp. 31.1–31.10.

Improvement of Tip Leakage Loss Model for Axial Turbines

Byung Nam Kim [1,3] **and Myung Kyoon Chung** [2,3]

Introduction

Tip leakage has a significant effect on the aerodynamic and thermal performance of gas turbines. Losses from the leakage flow often account for as much as one third of the total loss through a turbine stage. Among the recent experimental studies, Bindon (1989) measured the flow field in the tip gap and the subsequent mixing region in a linear cascade of turbine blades. He suggested that the tip leakage loss consists of two components, i.e., the internal gap loss and the mixing loss. In addition, he demonstrated that the fluid of low total pressure contributes significantly to the mixing loss after the flow leaves the gap. Based on the above-mentioned experimental observation and the three-dimensional N–S calculation of Storer and Cumpsty (1994), the present study is aimed at improving a tip leakage loss model that is consistent with the physics of the real leakage flows.

Development of a Tip Leakage Loss Model

The kinetic energy associated with the gap velocity normal to the blade chord, defined by $\Delta E = \int_{\dot{m}_g} 0.5 V_N^2 d\dot{m}_g$, is not recovered downstream and thus constitutes the major portion of the tip leakage loss. Assuming that the fluid is accelerated normal to the chord entirely by the pressure difference between the suction side and the pressure side, V_N may be estimated by $V_N = [2\lambda(P_{PS} - P_{SS})/\rho]^{1/2}$.

The tip unloading factor, λ, takes account of the flow resistance in the gap. Then, the following tip clearance loss coefficient can be obtained by the same derivation procedure as used by Yaras and Sjolander (1992):

$$Y_{\text{gap}} = 2K_E\sigma \frac{\tau}{h} C_D \lambda^{1.5} \frac{\cos^2(\alpha_2)}{\cos^3(\alpha_m)} C_L^{1.5}, \quad (1)$$

Note that the factor $\lambda^{1.5}$ does not appear in the work of Yaras and Sjolander (1992). Here, σ is the solidity (σ = blade chord/spacing), τ the tip gap height, h the blade span, C_D the discharge coefficient, and C_L is the lift coefficient.

The discharge coefficient is a measure of the area blocked by the tip separation bubble and the tip-wall boundary layer. Yaras et al. (1989) found that C_D of 0.577 gives a very satisfactory distribution of the leakage flow along the blade chord for 2.8 percent axial chord clearance. Dishart and Moore (1990) obtained C_D of about 0.7 from their experiment. However, from our semi-three-dimensional flow calculations (Kim, 1996), we found that an average value for a flat tip configuration is 0.67.

Now, consider the kinetic energy loss in the mixing region between the clearance discharge and the mainstream. A simplification of the theory is made by a method similar to that of Denton (1993) for the case when the flow rate of one of the streams is small. Consider a case where the fluid is injected with a small mass flow rate, $\dot{m}_c$, at an angle ζ and with velocity V_c into a mainstream flow, which has a mass flow rate $\dot{m}_m$ and velocity V_m (see Fig. 7 of Denton, 1993). When the flow is assumed incompressible and the pressure of the injected fluid is the same as that of the mainstream, the following formula for the total entropy creation, or pressure loss over the whole flow, can be obtained from the governing equations in Denton (1993):

$$T\dot{S} = -\dot{m}_2 \frac{\Delta p_0}{\rho} = V_2^2 \dot{m}_2 \cdot \left(\frac{\dot{m}_c}{\dot{m}_2} \sin\zeta\right) \cdot \left[2 - \frac{V_c}{V_2}\cos\zeta - \frac{\dot{m}_c}{\dot{m}_2}\sin\zeta\right], \quad (2)$$

where $\dot{m}_c = 0.3\rho V_c \cdot \tau \cdot c$ and $\dot{m}_2 = \rho V_2 \cdot h \cdot s \cdot \cos\alpha_2$. Here, c is the blade chord and s is the blade spacing.

According to Yaras and Sjolander (1992), the normal component of tip leakage jet speed in the suction side of a blade, V_c, is $C_D V_2 \sqrt{\lambda C_L}$. The factor 0.3 is introduced in the expression for $\dot{m}_c$ since the mixing loss starts to rise significantly at 70 percent chord (Bindon, 1989). Then the mixed-out loss of tip leakage jet, Y_{mix}, is obtained from Eq. (2) by the definition, $Y = 2\Delta p_0/\rho V_2^2$ as follows:

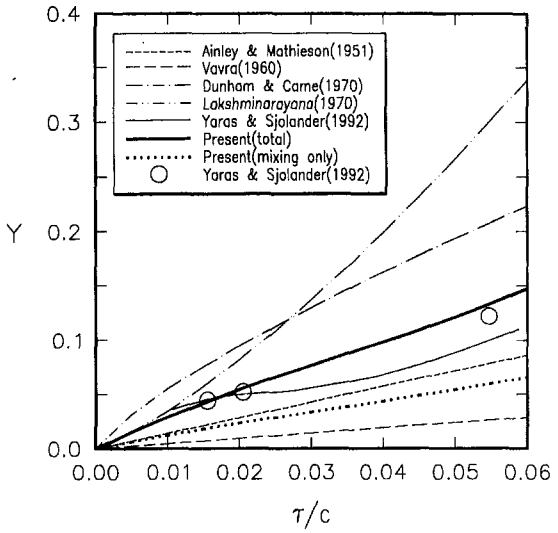

Fig. 1 Comparison between tip leakage loss predictions and measurements

[1] Graduate research assistant.

[2] Professor, to whom communication should be addressed: telephone: 82-42-869-3210, 5210; Fax: 82-42-861-1694; e-mail: mkchung@convex.kaist.ac.kr.

[3] Department of Mechanical Engineering, Korea Advanced Institute of Science and Technology, Yusong-ku, Taejon, 305-701, Korea.

Contributed by the Turbomachinery Committee of THE AMERICAN SOCIETY OF MECHANICAL ENGINEERS. Manuscript received by the Turbomachinery Committee March 15, 1996. Associate Technical Editor: R. A. Delaney.

$$Y_{\text{mix}} = 2 \cdot \left(\frac{\dot{m}_c}{\dot{m}_2} \sin \zeta \right) \cdot \left[2 - \frac{V_c}{V_2} \cos \zeta - \frac{\dot{m}_c}{\dot{m}_2} \sin \zeta \right], \quad (3)$$

For simplicity, Eq. (3) is evaluated using a mass-averaged mean angle, $\bar{\zeta}$, of about 50 deg (Storer and Cumpsty, 1994).

Model Validation

Figure 1 compares various model predictions of Y ($= Y_{\text{gap}} + Y_{\text{mix}}$) with experimental data of Yaras and Sjolander (1992) for a turbine cascade. The models of Dunham and Came (1970) and Lakshminarayana (1970) were derived by considering the momentum balance around the cascade. The momentum balance is assumed based on fully mixed-out conditions and since such conditions are approached about one axial chord length or farther downstream (Yaras and Sjolander, 1992), these models overestimate the leakage loss. The models of Ainley and Mathieson (1951), Vavra (1960), and Yaras and Sjolander (1992) underestimate the leakage loss. However, the present model predictions show best agreement with the data.

The decrease in stage efficiency due to the tip clearance as defined by Lakshminarayana (1970) can be derived from Eqs. (1) and (3) in the following form:

$$\Delta\eta = 2 \cdot K_E \cdot C_D \cdot \frac{\tau}{h} \cdot \lambda^{1.5} \cdot \sqrt{\frac{\psi \cdot \phi}{\sigma \cdot \cos^3(\alpha_m)}} + \frac{\phi^2}{\psi \cdot \cos^2(\alpha_2)} \times 2 \cdot \left(\frac{\dot{m}_c}{\dot{m}_2} \sin \zeta \right) \cdot \left[2 - 3 \frac{V_c}{V_2} \cos \zeta - \frac{\dot{m}_c}{\dot{m}_2} \sin \zeta \right]. \quad (4)$$

Figure 2 displays a comparison of predictions by the present and other prominent models with Kofskey and Nusbaum's data (1968). As can be seen, the present model is superior to others in performance prediction.

According to Yamamoto (1989), the incidence effects on the blade loading at a tip are seriously distorted for high-turning blade rows with blunt leading and trailing edges. These are attributed to the flow separation and associated loss generation in a leading edge. From Yamamoto's (1989) turbine cascade data at off-design operation, the blade unloading factor λ at the tip under off-design conditions is assumed to have a relation with design conditions λ_d and C_{Ld} as:

$$\lambda = \lambda_d \cdot \frac{C_L}{C_{Ld}}, \quad (5)$$

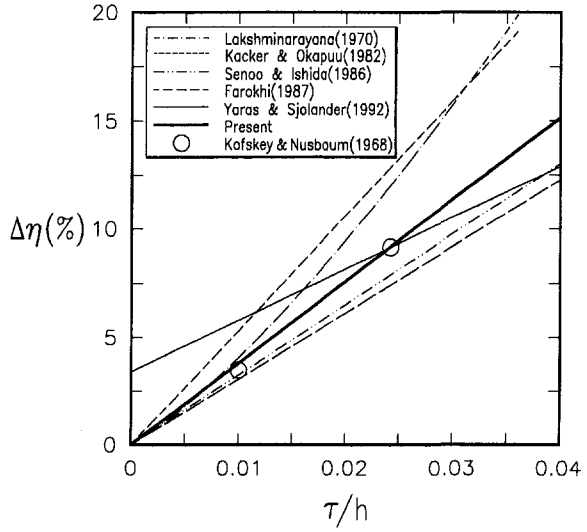

Fig. 2 Decrease in stage efficiency with clearance for an axial flow turbine

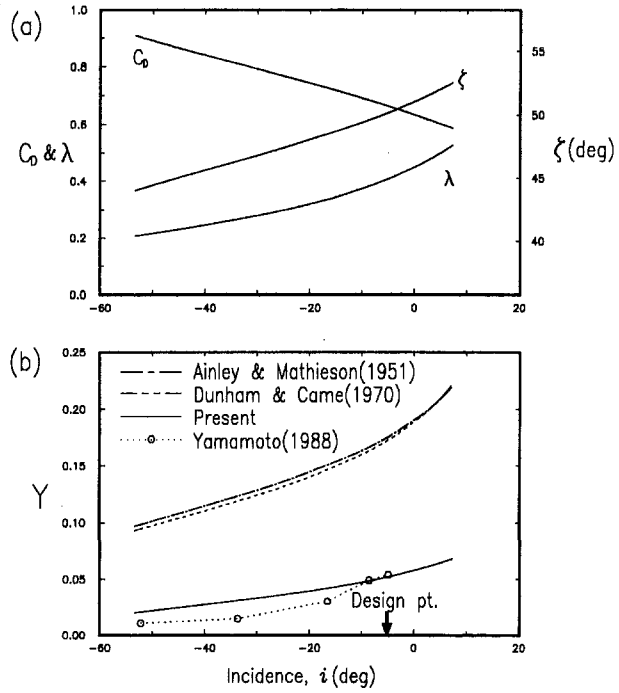

Fig. 3 Comparison of tip leakage loss predictions with experimental data of Yamamoto (1988)

where λ_d is 0.4 from Yamamoto (1989). The variation of C_D under off-design conditions may be inferred from the potential flow analysis of Heyes et al. (1992) for a flat tip. C_D may be represented by

$$C_D = C_{Dd} \cdot \frac{\sqrt{C_1 + 2C_{Ld}}}{\sqrt{C_1 + 2C_L}} \quad (6)$$

where the constant C_1 is $(1 - 2C_c + 2C_c^2)$ and C_c is a contraction coefficient. Finally, the following correlation of ζ is obtained from the approximate formulation of Storer and Cumpsty (1994):

$$\tan \zeta = \tan \zeta_d \cdot \sqrt{\frac{C_L}{C_{Ld}}} \cdot \sqrt{\frac{\cos \alpha_{md}}{\cos \alpha_m}}. \quad (7)$$

The variations of λ, C_D, and ζ with the incidence angle are shown in Fig. 3(a). Figure 3(b) compares the tip leakage losses at off-design operations predicted by Ainley and Mathieson (1951), Dunham and Came (1970), and the present model with experimental data of Yamamoto (1988). The former two conventional models grossly overestimate the tip leakage loss for the Yamamoto (1988) cascade with high turning and thick blades. However, the present model predicts the tip leakage loss with reasonable accuracy.

Conclusions

In order to represent the effect of flow resistance in the gap, a tip unloading factor, λ, was introduced in the gap loss, Y_{gap}. The mixing loss model, Y_{mix}, has been derived by considering the continuity and the momentum balance over the whole flow including the wake region. The resulting model equation is expressed in terms of the mean leakage jet angle, $\bar{\zeta}$, the mass ratio between the clearance flow and the mainstream and the ratio, V_c/V_2. The model predictions are very successfully compared with published data. In addition, the blade unloading at the tip and the underturning of the air outlet angle due to the leakage jet have also been investigated to devise a successful

prediction method for the rotor work deficiency under off-design conditions.

References

Bindon, J. P., 1989, "The Measurement and Formation of Tip Clearance Loss," ASME JOURNAL OF TURBOMACHINERY, Vol. 111, pp. 257-263.

Denton, J. D., 1993, "Loss Mechanisms in Turbomachines — The 1993 IGTI Scholar Lecture," ASME JOURNAL OF TURBOMACHINERY, Vol. 115, pp. 621-656.

Dishart, P. T., and Moore, J., 1990, "Tip Leakage Losses in a Linear Turbine Cascade," ASME JOURNAL OF TURBOMACHINERY, Vol. 112, pp. 599-608.

Heyes, F. J. G., Hodson, H. P., and Dailey, G. M., 1992, "The Effect of Blade Tip Geometry on the Tip Leakage Flow in Axial Turbine Cascades," ASME JOURNAL OF TURBOMACHINERY, Vol. 114, pp. 643-651.

Kim, B. N., 1996, "A Numerical Study on Flow and Heat Transfer and Development of Tip-Leakage Loss and Broadband Noise Model for Axial Flow Turbomachinery Tip Gaps," Korea Advanced Institute of Science and Technology, Ph.D Thesis.

Kofskey, M. G., and Nusbaum, J., 1968, "Performance Evaluation of a Two Stage Turbine for Two Values of Tip Clearance," NASA TN D 4388.

Storer, J. A., and Cumpsty, N. A., 1994, "An Approximate Analysis and Prediction Method for Tip Clearance Loss in Axial Compressors," ASME JOURNAL OF TURBOMACHINERY, Vol. 116, pp. 648-656.

Yamamoto, A., 1989, "Endwall Flow/Loss Mechanisms in a Linear Turbine Cascade With Blade Tip Clearance," ASME JOURNAL OF TURBOMACHINERY, Vol. 111, pp. 264-275.

Yaras, M. I., Zhu, Y., and Sjolander, S. A., 1989, "Flow Field in the Tip Gap of a Planar Cascade of Turbine Blades," ASME JOURNAL OF TURBOMACHINERY, Vol. 111, pp. 276-283.

Yaras, M. I, and Sjolander, S. A., 1992, "Prediction of Tip-Leakage Losses in Axial Turbines," ASME JOURNAL OF TURBOMACHINERY, Vol. 114 , pp. 204-210 [other references cited in figures are well documented by Yaras and Sjolander (1992)].